



# LUND UNIVERSITY

## Aspects of Optical Broad Band Spectroscopy and Information Extraction - Applications in Medicine and Ecology

Brydegaard, Mikkel

2012

[Link to publication](#)

*Citation for published version (APA):*

Brydegaard, M. (2012). *Aspects of Optical Broad Band Spectroscopy and Information Extraction - Applications in Medicine and Ecology*. [Doctoral Thesis (compilation), Atomic Physics]. Tryckeriet i E-huset, Lunds universitet.

*Total number of authors:*

1

### General rights

Unless other specific re-use rights are stated the following general rights apply:

Copyright and moral rights for the publications made accessible in the public portal are retained by the authors and/or other copyright owners and it is a condition of accessing publications that users recognise and abide by the legal requirements associated with these rights.

- Users may download and print one copy of any publication from the public portal for the purpose of private study or research.
- You may not further distribute the material or use it for any profit-making activity or commercial gain
- You may freely distribute the URL identifying the publication in the public portal

Read more about Creative commons licenses: <https://creativecommons.org/licenses/>

### Take down policy

If you believe that this document breaches copyright please contact us providing details, and we will remove access to the work immediately and investigate your claim.

LUND UNIVERSITY

PO Box 117  
221 00 Lund  
+46 46-222 00 00

**ASPECTS OF OPTICAL BROAD BAND  
SPECTROSCOPY AND INFORMATION EXTRACTION**  
-  
**APPLICATIONS IN MEDICINE AND ECOLOGY**

Mikkel Brydegaard Sørensen

Doctoral Thesis  
2012



LUND UNIVERSITY

ASPECTS OF OPTICAL BROAD BAND SPECTROSCOPY AND INFORMATION EXTRACTION  
APPLICATIONS IN MEDICINE AND ECOLOGY

© Mikkel Brydegaard Sørensen  
All rights reserved  
Printed by Tryckeriet i E-huset, Lund, 2012

Applied Molecular Spectroscopy and Remote Sensing Group  
Division of Atomic Physics  
Department of Physics  
Faculty of Engineering, LTH  
Lund University  
P.O. Box 118  
SE-221 00 Lund  
Sweden

<http://www.atomic.physics.lu.se>

Lund Report on Atomic Physics: LRAP-462  
ISSN: 0281-2762  
ISBN: 978-91-7473-353-2

- *To Anna and Aske*

# Abstract

---

The present thesis describes a number of aspects of modern electro-optical measurement technology also known as bio-photonics; this includes instrumentation, applications, sample interaction and data interpretation. The methods employed operate over several domains, and light measurements are discretized both in intensity, space, angle, time, polarization and energy. Mainly the spectral domain is investigated over two orders of magnitude from deep ultraviolet to thermal infrared, and mainly broad spectral features in solid and liquid samples are studied. The intensity employed ranges from microwatts to megawatts, time processes are studied between hundred picoseconds to weeks and measurement are carried out from the micrometer scale and up to hundreds of meters. An important aspect of this thesis is the development of realistic instrumentation with the intention that research should benefit the supporting society; this is a key point for the success of academic research in the developing world but also goes hand-in-hand with innovation, commercialization and entrepreneurship in Scandinavia. For this reason the thesis also encompasses a number of patent applications filed during the thesis work. Most of these realistic setups are based on spectroscopy using inexpensive light emitting diodes. Their application for medical diagnosis has been demonstrated with fiber sensors in the context of oncology, and microscopy in relation to parasitology. The thesis also covers optical diagnostics of animal populations of different species on the habitat scale; these studies are pursued by the use of laser radar (lidar) or telescopes. In these areas novel approaches for remotely classifying marked or unmarked flying animals open for the investigation of a new type of questions in field entomology and ornithology. In optical applications for medicine as well as ecology the understanding of the light interaction with complex biological tissue types is essential. Several aspects of such interaction are treated in the thesis. The complex optical interrogation together with the broad and overlapping spectral features in solid samples implies that an empirical approach of data evaluation and computer learning is often more valuable than forward modeling of expected signals. An ongoing theme throughout this thesis is data reduction and chemometrical evaluation. Here discrete light measurements and linear algebra form the basis for advanced statistical evaluation. This applies to the spectral domain where redundancy can be removed, but also topics such as dynamical processes and texture analysis are approached in the temporal and spatial domains, respectively.

# Populärvetenskaplig sammanfattning

---

Optoelektronik genomgår för närvarande en otrolig utveckling, inte minst på grund av de senaste årtiondenas kommersialisering och utveckling av hemelektronik som kompaktdiskar och digitalkameror. Denna utveckling har drivit en blomstrande global tillväxt för optoelektroniska företag som varje år utvidgar sina erbjudanden av optiska komponenter i hård konkurrens. Utvecklingen innebär också att det finns en stor potential för skraddarsydda specialsystem för inspektion, kvalitetskontroll och övervakning, vilka kan ersätta manuell kvalitetsinspektion, och ge mycket mer konsistenta och kvantitativa resultat. Dessutom erbjuder optisk mätteknik lösningar som ligger utanför den mänskliga synens begränsningar. Till exempel kan man använda mikroskop, teleskop och satellitövervakning för att studera fenomen som är för små, för långt bort eller för stora för det mänskliga ögat. Det finns också fenomen som sker alltför snabbt för att vi ska kunna uppfatta dem; dock kan pulserade lasrar upplösa fenomen, som inträffar på mindre än en miljarddel av en sekund. Andra situationer kräver observationer över lång tid, och här kan outtröttlig datorstyrd övervakning registrera optiska signaler över veckor och år. Den mänskliga synen är också begränsad vad gäller antalet färger hos ljuset som vi kan se skillnad på, och mycket information om vår omgivning ligger utanför det område vi kallar synligt ljus. I motsats till de tre våglängdsband den mänskliga synen kan uppfatta är optoelektronik känslig från djupt ultraviolett ljus till termisk infraröd strålning, och spektrometrar och multispektrala bildsystem med tusentals våglängdsband kan idag köpas eller byggas av amatörer. I modern optisk mätteknik kvantifieras ljusets intensitet, våglängd, ursprung och detektionstidpunkt i siffror på datorer. Detta kan på kort tid generera enorma mängder information. För en väl tillrättalagd optisk analysmetod har ljusets ursprungliga egenskaper påverkats av provets kvalitet eller sammansättning. Detta kan till exempel avspegla den kemiska sammansättningen eller provets mikrostruktur. Informationen som erhålls kan vara mångdimensionell och svåröverskådlig för den mänskliga hjärnan. Det finns dock systematiska tillvägagångssätt för tolkning av sådana stora dataset, till exempel så kallade kemometriska metoder som bygger på linjär algebra, matrisformulering och avancerad statistik. Utvärderingen görs ofta med hjälp av datorprogram som tränas med expertsvar från t.ex. en läkare eller ekolog. Dagens datorkraft innebär att analysen utförs direkt, och tillsammans ger optisk mätteknik och datorutvärdering möjligheten att omedelbart utnyttja data. Detta är värdefullt, t.ex. inom medicinsk diagnostik. Andra egenskaper som kännetecknar optisk mätteknik är att den är icke-invasiv, d.v.s. att den stör provet minimalt, och att diagnostiken kan upprepas om och om igen över långa tidsperioder.

I denna avhandling belyses främst aspekter hos fasta eller flytande prov, som kännetecknas av att ha bredbandig spektral information. Exempel på användning finns inom medicinen där förslag på förbättrad cancerdiagnostik av vävnader ges. Detta åstadkoms typiskt med utveckling av fiberoptiska metoder i kontakt med provet. Det ges även förslag till hur infärgningsfri malariadetektion i blodprov kan erhållas med enkla medel och ombyggnad av traditionella mikroskop. På större skala ges exempel på tillämpningar för analys av luftvolymmer med avseende på insekter och fåglar. Elektrooptiska tillvägagångssätt med teleskop möjliggör kvantitativ icke-invasiv analys av insekters beteende på habitatnivå. Genom att märka individer med fluorescerande pulver kan till exempel spridning och levnadslängd uppskattas. Laser-radar eller lidar kan till skillnad från traditionell radar ge färginformation. I denna avhandling visas hur detta kan användas för klassifikation av nattmigrerande fåglar som flyger på hög höjd. Detta har stora implikationer för biologernas möjligheter att studera migrationsmönster hos enskilda arter, något som är av centralt intresse för migrationsforskning. Fåglar och insekter kan flyga långa sträckor och kan transportera parasiter, virus, frön eller pollen mellan olika kontinenter. Förbättrade

övervakningsmöjligheter kan föröka förståelsen av sjukdomspridning för människor och boskap. Gemensamt för optisk mätteknik inom medicin och ekologi är att det grundläggande samspelet mellan ljus och biologisk vävnad är detsamma eller liknande. En central punkt i denna avhandling är därför att beskriva olika aspekter av denna interaktion, som i sin tur ger upphov till olikheter i de optiska signalerna. En annan central aspekt i avhandlingen är realistisk instrumentering. Detta innebär att man med små medel och klokt utformad design kan åstadkomma tekniker som kan användas i verkligheten och gynna lokalsamhället genom t.ex. tillämpningar av teknikerna inom hälsa eller lantbruk. Detta är väsentligt både inom innovation och entreprenörskap, men även för att motivera vetenskaplig aktivitet och få uppbackning och stöd från befolkningen, inte minst i utvecklingsländer. Ljusdioder och teleskop för amatörastronomi är två exempel på utrustning som utnyttas för realistisk instrumentering i denna avhandling.

# List of publications

---

This thesis is primarily based on 16 papers, and secondarily on 4 filed patent applications. Papers are referred to by their Roman numerals in the text, and patent applications are preceded by the capital letter P followed by a numeral.

## Publications

- I) **M. Brydegaard**, and S. Svanberg, "Simulation of multispectral X-ray imaging scenarios by means of Wien shift optical spectroscopy," *Am. J. Phys.* **78**, 170-175, 2010.
- II) **M. Brydegaard**, Z. Guan and S. Svanberg, "Broad-band multi-spectral microscope for imaging transmission spectroscopy employing an array of light-emitting diodes (LEDs)," *Am. J. Phys.* **77**, 104-110, 2009.
- III) **M. Brydegaard**, A. Merdasa, H. Jayaweera, J. Ålebring and S. Svanberg, "Versatile multispectral microscope based on light emitting diodes," *Rev. Sci. Instr.* **82**, 123106, 2011.
- IV) A. Merdasa, **M. Brydegaard**, S. Svanberg and J. T. Zoueu, "Staining-free malaria diagnostic by multispectral and multimodality LED microscopy," Submitted.
- V) **M. Brydegaard**, A. Runemark and R. Bro, "Chemometric approach to chromatic spatial variance. Case study: Patchiness of the Skyros wall lizard," *J. Chemometrics* **26**, 246-255, 2012.
- VI) L. Mei, P. Lundin, **M. Brydegaard**, S. Gong, D. Tang, G. Somesfalean, S. He and S. Svanberg, "Tea classification and quality assessment using laser induced fluorescence and chemometric evaluation," *Appl. Opt.* **51**, 803-811, 2012
- VII) **M. Brydegaard**, N. Hosseini, K. Wårdell and S. Anderson-Engels, "Photobleaching-insensitive fluorescence diagnostics in skin and brain tissue," *IEEE J. Photonics* **3**, 407-421, 2010.
- VIII) A.J. Thompson, **M. Brydegaard** Sørensen, S. Coda, G. Kennedy, R. Patalay, U. Waitong-Bramming, P.A.A. De Beule, M.A.A. Neil, S. Andersson-Engels, N. Bendsoe, P.M. French, K. Svanberg and C. Dunsby, "*In vivo* measurements of diffuse reflectance and time-resolved autofluorescence emission spectra of basal cell carcinomas," *J. Biophot.* **5**, 240-254, 2012.
- IX) **M. Brydegaard**, A.J. Thompson, C. Dunsby, S. Andersson-Engels, N. Bendsoe, K. Svanberg and S. Svanberg, "Complete parameterization of temporally and spectrally resolved laser induced fluorescence data with applications in biophotonics," Manuscript in preparation.
- X) **M. Brydegaard**, Z. Guan, M. Wellenreuther, and S. Svanberg, "Insect monitoring with fluorescence lidar: Feasibility study," *Appl. Opt.* **48**, 5668-5677, 2009.

- XI) Z. G. Guan, **M. Brydegaard**, P. Lundin, M. Wellenreuther, A. Runemark, E.I. Svensson, and S. Svanberg, "Insect monitoring with fluorescence lidar techniques: Field experiments," *Appl. Opt.* **49**, 5133-5142, 2010.
- XII) A. Runemark, M. Wellenreuther, H. Jayaweera, S. Svanberg and **M. Brydegaard**, "Rare events in remote dark field spectroscopy: An ecological case study of insects," *IEEE JSTQE Photonics for Environmental Sensing (PES)* **18**, 1573-1582, 2011.
- XIII) **M. Brydegaard**, P. Lundin, Z.G. Guan, A. Runemark, S. Åkesson and S. Svanberg, "Feasibility study: Fluorescence lidar for remote bird classification", *Appl. Opt.* **49**, 4531-4544, 2010.
- XIV) P. Lundin, P. Samuelsson, S. Svanberg, A. Runemark, S. Åkesson and **M. Brydegaard**, 'Remote nocturnal bird classification by spectroscopy in extended wavelength ranges', *Appl. Opt.* **50**, 3396-3411, 2011.
- XV) **M. Brydegaard**, P. Samuelsson, M.W. Kudenov and S. Svanberg, "On the exploitation of mid-Infrared iridescence of plumage for remote classification of nocturnal migrating birds," Submitted.
- XVI) P. Lundin, **M. Brydegaard**, A. Runemark, S. Åkesson, L. Cocola, and S. Svanberg, "Passive unmanned sky spectroscopy for remote bird classification," *Proc. SPIE* **8174**, 81740J, 2011.

### Patent applications

- P1) US provisional patent application on "Instrument for acquisition of fluorescence, absorption and scattering properties", **Mikkel Brydegaard**, US60/916,813, expired.
- P2) Patent application on "Instrument and methodology for acquisition of multiple coupled optical properties in volumes", **Mikkel Brydegaard**, Sweden, 0900253-6, Submitted 2009, pending.
- P3) Patent application on "Sensor head for acquisition of spectra and multispectral images based on semiconductor light sources and black body calibration." **Mikkel Brydegaard** and Sune Svanberg, Sweden, 0900425-0, Submitted 2009, expired.
- P4) Patent application on "Multimode imaging spectrometer for angular resolved optical diagnosis on micro scale" **Mikkel Brydegaard**, Sune Svanberg and Aboma Merdasa, Sweden, 0901398-8, Submitted 2009, expired.

# Table of Contents

---

<b>1. Introduction</b>	<b>11</b>
1.1 Spectroscopy, imaging and vision	11
1.2 Innovations and realistic instrumentation	12
1.3 Bio-medical aspects	13
1.3.1 Malaria	13
1.3.2 Cancer and malignancies	16
1.4 Instrumentation, electronics, mechanics and optics	20
1.5 New lidar applications tested in field campaigns	21
<b>2. Light and light-matter interaction</b>	<b>22</b>
2.1 Description of light	22
2.1.1 Rays	22
2.1.2 Waves	22
2.1.3 Particles	23
2.1.4 Reciprocity	24
2.2 Properties of light	25
2.2.1 Intensity	25
2.2.2 Location in space and time	26
2.2.3 Propagation direction	26
2.2.4 Frequency/Energy	26
2.2.5 Polarization	27
2.2.6 Phase	28
2.3 Altering of light properties	28
2.4 Surface effects	30
2.4.1 Reflection	30
2.4.2 Transmission and refraction	31
2.4.3 Diffraction	32
2.4.4 Multiple surface interference	32
2.4.5 Lambertian emission constraints	33
2.4.6 Thermal regime	34
2.4.7 Sub-wavelength effects	35
2.5 Volume effects	35
2.5.1 Refraction	35
2.5.2 Absorption	37
2.5.3 Fluorescence	39
2.5.4 Scattering	45
<b>3. Instrumentation</b>	<b>52</b>
3.1 Light sources	52
3.1.1 Light emitting diodes	52
3.1.2 Arcs / Flashes	57
3.1.3 Lasers	58
3.1.4 Filament bulbs	61
3.1.5 The Sun	62
3.2 Detectors	63
3.2.1 Photodiodes	63
3.2.2 Photo-multiplier tubes	64
3.2.3 Array detectors, CCD and CMOS	65
<b>4. Resolving and discretizing light</b>	<b>69</b>
4.1 The intensity domain	71
4.2 The spectral domain	73
4.3 The spatial domain	79

4.4	The angular domain	84
4.5	The temporal domain	89
4.6	The polarization domain	96
<b>5.</b>	<b>Computational methods</b>	<b>99</b>
5.1	Preprocessing	99
5.1.1	Intensity calibration and normalization	100
5.1.2	Spatial calibration	102
5.1.3	Spectral calibration	103
5.2	Color spaces	103
5.3	Description of variance	105
5.4	Histograms, images and spectra	106
5.5	Outliers and rare events	107
5.6	Data reduction and factorization	108
5.7	Multivariate regression models	111
5.7.1	Projection of maximum separation	111
5.7.2	Link function	113
5.8	Fitting, training, evaluation and prediction	113
5.9	Unsupervised clustering	116
5.9.1	Hierarchical clustering and dendrograms	116
5.9.2	Mixed Gaussian distributions	118
5.9.3	Centroids	119
5.10	Confusion matrixes	119
5.11	Dynamic processes	120
5.11.1	Fourier processes	120
5.11.2	State space concept and vector field models Trajectories	121
5.12	Correlations	124
5.13	Raytracing	125
<b>6.</b>	<b>Conclusion and outlook</b>	<b>126</b>
6.1	Optics and bio-photonics	126
6.2	Entrepreneurship and capacity building in the developing world	127
6.3	Scattering and dynamical contrast in medicine	128
6.4	Ecology and biosphere monitoring	130
	<b>Acknowledgements</b>	<b>133</b>
	<b>Publications and author contributions</b>	<b>136</b>
	<b>References</b>	<b>141</b>

---

# Chapter I

## 1. Introduction

---

### 1.1 Spectroscopy, imaging and vision

Optical diagnostics is the discipline of using light to reach conclusions on objects in our surroundings. Optical diagnostics is applied in almost any research fields; examples are medicine<sup>1, 2</sup>, ecology<sup>3</sup>, food science<sup>4</sup> and combustion science<sup>5</sup>. The corresponding outcome of such optical analysis could answer questions such as: Is a patient healthy? How does an animal population use a habitat? Is a fruit tasty? How efficient is an engine? In many situations we can come a long way by using the three spectral bands in our eyes and this is often done without further consideration. Examples are shown in Fig. 1.1.



*Fig. 1.1. The three spectral bands in our natural color vision improve object detection and quality control. To the left the rowan berries are difficult to contrast to the surroundings in a black and white image, whereas the berries are easily identified in the color picture. To the right the estimation of the maturity grade of bananas becomes easier when considering the color case. These are examples of application of multispectral imaging in our every day life.*

Red-green color blind people, however, are constantly reminded by their comrades that there is some information that they are missing which is apparent to all others, and they quickly find themselves wondering: What if I would have had one more spectral band? What would I see then? Recent research in animal vision has found birds and reptiles with four spectral bands, insects with six bands and mantis shrimps with up to sixteen spectral bands. This leaves the non-colorblind people with a similar feeling: What are we missing? Luckily we can use technology and electro-optical measurement techniques to meet our curiosity and visualize, detect or quantify information inaccessible to the naked eye. Well known examples of visualization outside our spectral sensitivity are, e.g., the detection of a broken bone through tissue by using medical X-ray, or detection of a drowning person in a sea rescue mission using a thermal infrared camera. But even within the spectral region visible to us, tiny spectral details are inaccessible to the broad spectral bands in our eyes; one example is the narrow sodium Fraunhofer lines in the middle of the visible region. A systematic way of acquiring spectral information is to use spectrometers or hyper-spectral imagers, and a systematic way of interpreting the spectral information is chemometry and multivariate analysis. These aspects will be demonstrated on a number of selected examples throughout this thesis.

## 1.2 Innovations and realistic instrumentation



*Fig. 1.2.1. The author of the thesis spent considerable time in organizing and contributing to international workshops mainly in African and South American countries but also in Asian and European countries. Key achievements are the planning of a number of building workshops with hands-on experience on realistic instrumentation, which resulted in the establishment of a Pan-African research network for applied spectroscopy and imaging. Realistic instrumentation is also attractive both for the industry and research in the developing world, because of the low cost and simplicity.*

The present thesis has partly been financed by a national innovation initiative; in this relation a number of patent applications have been submitted during the thesis work and also an award winning company was founded. For this reason, apart from peer reviewed journal papers, even patent applications are referred to throughout the thesis. The applications are either pending or have timed out, meaning that they are publicly available. Considering the partial financing it is also relevant to comment on the thesis work from an innovation perspective. Apart from fundamental basic research where scientists out of curiosity pursue the ideas that they judge most promising and novel regardless of application, it is also fair that the benefit of the general public from the work that they carried out is evaluated. This aspect is valid not the least since the expenses for research are mainly covered by the general public. From the point of view of the researcher it brings great satisfaction to see applications of the research. From the point of view of the general public the outcome of research, apart from teaching of professionals, can for example be fascinating results for general amusement, it can be results improving the public health, or research leading to a product or service which can be sold. The final aspect is thought to improve the national economy and is referred to as innovation or entrepreneurship. Such terms have been extensively promoted by politicians in Scandinavia, arguing that the survival of welfare societies depends on our existence as a knowledge society and the export of high-tech products, as if Scandinavians should be better suited for this function. As a consequence of the debate, a jungle of innovation offices, institutions and initiatives have been established to promote innovation and entrepreneurship.

The concept of a knowledge society assumes that national researchers secure their intellectual property (IP) by patent applications; however, already at this stage a number of conflicts arise; firstly good research project tend to look for solution for a broad range of problems, whereas a new coming successful entrepreneur must focus on solving one specific problem in a small niche. Secondly, science and academic careers are pushed forward by submission of results to conferences and journals, whereas the strategy in intellectual property is normally to withhold all information until the idea is mature enough to be submitted as a patent application. Consequently, patent applications submitted by academic staff are often submitted in a rush at an early stage with the result that the applications proceed to the international level with the associated costs before the product is ready or before the cost can be covered by any investor. At institutions like the Massachusetts Institute of Technology in the USA the inventions are mainly the property of the institution with the consequence that the university has a professional unit dedicated to secure and develop intellectual property. In Sweden inventions are the intellectual property

of the individual inventor in academia; therefore it is also up to the individual to cover the costs of patenting. It is for the same reason, also up to the inventor to write the claims in the patent application and manage the financing for the development of the invention, although their interest and specialization might be entirely different from legislation and economics. For the case of young master or doctoral students in academia it implies that they do not in general have the economic means to cover the cost of international patenting and the following costs to develop a product. Established academic staff normally has secure positions and do not have the motivation or time to risk launching themselves into an entrepreneurship adventure. This lack of a coherent plan for idea development forces academic innovators to turn to either the jungle of innovation offices or private investors. This leads to time consuming meetings where academic staff spends hours on lecturing on their topic of specialty for a community of economists and managers. It should be clear that the interest of a skilled private investor is not to safeguard the national economy by establishing long-term national industry, but to take a short-term risk before reselling the intellectual properties with more value added by short-term employed engineers and scientists in the initial phase. From the point of view of the researcher the large number of innovation offices can seldom offer any really useful craftsmanship in terms of assistance with patenting, financing or entrepreneurship management. Here, some weaknesses of the national innovation system have been pointed out, indicating that there is room for considerable improvement.



*Fig. 1.2.2. In view of difficulties frequently encountered in the academic innovation process the ever actual Emperor's New Clothes by the famous Danish writer Hans Christian Andersen might come to mind.*

## 1.3 Bio-medical aspects

### 1.3.1 Malaria

In this thesis several optical measurements on blood smears from patients suffering from malaria appear. These measurements on thin blood smears are mainly acquired by Aboma Merdasa during his master thesis work and visit to Ivory Coast. The author of this thesis was one of the master thesis supervisors in this relation, and the application was suggested by Jeremie Zoueu from Ivory Coast. Malaria refers to a disease with similar symptoms caused by infection by a range of mosquito borne parasites. The discovery and understanding of the infection and transmission, by Ronald Ross, was awarded the second Nobel prize in physiology or medicine. Despite the long history of knowledge of malaria, the disease is still responsible for 200-300 million infections, and 1-2 millions deaths per year.

The disease is caused by different protist eukaryotic microorganisms belonging to the family *Plasmodium*. The life cycle of the parasite is exceedingly complicated, and involves

a large number of life stages both in the mosquito (the vector and definitive host) and different organs in the human body (the secondary host).

Different species of the *Plasmodium* parasites can be encountered at all tropical continents - Africa, the Americas, Asia and Australia. However, 75% of the infections are caused by the *Plasmodium Falciparum* parasite, which is also the most lethal one. Out of this 98% infections occur in the African continent and 75% of the infected are children below 5 years of age. Apart from affecting humans, *Plasmodium* parasites can also be found in animals like birds, reptiles and many mammals. When considering migrating birds this implies that Plasmodium parasites can be even be encountered in Scandinavia. However, for the parasites to spread and survive, continuous mosquito breeding through the year is required. This is currently not the case in Scandinavia.

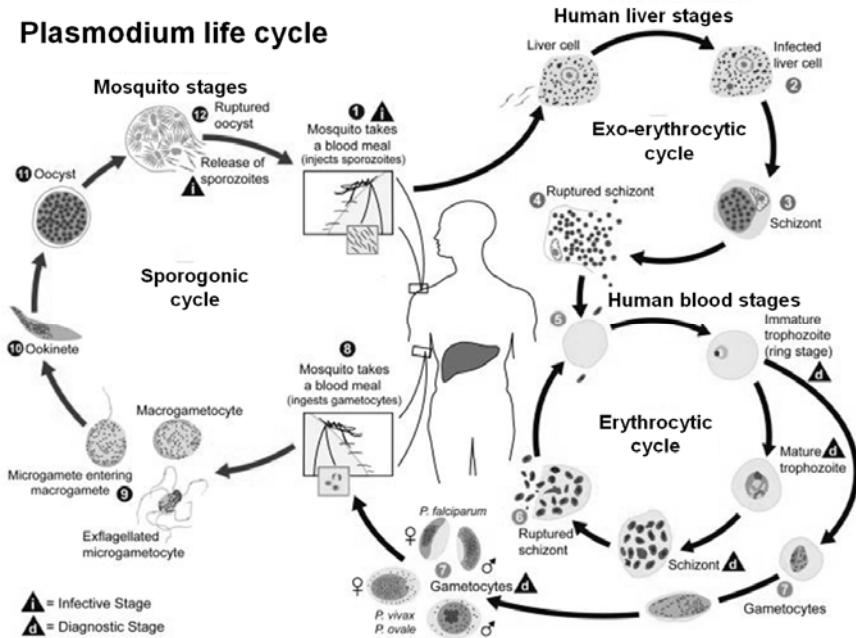


Fig. 1.3.1. The life cycle of *Plasmodium Falciparum* involves a large number of stages in different organs of both the human and the mosquito host. The human host serves mainly as food chamber and energy harvesting, while the mosquito host serves as bedroom for fertilization. Public domain image, obtained from the Center for Disease Control, CDC, USA.

The life cycle of *Plasmodium Falciparum* involves human infestation by parasite spores (Sporozoites) in the infested mosquito saliva after the sting. The spores are carried by the circular system in the human body to the liver and infest the liver cells (hepatocytes); they remain in the human liver for five days and form Trophozoites. Each time in the life cycle the parasite enters a new cell it discards its cell penetrating apparatus (apical complex), and undergo Schizonic development referring to nuclei division without cell division. Eventually the liver cell with the replicate parasites (scizont) ruptures and releases Merozoites into the blood stream. The Merozoites measure 1µm and are selfpropelled (motile stage), they can be encountered in the blood stream for one minut before entering the red blood cells (RBC, erythrocytes). Again they discard their apical complex and undergo schizonic development. Once in the RBC the parasite enters its ring state, then its trophozoite stage and finally its schizont stage. In the RBC they metabolizes 80% of the heamoglobin and grow to half a volume fraction of the RBC. The RBC does not increase in size but loses its ability to deform<sup>6</sup>. When the RGB ruptures 16-18 new merozoites are

released into the blood stream, and the circle repeats with exponential growth. The human host can survive infested fractions up to 5%. During the circular process in the human blood (erythrocytic stage), a fraction of the Merozoites develops into sexually different gametocytes; these remain in the RBC to mature for ten days. The survival success of the parasite relies on a second mosquito sting upon which the gametocytes enter the mosquito mid gut in terms of a blood meal. Once in the mosquito host the gametocyte leaves the RBCs, the male genetic code (DNA) divides three times into eight pieces which combine with microgametes in a process referred to as exflagellation. The fertilized zygote cell develops into an ookinete which transverses the mid gut peritrophic membrane and develops into a oocyst. The oocyst can grow up to the size of 100  $\mu\text{m}$  over two weeks, and upon rupturing new sporozoites are released and find their way to the saliva gland of the mosquito host. In summary, the parasite harvests energy and metabolizes in the human hosts whereas fertilization occurs in the mosquito host.

Malaria constitutes one of the major selection pressures in modern human evolution; this has caused a number of unfavorable hereditary diseases, such as sickle cell anemia, to be selected for since it increases the resistance to malaria. Whereas the blood disorder trait is lethal when inherited from both parents (homozygosity) it provides partial malaria resistance when inherited from one parent (heterozygosity). This is a classical example of a counter active equilibrium in evolutionary biology. From the initial sting, it takes 1-2 weeks before any symptoms of *Plasmodium Falciparum* induced malaria occur. The symptoms are headache, muscle fatigue, nausea, vomiting, dry cough, enlarged spleen, repeating chills and sweatings. A characteristic fever pattern (tertian fever) with a periodicity of three days is observed for *Plasmodium Falciparum*. Infection of pregnant women increases the risk for still births, low birth weight and infant mortality. Malaria cannot be diagnosed immediately after infestation and not until the parasites leave the liver and enter the circulatory system. The diagnosis of malaria is dominated by bright-field microscopy of stained thin blood smears, but even antigen test sticks have been developed<sup>7</sup>. Several advanced optical methods have been demonstrated<sup>8-11</sup>, most of which would not be implementable in the field due to the sophisticated equipment. In Papers III and IV we suggest how imaging scattering spectroscopy might provide instant evaluation of unstained thin blood smears.

Malaria can be fought on many different levels out of which some are less environmentally friendly than others; the mosquito habitat can be destroyed, e.g., by drainage, the mosquitoes can be killed with insecticide spraying, e.g. DDT (dichlorodiphenyl trichloroethane,  $\text{C}_{14}\text{H}_9\text{Cl}_5$ , vector control), fish predating on mosquito larvae can be released in the wetlands, stings can be prevented by improved housing, mosquito nets and indoor spraying. The host seeking mechanism can be inhibited. The development in the human host can be prevented or treated by drugs such as chloroquine phosphate or atovaquone/proguanil. However, the cost of such preventive drugs is far beyond economic capacity of most residents in malaria risk zones. Additionally, the drugs can produce allergy, sleeplessness, mental and emotional unbalance and are thus only suitable for short period prevention. As a consequence of the efforts of fighting malaria, resistance has evolved, both in terms of mosquitoes becoming resistant to insecticides and parasites becoming resistant to antimalarial drugs. Especially *Plasmodium Falciparum* has developed resistance to chloroquine, the mildest of the antimalarial drugs. Eradication of malaria has been successfully demonstrated in south Europe and in America through combined vector control and human treatment<sup>12</sup>. Some of the more creative approaches to deal with the malaria problem include release of genetically modified mosquitoes preventing the parasite from developing in the mosquito hosts<sup>13, 14</sup>, solar induced photo dynamic therapy (PDT) targeting the mosquito larvae<sup>15</sup>, and certain substances from a transgenic process from sea cucumbers inhibiting development of the parasite in the

mosquitoes<sup>16</sup>. Both airborne imaging and lidar techniques<sup>17</sup> have been used for correlating vegetation types to the preferred habitats of malaria vectors for epidemiological studies.



Fig. 1.3.2. Atmospheric haemoglobin in terms of an clearly visible blood meal inside an *Anopheles* mosquito by dark field imaging. Public domain image, obtained from the Center for Disease Control, CDC, USA.

The fact that malaria parasites are transmitted via insects, classifies it as a vector borne disease. Vector borne diseases can also be inflicted by bacteria such as *Borelia*, or viruses such as Dengue fever. The vectors transmitting malaria parasites are the mosquitos of the genus *Anopheles*, including more than 460 species of which more than 100 transmit malaria to humans. In particular the *Anopheles Gambiae* transmits *Plasmodium Falciparum*. *Anopheles* progresses through four life stages; eggs, larvae, pupae and imago (adult mosquitoes). The eggs are layed in the water surface and hatch into larvae after three days in tropical regions. The larvae undergo four instars (development stages) during the time of one week. Between instars they shed their exoskeleton to allow growth. Unlike other mosquito larvae *Anophele* larvae have no legs and no siphon (snorkel device) but a spiracle (breath hole) in the abdomen. Therefore, the larvae abdomen must be aligned with the water surface. The larvae feed on algae. After the fourth instar the larvae develop into pupae, from which the imagoes emerge after three additional days. The duration of the entire aquatic stage is 1-2 weeks. The adult *Anopheles* can be recognized by having black and white patchy wings and by their resting position with elevated tail. The imago of some *Anopheles* species are active at night (nocturnal) and most species at dusk and dawn (crepsular). The sex of *Anopheles* can be distinguished by the fundamental wing beat frequency<sup>18, 19</sup>. The males form swarms into which the females enter to become fertilized. Both sexes feed on nectar from flowers; however, the females require a blood meal in order to develop eggs. The female locates their human or animal hosts by use of odor<sup>20</sup>, CO<sub>2</sub> exhaust<sup>21</sup> and body heat. When the host is infested with malaria parasites, the *Plasmodium* gametes are transferred to the mosquito mid gut in the first visit. The blood meal clearly changes the spectral signature and wingbeat frequency of the individual. The blood meal can double the weight of the female mosquito<sup>22</sup>, and she needs 3 days rest to digest it, after which she lays the eggs directly on the water surface. Here after the females resume host seeking, upon the second visit the mosquito might transmit the *Plasmodium* sporozoites through their saliva. Hence, the parasites survival relies on at least two host visits, where the first one must be to an infested individual. However, the imago mosquito stage only survives in nature for two weeks. Age determination of *Anopheles Gambiae* has been demonstrated by near infrared spectroscopy<sup>23, 24</sup>. Apart from *Anopheles* being a malaria vector it has also been proposed to transmit a virus increasing the risk for developing brain tumors<sup>25</sup>.

### 1.3.2 Cancer and malignancies

Infectious causes is claimed to account for 25% of all cancers in Africa and 10% of cancers in Europe. Apart from age, this makes infections the second most important cause for cancer following the usage of tobacco<sup>26</sup>. Especially virus, whose replication relies on inserting themselves in the genetic code of the host can cause insertion of overactive oncogenes resulting in uncontrolled cell division. Examples are Hepatit B and C, Herpes

and human papilloma virus. Both bacteria, such as *Helicobacter pylori*, and parasites can cause cancer, e.g., through triggering by chronic stomach inflammations. Even parasites, such as the snail fever, can trigger, e.g., squamous cell carcinoma following the inflammation caused by worms and eggs in the host. The risk of cancer is highly inheritable, but also environmental parameters are important for the development of the disease. Such parameters include diet and occupational exposure to carcinogenic substances, such as arsenic, cadmium, benzene, radon or vinyl chloride. Other causes of cancer are exposure to carcinogenic radiation. In order of significance, this refers to neutrons, and ionizing charged particles from nuclear processes, ultraviolet light below 330 nm, and disputedly, radio frequency radiation from telecommunication.

The main mechanism of carcinogenic radiation is the ionization of water into OH radicals, which in turns react with the bases in the nuclei of the cell. Due to the double helix structure and the inherent repair mechanisms only a double simultaneous breaking leads to permanent DNA damage. Therefore, the risk of DNA damage does not relate to the radiation intensity linearly. This also explains why ion traces from charged particles are much more harmful than an equivalent dose of photons. Most animals have developed melanins for protection against the natural carcinogenic ultraviolet light, while in the botanical kingdom the most exposed species have developed UV absorptive waxes<sup>27</sup> to protect their genetic code. In the radio frequency regime the main arguments for carcinogenicity are interference with thermal receptors and altered perfusion due to triggering of voltage dependent ion channels in the cell membranes<sup>28</sup>. One bizarre aspect of such bio-electrochemically interactions is that they relate not only to a matching frequency but even to a matching amplitude<sup>29</sup>. This is entirely contradictory to the fundamentals of traditional radiation dosimetry. The epidemiological evaluation of physiological reaction to telecommunications is complicated by rapid development of new communication protocols and telecom habits, in contrast to the long-term development of tumors.

In terms of brain tumors the most common occurrence (50%) is glioma, where glial cells fail to replicate correctly. This is also the most deadly form of brain tumor, with a survival prognosis of only 15 months, even with multimodality treatments. Glial cells account for half of the cells in the brain and are considered to be support cells for neurons and also responsible for adjusting the synaptic weights, the process of learning by chemical signalling. Even for healthy individuals glial cells continue to divide throughout life. Noteworthy is also the elevated levels of glial cells in the brain of Albert Einstein<sup>30</sup>. The standard treatment of gliomas are radiation therapy, chemotherapy and surgical excision. Also experimental treatment with photodynamic therapy (PDT) has been tested<sup>31</sup>. One type of radiation therapy is performed by neutron activated <sup>59</sup>Co and exposure to the gamma emission from the decay of <sup>60</sup>Co into <sup>60</sup>Ni at 1.17 and 1.33 MeV. Although the gamma radiation dose decays exponentially with the depth, the dose in the tumor can somewhat be optimized by engineered omnidirectional illumination - so-called stereotactic "surgery". Surgical resection involves opening of the cranium and of the functional tissue covering the tumour, without breaking the vessel system. The tissue removal is typically done by hand tools such as an ultrasonic suction device. An important aspect is the guidance of the surgeon. Normally the surgeon has magnetic resonance images (MRI) available to plan the operation. A few MRI systems are designed for real-time imaging during operations; however, they also induce a number of complications. Other guidance systems are based on real-time ultrasonic imaging combined with stereo vision<sup>32</sup>. However, the tumour contrast is not very clear in ultrasonic images. The surgeon also has a surgical microscope available for micro surgery, some systems have been developed to incorporate advanced fluorescence molecular imaging into the microscope<sup>33</sup>. In Paper VII one aspect of a fiber point probe<sup>34</sup>, for used for guidance during surgery, is treated.



*Fig. 1.3.3. Preparations for fluorescence guided brain resection at Linköping university hospital, Sweden. The fluorescence is measured by a custom made fiber optical probe. Microscope for microsurgery is suspended from the roof together with the strong operation theater lamp. In the background computer monitors for ultrasound and stereovision navigation are visible.*

Both the imaging surgical microscope system and fiber point probe rely on spectroscopic detection of a fluorescence tumour marker or sensitizer, Protoporphyrin IX (PpIX). PpIX occurs edemically in relation to the heme production chain referred to as the porphyrin synthesis. When PpIX is combined with  $Fe^{++}$  in the mitochondria, heme is formed which in turn is incorporated in haemoglobin in the cytoplasm of the RBCs. Heme is responsible for transporting oxygen and  $CO_2$  to and from the lungs<sup>35</sup>. The rate of porphyrin synthesis is limited by the concentration of  $\delta$ -aminolevulinic acid (ALA) which is in natural circumstances produced by the citric acid cycle and which is negatively regulated by glucose and heme concentrations. The recombination of PpIX with  $Fe^{++}$  is, however, rather slow, and the implication of this bottleneck is that artificially high levels of ALA, e.g. through administration, translate into elevated levels of PpIX. Healthy brains are protected by two barriers, the blood-brain barrier (BBB) and the blood-cerebrospinal fluid barrier (BCSFB). These membranes allow only the smallest molecules, such as  $O_2$ ,  $CO_2$  and hormones to pass into the brain and prevent ALA from entering. In malignant brain tumors, however, new blood vessels are typically formed (neovascularization) with the consequence that administered ALA will enter the tumor and increase the PpIX levels through porphyrin synthesis. Since PpIX is highly fluorescent it becomes a remarkably good marker for deliniating the brain tumors. Diagnosis with PpIX is based on illumination with blue light, while treating (PDT) using PpIX is based on illumination with red light, which will cause free triplet oxygen radicals and subsequent tumor destruction.

Apart from a highly skilled surgeon, the survival chances for individual suffering from brain tumours mainly rely on early detection. Early detection can be derived from symptoms such as increased intracranial pressure, headache, vomiting, nausea, somnolence, coma or asymmetric pupil dilation. Dysfunctional symptoms include impaired judgements, memory loss, disorientation, lack of recognition, changed personality and emotional behavior, loss of senses or vision.

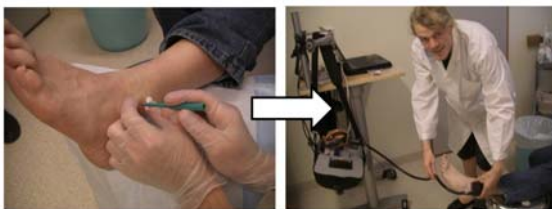


*Fig. 1.3.4. The long term goal of many fiber coupled optical diagnostic systems is the concept of optical biopsies. Here the idea is that painful intrusive punch biopsies (left) with long evaluation times are replaced by non-invasive optical interrogations (right) with instant evaluations. The prototype described in P3 is seen to the right; it is portable and controlled by a laptop computer.*

For other more prevalent forms of malignant tumors, such as breast cancer, early detection before symptoms appear can be achieved by massive screening. This can be performed by blood or urine tests or by medical imaging with ultrasound or MRI. A number of research projects aimed at optical mamography also exists<sup>36</sup>. Whereas the guided resection described

above relies on a tumor marker to accumulate in the tumour after several hours, most screening methods are thought to be based on intrinsic tissue contrast. In optical mammography, tissue discrimination can be based on the contents of water, lipids, blood and its oxygenation state. Also microstructural information in terms of the scattering coefficient can be used for a cancer criterion. In the more superficial dermatological screening, most research projects are oriented on fluorescence detection of, e.g., elastin, collagen, keratin, flavins and NADH<sup>37</sup>. Additionally, fluorescence lifetime measurements have been explored with the argument complimentary information in terms of the microenvironment of the tissue such as pH. Some aspects of this is covered in Papers VIII and IX.

Fluorescence diagnostics aiming at early detection of malignant disease and delimitation of tumour margins has been pursued at our division for almost 30 years (See, e.g. the reviews<sup>38, 39</sup>). Point monitoring<sup>40, 41</sup> as well as imaging instruments<sup>42</sup> have been developed. Endogenous fluorescence from native tissue constituents, as well as specific fluorescence from sensitizers, such as PpIX, has been utilized. While the techniques are powerful, sometimes outliers (false positives or false negatives) are observed. This observation initiated a search for non-malignant sources of fluorescence, and the hypothesis was that advanced glycation end product (AGE) could be responsible. Such substances are associated with several chronic diseases, such as diabetes<sup>43</sup>, renal<sup>43, 44</sup> or heart<sup>45</sup> failure and others. The idea is, that by understanding the different aspects of fluorescence, better fluorescence diagnostics of malignant tumors would result as well as a more exact evaluation of AGE levels.

During the studies towards this thesis, measurements with these goals have been carried out at the clinics for dermatology and oncology at the Lund University Hospital. Here fluorescence and reflectance measurements using the LED-based instrument presented in P3 and Paper VIII were carried out. The patients were all having suspicious skin lesions. Apart from optical measurements, the patient were also typically subjected to a routine biopsy for later clinical correct diagnosis based on histopathology making it possible to correlate to the optical measurements. Treatment was carried out with either cryogenic surgery, laser treatment or photodynamic therapy using light emitting diodes. The data from each patient thus included optical spectroscopic data, the clinical information, an immediate evaluation from the judgement of the clinician and a histopathological evaluation from a biopsy. The goal of the project is to predict the histopathological diagnosis from the optical data and thus replace a painful and intrusive punch biopsy with long evaluation time with a painless, non-invasive optical biopsy with immediate evaluation. AGE can be excited by ultraviolet light (UV) at 370 nm upon which they consequently emit blue light around 440 nm. The AGEs can be considered harmful and have been shown to provoke various diseases<sup>45</sup>, AGEs accumulate throughout life and there are currently no known substances to break down the most common AGE, glucosepane. Individuals suffering from diabetes are known to have increased concentration of AGEs<sup>46-48</sup>. The accumulation of AGEs is associated with the diet<sup>49</sup> and biological ageing<sup>50</sup>, or senescence, and thus also to oxidative stress<sup>51</sup>. Biological aging is attributed the shortening of the telomeres in each cell cycle. The telomeres in the end of the chromosomes carry redundant information protecting the information crucial for a functional cell replication. When shortening of the chromosomes exceeds the telomeres the replication fails and the likelihood to develop cancerous tissue increases. Thus by estimating the fluorescence from AGEs the biological age and the remaining length of the telomeres can be estimated, and with that the risk for developing malignant diseases. Optical spectroscopy constitutes an inexpensive and fast screening method where individuals with increased risk could be forwarded to more costly and advanced diagnostic procedures such as ultrasound or computerized tomographic diagnostics. In our analysis we have been able to predict the actual age of the participant to

a correlation of 80%; however, we have still not considered the biological age and the true AGE concentration. The current gold standard for estimating the AGEs concentration is mass spectroscopy (MS) and the biopsies from our campaign are still in queue and scheduled for MS; therefore the study<sup>52</sup> is not presented in this thesis. In practice the optical procedure also poses a large number of problems; the biological variance between individuals in terms of melanisation, superficial blood layers, subcutaneous fat, sweatyness, hairyness or wrinkles. Any of these factors will affect the optical signal. Invisible substances such as lotions, sunscreen or perfumes will in many cases spoil the measurement. The optical probe pressure also affects the acquired spectral data<sup>53</sup>. In order for an assessment of the AGE concentration to be insensitive to the mentioned parameters, the system must not only detect the AGE fluorescence but even retrieve any other varying parameter and compensate for their impact of the AGE estimation. This can be done with multivariate analysis which will be discussed in Chap. 5.

## 1.4 Instrumentation, electronics, mechanics and optics

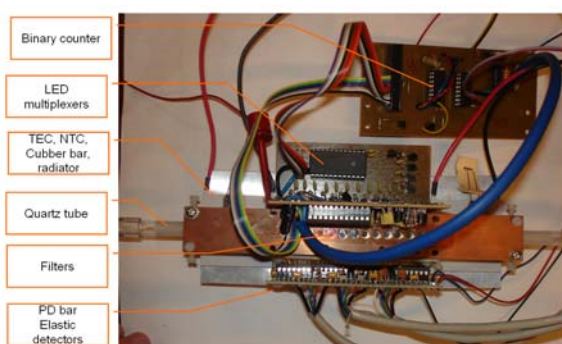


Fig. 1.4.1. Picture showing the prototype spectrometer for turbid liquids in P2. The setup consists of two perpendicular identical rows of LEDs. The LEDs are flashed and multiplexed in the kHz regime. There is one row of Si and InGaAs photodiodes for elastic detection and another of Si detectors with long pass filters for fluorescence detection. The circuit boards and supporting mechanics are made by the author of the thesis. Both P1 and P2 address the problem of disentangling optical properties such as absorption, scattering, fluorescence and refractive index.

Development of spectroscopic instrumentation has been carried out throughout the thesis work. Several instrument prototypes have been constructed. Especially light emitting diode (LED) based instruments have been explored. Due to their simplicity and low cost their application is attractive in new innovations. Prototype development in this aspect typically involved digital and analog circuit design with discrete components, computer aided design (CAD) of solid part in plastic and metals and also of printed circuit boards (PCB), exposure and development of PCBs with NaOH, and etching with H<sub>2</sub>O<sub>2</sub> and HCl, drilling, mounting and soldering. Computer interface programming was typically written in LabView or Matlab.

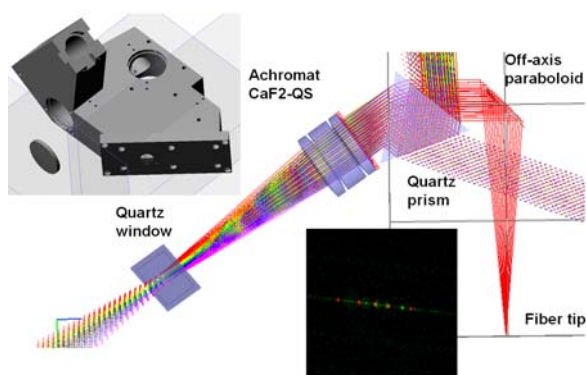


Fig. 1.3.3. Computer aided design of solid parts and ray tracing for stray-light analysis was carried out during the thesis work in relation to development of optical instrumentation. This contact prism spectrometer presented in P1, exploits perpendicular dispersion to simultaneously perform excitation-emission matrix spectroscopy and migration distance resolved elastic backscattering.

## 1.5 New lidar applications tested in field campaigns

Throughout the thesis work several ecological field campaigns have been conducted<sup>54</sup>. These were either pursued using a mobile laser radar laboratory<sup>55</sup> or with smaller passive portable equipment based on amateur telescopes. The durations of the field campaigns have ranged from two days to two weeks. The experiments were typically managed by three to four persons. In contrast to the individual laboratory work at the department, the campaigns are full-team efforts where the project has the full dedication of the participants without interruption by emails and meetings. Whereas measurements performed in the lab can always be redone or refined another day, the measurements from the field campaign are not redone, with the implication that data must be presented in the state it has. The success of outdoor experiments is highly sensitive to the weather conditions, and only during a fraction of the time assigned to the campaign the conditions are feasible. The conditions to be met include temperature, wind, fog, rain, cloudiness and sunlight. The will of animals further reduces the chance of success. Passive techniques are especially sensitive to environmental conditions, and in one unpublished experiment including the usage of moonlight for bird classification, even a full moon criterion had to be met during the migration season. The field work typically involves an operator positioned next to a telescope monitoring the signals live as they are being stored digitally. The operator keeps a logbook recording exact times of all events occurring, such as calibration events, or controlled releases and any changes to the setup. The operator communicates with the field personnel via walkie-talkie, the field personnel typically works several hundreds meters away from the operator and much of the time is spent on locating and overlapping a laser beam and the field of view (FOV) of the telescope. This is not necessarily trivial since both the beam and the FOV form two imaginary invisible cones. When the beam and FOV are partly overlapping the tuning procedure can be based on the optimization of the returning signal, see Fig. 1.5.1. When there is no overlap, the invisible ultraviolet beam must be located in the field with a fluorescence marker, sometimes in full daylight. When the detection is based on a fiber coupled spectrometer a convenient method for visualizing the FOV in the field is to swap the detection fiber to, e.g., a high pressure discharge lamp. This turns the invisible FOV into a bright spot in the remote location. The problem of overlapping arises due to the fact that small angular deviations between the beam and the FOV translate into large displacements at the remote location. A key to successful laser radar measurements is confinement of light in all possible domains; time, space, angle, and energy. These topics will be discussed in Chap. 4.



*Fig. 1.5.1. The river site of Klingavalsån where several campaigns were carried out. In the background several vehicles can be seen, the white trailer is a 40 kVA diesel power plant powering the lidar. The mobile lidar itself is constructed in a green Volvo truck. In the foreground, Prof. Sune Svanberg is communicating with the operators in the lidar while producing a fluorescence return echo from a stick for signal optimization.*

---

## Chapter II

# 2. Light and light-matter interaction

---

### 2.1 Description of light

In this thesis three complimentary ways are used to describe light, namely; as rays, as waves and as particles<sup>56</sup>. The three models are appropriate in different situations and for reaching different conclusions. In general, the photon particle concept becomes increasingly popular when describing high energy wave packets in the gamma and x-ray region, whereas the wave concept becomes increasingly popular when the wavelength increases to the terahertz and radio wave regime. In the optical region, from ultraviolet to infrared, all models are used to explain a plurality of phenomena.

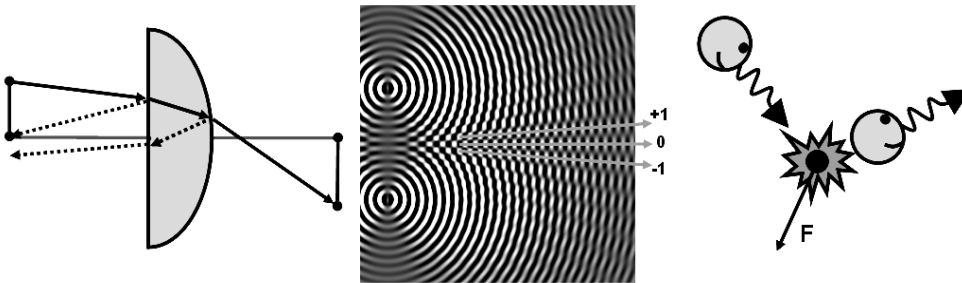


*Fig. 2.1. Left: A ray refracted in a planoconvex lens and secondary reflexes according to Snell's and Fresnel's equations. Middle: Wave-model of the refraction and interference orders of the electrical field following a double slit. Right: Scattering of a photon by a particle transferring linear momentum to the particle.*

#### 2.1.1 Ray models

Rays form the oldest understanding of light, and can be found in early geometrical optics of great importance; examples are Euclid of Alexandria dealing with perspectives in 300 BC, or Ibn Sahl dealing with refraction in lenses in the 10<sup>th</sup> century<sup>57</sup>. Ray models have throughout times been the most valuable models for engineering optical instruments. Following the explosion of computational power in the last decades, including the newly introduced graphical parallel processors, ray tracing of massive amounts of rays allows for refined analysis of stray light and non-ordinary rays in complex optical systems. Ray tracing is also the most advanced method employed when rendering computer graphics providing the most realistic cinematic images. Traditional ray-tracing is incapable of explaining most advanced properties of light such as diffraction, interference or absorption; however, a number of workarounds have been implemented in modern ray-tracing software. Modern ray-tracing programs and powerful computers can also, to some extent, simulate diffusely scattered light. Throughout the thesis work, ray tracing was employed for estimating the location and strength of non-ordinary rays and stray light (e.g. P1) and for estimating angular sensitivity lobes in microscope objectives in Paper III. This is similar to the form factor problem for telescopes.

#### 2.1.2 Wave models

James Clark Maxwell's equations led to a significant advancement of the understanding of light, capable of explaining diffraction and interference such as the famous Thomas Young double-slit experiment and, for example the Dane Ludvig Lorenz' and the Gustav Mie's

scattering lobes for spherical particles. Further, the complete description of the propagating electromagnetic transverse waves gives a reasonable account of the polarization of light. The wave model is incapable of describing light absorption which is determined by the wave frequency rather than the wave amplitude. A complete computation of the electromagnetic field in an optical system or a complex biological sample is often impossible, unfeasible and unusable; instead generalized derivatives of the wave model are used. Examples hereof are the resolution criterion of Ernst Abbe and John William Strutt Rayleigh, scattering theory by Gustav Mie or the Kramers-Kronig relations discussed in Paper XV and P2. The wave model is required for explaining and understanding the operation of most spectrometers, whether the concept is a grating-based polychromator as in Papers VI-IX, or Fourier transform spectrometers as in Papers XIV-XV. The wave interpretation is also required to explain effects arising from dominant spatial frequencies<sup>58</sup> in ordered samples such as crystals, films or biological matrices. Ordering in the latter context relates to thin film effects and structural and iridescent colors, which are discussed in Papers XV-XVI. The spherical wave solution from a point source can be expressed as:

$$U = \frac{U_0}{r} e^{2\pi i \left( \frac{\tilde{n}r - ct}{\lambda_0} \right) - \varphi} \quad \text{Eq. 2.1.2}$$

Here,  $U$  is the electric field,  $U_0$  is the source strength,  $r$  is the distance from the point source, the real part of  $n$  is the refractive index and the imaginary part is absorption,  $c$  is the speed of light in vacuum,  $t$  is time,  $\lambda_0$  is the vacuum wavelength and  $\varphi$  is the phase delay. Light beams or solutions from optical components such as lenses or gratings can in turn be found by adding a large number of point sources. The wave model provides an easy explanation to how odd and even harmonic generation can be achieved in asymmetrical and symmetrical media, and also how harmonic generation relates to pulse duration, amplitude and polarization.



*Fig. 2.1.1 Physics was “easy” in the 19<sup>th</sup> century. The Danish physicist Hans Christian Ørsted accidentally discovered electromagnetism on his messy table as he short-circuited a Volta pile and noticed the reaction of a nearby compass needle.*

### 2.1.3 Photon models

The concept of discrete packets of energy, photons, was introduced by Max Planck out of necessity for avoiding so called ultraviolet catastrophe and is also needed in Albert Einstein’s description of the photoelectric effect leading to all following quantum mechanics. Describing light solely as photons fails to explain phenomena such as diffraction or interference, and the photon model becomes particularly bizarre and unfeasible in relation to Thomas Young’s double-slit experiment where a single photon seems capable of traveling two different ways and then interfere with itself. The Copenhagen interpretation of these particles implies that each quantum has a probability for being absorbed by an atom or a molecule and a probability for being scattered. Others still

claim that classical mechanics equally well explains processes such as ionization<sup>59</sup>. Some renowned physicists still refuse to accept the existence of photons<sup>60</sup>; however, individual photon quanta are daily being registered in the gamma and x-ray region, as glimpses of light produced in scintillators, even in commercial equipment for food and pollution analysis, see Fig. 2.1.3.



Fig. 2.1.2 The Danish physicist Niels Bohr (right) enjoying an uncertain number of Carlsberg beers for lunch. One of his passions was philosophy and he is considered as one of the fathers of quantum mechanics featuring probabilities rather than determinism.

In the optical region the concept of photons occurs directly in relation to single photon counting in biophotonic instrumentation for time-of-flight (TOF)<sup>61,62</sup> or fluorescence lifetime measurements<sup>63</sup>, (Papers VIII-IX). Throughout this thesis, a fruitful interpretation of spectra and images is in terms of photon histograms, in one or two dimensions, respectively - this is discussed in Paper V. The idea of photons also forms the basis for photo-migration random-walk Monte Carlo statistical evaluation. Although such simulations have not been carried out in this thesis, the concept of the photo-migration penetrates the thoughts behind most of the papers (e.g. VII and XIII).

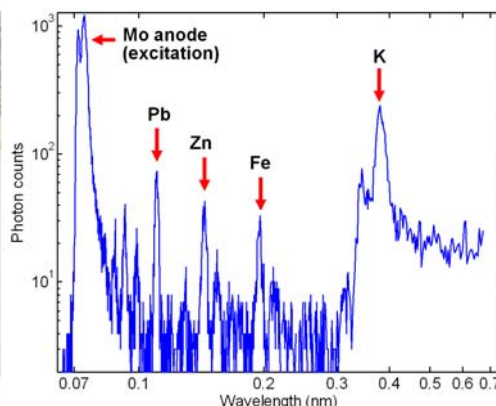


Fig. 2.1.3 Left, The roads are preferred placed for the distributed drying process of Venezuelan cacao seeds. Right, Single photon counting in total reflectance x-ray fluorescence spectroscopy (TRXF) reveals accumulation of considerable amounts of lead in the final food product. Photo and measurement by the author of the thesis.

## 2.1.4 Reciprocity

A concept used in all the above-mentioned light models, is that the light propagation is in many cases subject to the reciprocity theorem. This means that light will travel the same route if the propagation is reversed, or if the radiation source and detector are interchanged. This mindset is fruitful and simplifies matters in many situations, not the least when estimating interrogation volumes in optical spectroscopy. The theorem is used concretely in several of the papers; in Paper III it is used to estimate the angular sensitivity lobes, and in Paper II it is used for the design of a low-cost multispectral imager.

## 2.2 Properties of light

Spanning across the various models for the nature of light as mentioned in Sect. 2.1, light can be summarized by distributions of several properties of the light. The properties are intensity, localization, propagation direction, frequency/energy, polarization and phase. When using light for a diagnostic purpose, regardless if the application is for fundamental understanding, medical applications or environmental monitoring, the optical interrogation is based on the comparison of a subgroup of these properties before and after interaction with the studied sample. If the optical investigation scheme is considered appropriately, the light properties are chosen for the light to interact with the sample according to a phenomenon related to the sample property of interest. A successful optical interrogation implies that when the original light properties are compared to the detected properties a certain conclusion can be reached.

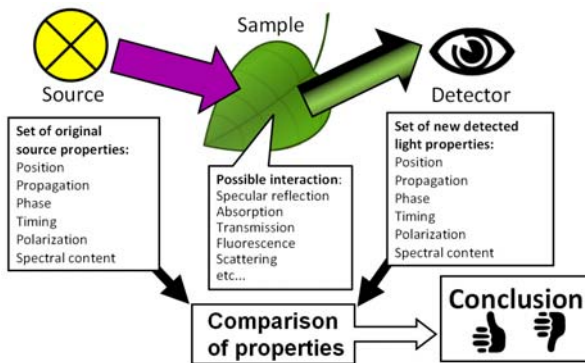


Fig. 2.2.1 The discipline of optical diagnostics is based on the comparison of a set of know source properties to a set of detected properties. A successful optical diagnostic ensures that the correct conclusion is reached.

### 2.2.1 Intensity

The intensity of light represents the amount of power transferred by the light rays - it represents the amplitude squared in the wave interpretation and the number of photons in the particle interpretation. An important observation is that intensity from a point source in a non-absorbing media decreases with  $1/r^2$ , this can be concluded by taking the square of Eq. 2.1.2. This is also in accordance with conservation of energy when taking the spherical integral of the intensities at any given distance.

$$I = U^2 = \frac{U_0^2}{r^2} \underbrace{\left| e^{\pi i \left( \frac{nr-ct}{\lambda_0} \right) - \varphi} \right|^2}_I = \frac{I_0}{r^2} \quad \text{Eq. 2.2.1}$$

A number of measures of intensity exists; when emission of a light source is integrated over all emission angles the quantity is given by Watts ( $W=J/s$ ). This quantity is typically indicated on commercial light bulbs and when compared to the electrical power consumption, in also given in Watts, an efficiency is obtained. When light impinging on a surface is considered the irradiance  $W/m^2$  is useful. As an example the maximal potential for a solar cell can be estimated from the solar irradiance which is no more than  $1.2 \text{ kW/m}^2$  at noon at equator equinox. Radiative flux carries the same unit and is mainly the quantity estimated in photomigration simulation and acousto-optic imaging<sup>64</sup>. The irradiance term  $TW/cm^2$  is popular for comparing ultra intense lasers, and different physical phenomena such as relativistic particle acceleration are often indexed on this scale. Pulsed sources are typically specified by Joule per pulse (J) together with the pulse duration and shape. This produces the peak power in Watts; together with the repetition rate it produces an average power also in Watts. In particular, the peak power determines the manner and significant effects when the light interacts with a sample or optical component. Given that a infinitely

collimated beam can in many situations be focused to a spot size close to the diffraction limit, important measures of diverging and collimated light are radiant intensity (W/sr) and radiance (W/sr m<sup>2</sup>). In spectroscopy where photons are sorted in bins according to energy, the intensity in each bin will scale along with the bin size, thus spectral power (W/nm), spectral intensity (W/nm m<sup>2</sup>) and spectral irradiance (W/sr nm m<sup>2</sup>) are introduced. Apparent magnitude is an inverse logarithmic measure used for brightness of celestial bodies when observed from the earth. A whole range of quantities based on candela such as lumen and lux is extensively used in the lighting industry. These last mentioned measures are based on human vision physiology and are mainly useless apart from in vision and display technology.

### 2.2.2 Localization in space and time

Whereas continuous wave (CW) radiation can be confined in space in a so-called light beam with a given width and divergence, pulsed radiation is additionally confined along the propagation direction forming a “bullet” traveling with the speed of light in the current medium. This analogy is popularly used in the context of, e.g., lidar; for example, where the localization of a light pulse propagates in the atmosphere with the speed of light profiling a narrow path along the beam. Whereas such a pulse is easily explained either by a location of a bunch of particles, or as a wave envelope, rays and most ray-tracing tools do normally not describe a spatio-temporal extension along the propagation direction and the simplest forms of rays are considered as infinite lines without a beginning or an end. By multiplying with the speed of light in the propagation medium the pulse duration can be converted to a physical pulse length with extension in space.

### 2.2.3 Propagation direction

The light propagation can be understood as the velocity vector of the photon particles, the vector perpendicular to the wave front in the wave model, and the direction of rays themselves. Whereas a very broad wave front has a very defined propagation direction, light passing through narrow passages experiences diffraction, and the propagation in terms of particle movement becomes uncertain. The diffraction angle  $\theta_{min}$  relates to the wavelength,  $\lambda$ , and slit width,  $d$ , as follows:

$$\theta_{min} \sim \sin^{-1}\left(\frac{\lambda}{d}\right) \quad \text{Eq. 2.2.3}$$

This relation in general sets the limit for optical resolution. The theoretical concept of light traveling in only one direction is referred to as collimated light in contrast to omnidirectional or Lambertian emission. In practice, lasers can provide very collimated light, but the emission will always be subject to minimal divergence, whereas filament bulbs typically emit omnidirectionally.

### 2.2.4 Frequency/energy

The frequency of an electromagnetic wave is directly proportional to the particle energy quantum. Throughout this thesis the term wavelength is used for energy in the spectral domain. More accurately, this refers to the vacuum wavelength:

$$\lambda = \frac{hc}{E_{phot}} = \frac{c}{f} \quad \text{Eq. 2.2.4}$$

Here  $h$  is Planck’s constant,  $E_{phot}$  is the photon energy and  $f$  is the frequency. The theoretical concept of light with a single wavelength is referred to as monochromatic light

in contrast to white or broadband light. In practice, lasers can provide extremely monochromatic light enabling resolving of tiny details in a spectrum such as hyperfine structure, isotopic line shifts, pressure or Doppler line broadening, or even the Lamb shift, with origins deep in the quantum electrodynamics - all these issues are outside the scope of this thesis. The sun, filament bulbs, or synchrotrons are examples of broadband light sources.

Fourier analysis on an enveloped wave or a light pulse leads to the conclusion that only continuous waves have a well defined frequency, whereas the frequency of short light pulses is uncertain. In the particle paradigm this is compatible with the uncertainty relations of Werner Heisenberg.

$$\Delta x \Delta p = \frac{h}{4\pi} \quad \text{Eq. 2.2.5}$$

Here the  $\Delta x$  and  $\Delta p$  are the uncertainties of position and momentum, respectively. In this thesis the shortest pulses employed are in the picosecond range and the demands on the spectral purity are low because of the dull solid state spectra of the substances studied. Therefore the spectral broadening of light pulses is not relevant. The same equation and dilemma does, however, appear through Fourier transforms in relation to digital signal processing (DSP) in various papers.

## 2.2.5 Polarization

The polarization can be associated with transverse oscillation orientation in the propagating wave model. Discrimination is often done between random/unpolarised, linearly polarized, and circularly left/right hand polarized light. In the particle model photons are typically denoted by  $\pi$  and  $\sigma$ , and correspond to different transitions in free atoms. Atoms arranged in periodic crystals often have preferences for polarization, e.g. difference in refractive index or nonlinear coefficients,  $\chi$ . Single molecules or molecules aligned in certain arrays also have polarization preference for, e.g., absorption or fluorescence<sup>65, 66</sup>. Organisms with compound or asymmetric eyes are sensitive to polarization to various extent. Almost any optical system which is not cylindrically symmetric around the optical axis is sensitive to different polarizations; this is the case for, e.g., diffraction gratings, beam splitters and prisms. An accurate description of the polarization can be given with Stokes parameters,  $S_0$ - $S_4$ ; these can in turn be interpreted in terms such as intensity, degree of polarization, orientation of polarization and degree of circular polarization. Circular polarization, and circular dichroism (CD spectroscopy), meaning differential absorption of left and right hand polarized light, is related to the chiral molecules. This have been proposed to be utilized in the search for extraterrestrial life<sup>67</sup>. Further, certain advanced biological nano retroreflectors have been demonstrated to selectively reflect spectral features in left-hand polarized illumination<sup>68</sup>.

In this thesis mostly a crude discrimination between co-polarized and de-polarized light is discussed, e.g. in Papers III, X, XI and XIV. This discrimination compares the detected intensity parallel and perpendicular to the original polarization, and typically relates to the coherent and incoherent part of reflectance, respectively. This will be discussed in details in Sect. 2.5.4. In a simple view photons having scattered once remember the original polarization whereas multiple scattered photons tend to forget their original polarization. Aspects of polarization in relation to frequency doubling in crystals were dealt with in relation to Paper XIV but are not discussed further in the paper. Refined analysis of all four Stokes parameters was attempted in the context of Paper XV; however, the data could only partly be presented in the paper.

## 2.2.6 Phase

The phase is easiest interpreted in the wave model as an offset to the temporal-spatial propagation of the wave front. From the gamma ray regime and, through the X-ray, ultraviolet (UV), visible (VIS), and infrared (IR) region the electromagnetic frequency is too fast to allow direct recording with any available detector. As a consequence, not the oscillating electromagnetic field,  $E$ , but the strictly positive intensity,  $I=E^2$ , can be directly recorded. Although the phase of light cannot be directly recorded, interferometric detection schemes allow phase sensitivity. This is often achieved by splitting the light source beam into two parts, one part interacting with the sample and another part acting as a reference beam. When combining the beams after the sample interaction phase delays will cause constructive or destructive interference which in turn can be registered as intensity changes. Interferometric schemes are often complex in design and highly vibration sensitive. Examples of interferometric schemes are Fourier Transform Spectroscopy, Optical Coherence Tomography<sup>69</sup>, Doppler lidar<sup>70, 71</sup> and vibratometry<sup>72</sup>. One important aspect in this context is the coherence length of the light source - a measure in time or space of the extension, for which the light remains in phase with itself.

The phase can easily be manipulated and delayed by letting the light pass through refractive media. One interpretation of a simple convex lens is as a phase delay which is large in the center and smaller in the periphery. Such an engineered delay causes the wave front to focus at a certain distance, and this is the basis of image formation. In the regime of radio waves or the non-electromagnetic ultrasonic waves the phase can be directly recorded. Here such focusing can be achieved by electronically introducing delays from receiver elements in phase arrays leading to lens-less imaging and post focusing techniques. Phase arrays are popular in technologies such as Very-Long-Baseline-Array (VLBA) radio astronomy, defense radars, earth observation, medical ultrasound and geological seismic sounding. Recently, direct phase sensitivity has also emerged in the field of terahertz technology<sup>73, 74</sup>. A non-technological example of application of phase arrays is the dolphin yaw, which the dolphin uses to localize prey and flock members by ultrasonic clicks. However, the beam steering and collimation used by dolphins are achieved by a conventional acoustic lens and a reflector<sup>75-78</sup>.

In the present thesis, interferometric schemes have only been used in integrated instruments, such as the Fourier Transform Spectrometer (FTS) used in, e.g., Paper XIV. The concepts of phase, phase delay, constructive and destructive interference are central for the understanding of optical components, including lenses, prisms, gratings and not the least interference filters and optical coatings. In biology, phase is essential for the understanding of thin film effects in insect wings<sup>79</sup> or feathers<sup>80</sup>, for structural colors (Paper X)<sup>81</sup> and iridescence (Paper XV).

## 2.3 Altering of light properties

In Sect. 2.2 the properties of light were discussed and it was emphasized that optical diagnosis, regardless of the application area, is based on the comparison of a set of these properties before and after sample interaction. When light interacts with the matter in a sample, there are a large number of mechanisms, processes or phenomena which are capable of changing the properties. Rough distinction is made between light conserving its original property and light with new properties following the sample interaction. Examples of terms used for light conserving its property are elastic for the energy, ballistic for the propagation, or coherent for the phase. As such, in the physics community, the phenomena are often classified as either elastic processes or inelastic processes. In the computer graphics rendering community including ray tracing software, phenomena are normally

classified as either surface or volume effects. In the following section we will use this distinction.

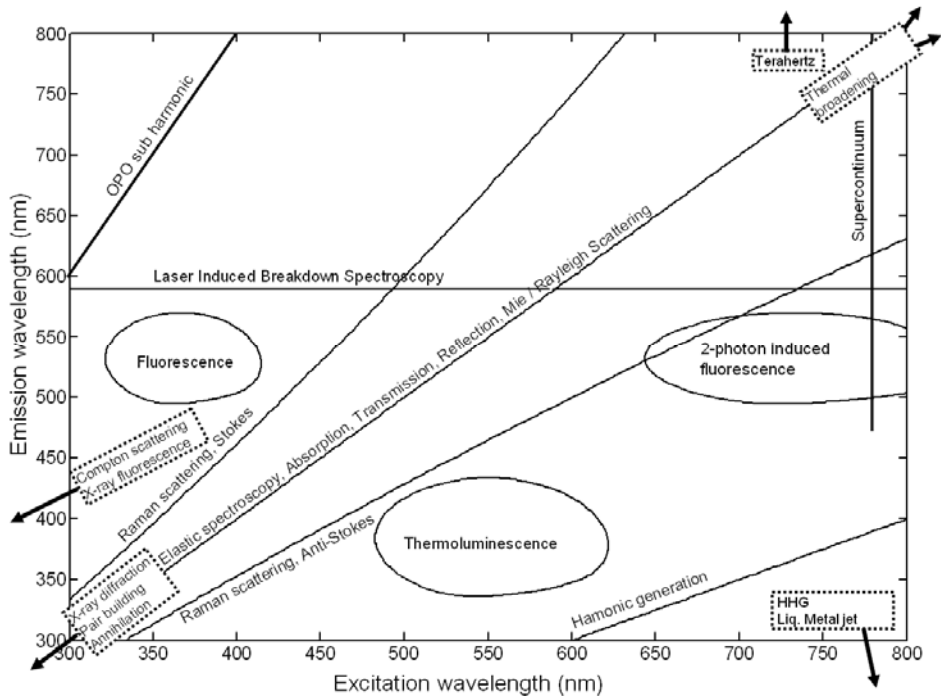


Fig. 2.3.1: One way to overview various optical processes and spectroscopic methods is to consider the illumination wavelength versus the detected wavelength, in a so-called excitation-emission matrix. The strongest and easiest measurable effects are the elastic effects encountered on the diagonal; those include absorption, transmission, reflection and elastic Mie or Rayleigh scattering. In bio-photonics the second strongest process is often fluorescence and after that Raman Stokes, whereas weak anti-Stokes scattering sets large demands on the instrumentation. Toward the thermal regime the elastic effects smear out because of thermal broadening. Processes such as two-photon induced fluorescence and harmonic generation scale with the intensity squared. Laser induced breakdown (LIBS<sup>82</sup>) occurs after reaching the intensity threshold for plasma formation, this threshold is spectrally dependent but the emitted wavelength lines are independent of the excitation wavelength. Super-continuum generation transforms short intense laser pulses to broad band emission. Optical parametric oscillators provide the possibility for partitioning laser photons in less energetic photons. High peak intensity infrared lasers are capable of producing terahertz, and extreme UV through high-harmonic generation, or X-rays with liquid metal jet targets. Toward the energetic region, inelastic processes such as x-ray fluorescence and Compton scattering become increasingly significant.

The phenomena governing the photonic interrogation depend to a large extent on the type of sample, the measurement geometry and instrumentation which is optimized for accessing a certain process. Different phenomena also become increasingly or decreasingly important in different regions of the electromagnetic spectrum. One example is the X-ray region, where Compton scattering might be considerable and the refractive index insignificant, whereas Compton scattering is irrelevant in the terahertz region but the refractive index is highly important. In the following section the processes relevant for this thesis will be reviewed.

## 2.4 Surface effects

### 2.4.1 Reflection

An optical surface or interface is characterized by an abrupt change in space of refractive index. An electromagnetic wave impinging on such a surface will partly be reflected and partly be transmitted. The reflected light will have a new propagation direction which is the original propagation mirrored in the surface normal. This part of the reflectance from an object is typically referred to as the specular reflection or coherent reflectance. One example of a well-known specular reflection is the white spot when depicting a tomato, the spot is located exactly where the surface normal directs to the point half way between the light source and the objective. The light in the specular reflection remembers its original propagation, its phase and its polarization. Unpolarized light can, however, become polarized when the incidence to the surface normal is large. Since the refractive index in many situations varies exceptionally slowly over the spectral domain, the illumination spectrum is mainly conserved in the specular reflection. Since the specular reflected light bounced off the surface of objects, it can generally be considered not to carry any information of what is inside the object. We will later see that most of these properties are opposed to the incoherent reflectance originating from volume effects. In many situations the specular reflection is rejected since it causes more disturbance for unknown geometries than it brings information; this is the case, e.g., in Papers V and XIV.

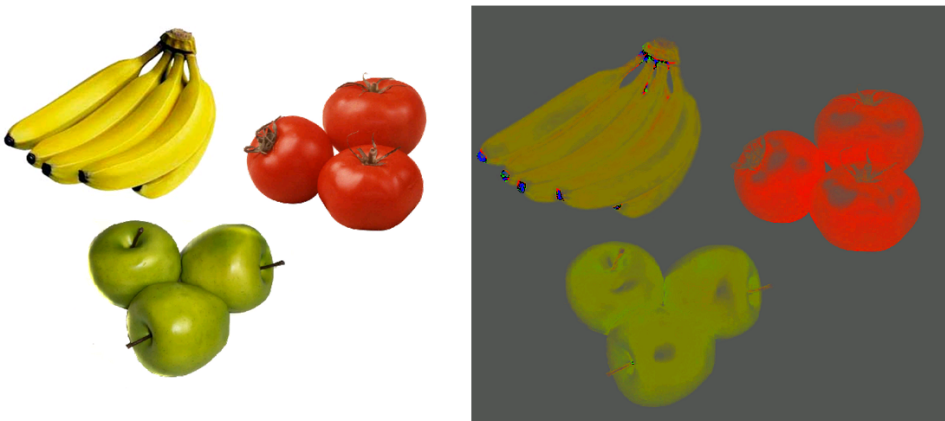


Fig. 2.4.1. Spectral identification, e.g. in machine vision, can be improved by auto normalization – a method cancelling out geometrical effects and shades of the same color. The so called dimension-less image to the right is constructed by dividing each pixel by the intensity or the sum of all spectral bands. The method can be further improved by discarding the specular reflexes by de-polarized photography.

Experimentally, reflectance is measured as:

$$R = \frac{I_{sample} - I_{dark}}{I_0 - I_{dark}} \quad \text{Eq. 2.4.1}$$

Here,  $I_{sample}$  is the intensity recorded from the sample,  $I_{dark}$  is the intensity recorded with no light, and  $I_0$  is the intensity recorded from a white reference. In practice, the term is fuzzy, and does not only relate to the sample, but also to a great extent to the sampling geometry. Apart from sample properties, the absolute values of  $R$  depend on the spot size, the numerical aperture, and the incidence angles of both illumination and light collection. Distinction between specular, diffuse, coherent, and incoherent reflectance is often made.

## 2.4.2 Transmission and refraction

When light impinges on a surface of a transparent object, the propagation of the transmitted light is changed in accordance with Snell's law for refraction. The law was first described by Ibn Sahl in the year 984 and was then rediscovered by Willebrord Snellius half a millennium later:

$$n_0 \sin(\theta_0) = n_1 \sin(\theta_1) \quad \text{Eq. 2.4.2}$$

Here  $n_0$  and  $n_1$  are refractive indices of the two media, and  $\theta_0$  and  $\theta_1$  are the propagation angles in either media. This equation can be derived by drawing the wave front propagation for the wave model, and is used extensively in ray tracing, where it forms the basis for focusing and image formation using lenses, spherical aberration analysis or describing spectrometers using dispersing prisms.

So far we discussed the propagation of light reflected from or transmitted through a surface. The amount of reflected light intensity can be described by the Fresnel equations from year 1818.

$$\begin{aligned} I_R &= I_0 R & I_T &= I_0 T \\ R_s &= \left( \frac{n_0 \cos \theta_0 - n_1 \cos \theta_1}{n_0 \cos \theta_0 + n_1 \cos \theta_1} \right)^2 & R_p &= \left( \frac{n_1 \cos \theta_1 - n_0 \cos \theta_0}{n_0 \cos \theta_0 + n_1 \cos \theta_1} \right)^2 \\ T_s &= 1 - R_s & T_p &= 1 - R_p \end{aligned} \quad \text{Eq. 2.4.3}$$

Here  $I_R$  and  $I_T$  are reflected and transmitted intensity, respectively. The amount of light leaving off the surface normal differs depending on the orientation of the polarization. The index  $s$  implies that the electric field oscillates perpendicular to the plane formed by the propagation vector and the surface normal, whereas the index  $p$  refers to light with an electrical field oscillates in the plane formed by the propagation vector and the surface normal. A special condition arises for the  $R_p$  at the so called Brewster angle, where the reflectance completely vanishes. The Brewster angle, named after the David Brewster, is to a large extent used in high-power laser design to induce polarization preferences or to avoid reflectance which could potentially damage the laser; this is, e.g., the case for the Nd:YAG laser used in the lidar Papers X, XI, XIII and XIV. The polarization in combination with the Fresnel equations was explored to solve the inverse problem of experimentally estimating the angular sensitivity lobes in Paper III; see<sup>83</sup>. A consequence of the Fresnel equations is that most spectrometers are highly sensitive to polarization orientation. However, in this thesis, spectrometers are in general coupled to multimode fibers which scramble any polarization preferences. Apart from optical design consideration, the Fresnel equations relate to several issues in biology; one consequence is that any non-cylindrically symmetric eye in animal vision is potentially sensitive to polarization. Such features relate to navigation based on sky polarization<sup>84</sup>, perception of structural colors, water body surfaces, or insect wing membranes<sup>85</sup>.

When approaching large-incidence angles essentially any surface becomes highly reflective. This is referred to as grazing incidence and is extensively exploited in the high-energy region of the electromagnetic spectrum where light penetrates most materials. Examples are monochromators for synchrotrons or telescopes in gamma astronomy.

In analogy with reflectance, the transmittance is experimentally measured as:

$$T = \frac{I_{\text{sample}} - I_{\text{dark}}}{I_0 - I_{\text{dark}}} \quad \text{Eq. 2.4.4}$$

In practice, also this term is fuzzy, and does not only relate to the sample, but also to a great extent to the sampling geometry. Apart from sample properties, the absolute values of  $T$  depend on the spot size, the numerical aperture, and the incidence angles of both illumination and collection. Distinction between collimated and total transmittance is often made.

### 2.4.3 Diffraction

A surface with ordered structures or dominant spatial frequencies along the surface will act as a diffraction grating. This was discovered by James Gregory, when he observed sunlight passing through a delicate seabird feather in the year 1673; the earliest known application of diffraction gratings. From the wave interpretation, we understand the resulting reflectance as a linear summation of the complex wave from each single structure as if they were interfering point sources. One result from such a summation is that the propagation preference relates to the wavelength of light divided by the periodicity of the surface structures. Another result of the summation of the complex fields is that when such a surface is illuminated by monochromatic light, the extent to which the reflected light is collimated not only depends on the original collimation but also on the number of structures illuminated, meaning the extent of the surface illuminated.

$$d(\sin(\theta_0) + \sin(\theta_m)) = m\lambda \quad \text{Eq. 2.4.5}$$

Here  $d$  is the periodicity of the grooves, and the integer  $m$  is the diffraction order.  $\theta_0$  is impinging angle and  $\theta_m$  is the direction in which order  $m$  constructively interferes for the given wavelength. By changing the spatial waveform of the structures on the surface or the relative strength and phase of the spatial harmonics the diffracted energy can be redistributed among the diffraction orders. In optical design of diffraction gratings for spectrometers this is referred to as blazing and substantially improves the throughput sensitivity and stray light rejection in spectrometers; also blazing angle allows optimization of a certain wavelength region. In diffraction gratings the ordered structures are in general produced by diamond ruling or holographic exposure, and the periodicity is measured in grooves per centimeter. Grating based spectrometers are used throughout the papers of this thesis. An example of a diffraction grating encountered in daily life is the surface of modern compact discs.

### 2.4.4 Multiple surface interference

Reflectance from two or more interfaces with a well defined separation will give rise to thin film effects, where certain wavelength region are suppressed due to destructive interference and other regions will be enhanced due to constructive interference. When the spacing becomes small in relation to the wavelength, broad spectral features arise. Examples from daily life are soap bubbles, insect wings<sup>79</sup> or the nanostructures in pigeon neck feathers<sup>80</sup>. In optical design this effect is exploited by vaporizing different substances on optical surfaces in optical coatings, interference filters and dichroic beam splitters, utilized, e.g. in Papers X, XI, XIII and XIV. When the spacing is large the spectral features can become extremely narrow, permitting some of the most accurate spectroscopic methods, e.g., by Fabry-Perot interferometers or causing a substantial amount of trouble in form of fiber fringes<sup>86</sup>. This will not be discussed further in this thesis. Spectral features reflected from or transmitted

through multi-layer surfaces will displace towards lower wavelength when the angle of incidence increases according to the formula:

$$\lambda_c = \lambda_0 \sqrt{1 - \frac{\sin^2(\theta)}{n_{eff}^2}} \quad \text{Eq. 2.4.6}$$

Here  $\lambda_c$  is the wavelength of the spectral feature,  $\lambda_0$  is the wavelength of the feature at normal incidence,  $\theta$  is the angle of incidence in respect to the surface normal and  $n_{eff}$  is the effective refractive index. This is the background for the iridescence effect where the color or spectral signature for a certain object changes depending of the angles of observation and illumination with respect to the surface normal. Such effects are discussed in detail in Papers XIV and XV.

### 2.4.5 Lambertian emission constraint

All light passing surfaces is subject to a special constraint called Lambertian emission or reflection. When applying the reciprocity theorem, the Fresnel equations give some clues that transmission or emission from any surface should vanish quickly as the angle of incidence increases, but even the conservation of brightness and energy principle, and infinitesimal calculus, lead to the conclusion that  $m \geq 1$  for the following equation:

$$I = I_0 \cos(\theta)^m \quad m \geq 1 \quad \text{Eq. 2.4.7}$$

Here  $I_0$  relates to the absolute intensity emitted,  $\theta$  is the direction the light leaves the surface in respect to surface normal, and  $m$  is the degree of ‘‘Lambertianess’’. Consider for instance an image of the sun. Towards the periphery of the sun the ratio between the footprint area on the sun surface and the image area increases with  $(1-r^2/R^2)^{-1/2}$ . Through infinitesimal calculus it can be derived that an  $m$  value less than one would lead to the consequence that all the power of the sun is emitted at the periphery and no light is emitted in the remaining area which is absurd. The same argument is valid for the reflectance of, e.g., the moon and all light emitted from any object subject to photonic investigation.

Surface scattering randomizes the propagation direction of light passing through surfaces. Surface scattering relates to the optical quality of components coupled to polishing and price, polishing and terms like surface roughness and scratches per  $\text{cm}^2$  are used. For many systems this effect is desired to have a minimal influence, since the consequence is a decrease in the performance, increased stray light or a broadened point spread function in imaging or lidar systems. However, in opal or frosted glass diffusers it is a desired effect. In this thesis such diffusers have been used for flat-field image calibration, merging of optical beams and phase scrambling in order to avoid speckle formation (Papers II-IV). An ideal diffuser converts light with a single propagation direction into a Lambertian source. According to the conservation of brightness principle, the reverse operation should not be possible. Nevertheless, this topic has lead to substantial discussion during the thesis work, since diffusers are subject to the reciprocity theorem, also the phenomena can be reversed with, e.g., complex conjugate reflection<sup>87</sup>.

### 2.4.5 Thermal regime

Towards the infrared regime surfaces emit light as a mechanism to dissipate heat, complimentary to the heat convection. The spectral distribution of the light from a perfect black body is given by the Planck distribution:

$$I = 2hc^2 \lambda^{-5} \left( e^{\frac{hc}{\lambda kT}} - 1 \right)^{-1} \quad \text{Eq. 2.4.8}$$

By setting the derivative equal to zero the Wien shift relation is obtained with the form:

$$\lambda_{max} = \frac{b}{T} \quad \text{Eq. 2.4.9}$$

This implies that black bodies such as, e.g., filament lamps can be used as tunable wavelength sources if the temperature is varied. This curiousum is exploited in Paper I for the purpose of multispectral imaging. A parallel to the behavior of the Bremstrahlung in the X-ray regime is also drawn. In the same paper it is also demonstrated how unknown response functions of spectrometers together with the absolute temperature of a filament can be determined with the only assumption that temperature relates linearly to the electric resistance. By integrating the Planck distribution along the spectral domain the Stefan-Boltzmann law is obtained:

$$P = \varepsilon \sigma A (T - T_{amb})^4 \quad \text{Eq. 2.4.10}$$

The law describes the total flux of radiative energy from a surface. Here the emissivity,  $\varepsilon$ , has a value between 0 and 1. When  $\varepsilon$  is 1 it describes a perfect black body, and when  $\varepsilon$  is 0 it describes a perfect mirror.  $\varepsilon$  is normally given as a spectrally integrated value weighted with the Planck emission for objects with room temperature. Apart from surfaces, also partially transparent media have an emissivity. In this context  $\varepsilon$  is 0 when the medium is transparent and 1 when the medium is opaque. As a consequence the thermal emission observed in atmospheric windows corresponds to that of a Planck emitter with the temperature of the cold universe, whereas the emission in the opaque regions corresponds to that of a Planck emitter with the temperature of the atmosphere. In other words, the atmosphere or infrared optical components are incapable of emitting thermal radiation in the transparent regions. Insertion of an opaque cloud or a bird with ambient temperature will, however, permit emission in the atmospheric windows. Such considerations have been discussed extensively in the context of Paper XV.

A spectrally featured emissivity not only weights the Planck distribution linearly. This is because the energy of the photons in the spectral regions where emission is not allowed, will remain within the sample, and eventually be converted to photons capable of escaping the object. In this sense, light-matter interaction in the thermal regime can be expected to be highly inelastic. The suppression and pop-up effect resembles the effects in hole-burning spectroscopy and depletion in biomass spectra in population ecology. This is discussed in relation to thermal photo migration in combination to microstructures in Paper XV. An obvious example is the animal heat uptake by visible sunlight absorption by melanin, where the heat is partially reemitted at thermal wavelength. Such heat uptake is crucial for insects and reptiles lacking thermal regulation. Therefore the melanization can be expected to vary with latitude. Thermal biology and animal heat uptake have been briefly discussed in Paper X.

## 2.4.5 Sub-wavelength effects

When the geometrical features through which light waves propagate become small in relation to the wavelength a number of phenomena occur. In this regime reflection cannot be explained solely from the change in refractive index as by the Fresnel's equations, here, even the thickness-wavelength ratio comes into play. In transmission through an absorptive medium light does not necessarily decay exponentially as we will discuss in the next chapter. In fact, transmission might even increase by increased slab thickness<sup>88</sup>. A number of confusing terms such as effective refractive index<sup>89</sup>, plasmonics or extraordinary transmission<sup>90</sup> arises. Although the effects have been known for over a century<sup>91</sup> and are extensively used in optical thin film coatings<sup>92</sup>, e.g. in evaporated metallic film beam splitters, sub-wavelength photonics is still today an active research area. This is in particular interesting due to the new possibilities of nanofabrication. Some of the ongoing trends are meta-materials with negative refractive index<sup>93</sup> and photonic crystal fibers<sup>94</sup>. Evanescent field fiber gas sensors are emerging<sup>95</sup>. Microscopy and spectroscopy based on the evanescent field is commercially available in terms of attenuated total internal reflection Fourier transform spectroscopy (ATR-FTIR). In this thesis sub-wavelength effects become of significant importance for the thin wing membrane of insects in the visible and near infrared (NIR), and also in relation to fibrous materials such as plumage in the infrared regime. In Paper XIV and XV the transmittance of feathers beyond thermal infrared (TIR) is mainly assigned to this effect. The general tendency is that transmission for thin films increases with the wavelength-thickness ratio,  $\lambda/d$ . However, both minima and maxima can be encountered. In an early study<sup>91</sup> transmission,  $T$ , for thin films are suggested:

$$T = 1 - \frac{4\pi n^2 k d}{\lambda} \quad \text{Eq. 2.4.11}$$

Here  $n$  is the refractive index and  $k$  is the imaginary part of refractive index.

## 2.5 Volume effects

### 2.5.1 Refraction

Propagation of a light beam in a medium can be understood as constructive interference between induced oscillations in a plurality of dipoles of the medium. With similarity to classical mechanics each such dipole has certain inertia, with the results that the oscillation is not induced instantaneously. Therefore light travels slower in a medium than it does in the case of a vacuum. The ratio between the wave front propagation in a medium and that in vacuum is referred to as the refractive index.

$$n = \frac{c_m}{c_0} \quad \text{Eq. 2.5.1}$$



*Fig. 2.5.1.* Danish scientist Lene Vestergaard Hau managed to slow down light to walking speed and eventually stop it momentarily<sup>96</sup>.

As discussed previously, changes in refractive index lead to effects such as reflections and change of propagation directions. When refractive index is applied as an operator on a propagating electromagnetic wave, described by a complex oscillation, an imaginary part of such an operator will result in damping or attenuation of the wave as it propagates. For this reason absorption is sometimes referred to as the imaginary part of refractive index. As can be understood from the term induced oscillation the delayed propagation can be considered as a causal phenomenon. A special mathematical relation applies to the real and imaginary part of a causal operator, the so called Kramers-Kronig relation.

$$n(\omega) = 1 + \frac{c}{\pi} \int_0^{\infty} \frac{\mu_{abs}(\Omega)}{\Omega^2 - \omega^2} d\Omega \quad \text{Eq. 2.5.2}$$

This relation implies that the refractive index is tied to absorption and visa versa. Since the integral covers a singularity, practical application of the equation involves residue calculus. The relation is a derivative-like relation, but becomes increasingly important<sup>97</sup> with the wavelength  $\lambda$ . Also the refractive index converges to two different values for shorter and longer wavelength, respectively, where the refractive index on the longer side converges to a higher value than on the shorter side. The relative increase of the refractive index on either side far from resonance is proportional to the absorption line strength. One consequence of the relation is that the refractive index is increased on the longer wavelength slope of an absorption band and decreased on the shorter wavelength slope of such an absorption feature. The relation governs properties of all optical materials. One consequence is, for instance, in prism spectrometer design; here a steep refractive index slope is desired for high spectral dispersion. However, steep slopes are only achieved for materials with large nearby absorption, thus the prism becomes increasingly opaque. This issue was part of the consideration for P1. Since the refractive index not only determines the sample surface reflectance but also reflectance from particles or inclusion in turbid or fibrous media, and appear directly in the Mie scattering equation, the Kramers-Kronig relation has a large impact on the scattering coefficient for, e.g. blood<sup>98</sup>. This will be discussed more in the follow section. The interplay between refractive index, absorption and scattering is discussed in detail in Paper XV and P2<sup>99</sup>.

Certain crystals used in optical components demonstrate birefringence, that is, different refractive index depending of the orientation of the polarization and the direction of propagation in respect to the crystal axis. Furthermore, birefringence can be altered in some material subject to a strong electrical field; this is referred to as the Pockels effect and can be used, e.g., for fast electro-optical switching, e.g., in Q-switched lasers. The Pockels effect relates linearly to the applied electrical field. The quadratic dependence of the refractive index in relation to the electric field is referred to as the Kerr effect. From the point of symmetry around zero field, it can be understood that the Kerr effect does not require a crystal, in fact it is particularly strong in certain liquids. When the electric field is induced by an intense and typically pulsed laser light wave the topic is referred to as non-linear optics. The refractive index dependence on the field strength is often expanded on a polynomial basis, and the polynomial coefficients are referred to as  $\chi^{(1)}$ ,  $\chi^{(2)}$  ...  $\chi^{(n)}$  or the electric susceptibility. A main discipline in nonlinear optics is the harmonic generation where the frequency of lasers can be doubled, tripled or many doubled. In, e.g., Paper XIV such an approach is used to convert a infrared laser at 1064 nm first into green light at 532 nm and secondly into ultraviolet (UV) light at 266 nm. The Kerr effect also relates to the phenomena of self focusing and laser filamentation. In the latter case ultra intense laser

pulses can break the normal divergence leading to long plasma guides emitting continuous white light in a backscattering<sup>100</sup>.

### 2.5.2 Absorption

When light propagates in a medium, there is a certain probability per unit length that the energy quantum of the photon is taken up by the medium. This is referred to as the absorption process. Albert Einstein got the Nobel prize for the explanation of the photoelectric effect, where the probability for this to happen relates to the photon energy rather than the intensity of the light of insufficient quantum energy. In a classical conception of waves this would correspond to the probability of a village to get destroyed by a tsunami relating not to the amplitude of the tsunami but to the wavelength, thus the probability would be greater for a thousand of ripples than for a single broad wave which is absurd. A more fruitful conception of absorption is provided by the photon particle model, where the particle energy can be transferred to potential energy of electron configurations in the atom. In the visible regime the photon energies typically correspond to those required for electronic transitions of the outer electrons. For gases this gives rise to extremely narrow absorption lines<sup>101</sup> which are unlikely to overlap between different gases. The strength of every such line corresponds directly to the concentration of a certain gas. Absorption lines by gases additionally provide information on temperature and pressure. Such aspects constitute a large field of investigation<sup>102</sup>, but in this thesis gas absorption is only discussed briefly in Papers XII and XVI. For solids and liquids, the outermost electron orbits are heavily perturbed by interaction with neighboring molecules, with the consequence that the electronic transitions in solids and liquids become largely undefined giving rise to broad absorption bands which overlap between different substances. These bands additionally include electronic transitions between various combinations of vibrational states. To interpret such overlapping spectra into a meaningful conclusion, multivariate analysis methods are often required; this will be discussed in Chap. 5. One exception where solids show narrow absorption lines are in rare earth elements, where visible radiation can be absorbed in transition to an unfilled shielded electron orbital. For this reason, rare earths are often exploited in solid state lasers, e.g. the Neodymium doped laser, which is utilized in Papers X, XI, XIII, and XIV.

For the less energetic photons in the infrared, absorption is mainly associated with vibrational transitions for molecular bonds. Examples in this thesis can be found for the NH and OH stretch modes in the MIR in Papers XIV and XV. In the microwave regime photon energies correspond to rotational transitions; one example hereof is the water absorption in microwave ovens.

Towards the more energetic part of the spectrum starting from UV light, photons potentially have the energy to ionize molecules and create free radicals. Such radicals can be carcinogenic and constitute a potential safety concern when working with high pressure discharge lamps, xenon flashes or UV lasers, e.g. in Paper XIII. Further down in the spectrum, X-rays are additionally associated with excitation of inner shell electrons, described by the simple Moseley law. Elementary X-ray absorption is utilized in, e.g., medical x-ray and computerized tomography. Eventually, gamma photons are associated with nuclear transitions.

The fact that absorption corresponds to a constant probability per unit length for a photon to be eliminated leads to the simple linear differential equation:

$$\frac{dI}{dx} = -\sum_m C_m \sigma_{m,\lambda} \rightarrow I = I_0 e^{-x \sum_m C_m \sigma_{m,\lambda}} \rightarrow T = e^{-x \sum_m C_m \sigma_{m,\lambda}} \quad \text{Eq. 2.5.3}$$

$$A = \log_{10} \frac{I_0}{I} = \log_{10}(e) x \sum_m C_m \sigma_{m,\lambda} = \log_{10}(e) x \sum_m \mu_{abs(m,\lambda)}$$

Here  $I$  is the transmitted intensity,  $I_0$  is the impinging intensity,  $m$  is the running index of the substances involved,  $C$  is concentration,  $\sigma$  is the absorption cross section,  $x$  is the path length,  $T$  is transmittance,  $A$  is absorbance,  $\mu_{abs}$  is the absorption coefficient. Here the transmittance is an exponential decay. Given that the path length,  $x$ , and absorption cross sections,  $\sigma$ , for all involved substances are known, one can relate the concentrations of all involved substances to the transmission. This is referred to as the Beer-Lambert law. This forms the basis for most of the simplest types of applied spectroscopy; namely absorption spectroscopy. Absorption spectroscopy is a returning subject in all papers in the thesis. In biophotonics, the substances which contribute to a significant absorption imprint in the spectral signature are termed chromophores. Examples of typical chromophores in this thesis are hemoglobin, carotenoids or melanins. It is often considered that each such chromophore has one associated spectral component,  $\mu_{abs}$ , which acts independently, and that the combined absorption effect is a linear combination of the constituent times their volume fraction. In matrix formulation this forms the simple relation

$$A_\lambda = x S_{\lambda,m} C_m \quad \text{Eq. 2.5.4}$$

Here  $A$  is a vector of absorbance measured at discrete wavelengths,  $x$  is a scalar path length,  $S$  is matrix with absorption cross sections for each spectral band and each substance,  $C$  is a vector of concentration of each substance involved. As we shall see later, the path length is, however, not trivial to determine in many situations. Approaches to this problem include probe volume estimation by spectral normalization from an intrinsic spectral features with an absorption from, e.g. water<sup>103</sup> or time-of-flight (TOF) spectroscopy<sup>104</sup>.

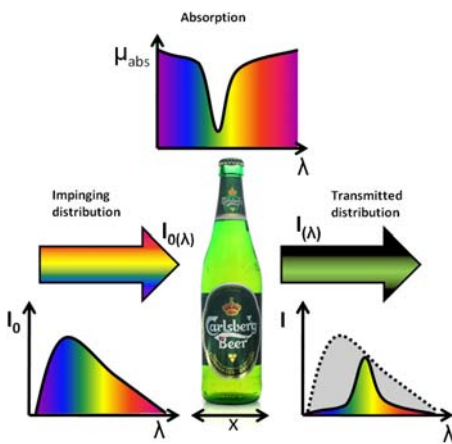


Fig. 2.5.2. The Beer Lambert law describes the exponential decay of intensity for light propagating in an absorptive medium. The decay arises due to the constant survival chance per unit length.

As can be seen from the solution the detected intensity relates linearly to the impinging intensity. This assumption holds true for low intensities where the Boltzmann distribution implies that most systems are in their ground state. However, ground states can become depleted with the consequence that the absorption coefficient decreases. In summary,

Schrödinger's famous cat might be black when photographed with a 1 J, 10  $\mu$ s flash, but grey when photographed with the same flash energy lasting only a femtosecond. Such saturable absorbers enable fast lasers as used in Paper VIII and IX. For very high intensities achieved with fast laser pulses, molecules or atoms can experience the energy of two identical photons as one photon with twice the energy. Such approaches are useful in biophotonics and confocal microscopy to compromise the dilemma between depth penetration and resolution. This is in analogy with harmonic imaging in medical ultrasound. The probability for a two-photon absorption scales with the intensity squared, three photon absorption scales with the cubic intensity, and so forth. This also implies that the spatial extension of the volume where light is absorbed gets increasingly confined for multi-photon absorption<sup>105, 106</sup>.

An interesting detail regarding the absorption coefficient,  $\mu_{a,n}$ , in relation to bio-photonics, is that the unit is typically given in inverse centimeters. As such, the inverse is referred to as the mean-free-path and has the unit of a physical length; this means that the light-sample interaction is completely different for samples of different sizes, even if the constituents are resembling. A consequence is that many approaches in biophotonic, are more feasible for infants<sup>107, 108</sup> and small animals<sup>109</sup> than for adults, whereas X-ray techniques provide large absorption contrast on full grown humans, while that technology cannot be directly scaled to applications for, e.g., insects. Reversibly, technology for high-resolution neurological functional imaging of the brain in, e.g., fruit flies<sup>110</sup> might never be applied in humans. In general, the absorption of biological tissue is low for near infrared (NIR) and increases towards green and blue and leaves tissue mainly opaque in the UV region. Towards the mid infrared (MIR) and thermal infrared (TIR) regions water becomes entirely opaque.

There are several energy routes for the molecules to dissipate energy following electronic excitation by absorption. The most likely one is that the electron returns through non-radioactive decay, converting the potential energy to heat dissipation. An example in entomology is the ant burning with magnifying glasses sometimes performed by children. In more sophisticated bio-photonics the effect has recently been exploited in ultrasensitive opto-acoustic breath analysis<sup>111</sup> or opto-acoustic imaging<sup>112</sup>. The energy can also be used to break the molecular bonds, referred to as bleaching or ablation, the energy can be transferred to other molecules and drive photochemical processes such as photosynthesis, or cause cell destruction in photodynamic therapy, PDT<sup>113</sup>. Bleaching and photokinetics are discussed in Papers III and VII. Eventually the excited molecules can decay to their ground state by emission of fluorescence.

### 2.5.3 Fluorescence

Although David Brewster observed fluorescence of chlorophyll already in 1833, it is generally considered that the phenomenon was discovered in the year 1852 by Sir George Gabriel Stokes, while observing a solution of quinine through his glass of yellowish wine<sup>114</sup>. The quinine was illuminated sidewise through a blue colored mosaic window. His setup resembles that used in a modern fluorescence spectrometer of today, except that the sources today are either lasers, light-emitting-diodes or high-pressure discharge lamps, and, further, drinking wine in the laboratory is generally not considered being a good practice. Since the resulting photons have less energy than the impinging photons, fluorescence is referred to as an inelastic effect with analogy to elastic and inelastic collision in classical mechanics. Examples of fluorescence from the daily life are fluorescence marking of money bills and passports and also fluorescent marking pens for office work. Such pens are capable of altering the apparent reflectance of white paper beyond hundred percent; this will be discussed more in Chapt. 3.

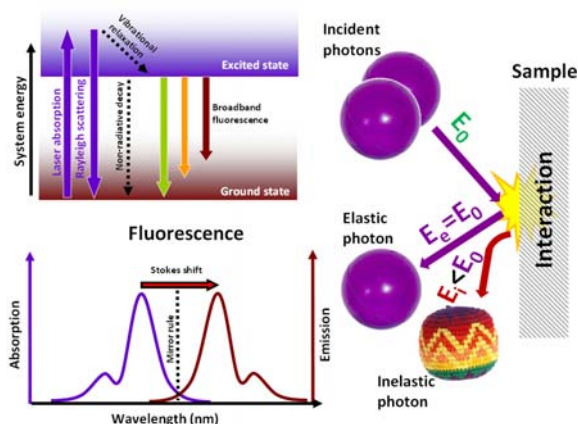


Fig. 2.5.3. Upper left: A molecular system is electronically excited from its ground state to an excited state by a purple laser. Because the excited electronic state has many vibrational bands excitation or absorption can be achieved over a broad range of energies. The system subsequently relaxes through either elastic scattering, heat conversion or fluorescence. Since the fluorescence transitions can occur to a broad band of vibrational bands in the electronic ground state, the emitted fluorescence is broad. Lower left: The symmetry between the phenomena of absorption and fluorescence produces a mirror effect along the spectral domain. The energy lost through vibrational relaxation gives rise to a Stokes shift displacing the emitted light toward the red end of the spectrum with respect to the original light. Right: Illustration of photons arising from elastic and inelastic scatter.

In this thesis fluorescence mainly refers to the spontaneous emission following an electronic excitation. Apart from this process there is also stimulated emission triggered by a second photon shortly after the excitation. The result is a superimposed identical copy of the photon, with all the same properties in terms of energy, propagation, phase and polarization. This is exploited in lasers as used throughout this thesis. Polarization preferences of fluorescence light can additionally appear in polarization anisotropy fluorescence measurements. Such preferences relate to the orientation of ordered molecules or crystallization and generally require a microscopic scheme. This issue is not discussed further in this thesis since the polarization of light will in most cases be scrambled prior to the absorption in all detection schemes presented here. Stimulated emission is in all respects identical to absorption which could also be redundantly termed stimulated absorption. Due to this symmetry, also absorption and fluorescence share similar properties. Therefore the discussion regarding spectral linewidth of the fluorescence from gases<sup>115</sup>, rare earths<sup>116</sup> and X-ray induced K-shell transitions (See Fig. 2.1.3) is also identical to that of the previous section. Since this thesis treats optical spectroscopy in solids we once more conclude that advanced mathematics is required to interpret fluorescence spectroscopy.

During the fluorescence process electrons are mainly excited from the lowest vibrational states in the electronic ground state to a vibrational state (determined by the Franck-Condon principle) in the excited state. Prior to the following emissive decay the molecules relax to the lowest of the vibrational states in the excited electronic state. Hereafter the electron returns to a vibrational state in the electronic ground state, eventually followed by a second vibrational relaxation. The potential energy loss during the vibrational relaxation is referred to as the Stokes shift of the emitted light. From the energy conservation principle it can be concluded that the emitted light is less energetic and therefore the fluorescence emission in general has a longer wavelength than the exciting wavelength. The fraction of absorbed photons which is remitted as fluorescence is termed the quantum yield. An absorber or chromophore with significant and detectable quantum yield is termed a fluorophore in biophotonics contexts. Typical examples of endogenous fluorophores measured in this thesis are keratin and chlorophyll. Fluorophores such as psittacofulvins, porphyrins and rhodamines are also occasionally present in animal pigmentation, e.g., in some parrots where they are thought to play a role for sexual signaling<sup>117</sup>. Red colors are produced by fluorescence in fish species<sup>118</sup>. Red fluorescence is also used in cosmetic products for humans<sup>119</sup> desiring to increase their popularity<sup>120</sup>. In this thesis, laser induced fluorescence (LIF) is induced on various fluorophores with UV or blue light ranging from 266-445 nm,

e.g. in Papers XIV and IX, respectively. The detected emission light is mainly in the blue-green region for most intrinsic fluorophores, but for protoporphyrin IX (PpIX) and chlorophyll red and near-infrared light is emitted. Just as chromophores have associated absorption spectral component vectors, also fluorophores have associated emission spectral distributions referred to as spectral components. When a fluorescence spectrum from a mixture of several fluorophores is recorded, it can in theory be linearly decomposed by projecting the measurement on a set of fluorescence components expected in the sample. In theory the concentration of fluorophore can be concluded from the linear coefficients of such spectral decomposition.

In the simplest case the emission spectrum from a fluorophore is related to the absorption for the fluorophore through the Kashas rule, popularly known as the mirror rule:

$$\lambda_{ind} = \frac{\lambda_0 \lambda_{em}}{2\lambda_{em} - \lambda_0} \quad \text{Eq. 2.5.5}$$

$$F = Q \sigma_{abs}(\lambda_{ind})$$

Here,  $F$  is fluorescence intensity,  $Q$  is the fluorescence quantum yield,  $\sigma_{abs}$  is the absorption spectrum,  $\lambda_0$  is the mirror wavelength,  $\lambda_{em}$  is the emission wavelength and  $\lambda_{ind}$  is the indexing in the absorption spectrum. The intensity registered from a fluorophore is thus given in a two-dimensional excitation emission matrix (EEM), which in the simplest case is the product between the absorption and emission spectral components. Such a kind of double spectroscopy provides an additional dimension for discrimination between samples. This can for example be exploited for estimation of the pure spectral absorption and emission components<sup>121</sup>. In many aspects the data of the EEM resemble those of other two-way spectroscopies such as lifetime spectroscopy, double mass spectroscopy (MS), or gas-chromatography-mass-spectroscopy (GC-MS). The *EEM* for an infinitely small volume can in the simplest case be given:

$$EEM_{\lambda_{ex}, \lambda_{em}} = A_{\lambda_{ex}, m} C_{m, m} F_{m, \lambda_{em}} \quad \text{Eq. 2.5.6}$$

Here *EEM* is the matrix with fluorescence intensities for corresponding discrete spectral bands for excitation and emission;  $A$  is a matrix with the absorption in each spectral band for the present fluorophore,  $C$  is a diagonal matrix with the concentrations of each fluorophore,  $F$  is a matrix with the fluorescence spectra of each fluorophore. The EEM can be measured directly on complex samples such as skin tissue<sup>122, 123</sup> or vegetation<sup>124-126</sup>. In the simplest case the EEM is the sum of the EEMs for each fluorophore; however, there are many examples of situations where one fluorophore transfers its energy or pumps another fluorophore. This is for instance the case for waxed leafs, here the wax absorbs UV and emits blue light, which in turn is absorbed by chlorophyll and reemitted in the NIR.

Since fluorescence is a secondary effect following absorption and since the quantum yield is strictly less than one, the inelastic fluorescence is always a weaker phenomenon than elastic effects such as absorption. In most situations, long-pass filters are required to suppress the elastic photons in order to observe the inelastic photons. For the same reason the collected fluorescence in applied spectroscopy is normally heavily perturbed by the absorptive properties of the sample. Since fluorescence requires a prior absorption, and absorption requires a path length to occur, fluorescence is created omnidirectionally at a certain depth in the sample. When part of the fluorescent light subsequently travels to the surface of the sample before it can be collected, it is once again subject to absorption. This absorption can be by the same fluorophore or other present chromophores. This is referred

to as re-absorption emission quenching and is a returning theme throughout this thesis and several of the patent applications. (See, e.g., discussion in Paper XIII). Since part of the produced fluorescence is propagating inwards with the possibility of the light being reflected in the sample prior to detection, even coherent reflectance features can potentially make an imprint in fluorescence; see, e.g., Paper X. These types of entanglement between fluorescence, absorption and reflectance can be exploited in several ways; one example is the absolute chlorophyll concentration determination which is possible by comparing the two emission peaks of chlorophyll. Here the short wavelength peak is reabsorbed by chlorophyll itself when the concentration is high.

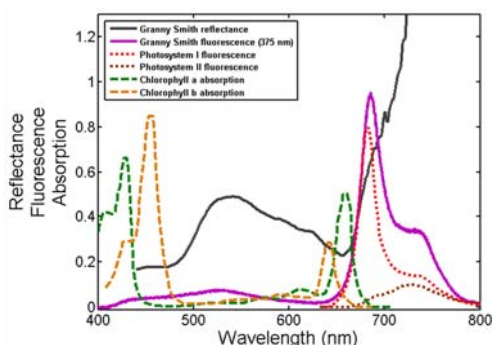


Fig. 2.5.4: Fluorescence and reflectance of Granny Smith apples measured by P3, the literature absorption and fluorescence spectra of associated chlorophyll are superimposed<sup>127</sup>. The fact that the absorption partly overlaps the fluorescence enables the estimation of the absolute chlorophyll concentration. The NIR reflectance exceeds 100% because it was measured by a white LED with low emission in the NIR and because the sample is highly fluorescent in this region.

It is in general not trivial to derive quantitative measures from fluorescence emission in applied spectroscopy. However, one way is to use a spectral feature of an intrinsic molecule relating to the volume probed. This is done in fluorescence spectroscopy on water purity where the probe volume can be derived from the water Raman emission<sup>128-130</sup>. Similar tissue-matrix normalization is performed, e.g., in Paper VII where fluorescence is normalized by the signal from tissue autofluorescence. Spectral ratio normalization is an on-going theme throughout this thesis. A final example on exploitation of emission re-absorption is the remote classification of birds in Papers XIII and XIV. Here the source of fluorescence emission can be associated with a single fluorophore, namely  $\beta$ -keratin. The presence of a plurality of chromophores such as melanins and carotenoids leaves a strong absorption imprint allowing discrimination between bird species.

In many other situations re-absorption of fluorescence causes great annoyance, and many efforts of retrieving the so-called intrinsic fluorescence have been made. The history of those efforts is reviewed in Paper IX. One way to correct retrieved fluorescence emission for re-absorption is to simultaneously record the elastic sample properties and subsequently compensate the fluorescence data. However, as we shall see in the next section, this is not trivial either, since reflectance is governed both by absorption, refractive index, scattering and anisotropic scattering, and thus measuring only the reflectance poses problems of an underdetermined system of equation. This is why several measurement geometries are employed, e.g., in Paper 3. The challenges related to this and a possible solution have been extensively reviewed in P2.

Other approaches for obtaining re-absorption-free fluorescence relies on time resolved fluorescence. Following excitation the system remains in the excited state with a certain probability per unit time of decaying to a lower energetic state. In the simplest case this leads to an exponential decay with a particular resulting lifetime. In general, the lifetimes are shorter for transitions with higher energy; additionally molecules with long lifetime typically have a low steady-state emissive yield, since they cannot be subject to a new fluorescence process as long as they are in their excited state. Most fluorophores in

biological tissue have lifetimes in the order of one nanosecond. In the simplest case the fluorescent decays exponentially from a single energy level to the ground state following excitation by a Dirac pulse.

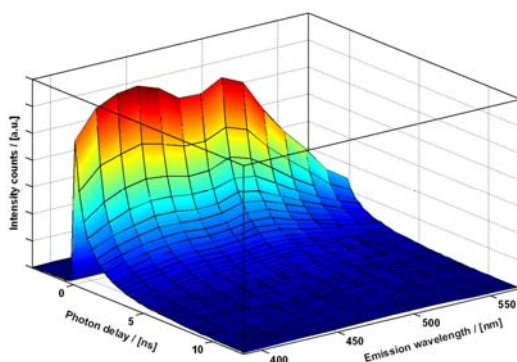


Fig. 2.5.5. Broad band fluorescence lifetime surface of the unpigmented keratin plumage of a Herring gull. The measurement is performed by spectrally resolved single photon counting induced by a mode locked laser. The analysis generally confirmed that the only significant fluorophore is keratin, whereas chromophores such as melanins and carotenoids merely serve as emission quenchers

Most fluorophores yield not one but several decay lifetimes, and when embedded in complex tissue matrices, complex mother and daughter activity might occur. This would for instance be the case for the example of waxed leaves above. In Paper IX such complex electron population dynamics are related to population dynamics in nuclear physics, robotics and ecology, and it is demonstrated empirically that the number of spectral components, or energy populations, are the same as the number of dynamical states or lifetimes. The numerical fitting of multiple exponentials is exceptionally ill conditioned. Once the lifetimes are obtained, the argument is often that they reflect both the type of fluorophore and also the micro environment, such as the pH<sup>114, 131</sup> or temperature<sup>132, 133</sup>, which should then form the basis for an optical diagnosis. Fluorescence lifetime instrumentation is in general much more costly and sophisticated than steady state instrumentation. The diagnostic benefit and complimentary information of this approach is currently the subject of much investigation.

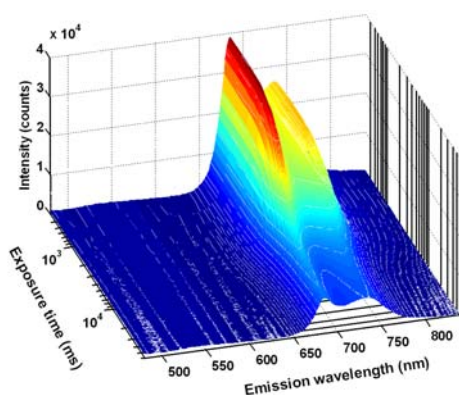


Fig. 2.5.6. LED induced fluorescence (410 nm) of vegetation. The fluorescence spectra from vegetation change shape according to exposure time, power, temperature, moisture, stress and other factors. These measurements were performed during a workshop in Bamako, Mali<sup>134</sup>.

As shortly mentioned before; an excited chromophore not only has a probability of fluorescing, but also has an additionally probability of breaking up. This is referred to as bleaching. In most situations this effect is very slow in comparison to the fluorescence lifetimes. Furthermore, it is irreversible, while a molecule can fluoresce numerous times. In

Paper VII the phenomenon is studied over seconds and minutes. Bleaching causes the fluorescence component of the bleached substance to decay over time. The thereby produced rest products can in turn alter the fluorescence by absorption or fluorescence with new spectral components. Bleaching can also potentially change the interrogation volume, since the bleaching substance might cease to absorb and thus excitation light is deposited at greater depths. Once again such time evolution can be described by population dynamics, where population this time refers to the various molecular species in the interrogation volume. There are several reasons why bleaching spectral components might not bleach to zero as time goes to infinity: The molecule subject to the bleaching might continuously be produced in, or perfuse into, the optical interrogation volume. Another possibility is that the micro environment around the fluorophore might either permit or inhibit bleaching; this could for instance be the case for substances found both extra- and intra-cellularly. The origin of such behavior can be derived from power analysis, where the bleaching process is studied as a function of excitation power. From this we can also understand that fluorescence from a sample undergoing a bleaching or photo kinetic process does not relate linearly to the excitation light. For similar reasons discussions arise regarding fractionated light dose and the temporal distribution of intensity administration during PDT<sup>135</sup>. For ionizing- and potentially carcinogenic radiation, such as X-rays or the UV in Paper XIV, distinction must often be made between pulsed and continuous doses because of the DNA repair mechanism<sup>136</sup>.

The energy of excited chromophores might also drive photochemical processes. A well known example is the photosynthesis by chlorophyll. One aspect of the associated Kautsky processes is briefly demonstrated in Paper III. A more profound analysis of the photokinetic parameters from live vegetation has proven valuable for sex discrimination of young nutmeg plants. The trees take decades to mature and only the female plant produces crop - thus a rapid optical discrimination during the plantation stage would greatly increase the crop yield<sup>137</sup>.

In more exotic examples molecules have the probability of flipping between a bright fluorescence state and a dark state. To observe such phenomena single molecule detection is required and therefore this research is typically associated with fluorescence microscopy. One particular interesting application of blinking molecules is as a fluorescence sensitizer for the formation of super resolution images, the so called STORM and PALM methods<sup>138-140</sup>. Neither super-resolution methods nor blinking molecules are part of this thesis, but retrieval of information beyond the Abbe criterion is demonstrated in Paper XV. Blinking aerosols are also discussed in Paper XV. In the Papers XI, XII and XIV blinking aerosols are being measured, but the sample rates have been too slow to exploit this property. Other groups have, however, exploited this for frequency and waveform identification<sup>141, 142</sup> and even patented remote detection of blinking aerosols also known as insects<sup>143</sup>.

Fluorescence sensitizers are extensively used to detect several sample properties by fluorescence; properties which do not yield any specific fluorescence signature by themselves. One example is the cancer seeking marker PpIX. The precursor  $\delta$ -aminolevulinic acid is administered either as a skin lotion or by intake with orange juice, and within hours PpIX accumulates in malignant tumors due partly because of differences in hormone concentration. In open brain surgery of tumors it works particularly well because of the destruction of the blood-brain barrier in tumors. When PpIX is excited by blue light it emits a clearly distinguishable red fluorescence component. A special property of PpIX is that when exposed to red light it can transfer excited energy to locally dissolved oxygen and create a reactive form of oxygen (singlet oxygen) which causes cell death/necrosis. This is exploited in PDT for curing, e.g., skin and prostate cancer. Fluorescence sensitizers are extensively used in microscopy where they bind to various

organelles in cells or react to pH enabling visualization of the acidity in cells and their nuclei<sup>144</sup>. In this thesis fluorescence powder sensitizers have been used to mark different groups of insects in Paper XI. This technique provides remote discrimination of insects which would not differ in their spectral signature. Insect lifespans and dispersion rates between habitats can be assessed by such methods. Remarkably, insects themselves have also been used as sensitizers; single molecule detection by lidar is in general not possible. Many insects, however, have extraordinary olfactory capabilities. One research group demonstrated how trained honeybees can be monitored by lidar and be correlated with the fumes emerging from landmines<sup>145</sup>.

## 2.5.4 Scattering

Single scattering refers to the process where photons instantly change their propagation direction. The origin of the effect can be associated with several elastic phenomena; Rayleigh scattering from dipoles such as molecules, Mie scattering from refractive spheres or random refractions by internal interfaces in turbid matrices. There are also inelastic scattering processes such as Raman scattering and Compton scattering. However, the relative probability of Raman scattering is negligible in comparison to elastic scattering, and Compton scattering only becomes significant for photons in the X-ray region. Rayleigh scattering is considered to be the dominant scattering process when the scatterer size is much smaller than the scattered wavelength. However, the process is in general much weaker than situations where Mie scattering occurs. The Rayleigh scattered intensity relates to the wavelength with a factor  $\lambda^{-4}$  with the implication that blue light has a higher scattering probability and red light has a low scattering probability. Rayleigh is polarization maintaining with the implication that perpendicularly scattered un-polarized light becomes linearly polarized since transverse waves cannot be polarized in their propagation direction. A daily example is the blue sky and red sunset; see Fig. 2.5.7.

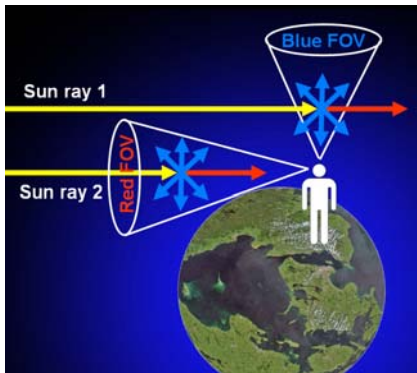


Fig. 2.5.7. At zenith observation a thin atmospheric slab is observed. In this situation mainly single scattered blue and polarized photons are seen. At sunrise and sunset direct observation of the sun occurs through a thick atmospheric slab. In this situation mainly ballistic unpolarized red photons are seen.

The single scattered light from the sun is linearly polarized in the arc perpendicular to the direction of the sun; however, atmospheric interaction is only close to single scattering when a thin atmospheric slab is observed close to zenith. Several animal navigation systems have been demonstrated to be based on the sky polarization. The angular scattering lobes of Rayleigh scattering are dull and do not provide much information regarding the scattering particles.

$$I = I_0 \frac{8\pi^4 \sigma^2}{\lambda^4 R^2} (1 + \cos^2 \theta)$$

Eq. 2.5.1

The particle perception of Rayleigh scattering is that the light excites the scatterer to a so-called virtual level with immediate de-excitation to the original state. When this de-

excitation ends in the same electronic state but for a higher or lower vibration state, the process is referred to as Raman scattering forming the basis of Raman spectroscopy<sup>146</sup> and related methods such as coherent anti-Stokes Raman spectroscopy (CARS)<sup>147</sup>. The energy difference of the exciting photons and the scattered ones can be related to vibration bonds of the molecules, and the methods are sometimes considered as a way to translate information available in the infrared into the visible regime. The spontaneous Raman effect is typically three orders of magnitudes weaker than Rayleigh scattering and typically weaker than fluorescence from most biological samples. When the scatterer is excited to a virtual level from a vibrational state which is not the ground state, and de-excites to the vibrational ground state, the scattered photons are more energetic than the impinging photons. This is referred to as anti-Stokes scattering, and can also be exploited for vibrational spectroscopy. Even if anti-Stokes scattering is less likely to occur than Stokes scattering, there are certain advantages of this, since the anti-Stokes components do not have to compete with fluorescence in the opposite triangle of the EEM.



*Fig. 2.5.9. Ludvig Lorenz derived a precise description of light scattered from a sphere and published the results in Danish twenty years earlier than Gustaf Mie. From this we can learn that knowing Danish is advisable for the successful physicist. Ludvig also derived Maxwell's equations, Advogados number and the Lorentz-Lorenz equation relating the refractive index to the polarizability. In his coffee breaks he would discuss maths with Christian Christiansen<sup>148</sup> whom we will hear more about later in this chapter.*

Mie scattering refers to solutions to Maxwell's equations for waves interacting with spherical particles. Apart from the dependence on the size of the scatterer, it is considered that the probability relates to the wavelength with an approximate factor of  $\lambda^{-2}$ : however, the scattering coefficient also scales with the difference in refractive index between the particles and the surrounding medium, both of which might not be spectrally flat in the region of interest. The Mie scattering lobes explain complex interference within the particle. When the wavelength is comparable to the particle size, detailed scattering patterns appear. Further, the scattering lobes differ considerably depending on the impinging polarization. Refined analysis of the lobes from single scattering including spectral, angular and polarization analysis can provide detailed information of the particle size, refractive index and absorption. Naturally occurring particles do, however, not have one particle size but typically a broad distribution of sizes, with the implication that the lobes are smeared out to a great extent. Nevertheless, natural situations do occur where preferences in scattering directions survive. The rainbow<sup>149</sup> is one example out of many other<sup>150</sup> intriguing atmospheric scattering phenomena.

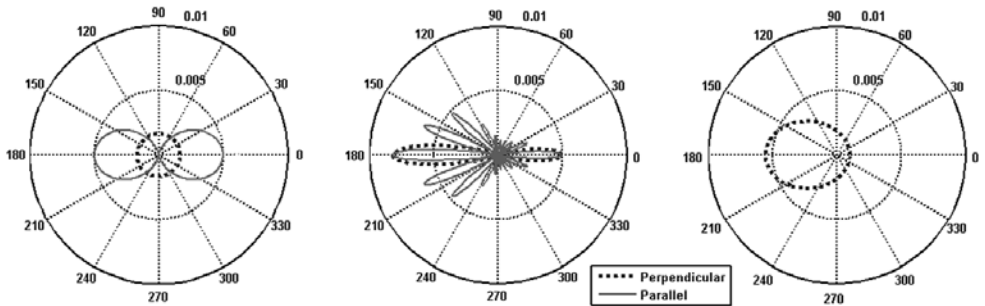


Fig. 2.5.8: Example of angular scattering probabilities according to Rayleigh and Mie theory; light impinges from the left in all subfigures. The outermost right is the corresponding Henyey gravitational point approximation of the Mie distribution. This particular example is scattering from 11  $\mu\text{m}$  water droplets at a wavelength of 2.9  $\mu\text{m}$  and shows a negative anisotropy factor with dominating back scattering. Parallel and perpendicular refers to the polarization and implies that the incident electric field is parallel or perpendicular to the plane of the plot<sup>151-153</sup>.

$$p = \frac{1 - g^2}{4\pi(1 + g^2 - 2g \cos \theta)^{\frac{3}{2}}} \quad \text{Eq. 2.5.2}$$

In several relations the detailed scattering lobes of the Mie type are mimicked by a simpler Henyey Greenstein function (Eq. 2.5.2), with a simple parameter,  $g$ , describing to what extent light is scattered in the forward direction. As we shall see in Chaps 3 and 4, the concept of scattering lobe polar plots is not only fruitful for the understanding of scattering processes but also for understanding instrumentation and detection schemes such as transmission and reflection measurements. This paradigm is introduced in Paper III but also helps the understanding of, e.g., Papers IV and XII. One fruitful result of the photon particle perception for Mie scattering, which is not apparent for the wave model, is the conservation of linear momentum. When photons change propagation direction by collision with particles the linear momentum must be conserved for the entire system. Thus photons transfer momentum to the particles. This can be exploited in laser tweezers, which can be used to manipulate particles on a microscopic scale or to measure extraordinary small pico Newton forces<sup>154</sup>.

Although the understanding of the details of single scattering processes is amusing, the outmost important aspect of scattering in relation to this thesis is the number of scattering events. More specifically, if scattering has occurred once or more than once, reflected light following either of the two cases is named the coherent or incoherent part of reflectance. This is of importance, because photons can potentially lose all memory of where they came from and what polarization they had, after only two scattering events. As already touched upon the blueness and polarization of the sky only exist because the observed light is scattered once. Had the atmosphere been ten times thicker the sky would neither be blue nor polarized. The conclusion can be reached turning the view to the horizon and watch how a thick atmospheric slab becomes increasingly pale.

Most biological samples scatter to an extent that the light enters what is referred to as the diffuse regime. Here the light no longer propagates in straight rays or in any well defined wave front, and the most fruitful perception is the particle model. The impinging photons will experience a random walk. Such random walks or so called photon-migration can be simulated for billions of photons by parallel Monte Carlo simulations<sup>155</sup>. Approximations of such behavior can also be made with the analytical diffusion equation<sup>156</sup>. Examples of highly scattering samples are: clouds<sup>149, 157, 158</sup>, canopies<sup>159, 160</sup>, snow<sup>161, 162</sup>, salt<sup>163</sup>, river water<sup>164</sup>, milk, fruits<sup>165</sup>, bread<sup>103</sup>, wood<sup>166</sup>, ceramics<sup>167</sup>, powders, porous media such as tablets<sup>168</sup>, human tissue<sup>37</sup>, and fibrous materials such as plumage<sup>169</sup> in Papers XIII-XV. The

sample properties governing such random walk are refractive index, the absorption coefficient, the scattering coefficient and the anisotropic scattering coefficient. The scattering coefficient,  $\mu_s$ , is the inverse of the scatter mean-free-path, and is typically measured in  $\text{cm}^{-1}$ . The scattering probability is often assumed to be constant per unit length; this assumption is reasonable for small suspended particles in the atmosphere or in aquatic solutions. However, for quasi-ordered biological matrices this might not always be the case. Further, following the Greenstein-Henyey simplification the reduced scattering coefficient is deduced,  $\mu'_s = \mu_s (1-g)$ . The inverse is the path length after which it can be assumed that light has lost all memory of the original propagation direction. Some research groups<sup>156</sup> claim the spectral dependence of  $\mu'_s$  to have the form:

$$\mu'_s = a\lambda^{-b} \quad \text{Eq. 2.5.3}$$

Here  $a$  is a measure on the amount of scattering and  $b$  carries information on the scatter size. In general in radiative transport the introduction of a scattering *constant* presumes that photons have a *constant* probability for scattering per unit length. This would imply that the distribution of path lengths between each scatter event would decrease exponentially. However, in ordered tissue this might not always be the case<sup>81</sup>, in particularly in situation where the coherent scattering is promoted in respect to the incoherent scattering<sup>69, 81, 170</sup>. The claim in Eq. 2.5.3 also assumes that refractive indices are constant throughout the spectral region of interest. In the NIR tissue optical window from 600-1000 nm this is in most cases true in biomedical optics and Eq. 2.5.3 can be fitted to experimentally determined scatter coefficients. In other situations and spectral ranges where strong absorption bands are present, this is entirely untrue, even for some of the most common constituents of human tissue such as water<sup>153</sup> and hemoglobin<sup>98</sup>. In the latter case the Kramer-Kronig (KK) relations, discussed previously, induce large deviation from the normal dispersion around the strong absorption of hemoglobin around 420 nm. Such change of refractive index in turn has a large impact on both the scattering coefficient,  $\mu_s$ , and the scattering anisotropy factor,  $g$ . Contrary to a widespread notion, scattering spectra can carry imprints of the absorption features.

When  $\mu_s$  is added to  $\mu_a$ , the total attenuation or extinction coefficient,  $\mu_{att}$  is obtained. This coefficient describes the length over which the coherent ballistic light vanishes. Since the scattering coefficient as well as the absorption coefficients are measured in  $\text{cm}^{-1}$ , the sample interaction entirely depends on the size of the sample. As discussed previously, methods which are hopeless to apply in adults might be feasible for infants<sup>107</sup>, and just as X-rays can provide detailed anatomical tomography for humans, it is entirely unusable for the anatomy of fruit flies yielding no contrast. Reversely, optical confocal microscopic methods only penetrate few hundreds  $\mu\text{m}$  into the human body, whereas the same methods provide amazing anatomical images of fruitflies<sup>171</sup> and provide functional *in-vivo* imaging of action potentials between single neurons<sup>110</sup>. Noteworthy, changing the spectral regime not only changes optical coefficients and penetration, but also changes the mechanism providing the contrast. In the previous example, X-ray imaging is based on atomic species contrast, whereas visible confocal microscopy is based on molecular contrast. In conclusion, certain studies might only be carried out on samples of appropriate size.

The anisotropic scattering coefficient, or  $g$ -factor, is a summation of the single scattering lobes discussed above, indicating to what extent light is scattered omnidirectionally and to what extent light is scattered in a forward direction. The value of  $g$  is 0 for omnidirectionally scattering and 1 for strictly forward scattering. As seen in Fig. 2.5.8 the value can even be negative indicating preferences for backscattering.

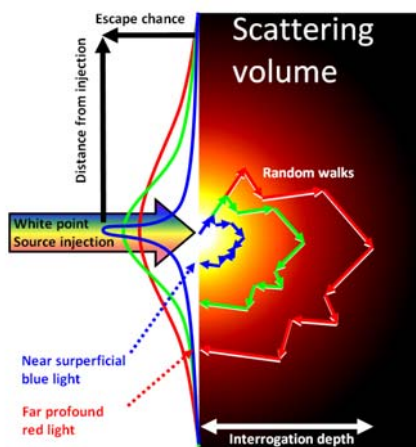


Fig. 2.5.9. The concept of scaling random walks is a fruitful result of Monte Carlo simulations. The concept is based on the point: What would a particular random walk have looked like, had the scattering coefficient been different? The answer is a simple isotropic scaling. The effect of absorption can be applied by considering the path length prior to the escape from the sample.

When summarizing millions of random walks, a number of features can be extracted: To what extent are the photons absorbed in the sample? To what extent are they transmitted? To what extent are they reflected? What is the mean depth they reach? What is the mean distance of surface escape in respect to the incidence point? By the reciprocity principle identical simulation can be performed for both the illuminating light or beam profile and the observed light or field of view (FOV). The product between intensity flux-field generated by the illumination and the flux-field reaching the detector constitutes the interrogation volume, i.e. the volume which has been interrogated by the light. This term will appear in various places throughout the papers of the thesis. In fluorescence spectroscopy where UV light impinges on the sample, the interrogation volume is often very superficial and extending few micrometers down in the sample, in NIR absorption spectroscopy interrogation depth can be centimeters, or even trans-illumination can be achieved, e.g., of the human skull<sup>172</sup> or a container with seeds.

Simulations of photomigration are often based on numerous simplifications and assumptions. As a consequence, the obtained results can deviate considerably from reality, and often these kinds of simulations are of limited practical use. The approach throughout this thesis has been instrumental, empirical and applied and no photomigration simulations were carried out. However, the mere idea of photo-migration and the awareness of the multiple aspects governing the sample interaction are highly beneficial for interpreting results and designing measurement schemes. The paradigm of photomigration has been extensively used in P2. In this construction for liquid spectrometry the refractive index, absorption, scattering, anisotropy and fluorescence spectra are disentangled by the use of combinatorial light paths. The approach of having more steady-state unique and complimentary measurands than unknown sample properties, is known from integrating sphere methodology<sup>173</sup> and spatially resolved methods<sup>174-176</sup> also pursued in P1. The task of disentangling absorption and scattering has produced vast piles of creative inventions during the last two decades. Some of the more sophisticated methods rely on time-of-flight spectroscopy where the photo migration travelling time is recorded in picoseconds<sup>104, 177</sup>. The idea is to assume a refractive index and in this way convert the travelling time to a path length after which the absorption coefficient can be determined. The refraction index is, however, not easily determined. It relates to the absorption through the Kramers-Kronig relation (KK) and further the sample might not be homogeneous throughout the interrogation volume.

One fruitful outcome for the understanding of the complex mechanism of random walk is the concept of scaling. Consider a random walk for a single photon not being subject to

absorption; see Fig. 2.5.9. If the scattering coefficient would have been less the entire walk would simply scale up, and if the scattering coefficient would have been larger, the mean-free-path would have been shorter and the entire walk would simply scale down. The absorption can in term then simply be applied to the length of the walk. This concept can explain how the microstructure of snow can be studied from a satellite at hundreds of kilometer altitude. When the snow microstructure collapses over time, the scattering coefficient decreases, the mean-free-path gets longer, the entire interrogation path length increases and the infrared absorption imprint of snow increases. This is one example on how incoherent reflectance can carry information regarding microstructure, which can be retrieved from far distances. This is discussed in details in Paper XV.

As said above, the scattering coefficient is defined as a constant probability of scattering per unit length, and thus a macroscopic unit requiring that the tissue can be considered homogeneous within this volume. For highly structured tissue this may not hold true. For human tissue it is considered that the main scatterers are the cell membranes, mitochondria and the nuclei. However, cells have a size and are to some extent positioned periodically. One way to quantify this is to map the refractive index tomographically in 3D and take the spatial spherical power spectrum<sup>81</sup>. Such analysis will reveal if there are dominant spatial frequencies, with the implication that there are preferred distances between the scatter events. If there are, then so called structural colors will appear in the coherent part of the reflectance. If the 3D spatial power spectrum is spherical symmetric then spectral features with a fixed wavelength appear. If the power spectrum is asymmetric, iridescent colors appear, the center wavelength of which depends on the angle of illumination and observation. One way to distinguish such colors from incoherent colors is to separately record the co-polarised and de-polarized reflectance; this was done in Paper X. The same methods are used in biomedical studies<sup>170, 178</sup>, where structural colors were even demonstrated from human tissue and correlated with the cell size for cancer diagnostics. Another example of ordered structures in the human body is the collagen fibers in the cornea<sup>179</sup>. Structural colors also appear in Papers XII-XV. The concept of dominant spatial frequency relates to technologies like Bragg gratings and X-ray diffraction in the area of crystallography<sup>180</sup>. However, the dominant spatial frequencies in biological systems are usually not as well defined as in crystals.

In the context of tomographic imaging of inclusions in turbid media, the scattering poses a severe challenge. Because of the random walk behavior the information on where the received photons have been is difficult to determine. In computerized tomography in the X-ray region the effect of Compton scattering is reduced by adding laminated collimators to the detectors, which only allows photons with the initial propagation direction of the source to pass, the so-called ballistic photons. In the visible regime and on the scales of human diagnostics, scattering is much more severe. Some approaches are referred to as diffuse optical tomography (DOT)<sup>181, 182</sup>, and are attempts to solve the inverse problem numerically. This is in many aspects similar to de-convolution with the point spread function. Such methods are used in astronomy and microscopy, and the results are normally poor. The reason for this is that even for a perfect photo-migration model, the working principle of deconvolution is that spatial resolution is traded on expense of dynamic resolution and certainty (signal to noise ration, SNR). This will be discussed more in Chapt. 4. An alternative strategy to the ill-conditioned inverse problems is the use of ballistic light. Ballistic light is not scattered, and thus provides high spatial information about the turbid medium. A challenge is that the ballistic photons quickly become outnumbered by the scattered ones. Ballistic light can be observed naturally, e.g. in the atmosphere, in some cases under the right conditions, for instance when the cloud conditions are right, a sharp edge of the sun can be seen through the cloud layer.

Apart from preserving its propagation, ballistic light is also the first to arrive through a turbid sample. With pulsed mode locked lasers and time-resolved detection in the picosecond regime, the photo migration traveling time can be recorded. The earliest light to arrive has also travelled in straight paths and can provide sharp imprints of inclusions inside the turbid medium<sup>183</sup>. Steady state detection in combination with or promoting of ballistic photons has also been suggested in spectral regions with high absorption of, e.g., water. Here the idea is, that the longer path lengths of the non-ballistic light in comparison to that of the ballistic propagation will result in a strong suppression due to absorption<sup>184, 185</sup>. An additional way to selectively promote ballistic photons from turbid samples is to find a certain spectral point where the refractive index of the matrix medium intersects the refractive index of the scatterers. This was investigated by the doctoral supervisor of Niels Bohr, Christian Christiansen, and is termed the Christiansen effect. Originally the effect was studied for solution with glass powders<sup>186, 187</sup>, but the effect has also been demonstrated to occur naturally in relation to aerosol particles<sup>157, 188-195</sup>. The effect is tightly related to the Kramers-Kronig relation and for this reason it primarily shows up for air-solid matrices towards the infrared<sup>196</sup> and terahertz<sup>197</sup> regime. In Paper XV the details of the interplay between refractive index, absorption, scattering are discussed for bird plumage and is tied to the Christiansen effect and the Kramers-Kronig relations.



*Fig. 2.5.10. The Danish physicist Christian Christiansen was born in Vostrup in the darkest part of Jutland and dreamt of becoming an engineer like the author of this thesis. Instead he ended up in physics, experimenting with abnormal dispersion, crystallography, magnetism, heat conduction and spectroscopy on liquid and powder mixtures. He was the doctoral advisor of Niels Bohr.*

The idea of photon migration in bio-photonics mainly considers elastic photon-migration. Fluorescence processes can be included by estimating an absorption field of the energetic light in the sample, and then consider this absorption field as a secondary light for fluorescence light. When approaching the thermal IR regime, photo migration becomes highly inelastic in the sense that each volume element absorbing a photon will increase its local temperature and in term emit a new thermal photon. In contrast to fluorescence, the energy of the emitted photon can be either higher of lower than that of the impinging photon. In fibrous or porous media this constitutes a highly complex situation where absorption, emissivity, scattering, refractive index, Christiansen effects and the evanescence effect interplay. In Paper XV it is speculated how such inelasticity and spectral broadening might enhance structural colors.

---

# Chapter III

## 3. Instrumentation

---

### 3.1 Light sources

#### 3.1.1 Light emitting diodes

The light emitting diode (LED) was introduced as a commercial light source 1962 by Nick Holonyak Jr. while working at General Electric Company<sup>198</sup>. The device is an extremely simple, robust, compact and inexpensive light source. The operation is based on a pn-junction semiconductor, where an electron instantaneously decreases its potential energy from the energetic conduction band to lower valence band. A popular description in solid state physics is referred to as radiative recombination of electron and hole pairs. The energy drop experienced by the electron is referred to as the bandgap,  $U_0$ ; this value depends on the material choice and doping, and is specified in the datasheet of the devices. The band gap can also be estimated with a simple multimeter, by measuring the currently-voltage dependence (UI-curve) and extrapolating the U to zero current. In an ideal case with a direct band gap the emitted wavelength corresponds reciprocally to  $U_0$  through Planck's constant.

$$\lambda = \frac{h}{U_0} \quad , \quad h = 1240 \text{ nm eV} \quad \text{Eq. 3.1.1.}$$

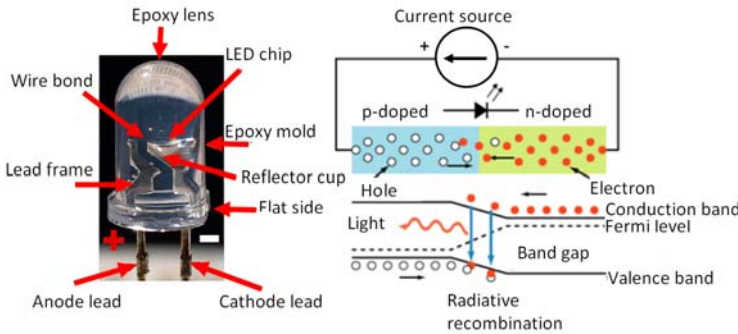


Fig. 3.1.1. Left: common epoxy casing of LEDs. The epoxy serves both for stabilizing the parts, focusing and index matching. The chip is placed in a reflecting cup, which is also the cathode lead. Right: Common diagram in solid state physics showing a representation of the potential energy drop in a LED bandgap. Public domain images adapted from Wikipedia.org.

LEDs are produced in a large variety of casings, but the most common and inexpensive form is the molded epoxy dome shown in Fig. 3.1.1. The epoxy serves both for fixing the anode and cathode leads, for improving emissive yield through index matching from the semiconductor material, increasing the so-called escape cone. The molded dome together with the cathode reflector cup, in which the chip is mounted, also serves for beam collimation. The collimation is determined by the chip size, the dome curvature and the chip position within the mold. The chip size is in the order of hundred micrometers and the collimated light can be potentially harmful to the human eye, although safety regulations have not been fully established. Epoxy can be made transparent from 350-1700 nm. LEDs have been demonstrated with emission wavelength down to 210 nm<sup>199</sup>. LEDs are commercially available from 240-4800 nm<sup>200</sup>. Deep UV LEDs are typically mounted in a can with quartz window or lens, whereas MIR LEDs and optically pumped LEDs are

typically mounted in an exposed configuration with a Si ball lens directly attached onto the chip. In most cases beams are strictly diverging, but some options based on ball lenses offer a focus at short distance. The spectral bandwidth of the emission often just referred to as full-width-half-maximum (FWHM) generally relates to the peak emission wavelength with a factor square,  $FWHM \sim \lambda_{peak}^2$ ; typical values are 15 nm FWHM at 405 nm and 40 FWHM at 810 nm. Such band width is mainly suited for acquiring solid-state spectra of, e.g., biological tissues; in P2 each band is additionally split in two by long pass filters, this resembles the function of oil droplets in bird retinas<sup>201</sup>. A few application of LEDs in gas sensing have been demonstrated by gas correlation techniques in the UV<sup>202</sup> or with optically pumped LEDs in the MIR<sup>203</sup>. Temporal response of LEDs in commercially available units goes down the order of hundreds of picoseconds<sup>204</sup>; this is mainly achieved by electrical impedance compensation.

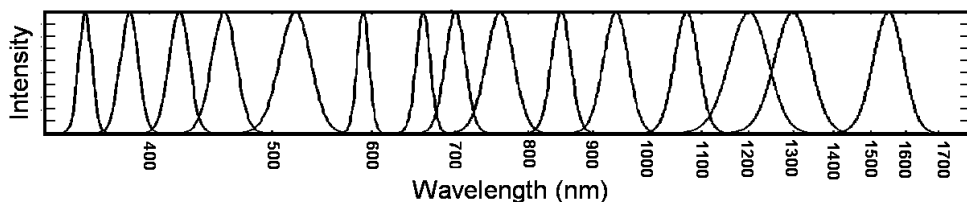


Fig. 3.1.2. Band positions and widths of LEDs used in P2. The range covers five multiples of wavelength span, three different detectors are employed throughout the regions.

An idealized LED conducts current perfectly as soon as the voltage is larger than the bandgap. In practice, the semiconductor material has a finite conductance, with the consequence that the UI curve has a slope similar to that of resistors for voltages greater than  $U_0$ ; see Fig. 3.1.3. The device might even conduct a weak current for voltages lower than  $U_0$ . This is referred to as shunt resistance or sub-threshold turn on.

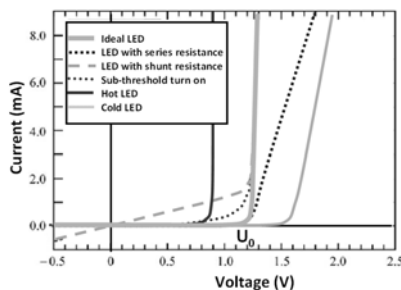


Fig. 3.1.3. Idealized LED and effects found in practice. Note that the effects are exaggerated.

Full exploitation of LEDs for optical diagnostic instrumentation requires profound insight into the interaction between the operation of the device and the temperature of the LED chip. The ratio between electrons passing the device and photons emitted is referred to as the emissive yield,  $\eta$ . This efficiency is steadily increasing year by year thanks to improved technologies regarding doping purity, index matching methods and structured interfaces preventing internal reflections. The general trend is that optical output power for a device doubles every three year. The electrical power entering the device is given as  $P_{elec} = UI$  and the optical energy leaving the device is given as  $P_{phot} = \eta UI$ . The remaining power is converted to heat in the device  $P_{heat} = P_{elec} - P_{phot} = UI(1 - \eta)$ . This heat is mainly dissipated by heat conduction through the cathode lead. Thus the dissipated heat scales linearly with the

temperature difference between the chip and the ambient,  $P_{diss} = \Delta Tk$ . The chip temperature is therefore ruled by the differential equation:

$$\frac{\delta T}{\delta t} C = P_{elec} - P_{phot} - P_{diss} = UI(1 - \eta) - \Delta Tk \tag{Eq. 3.1.2}$$

C is the heat capacity of the device. The main limitation for the maximal current tolerance for a LED, determining the output power, is the thermal dissipation. High power LEDs are often mounted directly on aluminum plates rather than arranged in epoxy molds. This increases the thermal conductance and allows higher steady state electrical and optical powers. One aspect of this slow thermal constraint is that the devices can operate beyond the max current tolerance for short times below one millisecond. This allows pulsed operation where the emitted intensity can typically be a factor 10 higher than the steady state power during 10% of a duty cycle, the remaining 90% off-time is required for cooling. This approach was implemented in P2. Pulsed operation should be complemented by a high-pass safety circuit which would switch off the device in case of any hang ups caused e.g. by software. Attending to the efficiency,  $\eta$ , it is noteworthy that increasing the efficiency from, e.g., 60% to 80% not only implies 33% more light, it also implies 50% less heat; therefore the current can be increased by a factor two with the consequence that increasing  $\eta$  by 20% units from 60% to 80% allows the output power to increase to 267%. This is one explanation for the exponential technological development of LED output powers. To further increase the complexity of the thermal interactions  $\eta$  is highly sensitive to temperature. Generally, the efficiency decreases exponentially with increasing temperature.

$$\eta = \eta_{amb} e^{\frac{T_{amb} - T}{Tk}} \tag{Eq. 3.1.3}$$

This means that when turning on the LED at a constant current, the temperature increases, the efficiency decreases causing the temperature to rise additionally due to an increased fraction of the electrical power turned into heat. This is a great difficulty with high power LED in the lighting industry. In diagnostic applications, as in this thesis, it implies that whenever a LED is used, the light emission might vary with time. For instance, the chip temperature is increased when in operation and could vary in a sequence of subsequent measurements, which is of particular importance when acquiring reference data. Then the emitted power is less although the driving current is constant. The thermal dependence of  $\eta$  is in general larger for lower  $U_0$  or red LEDs than for blue LEDs. Failing to account for such effects when using LED for spectroscopy could not only scale the absolute acquired spectrum but even tilt it.

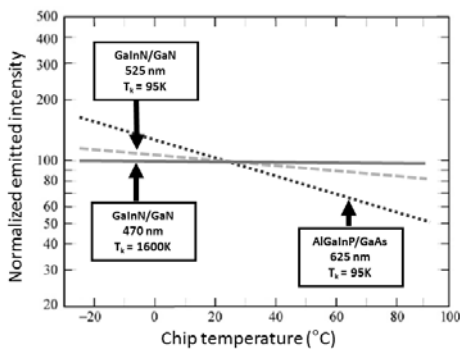
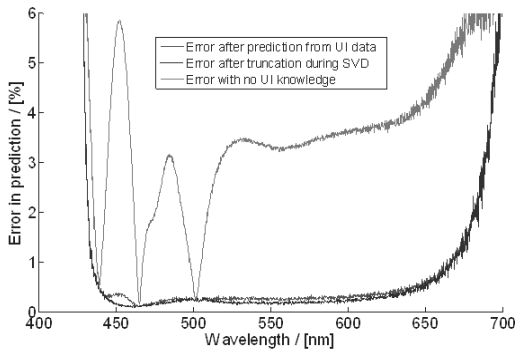


Fig. 3.1.4. Thermal dependence of the emissive yield of LEDs. Red LEDs are more susceptible to temperature changes than blue LEDs. This is an important detail in analytical applications. Data from Toyoda Gosei Corp. 2004

To further complicate the performance of LEDs in relation to the chip temperature, the entire UI characteristic curve changes considerably depending on the temperature<sup>205</sup>. Increased chip temperature has mainly two consequences; the band gap  $U_0$  diminishes and the semiconductor conductance increases; see Fig. 3.1.3. This is the reason why LEDs should always be operated by a constant current source and not a constant voltage source, since the last mentioned fact would result in an unstable vicious circle where increasing temperature causes increased current with the consequence of a burned device. Adding the thermal impact on quantum yield, Eq. 3.1.3, and the IU characteristics to Eq. 3.1.2 the following is obtained:

$$\frac{\delta T}{\delta t} C = U_T I_{set} \left( 1 - \eta_{amb} e^{\frac{T_{amb}-T}{T_1}} \right) - (T - T_{amb}) k \quad \text{Eq. 3.1.3}$$

As much as the thermal dependence of the UI curve complicates the use of LEDs, it can also be of great help. If the driving circuitry is designed in a manner allowing the UI curve to be measured simultaneously during the operation, the UI curve provides precise information on the chip temperature. From this value the precise absolute emission spectrum can be predicted. For simple LEDs this is mainly a matter of absolute emission power, whereas the FWHM increases in the order of 1% per Kelvin<sup>205</sup> and the spectral shift is a very small effect in the order of 0.006% per Kelvin<sup>206</sup>. The absolute emission intensity was adjusted for, e.g., in P2<sup>99</sup> and P4. For white LEDs, which are 470 nm InGaN devices coated with down-converting Ce:YAG producing a yellow emission, the spectral emission relates to the device temperature in a complicated manner including several pivot points. In P3 and Papers VIII, IX, XIII and XIV the reflectance is measured with such devices in the range 440-700 nm. The reflectance is calculated by dividing the intensity from the sample with a light spectrum predicted from the UI characteristic curve. The improvement of taking advantage of the UI curve is illustrated in Fig. 3.1.5.



*Fig. 3.1.5. Reflectance measurements using LEDs should take advantage of the information regarding the chip temperature available by measuring the UI characteristic online. Doing this can increase the accuracy by an order of magnitude. Here several spectra are acquired of the same gray reference with different instrument temperature. The upper curve is the expected error when no UI information is considered. The lower curve the error when correctly predicting the three detectable spectral components. The middle curve is a simple polynomial prediction of the spectral scores. The procedure will be explained further in Chap. 5.*

LED based instrumentation for optical diagnostics often exploits the low cost of LEDs and reciprocity principle. Here, typically an array of LEDs is implemented for the purpose of added spectral bands or acquisition of geometrical features. The price of the standard epoxy LED used in this thesis is in the range 0.1-10 dollars, the cost of deep UV LEDs such as the one used in Paper XIV is in the order of 100 dollars. Since the detectors and associated amplifiers and DAC are often more costly than LEDs and drivers, many systems have a plurality of sources and a single detector. This is the case for the multispectral microscopes in P4, Papers II-IV and also a commercial macro imager<sup>207</sup>. Such instruments are based on LED multiplexing, where one LED is turned on at a time. One advantage of this is that LEDs can be driven beyond their steady state thermal limit and will cool down while other LEDs are active. A LED multiplexing spectrometer can be assembled by anyone using

standard components from a hobbyist shop. Variations appear in several publications<sup>208-210</sup> and patent applications<sup>211-213</sup>. Multiplexing LED spectroscopy often requires some sort of beam combination, especially for multispectral imaging where high demands on spatial homogeneity of the illumination are required. This can be achieved by several means; examples are costly dichroic beam splitters or inefficient fiber couplings. In P3 and Paper VIII coaxial intersection and a cylindrical symmetry is employed; another approach is to employ opal diffusers or diffusely reflecting white cavities; this is employed in P4, Paper 3 and in a commercial solution<sup>207</sup>. In general, LED multiplexing has much higher photon economy than spectroscopy on the detection side where the majority of the light is discarded by filters or spectrometer slits.

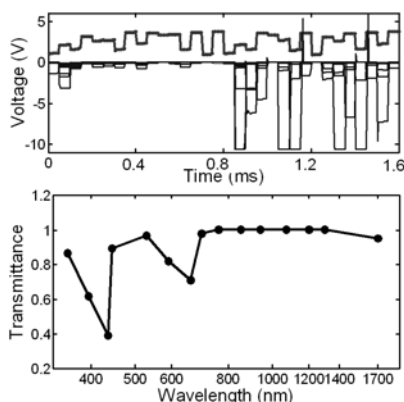


Fig. 3.1.6. Top: Time sequence of complete scans through all 30 sources in P2; see bands in Fig. 3.1.2 and instrument in Fig. 1.4.1. The positive curve is the common anode voltage related to the emitted wavelength, negative curves are the intensity signals received by all detectors. Bottom: Acquired transmittance for green household colorant covers a span of five multiples of wavelengths. This can hardly be achieved by any conventional grating based spectrometer<sup>99</sup>.

LEDs have been employed as excitation sources in fluorescence spectrometers<sup>214</sup>. A particular advantage is the use of several LEDs for multi-excitation fluorescence spectroscopy<sup>125</sup>. This can even be exploited for instantaneous acquisition of EEMs<sup>215</sup>. The methods becomes increasingly attractive as the efficiency of blue and UV LEDs increases. At present, single UV LEDs at 360 nm can deliver several hundreds of milliwatts continuously. The power can be increased by pulsed operation or LED chip configuration if brightness is not the constraint. At lower wavelength the emission power are much lower though. One important detail when using LEDs for fluorescence spectroscopy is the clean up of the light. Although solid state physics theory<sup>216,217</sup> claims that the spectral emission is given by

$$I_{\lambda} = \sqrt{\frac{hc}{\lambda} - U_0} e^{-\frac{hc}{kT\lambda}}, \quad \text{Eq. 3.1.4}$$

indicating a clear cut off wavelength towards longer wavelength at  $hc/U_0$ , in practice the spectral emission rather resembles a Gaussian. Therefore it is necessary to suppress the long wavelength tail of the emission with short pass filters to achieve high performance fluorescence spectroscopy<sup>218</sup>; this is implemented in P3 and Paper VIII. Thanks to the fast modulation times, LEDs can also be used to measure fluorescence lifetimes. This is either achieved through recording the attenuation and phase shift in the frequency domain<sup>219-221</sup> or preferably by time correlated single photon counting<sup>204</sup>. LEDs are particularly attractive in time correlated single photon counting (TCSPC) due the low requirements on emission powers. Identical detection schemes can also be used with elastic techniques for the purpose of time of flight spectroscopy, where the scattering and absorption can be separated<sup>222,223</sup>. This can be implemented in diffuse optical tomography (DOF) where the blood oxygenation in the brain can be monitored in respect to various stimuli<sup>172</sup>.

An interesting aspect of LED applications is the reverse operation as photo sensitive detectors. Although devices are optimized for specific purposes, in general any optical transparent pn junction can operate either as a LED, as a photo voltaic or as a photodiode. The operation can be summarized by the quadrant of the operation point on the UI curve; see Fig. 3.1.7

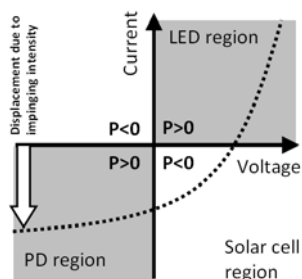


Fig. 3.1.7. LEDs can in general operate in different regimes: As LEDs, as Photodiodes, or as Photovoltaics. The regime is determined by the quadrant in the UI characteristics where the operation point is.  $P$  denotes the power consumed by the device.

When LEDs are used in reverse voltage mode as photodiodes they become spectrally selective devices, comparably to a traditional photodiode with band pass interference filter attached, but to a percent of the cost. The spectral sensitivity bands are encountered right next to the emission bands, displaced towards lower wavelengths in relation to the emission bands<sup>224</sup>. This shift is identical to the discussion regarding Stokes shifts, mirror rules and absorption and fluorescence spectra in Chap. 2 Sect. 2.5.3. One application of LED as detector in remote sensing and atmospheric studies are long-term sun photometry measurement of total air mass, aerosols and water vapor; see, e.g.<sup>225</sup>.

### 3.1.2 Arcs / Flash lamps

Short arcs discharge lamps and flash lamps are used in several of the papers. The devices are either used to produce white light for elastic spectroscopy or internally in lasers for pumping purpose. Both devices are quartz envelopes containing Xe gas and/or Hg vapor and two or three electrodes. Although carbon arc lamps were presented as early as 1802, the Xe-Hg arc, which is most commonly used today, was not developed until Second World War in Germany. Here they were applied in search lights for anti air warfare. The short arcs were ideal for this purpose due to the fact that they produce very intense light in a very small discharge volume, providing brightness beyond any other existing light sources at the time, and thereby also allowing collimating light beyond what was previously possible. The light sources, have since then also been developed for projectors for cinematic entertainment. The pressure in short arc lamps ranges up to 100 atmospheres and can be considered explosive in case of an envelope fracture. Thus handling requires severe protective wear. The most powerful short arc lamps are water cooled, and the envelope increases in temperature to an extent where afterglow of the quartz can be seen long after operation of the device. Fingerprints on the quartz envelope would most definitely turn into coal and cause tensions in the envelope eventually making it explode. Many such devices also emit a considerable amount of carcinogenic UV so that skin exposure should be avoided. Further, this UV light also produces toxic ozone from oxygen, and room ventilation is advisable. The high pressure requires an ionization pulse of up to 100 kV, but once operating the voltage drop is four orders of magnitudes, but with currents as high as 100 A. From this it can be understood that the peripheral driving and cooling circuitry is extensive. The emission spectrum is continuous from 200-2000 nm but included several spikes related to the atomic lines of Xe and Hg. Both the intensity and the spectral shape of the light sources are inherently unstable and affected by plasma oscillations, so although the source is bright it is not ideal for analytical applications unless the output is continuously monitored.

Flash lamps are also mainly based on Xe and is in general the same as short arcs but operate pulsed in an entirely different domain with high voltage pulsed and lower average current and pressure. They constitute user friendly and compact sources, which can be encountered in flashes for compact cameras and cell phones. The pulsed operation enhances the fraction of light emitted in the UV region; in bio-photonics they are popular for elastic spectroscopy in the UV-VIS regime. In this thesis a compact fiber coupled Xe flash was used. Although pulsed, such devices are often used as continuous light sources at repetition frequencies in the order of 100 Hz. This is not optimal in terms of collecting dark current, considering that the light source is off during 99.9% of the exposure time. However, by integrating measurements over a second fairly stable intensity and spectral shape is obtained even if the individual pulses vary considerably. High power flash lamps are also extensively used for laser pumping including the first operational laser<sup>226</sup>. In that laser the flash lamp was coiled around the laser crystal. Modern solid-state lasers use linear flashlamps aligned parallel to the crystal. The entire assembly of laser crystal and flash tubes is placed in either a diffusely white reflecting cavity or with flash lamp and laser rod at the foci of a cylindrical elliptical reflector, ensuring maximal transfer of energy from the flash lamp to the crystal.

### 3.1.3 Lasers

Light amplification by stimulated emission of radiation or lasing, can be achieved in a so-called gain medium with negative electronic temperatures or electronic population inversion rather than the Boltzmann distribution in normal conditions. Laser action occurs naturally in certain hot star environments<sup>227</sup>, in the thermal infrared CO<sub>2</sub> 10.33  $\mu\text{m}$  line in the upper Martian atmosphere<sup>228</sup> and possibly on earth at the 337 nm UV nitrogen line during lightning storms<sup>229</sup>. Stimulated emission was introduced by Albert Einstein in the early twentieth century. Following development of the maser (microwave amplification by stimulated emission of radiation) the first laser in the optical regime, based on chromium doped ruby, was demonstrated by Theodore H. Maiman in 1960<sup>226</sup>. Today, 50 years later, laser refers to devices from anything between tiny structures of a few microns (vertical-cavity surface-emitting laser, VCSEL<sup>230</sup>) for communication, to large scale facilities of hundreds of meters for fusion experiments (National Ignition Facility, NIF<sup>231</sup>). The peak powers of lasers today reach petawatts and average powers of megawatts<sup>232, 233</sup>. The high peak powers enable experiments investigating non-linear and relativistic optics, whereas high average powers have welding and cutting applications in material processing, and as weaponry<sup>233, 234</sup>. Smaller diode lasers are extensively used in commercial electronics for computer communication and optical storage. Today stimulated emission can be obtained at wavelength from x-ray to microwaves extended by the introduction of free electron lasers (FEL)<sup>235</sup>. The range for compact and practical applications is, however, much more limited. Extensive literature<sup>236</sup>, courses, and research cover the physics, design, construction and countless applications of lasers (See, e.g. <sup>237</sup>). In this thesis commercial lasers are used as light sources for diagnostic purpose. This is particularly attractive since the lasers can be made to produce emission approaching theoretical Dirac functions in all imaginable domains: spectral content, spatial origin, propagation angle, temporal pulses and polarization. These domains will be discussed in details in the next chapter, but in general optimal instrumentation has Dirac-like instrumental functions, matching the fact that arbitrary responses from samples can always be described as a sum of Dirac functions. For non-optimal instrumentation with broad response functions, e.g. in time or space, the Dirac response is often approached computationally by deconvolution by the impulse response or point spread function, respectively. However, although such approaches improve the temporal or spatial resolution they also increase the uncertainty of the estimate.

In this thesis three types of UV lasers in the range 266-445 nm are used for exciting fluorescence; continuous wave (CW) diode lasers (LD), flash-lamp pumped solid state lasers, and mode locked lasers. The blue CW lasers are typically devices packaged in Ø5 mm cans, and have experienced a steep exponential technological development of efficiency and output powers through the last decade. Especially their applications for Blu-Ray video discs for home entertainment operating at 405 nm wavelength have driven the development. The cost per output power unit of the devices themselves is comparable to that of LEDs. However, the peripheral driving circuitry is slightly more sophisticated and requires fast response to insure that the LD does not burn itself. A considerable advantage over LEDs is, however, that the brightness and total output power can scale beyond what can be produced by LEDs. Today blue CW LD modules emitting in the order of 1W are available to the general public for the cost of 100 dollars<sup>134, 238</sup>, research grade products with proper specification cost in the order of 1000 dollars, however. As a comparison light focused from such devices easily reaches irradiances per unit area a million times stronger than full daylight at the equator. As an example such light is strong enough to burn through most organic materials, and there are several potential associated laser safety concerns both in relation to eye safety and fire safety when operated.

The operation principle of pumping and thermal dependence resembles those discussed for LEDs; however, the geometry of the simplest LDs differs in the way that light is emitted from a polished side of the depletion layer. As a consequence cylindrical lenses are often required to achieve a circular symmetrically beam. Also LDs are typically installed in a can in front of a photodiode to monitor and control the emitted power. Laser diodes are typically commercially available at the discrete wavelengths 375, 395, 405, 445, 473, 525, 635, 660, 760, 808, 980 and 1550 nm. The simplest devices have a couple of nanometers broad multimode emission which is an order of magnitude narrower than LEDs, other single mode LDs emit a much narrower width and can be used for gas sensing<sup>101</sup> or laser cooling<sup>239</sup>. In these applications the spectral line is shifted by controlling current and temperature. Although the device is referred to as CW it is in general operated in a modulated manner, and all LDs can be logically TTL modulated up to the order of kilohertz. This improves diagnostic application in terms of lock-in detection. This is for instance the case in Paper VII, for the purpose of background subtraction which is crucial for the application in a clinical operation theater. For telecom purposes modulations up to gigahertz are achieved.

The solid state laser used in the lidar Papers VI, X, XI, XIII, XIV is a table top laser with a gain medium of Neodymium doped YAG crystal rods ( $\text{Nd:Y}_4\text{Al}_5\text{O}_{12}$ ). Apart from the optical assembly taking the space of a small table, there is also an associated power supply with the size of a small fridge, a pump station for cooling water and gas tubes for nitrogen flushing. In total, the various parts of the light source add up to more than one hundred kilograms. The size and weight of the power supply is mainly due to the large high voltage capacitors with the size of car batteries, which are used to accumulate the energy disposed in the flash lamps. The cost of such systems is around 100000 dollars. The operation of modern devices normally requires 20 minutes of warm-up for thermal stabilization and long term operation is associated with continuous maintenance in terms of changing flash lamps, cooling water, filters and nitrogen. Some improvement in terms of simplicity of operation can be achieved by air cooling and pumping by LEDs or LDs. Despite the bulkiness, flash lamp pumped Nd:YAG lasers are the most common for lidar applications and form the basis both for networks of aerosol monitoring lidars<sup>240</sup>, for most fluorescence bio aerosol lidar work<sup>241</sup> and diode pumped Nd:YAG for some of the few existing space borne lidars<sup>242</sup>. Such laser systems typically emit pulsed radiation with repetition frequency in the range 10-50 Hz which is a considerable limitation for the biosphere monitoring examples presented in this thesis. Another research group also makes use of solid state Nd:YAG laser

for biosphere lidar monitoring<sup>142, 243</sup>, with repetition frequencies in kHz but with much weaker pulses. This is referred to as micro lidar and can mainly be exploited for elastic spectroscopy in lidar relations.

The optical scheme of the Nd:YAG laser, used in this thesis, consists of four water cooled highly reflecting white cavities made from highly scattering ceramics. The cavities are arranged in a U-shape which highly reflecting laser line mirrors folding the beam. Each cavity houses a Nd:YAG rod and two parallel flash tubes used to pump the lasing medium from the side. When the energy in the capacitors in the power supply discharges through the inert gas in the flash tubes, the gas is ionized and the cavities are flooded with light for several microseconds. The light is absorbed by various lines of the neodymium ions throughout the wide spectral range, leaving the ions in an excited state. The neodymium YAG laser in turn commonly emits at 1064 nm. By incorporating a Brewster angled plate in the cavity a clean linear polarization of the output beam is achieved. Such laser emission occurs in bursts of spontaneous pulses within the flash lamp envelope. The laser is then operated in the so-called long pulse mode. A special fast electro-optical polarization switch known as a Pockels cell or a Q-switch is positioned between the first and the last two cavities preventing lasing from occurring spontaneously. The inhibiting function of this device can be compared to control rods in a nuclear reactor. By tuning the relative delay from the flash discharge to the opening the Q-switch lasing can be postponed to a point where the gain medium is saturated, and all energy can be released in a single pulse of an approximate duration of 16 ns with an energy in the order of 1J for the case of the system used in this thesis. Such high peak intensities are well suited for frequency doubling, tripling and quadrupling (SHG, THG and FHG). This is achieved with non-linear crystals positioned in an oven prior to the laser exit. The harmonics are emitted coaxially with the fundamental, and later separated by dispersion in a Pellin-Broca prism; the unwanted parts are dumped in thermally dissipating beam stops. The harmonic generation is highly sensitive to the temperature of the crystal, the orientation of the doubling/mixing crystal lattice, the divergence and polarization degree of the fundamental laser because of strict requirements for phase matching. The resulting wavelengths are 532, 355 and 266 nm, mentioned in order of decreasing generation efficiency. A considerable amount of time, during the lidar studies, was put in tuning the angle of the doubling crystals in order to find the optimal condition; especially for FHG in Paper XIV where thermal stabilization could not be implemented. According to the specification 80 mJ of 266 nm light should be achieved, we were able to get 20 mJ. The radiation is invisible but can be detected either with an indicator of white paper fluorescence or photo-acoustically on the termination, using the naked ear. The temporal pulse envelope decreases with the harmonic order, thus for the 266 nm radiation we obtained pulses of approximately 5 ns duration. In lidar context this corresponds to a spatial pulse length of 1.5 m and determines the minimum distance between two separable objects coaxially, without deconvolution methods. The orientation of polarization also changes 90° for each harmonic order. Both the fundamental and the doubled Nd:YAG are potentially harmful to the human eye and safety eyewear is required. The third harmonic at 355 nm is invisible to humans and less dangerous because of corneal blocking but still safety eyeglasses are needed. The wavelength is covered by avian vision and is not eye-safe for birds. However, we found that the third harmonic did not permanently damage the visual function of the damselflies in Paper X. This might be explained by the alternative eye-design of compound eyes. The fourth harmonic is not transmitted by the cornea of neither birds nor humans, it is therefore not focused on the retina, and eye-safety in the far field is not a concern. However, the radiation can be considered carcinogenic and for this reason Latex gloves and acrylic glasses were used by the personal operating at the remote target location.

Mode locked lasers as the ones used in Paper VIII and IX, can be understood as several superimposed continuously emitting lasers, emitting at different and equally spaced spectral lines. Such periodic lines are referred to as longitudinal modes, and are associated with the multiple wavelengths giving rise to constructive interference between themselves in laser cavities. If the lasing lines maintain a fixed phase relationship in respect to each other, constructive interference will only occur seldom between all modes whereas destructive interference will dominate for the remaining time. The consequence of this is that although each lasing line is emitting continuously the sum of the laser lines will be pulsed. The larger span of modes the shorter the pulse. Therefore, the device needs to support lasing in a broad range based on a broad fluorescence of the gain medium. For example, a HeNe gas laser can support 3 modes, whereas a solid state titanium sapphire laser can support up to 250000 modes. Through a Fourier paradigm, it can also be concluded that a Gaussian apodization of the laser lines produces single Gaussian temporal pulses with very large contrast to the off period. In order to achieve a fixed phase relationship between the laser lines a device referred to as a semiconductor saturable absorption mirror (SESAM) is used. Such a mirror has an intensity dependent reflectance and promotes laser pulses with high intensity which are also the continuous laser lines with a fixed phase relation shift with respect to each other. The repetition frequency of a mode locked laser is given by the round-trip time in the laser cavity and cannot be controlled during operation. The applications of mode-locked lasers include frequency combs, ultra precise clock defining the second, sources for chirped pulse amplification for ultra intense light-matter interaction studies and pump-probe schemes in femtochemistry. In biophotonics, mode-locked laser are popular in non-linear microscopy such as two-photon, coherent anti-Stokes Raman spectroscopy (CARS<sup>147</sup>) or harmonic generation microscopy<sup>179</sup>. On a macro scale biophotonic applications includes time-correlated-single-photon-counting (TCSPC) which can be used for time-of-flight (TOF) or fluorescence lifetime spectroscopy (FLS). FLS was employed in Paper VIII and IX. The low demands on intensity for mode-locked lasers used in TCSPC implicates that they are typically shoe-box sized devices emitting pulse energies of few nano joules with repetition frequencies in the multi Megahertz regime. Even mode-locked lasers are suitable for harmonic generation, and one of the sources used in Paper VIII and IX is a tripled Nd:YAG laser as discussed in the previous paragraph.

### 3.1.4 Filament bulbs

Following Thomas Edison's pioneering work in inventing and fabricating long lasting filament light bulbs in the end of the nineteenth century, the gas filled tungsten bulb was developed. These inventions encouraged the development of public power grids and extended the usage of the hours after dark. Initially filaments were made from carbon wires, the element with the highest known melting point. Today filaments are mainly made from tungsten with the second highest melting point at 3695 K, and the operation temperature is slightly below. The emission process is the black body radiation and the spectral content is given by the Planck distribution discussed in Chap. 2 and Paper I. The peak emission wavelength is given by the reciprocal relation in Wien's displacement law. Although the operating temperature of tungsten filaments is high, it is only half of the temperature of the surface of the Sun, and since the peak emission of the Sun is in the center of the combined human sensitivity band, filaments peak at twice the center wavelength of human vision. This partial overlap implies poor efficiency for lighting applications.

$$\eta = \frac{\int Planck(T, \lambda) S(\lambda) d\lambda}{\int Planck(T, \lambda) d\lambda} \quad \text{Eq. 3.1.5}$$

The efficiency can be increased as the temperature approaches that of the sun. This can partly be achieved with halogen lamps where the halogens ensure increased metal vapor re-

condensation on the filament. Halogen lamps are typically associated with quartz envelopes also allowing improved transmission of ultraviolet part of the black body radiation. The emission of many high pressure discharge lamps are also partially due to black body emission, and one research area is the development of solar simulators for testing photovoltaic devices under controlled natural-like conditions. Black body light sources with much higher temperatures and emission in the X-ray region can be achieved by pulsed laser induced plasmas and, e.g., liquid metal jet technology<sup>244</sup> such sources also include spectral lines following the cooling of the plasma. Although filaments are slow and not very bright they are excellent sources for steady state elastic spectroscopy due to their high stability and continuous emission spectra. Filaments are popular in both spectroscopy with Si or InGaAs polychromators, and in FTIR spectrometers. Elastic spectroscopy in the UV region can be achieved with filament lamps. However, this is typically done with tungsten-deuterium lamps, where the deuterium is responsible for a broad UV peak emission at 250 nm. The spectral emission of these sources is bimodal rather than Planck distributed. The sources are popular for studying animal UV coloration and vision. However, one potential concern when measuring reflectance with these sources is the fluorescence excited by the deep UV part of the emission.

In contrast to LEDs, filaments are self stabilizing at a fixed voltage. This is because increased temperature yields increased resistance and therefore decreased current and decreased power. The resistance of filaments relates to the temperature by a straight slope. When neglecting ambient temperature and heat conduction, the voltage current characteristic can be approximated by the solution to the equation:

$$U = I \left( k_1 + k_2 \sqrt{\frac{UI}{\sigma}} \right) \quad \text{Eq. 3.1.6}$$

Here  $k_1$  and  $k_2$  are the temperature coefficients of the filament. The UI curve has a sigmoid-like shape. In Paper I this relation is exploited in a method which simultaneously finds the thermal coefficients, the absolute temperature of filaments and the response curve of spectrometers. This is done by minimizing the variance between a set of transmittance spectra acquired with different source voltages. The situation where assessment of the UI curve of the source improves the prediction of the emitted light spectrum resembles that of LED calibration in Sect. 3.1.1.

### 3.1.6 The Sun

Detection schemes based on the light originating from the Sun or the Moon are referred to as passive techniques. Even methods based on black body radiation in the thermal infrared region falls under this category. In this thesis sunlight was mainly exploited in Paper XII and Paper XVI; also sunlight reflected by the moon was attempted in relation to Paper XVI. The energy maintaining the high temperature of the Sun arises from fusion of atomic nuclei with low atomic numbers, where the total energy per nucleon system decreases as the nuclei converge toward Fe (predicted by the semi-empirical mass formula). The main processes are the proton-proton chain reaction where hydrogen nuclei are converted into helium, and the carbon cycle, where carbon nuclei are turned into nitrogen and oxygen through proton bombardment, and finally releasing an alpha particle and returning to the initial carbon isotope. Even in this process the final product, except for the energy surplus, are  $\alpha$ -particles. The spectral emission of the Sun can be described as a Planck radiator peaking in the cyan region around 500 nm, the effective surface temperature is 5778 K. However, the spectrum is lacking wavelengths since a large number of narrow dark lines throughout the spectrum, known as Fraunhofer lines, are present. The lines are generated due to absorption of either the solar or the terrestrial atmosphere. In the infrared region

several broad regions are opaque due to H<sub>2</sub>O and CO<sub>2</sub> vibrational absorption, the remaining clear regions are therefore referred to as atmospheric windows. Remote sensing methods are often restricted to these windows. The infrared absorption of CO<sub>2</sub> relates to the discussion regarding green house effects and the global energy budget<sup>245</sup> which delicately determines the average temperature on earth. While few degree changes in average does not affect human welfare directly, it has a large impact on organism such as plants and insects who are unable to regulate their temperature, and tiny perturbations of fragile ecosystems quickly escalates into major humanitarian tragedies such as failed crops seasons or epidemics. The green house effect and radiative transfer towards the thermal infrared resembles the inelastic effect of fluorescence in the sense that highly energetic light becomes less energetic light after sample interaction, which in this case is the earth. In the NIR O<sub>2</sub> and H<sub>2</sub>O absorbs at several narrow bands<sup>103</sup>, one aspect of such line was briefly explored in Paper VI. The overlap of the lines with the fluorescent emission of chlorophyll also allows solar induced fluorescence in full daylight<sup>246</sup>, the effect can also be noticed in Paper XII. In the blue region the pollutant NO<sub>2</sub> absorbs. This gas can be monitored from space and can serve as an indicator of car activity<sup>247</sup>. The lower limit for atmospheric transmittance is constrained by the absorption of O<sub>3</sub> and relates to depletion of the ozone layer and resulting carcinogenic radiation. Using sunlight for remote sensing means access to a powerful broadband light source with continuous intensities up to 1 kW/m<sup>2</sup>. Although much higher intensities can be achieved per spectral or temporal unit with laser, such average intensities are difficult and costly to achieve by any other means. A major difficulty with solar based measurements are the changing atmospheric conditions which change the spectral content of the light impinging in the field of view (FOV). Both the length of the atmospheric slab, the angle of incidence, aerosols, clouds, fog and countless other atmospheric phenomena occur. In Paper XII this is dealt with by repeatedly taking reference spectra of the light spectra impinging on the FOV throughout the day. This particularly works in clear-sky condition where the solar irradiance is very stable. In cloudy conditions, however, the intensity becomes extremely unstable to an extent that it is difficult to distinguish the static signal and the rare events sought for in Papers XII and XVI.

## 3.2 Detectors

### 3.2.1 Photodiodes

The operation and architecture of photodiodes (PDs) is in many ways equivalent to that of LEDs, except that the devices are instead optimized for detection and operated in reverse direction in the third quadrant of the UI plot; see Fig. 3.1.7. The most common and inexpensive PDs are made of Si with a band gap around 1 μm, with broad sensitivity between 350-950 nm and peak sensitivity in the NIR around 800 nm. Such devices can be purchased from 1 dollar. Narrow-band so-called intrinsically selective PD and UV enhanced Si or GaN PDs are also available. NIR PDs made of InGaAs or Ge can cover the wavelengths 0.7-2.4 μm are widely available due to the fiber telecom technology operating at 1550 nm. In the MIR PDs can be made from InSb; other related detectors include, e.g. PbSe or HgCdTe photoconductive and InAs photovoltaic detectors which are operated in the first and forth quadrant in Fig. 3.1.7, respectively.

When a reverse voltage is applied to a PD the depletion layer physically increases in size, a photosensitive volume is created where photons with appropriate energy can produce electron-hole pairs which will migrate to the cathode and anode respectively creating a measurable photo current  $I_{PD}$ . An importance aspect of PDs is the time constant,  $\tau$ , determined the bandwidth and detection speed.  $\tau$  is determined by the product of the capacitance of the PD,  $C_{PD}$ , and the load resistance,  $R$ ; see Fig. 3.2.1. The PD capacitance is determined by the sum of two contributions; the active area over the thickness of the depletion layer (proportional to the reverse voltage) and the migration time of the electron-

hole pairs. The last mentioned increase with the thickness of the depletion layer. From the circuit example in Fig. 3.2.1 it can be understood that the output signal  $U_{out} = -I_{PD} * R$ . Thus the gain and sensitivity can be increased by increasing the reverse resistor, R. However, increasing R also implies increasing  $\tau$ . Thus a trade-off between sensitivity and bandwidth must be made. This is inevitable considering the limited amount of photons impinging per time unit, it is also equivalent to the trade off between bright pictures and motion blur in choosing an appropriate exposure time in photography.

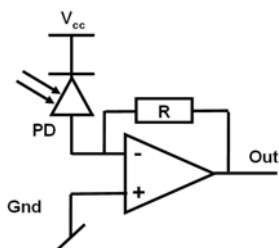


*Fig. 3.2.1. Simplified configuration for high speed photo diode configuration. Impinging light displaces the IU curve towards negative currents (See Fig. 3.1.7).*

PDs are typically packed in metal can casings ranging in size according to the active detection area. The detection area ranges in typical values between 100  $\mu\text{m}$  to 1 cm. In bio-photonics applications for detecting low brightness light, e.g. after photo migration, the sensitivity can be increased by employing large area PDs<sup>107</sup>. PD are available in linear arrays, e.g. for line scan or spectroscopy or in quadrant configuration, e.g. for tracking or alignment purpose.

Intrinsic gain can be achieved in PDs by a cascade phenomenon, where electron-hole pairs are multiplied in a strong electrical field. Such devices are referred to as avalanche photodiodes (APDs). They operate with reverse voltages of several hundreds volts, are much more costly than PD and are generally only available with small active areas.

Just as temperature changes the emission profile of LEDs, it also changes the sensitivity profile of PDs. Generally, increased temperature implies increased sensitivity at longer light wavelengths. Also increasing temperature increases the dark current; the current measured in complete darkness. Si and InGaAs PD are used in P2; in this setup thermal dependence of both LEDs and PDs was compensated for simultaneously.

### 3.2.2 Photo-multiplier tubes

Throughout the last half of the 19<sup>th</sup> century scientist learned to produce a variety of vacuum tubes and cathode ray tubes. One such tube culminated in the discovery of X-rays and the first Nobel prize in physics. In the other end of the spectrum, Heinrich Hertz was interesting in radio transmission with spark gap tubes. He was the first in a long row of Hertz scientists<sup>248</sup>, and discovered the photoelectric effect. Throughout the following century the effect contributed to a large number of Nobel prizes, and the electronic light detection and mastering of electron acceleration in vacuum tubes was refined, mainly driven by the desire for realistic applications of television. In 1934 the first photomultiplier tube (PMT) was produced. The device is still today the most sensitive light detector and is extensively used in scientific equipment ranging from the IceCube neutrino observatory at Antarctica<sup>249</sup> to confocal microscopes in bio-photonics<sup>171</sup>. The operation of PMTs is based on a photon releasing an electron from the window of the device, which is typically internally coated with an alkali metal photocathode. The electron is accelerated towards an array of dynodes, the dynodes have a range of electrical potentials produced by a high voltage divider. At the electron impact with each dynode, secondary electrons are emitted and accelerated. This cascade effect produces a large bunch of electrons which is eventually collected at the

anode producing a short current pulse which can be registered over a low impedance device. Depending of the material of the PMT cathode sensitivity in different regions can be achieved. The devices are extensively used for ultraviolet and visible detection. For higher energies in the regime of X- and gamma-rays and other particles, scintillators are used. They produce glimpses of light which are in term detected. The speed of PMTs allows recordings down to the range of hundred picoseconds, constituting the fastest direct opto-electronic detection. When applied in single photon counting methods, such as fluorescence lifetime or gamma spectroscopy, the time events are identified at the rising flank at the point where the current pulse has reached half of the maximum. This intensity insensitive method allows high timing precision and be compared to deconvolution; however, this is done electronically. In Papers VIII and IX miniature multi cathode PMTs are used for spectrally resolved fluorescence lifetime spectroscopy. The high voltage used to produce the cascade effects complicates the use of PMTs and the device is preferably often avoided for clinical *in-vivo* applications for this reason.

Much larger PMTs are typically used in lidar applications with accelerating voltage of 2 kV. Here PMTs are typically employed to detect, e.g. the green and UV harmonics of Nd:YAG lasers. The fundamental infrared emission is mostly detected by APDs. In lidar, the backscattered light is collected by a telescope and focused onto a pinhole. Following the pinhole the rays are collimated and fed through various dichroics or polarization beam splitters<sup>250</sup>. Several PMTs detects the co- or de-polarized elastic returns as well as various spectral bands. The spectral bands can be different harmonics of the emitter<sup>251</sup>, Raman bands of nitrogen or water vapor<sup>146</sup> or fluorescence bands<sup>241</sup>. The PMTs are usually equipped with narrow band interference filters to confine their spectral sensitivity, and limit their sensitivity to background light, e.g. from the sun. A key to success in lidar is confinement: confinement of the divergence of the transmitted beam by a beam expander, confinement of the field of view (FOV) set by the size of the pinhole, confinement of the spectral range retrieved. For demanding daytime fluorescence application with high background levels, the high voltage of the PMTs can be gated or ramped in synchronization with laser pulses. This limits the detection to the short time intervals following laser emission and protects the PMT to large background currents which would cause damage. PMTs are used in the lidar Papers X, XI, XIII and XIV.

### 3.2.3 Array detectors, CCD and CMOS

Following the invention of the television<sup>252</sup> in 1908 and the commercialization a decade later, electronic image display and recording were achieved by cathode tubes much along the lines of existing technology of vacuum tubes, and the photo multiplier tubes described above. The spatial resolution was managed by analogically scanning an electric or magnetic field, steering the beam of electrons produced by the photons in the photocathode and subsequently producing photons on a phosphorous screen. The receiving device was referred to as a vidicon, and the entire process of collecting images, transmitting them and reproducing them was done analogical and the concept of discretizing space was therefore not an issue during this process. Much later in 1969, at AT&T Bell Laboratory, work aimed at developing computer memories resulted in the Charge Coupled Device (CCD). This invention was an electronically shift register device with a discrete number of elements referred to as a pixels. The device revolutionized electro-optics, astronomy and spectroscopy, and the inventors were awarded the Nobel prize in physics in 2009. The CCD is capable of accumulating electronic charge produced through the photo-electrical effect on the individual pixel elements. The charges can in terms by moved to the edges by applying a sequence of opposite changes on the backside of the pixels. The original device consisted of 8 pixels in a line, today both such linear arrays with readout up to 100 kHz and imaging 2D arrays with readout up to 1 kHz exist with several billions of pixels. A large

number of varieties of specialized CCDs exists, such as back-thinned CCDs and intensified CCD. Despite the digital nature of the shift-registering, CCDs are analog devices and relies on external circuitry to produce the multiplexing sequences moving the charges and converting the electric charges into digital values. In the 90<sup>th</sup> an additional imager was developed - the Complimentary-Metal-Oxide-Semiconductor (CMOS) imager<sup>253</sup>. This technology is compatible with the one used in relation to the production of microprocessors, and this allowed fabrication of single chips including, imagers, readout electronics, analog digital conversions, image compression algorithms and communication protocols, and many other specialized features. CMOS imagers consist of arrays of photodiodes and their accumulated current is stored on a separate capacitor in each pixel. CMOS imagers currently undergo fast technological development, whereas CCDs are more mature and stagnated. The applications of CMOS are today widespread in commercial electronics such as digital still cameras, cell phones, and scanners. CMOS imagers are also found in advanced equipment such as satellites or in large formats for medical X-rays where they now substitute the slow process of developing X-ray films. In spectroscopy, spectra were previously recorded by the time consuming process of mechanically scanning a monochromator across the spectral range of interest; today linear array detectors and polychromators allow instantaneous recording of spectra over wide spectral ranges. Several efforts can be made to increase or extent the spectral response of CCDs. Scientific CCD are often “back thinned” and light impacts on the chip from behind instead. This option allows new chip geometries where light has to travel less inside the silicon before it generates the photon charge. Because of bulk absorption in silicon, especially in the blue region, back-thinned CCDs increase quantum efficiency significantly. However, it decreases the red response. Coatings for improving transmission and trapping photons inside the sensitive region can also be applied. Generally, long wavelength response extension is limited by the photon lack of energy to get the electron over the band gap, while blue or UV response extension is limited by the penetration depth for the light in the sensor chip. The last mentioned limitation can be overcome by down-conversion; this technique refers to a phosphor coating which transforms UV efficiently into longer wavelengths where better spectral response prevails. Similar solutions are found in deep sea animal vision systems<sup>254</sup>. This is the case for the Ocean Optics spectrometers used in various papers in this thesis. The window of linear array detectors in compact spectrometers can be coated with long pass filters, which can suppress higher order diffraction orders of light with half the wavelength belonging in a given position of the sensor; this allows spectra to be recorded over several multiples of the wavelength.

The use of 2D arrays in spectroscopy includes streak cameras<sup>61</sup> acquiring hundreds of spectra in nanoseconds, they also form the basis for push-broom imagers<sup>255</sup> used in satellites<sup>256</sup>, in rolling-band inspection systems<sup>257</sup>, multispectral imaging by time multiplexing as in Paper III or spectro-spatially resolved measurements in the diffuse optical regime as in P2. In this thesis, linear CCDs are used in most spectrometers, CMOS imagers are employed in Papers I-V. An intensified CCD was used for acquiring spectra remotely in Paper X and XIV. Such devices are based on the sandwiching of a micro channel plate, with high voltage supply, and a CCD. The function of the micro channel plate is similar to the PMT. Apart from improved sensitivity in respect to dark current<sup>258</sup>, an intensified CCD also allows fast gating in the nanosecond regime<sup>259</sup>.

Accumulating imagers have a maximum limit of accumulated signal. This is generally referred to as *full well capacity*. If one desires to make a type of image of a still standing rain cloud, one could arrange an array of buckets (pixels) on the ground and derive the shape and density of the cloud by measuring the level in each bucket after a certain rain *exposure time*. Putting out a finite and discrete number of buckets is referred to as spatial discretization. The total size of the array of bucket would be the field of view, and if the

buckets are put right next to each other the spatial resolution would be equivalent to the diameter of the buckets. If all buckets are put in at one instance of time and collected in another instance of time, it is referred to as a *global shutter*. If buckets are put one by one by a man, and later collected one by one in the same orders as they were put by another man we call it a *rolling shutter*. In the last case the exposure time corresponds to the time a single bucket was standing in the rain, not the time for producing the entire image. The two shutter techniques will give the same result as long as the cloud remains still during exposure. Inexpensive CMOS imagers typically come with *rolling shutters*. With a rolling shutter the image frames are not orthogonal to the time axis. Image artefacts occur when the scenery is moving or the illumination changes. For this purpose most webcams have the option to compensate for indoor/outdoor illumination and 50/60 Hz power frequency.

The bucket volume would be the *full well capacity*. The ratio between bucket-filled area and the total area is referred to as the *fill factor*; for a CCD this factor is close to one whereas a CMOS has lower fill factors due the pixel circuitry for amplification, accumulation, reset and read out. Also the CMOS pixels can be L shaped, which can generate certain artefacts in the images under special conditions<sup>260</sup>.

If the cloud in some place is particularly dense the rain will fill up the bucket completely at certain places. We refer to this phenomenon as *saturation*. Saturation destroys the relation between the buckets, since there is no way of knowing if the cloud was just slightly denser at this spot or if it was many million times denser for some reason. One way to deal with this is to change the exposure time and take several pictures - one of the million times bigger spike and one of the rests of the cloud, with the saturated buckets. This can be done with CMOS imagers and is referred to as high dynamic mode. However, this will not be possible on the CCD since charge from one pixel will spread to neighbouring pixels. This can be understood as water not only floating over the bucket side and wasting the water, but even distorting the neighbouring pixels by spilling water into those buckets as a result of the saturation. This phenomenon is referred to as *blooming*. Now we imagine that every bucket has centimetre marks to quantify the rain levels. Converting the levels into cm would be called dynamic *discrimination*, and the spacing between the marks would be the *dynamic resolution*. A level change smaller than  $\frac{1}{2}$  cm will be neglected. *Dynamic resolution* is mostly specified in bits or dB. E.g., 8 bit resolution means discrimination in  $2^8 = 256$  levels, between the determined min and max value. Special CMOS imagers might be *logarithmic*<sup>261</sup>; this corresponds to having cone-shaped buckets, where little rain gives big level change, while much rain gives less level change. Certain new CMOS imagers also features a high-dynamic mode, where multi exposures of different duration are merged into a single intensity scale covering a large number of magnitudes. Although such an approach does not overcome the stray light and the slopes of the point spread function (PSF) of the optical systems, in constitutes a significant advancement and many new opportunities in spectroscopy with large contrasts or bio-photonics<sup>176, 262</sup>. To finish this small illustrative example, think of *dark current* and noise as random contribution to the bucket array as the birds flying over and dropping leftovers in the buckets. Some buckets might be broken whereas others might not have been emptied properly from earlier use; this constitutes to *salt and pepper noise* and is common for CMOS imagers. The read out process constitutes an additional noise source, therefore the signal-to-noise ratio (SNR) is better for one image than for the sum of two images with half the exposure time.

In quantitative measurements and spectroscopy, detector linearity is of outmost importance, in this relation especially the thermal dependence of array detectors in polychromators. Compact USB spectrometers give the impression of a simple and reliable device providing a digitalized distribution of light intensities versus wavelengths. In practise, the instrument temperature changes a number of features in the spectrometers, thermal expansion changes the slit-width, the focal lengths of the collimating optics, and most importantly the number

of grooves per unit length. Apart from these mechanical changes, temperature also increases the dark current on the CCD and displaces the spectral response toward longer wavelengths. Modern compact spectrometers used in this thesis, report the chip temperature together with the spectrum. However, the temperature profile might not be homogeneous, since it may be optically induced through a given spectral signature impinging on the chip. This gives rise to nonlinearity, where traces of a smeared-out version of the light spectrum can be recorded shortly after the actual optical signal.

Traditionally, color images were formed by using dichroic beam splitters and one imaging chip for each spectral band. The method can still be encountered in some contexts, but the vast majority of color imagers are detector arrays with colour filters superimposed on the chip, like the commercial camera used in Paper V. In this way only certain bandwidths of light are able to activate certain pixels. The method is referred to as a Bayesian color filtering. One colour pixel is later created from four original pixels. As can be understood, photon economy is poor since light is lost in the filters, and furthermore, spatial resolution is impaired since it requires several pixels to create one colour pixel. The superimposed colour filters emulate the human eye in respect to wavelength, which means that they are broad and overlapping which is not optimal from a spectroscopic point of view.

---

## Chapter IV

### 4. Resolving and discretizing light

---

We have previously discussed the various properties of light, and described how the conclusions from optical diagnostics are derived by comparing these properties before and after sample interaction. In this chapter we will see that whenever a light measurement is carried out, the properties are quantified in a discrete manner. In mathematics different departments often treat continuous analytical mathematics, and discrete numerical matrix algebra. In most cases the phenomena can be described equivalently in either domain; however, the simplicity of the description might differ considerably. In the physics and biophotonics community the preferred domain is often the continuous notation. The discrete domain is often associated with applied mathematics, informatics and computer science such as digital signal processing (DSP), image processing or control theory. But even long before the time of computers, optical scientists recorded diffraction angles in rulers with certain grid precision. In this manner the continuously various propagation property was discretized into a quantity with a certain numbers of digits. The truncated number of digits reflects the precision allowed by the instrumentation. The process of converting a continuous changing quantity into a number with finite digits is referred to as discretization.

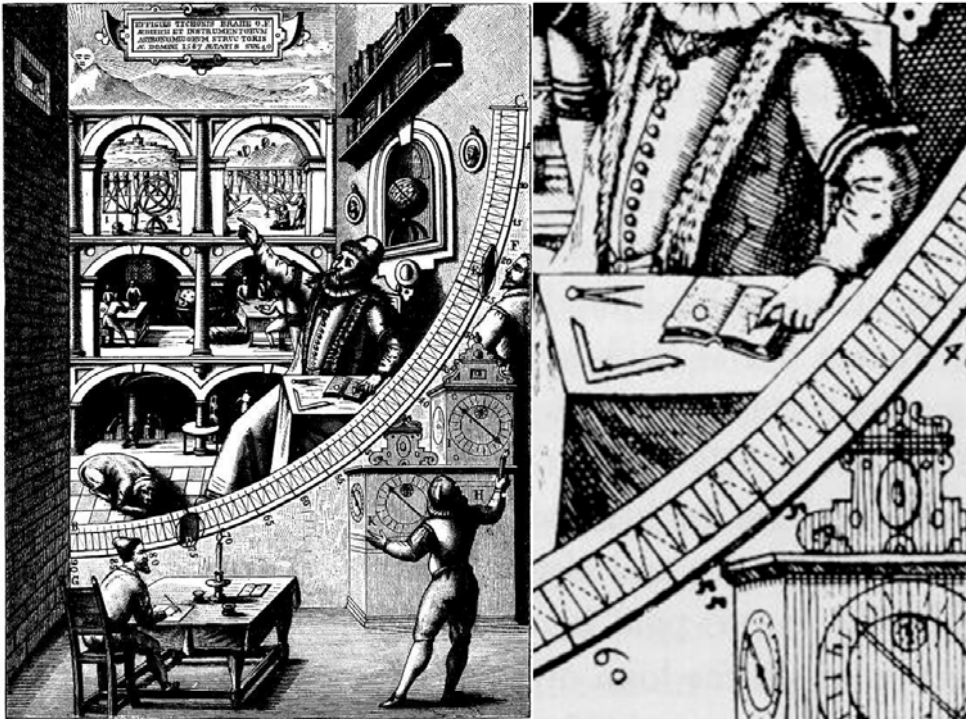


*Fig. 4.1. Apart from his nose prosthesis made from silver which he got after a duel, the famous Danish astronomer Tycho Brahe was known for high precision instrumentation. In the illustration the light propagation is discretized on the grids on an arc. Note the saw-toothed diagonal lines within each grid; these additionally increased the read-off precision. A comparison to the digital bits of modern times should be made.*

Similarly, also light intensity and detection time were recorded on analogue oscilloscopes throughout last century. The light on the phosphorous screen was in turn related to the grid on the screen and converted into quantitative numerical observations with a given number of significant digits. Discretization not only takes place for the purpose of science communication and quantitative analysis. Even in vision physiology light is persistently discretized in all domains. In our eyes the light propagation is discriminated in a finite number of sensory cones or rod cells, and the photon energy of the light is discretized in a number of spectral bands.

Whenever a light measurement is carried out it is always discrete and quantifies the light properties in all the domains. The measurement starts and ends at a certain time giving a certain exposure time, the detector has a certain spectral sensitivity band and the detector collects light with a confined propagation direction originating from a confined space. This paradigm is explained in Paper III where a comparison chart of terms and similarities in different domains can also be found.

Dealing with numerous types of optical instrumentation such as photo multiplier tubes (PMT), lidars, color cameras, multispectral imagers, hyper-spectral imagers or spectrometers becomes infinitely simpler by the paradigm that they are all the same; they simply have different number of bins along each domain: intensity is recorded with different precision; they have a different number of pixels, different sensitivity lobes, spectral bands or time slots. The aforementioned terms for the resolution generally refer to the smallest resolvable features in the different domains. Another aspect is the range in the various domains; such terms could be footprint size, numerical aperture, spectral range, or recording length.

In many situations it is beneficial not only to consider discretization on the detection side, but even on the illumination side. In elastic spectroscopy, a narrow gas absorption line can be measured with a broad lamp and a high-resolution spectrometer, alternatively the same result can be achieved with a broad band sensitive photodiode and a single-mode tunable diode laser<sup>263-265</sup>. The last mentioned approach offers improved photon economy but worse signal-to-background rejection. Imaging of fast phenomena can either be achieved by continuous illumination and a fast shutter or a continuously open shutter and a fast flash; this for instance in the case in particle imaging velocimetry (PIV)<sup>266</sup>. When the light does not preserve its original property it can be beneficial to discretize both on illumination and detection. Fluorescence EEM spectroscopy is one example of double discretization. The traditional collection of EEMs is sequentially scanning of two monochromators<sup>122</sup>, one for the illumination and one for the detection. Another example is the imaging of photons whose propagation has changed after the sample interrogation. Examples are diffusely reflecting objects illuminated by a point source imaged onto the surface. The incidence point is then scanned in x-y and images are sequentially collected<sup>175, 182</sup>. The last mentioned detection scheme provides additional information regarding both absorption and scattering of the image in contrast to a reflectance image where the entire surface is illuminated simultaneously. As can be understood in these two examples the resulting data are multidimensional, and often one data dimension is created from another physical dimension by certain assumptions. In the mentioned example the time domain is featured for sequential collection, and the assumption is that the sample does not change during the collection time - in other words when, e.g., the spectral domain is created over time, the time and spectral axis are not orthogonal. In push-broom imagers used in copying machines and satellites, the spatial y-axis is reconstructed by the use of time; thus the y-axis is not orthogonal to the time axis. One detection scheme where both EEM and spatial resolved photo-migration are acquired instantaneously was submitted as P1 during this thesis work. Also a further scheme was submitted for patenting; P2.

As can be understood from the above, conversions between different physical dimensions can be achieved, and the operation of many optical components and instruments can be seen as a conversion between different domains. A lens converts the propagation direction into a position in the focal plane, a grating converts photon energy into different propagation directions, a streak camera converts picoseconds delays into a spatial projection on an imaging chip and a lidar converts spatial distances into delay times.

In the following of this chapter the discretization along the intensity, spectral, spatial, propagation, temporal and polarization domains will be discussed. Other domains such as phase or sample temperature<sup>133, 267</sup>, static electric<sup>268</sup> or magnetic<sup>269</sup> fields could be imagined, but are outside the scope of this thesis. Also discrimination between source and detector domains could be imagined; however, we refer to the paradigm in Paper III, that discretization along domains can in many situations be achieved equivalently by discretization on the source or detection side. The classical approach in pushing science is to operate in either extreme of these domains: What happens when we detect a single photon quantum<sup>116, 270</sup>? How intense can we make light<sup>271</sup>? How energetic light can we produce<sup>272</sup>? How small things can we see<sup>273</sup>? How old light can we detect<sup>274</sup>? How short light pulses can we make<sup>275</sup>? The approach in this thesis is not to pursue these ideas, but to demonstrate creative interdisciplinary applications of optics in the intermediate regimes.

#### 4.1 The intensity domain

The wave interpretation of the intensity of light is defined as the electric field squared. Therefore intensity is positive definite. In the particle perception, intensity is the flux of photons per unit time. Thus, the lowest intensity monitoring is referred to as single photon counting, as in Papers VIII and IX. In these studies the intensity is purposely attenuated to an extent where multiple photon detection is very unlikely in order to avoid pile-up. Similar techniques based on scintillators are used in X-ray and gamma spectroscopy. Here not only the quantity and time occurrence, but even the energy can be recorded. When summing up photon counts the values are discrete, positive definite and therefore Poisson distributed. As the count increases the distribution approaches a normal distribution, after which normal operators of mean and variance can be applied. The highest human-made peak intensities are produced by confining the energy in very short pulses. This is typically done using mode locked<sup>276</sup> lasers and the chirped pulse amplification schemes<sup>277</sup>, and produces peak power in the terawatt or even petawatt range with the capability of producing laser filamentation<sup>100</sup> or relativistic accelerated electrons and protons<sup>271</sup>. The high peak intensity in short pulses can also be used to pile the photon in top of each other and produce highly energetic photons by high harmonic generation (HHG)<sup>278</sup>. The highest average powers are currently produced by chemical DF lasers continuously delivering megawatts in collimated beams. Such lasers are developed for laser warfare<sup>233</sup>. In this thesis intensity is used for peaceful optical diagnostics in medicine and environment. The powers employed on the samples in this thesis range from 10  $\mu$ W in the single photon counting, (see Papers VIII and IX), through typically 10 mW in LED spectroscopy, (e.g., Papers III and X), approximately 1 W with passive sunlight methods (Paper XII), and to 1 MW with lidar methods, (e.g., Papers XI and XIII). Similarly to this, the intensity in our natural surroundings also varies over many magnitudes in a logarithmic manner. The natural variation of intensity is closely related to geometry and one way to cancel out geometrical effects is by ratio building between intensities in different spectral bands. This is used, e.g., in differential absorption lidar (DIAL)<sup>279</sup>, normalized difference vegetation index assessment (NDVI) in satellite imaging, and in vision systems for robots<sup>280-283</sup>.

It is also considered that intensity information is separately neurologically wired in most animal vision systems<sup>85</sup>. The sensitivity of many organisms approaches single photon counting<sup>284</sup>, and some of the most sensitive eyes are encountered in cephalopods at kilometer sea depths<sup>285</sup>. Lens based eyes are easily permanently damaged with only few milliwatts of impinging collimated power; risk is increased for NIR lasers and pulsed lasers. Therefore, an important aspect and constraint of lidar applications is laser eye safety for humans and animals.

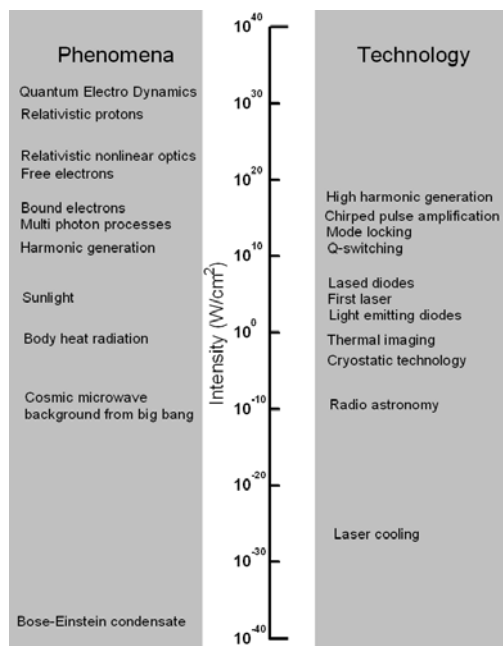


Fig. 4.1.2 Intensity overview chart. A number of different interaction processes, phenomena and technologies dominates at different peak intensities. Lasers play important roles throughout the dynamic range.

Even for entirely dark circumstances, photo-detectors will produce a signal; this is referred to as dark current. Often the dark current needs to be measured to define the true zero level, e.g., in Papers III and IV. In some situations, e.g., for fluorescence lifetime measurement or lidar applications in, e.g., Papers VIII and XIV, the dark level can be estimated from the pre-pulse level. In other situations, e.g., for the spectrometer in Papers VII and XII, the dark level can be estimated from a spectral region which can be assumed to be dark due to the blocking of a filter or of the atmosphere, respectively. However, one should be aware that the linear CCD in

spectrometers does not have one single temperature but a spatial temperature profile responding to the light intensity impinging on the sensor, and since the dark current increases with the detector temperature it creates a number of complications. Detectors are often cooled by Peltier elements or liquid nitrogen for demanding applications. Detector cooling produces a large amount of complications related to water vapor condensation or the use of vacuum chambers; therefore it is preferably avoided in applied instrumentation. In this thesis, detector cooling was applied in Papers XIV and XV in relation to thermal imaging.

Detector noise can be of various origins: the fact that light is absorbed in energy quanta leads to the *shot noise* limited detection under optimal conditions. However, thermal white noise is often the limiting factor. The noise typically scales with the frequency bandwidth in electronic band-pass filters or lock-in amplifiers, which are applied in demanding applications. Detector noise also tends to have a pink power spectrum, attenuating for increasing frequency, and increased signal to noise can therefore be achieved by increasing the modulation frequency in active detection schemes. This is implemented in GASMAS<sup>286</sup> or during this thesis in the prototype of P2. It also poses a fundamental dilemma for lidar systems: should an optimal lidar system emit low power pulses with a fast repetition frequency<sup>142, 145, 243, 287</sup> or high power with a slow repetition frequency as in this thesis? The dilemma somewhat relates to the term read-out noise, summarizing the noise added during electronic amplification and digital-analog conversion. The implications of read-out noise in CCD and CMOS is that it is preferable in terms of SNR to acquire one spectrum with twice the exposure time instead of averaging two spectra with half the exposure time. However, the same is not necessarily true for the signal-to-background ratio, SBR; see, e.g.,

the discussion in Paper VII. The SBR also suffers considerably when changing from, e.g., spectral discrimination on the detection to discrimination on the illuminating side; see, e.g., Paper III.

The acquisition speed and the sensitivity are related in such a way that the product is constant for a given detector. For cameras, long exposure gives large intensity signals but poor frame rate and motion blur. This is equivalent for photodiodes where a large resistor in series produces a large voltage drop from the photocurrent, but a large resistance in combination with the capacitance of the photodiode also gives rise to a slow time response and the same goes when increasing the detector area. One way to understand this is to think of a photo detector as a bucket collecting photon rain: Either it is left for long time and large photon levels can be recorded without the knowledge of exactly when it rained, or the bucket is emptied continuously with the results of a precise description of when it rained but the low quantities produce large uncertainty of how much it rained.

As discussed in the beginning of this chapter, the levels are quantified, e.g., by marks on the side of the bucket, the marks have a certain spacing and the read-out can be carried out with a certain precision. In practice, in modern electro-optics the electrical signal from the photon detector is fed to an analogue-to-digital converter (ADC), transient digitizer or digital oscilloscope. This component typically compares the analog noisy signal to an iteratively adjusted reference signal produced by a digital-to-analogue converter (DAC) and a digital number. The number of digits precision to which the level is discretized is the number of bits. Light measurements in consumer electronics like webcams and cell phones are done with a precision of 8 bits, forcing the intensity into one out of  $2^8 = 256$  intensity levels. Cameras employed in industrial inspection discretize with a precision of 10 or 12 bits yielding  $2^{10}=1024$  and  $2^{12}=4096$  levels, respectively; such cameras are employed in, e.g., Papers III and IV. Higher dynamical resolution than 12 bit in light recording is not possible without detector cooling and vacuum encapsulation. Scientific imagers exist with up to 16 bits resolution ( $2^{16}=65536$  levels) but the cost scales linearly with the number of intensity bins or exponentially with the number of bits. Some new CMOS imagers feature a high dynamic range mode with multiple exposures. From the dynamical resolution also the amount of colors specified in computer science is found: An 8 bit RGB camera digitizes light in  $2^8$  levels in 3 bands, every outcome of a measurement in a pixel will thus be 1 out of  $2^{8*3} = 16.777.216$  colors. Nowadays this is also the number representable on computer monitors. One aspect of this vast information is exploited in Paper V. Miniature spectrometers such as the one used in Paper XII, have a dynamic range of 16 bits and 4096 spectral channels. Thus the color space or a measurement can fall into one of more than  $10^{18000}$  outcomes! This number is larger than the numbers of elementary particles in the universe. Producing a look-up table for interpreting the results from such an instrument would be absolutely useless and take more than an eternity. In Chap. 5 it will be discussed how to approach the interpretation of such information in an analytical and systematical way. It should, however, be noted that un-cooled spectrometers such as the one in Paper XII, has a noise level already after the 10<sup>th</sup> bit and that all 4096 spectral bands typically are not independent because of the broad slit width.

## 4.2 The spectral domain

The spectral domain provides discretization of the energy of the photon quanta. Throughout this thesis the spectral domain is indexed with the use of light vacuum wavelength,  $\lambda$ . Because wavelength relates reciprocally to the photon energy, the wavelength is strictly positive definite. Other notations include eV typically commonly used in solid state physics and in the high-energy region of X-ray and gamma, wavenumber  $\text{cm}^{-1}$  typically used in infrared spectroscopy, and Hz used in radar and radio relations. Throughout the

electromagnetic spectrum the light interacts with matter according to a long list of mechanism of difference relevance in different regions of the spectrum; see Fig. 4.2.1.

### Spectral domain in general

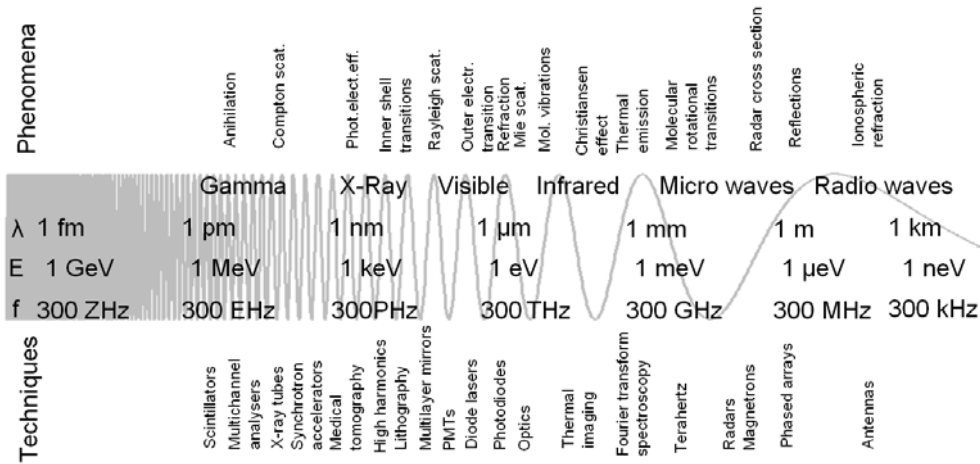


Fig. 4.2.1. Spectral overview showing important terms and technologies in respect to the wavelength of light.

Apart from Fig. 2.1.3 in the introduction, the papers in this thesis covers the optical spectral range 250 nm to 25  $\mu$ m. The lidar studies, e.g. XIV and XI, induce fluorescence at 266 nm and 355 nm, respectively. LED and laser diode induced fluorescence fiber probing is presented in the range 250 nm – 435 nm. The fluorescence emission from endogenous fluorophores mainly appear in the UV-green region (350-550 nm), the fluorescence from PpIX and Chlorophyll appear in the red (635 nm) and NIR (680 nm), respectively. The iridescent features of feather have additionally been explored in the MIR (3-5  $\mu$ m) and TIR (7-25  $\mu$ m).

Whereas the electric field oscillations are directly recorded for radio waves and thus the frequency can be determined, only the intensity can be acquired from the infrared to the gamma region. The simplest form of measuring the intensity of light is by letting a black object absorb the light and consequently measure the temperature increase. This corresponds to the very broad-band bolometer detectors, which are popular for low-cost thermal imaging, but are exceptionally slow in response and poor in sensitivity. Bolometers also appear in nature in TIR and MIR vision of cold blooded organism. One example is the pit organ of the viper, where heat is detected in a suspended membrane in a cavity with close resemblance to a pin hole camera<sup>288, 289</sup>.

More commonly different detectors, appropriate in different spectral regions due to the band gaps, are used as absorbing detectors. During this thesis, detectors of HgTeCd, InSb, PbSe, InGaAs were used in the infrared region (Papers XIV-XV). In the NIR and VIS region Si detectors are the most common and inexpensive. The forms are either photodiodes or CCD arrays in cameras or spectrometers, which are used throughout the thesis. Alkali PMTs are the most sensitive detectors in the blue and UV region; such units were used in the lidar and lifetime Papers, VIII-XI. UV sensitivity can also be achieved by Si detectors through coating the detector by a fluorescent material which converts the UV into VIS. This is the case, for the compact spectrometers covering wavelengths down to 180 nm, e.g. Paper XIV. Similar methods have been encountered in deep sea vision systems<sup>254</sup>. The same approach is used in the X-ray and gamma region; here scintillators

convert the highly energetic photons. A special detail in this process is that the intensity of the flashes can be correlated with the photon energy. This can be analyzed with multi-channel analyzers (MCA), where spectroscopy can be performed without dispersing the radiation in different directions.

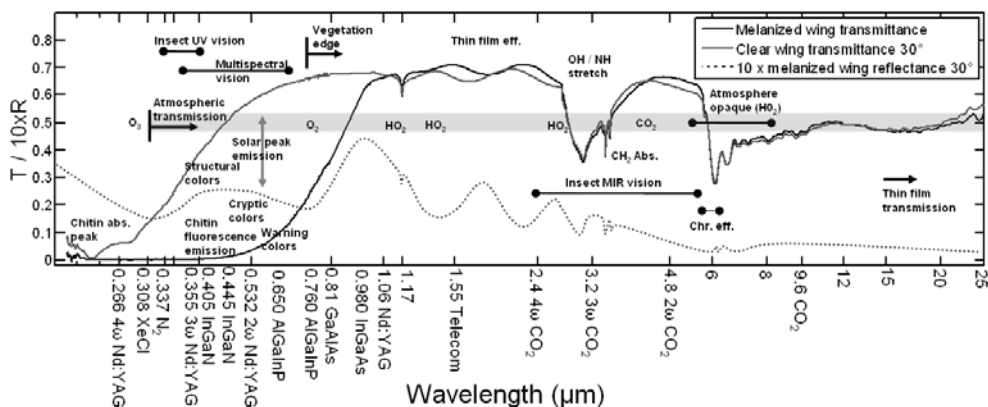


Fig. 4.2.2. Broad band transmission and reflectance spectra from a melanized and clear damselfly wing of the species *Calopteryx Splendens* discussed in Paper X-XII. Several related natural phenomena are marked throughout the spectrum as well as common commercially available lasers<sup>290</sup>. The spectra are assembled from various instruments, from 220-820 nm the source is a Xe flash and the detector is a UV enhanced CCD polychromator, from 0.9-25 μm the spectrum is measured by a FTIR instrument with either a InGaAs detector in the MIR or a HgCdTe detector in the TIR.

The band-gap of absorbing molecules is also the basis of our natural spectral discrimination where different types of rhodopsins provide us with trichromatic vision. The spectral sensitivity or quantum efficiency refers to the ratio between photons impinging on the detector and the signal reported by the detector. The spectral response of each distinct photoreceptor is referred to as the spectral bands of a vision system or instrument. The intensity reported for a spectral band is the product between the sensitivity curve and the impinging light spectrum integrated over the entire spectral domain. Since we happen to have three spectral bands, namely red, green and blue, we consider that light spectra perceived by humans to fall into a 3D color space; see Paper V. We have given names to different positions in this color space, e.g. orange, pink or beige. The corners of this color cube are referred to as primary colors, referring to colors where the bands are either on or off. This corresponds to 1 bit dynamical resolution and gives  $2^{1*3}=8$  colors which are: red, green, blue, black, white, cyan, magenta and yellow. The first three are referred to as additive colors emitted, e.g., by a computer screen and projectors; the latter three are referred to as subtractive colors and are used by painters and color printers. It is thought that trichromatic vision of primates including humans is a result of a recent mutation selected for due to the benefit for estimating the maturity of fruits<sup>291</sup>. People suffering from color blindness and most mammals have only a blue and a yellow spectral band and might refer to colors in a 2D plane<sup>292</sup>. Such reduction can easily be understood and is comparable to the familiar concept of black and white images. In contrast, most birds<sup>201, 293</sup> and reptiles<sup>294</sup> have four spectral bands. Thus, their color space is 4D and it is exceedingly difficult to grasp and communicate such visual information to humans. Behavioral studies involving birds and reptiles are considerably complicated because it is not apparent to humans what the study species perceives from its environment. Careful experimental considerations regarding illumination and concealment materials have to be done, since white lamps designed for humans might not at all be “white” to birds and reptiles, and transparent plastic terrariums might not be transparent to the UV. For this reason biologist are often forced into the domain of optical spectroscopy and detailed spectral analysis of both the coloration<sup>295, 296</sup> and the vision system<sup>85</sup> must be taken into account. One patent

application regarding special eyeglasses suggests how to increase human spectral bands to six by dividing each band by filtering in an upper and lower half for the right and left eye, respectively<sup>297</sup>. For this to work, the user must, however, be trained to distinguish the colors, and 56 new words for the primary colors ( $2^{1^6} \cdot 2^{1^3} = 56$ ) must be invented. For insects the spectral bands can be more than four<sup>298</sup>, and up to 16 spectral bands have been demonstrated in the case of the Mantis Shrimp<sup>299</sup>. In respect to the latter case, it has been proposed that such development is related to spectrally increasing the contrast in its turbid living environment. This is similar to the reasoning regarding added spectral bands in medical diagnostic tools for improved diagnostic contrast for diseases in turbid human tissue<sup>37</sup>. However, the vision bands in organisms are also closely tied to the spectral details of the coloration of the same and interacting species including food sources (e.g. the coloration of flowers in relation to pollination)<sup>300</sup>. Analogously, spectral analysis of human clothing and advertisement would show not much more than three spectral components, whereas the coloration and photonics tricks played by the mantis shrimp are extraordinary.

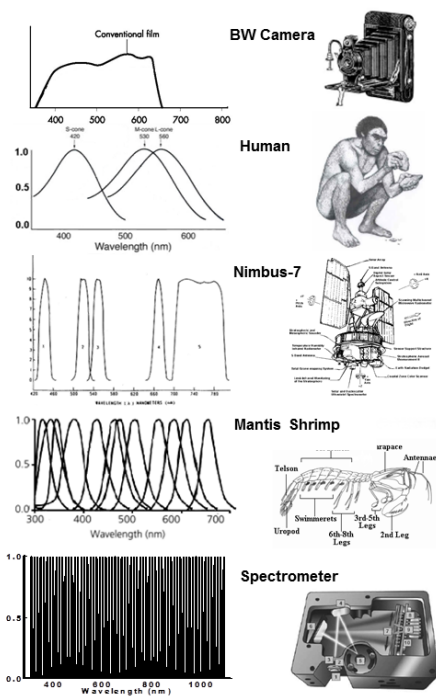


Fig. 4.2.3. Similar to pixels, time frames or intensity bins in other domains, light energy is discretized by a finite number of spectral bands. Discrete spectral bands are found both in zoology and technology and vary from one in monochrome imagers to thousands in high resolution spectrometers or hyperspectral imagers. The number of bands is identical to the dimensionality of the color space and relates exponentially to the number of colors which can be retrieved.

Generally, the band shape, width and center position varies, but the bluest spectral bands found in the animal kingdom are constrained by the opacity of ozone at 300 nm, below which the ambient light is negligible. Some of the reddest bands for terrestrial animals peak just below the Chlorophyll edge at 660 nm and can be found in Caribbean lizards<sup>294</sup>. The amount of ambient NIR light in, e.g., dense forest is an order of magnitude larger than visible light, but one argument against NIR vision in biology is that the photon energy is so low that the visual signal becomes noisy. Nevertheless NIR sensitivity has even been reported in spotlight fish<sup>301-303</sup>.

Apart from traditional eyes, broad band MIR receptors have also been found in certain beetles<sup>288, 304</sup>. The function of such receptors has been proposed to warn the organism against forest fires in time.

The use of spectral filters for spectral discrimination is popular in both technology and biology. Birds are known to have developed oil droplet filters superimposed on their cones on their retinas<sup>201</sup>. The filters have a cut-off wavelength in the center of the natural sensitivity band of the receptors, and they alter the effective band to only half the width. Thus they sacrifice absolute sensitivity to gain spectral resolution and non-overlapping bands. An even more extreme example are the many deep sea predating fish which has a spectral long-pass filter in the cornea to distinguish down-welling natural radiation from synthetic radiation produced by the prey trying to hide their silhouettes<sup>305</sup>. By developing this the fish are blinded from natural sunlight in order to detect its prey. Filters can either be

of absorptive nature with dull spectral features and of high contrast, or interference based, with sharp edges but low suppression ratio. Mainly absorption longpass and shortpass filters are used throughout this thesis. Longpass filters are typically employed to suppress elastic light in fluorescence detection, whereas shortpass filters are mainly employed to clean up excitation light from LEDs; see, e.g., Paper VIII or P2.

A classical example of filter-based multispectral imaging, is color astrophotography with monochrome cameras and filter wheels. Here images of a static scene are taken for each wavelength band sequentially<sup>306</sup>. Often such filters are narrow-band interference filters matching atomic emission lines, allowing the mapping of the elementary distributions. In commercial color cameras such as the one employed in Paper V, tiny interference filters are coated directly on the pixels of the imaging chip in a Bayesian manner. From this we can understand that one color pixel is created from four original pixels<sup>253</sup>, and that the different bands are acquired from different spatial origins. This is similar to vision systems in biology, but one consequence of this in respect to orthogonality between the spatial and spectral domains, is that when imaging a black and white checker pattern of comparable size to the pixels the color can vary drastically.

When interference filters are tilted to 45° they are referred to as dichroic beam-splitters, transmitting one part of the spectrum and reflecting the other part perpendicularly to the initial optical axis. Dichroic beam splitters allow simultaneous acquisition of many bands by the use of several detectors. Such schemes are employed with PMTs throughout the lidar studies in this thesis, Papers X, XI, and XIII-XV. Beam splitter schemes can even be employed for imaging detectors<sup>307</sup>.

Array detectors such as linear or imaging CCDs or CMOS, can be used to create instruments with a vast number of spectral bands. Such instruments are referred to as spectrometers or polychromators (in contrast to monochromators which were previously more common). This is done by dispersing the light with a grating or a prism, converting the spectral dimension into a spatial dimension, and projecting this on the sensor. Today and throughout this thesis, grating based spectrometers are the most common ones. A prism based spectrometer was, however, designed in relation to P1. Both gratings and prisms disperse parallel light in different directions according to the wavelength. In order to make light parallel it is fed through a narrow slit which is placed at the focal distance from a concave mirror. The light impinges on the grating, and then on a second concave mirror converting the propagation direction to a position in the focal plane, where the array detector is placed. Modern optical design allows producing concave gratings combining the operations. Eventually the transfer function from the slit to the detector is an imaging operation for a single wavelength, with the consequence that a high spectral resolution is achieved by a narrow slit which conversely means low signal and long exposure. This is a common dilemma. In this thesis mostly wide slit widths are used to achieve a strong signal at fast speed. Even so, some of the stronger gas absorption bands can still be detected; see, e.g., Paper XII. Grating spectrometers have not one but several diffraction orders. This implies that, e.g., 355 nm UV light will also appear at 710 nm as if it was NIR. Most spectrometers employed in this thesis have installed higher order rejection filters. Since the spectrum is measured by different positions on the linear array, the longer sensing part of the array can be coated with long pass filters preventing the higher order diffracting from the UV from being detected there. Today compact spectrometers can be made with the size of a palm.

The fact that the slit is imaged on the array detector can be exploited by so-called push broom sensors. Here the linear array is substituted by a 2D imaging array; thus one axis corresponds to the spectral domain and the other corresponds to the spatial dimension along

the slit. When the depicted scenery is scanned over the slit a hyper-spectral image is created with continuously distributed spectral bands in each spatial pixel. This detection scheme is particularly popular for industrial inspection of materials on running belts<sup>257</sup> or in aerial and satellite monitoring<sup>256</sup> where the continuous scanning motion is inherently present. A particularly clever push-broom design is the prism-grating-prism (PGP) device<sup>257, 308</sup>, where the hyper-spectral push-broom function is achieved on a single optical axis and assembled in a tube. Inserting the PGP tube between any existing objectives and cameras converts any imaging system into a hyper-spectral imaging system, be it a microscope or a telescope.

Spectral discrimination can also be achieved through the Fourier domain by an interferometer. This is referred to as Fourier transform spectroscopy (FTS), or commonly Fourier transform infrared spectroscopy (FTIR). The classical design is based on a Michelson interferometer, where light is divided in two beams by a beamsplitter. One part is reflected by a stationary retro-reflector, whereas the other part is reflected off a displaceable retro-reflector which is scanned linearly back and forth in time. When the two beams are recombined in the same beamsplitter, constructive or destructive interference occur depending on the path length difference in the two branches and the wavelength of the light. This interference is measured by a photo detector perpendicular to the incident light, producing a time-domain signal referred to as the interferogram. When monochromatic laser light impinges on the system a squared sine wave is produced on the detector. The signal is then typically high-pass filtered electronically centering it on zero. Frequency analysis or the Fourier transform of such a signal will produce a single Dirac function with resemblance to the light spectrum of the impinging laser. By applying the superposition principle and seeing white light as the sum of infinitely many closely spaced laser lines, it can be understood that each single wavelength of the light produces its own frequency in the interferogram and that the broad white light produces as equivalently broad Fourier transform of the interferogram. If the photo detector is replaced by an imaging array, interferograms and spectra are acquired in every pixel of the imager. An FTIR instrument was used in Paper XIV and an imaging FTIR instrument in Paper XV.

Spectral discrimination can also be achieved by other interference techniques such as fiber Bragg gratings or acousto-optic filters. In the latter case, grooves are generated by standing sound waves and can be modified by changing the frequency of the sound. Tunable wavelength filters without moving parts based on polarization also exist for limited spectral ranges<sup>309</sup>.

So far we have only discussed spectral discrimination on the detection side, when performing spectroscopy on the diagonal of the EEM; see Fig. 2.3.1. We can equivalently discretize before or after the sample interaction. Discretizing the source wavelength can greatly increase the photon economy and sensitivity of a technique. This is the case for differential absorption lidar (DIAL)<sup>279</sup> or tunable diode laser absorption spectroscopy (TDLAS) in GASMAS<sup>103</sup>. Here, the tunable laser is scanned over gas absorption lines and recording is made by a single detector covering the scan range. The number of effective spectral bands for such systems is thus defined by the number of scanning steps of the light source, and the width of the effective spectral bands are essentially defined by the width of the laser emission. Since laser emission can be exceptionally narrow, fine spectral details can be resolved, and conclusions, not only on the gas concentration, but even on the temperature<sup>5</sup>, isotopic composition<sup>263</sup>, pressure<sup>165</sup> and nano porous confinement<sup>167</sup> can be reached. On a much broader scale spectral source discrimination was employed in Papers I-IV. The difference between discretization on the source side and the detection side is that the EEM is either integrated along the emission dimension or the source dimension, respectively. When the elastic effects on the diagonal are dominating the two approaches are equivalent. When attempting to measure the reflectance in a scenario with strong

fluorophores, this can potentially cause the reflectance to exceed 100%. The effect can be seen in satellite imaging from chlorophyll where the near infrared reflectance spectrum from water bodies with high algae content cannot be entirely explained from the absorption spectra of the involved species<sup>310</sup>. Along those lines, special caution should be displayed in biology when measuring reflectance of animals in the UV region. Such measurements are typically performed with deuterium-tungsten lamps emitting intensively in the deep ultraviolet (DUV) which could potentially be downconverted by, e.g., keratin or chitin and reappear at the UV and blue region.

In a dedicated fluorescence spectroscopy setup, discrimination on both the source and the detection side is in general always performed. Emission spectra are associated with their excitation wavelength. In the analytical chemistry community clear substances are measured in cuvettes. Here white light is collimated and passed through a motorized scanning monochromator and impinges on the cuvette; fluorescence light is then collected perpendicularly and fed through a second scanning monochromator before being detected. For such simple geometries and substances, the EEM can be reduced to the absorption spectrum and the emission spectrum, which are often shown next to each other. In the simplest cases these are mirrored distributions. For more complex samples the entire EEM most often must be acquired and taken into account. It can be measured by similar approaches using contact fiber probes<sup>122, 123, 311</sup> in some cases replacing the monochromators by filter wheels. In this thesis the excitation light is varied by switching between different LEDs or laser sources emitting in different wavelength; see, e.g., Papers VIII-IX and XIV. In applied fluorescence spectroscopy it is an advantage to measure the elastic reflectance both at the excitation wavelength and at the emission wavelength. Such a procedure allows to compensate for re-absorption effects and to recover the intrinsic fluorescence by consideration of the total escape chance<sup>312, 313</sup>.

However, rejection of the elastically scattered excitation light is also an important aspect in fluorescence spectroscopy. This is done by three complimentary approaches; by discriminating the light with the original propagation direction, by selectively reflecting off the spectral region of excitation and by absorbing the excitation light in detection through long pass filter. In total-reflection X-ray fluorescence (TRXRF) used for elementary analysis of, e.g., heavy metals in food inspection (See Fig. 2.1.3), no spectral filters are appropriate and the method relies on grazing incidence of the excitation light and detection at normal incidence; the geometry resembles that of Paper VI. In the monostatic lidar Papers X, XI, XIII and XIV, the excitation and detection angle must necessarily be the same. In this case the elastic back scatter is first separated by a dichoric filter and then completely suppressed by an absorption long pass filter. In Papers VIII, IX and P3 both the angular method and a long pass filter is used. When detecting weak fluorescence it is a potential risk to expose the longpass filter to the excitation light, since the filter itself might fluoresce.

### **4.3 The spatial domain**

The optical discretization of space is commonly associated with the pixels in CCD and CMOS imaging chips. However, whenever any light measurement is performed the collected photons originate from a discrete and confined area or volume. In the x-y dimensions, space can be discretized by imaging systems, where every pixel on the imaging chip is imaged to a corresponding square in the object plane. Imaging systems convert photon propagation direction into a physical position; therefore it can often be conceptionally difficult to distinguish spatial discretization from angular discretization. In this thesis spatial discretization refers to position on the sample surface where the detected light originates from, while angular discretization refers to distinguishing light emitted from the same spatial position in different propagation angles. In microscopy spatial resolution is

given in terms of the smallest separable distance. When the depicted objects are far away, like in the case of stars in astronomy, spatial and angular discrimination become the same and the terms angular and spatial resolution are used synonymously. One of the simplest form of imaging consist of a small pinhole followed by an image plane - the different propagation directions of light would then separate at different spatial positions in the image plane. Pinhole cameras have the advantages of having an infinite focus depth and no aberrations including chromatic aberration. However, the photon collection efficiency is exceptionally poor. Pinhole camera can be encountered in the natural vision of many species; also it is considered that the eyes of mammals including our own evolved from pinhole cameras. Because of the opacity for biological tissue and water in the MIR and TIR regime, thermal sensing organs in the animal kingdom are exclusively based on the pinhole principle.

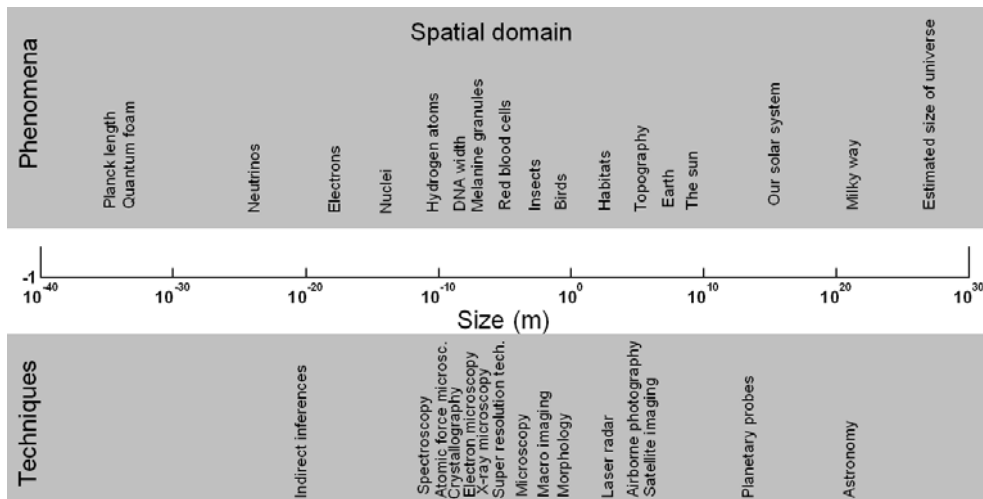


Fig. 4.3.1. Spatial overview for comparison of size and applicable imaging techniques.

With similarity to the other domains discussed, the space spans vast magnitudes from approximately  $10^{27}$  m of the known universe down to the quantum foam and the Planck length at  $10^{-35}$  m. Several attempt to make such scales understandable have been made. Observations at astronomical scales to a great extent rely on optical techniques. Microscopic methods down to approximately 10 nm can be achieved optically with super-resolution or extreme UV methods. Smaller molecular and atomic features can be inferred optically indirectly in the spectral domain. The work in this thesis ranges from molecules around 1 nm, through arrangement 100 nm sized nano spheres in damselflies, through barbules and RBC of several micron size, through macro imaging on the millimeter and centimeter scale, through meter long-lidar pulses up to animal habitats of hundreds of meters.

More efficient imaging is achieved with spherical lenses; such lenses are mainly characterized by their focal length due to surface curvature, and by their aperture. Lens based vision was used by vertebrates for more than half a billion years. The earliest known man made lens is the Nimrud lens dated to 750 years BC from ancient Assyria. The operation of lenses is to convert parallel light propagation direction into a spatial position in the focal plane. Image formation with lenses can be understood with ray tracing and Snell's equation of refraction as described by Ibn Sahl already in the tenth century. It can also be understood from the perspective of the wave model; a point source in the object plane emits an omnidirectional light wave diverging in a spherical manner; part of the spherical wave is collected by the lens aperture, the wave in the center of the lens experiences a relative delay

in respect to the wave in the periphery, and this causes the wave front to converge unto an imaged point in the image plane. Since the delay is introduced by the refractive index in the optical material, lens-based imaging systems are known as refractors. A major disadvantage when using refractors for spectrally resolved imaging is that the refractive index is different for different wavelengths; thus the focal length is different for different colors.

$$\frac{1}{f} = (n_1 - n_0) \left( \frac{1}{R_1} - \frac{1}{R_2} + \frac{d(n_1 - n_0)}{n_1 n_0 R_1 R_2} \right) \quad \text{Eq. 4.3.1}$$

In commercial color imagers chromatic aberration is overcome by the use of duplet or triplet lenses. Here convex and concave lenses of different materials are employed alternately to produce an equal effective focus length at two or three wavelengths, respectively. The magnification, the image and object plane relate to the effective focal distance through the lens formula:

$$\frac{1}{f} = \frac{1}{a} + \frac{1}{b} \quad \text{Eq. 4.3.2}$$

However, this formula is only a first order truncation of the true solution, and it is based on assumptions such as that the lens is thin and that the depicted scene is close to the optical axis. Finally, lenses cannot be produced with very large apertures. For spectrally broadband applications imaging can be achieved by curved reflective mirrors instead. This is an advantage because the focal length remains the same regardless of the wavelength. Also mirrors can be made exceptionally large; the largest optical imager in the world will be the Giant Magellan Telescope (GMT) which has a segmented aperture of an equivalent to 25 m in diameter. Since the number of photons collected scales with the aperture squared, the GMT is a factor ten thousand more sensitive than the Newtonian telescope used in, e.g., Paper XII. Papers III and IV exploit recently available reflecting microscope objectives (e.g. by Edmunds Optics Inc) to maintain focus from UV to NIR. These devices are inspired by the Cassegrain telescope. Both Newtonian and Cassegrain reflectors suffer from an obscuration by the secondary mirror. This partly reduces the collection area but also complicates the simple terms numerical aperture and acceptance angle used for refractors. In remote sensing and lidar these issues is referred to as the form factor problem<sup>315, 316</sup>. Similar issues affect the angular sensitivity lobes discussed in Paper III. The form factor can be measured experimentally by inserting an object with a known cross section into the field of view at various positions. It can also be measured by detection of the nitrogen Raman signal<sup>146</sup> or by comparing vertical and horizontal sounding<sup>317</sup> with the assumption that horizontal profiles are homogeneous. Finally, it can be estimated numerically by ray tracing or by analytic functions such as<sup>315</sup>:

$$G_{(r)} = \frac{G_0 (1 + \tanh(\frac{r-r_0}{R}))}{r^2} \quad \text{Eq. 4.3.3}$$

The performance of imaging systems in terms of spatial resolution can be described by the point spread function (PSF). This is the image of an infinitely small point and the smaller the PSF the better the imaging system. An equivalent measure is the modulation transfer function (MTF) which is determined by varying spatial frequencies, and thus relates to the PSF through the Fourier transform. The PSF should be compared to the impulse response in the time domain, or a spectrometer response to a laser line in the spectral domain. The PSF in Paper III is just below 1  $\mu\text{m}$  which is close to the diffraction limit, since the numerical aperture is not very high for the objective employed. The transverse resolution in Paper V is

in the order of 100  $\mu\text{m}$ . For the lidar papers, e.g. XIV, the PSF is approximately 10 cm at the sample location. From the Abbe/Rayleigh resolution criterion there are two obvious ways to achieve high resolution - one is to increase the numerical aperture. This is done in microscopy by immersion objectives or complimentary  $4\pi$  objectives<sup>318</sup>. In astronomy it can be done by interferometric combination of light from several telescopes<sup>319</sup> or by phased arrays in the radio-wave region<sup>320</sup>. Another approach is to image with shorter wavelengths toward the X- and gamma-rays. The largest problem by doing so is to construct imaging mirrors which reflect in that spectral region. However, it can be overcome by using multilayer mirrors<sup>248</sup> or grazing incidence mirrors<sup>321</sup>. However, in bio-photonics the tissue contrast in the X-ray region is weak on a small scale. Recently, methods beyond the Abbe criterion have also been developed for fluorescence imaging, so-called super resolution microscopy. Several such methods exist; all of them are based on fluorescence from small confined volumes; the locations of which can in turn be determined with precision beyond the Abbe criterion. One method is based on the suppression of fluorescence by depletion of the excited state on ring around the PSF, causing the PSF to diminish<sup>273</sup>. Another approach is based on inherently stochastically blinking molecules switching between a bright and dark state. Framing of the blinking single molecules behavior over time allows estimating their center position to a much higher precision than the width of the PSF<sup>138</sup>. The super-resolution techniques produce remarkably sharp images of tiny biological features such as axons of neurons<sup>322</sup> and constitute a major advancement of peering into the microscopic living world. From a cell biological point of view, the most important aspect of super resolution is the so-called co-location analysis, where fundamental question regarding the occurrence or organelles and certain proteins can be correlated in space. The analysis resembles the correlation analysis presented in the temporal domain in Paper XII. The resemblance between blinking fluorescence sensitizers and the blinking bee sensitizers<sup>142, 243, 287</sup>, should also be noticed.

It is important not to confuse spatial resolution limits with the ability to detect small objects or classify their sizes. Although our eyes cannot resolve the spatial extension of stars, we can still see them but their extension is given by the size of the point spread function in our eyes. Similarly, we can also see the light scattered from a single aerosol of just 100 nm diameter, and although the size is not resolved it can be determined from the scattering spectrum, or the color of the scattered light. This is exploited in multiband elastic lidars for profiling the aerosol size distributions<sup>240, 250</sup>. Similar phenomena arise in a number of situations where geometrical size can be inferred by details in the spectral domain. The most well known examples are atomic absorption lines related to the spatial electron distribution around the nuclei<sup>102</sup>. Broadening of narrow absorption lines might also describe the cell size of nanoporous materials<sup>167</sup> far below the probing wavelength. As discussed in Chap. 2, the infrared signature of snow recorded by satellites can describe the snow grain size on the micrometer scale<sup>162</sup>. Ordered or quasi-ordered samples such as crystals<sup>180</sup> or biological tissue<sup>81, 170</sup> can produce structural colors from which the dominant spatial frequency can be estimated; typically such features are sub-wavelength. The thickness of nanometer sized wing membranes can be inferred by the color vision of the naked eye<sup>79</sup>. In Papers X and XV such issues are discussed and the concept of remote microscopy is promoted.

Multispectral imaging and spatial resolution not only serve for mapping and geometrical distribution of diverse substance; it can also serve to describe the spatial variance, texture or patchiness of the same sample. This is a classical topic in the community of image processing where the traditional approach is to summarize the spatial frequency content<sup>323</sup>. In Paper V another aspect of multispectral texture analysis is discussed. The main argument of that paper is that the reflectance variance provided by the spatial resolution holds more information than the spatial average. This implies that a black and white zebra and a grey

donkey might have exactly the same reflectance spectrum for a high resolution spectrometer, whereas the two samples are easily distinguished by taking their spatial variance into account. The approach presented in Paper V might provide improved skin diagnostic methods in the future.

Just like both the excitation and emission wavelength can be discretized in the spectral domain for, e.g., fluorescence spectroscopy, this kind of double discretization can also be performed in the spatial domain. This is typically done by projecting a point source to the sample surface, and image both this point and the surrounding surface elements with an array imager. The projection of the point source is then moved and a new image is acquired. The detection scheme is usually developed for macro imaging of body parts or small animals<sup>175, 182</sup> but the method has also been demonstrated remotely in relation to snow monitoring<sup>161</sup>. This is a popular approach in biophotonics where photo migration causes upwelling of injected light in the neighboring regions. If the sample is assumed to be homogeneous in all three spatial dimensions, absorption, scattering and anisotropy coefficients can be deduced from the spatial profile of the upwelling light. For layered tissues or samples the method can provide depth information, since the light upwelling the furthest away from the incidence is also light most likely to have reached the deepest interrogation. The concept of spatially resolved measurement for the purpose of deducing optical constants is the core of P1. The fact that photo migration transports light impinging on one surface element to another, also quickly leads to the conclusion that reflectance from a certain sample taken with an imaging system and a flat field of white illumination gives one value. But reflectance of the same sample measured by a point probe will give rise to a different value. In general, the red reflectance will be lower in the latter case, since the long waved light are more prone to escape the field of view in a fiber probe configuration.

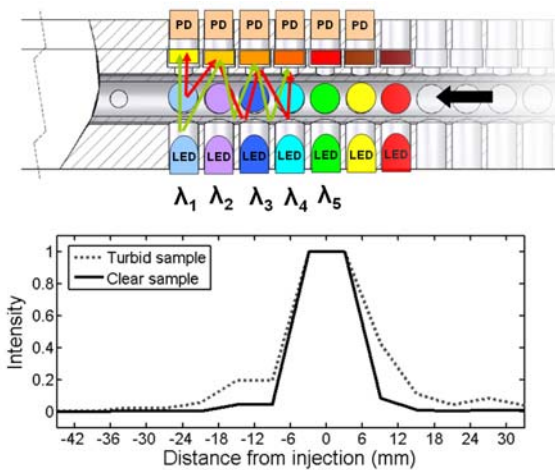


Fig. 4.3.2. Spatial resolution can be used for analyzing the escape chance of photons as a function of the distance to the point of injection. This is the case in P2 where the elastic light from each LED light source is detected by an array of photodiodes. See also Fig. 1.4.1, Fig. 3.1.2 and Fig. 3.1.6.

Imaging is not a compulsory part of spatial discrimination. In terms of contact methods light can be injected at one position and retrieved at other positions on the sample surface or in the sample volume. This can be done with multiple fiber probes, or by directly applying the sources and detectors<sup>324</sup>. In prostate cancer treatment by PDT a number of fibers are inserted with syringes into the tumor by rectal ultrasound guidance. The fibers are then used to irradiate the tumor tissue by red light for treatment. For improved treatment the same fibers are iteratively used for diagnosing the treatment progression. During the diagnostic phase of the procedure, light is injected in one fiber at a time and recorded by all other fibers, and the plurality of light paths allows a crude 3D reconstruction of the tissue<sup>325</sup>. Similar approaches known as diffuse optical tomography (DOF) have proved capable of

producing crude 3D maps of the oxygen consumption in the brain<sup>172</sup>. In P2 a large number of unique light paths are formed between LEDs and photodiodes along a transparent tube containing the sample, the many measurands allow the determination of a large number of optical coefficients.

Space can also be discretized in the z-domain along the optical axis. This can for example be achieved by focusing an imaging system with a short focal depth at different depth. This is the typical approach in confocal microscopy<sup>326</sup> and certain CW Doppler lidar schemes<sup>327</sup>. For phased array methods all three dimensions are discretized. In the optical region such approaches must instead be based on interferometric schemes, where constructive interference is achieved by surfaces matching the distance to the reference branch. Such methods are referred to as digital holography<sup>328</sup> or optical coherence tomography (OCT)<sup>329</sup>. These techniques typically provide an axial resolution in the order of microns. For longer ranges and remote sensing interferometry is unfeasible but axial resolution can be achieved by lidar. Here the axial resolution is mainly given by the laser pulse length, the detector response time and the sampling frequency. Deconvolution with the instrument response function (IRF) can yield improved axial resolution<sup>330, 331</sup>. The pulse lengths for typical lidar systems are 1-10 ns which correspond to spatial extensions of 30-300 cm. In Papers X, XI, XIII and XIV the axial resolution is approximately 150 cm. The range covered is up to a couple of hundred meters.

Distance information can also be determined without phase information or pulsed laser by triangulation. In the image processing community this is referred to as stereo vision. Most such systems have several fixed cameras employed and is calibrated by a well-defined geometrical object. Such systems with high-speed cameras have been used to study the detail of insect flight and insect interaction<sup>332</sup>. Other approaches to triangulation with a single camera assume that the scenario is still and application of advanced algorithm to reconstruct trajectory and orientation of a handheld moving camera, where after the complete 3D geometry of the surroundings can be reconstructed without calibration or priori knowledge<sup>333</sup>. In lidar, steady-state ranging can also be achieved by triangulation; this is referred to as bistatic lidar<sup>100</sup>. Here the transmitter and receiver are separated in contrast to mono-static lidar, where transmittance and detection are performed coaxial.

#### **4.4 The angular domain**

The concept of comparing particles scattered in different angles in respect to the incident angle has a long tradition in nuclear and particle physics. A famous example is the Ernest Rutherford experiment on a gold foil from which he could conclude that the nuclei of atoms are positively charged and very small. Today most target chambers in large-scale particle accelerators include the option for studying particles scattered in many different angles. In most cases such instrumentation is required to surround the sample. A number of similar schemes appear in the optical region. In order to achieve a high angular resolution both the illumination and detection should be collimated. Thus a collimated laser beam in the angular domain should be compared to a point source in the spatial domain, a monochromatic laser line in the spectral domain or a picosecond pulse in the temporal domain.

The absolute direction of light propagation in respect to gravity has a number of implications in ecology. In ocean environments, for instance, the ambient photon flux is mainly downwelling, as a result the eyes of many deep-sea fish point upwards and they observe their prey by their silhouettes, whereas other fish have been found to produce light on their bellies to reduce their silhouettes<sup>254, 305</sup>. Collimated light has been actively produced several millions years back by the ponyfishes and flashlight fishes projecting

beams of NIR light on their prey to detect their reflectance. Because of the spectral selectivity of chlorophyll derived retinal photosensitizes the NIR light is visible only to predators themselves<sup>301-303</sup>. Man-made collimated light was developed in relation to maritime navigation and lighthouses. During Second World War collimation of light was further developed for searchlights in relation to anti-aircraft warfare. Such searchlights were based on discharge arcs with high brightness and also formed the basis for the first lidars<sup>334</sup>. Considering imaging systems such as lenses or spherical mirror, we can conclude that since they convert propagation angles into a position in the focal plane, then it requires an infinitely small point source to create an infinitely collimated beam. However, following the construction of the first functional laser in 1960, light could be collimated beyond all previous experience. The reason for this is that stimulated emission in laser has a draining effect, where any preferences regarding propagation, wavelength or polarization quickly dominates and suppresses emission with less prominent properties. Therefore the spectral line width of lasers is much narrower than the normal system emission linewidth, the polarization of a Brewster angled cavity is much more polarized than unpolarized light passing through such a window, and the collimation is much higher than what can be explained geometrically by the length of the cavity.

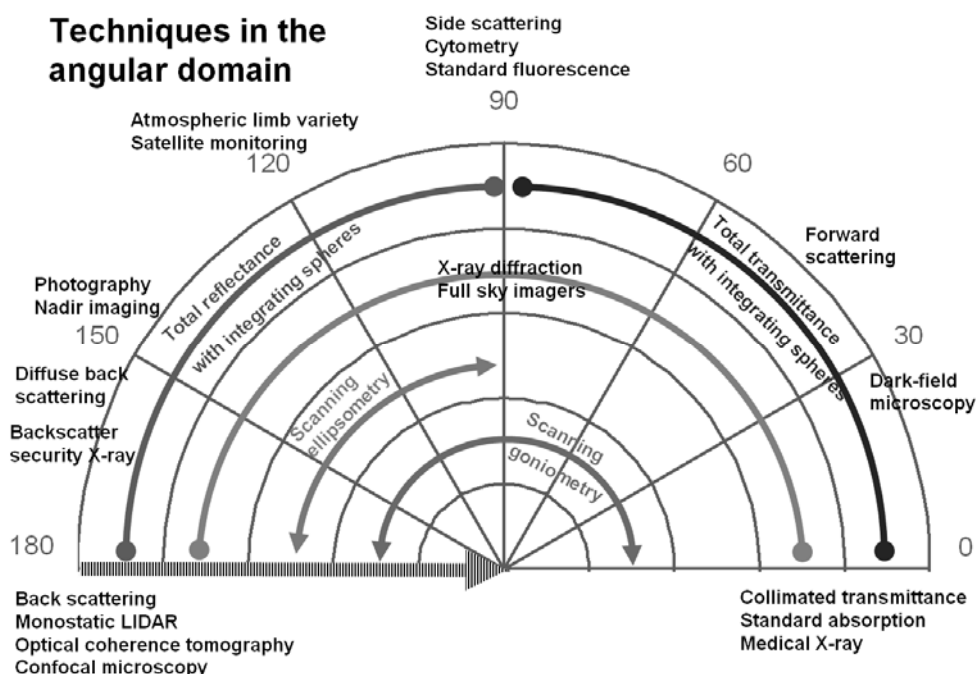


Fig. 4.4.1. Overview of different techniques in the angular domain. Here the situation is simplified to relating the detected angle in respect to the incident angle, the radial axis is not assigned anything. The striped arrow indicates incident light, the degree scale indicates the angle scattered. At 0° we find collimated transmittance and standard absorption measurement in, e.g., cuvettes in analytical chemistry. Medical X-ray and computerized tomography also belong to this group. At 30° typical dark-field microscopy is performed. The entire span from 0°-90° can be measured with integrating spheres in transmission modes. Cytometry and fluorescence is typically measured at 90°. Atmospheric limb monitoring of gases, e.g., by SCIAMACHY, can be performed at various scattering angles. Backscattering aerial or space-born imaging mainly depends on the latitude of the depicted area. Photography and backscatter X-ray for, e.g., airport security, are close to 180°. Techniques such as lidar, OCT and confocal microscopy are often limited to strict backscattering. The entire span from 90°-180° can be collected by integrating spheres in reflectance mode; traditional X-ray diffraction with film exposure normally samples the entire region from 0°-180°. Scanning methods include, e.g., ellipsometry and goniometry.

A summation of the scattering angle and angular sensitivity lobes explains a number of measurement geometries such as total transmission, collimated transmission, total reflectance, etc (See Fig. 4.4.1). In practice neither the source nor the detection can be infinitely collimated and the detected scattering is the spherical convolution between the illumination lobe and the detected lobe. This corresponds to the case where the PSF smears out the depicted scene by a 2D convolution in the spatial domain.

For scattering by spherical particles it is enough to relate the detected angle to the incident angle. Such polar scattering probability distributions are known from Mie scattering theory and differ depending on the incident or detected polarization. For non-spherical particles, sample surfaces or sample slabs the orientation of the surface normal will additionally influence the scattering probability distribution. This is the case for the red blood cells with shapes as biconcave discs studied in Papers III and IV. Certain samples may additionally have features in preferred directions along the surface. This is, for instance, the case for the feathers studied in Papers XIV and XV. Here the fact that the barbules are aligned in a certain direction along the surface implies that, e.g., a 45° reflectance measurement will yield different values when the sample is rotated around the surface normal. Samples where dominant spatial frequencies in the refractive index in any of the three dimensions are of the order of magnitude as the probing wavelength, can produce interference effects. Unless the spatial frequency spectrum is spherical symmetric<sup>335</sup> the sample will demonstrate iridescence, with the implication that the spectral signature of the sample changes significantly depending on the angles between the illumination, surface normal or detection. Iridescence is discussed for birds in Paper XV. Similar effects have been demonstrated for insect wing membranes<sup>79</sup>. Both these aspects are interesting since birds and insect wings are inherently self angular scanning. We have, however, not had the adequate instrumentation to demonstrate these aspects *in-vivo* in this thesis.

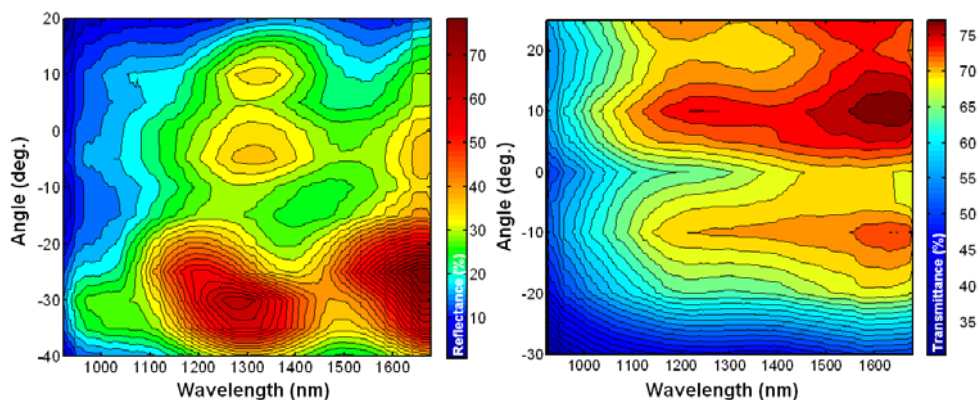


Fig. 4.4.2. Insects are self angular scanning up to several hundreds times per second. When the wavelength becomes large in comparison to the thickness of the wing membrane, iridescent features arise. Here infrared, reflectance and transmittance from a *Calopteryx Virgo* male wing change according to the angle of observation and illumination. The reflectance measurements are taken with the light source perpendicular to the field of view only rotating the wing. Zero angle correspond to 45° incidence of illumination and observation. The ballistic transmission for the same geometry is show to the right for reference. The spectrometer is a polychromator with an InGaAs array (StellarNet). Oscillations can be seen in the spectral domain, for three times thinner membranes of smaller insects this produces iridescent colors in the visible<sup>79</sup>.

In terms of instrumentation all detectors such as photodiodes or CCDs have an inherent angular sensitivity originating from the Fresnel equations and the layers that the light need to pass prior to detection. This sensitivity lobe is specified in the data sheets for most

photodiodes. This is in all respects identical to the angular emission lobes provided for LEDs, and both sensitivity and emission lobes can be approximated by the form:

$$I = I_0 \cos^m(\theta) \quad \text{Eq.4.4.1}$$

The lobe is often summarized by a single angular value where the intensity has dropped to half. Similarly, the emission of lasers is typically specified with a divergence angle and further a beam quality. The beam quality is a measure of how close the beam profile is to a Gaussian. This is particularly interesting since perfect focusing of parallel rays by, e.g., a lens will produce the Fourier transform scaled by the wavelength of the beam profile in the focal plane. The Gaussian function is the only function which remains intact through Fourier transformation and also the beam shape which produces the smallest focus with the highest energy density. This is identical to beam apodization in, e.g., medical ultrasound and radar and also has several equivalents in terms of mathematical windows and envelopes in digital signal and image processing<sup>336</sup>. The Fourier relationship between collimated beams and their focus can also be exploited for light-speed image processing<sup>337</sup>. In this thesis the lasers for lidar and telescopes typically exhibit a divergence of  $0.05^\circ$  of the beam or field of view, respectively. Some attempts to transilluminate birds by sun and moon light were made in relation to Papers XIV and XVI. Here the divergence is limited by the opening angle of  $0.5^\circ$  for both the celestial bodies. The LEDs and fiber tips in, e.g., Paper VIII, typically emit and collect light within a  $20^\circ$  cone, bare photodiodes with frosted glass in front, as in P2, collect light in a Lambertian manner corresponding to a half angle of  $60^\circ$ .

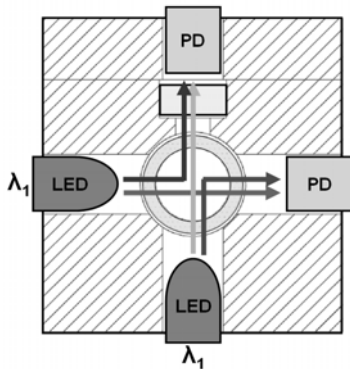


*Fig. 4.4.3. Both forward and side scattered light is retrieved by the combinatorial light path spectrometer in P2. Each light path in the shown cross section is unique either in terms of angular detection or in terms of filter configuration; compare to Fig. 1.4.1, Fig. 3.1.2, Fig. 3.1.6, and Fig. 4.3.2.*

Although all light sources and detectors emit and detect angular distributions, angular resolved instruments are characterized by discriminating several light propagations and having more than one angular sensitivity lobe, just as a spectral imager is characterized by providing more than one pixel and more than one spectral band. In analogy with the source-detector switching paradigm in Papers II-IV this can be achieved either by illuminating the sample from one direction and detecting scattered light in several direction, or by observing the sample from one direction and illuminating the sample from several directions. The latter option was chosen in Paper III, since the cost of the detector is hundred times larger than that of the source. The instrument in Paper III was inspired by previous work at our department with integrating spheres, where multi-lobed non-imaging spectrally resolved measurements were performed on tissue slabs<sup>173</sup>. In this setup, the total reflectance, total transmittance and collimated transmittance were discriminated in order to deduce the optical properties in tissues. In contrast to a single reflectance or transmittance measurement, the added angular lobes allowed estimation of absorption, scattering and anisotropy. However, estimation of refractive index would require an additional lobe since the system of equations would be underdetermined otherwise. This does not imply that

varying refractive index would not influence the estimated properties listed above. In many tissue optics studies the refractive index is assumed to have a certain value regardless of the wavelength. Also, the fact that several measurements are performed does not necessarily mean that the system of equation is well conditioned numerically. The situation, where even the simplest imaginable optical measurement of, e.g., absorption is entangled with refractive index or fluorescence, often leads to the conclusion that nothing can be measured accurately without measuring and compensating for all imaginable optical properties. This is extensively discussed in P2, and it is demonstrated in Jesper Borggren's master thesis<sup>99</sup> how substances giving rise to entirely different optical phenomena, such as absorption, scattering, fluorescence and refraction can be disentangled by measuring in a large number of unique optical path with different source and detector spectra bands, lobes and migration distances.

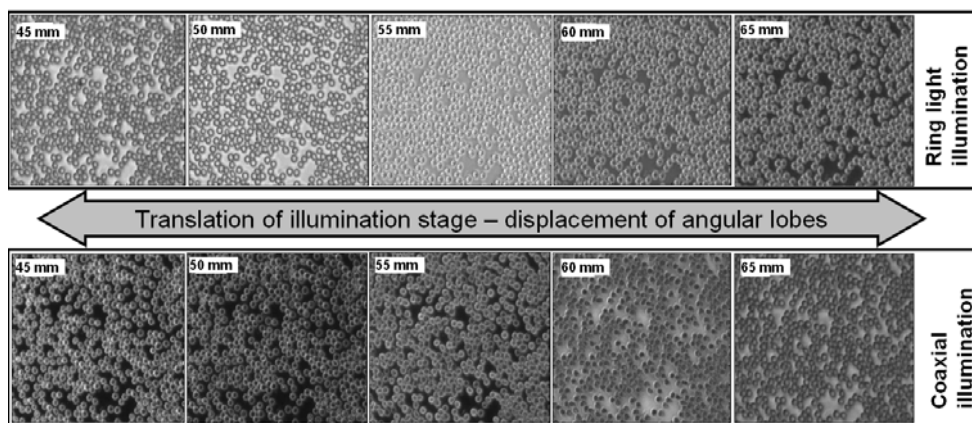


Fig. 4.4.4 The concept of numerical aperture becomes slightly more complicated when using reflecting microscope objectives. Similar discussion arises in relation to form factors of reflective telescopes. Above the effect of translating the illumination stage, and thus the impinging angles, in P3 is apparent, bright field becomes dark field and visa versa. The pictures depict a thin blood smear and are all acquired at the yellow wavelength 590 nm.

Other instrumentation with a few discrete angular sensitivity lobes includes particle analyzers and flow cytometers. The method is suitable for dilute solutions with cells or air with dilute aerosol particles. The typical approach is to let a continuous wave (CW) laser or light source illuminate a flow of clean liquid or air perpendicular to the flow. When a particle in the flow enters the beam light scatters elastically and inelastically in all directions. A few photo multiplier tubes (PMT) collect the flashes of backscatter, forward scatter and fluorescence in one or two spectral bands. Flow cytometry is widely used in pathology to classify the composition of dissolved tissues<sup>338</sup>. In air monitoring, cytometry-like methods is employed for warning systems against terrorism with bio-warfare aerosols such as anthrax<sup>339</sup>. Cytometry is interesting in the sense that it can process sample sizes of tenth of thousands in a minute. Such information has close relation to the information produced by spectral imaging and the details in Paper V. Also cytometry should be compared to the dark-field spectroscopy setup in Papers III and XII. The number of detectors and angular lobes can obviously be increased to a large number by introducing more detectors<sup>340</sup> or by using array detectors<sup>341</sup>. Thus, refined details of the Mie scattering lobes can be resolved; see Fig. 2.5.8.

More continuous angular scattering can also be resolved by using the time domain, and sequentially scanning of the detector over time around the scattering particles with respect to the illumination. This is referred to as goniometry<sup>342</sup> and was explored already in the 19<sup>th</sup> century in relation to crystallography. Such studies later evolved into X-ray diffraction with

film exposure and eventually revealed the nature of the double helix in 1953<sup>343</sup>. As discussed in Chap. 2 scattering, reflectance and polarization are closely related, and the area of detecting the back-scattering from surfaces as a function of angle, wavelength and polarization is referred to as ellipsometry. Ellipsometry is typically performed with polarized white light and a spectrometer with an additional polarization analyzer. The angle of both the illumination and detection is scanned sequentially and mostly the specular reflection is considered. Ellipsometry and imaging ellipsometry<sup>344</sup> are widely used in optical manufacturing for inspection of the consistency of optical metal multilayer coatings. Both refractive index and thickness can be deduced from the highly dimensional data produced by such instruments. Ellipsometry has provided insight into advanced color producing mechanism in insects<sup>345</sup> and could also provide precise information on, e.g., the thickness of insect wings<sup>79</sup>.



*Fig. 4.4.5. Automated polarimetric goniometer made from inexpensive LEDs, film polarizers, LEGO and controlled by a LabView compatible Mindstorm micro-processor. The setup was assembled during an exercise on scattering from powdered milk during a workshop in Lima, Peru<sup>346</sup>.*

Apart from changing the detection angle in respect to the illumination angle, other experiments involve fixed detection in respect to illumination, but sequentially scanning different orientations of the sample. Such experiments may reveal if the nature of a spectral signature is iridescent and structural, and the method has been used several times in relation to bird coloration<sup>80, 347-349</sup>. In this thesis we used this approach for transmittance in Paper XIV and for reflectance in Paper XV.

## 4.5 The temporal domain

The time domain is special with respect to, e.g., the spatial domain in the sense that it is causal; thus a given event can only affect events which follow. The oldest radiation detected by mankind is approximately 13.7 billion years old from the beginning of the universe. Historical solar light intensity impinging on the earth can be indirectly inferred by analysis of cosmogenic isotopes such as <sup>10</sup>Be in ice-core drilling<sup>350</sup> and geology. Such historical solar irradiance measures are valuable for the understanding of climate changes<sup>351</sup>. From the earliest days of mankind humans have been fascinated by gazing at stars, and although light could not be measured quantitatively, civilizations in each continent had dedicated clerks taking notice of cosmic phenomena and events. Old scriptures of cosmic events are still of interest in modern astronomy<sup>352</sup>. Important dates for, e.g., explosions of supernovas, whose afterglowing debris can still be observed are given. The first photograph was taken in 1826 by the French inventor Joseph Nicéphore Niépce and the first color photography by James Clerk Maxwell in 1861. Historical photographs are still today a valuable source for historians peering back in time. More consistent quantitative imaging of light, reflected from the earth's surface, has been carried out by the LANDSAT satellite imaging program since 1972. The images provided by this longest lasting earth observation program, throughout almost half a century, still provide countless aspects of the human impact on the environment such as deforestation and the formation of megacities during the same period. Satellite monitoring of seasonal time scales provide important forecast for,

e.g., upcoming drought disasters. Monitoring with sampling interval of weeks are used, e.g., to estimate the damage on human infrastructure by seismic activities and give overview much faster than anything that could be provided by any ground team<sup>353</sup>.

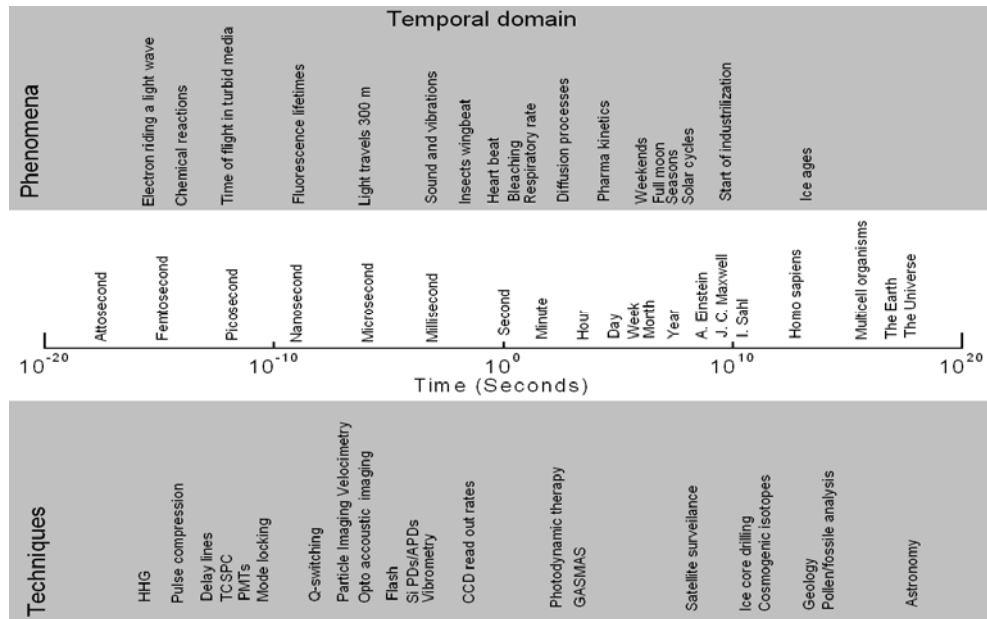


Fig. 4.5.1. Temporal overview of time units, phenomena and associated technology.

Daily sampling rates and spectrally resolved satellite imaging can reflect anthropogenic behavior and religious culture on the ground<sup>247</sup>. This can be achieved by measuring the atmospheric NO<sub>2</sub> column in the blue spectral region because this correlates with the car activity. When analyzing this in terms of week day, a dip can be seen on Sundays for Christian cities, on Saturdays for Jewish cities and on Fridays for Islamic cities. By measuring the relative depths of the dips the strength of the faith can be estimated and compared between, e.g., South and Central Europe. It is fascinating that mindreading can be performed from 785 km altitude. This study is also a good example of an optical acquisition that is neither extreme in spectral, temporal or spatial regime or resolution but using creativity and getting the idea of plotting the concentration against the week days novel results are produced. This is much along the lines of this thesis. The NO<sub>2</sub> dip in the week days should be compared with the absorption dip along the spectral domain: In the first case the type of religion is discriminated according to the weekday position and the faith estimated by the dip strength; in the latter case the type of gas molecule are discriminated by the wavelength position and the concentration by the absorption depth. From a mathematical point of view there is no difference except for the name on the axis. This has given rise to an emerging field sometimes referred to as dynamic contrast which can be superior to spectral contrast under the right conditions<sup>109</sup>. In the remote sensing community this is referred to as multi-temporal imaging as compliment to multi-spectral imaging<sup>354</sup>. In this thesis continued monitoring over many days was performed, e.g., in Paper XI. In this study insects were marked with fluorescent powder and released at time zero. The marked individuals reappeared the following hours and days. The counts will decay over time partly because the insect perish and partly because they disperse to neighboring habitats. Thus, this novel non-invasive day regime monitoring method provides a new tool for studying the migration of insects, much like diffusion of, e.g., gases can be studied by laser spectroscopy<sup>165</sup>.

With hour-based sampling rates details can be studied as the sun rises and sets. This cycle governs the temperature and most life on the planet. Hour-based sensing is typical in traditional lidar research. Here pollution of, e.g., NO can be associated with traffic rush hours and the effects of changing weather conditions on the atmospheric chemistry<sup>317</sup>. In Paper XII the comparative activity of two sexes of damselflies is measured during an entire day. By such monitoring their habits can be quantified: At which time do the males become active? When are the females active? A typical phenomenon is that the weather changes on the hour basis; this can be exploited for so called model excitation. Model excitation is a term from system identification<sup>355-357</sup> in control theory and robotics, and refers to the span of parameter values when building a mathematical model from empiric observations. This span will consequently determine the validity of the model. Thus, by monitoring over hours, the wind and temperature changes, and this affects the flight activity of either of the sexes. A comparative flight preference model can be constructed from this; see Paper XII. Such activity models relate to the species sensitivity and adaptation to climate changes. It also relates to the spreading of agricultural pests, pollinators and disease vectors.

The diffusion of substances can be studied on the scale of minutes, One example is gas diffusion in fruits<sup>165</sup> with implications to preservation and export possibilities for developing countries. The distribution of drugs in the body also occurs on the time base of minutes. This is referred to as pharmacokinetics and is of great importance for, e.g., the uptake and timing of PpIX for therapeutic PDT purpose<sup>358-360</sup> and diagnostic purposes as in Paper VII. The spatial distribution of such drugs or fluorescent sensitizers can also be recorded with a small animal imaging camera. Here every single pixel in the image contains fluorescence intensity as a function of time. The vector contains information of, e.g., when the drug arrives to the body part, how much does arrive and how long it stays. Some of the most extraordinary images in biophotonics are produced in this way<sup>109</sup>. This is referred to as dynamical contrast. The images provide contrast between different internal organs according to their function far beyond any contrast which can ever be achieved in the spectral domain. In another patent application by the author<sup>361</sup>, a method for quantifying the pharmacokinetic physical response of blood vessels when subject to, e.g., adrenaline is filed.

With sampling rates in the order of a second, photo-chemical kinetic processes can be observed. A well known example is the behavior of *in-vivo* chlorophyll fluorescence as a function of light exposure time; this is associated with the Kautsky processes. The effect can easily be acquired with simple instrumentation<sup>125, 126, 214</sup>; see even Paper III. The applications of recording of fluorescence spectra over time includes monitoring of plant condition and stress, e.g., due to external factors such as draught. The information in the dynamic evolution of spectra has also proven valuable for the determination of the sex of young nutmeg trees. As discussion in Sect. 2.5.3 this can potentially increase crop yield by introduction of unbalanced sex ratio in agriculture<sup>137</sup>. In relation to fluorescence spectroscopy bleaching phenomena also typically occur on this time scale<sup>362</sup>. In this thesis the bleaching process of PpIX is studied over minutes with samples rates in a fraction of second; see Paper VII. In particular, it is demonstrated how a clinical diagnostic method could be improved by taking the temporal evolution into account. One important parameter governing the temporal dynamics of light-driven chemistry is the absolute intensity of the driving light. From this it can also be understood that if attempting to acquire steady-state fluorescence spectra from a sample experiencing photochemistry, then the detected fluorescence intensities will not scale linearly with excitation intensity and the exposure time. As discussed in Sect.2.5.3 such power dependence can also be exploited to investigate the nature of the photokinetic processes; in many cases fluorescence will not bleach towards zero. This can be caused by continuous production or inflow in the measurement volume or inhibition from bleaching by the micro environment. One example of such excitation power analysis is performed in Paper VII. Examples of cyclic phenomena on the

minute and second timescale relevant in bio-photonics contexts are breath taking and heart beats. These two life indicators are extensively monitored by simple LED detectors in intensive care units<sup>363</sup>.

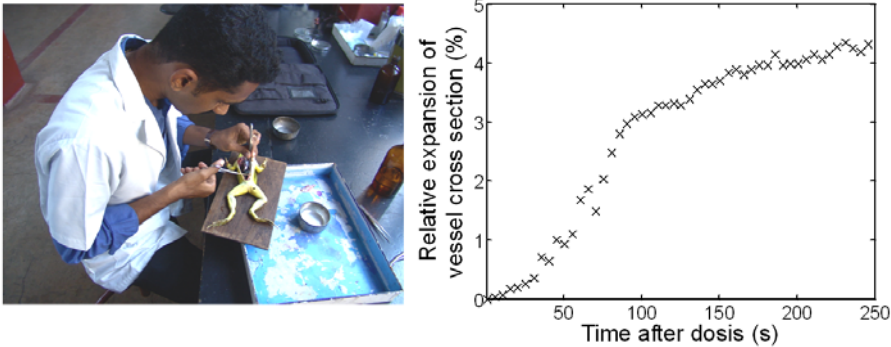


Fig. 4.5.2. Pharmacokinetics studies of physiological reactions in respect to time and dose of pharmaceutical agents. In this figure the expansion of a frog blood vessel is recorded as a function of time after administration of a vaso-active agent such as caffeine, histamine, adrenalin or other. The curve was recorded using a self-made digital microscope by the author at Manipal University Hospital, Udupi, India<sup>361</sup>.

Sampling on the millisecond time scale is typically the limit for simple un-intensified CCDs and CMOS in imagers and compact spectrometers. The time scale of action potentials emitted by the neurons in our brain is on the order of a few milliseconds. The speed of modern optics in bio-photonics allows such signals to be individually recorded and topographically mapped *in-vivo* in 3D in the brain of, e.g., fruit flies<sup>110</sup>. The technique is based on a fluorescence dye sensitive the release of  $Ca^{++}$  in the synapses when the potential arrives through the axons. Eventually such methods together with advanced statistics and system identification will help answering one of the biggest remaining questions in science: How does a brain work? Spectra are recorded on the millisecond basis in Paper XII. This is used to record insect occurrences on the same time scale; this allows time correlation analysis. Such correlation analysis can answer the question: given that a male is detected at time zero, what is then the probability of detecting another male or female 50 ms after? When a vector is correlated to itself as a function of lag it is referred to as autocorrelation. Time autocorrelations are always symmetrical about zero lag. When two different vectors are correlated as a function of time it is referred to as time cross correlation. The time correlations are quantitative measures of what in ecology is experienced as chasing. Chasing occurs, e.g., between sexes or between the same sex due to territorial protective behavior. Chasing also occurs between prey and predator related to the food chain. The phenomena of chasing could not previously we quantified to this extent and the approach can be expected to produce many novel experiments in behavioral ecology.

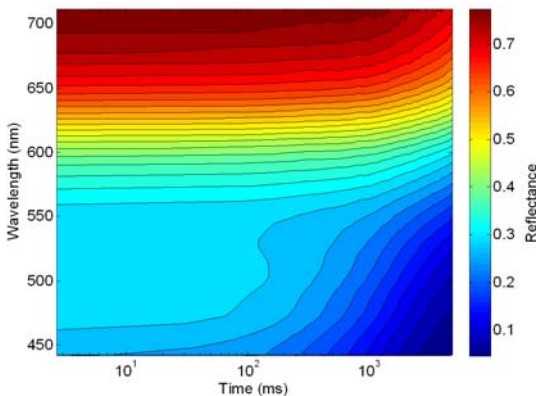


Fig. 4.5.2. Reflectance measurements of the oxygenation of fresh cola nut tissue when exposed to air. The measurement was done with the instrument in P3 during an international workshop in Bamako, Mali<sup>134</sup>. The spectral evolution can be explained by a linear combination of three spectra.

Optical sampling rates below one millisecond are extensively used, e.g., in vibratometry where mechanical vibrations and acoustics can be acquired by optical interferometric setups. In relation to remote monitoring of insects, such fast sampling has been particularly exploited to identify, e.g., honey bees by their wing-beat frequency<sup>142, 243, 287</sup>. It is noteworthy that some of the fastest vision systems known in, e.g., blowflies<sup>364</sup>, resolved frequencies up to 300 Hz and thus potentially retrieves wing beat modulation from their surroundings. When sampled much faster than the fundamental wing-beat frequency, refined chemometrics can be performed on the relative strength of the harmonics. Such waveform analysis has been demonstrated to discriminate different species of *Aphids*<sup>141</sup>. A similar discussion around birds appears in Paper XV. Two more examples in entomology is the application for analysis of insect hearing<sup>365</sup>, where the acoustic sensitivity spectrum of tiny body parts can be acquired. Vibratometry has also been performed on leaves in order to detect insect movement<sup>366</sup>. Sampling in the kHz regime is also common in schemes with lock-in amplification<sup>111, 286</sup>, simply to suppress noise. In P2 LEDs were multiplexed with several kilohertz; this not only allows lock-in detection but also the intensity of the LEDs could be increased by a factor of ten in comparison to what their steady-state thermal dissipation allows. Such fast multiplexing is a great advantage in low-cost LED spectroscopy and is easily achieved by homemade electronics. The time of discharges in flash lamps is in the order of ten micro seconds; thus this is also the pulse length of the flash-pumped Nd:YAG laser when in long-pulse mode. One microsecond is the time it takes for a light pulse to travel back and forth over the damselfly habitat in Paper XI.

When lasing is withheld by a Q-switch, the energy can be accumulated by the lasing medium and released in a single burst. This method is used in, e.g., Papers XI and XIV, to create laser pulses with the duration of around 10 nanoseconds and the energy of 1 Joule (for the fundamental emission). Because the energy is emitted over such a short time it implies a peak intensity towards 1 GW. Such intensity referring to the amplitude of the wave can potentially induce periodic changes to the refractive index, especially if a material with large nonlinearity is chosen. The induced changes in the refractive index will cause the peaks of the wave to travel at a different speed than the remainder of the wave; thus deforming the sine wave. Similar harmonic generation by high intensity can also occur for sound waves<sup>367-369</sup>; here the longitudinal pressure waves induces density difference in the air, and since the sound speed increases with the density it implies that the top of the pressure wave propagates faster than the rest, the wave is deformed and harmonics arise. The nonlinearity of air arises due to the fact that it is harder to compress than expand. As discussed in Sect. 3.1.4, in the Fourier domain this implies that harmonics are generated. Harmonics of light imply in the particle conception photons with multiple energy of the fundamental photon energy emitted by the laser. The conversion can be repeated and the fundamental wavelength of Nd:YAG lasers at 1064 nm can be doubled to 532 nm (SHG), tripled to 355 nm (THG) and quadrupled to 266 nm (FHG). In this thesis THG was used in, e.g., Paper X and FHG in Paper XIV. Since the operation of a doubling crystal can be seen as a square operator on the electrical field, it can also be understood that the envelope or pulse duration after harmonic generation also becomes faster<sup>236</sup>. Along these lines the 266 nm light has a pulsed duration of just 4 ns. In lidar contexts this corresponds to a light bullet with the spatial length of 120 cm. The echo from such pulsed can be recorded with PMTs allowing spatial resolution along the optical axis comparable to the pulse length. The standard procedure in lidar is then to convert the delay time into range by multiplying with half the speed of light<sup>370</sup>. Having created a spatial dimension from a temporal one, however, one has to consider that the light can be delayed for other reasons, one example is fluorescence from atomic mercury in DIAL measurements<sup>279</sup>. An interesting temporal detail regarding the laser used in Paper XIV is that inside the mobile laboratory, the blinking from the 20 Hz repetition can clearly be observed, whereas the light appears to be continuous when working with the beam in the field during night time. This can be

understood since the perceived temporal pulse profile is the convolution between the pulse shape and the detector response; see Paper III, and the temporal response of human night vision is much slower than the day-time response.

As discussed in Sect. 3.1.3 lasers can be mode-locked; the principle of this is to have a continuous wave laser cavity allowing a broad wavelength band to lase. By fixing the relationship between the phases of the longitudinal lasing modes, the many modes interfere destructively most of the time and no light is emitted. However, when all modes enter in the same phase, constructive interference is achieved and a very bright and short pulse is emitted. The pulse duration is typically in the order of picoseconds or femtoseconds, and the repetition frequency is typically in the Megahertz range. Since both the pulse width and repetition rate are the outcome of the geometry of the cavity, they are fixed and cannot be adjusted electronically like for the cases of a pulsed Q-switched laser. In the bio-photonics community mode-locked lasers emitting picosecond pulses are popular for the so-called time-correlated single-photon counting (TCSPC). This method makes use of electronics from nuclear physics, where scintillators are coupled to multichannel analyzers (MCA) for the purpose of X-ray fluorescence spectroscopy or gamma spectroscopy. MCA are specialized circuits capable of sorting pulses with different magnitudes into digital histograms with the speed of many MHz. In TCSPC photons produce pulses with fixed magnitude which are in turn multiplied with a time ramp synchronized with the repetition rate. This sorts the collected photons as a function of delay time. In bio-photonics TCSPC is used extensively for time-of-flight spectroscopy to estimate the photo-migration pathlength<sup>168</sup>, TCSPC can also be used to record fluorescence lifetimes<sup>371</sup>; this was the case in Paper VIII and IX.

A large research field emerged from mode-locked femtosecond lasers - femto chemistry. The timescale on which individual chemical reactions take place is explained. One popular approach here is the pump-probe scheme. Here the light is split in two parts and a delay in respect to each other is introduced by a so called delay line. The first arriving infrared laser pulse aligns the molecules in the direction of the electric field, and then a second blue pulse excites the molecules<sup>372</sup>. Because mode-locked lasers emit their energy in so short pulses the peak power can be much larger than for Q-switched lasers. This implies that essentially anything exposed to a high power femtosecond pulse will interact nonlinearly with the light. One application is to let the sample produce second or third harmonics. This has been demonstrated in microscopy where, e.g., the lipids in the cell membrane produce SHG, whereas, e.g. porphyrin containing molecules such as haemoglobin produce THG<sup>11</sup>. Further, the conversion yield depends on the polarization orientation with respect to the orientation of the molecules. Femtosecond pulses are in general so fast that no electronic detector can record them directly; instead one must use temporal correlation schemes with a reference beam from the original light.

As mentioned in Sect. 3.1.3 short pulses can be amplified by the chirped pulse amplification scheme, where ultrashort seeding pulses are chirped or distributed in time, amplified and then compressed to the original length. By this approach peak powers in hundreds of terawatts can be achieved. When intensities in this range impinge on noble gases, high harmonic generation (HHG) with odd harmonics ranging down to the extreme ultraviolet can be achieved. Even harmonics can be generated in a symmetric medium by inducing asymmetry with an additional laser field<sup>373</sup>. It can be understood that only odd harmonics can be produced since the gas has no preferences of directions and thus its nonlinearity must be symmetric around zero electrical field. Under the right conditions the harmonics can be phase matched and interference similar to that of mode-locking occur over a very broad wavelength range, producing the shortest light pulses ever created by

mankind, in the range of one hundred attoseconds. One example of a phenomenon occurring at this time scale is an electron riding on a light wave<sup>374</sup>.

The phenomena and techniques listed above can be sorted into three categories: transient, cyclic and correlation. Transient phenomena are, e.g., the Big Bang, deforestation, pharmacokinetics, bleaching and lidar echoes. Examples of cyclic phenomena are years, weeks, days, breath taking or wing beats. Examples of time correlations are the chasing between insects and the single-photon counting. While natural processes are inherently one or the other, instrumentation and experiment design can in many cases use any of the three modes to obtain the same results. Fluorescence lifetime can be recorded transiently following a laser pulse<sup>375</sup>, it can be measured in terms of attenuation and phase delay with frequency domain methods<sup>114, 219</sup> or by time correlation as in Papers VIII and IX. The latter approach is in general the most precise one.

From the vast span of times discussed above it can also be understood that in many experiments it is advantageous to have multiple time dimensions. A classical example is vertical lidar sounding. Here the fast time in nanoseconds describe the range travelled by the light, whereas passing clouds and changing atmospheric conditions can be observed on the hour basis; see, e.g.<sup>317</sup>.

A special temporal distinction, with importance for this thesis, is made between *static* or *quasi-static* signals and *non-static* signals. The term appears throughout Papers XI-XVI, and relates to the detection of rare events. Several approaches to this were pursued for the different experiments, but most of them are based on the creation of histograms, where outliers can be discriminated from system noise and the scattering from the distributed gases and aerosols.

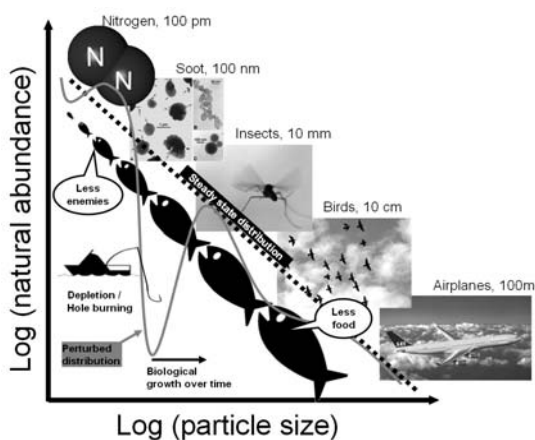


Fig. 4.5.3. The general tendency is that the natural abundance of atmospheric constituents decays with the particle size. When monitoring an air volume with lidar this implies that huge number of molecules and aerosols will always be detected, insects will be detected now and then and birds constitutes very rare events. In biology such distributions are referred to as biomass spectra and they are subject to several kinetic processes such as biological growth and prey-predator oscillations. Such oscillations arise due to the fact that most organism do not consume organism which are just slightly smaller than themselves, but organisms with is considerably smaller. The ecological discipline covering such aspect is referred to as population dynamics and related in many ways to electron population dynamics in atomic systems.

The histograms relate closely to what in population ecology is referred to as the biomass spectrum, and relates the natural abundance of particles and animal to their size. In one lidar study such a biomass spectrum is measured directly by plotting the likelihood against backscatter cross-section for the monitored air volumes<sup>376</sup>. Biomass spectra have been extensively investigated in marine biology in relation to industrial fishing. Here a certain net size can create depletion and burn a hole in the biomass spectrum. The hole will displace toward larger animal sizes because of biological growth of the individuals in the ecosystem. Further, such depletion will cause oscillations in the biomass spectrum, causing individuals with smaller body sizes to pop up from the static biomass spectrum since they suddenly experience no predators. Consequently, their prey will be depleted and so forth<sup>377</sup>.

<sup>378</sup>. Such behavior is in most respects identical to the behavior of electron populations, and absorption spectra subjected to hole burning and depletion, where the burned hole tends to pop up in another spectral region<sup>379, 380</sup>. In a atomic system, the sum of all populations is constrained by a finite number of electrons, in the ecosystem the sum of populations is in general constrained by the finite number of photons from the sun, driving the primary production. In the future such population dynamics phenomena could potentially be monitored directly by lidar on ecosystems by sorting rare events by their likelihood and magnitudes.

In atmospheric research the size and abundance of smaller atmospheric aerosols are traditionally measured by differential mobility analyzers (DMA). In this scheme inspired by nuclear physics and mass spectroscopy, aerosols are sucked in and ionized with radioactive material. Particles are in turn dragged by an air sheet and accelerated in a high voltage according to their mass/charge ratio. Particles with the right ratio will enter a slit and be counted individually in a cytometric approach. By scanning the high voltage a abundance-mass spectrum can be recorded<sup>381</sup>.

#### 4.6 The polarization domain

Where as the previously domains can by discretized by increased number of bins in order to achieved high resolution spectroscopy or imaging, the polarization domain is distinct in the sense that that light intensity and polarization can be completely parameterized by just four parameters. Four complimentary polarimetric measurements are therefore sufficient for a complete description, however additional measurement improve the estimate certainty<sup>382</sup>. These are either referred to as the Stokes parameters or a four element Stokes vector. Properties such as *intensity*, *degree of polarization* or *degree of linear polarization* (DOLP), the *orientation of the polarization* and the *degree of circularly polarization* can be derived from the Stokes vector. An example of such alternative representation is given:

$$\begin{aligned}
 S &= [s_0 \quad s_1 \quad s_2 \quad s_3] \\
 I &= s_0 \\
 DOLP &= \frac{\sqrt{s_1^2 + s_2^2}}{s_0} \\
 2\psi &= \tan^{-1} \frac{s_2}{s_1} \\
 2\chi &= \tan^{-1} \frac{s_3}{\sqrt{s_1^2 + s_2^2}}
 \end{aligned}
 \tag{Eq. 4.6.1}$$

When considering the Stokes parameters prior and after sample the change can be described as a linear matrix transform of the vector. This transform is referred to as the Müller matrix for the sample or optical element. Such applications of linear algebra and matrix formulation are also popularly used to describe ray location and propagation in multi element optical systems, in this paradigm the consecutive lenses, optical elements and free space is reduced to a cascade matrix multiplication<sup>56</sup>. In Müller calculus optical components such as linear polarizers and quarter wavelength plates have a particular associated linear transform; in ray transfer matrix analysis lenses and prisms have similar matrices transforming location into propagation or visa versa. Similar matrix formulations can also include the phase of light with applications for multilayer coatings analysis.

One of the instruments used in Paper XV is capable of measuring all four Stokes parameters<sup>383</sup>; this is achieved by an arrangement of birefringent wedge prisms projecting

different polarization part onto different areas of an infrared focal plane imager. The analysis was carried out to get more profound insight into the polarization nature of infrared structural colors in birds. The signal-to-noise ratio (SNR) did, however, not allow any definite conclusions.

The approaches to discretize polarization resemble many of those applied to perform spectral imaging. Four images can be taken sequentially in time through a linear polarizing filter. Here the filter is typically rotated in angles of  $0^\circ$ ,  $45^\circ$ ,  $90^\circ$  and  $135^\circ$ . Micro polarization arrays of differently oriented linear polarizers can also be placed on the individual pixels of the imager along the lines of commercial RGB imagers<sup>384</sup>. The light beam or image subject to polarization analysis can also be split into different propagations and be distribution to different detectors or different regions on an array detector<sup>385</sup>. One difficulty in the latter case is the exact overlapping of pixels which is required for applying arithmetic functions such as those in Eq. 4.6.1. With similarity to tunable wavelength filters polarimetric measurements can also be achieved electro-optically. This can be done with combination of linear polarizers, wave retarders and liquid crystals<sup>386</sup>, photo elastic modulators<sup>387</sup> or Pockels cells. As for the case of EEM fluorescence spectroscopy, both the source and detector can be subject to discrimination in active polarimetric measurements<sup>382, 388</sup>. This concept becomes particular valuable in situation where the sample has a preferred orientation. In metallurgical polarization microscopy the linear filter in front of the light source is simply referred to as the polarizer, whereas the second filter prior to the eye piece is referred to as the polarization analyzer.

Linear polarizers can be based on three principles; absorption of light polarized in a certain orientation (e.g. inexpensive polymer sheet), ballistic transmittance of one orientation while the perpendicular is scattered omni-directional (e.g. infrared wiregrid polarizers) and beam splitters diverging the two perpendicular orientation into two separate beams (e.g. the Glan-Thompson polarizer). Another main property of polarizer is the extinction ration a value that can vary from  $1:10^2$  to more than  $1:10^6$ . Absorbing polymer sheet polarizer, in the visible, are widely available and used in commercial devices such as computer and cell phone screens or 3D cinema glasses. A simple polarizer can be made, e.g. from a pile of tilted microscope cover slides at Brewster angle. Broad band and UV polarizers are mainly of the beam splitter type and are much more costly; examples are Glan-Thompson, Glan-Taylor, Wollaston or Rochon prisms. Such devices are constructed by two birefringent crystals typically calcite  $\text{CaCO}_3$ , which are fused together with perpendicular optical axis. In the infrared region polarizer are either by sheets with elongated metal particles or by an arrangement of sub-wavelength wire grid; even such polarizers are much more costly than visible sheets. Wiregrids or larger scales can also be used in the microwave region. For long waved technology antennas are in general always polarization sensitive. A particular advantage of performing synthetic radar sideways (side-looking airborne radar, SLAR) instead of nadir, is that complimentary information can be retrieved from both two polarizations of the emitted pulse as well as two additional polarization of the received echo. In this situation the sample orientation preference arises due to the orientation of gravity. Generally, the field of view is limited in polarizing beam splitters, whereas sheet polarizers are more suitable for wide field imaging applications.

Any optical system which is not cylindrical symmetric around the optical axis is potentially sensitive to polarization. This includes beam splitters, spectrometers, Newton telescopes but even some cylindrical symmetrical systems such as wide field fish-eye objectives<sup>386</sup>. Polarization sensitivity in both symmetrical and asymmetrical animal vision systems is currently subject to investigation<sup>389, 390</sup>, in the latter case asymmetry have been proposed on a cellular or molecular level on the retina. Techniques such as non-linear microscopy, where the sample generates second or third harmonics, can be expected to be polarization

sensitive in respect to the orientation of the molecules generating the signal<sup>391</sup>. Polarimetric imaging, in particular in the infrared region, is a hot research topic in relation to locating camouflaged metallic surfaces of military material in remote sensing<sup>384</sup>. A common feature is that such surfaces exhibit high degree of polarization. Polarimetric imaging applications more friendly to the entire humanity include all sky imaging for aerosol analysis<sup>392</sup>. Polarimetric measurement of a specular reflex from a surface measured as a function of incidence angle is referred to as ellipsometry. These techniques are extensively used for surface analysis, and inspection and characterization of optical coating in optical manufacturing. Further, ellipsometry can both be imaging or spectrally resolved<sup>393, 394</sup>. When the absorption of left and right handed polarized light are subtracted and resolved spectrally it is referred to as circular dichroism (CD) spectroscopy. This is mainly performed in the deep UV and have various applications in analytical biochemistry<sup>387</sup>.

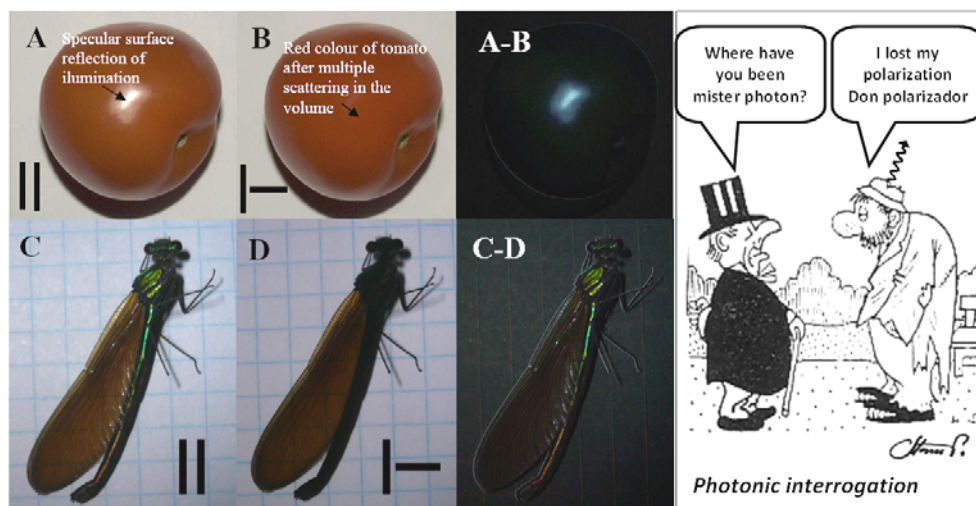


Fig. 4.6.1. The origin of colors of a tomato and a damselfly is entirely different, this can be confirmed by comparing the co- and de-polarized reflectance. The tomato maintains its color in the de-polarized or incoherent backscatter while the damselfly loses its colors. The coherent backscatter can be estimated from the difference; here only the white specular reflectance from the tomato survives while the green and goldish structural colors from the damselfly appear. In summary, photons which experience photon migration and penetrated deep into the sample lose the memory of original polarization, while superficial photons recall their initial polarization as well as their phase. The drawing to the right is adapted from the famous Danish cartoonist Robert Storm Pedersen.

Many schemes in optical instrumentation do not regard polarization or only a crude distinction between co-polarized and de-polarized light is made. This refers to the orientation of polarization in respect to the light source. These two components are extensively measured in elastic aerosol lidars improving the characterization of the aerosols. Here linearly polarized light is emitted by a pulsed laser; the returning light is then received by a telescope, fed through a pinhole, collimated, passed through a laser line interference filter and split by a polarization beam splitter onto two different PMTs. In industrial machine vision and inspection systems de-polarized imaging is popular to avoid specular reflections. This is in general achieved by two perpendicular polymer sheet linear polarizers in front of the white illumination and color camera objective, respectively. Polarization analysis throughout this thesis mainly aims at separating structurally induced colors from colors arising from absorption by chromophores. In Paper XIV we perform polarization analysis to investigate the penetration depth and absorption in diversely colored plumage in the deep UV.

---

## Chapter V

### 5. Computational methods

---

In contrast to spectroscopy on, e.g., narrow optical atomic emission lines or gas absorption lines with wavelengths highly specific to the substance, the absorption and fluorescence of most solids and liquids are broad and overlapping. For this reason advanced data interpretation is in most situations more beneficial than highly resolving instrumentation. In this chapter a number of aspects of statistics, chemometrics or multivariate analysis will be presented. For a tutorial example we will mainly consider data from seven types of fruits presented in Fig. 5.1. The discipline of multivariate analysis and chemometrics covers vast amount of aspects; generally there is not one unique correct solution but a range of creative approaches which will all work to some extent. There are also many incorrect evaluation ways, details and traps which can lead to the wrong conclusion. One such example is risk of information leakage when using multiple dark and bright references<sup>395</sup>. This can be caused through unique noise imprints in references spectra with are erroneously propagated to subsets of the data when normalized. Data evaluation can be rather in-transparent and infinitely complicated with many steps following each other; however, the robustness of evaluation tends to decay with the complexity of the evaluation. In properly performed multivariate analysis the main conclusion relates back to physical properties responsible for discrimination. This can be in terms of signatures of well known substances or absolute values of, e.g., reflectance. Such back reflections increase the value of the evaluation and enable readers to relate the study quantitatively to their own work. One example of such back reflections are the cluster mean spectra, e.g., in Papers IV and XII. Another general thumb rule for chemometrics is that it has to be implementable in practice. In this relation the concept of prediction is particularly important; see, e.g. Paper VI.



Fig. 5.1. Seven fruit types from left to right: Royal Gala, Red delicious, Granny Smith, Orange, Golden delicious, Lemon and Lime. The fruits were photographed in a depolarization configuration. Additionally fluorescence and reflectance spectra were obtained with P3 on three location on each fruit.

#### 5.1 Preprocessing and calibration

Although conclusions based on multivariate analysis can be reached regardless of any data preprocessing calibration, serves two different purposes; one, cancellation of instrument variance such as temperature, and two, communications of reliable quantitative values to the scientific community.

### 5.1.1 Intensity calibration and normalization

As explained earlier, spectroscopic methods such as reflectance or transmittance are highly dependent on the measurement geometry which should always be stated in details in relation to such measurements. This especially complicates the absolute calibration of scattering measurements<sup>83, 396</sup>; see, e.g., discussion in Paper III. Nevertheless, in elastic spectroscopy the most basic calibration involves subtraction of a dark level and division with a bright reference, e.g.

$$R = \frac{I - I_{dark}}{I_{white} - I_{dark}} \quad \text{Eq. 5.1.1}$$

This assumes a detection linearity of a first order polynomial; the concept can be expanded to include several gray references with certified absolute intermediate reflectances. One reason that the instrument response might not be described by a first order polynomial, is the situation, where a reflectance instrument partially reflects light from the sample back onto the sample. Such photon re-bounce would make bright samples appear brighter and dark samples appear darker. The biases caused by detector dark current; see Sect. 3.2, are absent in FTIR based spectroscopy since the detector signal is electronically high-pass filtered. In remote sensing, biases can also be of optical nature in terms of atmospheric scattering which might not be the focus of the investigation. In satellite imaging this is one aspect of atmospheric correction. Here the bias can mainly be explained by the Rayleigh scattering and is thus one of the main limitations of satellite imaging toward the ultraviolet. In Paper XII such scattering is subtracted by a temporal median filter. The same obstacle is common in submarine situations. Here, one approach to greatly enhance the contrast in weakly scattering condition is to use imagers with high dynamic range of 10 or 12 bits and perform contrast stretching; see Fig. 5.1.1. It is noteworthy that such dynamic spans cannot be communicated to humans, the data from medical MRI cover a large dynamic span. The radiologist often has to interactively scroll through the dynamic span to evaluate a case.

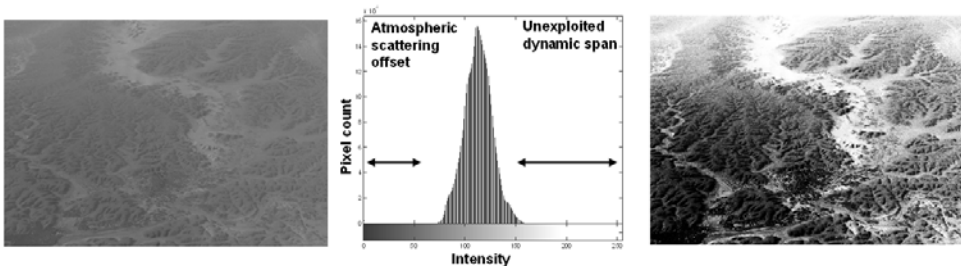


Fig. 5.1.1 Picture of a village in the Air mountain, Niger, taken by the author from cruising altitude of 10 km. In weak scattering conditions like airborne imaging or in submarine conditions, scattering contributes with an offset to all pixels. The offset is largest for the blue spectral band and smallest in the red band. In the image to the right the offset and low exposure has been mathematically corrected. This works particularly well for imagers with high dynamic resolution.

In spectrally resolved measurement the dark level can be estimated in spectral regions where darkness can be assumed; see Fig. 5.1.1 and Paper XII. In pulsed time and range resolved lidar measurements dark levels might be estimate from the pre-pulse period or the pre-echo level, e.g. Paper VIII and XIV. In imaging situations the dark level can be estimated from a region of interest of a black reference in the image. White references describing the combined efficiency of the source and detector can be measured no sample or only the sample holder in transmission mode. In scattering mode white references can be well characterized diffuse glass or opals which have near perfect Lambertian angular behavior. White reference in reflectance can be salt deserts in satellite imaging<sup>163</sup>. Kitchen

salt, NaCl, is one of the best optical materials in terms of transmission ranging from 200 nm to 20  $\mu\text{m}$  and the highly scattering powder is an excellent white reference throughout this region. On smaller macro scales white reflectance references are typically highly scattering Teflon also referred to as Spectralon. Although such commercial references are certified white from 300 nm to 2  $\mu\text{m}$ , one considerable issue with them is the chance of photons escaping the field of view (FOV). This implies that certified reflectance highly depends on the instrument measurement geometry and the footprint size of the sampled part of the reference. Following this argument it can be understood that the reference will not be equivalent for fibers and imaging instruments. White reference without photo migration for reflectance can also be spectrally flat specular reflections, e.g. from metals or glass surfaces.

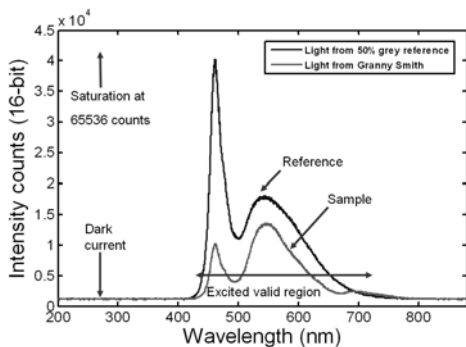


Fig. 5.1.2. In elastic reflectance spectroscopy an intensity vector from a CCD is recorded. The samples are related to a white or grey reference. The offset caused by dark current must be subtracted. The exposure time, gain and source power are adjusted to fill the dynamical span. Reflectance can be measured within the spectral region of emission of the source times the sensitivity of the detector.

In emission spectroscopy, encompassing laser induced fluorescence (LIF) and laser induced break down spectroscopy (LIBS), absolute light intensities are measured in terms of watts. This is complicated because the quantity greatly depends on the geometry. A number of measures such as watt per square meter, watt per steradian or watt per nanometer exists. In most cases of applied spectroscopy data are presented with arbitrary units on the intensity axis. For such plots to be meaningful, the intensity should, however, be comparable throughout the spectral region, since the emission peak wavelengths would otherwise not be correct. When emission is measured thermally with bolometers, the spectral instrument sensitivity can be assumed flat. With measurements by photodiodes, PMTs, CCD or CMOS, the spectral sensitivity function has to be measured and compensated for, however. In Paper I one novel approach to achieve this is presented.

In emission measurements of fluorescence lifetimes the detector linearity becomes extremely crucial. The linearity is typically expressed by a gamma factor:

$$I_{obs} = I_{true}^{\gamma} \quad \gamma \approx 1 \quad \text{Eq. 5.1.2}$$

A gamma factor deviating from 1 at, e.g., the fifth digit will produce an entirely different set of fluorescence lifetimes. This is one reason why single photon counting as in Paper VIII and IX is preferred over alternatives of transient recording<sup>375</sup> or frequency domain methods<sup>221</sup>.

In laser ranging the white reference relates to the form factor problem; see Sect. 4.3. In gas analysis or differential absorption lidar (DIAL) it can be estimated from the off-absorption-line shot. In aerosol lidar it can be estimated from the N<sub>2</sub> Raman Stokes emission from the main constituent of the aerosol matrix. In zoo-ecological applications like the ones presented in this thesis, white references relates to unpigmented reference birds and, e.g., the beam-bird overlap problem. Approaches to solve the latter problem includes recording

of the depolarized backscatter or analysis or the decreased return from later coming static echoes, e.g., from a termination or from the atmospheric scatter.

In many situations the absolute intensity, transmittance, reflectance, fluorescence or other measure cannot be accessed or its variance is not relevant for the topic of interest. In many cases this has to do with geometrical induces uncertainty. Therefore auto-normalization is applied in order to produce so called spectral shapes. Auto-normalization can have a number of forms, one example of such normalization is a reflectance spectrum:

$$I_{norm} = \frac{I - \mu_I}{\sigma_I}$$

Here,  $\mu_I$  is the mean intensity value in the spectral domain and  $\sigma_I$  is the intensity variance. Since the unit cancel out this is sometimes referred to as dimensionless processing. Examples of dimensionless processing and evaluation of the spectral shape are normalized difference vegetation index (NDVI) in satellite imaging, chromatic identification in machine<sup>282</sup> and animal<sup>85</sup> vision, DIAL lidar<sup>397</sup>, TDLAS<sup>398</sup> and high pass filtered FTIR spectroscopy<sup>399</sup>. Dimensionless quantities can also be made along other domains than the spectral; fluorescence lifetimes in TCSPC<sup>400</sup> and degree of polarization in polarimetric imaging<sup>401</sup> are examples in the time and polarization domains respectively. A common issue with all quantities mentioned above is that even if they are intensity insensitive, their certainty vanishes when the absolute intensity reaches the noise level.

In single photon counting in x-ray and gamma spectroscopy the intensity bins translate into spectral bands; see Fig. 2.1.3. The linearity curve is thus determined by the K or L shell emission lines (from Moseley law) from a reference sample with known elements. Here even the counts related to the fluorescence intensity are subject to additional white calibration, through known dilutions of the elements. This is in order to correct for different scintillator capture efficiencies at different wavelength. In both these relations higher order linearity polynomial are required.

### 5.1.2 Spatial calibration

For x-y calibration in images there are several approaches. A reference grid with known grid size can be placed in the objects plane, and landmarks can be selected. In the simplest form three landmarks are selected and thus no image distortion is assumed. This was done in Paper V. In Paper II a larger number of landmarks were selected to compensate for image distortion due to chromatic aberration. This kind of rubber-like stretching correction is based on polynomial planes and are popular in cartography for correcting image distortion and othogonalizing perspective, e.g., in airborne photography. Landmark selection is also closely related to image morphology<sup>402</sup>. The x-y calibration can also be roughly estimated through knowing the pixel size and magnification of the imaging system by geometrical optics; this was done in Paper IV. In wide field imaging systems, such as all-sky imagers the term spatial resolution does not make sense, and a position on the image sensor should preferably be associated with an angle rather than a position on a image plane.

The z spatial axis is obtained with techniques lidar, stereo vision, tomography, OCT or confocal microscopy. With stereo vision calibration is typically performed by selecting landmarks on a well defined 3D geometrical object as in 2D imaging. In lidar the range is determined by echo delay:

$$z = \frac{cAt}{2n} \tag{Eq. 5.1.3}$$

The axial resolution is thus limited by the laser pulse duration and the detector response time. In demanding applications de-convolution with the instrument response function (IRF) is performed.

### 5.1.3 Spectral calibration

In polychromators using array detectors, the spectral bands are given by pixels on the detector. The estimation of the center wavelength of a spectral band is determined by the spatial position or pixel number on the sensor. The relation between wavelength and position on the detector is often not exactly linear and is approximated by a polynomial, which is fitted empirically. This is done by measuring spectra from sources with known narrow spectral lines such as gas discharge lamps or lasers. Many modern compact spectrometers have built in polynomial coefficients providing the correct wavelength vector for the pixels. The very exact scale does not have any implications for the chemometric evaluation presented throughout this thesis, but is mainly a matter of proper scientific communication. The scale becomes crucial for those attempting to model light propagation from literature spectra. However, such attempts are very crude and depend on several instrumental factors. The characterization of broad spectral bands such as those of animals or satellites in Fig. 4.2.3, are done either with a broad-band lamp and a scanning monochromator, or with commercial test charts with narrow band reflecting checkers throughout the spectral region of interest. An arbitrary shaped spectral sensitivity band,  $S_\lambda$ , can be reduced to a number indicating the effective wavelength of the channel. This is done, e.g., with a gravitational point, see Eq. 5.1.4, and presumes spectrally flat illumination. For the effective wavelength of a band in an arbitrary illumination, the wavelength is the gravitational point of the product of the sensitivity and the illumination spectra. This is exploited in multiplexing LED spectroscopy throughout the thesis. In this case the white illumination and scanning monochromator is exchanged with a white calibrated polychromating spectrometer.

$$\lambda_{eff} = \frac{\int \lambda S_\lambda d\lambda}{\int S_\lambda d\lambda} \quad \text{Eq. 5.1.4}$$

## 5.2 Color spaces

Color theory fascinated a number of scientists throughout times; some of those were Leone Battista Alberti 1435, Leonardo da Vinci 1490 and Isaac Newton 1704. Throughout the 19<sup>th</sup> century the theories developed into more quantitative colorimetry and chemometry was boosted by analytical chemist such as the spectroscopist Robert Bunsen. In the early 20<sup>th</sup> century technologies such as color printing lithography required quantitative representation of colors and reproducibility. In 1931 the first CIE international standard was defined based on the physiological response curves of the human eye. The idea of such a color space is that each axis represents a primary color, i.e., the stimuli of only one of the three types of cone cells. In reality this cannot be achieved since the spectral bands overlap. All perceivable colors to humans are defined by a location in these spaces. At the early days of color television and color computer monitors quantitative additive color mixing became important and a number of additional representations appeared. The reason that colors are said to be indexed in a space is a mutation believed to have occurred in a common primate ancestor approximately fifty million ago, which caused a yellow ( $\lambda_{peak} \sim 540$  nm) spectral band to split into a red ( $\lambda_{peak} \sim 560$  nm) and green band ( $\lambda_{peak} \sim 530$  nm), apart from the blue ( $\lambda_{peak} \sim 430$  nm) band of the dichromatic ancestors. From this it is understood that most other mammals, e.g., horses would refer to a color plane<sup>292</sup> whereas bird would refer to a 4D color space, which there have been some efforts to make understandable<sup>201</sup>. The additive red-green-blue (RGB) color space has intensity or reflectance on the three axis, the eight

corners of the spaces are referred to as black, white, red, green, blue, cyan, magenta and yellow. In color printing subtractive colors representing absorption of red, green and blue are used. Those are cyan, magenta and yellow (CMY), respectively. The CMY and RGB color space relate to each other through a *not* operator,  $CMY=1-RGB$ . Further to save ink and improve contrast, a black ink is included. Thus the common term becomes CMYK.

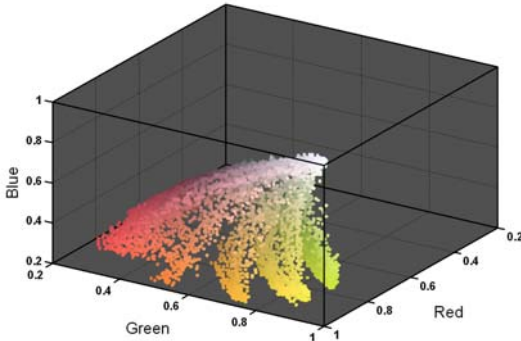


Fig. 5.2.1. The RGB pixels of the fruits in Fig. 5.1. can be represented by a scatter plot in a 3D RGB color space. The axes refer to the reflectance in each spectral band. Improved perception of the 3D distribution is achieved on the computer screen through the interactive ability to rotate the space. Perception of color spaces of higher dimensionality is very complicated. Although concentrations of observations are generally difficult to estimate from scatter plots several clusters can be seen.

Geometry and shades in natural conditions often induce large covariance of the absolute intensity of reflectance values. Therefore intensity or shade is often separated from the chromaticity. These two different measures are treated differently both in image compression and in neurophysiology, where they are referred as intensity channel and chromaticity channel. One way to calculate the chromaticity is through auto-normalization in each pixel,  $R/(R+G+B)$  and  $G/(R+G+B)$ . Such an operation reduces the dimensionality of the color space by one, and a chromatic plane is obtained. Color spaces are extensively discussed in Paper V.

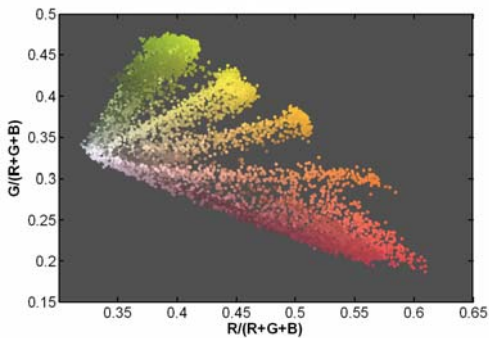


Fig. 5.2.2. Whereas the distributions from each fruit in Fig. 5.2.1 are prolonged towards origo, the auto-normalization in each pixel greatly reduces the variance induced by geometry; also the dimensionality is reduced by one. Still the prolongation of the distribution towards unity is caused by the edges of the fruits reflecting the white background; see Fig. 5.2.1. This 2D scatter plot displays the pixels according to their chromaticity.

Whereas the RGB color has a Cartesian nature, the same coordinates can even be expressed in a conic or cylindrical coordinate system. This gives rise to the hue-saturation-value (HSV) color space. While this representation has little to do with physics, it does relate to the experience of colors. The angular *hue* component represents the color on the so-called color wheel (a circular arrangement of red-yellow-green-cyan-blue-magenta-red). The *saturation* expresses how strong the color is, i.e. to what extent it is grey and to what extent it is one of the above mentioned. The *value* expresses the brightness or intensity with zero for black and one for white. In the physics and optical community the HSV color space is particularly beneficial to color code and communicate quantities of circular nature, for example the polarization orientation from the Stokes parameters or the phase of a signal, both which varies between 0 and  $2\pi$ , with the property that the value at 0 and  $2\pi$  are indistinguishable<sup>403, 404</sup>.

### 5.3 Description of variance

When considering a set of measurements an important aspect is the variance between the measurements. The variance becomes an issue in many different situations; what is the variance of energies between collected photons from the Sun? What is the variance in reflectance between pixels of an orange? What is variance in skin pigmentation in patients presenting themselves with suspected skin lesions? The variance arises between multiple assessments of a single parameter or between multiple reflectance spectra represented by points in, e.g., a 4096 dimensional colors space. The most fundamental value describing a set of measurements is the mean value which is the summed value over the number of observations. Mean,  $\mu$ , average or integral values are also often produced physically in the instrumentation. A photo diode records the spatial mean intensity within its sensitive area, and it temporally averages time changes faster than its rise time and integrates photons within the sensitivity band regardless of the energy. In many situations this is referred to as a low pass function. Apart from a mean value, observations will also have a spread - a standard deviation,  $\sigma$ , or a variance,  $\sigma^2$ . The value can be calculated numerically by:

$$\sigma^2 = \frac{\sum (x_i - \mu)^2}{N} \quad \text{Eq. 5.3.1}$$

Even variance or spread can be measured physically in various domains by introduction of a high pass filter, either temporally by electronic filters or spatially through Fourier optics<sup>337</sup>. Variance is important; consider for instant that you stand with each foot in a bucket; one full of 70 K liquid nitrogen and the other full of 470 K boiling oil, the average value would be a pleasant room temperature but the variance would make you highly uncomfortable. Variance is also referred to as the second statistical moment, suggesting that the measure can be generalized to describe additional features. The third and fourth moments are referred to as *skewness*,  $\gamma$ , and *kurtosis*,  $\beta$ , respectively, and can be calculated by:

$$\{\gamma_{m=3} \quad \beta_{m=4} \quad \dots\} = \frac{\sum (x_i - \mu)^m}{N\sigma^m} \quad \text{Eq. 5.1.1}$$

If the data are Gaussian distributed, the distribution can be completely described by the mean and the first mode, i.e. the standard deviation. The terms skewness, kurtosis and additional statistical modes are mainly used in cases where data cannot be assumed to belong to a well defined statistical distribution such as a beta or gamma distribution. Probability distributions can be classified firstly by whether they describe a continuous or a discrete parameter, and secondly, whether the parameter is unbound, semi-bound or strictly bound. Such distributions relate to various types of spectroscopies. Emission spectroscopies like fluorescence- (LIF) or laser-induced breakdown spectroscopy (LIBS) detect positive definite quantities and a set of such measured data would be gamma distributed. In the single fluorescence photon counting Papers VIII and IX, either a photon or no photon is detected and as a consequence the intensities are integer numbers. Further, since the photon count must at least be zero but has no upper bound, the distribution is semi-bound and thus it must be Poisson distributed. In Paper II, a continuously varying transmittance is measured in several pixels. Since transmittance is constrained between zero and one the variance between the pixels must be explained by a beta distribution. Fitting such distributions instead of using the simple mean and standard deviation ensures that the error bars for, e.g., the transmission remains in-between 0 and 100%. In the same paper there is also an example of a sample focusing effects causing transmittance to exceed 100%. Such effects would complicate the fitting of a beta distribution. There are also a number of probability distributions relating to physical phenomena; examples are the Planck

probability for emission of a thermal photon, or the Cauchy-Lorentz distribution describing the probability for absorption by a pressure broadened gas spectral line<sup>165</sup>.

## 5.4 Histograms, images and spectra

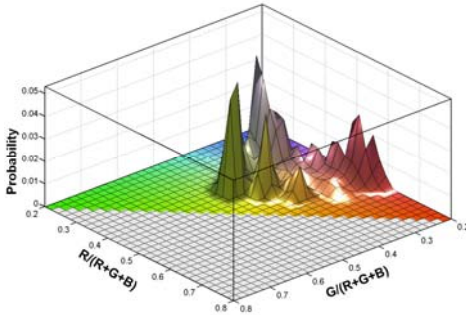


*Fig. 5.4.1. A 2D histogram of the chromaticity (Fig. 5.2.2) of the pixels from the seven fruits in Fig. 5.1. The probability plane is color coded with the corresponding chromaticity. The plane presents several modes corresponding to different fruit types.*

Spectral data with many mixing transition bands or complex patchy samples as in Paper V produce multimodal, apparently arbitrary, probability functions. For such distributions the statistical modes discussed above perform poorly for describing probability distributions. Instead, the probability distribution can be estimated empirically by producing histograms of the parameters and divide with the number of observation. As the number of observation goes towards infinity, the histogram converges towards the probability function. Thus, this approach works particularly well for large sample sizes arising in, e.g., imaging or flow cytometry. A given sample size allows either good probability estimate or a large number of histogram bins for high resolution. Histograms of photons can be constructed physically, e.g., by detector arrays. Here spectra can be understood as histograms of the photon energies (See Fig. 2.1.3), and images can be understood as 2D histograms where photons are binned according to their spatial origin. The concept of one dimensional histograms, e.g. of intensity in a single spectral band like in Fig. 5.1.1 can be expanded to two and more dimensions. This is explained in details in Paper V where considerable work was also put in visualizing this concept. Whereas scatter plots like the ones presented in Fig. 5.2.1 and Fig. 5.2.2 can communicate the spread of all observation, it is impossible to determine the observation density in a given location. In contrast 2D histogram planes can be quantitatively communicated on flat paper in the form of contour plots or color maps.

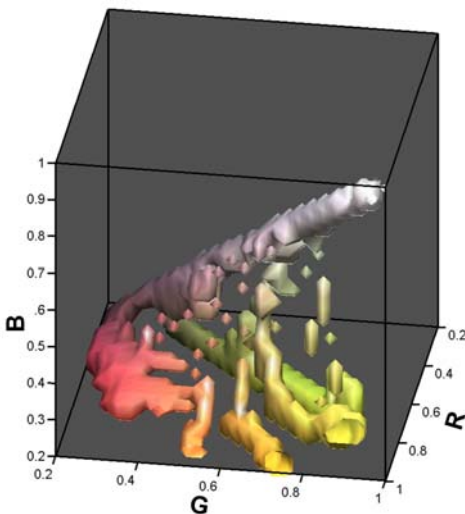


*Fig. 5.4.2. Iso-surface representation of a 3D probability distribution of the pixels in Fig. 5.2.1. from the image of seven fruits in Fig. 5.1. Several clusters can be observed. It should be noted how the clusters are prorogated towards origo.*

Probability fields or 3D histograms can be qualitatively visualized in flat figures by so-called iso-surfaces. Such a surface corresponds to a single contour line in a 2D histogram. Thus a decision regarding the fraction of the observation to be included by the iso-surface has to be made. In Paper XIV a 3D histogram from multiband lidar echoes is proposed for indexing and classification of nocturnal migrating birds. 3D probability fields also relate to the Copenhagen interpretation of quantum mechanics where probability of encountering, e.g., an electron close on a nuclei is defined as a density field, often expressed in a polar coordinate system.

Probability of higher dimensionality (ND) of ND-histograms can be calculated and used in multivariate analysis. However, they cannot be visualized, and additionally, the total number of bins increases with the number of bins along each dimensions to the power of the dimensionality. Therefore ND-histograms either rely on huge amounts of observations, provide either poor resolution or a very poor probability estimate. The same situation arises physically in optical instrumentation; the more properties of photons which are subjected to analysis and the finer the resolution, the less photons will meet the conditions and the weaker will be the signals in respect to the noise levels.

## 5.5 Outliers and rare events

Both the terms outliers and rare events are fuzzy in nature. Nevertheless, they have a large impact in many analytical applications and studies. Common operations such as the mean or the least-square regression, which will be discussed later in this chapter, will produce entirely different values if a single outlier is present in the dataset. Several criteria for outlier detection, such as Grubb's, Chauvenet's, Peirce's or Dixon's criteria have been proposed. Approaches to deal with outliers can be inclusion, automatic exclusion or preferably detection for closer inspection. In dermatological studies such as the ones presented in Papers VIII and IX, outliers could be caused by unexpected substances such as lotions or perfumes on the measurement location. In the ecological studies presented in this thesis, e.g., Papers XI and XII outliers might arise from species others than the focal species intersecting with the experiment. Such events can be minimized by marking with substances with very specific spectral signatures. Outliers also occur in optical instrumentation, e.g., if a PMT detector is struck by cosmic particles, this can be minimized by using several detectors where co-occurrence is expected as in Paper XIV. In Paper III outliers appear due to bad pixels in an CMOS imager chip; this can be dealt with by using a 2D median filter. The median function is particularly interesting in relation to outliers and rare events. Consider for instance the vector  $[6 \ 7 \ 7 \ 6 \ 7 \ 7 \ 255]$ ; the mean value is 42 whereas the median is a more representable value of 7. Whereas the median is used to avoid outliers in Paper III it is used to detect rare events of particular interests in Paper XII. Here a sliding median filter estimates the quasi-static atmospheric scattering level unaffected by spikes caused by the intersecting insects.

Model based learning by regression such as the one employed in Paper VI would suffer badly if the dataset had contained an outlier measurement or wrong expert answer. Hierarchical methods, which will be discussed later in the chapter, are entirely empirical observations without any learning, and are unaffected by outliers. In fact it is common practice in biology to purposely include a control outlier, e.g., a genetic sample from a related species to verify that it indeed falls out as an outlier in the dendrogram.

Rare events relate to risk management and certain probability distribution with so-called fat, long or heavy tails such as the Poisson distribution. Preferred ways to overview rare events and distinguish them from normally occurring observation is to produce histograms of the observation with a logarithmic probability axis. As an example damselflies occur in 1 out of

10000 spectra in Paper XII, a value which would not be observed in a linear plot. Similar histograms appear in Papers XIV and XVI. Apart from the field lidar studies presented in this thesis only very few lidar researchers concern themselves with rare events in lidar data. In one lidar study<sup>376</sup> positive echo spikes from air volumes were sorted in a histogram according to their statistical frequency and magnitude in terms of optical cross section. The spikes are among others assigned to insects. In a log-log histogram, the events can be explained as a straight line, as in Fig. 4.5.3. The ordinary return from the air matrix on the other hand was explained by a parabola corresponding to a Gaussian distribution.

## 5.6 Data reduction and factorization

Although resolution along all discussed domains can be increased to ultra precision measurements, especially with laser spectroscopy, the information does not necessarily scales with the resolution. Consider for instance emission spectroscopy of light at 588.9950 nm. Intensity at this wavelength can be associated with the content of Sodium, and is used, e.g., in astronomy. Measuring a second line at 589.5924 nm is also emitted by same element. The two lines are referred to as the Sodium D-lines and are separated due to the fine structure. Both these lines would vary with the content of Sodium, and thus one would find a large co-variance between the two measured intensities. One could also say that the information measured is redundant. We will return to the terms co-variance and redundancy later in this section. A common situation in science is that a large amount of measurement are done, and then compared to a model based on some theory with much less degrees of freedom (DOF). When the model parameters are adjusted to fit the data, the data are factorized. The benefit of having more data than model parameters is increased accuracy of the model parameters as well as improved model verification. In situations where the model can be described as a sum of linear terms or in situation where the model is approximated by a polynomial, e.g., in Paper XII, the model coefficients or factors can be found by least square regression (which will be discussed in Sect. 5.7). In models where this is not the case, e.g. Paper I, the coefficients are found through search algorithms such as the Gauss-Newton or the Levenberg-Marquardt algorithms. The latter two mentioned methods suffer from several disadvantages; they rely on iterations and are computationally demanding, they do not necessarily converge to a global minimum, and they rely on an approximately right initial guess. The initial guess problem can be very hard to provide for a model with many DOF, since the parameter space expands exponentially with the DOF. The complexity of theoretical models can often be chosen arbitrarily, covering details of less and less significance. An important aspect is thus the model selection problem; how many parameters to include and where to truncate. More important is to avoid over-fitting and ensure that the number of parameters is supported by the noise limits and natural variance of the data. These issues relate to the subject information theory covering terms like information criteria (such as Akaike's), data compression problems and information entropy. Data compression obviously has applications for computer science and telecommunication. Here compression has been developed in particular in relation to transmission and storage of multimedia data, such as sound (MP3), images (JPEG) and video (MPEG). Such lossy algorithms reduce data to what is physiologically perceivable and relevant to the human receiver; this could be in terms of hearable frequencies or resolvable spatial frequencies in images and movies. Lossless algorithms, such as the GIF algorithm are based on the construction of efficient hierarchical dictionaries specific to the dataset. Similar algorithms can be used for sequential compression; this is exploited in disciplines like computational linguistics and analyses of genetic sequences. In linguistics and literature, compression efficiencies from such algorithms have been shown to out-compete literature professors in terms of matching texts to the correct author<sup>405, 406</sup>. Other applications include deciphering of the language of other species and, e.g., anti-terror intelligence in the Internet age.

In spectroscopy a common property is that spectral features remain in the same wavelength, whereas, e.g, the intensity, absorbance or reflectance vary with the concentration of the associated substance. This implies that a spectral vector can be linearly decomposed into a number of spectral components. The number of components corresponds to the number of substances causing the variance of the optical properties within the dataset, the components could, e.g., relate to absorption of fluorescence spectral signatures. These spectral components could be measured from the pure substances. However, the interrogation geometry for the actual application in terms of probe configuration, scattering and sample layers might not be easily replicated. Even more empirical methods include principal component analysis (PCA) or singular value decomposition (SVD). These methods imply a change of coordinate system of the color space in a way such that the first axis is aligned with maximal co-variance in the original color space. The second axis is aligned to the remaining largest co-variance and so fourth. By this procedure the spectral signatures are sorted in order of significance, where the first ones are essential for the proper reconstruction of the spectra and the last components solely contain sample specific superimposed random noise. By choosing a truncation value, i.e. a number of spectral components the information can be separated from the redundancy and noise. PCA and SVD constitute cornerstones in chemometric evaluation<sup>407-409</sup>, and are today not only used in analytic chemistry but in all observational scientific disciplines.

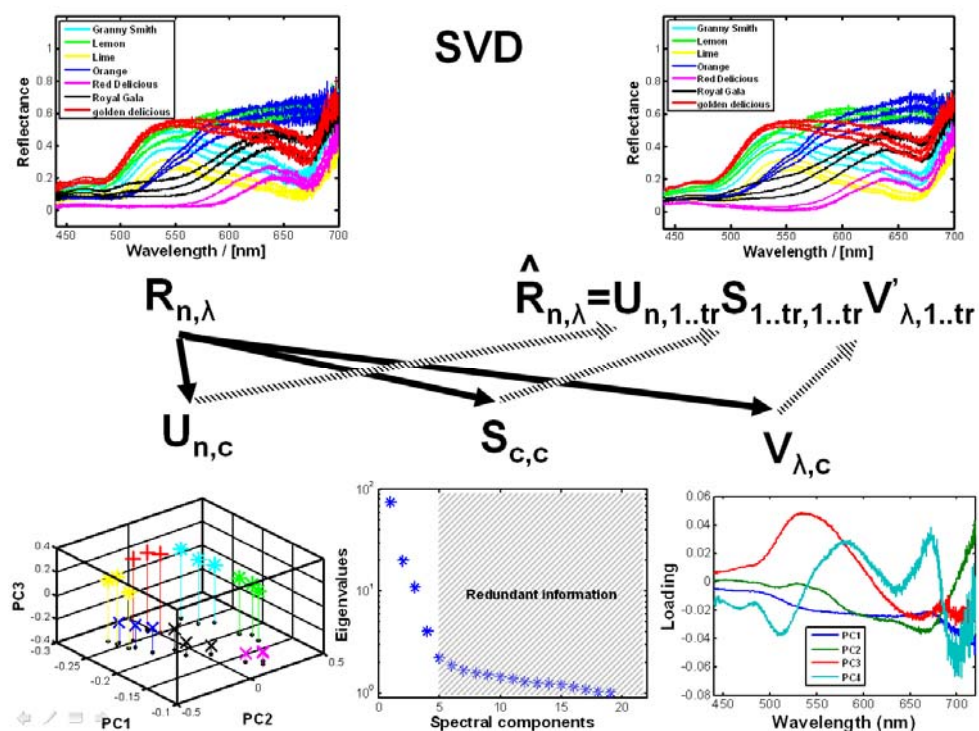


Fig. 5.6.1. With singular value decomposition (SVD) a matrix with reflectance spectra on the row can be decomposed into three new matrices according to the variance between the spectra. Here the columns of  $U$  contain scores of decreasing significance; the first few dimensions of scores can be displayed as scatter plots. The diagonal matrix  $S$  contains Eigenvalues in decreasing order. From their magnitude the number of independent linear components, or spectral components, can be estimated. The columns of  $V$  contain the spectral components in order of decreasing significance. The spectral components are linear combinations of the true spectral components of the involved substances. For a comparison the reconstructed spectra using four components are shown in the upper right corner.

The working horse of PCA is the SVD algorithm. In linear algebra SVD is a matrix decomposition method, this means that SVD splits a single matrix into several matrixes (three for SVD) whose product reproduces the original matrix. In this thesis three decomposition methods are used; SVD, QR and EIG (Eigen value decomposition). The SVD, QR and EIG matrix factorization techniques are, from a certain point of view, unique or analytical, meaning that they always produce the same factorized matrices for a particular input matrix. SVD is used in this thesis in relation to reducing spectra or probability distributions, QR is used for performing least square regression and EIG is used in relation kinetic or dynamic processes. To avoid a situation with a set of underdetermined equations, the factorized matrixes after decomposition are subjected to various types of constraints. Typical constraints include diagonal matrixes, lower or upper triangular matrixes, orthogonal vectors or normalized vector values. The SVD decomposes a matrix, e.g.  $R$ , into three new matrixes; see Fig. 5.6.1.

$$R_{n,\lambda} = U_{n,s} S_{s,s} V_{\lambda,s}' \quad \text{Eq. 5.6.1}$$

Here,  $n$  is the sample number,  $\lambda$  is the spectral band,  $s$  is the spectral component.  $U$  is a full matrix with the coefficients for the spectral mixing for each sample on the row and for each spectral component on the columns. The vectors of both  $U$  and  $V$  are unitary and ortogonal (othonormal).  $S$  only contains elements on the diagonal, the elements are strictly positive and referred to as spectral Eigen values. They are sorted in decreasing magnitude and the value constitutes to a weight factor for each spectral component. Thus, they relate direct to the significance of each spectral component. The columns of  $V$  are the spectral components, and a linear map of the true spectral signatures of the substances causing the variance within the dataset. The concept of decomposition and reconstruction, as well as the content of the various matrixes are visualized in Fig. 5.6.1. The concept is explained in details in Paper I.

Most PCA algorithms are based on SVD, but PCA differs from SVD by the fact that the mean is subtracted prior to the SVD. Since the mean is thereby lost, the original data cannot be reproduced from PCA parameters and the method is therefore not unique. For this reason PCA only plays a minor role in this thesis. The nomenclature from PCA has, however, been used in this thesis although it differs slightly between SVD and PCA. The three matrixes produced by PCA are referred to as *scores*, *latent* and *loadings*. *Score* is the product  $U S$  and typically appears in scatter 2D or 3D plots, *latent* is  $S^2/(N-1)$  and *loading* is identical to  $V$ .

Several widely different types of observations can be compressed simultaneously by SVD. This is, e.g., the case for transmittance, reflectance and scattering in Paper IV, or fluorescence and reflectance in Paper VIII. This is done by merging or concatenating, e.g. reflectance and fluorescence matrixes prior to the decomposition. When this is done, special care must be taken to weighting or normalize the values to comparable magnitudes, in a way such that, e.g., 16-bit fluorescence counts (0...65536) are not compared to reflectance (0...1). The advantage of a merged decomposition is that co-variance, e.g., the reflectance impact on the fluorescence can be analyzed. Multidimensional planes or fields can be decomposed, e.g. by temporally discarding the dimensions and arranging the observations from each sample in a single vector; this was done in Paper V. Alternatives include, e.g., the PARAFAC<sup>121</sup> method, this method is capable of parameterizing fluorescence EEM surfaces into sets of pure absorption and emission spectral components.

Parameterization and factorization of dynamical processes are subject to special considerations and will be discussed in Sect. 5.10.

## 5.7 Multivariate regression models

### 5.7.1 Projection of maximum separation

When desiring to reduce several parameters into a single concluding parameter, multivariate functions are used.

$$y = F(x_1, x_2, \dots, x_{tr}) \quad \text{Eq. 5.7.1}$$

The output of such a function can be a logical Boolean decision, e.g. sick or healthy, or it can be a graded quality of the sample. A typical situation in computer learning and diagnostic science is that  $x$  is measured by a new method under development, the true  $y$  is provided by an expert or a gold standard whereas  $F$  is often unknown. The Taylor theorem states that any analytical and continuous function can be approximated by a polynomial series. The most simple approximation is thus to linearize  $F$  by a hyper plane:

$$y = k_0 + k_1 x_1 + k_2 x_2 + \dots \quad \text{Eq. 5.7.2}$$

The bias coefficient  $k_0$  allows  $y$  to differ from zero in origo. This can be matrix formulated as:

$$Y = \underbrace{\begin{bmatrix} X_1^0 & X_1^1 & X_2^1 & \dots \end{bmatrix}}_{\Phi, \text{ regressor}} = \underbrace{\begin{bmatrix} k_0 \\ k_1 \\ k_2 \\ \dots \end{bmatrix}}_{\theta, \text{ model coefficients}} \quad \text{Eq. 5.7.3}$$

Here,  $\Phi$  is called the regressor and  $\theta$  is the model. The model coefficients,  $\theta$ , satisfying a global minimum of the least square method can be found:

$$\theta = (\Phi' \Phi)^{-1} \Phi' Y \quad \text{Eq. 5.7.4}$$

In practice, this is found through QR matrix decomposition which is much more computationally efficient than finding the inverse matrix of  $\Phi' \Phi$ . The vector terms in the regressor are referred to as base functions, and the operation is referred to as a projection of  $Y$  on  $\Phi$ . The example above is projection on a multidimensional first-order polynomial. The base functions can also be a recorded absorption of fluorescence spectrum from pure substances. When this is the case, the concentration of the respective substances can be estimated independently. In practice, the spectral signature can be perturbed in shape when embedded in a complex matrix. When the base functions are sines and cosines of increasing frequencies the projection is referred to as the Fourier transform. As discussed previously this operation appears naturally in many relations.

As can be understood from Eq. 5.7.3 the answer in vector  $Y$  is simply a linear mapping of the regressor  $\Phi$ . When the expert vector contains Boolean elements, this method is therefore also referred to as projection of maximal separation, and the function of the hyper plane can be understood as observing the data points,  $X_{1...tr}$ , in a  $tr$ -dimensional space from the angle, where  $Y \in O$  and  $Y \in I$  separates the most. Other related terms are linear discriminant analysis (LDA) or Fisher's linear discriminant analysis. When the  $Y$  contains gradual elements the method is referred to as a generalized linear model (GLM).

The fact that matrix formulation and linear algebra is used does not restrict  $F$  to be approximated only by linear functions. Following the Taylor argument,  $F$  can systematically be expanded or projected onto multidimensional polynomials of any given order, given that the sample size is large enough to provide an over-determined set of equations. The elements in the regressor can contain polynomial expansions, cross terms as known from the 2D Fourier projection, reciprocal terms or any other imaginable varieties.

$$\begin{bmatrix} x_1^0 x_2^0 & x_1^1 x_2^0 & x_1^2 x_2^0 \\ x_1^0 x_2^1 & x_1^1 x_2^1 & x_1^2 x_2^1 \\ x_1^0 x_2^2 & x_1^1 x_2^2 & x_1^2 x_2^2 \end{bmatrix} \rightarrow \underbrace{\begin{bmatrix} x_1^0 x_2^0 & x_1^0 x_2^1 & x_1^0 x_2^2 & x_1^1 x_2^0 & x_1^1 x_2^1 & x_1^1 x_2^2 & x_1^2 x_2^0 & x_1^2 x_2^1 & x_1^2 x_2^2 \end{bmatrix}}_{\phi} \quad \text{Eq. 5.7.5}$$

One way to interpret polynomials and cross products is by applying a fuzzy logic paradigm. Here mathematical equations can be translated to linguistic statements, through breaking down equation into three basic functions; 1-A, AB and A+B-AB, which correspond to the words *not*, *and* and *or*, respectively. The same form also appears in mathematical statistics. Consider for instance the capability of distinguishing bananas from tomatoes and apples by red and green reflectance. A good candidate is thus  $isBanana = R_{red}R_{green}$ , where both red *and* green reflectance has to be high.

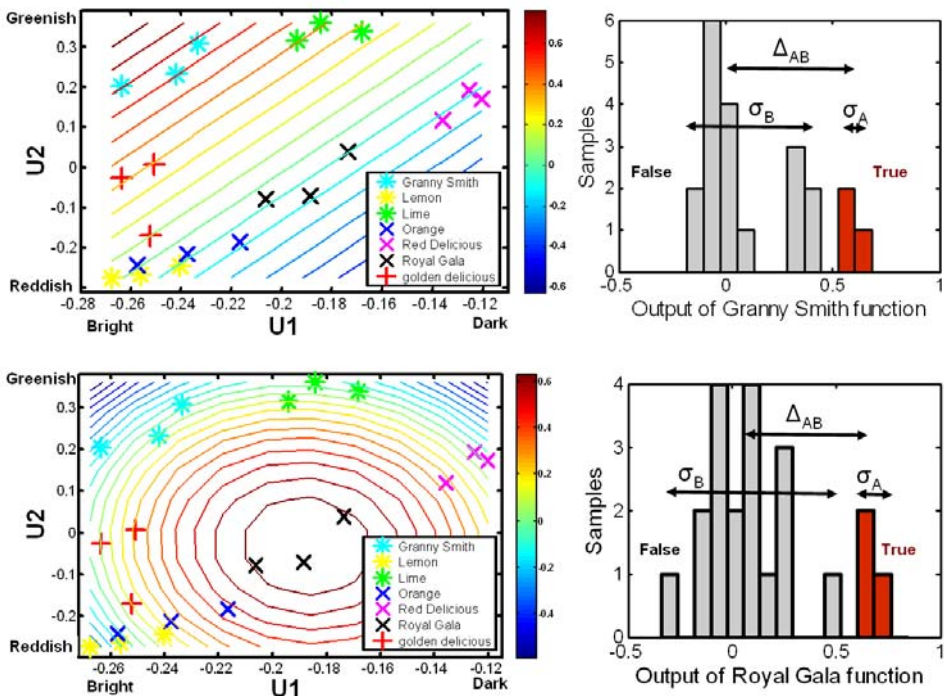


Fig. 5.7.1. When the reflectance of the seven fruits in Fig. 5.1. are reduced to a representation in a 2D color plane, regression contrast functions can be illustrated with contour plots. Upper left, scatter plot of the reduced representation of the fruits, a 2D plane separates the Granny Smith optimally from the rests by the 0.5 contour line. Upper right. When the plane is indexed at each sample position the output of the contrast function can be analysed in a histogram. A well performing contrast function has a large difference between true and false in terms of the within-group variances. Lower left, the Royal Gala is not easily separated from the rest by a 2D plane. By adding second order polynomial terms to the regressor, an optimal paraboloid can be found by linear regression. Lower right, the output of the paraboloid illustrates the discriminating ability.

In general, the practical usefulness and stability quickly degenerates as the complexity of models increase. One quality parameter of such contrast functions, is the difference of the function output with either groups in terms of the within-group variance of the output for

the true and false samples. In Fig. 5.7.1 two 2D regression models are illustrated with contour lines. In the upper case the Granny Smith apples are easily separable from the rest by a simple 2D plane. The output of the function for either group is showed to the right. In the lower case, the Royal Gala apples are situated within the remaining samples and requires a second order polynomial surface to separate them from the rest. The function terms are identical to Eq. 5.7.5 and have 9 degrees of freedom. The colored ring shows the contour of the paraboloid; the function value is shown to the right.

Regression models are not necessarily entirely empirical. In nuclear physics the semi-empirical mass formula contains regression elements which are based on several aspects of the understanding of atomic nuclei. In Paper XII a model for insect activity in relation to wind and temperature is estimated; however, the first polynomial order of wind is not included since the relation must be the same regardless of the sign of the wind speed. Therefore it can only include even polynomial terms.

### 5.7.2 Link functions

Improvements to linear regression models can also be achieved through link functions. If the expert answer is a positive definite quantity like a size, a weight or an age, a logarithmic link function can reduce the residuals between the true answer and the answer from the model. For a strictly bound parameter like a physiological evaluation grade between 1 and 10 as in Paper VI, a sigmoidal logistic link function can improve the performance. For a link function to be of practical use it must have an analytical and unique inverse function.

## 5.8 Fitting, training, evaluation and prediction

As the degree of freedom (DOF) of regression models reaches the sample size, the model will always answer infinitely correct. Such performance is not representative for a practical implementation of a method, since models or contrast functions with high complexity become highly unstable and the use of such models on a new measurement could result in any arbitrary value. We thus have to distinguish the terms *fitting*, *training*, *evaluation*, and *prediction*. When a regression model is applied on the same samples as the samples used during the regression it is referred to as fitting. An alternative is to divide the regressor,  $\Phi$ , and the expert answer,  $Y$ , into two groups. One training group or set used for regression and one evaluation group or set used to evaluate the predicting performance of the model. Consider a Boolean expert matrix,  $Y$ , where the rows correspond to the sample number and the columns correspond to one of the seven fruit types in Fig. Let the regressor,  $\Phi$ , be a simple hyperplane based on a truncated set of scores from the SVD decomposition,  $U_{n,1..tr}$ . Seven hyperplanes,  $\theta$ , separating the types can now be estimated:

$$\hat{\theta}_{1..tr+1,1..7} = \left( \Phi_{n \in \text{TrainSet},1..tr+1} ' \Phi_{n \in \text{TrainSet},1..tr+1} \right)^{-1} \Phi_{n \in \text{TrainSet},1..tr+1} ' Y_{n \in \text{TrainSet},1..7} \quad \text{Eq. 5.8.1}$$

The model can now be applied to separate a different group of samples:

$$\hat{Y}_{n \in \text{EvalSet},1..7} = \Phi_{n \in \text{EvalSet},1..tr+1} \hat{\theta}_{1..tr+1,1..7} \quad \text{Eq. 5.8.2}$$

The hat on the  $Y$  denotes that this is the predicted answer from the model in contrast to  $Y$  which is the true answer given by the expert or a gold standard method. Data can be tedious to collect; for example, in the case where a sample corresponds to a patient, e.g., in relation to P3, and where the number of patients is limited per day. The best way to make use of a data set with a limited sample size is the leave-one-out methodology. Here the training and evaluation steps described above are repeated  $N$  times. Each time the training set constitutes

of all but one sample, and the evaluation set is just the remaining one sample. The predicted answer for each sample is progressively calculated. The performance of the model can be measured, e.g., as the correlation between the elements in  $\hat{Y}_{1..7N}$  and  $Y_{1..7N}$ . The performance can be calculated as a function of truncation of model complexity; see Fig. 5.8.1. Whereas the performance of fitting shows a continuous increase, the performance of prediction shows a maximum. Such analysis and the point of maximal performance is a good candidate for making an optimal choice between inclusions of necessary information and keeping a model simple.

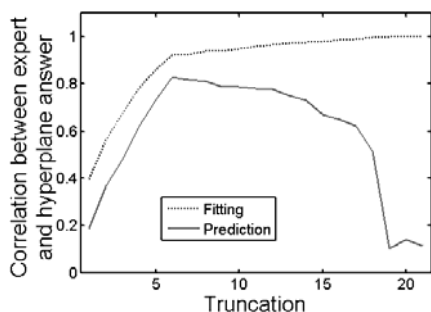


Fig. 5.8.1. Performance of hyper plane separation of the 7 fruit types as a function of truncation or dimensionality. Whereas fitting always converges to perfect performance as the degree of freedom (DOF) reaches the sample size, prediction will show a maximum as a trade-off between including sufficient information and not including irrelevant information.

A large research field in biophotonics is the disentanglement of optical properties in complex samples. The discipline attempts to tackle problems like separating scattering and absorption coefficients, e.g. by time-of-flight (TOF) spectroscopy<sup>61</sup> or spatially resolved methods<sup>175, 410</sup>. Other attempts include the recovery of intrinsic fluorescence<sup>313, 411, 412</sup>. The studies typically escalate into a jungle of partial differential equations in time and space for photo diffusion<sup>156</sup>, or large-scale forward Monte Carlo simulations which are not trivial to reverse for practical applications. Also the attempts typically focus on a few entangled properties, e.g., absorption and scattering, or absorption and fluorescence, whereas the remaining parameters like scattering anisotropy or refractive index are often presumed not to change. One reason why a general solution to separately acquiring all optical properties at all wavelengths in arbitrary samples has not been proposed, might be that both instrumentally and conceptually it is too complicated to comprehend and communicate in a scientific paper. Nevertheless, this task was the aim of both P1 and P2. In the master thesis<sup>99</sup> associated to P2, it is demonstrated that it is possible to independently predict the concentration of a substance with completely different types of optical properties, e.g. absorption, scattering, refractive index and fluorescence. This is achieved by an ignorant approach both instrumentally and in terms of data evaluation. In the instrument transmission in a large number of optical paths between combinations of source and detectors is measured. Through consideration of the basic optical interaction laws in Chap.2 it can be concluded that each type of optical property, such as scattering, anisotropy or refractive index, in the sample influences the transmittances in a different way. The combined action of all imaginable optical properties can be assumed to be very complicated; nevertheless we can consider the many transmittances measured as information related to each property, by reducing the information with singular value decomposition (SVD), the information regarding spectral content, forward scattering, side scattering, fluorescence, spatial broadening etc. within a given scenario can be summarized by the linear combination of a few components,  $V_{1..N_{sour}N_{det}, 1..tr}$ . The scores,  $U_{1..N, 1..tr}$ , of these components then contain the information essential to predict the concentration,  $C$ , of the substances independently. This was done by a hyperplane, Eq. 5.8.3, prediction with leave-one-out methodology as described above; see Fig. 5.8.2. The model uses a biased

regressor with the reduced representation in terms of scores from a truncated SVD; see Fig. 5.6.1.

$$C = [I \ U_{n,l..r}] \theta$$

Eq. 5.8.3

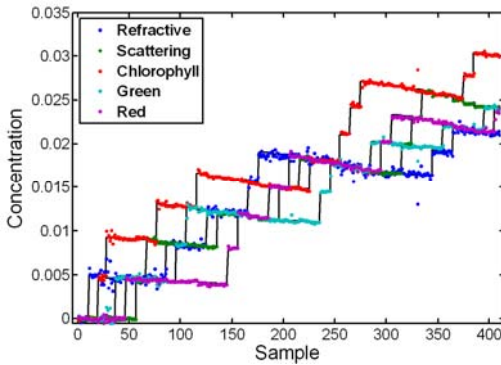


Fig. 5.8.2. Photomigration in scenarios where both absorption, scattering, fluorescence and refractive index changed typically requires advanced Monte Carlo simulations which are difficult to invert. Nevertheless accurate and independent estimates of substances with widely different impact on the migration can be estimated with linear hyper planes. In this case a 12D plane predicts the concentration of colorants, fluorophores, scatterers and refractors randomly added to a reservoir. The measurements are performed with the combinatorial light path spectrometer P2<sup>99</sup>. Apart from providing independent estimates the methods also covers a larger span of optical depths than traditional spectroscopic setups.

While emission and absorbance spectra decompose linearly into a number of spectral component equivalent to the number of substances influencing the spectra, this is not the case for transmission or reflection when the concentration varies over a large span. This is because of the Beer-Lambert law (see discussion in Section 2.5.2) where the transmittance relates to the concentration by an exponential decay. Such relation can obviously be approximated by a line or another low-order polynomial, but this does not change the fact that high concentrations causing a large optical depth will eventually decrease the transmittance down to the noise equivalent. Therefore precise estimation of low concentrations should be performed at the peak absorption, whereas precise estimations of high concentrations should be carried out at the flank of the absorption, see Fig. 5.8.3.

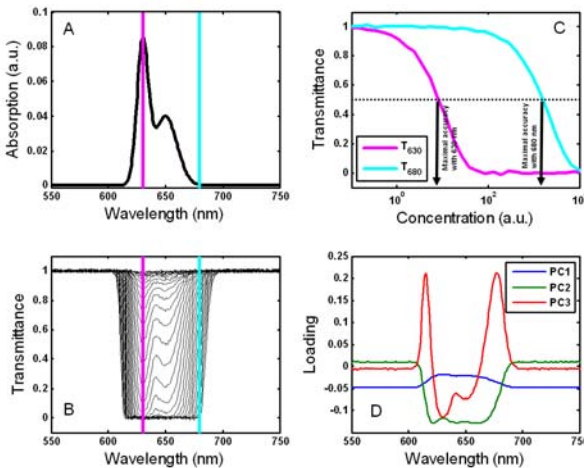


Fig. 5.8.3. Simulation of transmittance through a single fictive absorber (A). The absorbed band in the transmittance spectra depletes and broadens for high concentrations (B). The transmittance is plotted at two wavelengths against concentration (C). Best concentration estimates are obtained around 50% transmittance. Linear decomposition of the transmittance spectra produces a number of components (D).

When linear decomposition such as SVD is attempted directly, e.g., transmittance spectra covering a large span of concentrations, several spectral components are required to explain the depletion and the expanding flanks (See Fig. 5.8.3D). While, Beer-Lamberts law provides precise concentration estimates in concentration regions around 50% transmittance, a multivariate regression model, Eq. 5.8.4, is able to estimate the concentration over a large

span. The performance is compared to a Beer-Lambertian approach at the peak absorption and ant the flank in Fig. 5.8.4.

$$\log(C) = [I \quad U_{n,l,tr}] \theta \tag{Eq. 5.8.4}$$

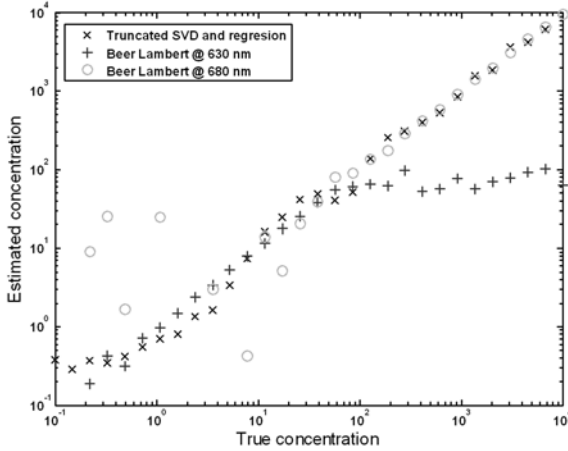


Fig. 5.8.4. Comparison between the Beer-Lambertian approach and SVD - multivariate regression approach to estimation of concentrations over a large span of optical depths. See Fig. 5.8.3.

## 5.9 Unsupervised clustering

As opposed to data evaluation through computer learning and training, multidimensional data can also be evaluated through unsupervised clustering methods. Such methods do not require an expert answer to operate; however, an expert answer is still useful for verifying the performance.

### 5.9.1 Hirarchical clustering and dendrograms

One approach to unsupervised clustering is the concept of analysing statistical distances. The distances refer to the process of applying norms pair wise between observations of measurements in a multi-dimensional space. A norm is a measure fulfilling a number of criteria such as returning strict positive values. Examples of norms are Pythagoras equation, which is a special case of a Euclidean norm, there are Manhattan or taxi norms and max norms. Even the correlations between, e.g., spectra or multivariate distributions as in Paper V, can serve for measuring the similarity of two samples. This is employed in another paper by the author<sup>413</sup>. The outcome of such pair-wise applications of norms is a reduction from scatter plots of high dimensionality into a description of the distance from one data point to all of the rest of the data points; this is also referred to as connectivity.

$$d_{ab} = \left( \sum_{m=1}^M |x_{a,m} - x_{b,m}|^p \right)^{1/p}, \quad p > 1 \tag{Eq. 5.9.1}$$

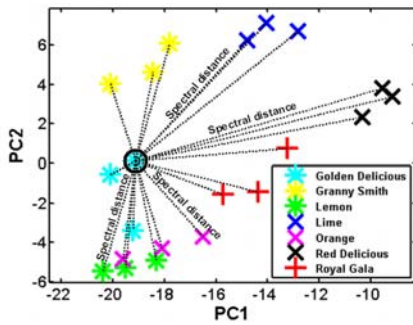


Fig. 5.9.1. Illustration showing Euclidean distances from one data point to all others in two dimensions. The process is repeated for all data points.

For such distances to work well it is important that the different dimensions are of comparable magnitudes. One way to ensure this is to maintain equal signal-to-noise ratios (SNR) in each dimension. This is the case for principal component analysis (PCA) scores or  $U$  weighted with  $S$ , as in Paper XII. Given a sample size of  $N$ , a total of  $(N^2-N)/2$  distances will be obtained. Note the different magnitudes on the axis in Fig. 5.9.1. Another approach is to use Mahalanobis distances which are scale invariant, due to normalization by subtraction of the mean and division by the variance. From the many distance a complete linkage structure can be calculated. The linkage function clusters all samples hierarchically by their similarity. The visualization of linkage structures are often plots referred to as dendrograms. In Fig. 5.9.2 the unsupervised hierarchical cluster dendrogram for the seven fruit in Fig. 5.1 is shown. The color threshold was set to divide the samples into seven groups. The basis for the distances in the figure is the scores for the first four spectral reflectance components of the fruits. A four-dimensional scatter plot can never be visualized on the two-dimensional paper of this thesis. The dendrogram, however, manages to reduce the dimensionally and sort the samples in similarity and visualize it. Although the algorithm is completely unaware of what it is sorting it only makes one mistake; see Fig. 5.8.2.

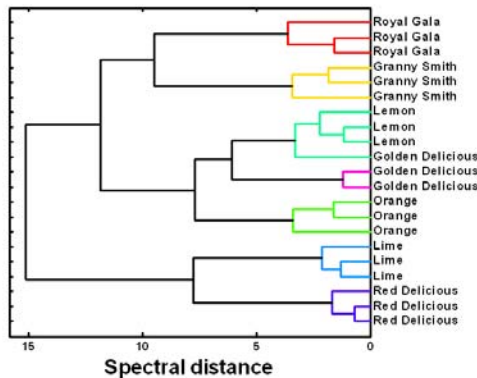


Fig. 5.9.2. In this case a dendrogram is able to present distances between samples in a 4D color space from a truncated SVD (see Fig. 5.6.1.) of the reflectances from the fruits in Fig. 5.1. 4D data are not easily communicated in any other way. A dendrogram can be understood from right to left as a series of  $\subset$  shapes, the width of each  $\subset$  represents the statistical distance between two samples of group of samples in a multidimensional space. Even if the method is completely unsupervised, the method is capable of sorting the samples in correct groups except for one mistake. The performance might be improved by choosing a higher truncation point, by normalizing the data or by concatenation with, e.g., fluorescence data.

In biology the gold standard for producing dendrograms is genetical distances, produced by tedious polymerase chain reaction (PCR) and genetic sequencing. However, dendrograms and hierarchical clustering in biology can also be produced, e.g., by morphological data. This was done extensively historically. The general public associates dendrograms with

heredity and family trees, the statistical distance axis is often confused with time; however, this presumes absence of evolutionary constraints and constant rate of mutation. Dendrogram are even suitable to plot in polar forms since there more details in the smallest branches than in the trunk.

Hierarchical clustering is an attractive tool since it is entirely empirical. This is of particular interest in relation to mistakes by the expert or odd and rare events. Consider for example a large number of dermatological fluorescence measurements from sick and healthy patients; see Fig 1.3.4. The medical doctor or the histopathologists might provide the correct answer in 99% of the cases, but one patient might wear an invisible layer of sun lotion or perfume and forget to inform about this. This event could give an entirely new spectral signature and a training approach would be entirely perturbed by such large deviation and to a high degree depend on whether or not this individual was judged sick or healthy. In hierarchical clustering, however, such outlier would be easily identified.

### 5.9.2 Mixed Gaussian distributions

Mixed Gaussian distributions are based on the paradigm that a distribution or a collection of observation can be explained by the sum of several normal distributions.

$$p = \sum_{m=1}^M a_m e^{-\left(\frac{x-\mu_m}{\sigma_m}\right)^2} \tag{Eq. 5.9.2}$$

Here  $M$  is the number of modes. In emission spectroscopy such as fluorescence spectroscopy, this somewhat intuitively relates to the observation from a number emission lines, with given center wavelength,  $\mu_m$ , and line width,  $\sigma_m$ . Features caused by re-absorption or scattering are, however less intuitive. In Fig. 5.9.1. the fluorescence signature from a Granny Smith apple (see Fig. 2.5.4) is approximated by a sum of six Gaussians. An advantage of mixed distributions over SVD or measured table data is that it can be communicated and reproduced with relatively few parameters. The disadvantages is that the fit entirely depends on the initial guess and a global minimum of residuals cannot be guaranteed. Form this it can be understood that the solutions are not unique. The fit is based on computationally heavy iterative search algorithms. In Fig. 2.5.4 the initial guess is a point in an 18-dimensional space and it was provided by the intuition of the author.

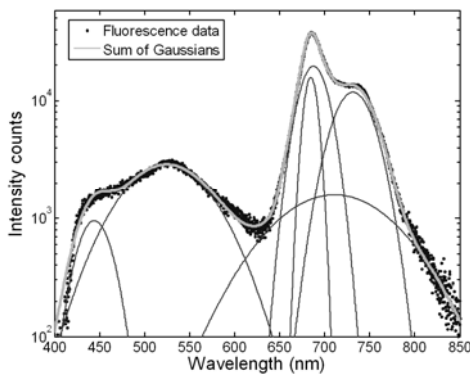


Fig. 5.9.3. Fluorescence from a Granny Smith apple and a mixed Gaussian approximation.

The degrees of freedom (DOF) for multi-dimensional mixed Gaussian distributions quickly increase with the dimensionality,  $D$ , according to:

$$DOF = M(1 + \frac{3}{2}D + \frac{1}{2}D^2) \tag{Eq. 5.9.3}$$

The square term arises because of co-variance. Mixed Gaussian distributions can be used for clustering simply by considering the dominant Gaussian mode at the location where an observation is made. For the case of the seven-fruit classification problem a mixed Gaussian clustering by the two first reflectance components, would imply 42 DOF. Even if the sample size would allow an over determined system of equations the fit an initial guess would be exceedingly difficult to find. Fig. 5.9.4 illustrates mixed Gaussian clustering into three groups. Such an approach is not unique, computationally heavy and performs for problems with many modes and high dimensionality.

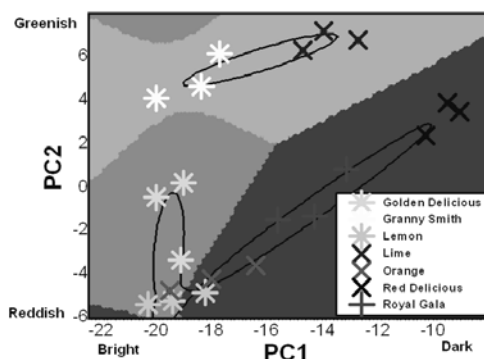


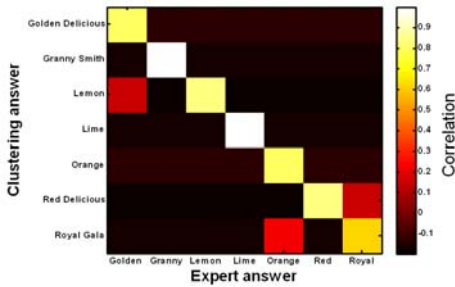
Fig. 5.9.4 Mixed Gaussian clustering of the seven fruits in Fig. 5.1., using the first two spectral components of reflectance.

### 5.9.3 Centroids

Centroids are theoretical points in the color space either produced from a mean value of samples clustered to a particular group or by the expectation values in mixed Gaussian distributions. The position of a centroid in a color space or SVD space, can be used to reconstruct centroid spectra for each group. This provides the opportunity to relate different clusters back to the physical difference dividing the clusters. This is done in Paper XII. Whereas inspection of the thousands of spectra recorded would require tiresome work, inspection of the few cluster centroid spectra could quickly be assigned to previous lab spectra from male and female insects in Paper X, as well as to the vegetation edge and terrestrial oxygen line in the NIR.

### 5.10 Confusion matrixes

When evaluating the performance of multivariate interpretation the scenario quickly becomes confusing, even for a simple two class problem; How many were classified correctly? How many of the sick were classified as sick? How many sick were classified as healthy? How many healthy were classified as sick? The situation only becomes more complex in a multiclass problem. One way to evaluate and visualize mistakes, when a gold standard method exist, it to produce a confusion matrix<sup>413, 414</sup>.



		Algorithm	
Expert	True negative	False positives	
	False negatives	True positive	

Fig. 5.10.1. When the hierarchical clustering methods from Fig. 5.9.2 is correlated with the classification by the fruit expert (the author) a confusion matrix is obtained. In this case the spectral truncation and thus the dimensionality of the color space was reduced to three. The correctly classified samples appear on the diagonal, and the algorithm mistakes off diagonal. From such plots confusion in multi cluster analysis can be overviewed. In this case a lemon and a Golden Delicious are confused, and additionally oranges, Royal Gala and Red Delicious are confused with each others.

## 5.11 Dynamic processes

### 5.11.1 Fourier transform

The Fourier transform is named after the French revolutionary and mathematician Jean Baptiste Joseph Fourier from the 18<sup>th</sup> century. His work included heat transfer and in particular Fourier series and the Fourier Transform. His doctoral thesis advisor was another famous mathematician, Giuseppe Luigi Lagrangia (Lagrange). The Fourier series implies that any given limited continuous analytical function or numerical series can be described as a the sum of sinuses and cosines. The Fourier transform is an analytical dictionary for transforming functions back and forth between the original and the Fourier frequency domain. In terms of linear algebra and matrix formulation, the Fourier transform can be understood as the projection of a numerical vector onto a set of sinus and cosine base vectors. Thus the coefficients can be found by least square regression or the particularly computationally efficient fast Fourier transforms (FFT). Although data transformed by FFT are identical and lossless, the interpretation can be facilitated in one or the other domain. The Fourier concept relates to a large number of physical and optical phenomena, such as Fourier optics, diffractions and Heisenberg's uncertainty. It is particularly efficient in describing periodic phenomena such as solar cycles, years and seasons, weeks, day cycles, breath takings or hearth beats, wing beats of insects, sounds and oscillations of the electric field referred to as light. With its many occurrences in nature it is worthwhile remembering some of the most fundamental aspects of the Fourier transform, even if not implemented in calculations. One such important aspect is the fact that anything which is short, sharp or fast produces a very broad Fourier counter part. Examples of implications are: illumination of a broad area of a diffraction grating can produce a sharp collimation and narrow spectral width in a spectrometer, or, in order to produce a short light pulse, it must contain a very broad spectral content.

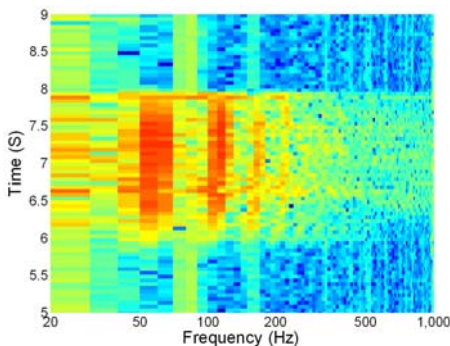


Fig. 5.11.1. The first results of passive sunlight scatter from a dragonfly species over Klingavalsån river nature reserve July 2012. The event was simultaneously remotely recorded by a Si quadrant photodiode, a compact spectrometer and an imager<sup>415</sup>. The intersection appears in the duration 6-8 seconds. Up to four harmonics are observed as well as a chirp around 6.6 s, the additional static vertical lines are electronic interferences.

When a time series is chopped in pieces and partially Fourier transformed a spectrogram or sonogram is obtained, see Fig. 5.6.1. This type of analysis is popular in speech recognition, analysis of animal communication and also for monitoring the wearing of machines and engines. One lidar group working with honey bees exploits such plots for the detection of their focal species<sup>287</sup>. The harmonic analysis of such plots from insects have been used for taxonomy<sup>141</sup>.

### 5.11.2 State space concept and vector field models

Kinetics or modeling of dynamical processes have been a traditional discipline in classical mechanics and chemical reaction kinetics for centuries. Initially the main interest was in understanding ballistics (e.g., Albert of Saxony, 14<sup>th</sup> century). Later the understanding was significantly improved by precise astronomical observations, e.g., by Tycho Brahe, Fig. 4.1, inspiring people like Johannes Kepler, Galileo Galilei and Isaac Newton. Following the industrial revolution and the invention of the steam engine the familiar James Clark Maxwell invented the centrifugal speed regulator. This closed-loop device is considered the starting point of the discipline of control theory. Other important figures from the same century inspiring to control theory include Pierre-Simon Laplace, Alexander Lyapunov and Harry Nyquist. In the late World War II, control theory was capable solving the unstable problem of balancing the famous Vergeltungswaffe 2 (V2) on top of the exhaust jet. The construction and the famous rocket scientist and visionary Werner von Braun was later exported to United States of America contributing to the USA-Soviet space race and most space technology used today. Whereas control theory was initially based entirely on mechanics, and later on analog electronics, the development of computers and microprocessors allowed real time control by complex algorithms. In this respect discrete time series and linear matrix algebra became important corner stones of control theory and dynamic modeling.

Whereas control theory concerns itself with designing optimal controllers, a complimentary part is the physical dynamic process or system subject to control. Mathematical descriptions of such processes can either be based on a number of presumptions and physical laws or they can be build empirically from time observations of the inputs to and outputs from the dynamical process (black box models, semi empirical models with some physical insight are some times referred to as grey box models). The discipline of building dynamical mathematical models empirically from measurement data is referred to as system identification. The span of input perturbations to the process during system identification is referred to as the model excitation. Model excitation can be in terms of frequencies of amplitudes fed to the dynamical system. As in optical elastic spectroscopy, the broader the model excitation, the better the description and validity of the model will be. The cause of the Chernobyl reactor disaster has been assigned to such a system identification test with increased perturbations to the control system. There are countless, more successful applications of system identification; in chemical process industry, robotics and automation advanced mathematical dynamical models can greatly increase the production and throughput rates in factories without increased costs. In commercial electronics such as compact disc drives, the dynamics of the optical pickups is regularly characterized and in cell phones communication the channels are characterized according to the multiple reflectance and interference from the changing surrounding geometry.

One of the main aspects of dynamical models is the number of dynamical states required to describe the behavior. These states often relate to populations of energies. As an example a simple pendulum has two dynamical states; those could be angle and angular speed, or potential and kinetic energy. A multi-joint robot will typically have two such states per joint<sup>355-357</sup>. In chemical reaction kinetics the state could be the concentration of various

substances. In population dynamics of ecosystems the states can be populations of different species or even more detailed populations of different age groups in different life stages<sup>416-419</sup>. In multi chain radioactive decays in nuclear physics the states would be population of different isotopes<sup>420, 421</sup>. In atomic or molecular physics the dynamical states could be the electron populations in different excited states as in Paper IX. Dynamical states can either be observable or non-observable.

A common assumption in dynamical modeling is that the process is deterministic and the value of the dynamical states in the next given instance is solely determined by the present value of the states and the given perturbation, e.g. from a controller. In the following we will not discuss external perturbations, but briefly note that they can be treated equally as the states of the system. A vector,  $X_t$ , containing the present values of the dynamical states, the dynamical systems can be considered in a state space. In time the system will produce a state space trajectory. Given the determinism, the trajectory can be described as:

$$X_{t+1} = F(X_t) \quad \text{Eq. 5.11.2}$$

Here  $F$  is a multivariate function or map producing a new set of dynamical states depending of the position in the state space. More commonly a differential function describing the change of states is considered:

$$\dot{X}_t = X_{t+1} - X_t = F(X_t) - X_t = \dot{F}(X_t) \quad \text{Eq. 5.11.3}$$

From such a description one can understand the system transfer function as a vector field, where any given position in the state space points are the state space position where the states will be in the next given instance. As for previously unknown functions; see e.g. Sect. 5.8.,  $F$  can be approximated by a multivariate polynomial. In the simplest case a linearization is obtained:

$$\dot{X}_t = X_t A \quad \text{Eq. 5.11.4}$$

Here  $A$  is referred to as the system matrix. Together with the initial condition  $X_0$ ,  $A$  gives a complete description of the temporal evolution of the system. Depending on the matrix eigen values of  $A$  the system has three solutions; exponential growth for real part positive Eigenvalues, decay to origo for real part negative Eigenvalues, and oscillations for Eigenvalues with zero real values, the latter never occurs in practice. Oscillations occur when  $A$  has a pair of complex conjugated Eigenvalues or when there are cyclic energy routes in the systems, e.g., the situation in a pendulum where kinetic energy transforms into potential energy and vice versa. In decay of radioactive nuclei or excited atomic or molecular systems this cannot occur and only a triangular system matrix is required to describe the dynamics. For processes which are not assumed to converge to the origin a bias term can be added. This is for instance the case for the bleaching in Paper VII.

$$\dot{X}_t = [I \quad X_t] A \quad \text{Eq. 5.11.5}$$

Similarly higher order polynomial approximations of  $F$  including cross terms, can be constructed. However, most general stability theory, is only valid for linear dynamics, and stability and convergence of non linear system can only be found or guaranteed in special cases, e.g. through Lyapunov theory. Even a single state second order polynomial or a triple state system with a cross term is capable of producing chaotic outcomes such as the Feigenbaum structure, sub-harmonics or the Lorenz attractors, respectively. Chaos implies

that the slightest deviation of the initial condition escalates with time to an extent that the state is entirely unpredictable after a given time. Regardless of the complexity and whether the model is linear or not, the model coefficients can be found empirically through least square regression, e.g.:

$$\begin{aligned} \dot{X} &= X_{t+1} - X_t \\ \Phi &= [I \quad X \quad X^2] \\ A &= (\Phi' \Phi)^{-1} \Phi' \dot{X} \end{aligned} \tag{Eq. 5.11.6}$$

In Paper VII and IX it is postulated that the dynamical states are observable and that they are the spectral components observed in the two scenarios. When decomposing a time series of spectra with SVD, the scores are a linear map of the actual concentration of substances or populations in fluorescence states. Since the dynamic is determined by a linear map of the populations, the change of scores over time can be described by a linear map of the inverse linear map of the scores themselves. Since an unknown linear map of another unknown linear map collapses into a single unknown linear map,  $A^*$ , we can write the evolution of  $U$  from Sect. 5.6:

$$\dot{U}_t = [I \quad U_t] A^* \tag{Eq. 5.11.7}$$

When considering reflectance spectra from a freshly cut cola nut; see Fig. 5.11.1 the Eigenvalues from SVD analysis reveal that the spectrum at any given instance can be described by the linear combination of three spectral component. This could be understood as one component describing the initial reflectance and two additional components describing the increased absorbance from oxidized rest products.

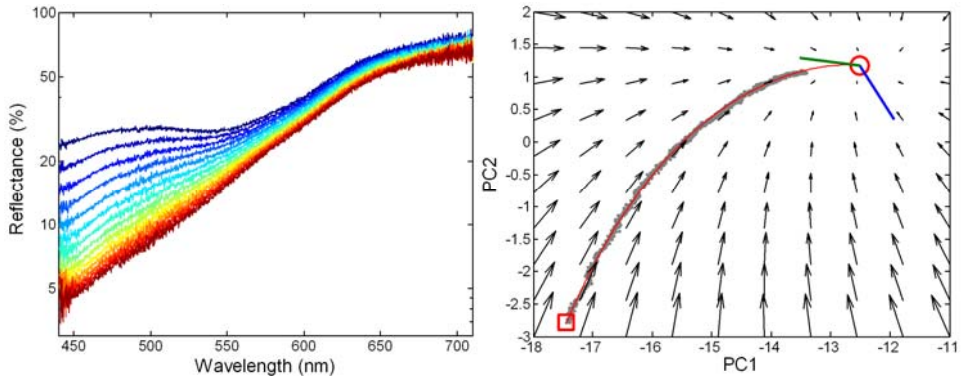


Fig. 5.11.1. Left, Sample reflectance spectra of the browning process due to oxygenation of a freshly cut cola nut (See Fig. 4.5.2). The time span from the initial (upper) spectrum to the last (lower) spectrum is 5 s. Measurements performed in workshop at Bamako university, Mali<sup>134</sup>. Right, When reflectance is recorded over time for the oxygenation of a fresh cut cola nut (See Fig. 4.5.2) the spectra can be explained by a linear combination of two spectral components. The content of either component are also the dynamical states of the system. In figure the measured state space trajectory for the two states are shown with blue dots. The biased linear dynamic model is plotted with a black line, the vector field of the system matrix is shown by arrows, the convergence point is marked by a circle, and two eigenvectors are plotted by a green and blue line. These vectors can be used to rectify the arbitrary coordinate system from the SVD.

Thus, the state space trajectory can be described by two dynamical states. Since it cannot be assumed that reflectance decays to zero at infinite time, a bias term is required as in Eq. 5.11.7. The system matrix  $A$  can be found upon regression and visualized by a vector field; see Fig. 5.11.1. The data points are shown in grey and the trajectory from the models is shown with a red line.

When the system matrix  $A$ , is subjected to Eigenvalue decomposition two results are obtained; the dynamical Eigen values or accumulation lifetimes which in this case are 1.53 and 2.36 s and also two Eigenvectors. The Eigenvectors relates to directions in the coordinate system produced by the SVD, the Eigenvalue decomposition is only unique to the extent that any scalar combination of the Eigenvectors solves the decomposition problem. Therefore the sign of the eigenvectors can always be chosen so that the projection of the state space trajectory produces positive entities. Such projections produce single exponential decays, additionally the directions of the eigenvectors can be used to rectify the arbitrary spectral components from the SVD into purely decaying spectral components, see Fig. 5.11.2. This is discussed in details in Paper IX and relates the DECRA algorithm<sup>422</sup>.

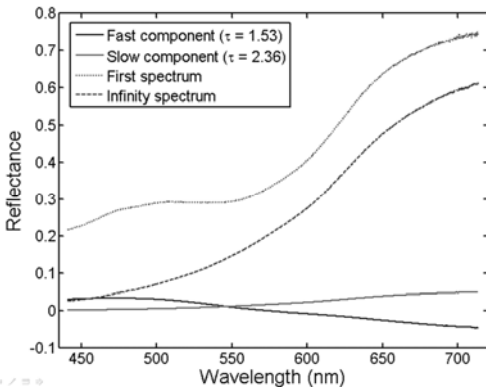


Fig. 5.11.2. Rectified spectra from cola nut oxygenation reflectance time series. The reflectance at any given moment can be entirely explained by the infinity spectrum plus two exponentially decaying spectral components. The time constants are in seconds.

## 5.12 Correlations

Correlations can be used as a measure of similarity of two vectors, planes or probability fields. As such direct correlation between spectra can be used a crude distance norm for hierarchical clustering of spectral data; see Sect. 5.9. Spectral correlation can also be performed optically and is exploited, e.g. in gas correlation spectroscopy<sup>202</sup> and imaging<sup>423</sup>. In another study by the author<sup>413</sup> 3D probability distribution of patchy lizard backs were correlated to the patchiness of their habitats to investigate cryptic coloration, in this case the elements from a 3D probability distribution is rearranged into a vector. The correlation between two vectors,  $a$  and  $b$  is given by

$$r_{ab} = \frac{\sum (a - \mu_a)(b - \mu_b)}{(N-1)\sigma_a\sigma_b} \quad \text{Eq. 5.12.1}$$

Correlations can also be calculated between to sets of data as a function of relative displacement. Image correlation as a function of x-y displacement can be used to locate objects and shapes of particular interesting in an image. Such operations can be achieved by digital image processing or with light speed with Fourier optics. Sliding cross-correlations highly resemble convolutions, corresponding to a multiplication in the Fourier domain. Sliding time correlations of process inputs and outputs are extensively used in robotics to characterize robot time responses. In Paper XII a sliding time correlation is applied to occurrences of two sexes in a damselfly population in a confined air volume. This analysis is a quantitative measure of the biological phenomena of chasing. The matrix correlation between a Boolean gold standard matrix and a predicted matrix in a multiclass classification problems produces the confusion matrix; see e.g. Fig. 5.10.1

### 5.13 Ray-tracing and Monte Carlo

Ray-tracing and Monte Carlo simulations are forward simulation of rays or photons producing intensity flux, e.g., through a plane on in a volume. The term raytracing typically refers to simulation of light in the community of optical engineering while Monte Carlo typically refers to simulations of photo migration in the biophotonics community. The term ray-tracing is also used in computer graphics and 3D rendering. In the latter case the aim is not necessarily to produce an accurate description of light propagation, but to produce realistic pictures. The consequence is, however, that well known optical phenomena are reinvented and given new redundant names, e.g. sub-surface scattering (SSS). The community of computer graphics and entertainment have, however, developed exceptionally powerful parallel graphics processors which are now being used for scientific computing. Ray-tracing in optical system design is typically aimed at analyzing aberrations, image distortions and stray light for the purpose of minimization (See e.g. Fig. 1.3.3). Common for ray tracing and Monte Carlo is that the simulation of rays or photons is typically followed by a statistical collection of rays or photons impinging on a plane of interest. In particular straylight from diffuse reflections is a computationally very heavy problem. The Monte Carlo approach in photomigration simulations can be considered superior in terms of precision in comparison to the diffusion model<sup>156</sup>. Such studies typically involve simple scenarios such as semi-infinite homogeneous media, tissue slabs or tissue models with a few layers. The outcome of such simulation are often general questions of interest; e.g, over which volume is the energy of a laser deposited for treatment, or what is the mean interrogation depth for a certain wavelength in optical diagnostics. For the statistical measures of a simulation to be accurate, highly resolved and noise-free, a very large number of simulated photons is required. However, since the random walk of each simulated photon is independent of the other simulated photons, the problem is ideal for parallel computing<sup>155</sup>. Other tricks to increase the computational efficiency is to save the photon flux field solutions for one scattering coefficient and then rescale the solution, should the coefficient change; even interpolation between solutions can be done. In situation where photons emerge from a source and are registered by a detector, another common trick is to change the detector into a second source and run two simulations. The intensity which can be expected by the detector is then the integrated product of the two flux field from each simulation. The computational benefit can be understood by the very small chance of a photon to walk all the way to the detector, whereas the chance of walking half way is much larger.

---

## Chapter VI

# 6. Conclusion and outlook

---

---

### 6.1 Optics and bio-photonics

In terms of optics and bio-photonics this thesis highlights a number of difficulties and opportunities with intermingled optical properties. In P2 a solution for direct prediction and disentanglement was proposed. In Paper XIII a relationship between reflectance and fluorescence was found which can be exploited to indirectly measure the reflectance with bird eye-safe fluorescence lidar. In Paper XV the properties of absorption, refractive index, scattering and ballistic transmittance were discussed and related to the Kramer-Kronig relationships and the Christiansen effect. Although the latter two effects have been known for a century there are only few studies where they are considered in atmospheric optics and optical analysis of fibrous and porous samples. Similarly, various aspects of both iridescent and non-iridescent structural colors have been discussed throughout the thesis. The possibility of structural colors in remote sensing is mainly an unexplored subject. However, they might be present in ordered tissue such as vegetation where complimentary structural information could be retrieved.

In terms of instrumentation, Papers I and VIII demonstrate improved estimates of spectral emission by assessment of the UI characteristic of the filament and LED light sources, respectively. In Papers II, III, VIII and P2-P4 some new schemes for ray combination in LED multiplexing are presented. In P2 the advantages of flashing and cooling in fast multiplexed LEDs are exploited. Paper III and Chap. 4 introduce the concept of discretizing along various domains; the paper and the chapter highlight similarities between the domains. The paradigm is not common in optical instrumentation but can be beneficial for future studies on the topic. Throughout the thesis and, e.g., in Paper II, several references to the fascinating world of animal vision were made. Although many such vision systems are not directly implementable for engineers, vision physiology constitutes a nice compliment to existing technological design of what vision systems could also be. It is pedagogically valuable to include this aspect even for technologists. Such an approach is popularly referred to as bio-inspiration.

New schemes for scattering imaging, and remote scattering, are introduced in Papers III and XII. The former features a fiber ring light illuminator and its implementation is much simpler than traditional beam shaping in dark field microscopy. Also the construction enables angular scanning such as the one presented in Fig. 4.4.4 and could equivalently be implemented in the back scattering mode. The remote dark-field setup in Paper XII yielded surprisingly good first results even if the detecting spectrometer was neither cooled nor intensified. The disadvantages of the method in Paper XII is the reliance on daytime, the clear sky conditions, and also the fixed interrogation volume. The method provides a broad spectral overview of what could be expected by a multi-band elastic lidar system, however. Such an active system would work independently of sunlight and black terminations, it would provide ranging as in Paper XI and could be scanned to produce 3D data.

In respect to the lidar community, this thesis highlights the presence of organisms such as insects and birds as natural atmospheric constituents. Terms such as rare events and quasi-static and non-static contribution are introduced. Particularly in Paper XIV the concept of

color spaces from imaging terminology is used to illustrate classification of birds. This could also be of use for empirical classification of other types of aerosols.

## **6.2 Entrepreneurship and capacity building in the developing world**

As the thesis was partially financed by a national innovation initiative several efforts were done in order to develop realistic prototypes and secure intellectual property rights. Most of these innovations were instrumentation based on inexpensive LED light sources; in particular P2 led to the establishment of a company (IdeaSpec I/S, Denmark) and was rewarded a Danish innovation price. The national infrastructure for promoting innovation and entrepreneurship is, however, currently immature, and despite the large number of people working on the issue no coherent plans for the development of ideas into business plans seem currently fully functional; see discussion in Sect. 1.2. As a result most of the ideas and projects initiated during the thesis work are on halt. As per recommendation from the financing innovation initiative, patent applications should be part of the academic evaluation of the doctor's defence. In contrast to peer-reviewed journal paper the cost for patent applications, however, are thought to be covered by the inventor. It is a highly unrealistic idea that a graduate student could cover the exponentially increasing cost associated with patent filing, or that the student would allocate the time necessary for the intense fundraising to achieve the means, apart from ordinary activities. Although an innovation first price was given to P2 by the Danish industry, and the grant could cover expenses for European filing and prototype components, it can only ensure project continuation for a few months salary, and the grant is negligible in comparison to most research grants (the grant constituted approximately 2% of the cost associated with this thesis).

Despite organizational problems, electro-optical instrumentation and inventions for realistically solving real-life problems constitute a highly relevant topic. The matureness can be associated with widely available, compact and robust semiconductor light sources, CCD and microprocessor for chemometrical evaluation. A large synergy between realistic technology for implementation in Scandinavian industry and realistic instrumentation for science in developing countries exists. A considerable amount of effort during this thesis work was spent on organizing workshops financed by the International Science Program (ISP) which operates with support from the Swedish International Development Cooperation Agency (SIDA). These activities fall under the category of capacity building, where the idea is to provide training and instrumentation for local formation of doctoral students. As opposed to many projects supporting lower stages of education, e.g. in the elementary schools, the projects pursued through this thesis works are costly and target only a few national candidates. The expectation from such persisting projects lasting for decades is to prevent so-called brain-drain, and to plant intellectual seeds with expected exponential growth. Here the main idea is the pride in the local formation of role models offering an alternative to pursue scientific careers abroad.

A common tendency is that many scientist in developing countries pursue science abroad with sophisticated instruments. Upon returning the projects cannot be pursued with the local means and the projects might be irrelevant to the local society and therefore downprioritized by the local government. One approach to increase the local interest in science is to pursue applied science for solving local problems, e.g. issues in health<sup>424</sup> or agriculture<sup>137</sup>. This has been one of the main considerations in organizing these workshops. A general tendency is that academics in developing countries are funded for their teaching and budgets for research and materials are commonly non-existing. In the workshops organized during this thesis work the expenses for traveling and accommodation of the participants and the materials were balanced. Other programmes such as the Network for

Low Cost Physics, by the Interdivisional Group for Physics for Development (IGPD), European Physical Society (EPS), suggests minimally costly scientific instrumentation, e.g., from stripping outdated consumable electronics. This approach was used throughout the childhood of the author at the local scrap yard in Copenhagen, but is becoming increasingly difficult along with the miniaturization and integration of most products, which are now seldom made from discrete parts.

Other more well founded programs include the Abdus Salam International Center for Theoretical Physics (ICTP). The center focuses less on materials and its main activity is to bring in scientists for long- or short-term training, originally in theoretical physics in a creative environment. The Center is now also encouraging experimental physics. A challenge is then to find the optimum time balance between time spent at the ICTP or elsewhere in the developing countries, and working with local students with the available equipment at the home institutions. In the ISP funded workshops organized by the author together with collaborators, a balance is sought and demands of active deliverance by the participants, including equipment construction, computational training and poster competitions are emphasized.

### **6.3 Scattering and dynamical contrast in medicine**

In the work on detection of malaria parasites in blood smear, in particular spectrally resolved scattering imaging proved promising. The ballistic transmittance of thin unstained tissue slides in bright field microscopy often shows low contrast except for strong chromophores such as hemoglobin. The specular reflectance also shows low contrast with signals primarily arising from the spectrally slowly varying refractive index. The scattering, however, arises from the cell membranes, the organelles such as mitochondria, the nuclei and parasites within the cells. Since the observed intensity in scattering or dark field microscopy scales from zero, the contrast can be increased by turning up the illumination power or exposure time. The Mie scattering lobes from organelles and parasites can be expected to vary considerably with the size of the scatterer. Thus, by spectral analysis, the scatterer size can be determined even if it is below the diffraction limit of the microscope. The contrast thus arises from physical sizes rather than the chemical compositions. For this reason future development of the spectrally resolved dark field techniques could lead to classification of species and life stages in parasitology. Studies involving spectrally resolved dark field microscopy are very few<sup>425</sup> to the extent of non-existent, despite the simplicity of rearranging the incident propagation of illumination. The community of dark field microscopy has mainly relied on old fashion beam shaping of broad band incandescent lamps, rather than modern fiber optical ring illumination and semiconductor light sources.

On larger macro scales, spectrally resolved single scattering can be achieved in reflectance of human tissue. This can be done by subtracting the depolarized incoherent backscatter from the co-polarized, thus obtaining the structural color of tissue<sup>170</sup>. As in crystallography but less ordered, this signature can be associated with the dominant spatial frequencies of refractive index which to a great extent is caused by the cell membranes. Considering that cancer cells are well known to be larger than their healthy counterparts, this can be extended to provide an discrimination in cancer diagnostics<sup>178</sup>. Similarly, detection deeper lying lesions has been proposed to be based on, e.g., increased water content or scattering coefficient<sup>36</sup>. Although a few studies exist on the topic, structural colors of human tissue are not a very widespread concept, even if some varieties of optical coherence tomography (OCT) show remarkably resemblance to spectroscopic setups<sup>69</sup>.

The societies of bio-photonics mainly consisting of opticians and physicists have proven capable of pushing the frontiers of biomedical imaging and microscopy. Remarkable 3D

topographical molecular imaging can now be produced *in vivo*, e.g., with scanning fluorescent confocal microscopes<sup>171</sup> or opto-acoustical imaging<sup>112</sup>. Regardless of the quality, spectrally resolved 3D tomographical maps with multiple chromophores are not easily interpreted or communicated and therefore hard to implement in practice. One method of interpreting such data is image summation and tissue texture analysis, where one approach is presented in Paper V. An observed tendency in the bio-photonics and tissue spectroscopy community is that its members mostly use sophisticated instrumentation such as time-of-flight (TOF) spectroscopy and troublesome inverse problems such as diffuse optical tomography (DOT), and take less advantage of computational advances of empirical direct prediction approaches from the chemometric or control communities. All though the first mentioned aspect is important for the understanding of the physical background for light-tissue interaction, a broadened approach could improve the understanding of information theory, noise levels and model selection. This can avoiding the risk of over-fitting or extracting more information from data than what is available with the given detection limits.

A hot topic in bio-photonics is fluorescence lifetime measurements implemented to great extent in microscopy<sup>63, 426</sup>, macro imaging<sup>427</sup> and spectroscopy like in Paper VIII and IX. The mixed multiple decays are, however, considerably ill-conditioned, and further in Paper IX, we indicate that the lifetime information is partially redundant with the spectral information. The arguments for lifetime measurements are often avoidance of geometrical effects and absorption quenching of fluorescence excitation and emission, as well as assessment of the fluorophore microenvironment. The spectral emission profiles are, however, also known to depend on the micro environment. Whereas all other spectroscopies provide values which correspond to the composition of the sample, life times are frequently considered to be independent of concentrations. This is a truth with limitations since a low concentration of a given substance would inevitable lead to a large uncertainty in the lifetime estimate. Therefore lifetime values are not trivial to integrate in traditional chemometric evaluation and traditional statistics.

In Paper VII a bleaching process is studied in details and promises improvements to an existing spectral method when the measurements are additionally temporally resolved. As in Paper IX the kinetic evolution of the spectra can be described by a simple linear model discussed in Sect. 5.10.2. The approach is in the category of dynamical contrast, where including the temporal domain increases the amount of complimentary information retrieved.

Although one of the arguments for employing optical diagnostics is the non-intrusive nature, bleaching analysis might bring complimentary information<sup>362</sup> in many situation where bleaching is either motivated, acceptable or not a concern. The recent development of inexpensive high power violet and blue laser diodes<sup>134</sup>, imply that the main limitation for bleaching times is thermal destruction of the sample. A parallel from bleaching spectroscopy to tandem mass spectroscopy<sup>428</sup> (MS/MS) should be made. In bleaching spectroscopy an initial substance is measured, then broken into fragments and measured again etc. In MS/MS the sample is first ablated into fragments with high Daltons, then fragmented again and analyzed, thus increasing the information extracted. By detailed power irradiance analysis phenomena such as production and inflow can be optically assessed, and provide a chemical specific alternative to Doppler OCT. Finally, spectral rectification such as that presented in Paper IX can extract the signatures of overlapping spectral signature due to their different destruction rates.

## 6.4 Ecology and biosphere monitoring

While the entomological studies in this thesis have focused on the Calopterygid damselfly species *Calopteryx* and describe spatial and temporal habitat use and interactions, the new techniques for insects monitoring developed throughout this thesis have a large potential to answer novel questions in many areas of ecology. In the future the techniques may be used to improve our understanding of migration ecology, for agricultural pest monitoring, analysis of vectors spreading diseases to human or domestic animals, for monitoring of agricultural pollinators. It can be used to study interactions between, for instance, prey and predators, as in Paper XII, to study insect flight physiology, and in conservation ecology, where it may give information on the impact of agricultural monocultures on the biodiversity and vice versa.

In respect to detailed taxonomic quantitative monitoring methods for surveillance of the marine biosphere, a lot of work has been done on large scales<sup>429</sup> using monochromatic autonomous submersible holographic imagers<sup>430</sup>. Here organisms are classified by image analysis according to their morphology. At present there are no table values for the optical cross section for insects, as there is for other atmospheric constituents. The remote optical classification problem of insects resembles the radar cross section (RCS) classification problem for airplanes. Apart from the type of insect, the wavelength and the polarization, such optical cross sections additionally depend on pitch, roll and heading orientations and even the phase in the wing beat cycle. A few studies associate radar echoes to insects. However, the discrimination between species is very limited. Current field methods mainly includes manual observation during day time and the use of insects traps for quantitative counts. The last mentioned method has large biases in terms of species, genders and life stages caught. The sample rate of distributed trap arrays is down to the order of once per day, the information on flight direction is very limited and the trap monitoring method is highly intrusive and perturbing in contrast to the optical techniques presented here. In Paper XI a unique marking and detection strategy for insects is presented. This method provides an entirely new way of studying insects. This method makes it possible to compare insect of the same species, gender which are for instance released at different locations, and to study differences in behavior between groups such as for example resident and immigrating individuals.

In respect to the opportunities for electro-optical monitoring of the unstained biosphere, here in particular classification of the constituents of the zoosphere, one has to consider the reasons why different species, genders or life stages differ in optical properties. In the UV and VIS, animals might differ because of gender specific sexual selection, selection for aposematism (warning coloration), selection for cryptic coloration or selection for melanization to increase the heat uptake from the sun (see Fig. 4.2.2). Sexually selected colors are often a trade-off between impressing on the opposite gender and the risk of being spotted by a predator. There are many examples of sexually selected bright colors differing considerably from the natural surroundings and appearing both in UV<sup>431</sup>, blue<sup>432</sup>, or red<sup>120</sup> regions. Cryptic colors are ment to make the individual blend into the environment and prevent either the predator or the prey from spotting the cryptically colored individual. Incubating species and sexes are for instance often cryptically colored as they spend large amounts of time on the nest and hence are very exposed to predation. Cryptic coloration depends on both the habitat and the ecology of the species. Many nocturnal species are often dark and spectrally dull, even if they live in a green forest, as is the case for many nocturnal insects and bats. In marine biology cryptic appearance even includes transparency, e.g. in jelly fishes or shrimps, reflections of the surrounding laterally light flux, e.g., in herrings, or even bioluminescence mimicking of the down welling natural sunlight<sup>305</sup>. Warning colors are in general yellow, orange or red with black patches and typically found

in venomous species or species mimicking such. Melanins are the pigments which are most frequently used to control heat uptake. The use of pigments for controlling body temperature is particular for ectotherm organisms such as insects.

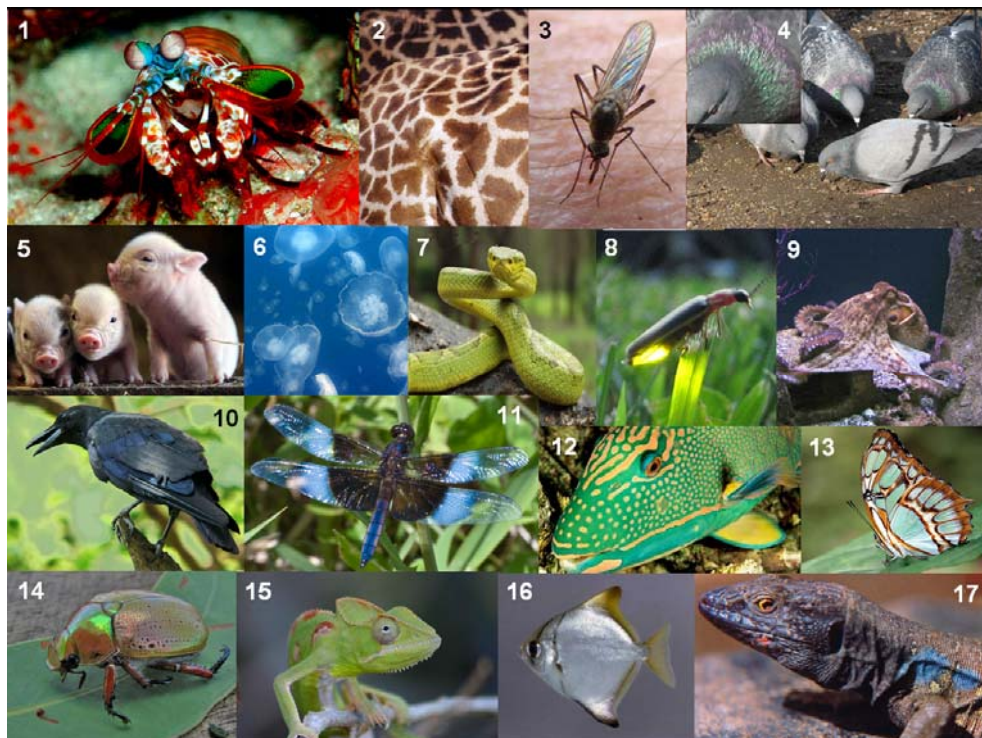


Fig. 6.1. Few examples of the diversity of animal coloration and photonics. From upper left to lower right: 1) The mantis scrimp has a 16-band multispectral polarization vision<sup>85, 299</sup> and manipulates its appearance with polarization dichroism<sup>433</sup>. 2) Patchiness such as that of giraffes or zebras has been proposed to trick the polarization vision of blood sucking tapenides to reduce their attacks<sup>434</sup>. 3) Thin film interference in a mosquito wing<sup>79</sup> produces a sinusoidal reflectance in the spectral domain observed as magenta and cyan shades. 4) The same physical phenomena arising due to nano-arrangement of melanin granules in pigeon neck feathers<sup>30</sup>. 5) Appearance of piglets is governed by photomigration<sup>156</sup> and tissue optics much like in biomedicine. 6) Jellyfish and shrimps achieve near transparency by index matching<sup>305</sup>. 7) Cold blooded insects<sup>288, 304</sup>, and reptiles<sup>435</sup> like this green python snake use pinhole like pit organs for thermal imaging. 8) Bioluminescence, e.g. by the firefly, is used for signaling, luring prey<sup>254</sup>, avoiding silhouettes<sup>305</sup> or illuminating prey by infrared beams<sup>302</sup>. 9) Cephalopods replay colored textures on their skin to mimic shadows from ocean ripples or a moving background<sup>436, 437</sup>. 10) The absorption of melanin controls the heat uptake by sunlight and is found throughout the animal kingdom, here in a raven. 11) Non-iridescent metallic blue and green colors, e.g. in this dragon fly are produced by spherically by symmetric nanosphere arrangements<sup>335</sup>. 12) Yellow long pass filters increasing contrast on expense of sensitivity are encountered both in avian vision<sup>201</sup> as well as in marine biology<sup>305</sup>, here a parrot fish. 13) The color producing nanostructures of butterflies have fascinated electronmicroscopists and the sub-wavelength photonics community<sup>58</sup>. 14) Chiral retroreflectors in certain beetles produce color signatures only in left handed polarized light<sup>68, 345</sup>. 15) Chameleons change their coloration by contracting or displaying a set of chromatophores. 16) Highly reflecting fish scales is another way to mimic the vertical photon flux and decrease contrast to the surroundings<sup>438</sup>. 17) The fluorescence process is used in sexually selected colors<sup>117</sup> and in down conversion in vision<sup>254</sup> and red appearances<sup>118</sup>. Public domain images from Wikipedia.

Apart from colors or optical properties that are selected for, as they give the organisms an advantage, there are also a range of properties which simply arises due to the physical or chemical construction of animal skin, fur, plumage, scales, exoskeleton etc. In the deep UV and MIR, compounds such as chitin, keratin and waxes have several absorption bands which could be used for identification<sup>399</sup>. The fact that the imago stage of many insects emerges from a tight pupae implies that newly hatched individuals have soft and flexible

wings which harden during the following days. In optical properties this translates into young individuals having more glittering wings in comparison to the older ones. A few studies have suggested age determination from the optical properties<sup>23</sup>. Remote applications of this would be a tool of great interest in empirical population dynamic studies and also for strategic minimal use of pesticides in agriculture. In the latter case insecticide spraying could be reduced by targeting pests in their most vulnerable life stage. The fact that blood meals clearly change the spectral signature of disease vectors (see Fig. 1.3.2) provides a tool for comparing behavior of individuals with and without blood meals<sup>22</sup>. An exciting fact is that tiny structures such as insect wing membranes or the repetitive barbules in feathers produce iridescent interference phenomena in the NIR and MIR. In particular, since insect and bird wings are self angular scanning, such phenomena promise remote acquisition of microscopical features or as introduced in this thesis, remote microscopy. Since interference effects are closely related to polarization, even remote ellipsometry can be considered; see discussion in Paper XV.

The fact that insects and birds must overcome gravity implies wing flapping and thus modulation of the optical cross section. The frequency is highly species and gender specific, but also depends on temperature, wind and payload. Apart from the fundamental frequency the strength and phase of the harmonics contain specific information on the species<sup>141</sup> and the heading direction. Detection of blinking insects and birds in the atmosphere in many ways relate to single molecule detection<sup>139, 382</sup> and flow cytometry<sup>338</sup>.

# Acknowledgements

---

Anna, thanks for appearing in my life and making it richer, thanks for your persistent patience, for forcing me to explore multivariate statistics, for encouraging me to pursue a doctoral degree, for messing up my thesis with insects, birds and lizards, and for your cute optimistic approach to scientific measurements and methodology.

Aske, little silly dude, thanks for coming to us, thanks for bringing perspective to me and Anna when we loose ourselves in irrelevant scientific details. An atto-second of your joy is worth a lifetime of exhaustion.

Far and Mor, thanks for a perfect childhood with all the opportunities and freedom I wish I can give my own son. Thanks for the practical skills, Mor, and thanks, Far, for introducing me to electrochemistry, thermodynamics, programming and HeNe lasers through a constant flow of scientific private lectures mixed with fairytales and criminal novels.

Sune, thank you so much for your confidence and patience throughout the years. Thanks for trusting in me, for your efforts to tame me, for introducing me to your scientific world and giving me so many opportunities and free hands. Thanks for being a role model with ever surprisingly unquestionable skills in practice and theory. Thanks for being a good friend. I wish you good luck with your Chinese adventures and Sino-Swedish collaboration..

Zuguang, thanks for all the common hard work and office sharing, thanks for the many dinners with your interesting specialties. I wish you good luck with the implementation of environmental monitoring in the People's Republic.

Patrik, it has been a pleasure to watch you descend from a disciplined Navy sailor, deep into a bearded academic troubling yourself with strange optical inventions. Thanks for the hard work and strange experiences at the many field campaigns. The early morning Zombie walk to the coffee machine with you was one of the last pleasures during my thesis writing. I wish all the best for your remaining doctoral period and for your new family.

Märta, thanks for being the only structured and organized individual in our group, thanks for sharing office and asking to my everyday life. We miss you.

Maren, the ever-reliable cornerstone when it comes to entomological expertise or borrowing of milk pumps. Thanks for all your detailed contributions to our manuscripts, for the many hours of common field work and for countless attempts to socialize me and Anna. I wish the best for you and your family and hope for a life long collaboration little by little.

Aboma, thanks for your hard, continued and sweaty efforts with the African workshops. Thanks for the wonderful Ethiopian dinners at your mother's place. I wish you good luck with your doctoral degree.

Hiran, thanks for your demanding help with the workshops, for being the only chief dancer and for contributing to damselflies and joyful spirit. We will not forget your downhill skiing in our courtyard.

Jesper, the director of IdeaSpec, thanks for the great master thesis and your lousily paid efforts to push commercialization forward. I am happy to know that you eventually choose the academic side and I am confident that you will constitute a disciplined and focused scientist. Good luck with your thesis work.

Per, the perfectionist, thanks for hard efforts at the field campaign and following. You did a great master thesis and we almost got it into Science. Do not worry so much of what it interesting and not, in my experience most scientific rabbit holes lead to Wonderland; it is just a matter of digging.

Jens and Majd, thanks for your efforts and good luck with your remaining thesis work.

Susanne, thanks for enthusiastically introducing me to the fascinating world of migration ecology and birds. Thanks for your efforts during our field campaign, for giving us a reason to fill our office with living zebra finches. I hope that technology and I will live up to your expectations regarding nocturnal bird watching.

Stefan, thanks for teaching bio-photonics and organizing brilliant summer schools, for supervising, for adopting me in the medical group, bringing me to your canoeing and BBQs and for your heroic last minute field effort when your family was expecting you for the opera.

Rasmus Bro, thanks for lecturing in chemometrics, for wasting time on lizards, for distrusting my future outside academia, and for your wonderful attitude in general. I hope we will see more of each other in the future.

Erik, thanks for the countless BBQs at your family's place, I know I have been busy the last couple of years but I would like to propose a round table discussion with you regarding the evolutionary benefit of death and the possible implementation of a communistic society on the 6<sup>th</sup> of October at 4:00, 2012.

Mathias, thanks for constantly coming into my office and complaining about the lack of public understanding of fundamental aspects of laser based relativistic particle acceleration. Thanks also for the thrilling attempts to release a plume of down from an airplane between laser beams and thunderstorms.

Frederik, the intrinsically optimistic entrepreneur who took the shortcut from Strandvejen to the Hven Biophotonics School in his luxury yacht. Thanks for the efforts of making something useful out of my inventions. I think we can honestly say that we did our best.

Lorenzo, Mei and Hu thanks for your assistance with birds, insects and telescopes at weird times of the day.

Gabriel, thanks and best wished for the continuation of the applied spectroscopy.

Niels, thanks for working with me at the hospital and practicing Danish with me.

Katarina, thanks for being so colorful and reminding the division of spectroscopy, thanks for common work at the hospital, for teaching me about medicine, thanks for the BBQs at your place, thanks for traveling around with me drinking Pisco Sour and handing out SPIE prizes. I wish that you and Sune will have a wonderful retirement when the time comes when, you do just what you feel like.

Minna, thanks for persistently smiling, for spreading good atmosphere and art at the division. Thank you for organizing wonderful excursions and summer schools.

Claes-Göran, Harriett and Camilla, thank you for your leadership and management of the Atomic Physics Division.

Bertil, thanks for computer assistance, cozy soldering sessions at your workshop, and thanks for the sausage club.

Alex, Chris, and Paul, thanks for the hospitality in London; sorry for being dizzy from *Borrelia*. I wish you good luck for the defense, Alex.

Neda and Nadine; thanks for your collaboration and for the time on the summer school, I wish you good luck with your defenses and future optics careers.

Can Xu, thanks for being a person I always can bother when I lost myself in thoughts about photons and math. I am happy on your behalf for your wonderful daughter and worry for her when I think of all the photonic babbling she will be exposed to.

Dmitry, my comrade, I look forward to the scheduled Pivo and Russian lessons once this thesis is defended.

Haiyan, thanks for the collaboration and best wishes for your maternity leave and remaining thesis work.

Pontus Svenmaker, Johan Axelsson, Thomas Svensson, thanks for being around for discussion and coffee, making the corridors less empty.

Arash, thanks for countless chess games during my master thesis when few other at the department wanted to speak to me. I shall not forget the crazy pub crawl and watermelon bowling in Hangzhou's shanty towns.

Marcus, thanks for sharing office during the master thesis and for being such a hopeless and successful theoretician.

Francois, the laidback and energetic Frenchman surrounding himself with optoelectronic scrap and low physics in the name of development. Whenever you are around you remind me of my childhood room flooded with high-voltage supplies and HeNe lasers. Thanks for the traveling in Peru and Cameroon and for introducing me to the Interdivisional Group of Physics for Development. I hope to be able to contribute more in the future.

Carsten, thanks for contacting me in the first place and thanks for the help with the post-doc application. The project is really interesting and I hope we will be able to pursue these ideas.

Jeremie, thanks for your dedication and sharing your malaria research with us, for receiving Aboma in Ivory Coast, for your persistent initiative resulting in the AFSIN research network, for making it to the Bamako workshop through bullet showers.

Ernst, thanks for believing and supporting in capacity building of African spectroscopists. I hope we can live up to your expectations and can show that science and formation of physics doctors in spectroscopy is possible and relevant in Africa.

Benjamin, Jojo, Paul, students and staff, thanks for the hospitality and contributions to the workshop in Cape Coast.

Mbaye, Salma, Ababacar, Amadou, thanks for the stay at your laboratory and great hospitality for me and Anna in Dakar. We shall not forget the crazy Djellaba dancing with Youssou N'Dour. I wish you all the best.

Abdrmane and Amadou Coulibaly, thanks for hosting a perfectly planned and timed workshop in Bamako on such short notice. I shall not forget the excursion to the founder of Mali's forge. I hope the troubles of your country quickly resolve with minimal damage for your countrymen and great historical remains.

Jonas Sandsten, thanks for your kind help with infrared instrumentation in relation to birds.

Else and colleagues, thanks for keeping me updated about your cows and persistently cleaning up the mess left by absent minded physicists.

Elisabeth Nilsson, thanks for teaching my first course in optics.

Lars Engström, thanks for teaching my first course in atomic physics and discussion throughout the years.

Sven-Göran Pettersson, thanks for teaching my first course in laser technique and for your efforts for public outreach.

Aura and colleagues at the Universidad Nacional de Colombia, Bogota. Thanks for the stay, the sightseeing, the hayaca and the culones; sorry about your bathroom.

Lazlo Saho, thanks for the stay at the nuclear physics laboratory and my participation in the first Venezuelan conference for Applied Nuclear Physics.

Enrique Iglesias and Vincent Piscitelli, thanks for the stay at your laboratories and introducing me to Venezuelan research in optics.

Ramesh Galigekere, thanks for the experiencing stay in Udupi.

Eric Warrant, thanks for great lectures, for reviewing and for answering all kinds of ignorant questions about animal vision.

Almut Kelber, thanks for providing prepared slides of Budgerigar retina for Paper II.

Richard Prum and Mathew Shawkey, thanks for inspiring scientific discussion over distance.

Jens Carlsson and PP Mekanik, for providing the best, quick, reliable, custom mechanical prototyping enabling us to conduct the workshops in Africa.

Louise, Alf, best possible parents in law, thank you so much for all the help and babysitting; you substantially improved the quality of the thesis.

Jara and Gardar, thanks for being the ultimate neighbors. Thanks for all the help, such a pity that we all have to leave the student housing; we will miss you.

Wikipedia and contributors, thank you for providing this wonderful tool for humanity. I hope that your efforts are soon recognized and that contributing becomes an academic duty in all fields of specialty.

This work benefited from financial support by:

The Swedish Research Council through a direct grant, and a Linnaeus Grant to the Lund Laser Center (LLC), the Innovation Driven Research Education (IDRE) program, the Product Innovation Engineering program (PIEp), the Lund University Medical Faculty and Region Skåne, the Knut and Alice Wallenberg Foundation, the International Science Program (ISP), Uppsala, the Kullaberg Foundation, an Alexander Foss Grant by the Danish Industry, the Lund Royal Physiographical Society, the Abdus Salam International Centre for Theoretical Physics (ICTP), the Interdivisional Group of Physics for Development (IGPD), European Physical Society (EPS), and the Puya Raimondi Foundation.

# Publications and author contributions

---

## Publications

- I) **M. Brydegaard**, and S. Svanberg, “Simulation of multispectral X-ray imaging scenarios by means of Wien shift optical spectroscopy,” *Am. J. Phys.* **78**, 170-175, 2010.

This paper is ment as a pedagogical inspiration for a simple student exercise. The paper discusses a curious analogy between *Bremstrahlung* in the X-ray regime and Planck emission in the near infrared regime. It also explains multivariate evaluation for beginners. From a professional point of view, it provides an interesting approach to intensity calibration of spectrometers with minimum a priori knowledge.

MB got this idea during his undergraduate studies based on lectures by his main supervisor; he later assembled the setup, performed the measurement, processed the data and wrote the manuscript draft.

- II) **M. Brydegaard**, Z. Guan and S. Svanberg, “Broad-band multi-spectral microscope for imaging transmission spectroscopy employing an array of light-emitting diodes (LEDs),” *Am. J. Phys.* **77**, 104-110, 2009.

This paper explains how multispectral imaging can be performed by amateurs with minimal resources. The instrument described in the paper was originally constructed for a local science exhibition, with the purpose of explaining the advanced research concept of multispectral imaging for the general public. The setup has encircled the world once and has also been used for live presentations in the USA, China, Italy, Peru, Colombia, Ghana, Senegal, Mali and Cameroun. Subsequently, this stimulated the establishment of a tropical research network, AFSIN, related to Papers III and IV. The paper constitutes an example of an exceptionally long and tiresome review process.

MB got this idea during his undergraduate studies; he later assembled the setup, performed the measurement, processed the data and wrote the manuscript draft.

- III) **M. Brydegaard**, A. Merdasa, H. Jayaweera, J. Ålebring and S. Svanberg, “Versatile multispectral microscope based on light emitting diodes,” *Rev. Sci. Instr.* **82**, 123106, 2011.

This paper describes a research platform for multispectral imaging. It is an improvement of the concepts presented in Paper II. Several features, such as reflectance and dark-field spectroscopy, were added. A particular improvement was the application of a reflective objective to avoid chromatic aberration. The paper introduces discretization along various domains in a consistent way, and helps the reader to see similarity between various optical terms in intensity, time, space, propagation and energy. The instrument was replicated in nine copies whereof the majority were distributed across the African continent, following a workshop in Ghana 2009.

The idea originated from Paper II, further MB contributed with suggestions of added features and engineering tricks in optical design, electronics and acquisition software. He performed several of the measurements presented as examples, evaluated the data, wrote the manuscript draft and introduced concept of discretization along different domains also penetrating Chap. 4 in this thesis.

- IV) A. Merdasa, **M. Brydegaard**, S. Svanberg and J. T. Zoueu, “Staining-free malaria diagnostic by multispectral and multimodality LED microscopy,” Submitted.

This paper is the outcome of Aboma Merdasa’s master thesis and collaboration with Prof. Jeremie Zoueu in the Ivory Coast. The paper presents how staining free malaria detection can be achieved with dark field imaging spectroscopy. It also presents the optimal wavelength for discriminating the parasites and forms a basis for the development of low-cost realistic instrumentation for the same purpose.

MB was one of the master thesis supervisors for the first author. MB further contributed during instrument design and construction. He suggested evaluation by multivariate methods and contributed to the manuscript.

- V) **M. Brydegaard**, A. Runemark and R. Bro, “Chemometric approach to chromatic spatial variance. Case study: Patchiness of the Skyros wall lizard,” *J. Chemometrics* **26**, 246-255, 2012.

This paper presents a new and alternative approach to texture analysis, to traditional methods based on spatial frequency analysis; the approach is based on the decomposition of probability distributions of various dimensionalities. Efforts were made to visualize such distributions in a pedagogical manner. The paper also discusses the analogy between ND histograms, spectra, images and probability distributions in quantum mechanics.

The paper is important in the sense of acceptance in a chemometrics journal, since chemometry penetrates several other studies presented in this thesis.

MB got the idea following paid assignments from the Lund University Biology Department. He constructed the setup, assisted in field work, wrote the code for statistical evaluation and visualization, and finally wrote the manuscript.

- VI) L. Mei, P. Lundin, **M. Brydegaard**, S. Gong, D. Tang, G. Somesfalean, S. He and S. Svanberg, "Tea classification and quality assessment using laser induced fluorescence and chemometric evaluation," *Appl. Opt.* **51**, 803-811, 2012

The paper is some of the outcome of Chinese collaboration with our research group. The paper illustrates the capability of fluorescence spectra to predict the quality and type of Chinese tea types, otherwise determined by tea tasting experts.

MB mainly contributed with guidance for multivariate evaluation. The tea was also photographed with the setup from Paper V. He also contributed to the manuscript.

- VII) **M. Brydegaard**, N. Hosseini, K. Wårdell and S. Anderson-Engels, "Photobleaching-insensitive fluorescence diagnostics in skin and brain tissue," *IEEE J. Photonics* **3**, 407-421, 2010.

This paper presents a method for parameterisation of bleaching processes in complex matrices. The clinical possibilities of using time-invariant parameters of such dynamical models are explored for the applications of more consistent diagnostics during brain surgery. Analogies to dynamics in nuclear physics, robotics and population dynamics in ecology are also drawn.

MB contributed to the acquisition software for the instrument, he then got the idea to use the dynamical information during the bleaching behaviour. He evaluated the data and wrote the manuscript draft.

- VIII) A.J. Thompson, **M. Brydegaard** Sørensen, S. Coda, G. Kennedy, R. Patalay, U. Waitong-Bramming, P.A.A. De Beule, M.A.A. Neil, S. Andersson-Engels, N. Bendsoe, P.M. French, K. Svanberg and C. Dunsby, "*In vivo* measurements of diffuse reflectance and time-resolved autofluorescence emission spectra of basal cell carcinomas," *J. Biophot.* **5**, 240-254 2012.

This paper is the outcome of a joint measurement campaign between our research group and an English group carried out at the Lund University Hospital. The English group brought an advanced instrument for spectrally resolved fluorescence lifetime spectroscopy. In parallel, measurement were also done with a multi-excitation steady-state spectrometer also being the prototype in P3. A total of 25 patients with suspected tumours were measured and the paper suggests that the lifetime change of blue light discriminates the lesions from healthy tissue.

MB constructed various varieties of the steady-state instrument; this included computer aided mechanical design, circuit design and soldering. He established advanced electronic routines for calibration and wrote the acquisition software. He participated in the measurement campaign, he then spent ten days in England merging the data sets from the two instruments, he guided the first author in multivariate evaluation and contributed to the manuscript.

- IX) **M. Brydegaard**, A.J. Thompson, C. Dunsby, S. Andersson-Engels, N. Bendsoe, K. Svanberg and S. Svanberg, "Complete parameterization of temporally and spectrally resolved laser induced fluorescence data with applications in biophotonics," Manuscript in preparation.

This paper is based on the same instruments and dataset as in Paper VIII but covers additional aspects. The historical background for fluorescence lifetime spectroscopy is reviewed. Then a systematic way of parameterising spectrally and temporally resolved fluorescence is presented. It is shown empirically that the two domains are partly redundant. Finally, the parameterization is presented in a clinical context, and the discrimination previously reported in Paper VIII is substantially downgraded.

MB constructed the steady-state instrument and wrote the acquisition software. He participated in the measurement campaign, he then spent ten days in England merging the data sets from the two instruments. He had the idea of matrix formulation and a dynamical state space approach to a unified parameterization, he evaluated the data set independently from the evaluation in Paper VIII and wrote the manuscript draft.

- X) **M. Brydegaard**, Z. Guan, M. Wellenreuther, and S. Svanberg, "Insect monitoring with fluorescence lidar: Feasibility study," *Appl. Opt.* **48**, 5668-5677, 2009.

In this paper we investigate the feasibility of fluorescence lidar techniques for remotely detecting and classifying insects. Clues on what to expect from the interplay between fluorescence and structural colours are given. Initial

attempts for fluorescence marking were also carried out. All measurements were carried out on *ex-vivo* specimens during winter time.

MB had worked with the third author with laboratory measurement of the reflectance of the same specimen. Together with the then recently published papers on honey bee detection with lidar, this evolved into the idea. He also contributed to the instrumentation, evaluated the data and wrote the manuscript draft.

- XI) Z. G. Guan, **M. Brydegaard**, P. Lundin, M. Wellenreuther, A. Runemark, E.I. Svensson, and S. Svanberg, "Insect monitoring with fluorescence lidar techniques: Field experiments," *Appl. Opt.* **49**, 5133-5142, 2010.

This paper is the outcome of the two week field campaign following Paper X. This paper constitutes an important progress for studying insects in the field. Powder marking and mark-without-recapture are demonstrated. This gives new insight in the comparative behaviour of several marked groups both in time and in space on the habitat level. In the future this will also shed new light on dispersal rates and migration of, e.g., agricultural pests, pollinators and disease vectors.

MB took the initiative for this campaign and contributed to the instrumentation and participated in the measurement campaign. He contributed with evaluation of a subset of the data where he started the work of separating the static lidar signal from rare events; this aspect was further developed in Papers XII, XIV and XVI. He also contributed to the manuscript.

- XII) A. Runemark, M. Wellenreuther, H. Jayaweera, S. Svanberg and **M. Brydegaard**, "Rare events in remote dark field spectroscopy: An ecological case study of insects," *IEEE JSTQE Photonics for Environmental Sensing (PES)* **18**, 1573-1582, 2011.

This paper is the outcome of a one day experiment on the same field site as where the study in Paper XI was carried out the previous year. The paper describes a realistic low-cost method for remote sensing of insects. The setup is portable by a small field team and based on the scattering of sunlight. This initial attempt showed surprisingly good performance in comparison to the heavy equipment previously employed in Paper XI. A particularly interesting detail of insect occurrences detected with fast electro-optics is the aspect of time correlations to quantify insect interactions. This will bring entirely new opportunities in ecological field entomology in the future.

MB got the idea from the work related to Paper III; he first suggested the experiment in relation to collaboration with Mali, and he then took the initiative to conduct a mini campaign in Sweden. He wrote the acquisition software and contributed in setting up the experiment, evaluated the data and wrote the manuscript draft. The author order reflects MB's role as supervisor in the project.

- XIII) **M. Brydegaard**, P. Lundin, Z.G. Guan, A. Runemark, S. Åkesson and S. Svanberg, "Feasibility Study: Fluorescence lidar for Remote Bird Classification", *Appl. Opt.* **49**, 4531-4544, 2010.

This paper resulted since accidental bird hits occurred during the measurement presented in Paper XI. Subsequently *ex-vivo* specimens were acquired from the Lund Zoological Museum and were brought into the field. The paper relates reflectance and fluorescence from bird plumage and demonstrates how the coloration of birds can be remotely measured by fluorescence lidar. This is of particular interest for classification of migrants which typically travel by night; it also represents a progress in comparison to the radars currently employed, which cannot provide any chemical information.

MB participated in the measurement campaign, contributed to the instrumentation and data evaluation and wrote the manuscript draft.

- XIV) P. Lundin, P. Samuelsson, S. Svanberg, A. Runemark, S. Åkesson and **M. Brydegaard**, 'Remote nocturnal bird classification by spectroscopy in extended wavelength ranges', *Appl. Opt.* **50**, 3396-3411, 2011.

This is the outcome of a two week campaign following the success of Paper XIII. In this paper the method from Paper XIII is considerably improved and made eye-safe to birds by lowering the excitation wavelength. An uncertainty in Paper XIII regarding excitation quenching in plumage was clarified by polarization analysis. Passive scattering from birds was investigated in the NIR showing imprint of chlorophyll and atmospheric oxygen. This experiment later led to Paper XII and XVI. Initial investigation of the MIR signature of bird was carried out. This was the basis for the master thesis of Per Samuelsson and led to the results in Paper XV. The paper presents a few *in-vivo* measurements of wild and released specimens but unfortunately the migratory flux was sparse at the time and location.

MB took the initiative and drafted an application for a research grant to finance the campaign; he then coordinated several parallel experiments ranging over a broad range of wavelengths. He guided and contributed to the data evaluation and manuscript. He was one of the master thesis supervisors for Per Samuelsson. The author order reflects MB's role as supervisor in the project.

- XV) **M. Brydegaard**, P. Samuelsson, M.W. Kudenov and S. Svanberg, “On the exploitation of mid-Infrared iridescence of plumage for remote classification of nocturnal migrating birds,” Submitted.

This paper is the outcome of several experiments following the master thesis of Per Samuelsson. The paper explains in details how not only chemical but even micro-structural information can be retrieved from night migrating birds due to an inherent iridescence in combination with wing self angular scanning. Discussion in the paper covers several advanced aspects in physics such as super resolution, spectral broadening, the Kramers-Kronig relation and the Christiansen effect. The paper also represents several hard efforts to demonstrate the effects in field *in-vivo*. This was instrumentationally difficult and only a fraction of the attempts were successful.

MB noticed the first traces of iridescent effects, he was one of the master thesis supervisor of Per Samuelsson and he contributed to the instrumentation and data evaluation. MB wrote the manuscript.

- XVI) P. Lundin, **M. Brydegaard**, A. Runemark, S. Åkesson, L. Cocola and S. Svanberg, “Passive unmanned sky spectroscopy for remote bird classification,” Proc. SPIE **8174**, 81740J, 2011

This paper is a continuation of the passive detection scheme employed in Paper XIV. The paper investigates the behaviour of the terrestrial oxygen-A Fraunhofer line in relation to scatter events by birds. The aim of this attempt was to relate the absorption imprint of the gas to the altitude of the bird passively. The results were arbitrary but did not exclude the possibility of future passive altitude estimation if the method is refined.

MB had the idea for the experiment, set up the experiment and wrote the acquisition software. He also made suggestions to the data evaluation and contributed to the manuscript.

### Patent applications

- P1) US provisional patent application on “Instrument for acquisition of fluorescence, absorption and scattering properties”, **Mikkel Brydegaard**, US60/916,813, expired.

This detection scheme was elaborated during the master thesis of Mikkel Brydegaard. It is based on a double spectrometer principle where white light is dispersed once prior to sample interaction and once more perpendicularly following the sample interaction. The instrument instantaneously acquires fluorescence spectra with all excitation wavelengths as well as the elastic coefficients for absorption and scattering spectrum. The invention was the initial starting point of the thesis work but was delayed by the mechanical workshop to an extent that other more feasible projects become the focus.

MB invented the scheme and wrote the text which was submitted.

- P2) Patent application on “Instrument and methodology for acquisition of multiple coupled optical properties in volumes”, **Mikkel Brydegaard**, Sweden, 0900253-6, Submitted 2009, pending.

This project was inspired by P1 but with a much simpler construction and intended for monitoring of liquids. The concept is based on a large amount of combinations of unique light path between an array of detectors and sources; this was inspired from previously implemented PDT schemes at the division. The result was an instrument with a cost of a fraction of that of conventional spectrometers. The instrument acquires fluorescence, refractive index, absorption, scattering and anisotropic scattering coefficients for all excitation wavelength between 350 nm and 1700 nm. The prototype demonstrated disentangling of all aforementioned sample properties. The project was the basis for the master thesis of Jesper Borgren as well as the foundation of the company IdeaSpec I/S. The project was awarded an innovation price of 100.000 DKK by the Federation of Danish Industry.

MB invented the scheme and wrote the extensive text which was submitted.

- P3) Patent application on “Sensor head for acquisition of spectra and multispectral images based on semiconductor light sources and black body calibration.” **Mikkel Brydegaard** and Sune Svanberg, Sweden, 0900425-0, Submitted 2009, expired.

The idea for this instrument was developed during the master thesis of Mikkel Brydegaard. The instrument captures fluorescence spectra induced by an arrangement of LEDs with different excitation wavelength, the instrument also captures the elastic reflectance. The patent application also encompasses several advanced methods for LED calibration. The prototype has been modified several times and used in, e.g., Paper VIII and XIV. Like the instrument presented in Paper I it also encircled the globe and have been used extensive for live demonstration in China, Italy, Peru, Colombia, Ghana, Senegal, Mali and Cameroun.

MB further developed the concept of a previous prototype developed in the group.

P4) Patent application on "Multimode imaging spectrometer for angular resolved optical diagnosis on micro scale" **Mikkel Brydegaard**, Sune Svanberg, Aboma Merdasa, Sweden, 0901398-8, Submitted 2009, expired.

The idea for this originated from Paper II but includes the feature of angular discrimination inspired from previous activities with multi integrating sphere measurements at the division. In respect to Paper II the filed application also had a solution for chromatic aberrations and presented electronic routines for LED stabilization.

MB had the idea for the setup and emphasized the need for additional angular lobes. He also wrote the draft of the text filed.

# Reference

---

1. D. A. Boas, C. Pitris, and N. Ramanujam, *Handbook of Biomedical Optics*, (CRC Press, 2011).
2. V. Tuchin, *Tissue Optics: Light Scattering Methods and Instruments for Medical Diagnosis*, 2nd ed., (SPIE Publications, 2007).
3. S. Johnsen, *The Optics of Life: A Biologist's Guide to Light in Nature*, (Princeton University Press, 2011).
4. D.-W. Sun, *Hyperspectral Imaging for Food Quality Analysis and Control*, (Academic Press, 2010).
5. K. Kohse-Höinghaus, R. S. Barlow, M. Aldén, and J. Wolfrum, "Combustion at the Focus: Laser Diagnostics and Control," *Proc. Combustion Institute* **30**, 89-123 (2005).
6. D. A. Fedosov, H. Lei, B. Caswell, S. Suresh, and G. E. Karniadakis, "Multiscale Modeling of Red Blood Cell Mechanics and Blood Flow in Malaria," *PLoS Comput. Biol.* **7**, e1002270 (2011).
7. K. Abba, J. J. Deeks, P. Olliaro, *et al.*, "Rapid Diagnostic Tests for Diagnosing Uncomplicated *P. Falciparum* Malaria in Endemic Countries," *Cochrane Database Syst. Rev.* **6**, 8122 (2011).
8. S. Cho, S. Kim, Y. Kim, and Y. Park, "Optical Imaging Techniques for the Study of Malaria," *Trends Biotech.* **30**, 71-79 (2012).
9. C. Yuen and Q. Liu, "Magnetic Field Enriched Surface Enhanced Resonance Raman Spectroscopy for Early Malaria Diagnosis," *J. Biomed. Opt.* **17**, 017005 (2012).
10. B. R. Wood, A. Hermelink, P. Lasch, *et al.*, "Resonance Raman Microscopy in Combination with Partial Dark-Field Microscopy Lights up a New Path in Malaria Diagnostics," *Analyst* **134**, 1119-1125 (2009).
11. J. M. Bélisle, S. Costantino, M. L. Leimanis, M.-J. Bellemare, D. Scott Bohle, E. Georges, and P. W. Wiseman, "Sensitive Detection of Malaria Infection by Third Harmonic Generation Imaging," *Biophys. J.* **94**, L26-L28 (2008).
12. R. M. Packard, *The Making of a Tropical Disease: A Short History of Malaria*, (The Johns Hopkins University Press, 2007).
13. L. Alphey, C. B. Beard, P. Billingsley, *et al.*, "Malaria Control with Genetically Manipulated Insect Vectors," *Science* **298**, 119-121 (2002).
14. K. Raghavendra, T. K. Barik, B. P. Reddy, P. Sharma, and A. P. Dash, "Malaria Vector Control: From Past to Future," *Parasitol. Res.* **108**, 757-779 (2011).
15. C. Fabris, R. K. Ouedraogo, O. Coppellotti, *et al.*, "Efficacy of Sunlight-Activatable Porphyrin Formulates on Larvae of *Anopheles Gambiae* M and S Molecular Forms and *An. Arabiensis*: A Potential Novel Biolarvicide for Integrated Malaria Vector Control," *Acta Trop.* **123**, 239-243 (2012).
16. S. Yoshida, Y. Shimada, D. Kondoh, Y. Kouzuma, A. K. Ghosh, M. Jacobs-Lorena, and R. E. Sinden, "Hemolytic C-Type Lectin CEL-III from Sea Cucumber Expressed in Transgenic Mosquitoes Impairs Malaria Parasite Development," *PLoS Pathog.* **3** (2007).
17. K. A. Hartfield, K. I. Landau, and W. J. D. v. Leeuwen, "Fusion of High Resolution Aerial Multispectral and Lidar Data: Land Cover in the Context of Urban Mosquito Habitat," *Remote Sensing* **3**, 2364-2383 (2011).
18. G. Gibson and I. Russell, "Flying in Tune: Sexual Recognition in Mosquitoes," *Curr. Biol.* **16**, 1311-1316 (2006).
19. G. Gibson, B. Warren, and I. J. Russell, "Humming in Tune: Sex and Species Recognition by Mosquitoes on the Wing," *J. Assoc. Res. Otolaryngol.* **11**, 527-540 (2010).
20. W. Takken, "The Role of Olfaction in Host-Seeking of Mosquitoes: A Review," *Internat. J. Trop. Insect Sci.* **12**, 287-295 (1991).
21. M. F. Bowen, "The Sensory Physiology of Host-Seeking Behavior in Mosquitoes," *Ann. Rev. Entomol.* **36**, 139-158 (1991).
22. M. H. Hall, S. M. Dutro, and M. J. Klowden, "Determination by near-Infrared Reflectance Spectroscopy of Mosquito (*Diptera: Culicidae*) Bloodmeal Size," *Entomol. Soc. Am.* **27**, 76-79 (1990).
23. V. S. Mayagaya, K. Michel, M. Q. Benedict, G. F. Killeen, R. A. Wirtz, H. M. Ferguson, and F. E. Dowell, "Non-Destructive Determination of Age and Species of *Anopheles Gambiae* S.L. Using near-Infrared Spectroscopy," *Am. J. Trop. Med. Hyg.* **81**, 622-630 (2009).
24. M. Sikulu, G. F. Killeen, L. E. Hugo, *et al.*, "Near-Infrared Spectroscopy as a Complementary Age Grading and Species Identification Tool for African Malaria Vectors," *Parasit. Vectors* **3**, 49 (2010).
25. S. Lehrer, "Anopheles Mosquito Transmission of Brain Tumor," *Medical Hypotheses* **74**, 167-168 (2010).
26. H. zur Hausen, "Viruses in Human Cancers," *Science* **254**, 1167-1173 (1991).
27. J. F. Jacobs, G. J. M. Koper, and W. N. J. Ursem, "UV Protective Coatings: A Botanical Approach," *Progr. Org. Coatings* **58**, 166-171 (2007).
28. L. G. Salford, A. E. Brun, J. L. Eberhardt, L. Malmgren, and B. R. R. Persson, "Nerve Cell Damage in Mammalian Brain after Exposure to Microwaves from GSM Mobile Phones," *Environ. Health Perspect* **111** (2003).

29. C. L. M. Bauréus Koch, M. Sommarin, B. R. R. Persson, L. G. Salford, and J. L. Eberhardt, "Interaction between Weak Low Frequency Magnetic Fields and Cell Membranes," *Bioelectromagnetics* **24**, 395-402 (2003).
30. M. C. Diamond, A. B. Scheibel, G. M. Murphy Jr, and T. Harvey, "On the Brain of a Scientist: Albert Einstein," *Exp. Neurol.* **88**, 198-204 (1985).
31. A. Johansson, F. W. Kreth, W. Stummer, and H. Stepp, "Interstitial Photodynamic Therapy of Brain Tumors," *IEEE JSTQE* **16**, 841-853 (2010).
32. J. C. Richter, N. Haj-Hosseini, S. Andersson-Engels, and K. Wårdell, "Fluorescence Spectroscopy Measurements in Ultrasonic Navigated Resection of Malignant Brain Tumors," *Lasers. Surg. Med.* **43**, 8-14 (2011).
33. M. Hefti, G. von Campe, M. Moschopoulos, A. Siegner, H. Looser, and H. Landolt, "5-Aminolaevulinic Acid-Induced Protoporphyrin IX Fluorescence in High-Grade Glioma Surgery," *Swiss Medical Weekly* **138**, 180-185 (2008).
34. N. Haj-Hosseini, J. Richter, S. Andersson-Engels, and K. Wårdell, "Optical Touch Pointer for Fluorescence Guided Glioblastoma Resection Using 5-Aminolevulinic Acid," *Lasers in Surgery and Medicine* **42**, 9-14 (2010).
35. C. Bohr, K. Hasselbalch, and A. Krogh, "About a New Biological Relation of High Importance That the Blood Carbonic Acid Tension Exercises on Its Oxygen Binding," *Skandinavisches Archiv Für Physiologie* **16**, 402-412 (1904).
36. S. Fantini and A. Sassaroli, "Near-Infrared Optical Mammography for Breast Cancer Detection with Intrinsic Contrast," *Ann. Biomed. Eng.* **40**, 398-407 (2012).
37. M.-A. Mycek and B. W. Pogue, *Handbook of Biomedical Fluorescence*, (CRC Press, 2003).
38. R. Richards-Kortum and E. Sevick-Muraca, "Quantitative Optical Spectroscopy for Tissue Diagnostics," *Ann. Rev. Phys. Chem.* **47**, 555 (1996).
39. J. G. Fujimoto and D. Farkas, *Biomedical Optical Imaging* (Oxford University Press, USA, 2009).
40. S. Andersson-Engels, A. Gustafson, J. Johansson, U. Stenram, K. Svanberg, and S. Svanberg, "Laser-Induced Fluorescence Used in Localizing Atherosclerotic Lesions," *Lasers in Medical Science* **4**, 171-181 (1989).
41. U. Gustafsson, S. Pålsson, and S. Svanberg, "Compact Fiber-Optic Fluorosensor Using a Continuous-Wave Violet Diode Laser and an Integrated Spectrometer," *Rev. Sci. Instr.* **71**, 3004-3006 (2000).
42. P. S. Andersson, S. Montán, and S. Svanberg, "Multispectral System for Medical Fluorescence Imaging," *IEEE J. Quant. Electr.* **23** (1987).
43. J. W. Hartog, A. P. de Vries, H. L. Lutgers, *et al.*, "Accumulation of Advanced Glycation End Products, Measured as Skin Autofluorescence, in Renal Disease," *Ann. N.Y. Acad. Sci.* **1043**, 299-307 (2005).
44. N. J. McIntyre, L. J. Chesterton, S. G. John, *et al.*, "Tissue-Advanced Glycation End Product Concentration in Dialysis Patients," *Clin. J. Am. Soc. Nephrol.* **5**, 51-55 (2010).
45. J. W. L. Hartog, A. A. Voors, S. J. L. Bakker, A. J. Smit, and D. J. van Veldhuisen, "Advanced Glycation End-Products (AGEs) and Heart Failure: Pathophysiology and Clinical Implications," *European J. Heart Failure* **9**, 1146-1155 (2007).
46. R. Meerwaldt, R. Graaff, P. Oomen, *et al.*, "Simple Non-Invasive Assessment of Advanced Glycation Endproduct Accumulation," *Diabetologia* **47**, 1324-1330 (2004).
47. J. W. Hartog, A. P. de Vries, H. L. Lutgers, *et al.*, "Accumulation of Advanced Glycation End Products, Measured as Skin Autofluorescence, in Renal Disease," *Ann N Y Acad Sci*, 299-307 (2005).
48. H. L. Lutgers, R. Graaff, T. P. Links, L. J. Ubink-Veltmaat, H. J. Bilo, R. O. Gans, and A. J. Smit, "Skin Autofluorescence as a Noninvasive Marker of Vascular Damage in Patients with Type 2 Diabetes," *Diabetes Care* **29**, 2654-2659 (2006).
49. S. Bengmark, "Advanced Glycation and Lipoxidation End Products-Amplifiers of Inflammation: The Role of Food," *J. Parenteral and Enteral Nutrition* **31**, 430-440 (2007).
50. V. M. Monnier, V. Vishwanath, K. E. Frank, C. A. Elmets, P. Dauchot, and R. R. Kohn, "Relation between Complications of Type I Diabetes Mellitus and Collagen-Linked Fluorescence," *N. Engl. J. Med.* **314**, 403-408 (1986).
51. J. V. Glenn and A. W. Stitt, "The Role of Advanced Glycation End Products in Retinal Ageing and Disease," *Biochim. Biophys. Acta* **10**, 3 (2009).
52. M. Brydegaard, N. Vogler, N. Bendso, K. Svanberg, and S. Svanberg, "Fluorescence Diagnostics for Integrated Advanced Glycation End (AGE) Products and Malignant Disease Assessment," (To appear).
53. R. Reif, M. S. Amoroso, K. W. Calabro, O. A' Amar, S. K. Singh, and I. J. Bigio, "Analysis of Changes in Reflectance Measurements on Biological Tissues Subjected to Different Probe Pressures," *J. Biomed. Opt.* **13**, 010502 (2008).
54. K. Barup, M. Brydegaard, Z. Guan, *et al.*, "Multi-Disciplinary Lidar Applications," in *Laser Applications to Chem., Security and Environmental Analysis (LACSEA)*, (OSA, 2010).
55. P. Weibring, H. Edner, and S. Svanberg, "Versatile Mobile Lidar System for Environmental Monitoring," *Appl. Opt.* **42**, 3583-3594 (2003).
56. B. E. A. Saleh and M. C. Teich, *Fundamentals of Photonics*, 2nd ed., (Wiley-Interscience, 2007).
57. I. Sahl, "On Burning Mirrors and Lenses," (Baghdad, Persia, 984).
58. S. Kinoshita and S. Yoshioka, "Structural Colors in Nature: The Role of Regularity and Irregularity in the Structure," *Chem. Phys. Chem.* **6**, 1442-1459 (2005).

59. P. Grujic and N. Simonovic, "Insights from the Classical Atom," *Phys. Today* **65**, 40-46 (2012).
60. W. E. Lamb, "Anti-Photon," *Appl. Phys. B: Lasers and Opt.* **60**, 77-84 (1995).
61. C. Abrahamsson, T. Svensson, S. Svanberg, S. Andersson-Engels, J. Johansson, and S. Folestad, "Time and Wavelength Resolved Spectroscopy of Turbid Media Using Light Continuum Generated in a Crystal Fiber," *Opt. Expr.* **12**, 4103-4112 (2004).
62. A. Pifferi, A. Torricelli, P. Taroni, D. Comelli, A. Bassi, and R. Cubeddu, "Fully Automated Time Domain Spectrometer for the Absorption and Scattering Characterization of Diffusive Media," *Rev. Sci. Instr.* **78**, 053103 (2007).
63. A. Ehlers, I. Riemann, M. Stark, and K. König, "Multiphoton Fluorescence Lifetime Imaging of Human Hair," *Microsc. Res. Tech.* **70**, 154-161 (2007).
64. H. Zhang, M. Sabooni, L. Rippe, C. Kim, S. Kröll, L. V. Wang, and P. R. Hemmer, "Slow Light for Deep Tissue Imaging with Ultrasound Modulation," *Appl. Phys. Lett.* **100**, 131102 (2012).
65. M. Forster, D. Thomsson, P. R. Hania, and I. G. Scheblykin, "Redistribution of Emitting State Population in Conjugated Polymers Probed by Single-Molecule Fluorescence Polarization Spectroscopy," *Phys. Chem. Chem. Phys.* **9**, 761-766 (2007).
66. N. Mazumder, J. Qiu, M. R. Foreman, *et al.*, "Polarization-Resolved Second Harmonic Generation Microscopy with a Four-Channel Stokes-Polarimeter," *Opt. Expr.* **20**, 14090-14099 (2012).
67. W. B. Sparks, J. H. Hough, L. Kolokolova, *et al.*, "Circular Polarization in Scattered Light as a Possible Biomarker," *J. Quant. Spectrosc. Rad. Trans.* **110**, 1771-1779 (2009).
68. V. Sharma, M. Crne, J. O. Park, and M. Srinivasarao, "Structural Origin of Circularly Polarized Iridescence in Jeweled Beetles," *Science* **325**, 449-451 (2009).
69. J. Walther, M. Gaertner, P. Cimalla, A. Burkhardt, L. Kirsten, S. Meissner, and E. Koch, "Optical Coherence Tomography in Biomedical Research," *Anal. Bioanal. Chem.* **400**, 2721-2743 (2011).
70. G. J. Koch, J. Y. Beyon, B. W. Barnes, *et al.*, "High-Energy 2  $\mu\text{m}$  Doppler Lidar for Wind Measurements," *Opt. Eng.* **46**, 116201 (2007).
71. S. Kameyama, T. Ando, K. Asaka, Y. Hirano, and S. Wadaka, "Compact All-Fiber Pulsed Coherent Doppler Lidar System for Wind Sensing," *Appl. Opt.* **46**, 1953-1962 (2007).
72. C. J. Clark, D. O. Elias, and R. O. Prum, "Aeroelastic Flutter Produces Hummingbird Feather Songs," *Science* **333**, 1430-1433 (2011).
73. C. Wai Lam, D. Jason, and M. M. Daniel, "Imaging with Terahertz Radiation," *Reports on Progress in Phys.* **70**, 1325 (2007).
74. P. U. Jepsen, D. G. Cooke, and M. Koch, "Terahertz Spectroscopy and Imaging – Modern Techniques and Applications," *Laser & Photonics Reviews* **5**, 124-166 (2011).
75. D. Peter, "Dolphin Sonar—Modelling a New Receiver Concept," *Bioinspir. Biomim.* **2**, 19 (2007).
76. H. Ledford, "Better Sonar through Dolphin Teeth," *Nature news*, 2007.
77. S. Hemilä, S. Nummela, and T. Reuter, "Anatomy and Physics of the Exceptional Sensitivity of Dolphin Hearing (*Odontoceti: Cetacea*)," *J. Comparative Physiol. A* **196**, 165-179 (2010).
78. S. A. Dible, J. A. Flint, and P. A. Lepper, "On the Role of Periodic Structures in the Lower Jaw of the Atlantic Bottlenose Dolphin (*Tursiops Truncatus*)," *Bioinspir. Biomim.* **4**, 015005 (2009).
79. E. Shevtsova, C. Hansson, D. H. Janzen, and J. Kjaerandsen, "Stable Structural Color Patterns Displayed on Transparent Insect Wings," *PNAS* **108**, 668-673 (2011).
80. H. Yin, L. Shi, J. Sha, *et al.*, "Iridescence in the Neck Feathers of Domestic Pigeons," *Phys. Rev. E* **74**, 051916 (2006).
81. M. D. Shawkey, V. Saranathan, H. Pálsdóttir, J. Crum, M. H. Ellisman, M. Auer, and R. O. Prum, "Electron Tomography, Three-Dimensional Fourier Analysis and Colour Prediction of a Three-Dimensional Amorphous Biophotonic Nanostructure," *J. R. Soc. Interface* **6**, 213-220 (2009).
82. R. Perez, B. L. Barraclough, S. C. Bender, *et al.*, "The ChemCam Instrument for the 2011 Mars Science Laboratory Mission: System Requirements and Performance," *Planetary probe* (To appear).
83. J. Ålebring, "Multispectral LED Based Microscopy," Masters thesis (Lund University, Lund Report on Atomic Physics, 2012).
84. M. Dacke, M. J. Byrne, C. H. Scholtz, and E. J. Warrant, "Lunar Orientation in a Beetle," *Proc. R. Soc. B* **271**, 361-365 (2004).
85. E. J. Warrant and D. E. Nilsson, *Invertebrate Vision*, (Cambridge University Press, Cambridge, 2006).
86. T. Svensson, "Pharmaceutical and Biomedical Applications of Spectroscopy in the Photon Migration Regime " Doctoral thesis (Lund University, Lund, LRAP-392, 2008).
87. Z. Yaqoob, D. Psaltis, M. S. Feld, and C. Yang, "Optical Phase Conjugation for Turbidity Suppression in Biological Samples," *Nat. Photon.* **2**, 110-115 (2008).
88. R. S. Sennett and G. D. Scott, "The Structure of Evaporated Metal Films and Their Optical Properties," *J. Opt. Soc. Am.* **40**, 203-210 (1950).
89. S. Lönn and D. Kroon, "Utilizing Enhanced Backscattering for Determination of Scattering Properties in Turbid Media " Masters thesis (Lund University, Lund Reports on Atomic Physics, LRAP-436, 2011).
90. T. W. Ebbesen, H. J. Lezec, H. F. Ghaemi, T. Thio, and P. A. Wolff, "Extraordinary Optical Transmission through Sub-Wavelength Hole Arrays," *Nature* **391**, 667-669 (1998).
91. J. C. M. Garnett, "Colours in Metal Glasses and in Metallic Films," *Philos. Trans. R. Soc. Lond. A, Math. Phys.* **203**, 385-420 (1904).

92. O. S. Heavens, "Optical Properties of Thin Films," *Reports on Progress in Phys.* **23**, 1 (1960).
93. D. Schurig, J. J. Mock, B. J. Justice, S. A. Cummer, J. B. Pendry, A. F. Starr, and D. R. Smith, "Metamaterial Electromagnetic Cloak at Microwave Frequencies," *Science* **314**, 977-980 (2006).
94. P. S. J. Russell, "Photonic-Crystal Fibers," *J. Lightwave Technology* **24**, 4729-4749 (2006).
95. U. Willer, C. Bohling, P. Geiser, and W. Schade, "Infrared Evanescent-Field Fiber Sensor for *in Situ* Mapping of Volcano Gases," 504-507 in *Second European Workshop on Opt. Fibre Sensors*, (SPIE, **5502**, 2004).
96. L. V. Hau, "The Art of Taming Light: Ultra-Slow and Stopped Light " *Europhys. News* **35**, 33-39 (2004).
97. C. R. Schwarze, J. A. Gargas, J. H. Rentz, and M. Hercher, "Method for Obtaining Gas Concentration with a Phase-Based Metrology System," *Appl. Opt.* **37**, 3942-3947 (1998).
98. D. Faber, M. Aalders, E. Mik, B. Hooper, M. van Gemert, and T. van Leeuwen, "Oxygen Saturation-Dependent Absorption and Scattering of Blood," *Phys. Rev. Lett.* **93** (2004).
99. J. Borggren, "Combinatorial Light Path Spectrometer for Turbid Liquids," Master thesis (Lund University, Lund, LRAP-428, 2011).
100. J. Kasparian, M. Rodriguez, G. Méjean, *et al.*, "White-Light Filaments for Atmospheric Analysis," *Science* **301**, 61-64 (2003).
101. M. W. Sigrist, *Air Monitoring by Spectroscopic Techniques*, (Wiley-Interscience, 1994).
102. S. Svanberg, *Atomic and Molecular Spectroscopy : Basic Aspects and Practical Applications*, 4th ed., (Springer, Heibelberg, 2004).
103. M. Lewander, Z. Guan, L. Persson, A. Olsson, and S. Svanberg, "Food Monitoring Based on Diode Laser Gas Spectroscopy," *Appl. Phys. B: Lasers and Opt.* **93**, 619-625 (2008).
104. T. Svensson, E. Alerstam, D. Khoptyar, J. Johansson, S. Folestad, and S. Andersson-Engels, "Near-Infrared Photon Time-of-Flight Spectroscopy of Turbid Materials up to 1400 nm," *Rev. Sci. Instr.* **80**, 063105 (2009).
105. P. Svenmarker, C. T. Xu, and S. Andersson-Engels, "Use of Nonlinear Upconverting Nanoparticles Provides Increased Spatial Resolution in Fluorescence Diffuse Imaging," *Opt. Lett.* **35**, 2789-2791 (2010).
106. W. Denk, J. Strickler, and W. Webb, "Two-Photon Laser Scanning Fluorescence Microscopy," *Science* **248**, 73-76 (1990).
107. M. Lewander, A. Bruzelius, S. Svanberg, K. Svanberg, and V. Fellman, "Noninvasive Gas Monitoring in Neonatal Lungs Using Diode Laser Spectroscopy: Feasibility Study," *J. Biomed. Opt.* **16**, 127002 (2011).
108. P. Lundin, E. K. Svanberg, L. Cocola, *et al.*, "Non-Invasive Gas Monitoring in Newborn Infants Using Diode Laser Absorption Spectroscopy: A Case Study," in *Conference on Opt. Diagnostics and Sensing XII - Toward Point-of-Care Diagnostics/4th Meeting the Design and Performance Validation Phantoms Used in Conjunction with Opt. Measurement Tissues* (SPIE, **8229**, 2012).
109. E. M. Hillman, C. B. Amoozegar, T. Wang, A. F. McCaslin, M. B. Bouchard, J. Mansfield, and R. M. Levenson, "In Vivo Optical Imaging and Dynamic Contrast Methods for Biomedical Research," *Philos. Trans. A Math. Phys. Eng. Sci.* **369**, 4620-4643 (2011).
110. J. Kalb, T. Nielsen, M. Fricke, M. Egelhaaf, and R. Kurtz, "In Vivo Two-Photon Laser-Scanning Microscopy of Ca<sup>2+</sup> Dynamics in Visual Motion-Sensitive Neurons," *Biochem. Biophys. Res. Commun.* **316**, 341-347 (2004).
111. T. H. Risby and F. K. Tittel, "Current Status of Midinfrared Quantum and Interband Cascade Lasers for Clinical Breath Analysis," *Opt. Eng.* **49**, 111123 (2010).
112. P. Beard, "Biomedical Photoacoustic Imaging," *Interface Focus* **1**, 602-631 (2011).
113. M. R. Hamblin and P. Mroz, *Advances in Photodynamic Therapy: Basic, Translational and Clinical* (Artech House Publishers, 2008).
114. J. R. Lakowicz, *Principles of Fluorescence Spectroscopy*, 3rd ed., (Springer, New York, 2006).
115. J. Kiefer, Z. S. Li, J. Zetterberg, X. S. Bai, and M. Aldén, "Investigation of Local Flame Structures and Statistics in Partially Premixed Turbulent Jet Flames Using Simultaneous Single-Shot CH and OH Planar Laser-Induced Fluorescence Imaging," *Combustion and Flame* **154**, 802-818 (2008).
116. L. Rippe, M. Nilsson, S. Kröll, R. Klieber, and D. Suter, "Experimental Demonstration of Efficient and Selective Population Transfer and Qubit Distillation in a Rare-Earth-Metal-Ion-Doped Crystal," *Phys. Rev. A* **71** (2005).
117. K. E. Arnold, I. P. F. Owens, and N. J. Marshall, "Fluorescent Signaling in Parrots," *Science* **295**, 92 (2002).
118. N. Michiels, N. Anthes, N. Hart, *et al.*, "Red Fluorescence in Reef Fish: A Novel Signalling Mechanism?," *BMC Ecol.* **8**, 16 (2008).
119. C. C. Wang, A. N. Masi, and L. Fernández, "On-Line Micellar-Enhanced Spectrofluorimetric Determination of Rhodamine Dye in Cosmetics," *Talanta* **75**, 135-140 (2008).
120. A. J. Elliot and D. Niesta, "Romantic Red: Red Enhances Men's Attraction to Women," *J. Pers. Soc. Psychol.* **95**, 1150-1164 (2008).
121. R. Bro, "PARAFAC. Tutorial and Applications," *Chemometr. Intell. Lab.* **38**, 149-171 (1997).
122. M. S. Kim, Y.-R. Chen, S. Kang, I. Kim, A. M. Lefcourt, and M. Kim, "Fluorescence Characteristics of Wholesome and Unwholesome Chicken Carcasses," *Appl. Spectrosc.* **60**, 1210-1216 (2006).

123. R. A. Zângaro, J. Landulfo Silveira, R. Manoharan, *et al.*, "Rapid Multiexcitation Fluorescence Spectroscopy System for in Vivo Tissue Diagnosis," *Appl. Opt.* **35**, 5211-5218 (1996).
124. Y. Goulas, Z. G. Cerovic, A. Cartelat, and I. Moya, "Dualex: A New Instrument for Field Measurements of Epidermal Ultraviolet Absorbance by Chlorophyll Fluorescence," *Appl. Opt.* **43**, 4488-4496 (2004).
125. S. Ek, B. Anderson, and S. Svanberg, "Compact Fiber-Optic Fluorosensor Employing Light-Emitting Ultraviolet Diodes as Excitation Sources," *Spectrochimica Acta Part B: Atomic Spectrosc.* **63**, 349-353 (2008).
126. "Force A - See to Act", retrieved 2012, <http://www.force-a.eu/>.
127. R. Pedros, I. Moya, Y. Goulas, and S. Jacquemoud, "Chlorophyll Fluorescence Emission Spectrum inside a Leaf," *Photochem Photobiol Sci* **7**, 498-502 (2008).
128. N. Hudson, A. Baker, and D. Reynolds, "Fluorescence Analysis of Dissolved Organic Matter in Natural, Waste and Polluted Waters—a Review," *River Research and Applications* **23**, 631-649 (2007).
129. F. E. Hoge and R. N. Swift, "Airborne Simultaneous Spectroscopic Detection of Laser-Induced Water Raman Backscatter and Fluorescence from Chlorophyll a and Other Naturally Occurring Pigments," *Appl. Opt.* **20**, 3197-3205 (1981).
130. P. Kokkalis, A. Papayannis, R. Mamouri, G. Tsaknakis, and V. Amiridis, "The EOLE Lidar System, of National Technical University of Athens," in *Internat. Laser Radar Conference (26 ILRC)*, (2012).
131. M. Kneen, J. Farinas, Y. Li, and A. S. Verkman, "Green Fluorescent Protein as a Noninvasive Intracellular Ph Indicator," *Biophysical J.* **74**, 1591-1599 (1998).
132. G. Agati, "Response of the in Vivo Chlorophyll Fluorescence Spectrum to Environmental Factors and Laser Excitation Wavelength," *Pure Appl. Opt. J. Euro. Opt. Soc. Part A* **7**, 797 (1998).
133. G. Agati, Z. G. Cerovic, and I. Moya, "The Effect of Decreasing Temperature up to Chilling Values on the in Vivo F685/F735 Chlorophyll Fluorescence Ratio in *Phaseolus Vulgaris* and *Pisum Sativum*: The Role of the Photosystem I Contribution to the 735 nm Fluorescence Band," *Photochem. Photobiol.* **72**, 75-84 (2000).
134. M. Brydegaard and S. Svanberg, "Multispectral Imaging in Development," *Europhys. News* (2011).
135. H. S. de Bruijn, A. van der Ploeg - van den Heuvel, H. Sterenborg, and D. J. Robinson, "Fractionated Illumination after Topical Application of 5-Aminolevulinic Acid on Normal Skin of Hairless Mice: The Influence of the Dark Interval," *J. Photochem. Photobiol. B-Biol.* **85**, 184-190 (2006).
136. C. Tillman, G. Grafström, A. C. Jonsson, *et al.*, "Survival of Mammalian Cells Exposed to Ultrahigh Dose Rates from a Laser-Produced Plasma X-Ray Source," *Radiology* **213**, 860-865 (1999).
137. B. Anderson, P. K. Bush-Bassuah, and J. P. Teteh., "Discriminating Male and Female Nutmeg Plants (*Myristica Fragrans* Houtt), with the Use of Laser-Induced Chlorophyll Fluorescence Induction Kinetics and Multivariate Analysis," Submitted to *Appl. Spectrosc.* (2012).
138. B. Huang, M. Bates, and X. Zhuang, "Super-Resolution Fluorescence Microscopy," *Ann. Rev. Biochem.* **78**, 993-1016 (2009).
139. M. J. B. Rust, M. Zhuang, X., "Sub-Diffraction-Limit Imaging by Stochastic Optical Reconstruction Microscopy (STORM)," *Nat. Methods* **3**, 793-795 (2006).
140. S. Manley, J. M. Gillette, G. H. Patterson, H. Shroff, H. F. Hess, E. Betzig, and J. Lippincott-Schwartz, "High-Density Mapping of Single-Molecule Trajectories with Photoactivated Localization Microscopy," *Nat. Methods* **5**, 155-157 (2008).
141. A. Moore and R. H. Miller, "Automated Identification of Optically Sensed Aphid (*Homoptera: Aphidae*) Wingbeat Waveforms," *Ann. Entomol. Soc. Am.* **95**, 1-8 (2002).
142. E. S. Carlsten, G. R. Wicks, K. S. Repasky, J. L. Carlsten, J. J. Bromenshenk, and C. B. Henderson, "Field Demonstration of a Scanning Lidar and Detection Algorithm for Spatially Mapping Honeybees for Biological Detection of Land Mines," *Appl. Opt.* **50**, 2112-2123 (2011).
143. J. A. Shaw, "Optical Detection of Oscilating Targets Using Modulation of Scattered Laser Light," US 7,511,624 B2 (United States Patent 2009).
144. J. Llopis, J. M. McCaffery, A. Miyawaki, M. G. Farquhar, and R. Y. Tsien, "Measurement of Cytosolic, Mitochondrial, and Golgi Ph in Single Living Cells with Green Fluorescent Proteins," *PNAS* **95**, 6803-6808 (1998).
145. J. A. Shaw, N. L. Seldomridge, D. L. Dunkle, P. W. Nugent, and L. H. Spangler, "Polarization Lidar Measurements of Honey Bees in Flight for Locating Land Mines," *Opt. Expr.* **13**, 5853-5863 (2005).
146. D. N. Whiteman, Melfi, S. H., Ferrare, R. A., "Raman Lidar System for the Measurement of Water Vapor and Aerosols in the Earth's Atmosphere," *Appl. Opt.* **31**, 3068-3082 (1992).
147. T. Hellerer, A. M. K. Enejder, O. Burkacky, and A. Zumbusch, "Highly Efficient Coherent Anti-Stokes Raman Scattering (CARS)-Microscopy," in *Multiphoton Microscopy in the Biomed. Sci. IV*, A. Periasamy, ed. (SPIE, Bellingham, 2004), pp. 223-229.
148. H. Kragh, "Ludvig Lorenz and Nineteenth Century Optical Theory: The Work of a Great Danish Scientist," *Appl. Opt.* **30**, 4688-4695 (1991).
149. Y. Timofeev, *Theoretical Fundamentals of Atmospheric Optics*, (Cambridge International Science Publishing, 2008).
150. G. E. Shaw, "Observations and Theoretical Reconstruction of the Green Flash," *Pure Appl. Geophys.* **102**, 223-235 (1973).
151. C. F. Bohren and D. R. Huffman, *Absorption and Scattering of Light by Small Particles*, (Wiley, 1983).

152. C. Mätzler, "MATLAB Functions for Mie Scattering and Absorption," (Institut für Angewandte Physik, Bern, 2002).
153. G. M. Hale and M. R. Querry, "Optical Constants of Water in the 200-nm to 200- $\mu$ m Wavelength Region," *Appl. Opt.* **12**, 555-563 (1973).
154. M. Dienerowitz, M. Mazilu, and K. Dholakia, "Optical Manipulation of Nanoparticles: A Review," *J. Nanophot.* **2**, 021875 (2008).
155. E. Alerstam, T. Svensson, and S. Andersson-Engels, "Parallel Computing with Graphics Processing Units for High-Speed Monte Carlo Simulation of Photon Migration," *J. Biomed. Opt.* **13**, 060504 (2008).
156. S. L. Jacques and B. W. Pogue, "Tutorial on Diffuse Light Transport," *J. Biomed. Opt.* **13**, 041302 (2008).
157. P. Yang, B.-C. Gao, B. A. Baum, *et al.*, "Radiative Properties of Cirrus Clouds in the Infrared (8–13  $\mu$ m) Spectral Region," *J. Quantitative Spectrosc. & Radiative Transfer* **70**, 473-504 (2001).
158. J. A. Shaw and N. J. Pust, "Icy Wave-Cloud Lunar Corona and Cirrus Iridescence," *Appl. Opt.* **50** (2011).
159. R. Furfaro and B. D. Ganapol, "Spectral Theory for Photon Transport in Dense Vegetation Media: Caseology for the Canopy Equation," *Transport Theory and Statistical Phys.* **36**, 107-135 (2007).
160. A. Ounis, Z. G. Cerovic, J. M. Briantais, and I. Moya, "DE-FLIDAR: A New Remote Sensing Instrument for the Estimation of Epidermal UV Absorption in Leaves and Canopies," in *Proc. EARSeL*, 2000).
161. Z. Guan, M. Lewander, R. Grönlund, H. Lundberg, and S. Svanberg, "Gas Analysis within Remote Porous Targets Using LIDAR Multi-Scatter Techniques," *Appl. Phys. B: Lasers and Opt.* **93**, 657-663 (2008).
162. A. W. Nolin and J. Dozier, "A Hyperspectral Method for Remotely Sensing the Grain Size of Snow," *Remote Sensing Environ.* **74**, 207-216 (2000).
163. P. S. Barry, P. Jarecke, J. Pearlman, D. Jupp, J. Lovell, and S. Campbell, "Radiometric Calibration Validation of the Hyperion Instrument Using Ground Truth at a Site in Lake Frome, Australia," in *Imaging Spectrometry VII*, M. R. Descour and S. S. Shen, eds. (SPIE Int. Soc. Opt. Eng., Bellingham, 2001), pp. 242-246.
164. A. L. Odriozola, R. Varela, C. Hu, Y. Astor, L. Lorenzoni, and F. E. Müller-Karger, "On the Absorption of Light in the Orinoco River Plume," *Continental Shelf Research* **27**, 1447-1464 (2007).
165. U. Tylewicz, P. Lundin, L. Cocola, *et al.*, "Gas in Scattering Media Absorption Spectroscopy (GASMAS) Detected Persistent Vacuum in Apple Tissue after Vacuum Impregnation " *Food Biophys.* **7**, 28 - 34 (2012 ).
166. M. Sjöholm, G. Somesfalean, J. Alnis, B. Anderson, and S. Svanberg, "Gas Transport in Wood Assessed by Laser Spectroscopy," 505 in *Lasers and Electro-Opt. Europe, 2003. CLEO/Europe. 2003 Conference on*, (IEEE CLEO/Europe, 2003).
167. C. T. Xu, M. Lewander, S. Andersson-Engels, E. Adolfsson, T. Svensson, and S. Svanberg, "Wall-Collision Line Broadening of Molecular Oxygen within Nanoporous Materials," *Phys. Rev. A* **84**, 042705 (2011).
168. T. Svensson, M. Andersson, L. Rippe, S. Svanberg, S. Andersson-Engels, J. Johansson, and S. Folestad, "VCSEL-Based Oxygen Spectroscopy for Structural Analysis of Pharmaceutical Solids," *Appl. Phys. B: Lasers and Opt.* **90**, 345-354 (2008).
169. X. Wan, J. Fan, and H. Wu, "Measurement of Thermal Radiative Properties of Penguin Down and Other Fibrous Materials Using FTIR," *Polymer Testing* **28**, 673-679 (2009).
170. V. Backman, R. Gurjar, K. Badizadegan, I. Itzkan, R. R. Dasari, L. T. Perelman, and M. S. Feld, "Polarized Light Scattering Spectroscopy for Quantitative Measurement of Epithelial Cellular Structures *in Situ*," *IEEE JSTQE* **5**, 1019-1026 (1999).
171. J. Michels and S. N. Gorb, "Detailed Three-Dimensional Visualization of Resilin in the Exoskeleton of Arthropods Using Confocal Laser Scanning Microscopy," *J. Microsc.* **245**, 1-16 (2012).
172. E. Gratton, S. Fantini, M. A. Franceschini, G. Gratton, and M. Fabiani, "Measurements of Scattering and Absorption Changes in Muscle and Brain," *Proc. R. Soc. B* **352**, 727-735 (1997).
173. A. M. K. Nilsson, C. Sturesson, D. L. Liu, and S. Andersson-Engels, "Changes in Spectral Shape of Tissue Optical Properties in Conjunction with Laser-Induced Thermo-therapy," *Appl. Opt.* **37**, 1256-1267 (1998).
174. L. Wang and S. L. Jacques, "Use of a Laser Beam with an Oblique Angle of Incidence to Measure the Reduced Scattering Coefficient of a Turbid Medium," *Appl. Opt.* **34**, 2362-2366 (1995).
175. B. Yuan, S. A. Burgess, A. Iranmahboob, M. B. Bouchard, N. Lehrer, C. Bordier, and E. M. C. Hillman, "A System for High-Resolution Depth-Resolved Optical Imaging of Fluorescence and Absorption Contrast " *Rev. Sci. Instr.* **80** (2009).
176. J. Qin and R. Lu, "Measurement of the Optical Properties of Fruits and Vegetables Using Spatially Resolved Hyperspectral Diffuse Reflectance Imaging Technique," *Postharvest Biol. Tech.* **49**, 355-365 (2008).
177. H. Liu, B. Chance, A. H. Hielscher, S. L. Jacques, and F. K. Tittel, "Influence of Blood-Vessels on the Measurement of Hemoglobin Oxygenation as Determined by the Time-Resolved Reflectance Spectroscopy," *Medical Phys.* **22**, 1209-1217 (1995).

178. L. Qiu, V. Turzhitsky, R. Chuttani, *et al.*, "Spectral Imaging with Scattered Light: From Early Cancer Detection to Cell Biology," *IEEE JSTQE* **18**, 1073-1083 (2012).
179. F. Aptel, N. Olivier, A. Deniset-Besseau, J. M. Legeais, K. Plamann, M. C. Schanne-Klein, and E. Beaurepaire, "Multimodal Nonlinear Imaging of the Human Cornea," *Invest. Ophthalmol. Vis. Sci.* **51**, 2459-2465 (2010).
180. M. D. Graef and M. E. McHenry, *Structure of Materials: An Introduction to Crystallography, Diffraction and Symmetry* (Cambridge University Press, 2007).
181. A. Corlu, R. Choe, T. Durduran, *et al.*, "Three-Dimensional *in Vivo* Fluorescence Diffuse Optical Tomography of Breast Cancer in Humans," *Opt. Expr.* **15**, 6696-6716 (2007).
182. C. T. Xu, N. Svensson, J. Axelsson, *et al.*, "Autofluorescence Insensitive Imaging Using Upconverting Nanocrystals in Scattering Media," *Appl. Phys. Lett.* **93** (2008).
183. S. Andersson-Engels, R. Berg, S. Svanberg, and O. Jarlman, "Time-Resolved Transillumination for Medical Diagnostics," *Opt. Lett.* **15**, 1179-1181 (1990).
184. K. M. Yoo, F. Liu, and R. R. Alfano, "Imaging through a Scattering Wall Using Absorption," *Opt. Lett.* **16**, 1068-1070 (1991).
185. P. P. Ho and R. R. Alfano, "Early Light Imaging for Biomedical Applications," 8-13 in *Optical Sensing, Imaging, and Manipulation for Biological and Biomedical Applications*, (Proc. SPIE **4082**, 2000).
186. C. Christiansen, "Untersuchungen über die Optischen Eigenschaften von Fein Verteilten Körpern," *Ann. Phys. Chem.* **23, 24**, 293-306, 439-446 (1884, 1885).
187. C. V. Raman, "The Theory of the Christiansen Experiment," *Proc. Indian Acad. Sci.* **A29**, 381-390 (1949).
188. H. R. Carlon, "Christiansen Effect in IR Spectra of Soil-Derived Atmospheric Dusts," *Appl. Opt.* **18** (1979).
189. H. R. Carlon, "Contributions of Particle Absorption to Mass Extinction Coefficients (0.55-14  $\mu\text{m}$ ) of Soil-Derived Atmospheric Dusts," (U.S. Army Armament Munitions Chemical Command, 1988).
190. W. P. Arnott, Y. Y. Dong, and J. Hallett, "Extinction Efficiency in the Infrared (2-18  $\mu\text{m}$ ) of Laboratory Ice Clouds: Observations of Scattering Minima in the Christiansen Bands of Ice," *Appl. Opt.* **34**, 341-551 (1995).
191. W. P. Arnott, C. Schmitt, Y. Liu, and J. Hallett, "Droplet Size Spectra and Water-Vapor Concentration of Laboratory Water Clouds: Inversion of Fourier Transform Infrared (500-5000  $\text{cm}^{-1}$ ) Optical-Depth Measurement," *Appl. Opt.* **36**, 5205-5216 (1997).
192. C. G. Schmitt, "Infrared Emission (500-2000  $\text{cm}^{-1}$ ) of Laboratory Ice Clouds," (University of Nevada, 1998).
193. P. Yang, "Spectral Signature of Ice Clouds in the Far-Infrared Region: Single-Scattering Calculations and Radiative Sensitivity Study," *J. Geophys. Research* **108**, 4569 (2003).
194. H.-L. Huang, P. Yang, H. Wei, B. A. Baum, Y. Hu, P. Antonelli, and S. A. Ackerman, "Inference of Ice Cloud Properties from High Spectral Resolution Infrared Observations," *IEEE Trans. Geosci. Remote Sens.* **42**, 842 (2004).
195. M. M. Hedman, P. D. Nicholson, M. R. Showalter, *et al.*, "The Christiansen Effect in Saturn's Narrow Dusty Rings and the Spectral Identification of Clumps in the F Ring," *Icarus* **215**, 695-711 (2011).
196. M. J. Smith and R. T. Carl, "Applications of Microspectroscopy in the near-Infrared Region," *Appl. Spectrosc.* **43**, 865-873 (1989).
197. M. Franz, B. M. Fischer, and M. Walther, "The Christiansen Effect in Terahertz Time-Domain Spectra of Coarse-Grained Powders," *Appl. Phys. Lett.* **92**, 021107 (2008).
198. N. Holonyak and S. F. Bevacqua, "Coherent (Visible) Light Emission from  $\text{Ga}(\text{As}_{1-x}\text{P}_x)$  Junctions," *Appl. Phys. Lett.* **1**, 82-83 (1962).
199. Y. Taniyasu, M. Kasu, and T. Makimoto, "An Aluminium Nitride Light-Emitting Diode with a Wavelength of 210 Nanometres," *Nature* **441**, 325-328 (2006).
200. "Roithner Lasertechnik GmbH", retrieved 2012, [www.roithner-laser.com](http://www.roithner-laser.com).
201. T. H. Goldsmith, "What Birds See," *Scientific Am.* **295**, 68-75 (2006).
202. X. T. Lou, G. Somesfalean, Z. G. Zhang, and S. Svanberg, "Sulfur Dioxide Measurements Using an Ultraviolet Light-Emitting Diode in Combination with Gas Correlation Techniques," *Appl. Phys. B* **94**, 699-704 (2009).
203. B. A. Matveev, N. V. Zotova, N. D. Il'Inskaya, S. A. Karandashev, M. A. Remennyi, N. M. Stus, and G. N. Talalakin, "Towards Efficient Mid-IR LED Operation: Optical Pumping, Extraction or Injection of Carriers?," *J. Modern Opt.* **49**, 743-756 (2002).
204. "Picoquant", retrieved 2012, <http://www.picoquant.com/>.
205. H.-Y. Chou, C.-C. Chen, and T.-H. Yang, "Maintenance of Stable Light Emission in High Power LEDs," *Microelectronics Reliability* **52**, 912-915 (2012).
206. Y. Xi, T. Gessmann, J. Xi, *et al.*, "Junction Temperature in Ultraviolet Light-Emitting Diodes," *Jpn. J. Appl. Phys.* **44**, 7260-7266 (2005).
207. "Videometer A/S", retrieved 2012, <http://www.videometer.com/>.
208. P. C. Hauser, T. W. T. Rupasinghe, and N. E. Cates, "A Multi-Wavelength Photometer Based on Light-Emitting Diodes," *Talanta* **42**, 605-612 (1995).

209. M. Trtilek, D. M. Kramer, M. Kobliiek, and L. Nedbal, "Dual-Modulation LED Kinetic Fluorometer," *J. Luminescence* **72**, 597-599 (1997).
210. J. G. Schnable, P. J. Grochowski, L. Wilhelm, C. Harding, M. Kiefer, and R. S. Orr, "Portable LED-Array Vis-NIR Spectrophotometer/Nephelometer," *Field Anal. Chem. Tech.* **2**, 21-28 (1998).
211. A. D. Magnus Petterson, Hans Petterson, "Method and Device for Measurement in Blood," (United State Patent Application Publication 2007).
212. J. M. Carstensen and J. Folm-Hansen, "An Apparatus and a Method of Recording an Image of an Object.," EP1051660 (European Patent 2000).
213. L. Oppenheimer, "Spectrophotometric Blood Analysis," (United States Patent 1994).
214. K. B.-B. Paul, M. v. B. Hubertus, T. T. Ebenezer, and M. S. Christine, "A Portable Fibre-Probe Ultraviolet Light Emitting Diode (LED)-Induced Fluorescence Detection System," *Measurement Science and Technology* **19**, 025601 (2008).
215. S. J. Hart and R. e. D. JiJi, "Light Emitting Diode Excitation Emission Matrix Fluorescence Spectroscopy," *Analyst* **127**, 1693-1699 (2002).
216. G. Held, *Introduction to Light Emitting Diode Technology and Applications*, (Auerbach Publications, 2008).
217. E. F. Schubert, *Light-Emitting Diodes*, 2nd ed., (Cambridge University Press, 2003).
218. E. P. de Jong and C. A. Lucy, "Spectral Filtering of Light-Emitting Diodes for Fluorescence Detection," *Analytica Chimica Acta* **546**, 37-45 (2005).
219. P. Herman, Maliwal, B. P., Lin, H. J., Lakowicz, J. R., "Frequency-Domain Fluorescence Microscopy with the LED as a Light Source," *J. Microscopy* **203**, 176-181 (2001).
220. P. Herman, Vecer, J., "Frequency Domain Fluorometry with Pulsed Light-Emitting Diodes," *Ann. N. Y. Acad. Sci.* **1130**, 56-61 (2008).
221. B. T. Barbieri, E. Jameson, D. M., "Frequency-Domain Fluorescence Spectroscopy Using 280-nm and 300-nm Light-Emitting Diodes: Measurement of Proteins and Protein-Related Fluorophores," *Anal. Biochem.* **344**, 298-300 (2005).
222. S. Fantini, M. A. Franceschini, J. B. Fiskin, B. Barbieri, and E. Gratton, "Quantitative Determination of the Absorption Spectra of Chromophore in Strongly Scattering Media: A Light-Emitting-Diode Based Technique," *Appl. Opt.* **33**, 5204-5213 (1994).
223. A. Pifferi, J. Swartling, E. Chikoidze, *et al.*, "Spectroscopic Time-Resolved Diffuse Reflectance and Transmittance Measurements of the Female Breast at Different Interfiber Distances," *J. Biomed. Opt.* **9**, 1143-1151 (2004).
224. Y. B. Acharya, "Spectral and Emission Characteristics of LED and Its Application to LED-Based Sun-Photometry," *Opt. Laser Techn.* **37**, 547-550 (2005).
225. F. M. Mims, "An Inexpensive and Stable LED Sun Photometer for Measuring the Water Vapor Column over South Texas from 1990 to 2001," *Geophys. Res. Lett.* **29**, 1642 (2002).
226. T. H. Maiman, "Stimulated Optical Radiation in Ruby," *Nature* **187**, 493-494 (1960).
227. V. Letokhov and S. Johansson, *Astrophysical Lasers* (Oxford University Press, 2009).
228. M. J. Mumma, D. Buhl, G. Chin, D. Deming, F. Espenak, T. Kostiuik, and D. Zipoy, "Discovery of Natural Gain Amplification in the 10-Micrometer Carbon Dioxide Laser Bands on Mars: A Natural Laser," *Science* **212**, 45-49 (1981).
229. W. Silfvast, "Population Inversions in Lightning Discharges?," *Opt. Photon. News* **21**, 32-37 (2010).
230. F. Koyama, "Recent Advances of VCSEL Photonics," *J. Lightwave Techn.* **24**, 4502-4513 (2006).
231. C. A. Haynam, P. J. Wegner, J. M. Auerbach, *et al.*, "National Ignition Facility Laser Performance Status," *Appl. Opt.* **46**, 3276-3303 (2007).
232. D. Schuöcker and B. Holzinger, "CO<sub>2</sub> Laser with 65MW Pulses and 100kW Power, Concept and First Steps of Development," *Proc. SPIE* **7005**, 70051F-70051F-70012 (2008).
233. J. R. Albertine, "History of Navy HEL Technology Development and Systems Testing," in *Laser and Beam Control Technologies*, (Proc. SPIE, 2002).
234. J. R. C. J. R. Abertine, "Navy's High Energy Laser Weapon System," (1997).
235. R. Whitney, D. Douglas, and G. Neil, "Airborne Megawatt Class Free-Electron Laser for Defense and Security," in *Laser Source and System Technology for Defense and Security, Kissimmee, FL (US)*, (Thomas Jefferson National Accelerator Facility, Newport News, VA (US), 2005).
236. O. Svelto, *Principles of Lasers*, 5th ed., (Springer, 2009).
237. F. J. Duarte, *Tunable Laser Applications, Second Edition*, 2nd ed., (CRC Press, 2008).
238. "O-Like Dedicated Laser", retrieved 2012, <http://o-like.com/>.
239. D. Kielpinski, M. Cetina, J. A. Cox, and F. X. Kärtner, "Laser Cooling of Trapped Ytterbium Ions with an Ultraviolet Diode Laser," *Opt. Lett.* **31**, 757-759 (2006).
240. "A European Aerosol Research Lidar Network to Establish an Aerosol Climatology: EARLINET", retrieved 2012, <http://www.earlinet.org/>.
241. NATO, "Laser Based Stand-Off Detection of Biological Agents," SET-098/RTG-55 (North Atlantic Treaty Organisation, 2010).
242. NASA, "CALIPSO: Cloud-Aerosol Lidar and Infrared Pathfinder Satellite Observations," FS-2005-09-120-LaRC (NASA, 2005).

243. D. S. Hoffman, A. R. Nehrir, K. S. Repasky, J. A. Shaw, and J. L. Carlsten, "Range-Resolved Optical Detection of Honeybees by Use of Wing-Beat Modulation of Scattered Light for Locating Land Mines," *Appl. Opt.* **46**, 3009-3012 (2007).
244. P. A. C. Jansson, B. A. M. Hansson, O. Hemberg, M. Otendal, A. Holmberg, J. de Groot, and H. M. Hertz, "Liquid-Tin-Jet Laser-Plasma Extreme Ultraviolet Generation," *Appl. Phys. Lett.* **84**, 2256-2258 (2004).
245. J. T. Kiehl and K. E. Trenberth, "Earth's Annual Global Mean Energy Budget," *Bulletin Am. Meteorological Soc.* **78**, 197 (1996).
246. I. Moya, "A New Instrument for Passive Remote Sensing I. Measurements of Sunlight-Induced Chlorophyll Fluorescence," *Remote Sensing Environ.* **91**, 186-197 (2004).
247. S. Beirle, U. Platt, M. Wenig, and T. Wagner, "Weekly Cycle of NO<sub>2</sub> by GOME Measurements: A Signature of Anthropogenic Sources," *Atmos. Chem. Phys.*, **3**, 2225-2232 (2003).
248. M. Bertilson, O. von Hofsten, U. Vogt, A. Holmberg, and H. M. Hertz, "High-Resolution Computed Tomography with a Compact Soft X-Ray Microscope," *Opt. Expr.* **17**, 11057-11065 (2009).
249. A. Achterberg and M. Ackermann and J. Adams, *et al.*, "First Year Performance of the IceCube Neutrino Telescope," *Astroparticle Phys.* **26**, 155-173 (2006).
250. D. Althausen, D. Muller, A. Ansmann, U. Wandinger, H. Hube, E. Clauder, and S. Zorner, "Scanning 6-Wavelength 11-Channel Aerosol Lidar," *J. Atmospheric & Oceanic Tech.* **17**, 1469 (2000).
251. D. M. Winker, C. A. Hostetler, M. A. Vaughan, and A. H. Omar, "Mission, Instrument, and Algorithms Overview," PC-SCI-202.01 (NASA, 2006).
252. A. A. C. Swinton, "Distant Electric Vision," *Nature* **78** (1908).
253. T. S. L. Gerald C. Holst, *CMOS/CCD Sensors and Camera Systems*, 2nd ed., (SPIE, 2011).
254. E. Pennisi, "Light in the Deep," *Science* **335**, 1160-1163 (2012).
255. U. P. Gustafsson, E. McLaughlin, E. Jacobsen, *et al.*, "*In-Vivo* Fluorescence and Reflectance Imaging of Human Cervical Tissue," 521-530 in (SPIE, **5031**, 2003).
256. J. Pearlman, S. Carman, C. Segal, P. Jarecke, P. Clancy, and W. Browne, *Overview of the Hyperion Imaging Spectrometer for the NASA EO-1 Mission*, Igarss 2001: Scanning the Present and Resolving the Future, Vol. 1-7, (Proc. IEEE, New York, 2001).
257. E. Herrala, J. Okkonen, T. Hyvarinen, M. Aikio, and J. Lammasniemi, *Imaging Spectrometer for Process Industry Applications*, Opt. Measurements and Sensors for the Process Industries, Vol. 2248, (SPIE - Int Soc Optical Engineering, Bellingham, 1994).
258. A. Sjögren, M. Harbst, C.-G. Wahlström, S. Svanberg, and C. Olsson, "High-Repetition-Rate, Hard X-Ray Radiation from a Laser-Produced Plasma: Photon Yield and Application Considerations," *Rev. Sci. Instr.* **74**, 2300-2311 (2003).
259. A. P. Rinaldo Cubeddu, P. Taroni, A. Torricelli, G. Valentini, F. Rinaldi, and E. Sorbellini, "Fluorescence Lifetime Imaging: An Application to the Detection of Skin Tumors," *IEEE JSTQE* **5**, 923-929 (1999).
260. O. Yadid-Pecht and R. Etienne-Cummings, *CMOS Imagers: From Phototransduction to Image Processing*, (Springer, 2004).
261. "Photonfocus AG", retrieved 2012, <http://www.photonfocus.com/>.
262. N. Joshi, C. Donner, and H. W. Jensen, "Noninvasive Measurement of Scattering Anisotropy in Turbid Materials by Nonnormal Incident Illumination," *Opt. Lett.* **31**, 936-938 (2006).
263. R. Bartlome and M. W. Sigrist, "Laser-Based Human Breath Analysis: D/H Isotope Ratio Increase Following Heavy Water Intake," *Opt. Lett.* **34**, 866-868 (2009).
264. S. Svanberg, "Gas in Scattering Media Absorption Spectroscopy - Laser Spectroscopy in Unconventional Environments," 285 - 296 in *19th Internat. Conference on Laser Spectrosc.*, (World Scientific Publishing Co, 2010).
265. S. Svanberg, "Gas in Scattering Media Absorption Spectroscopy," in *Sixth Internat. Conference on Advanced Opt. Materials and Devices (AOMD-6)*, (Proc. SPIE, **7142**, 2008).
266. R. J. Bomphrey, "Insects in Flight: Direct Visualization and Flow Measurements," *Bioinspir. Biomim.* **1**, S1-9 (2006).
267. H. Yamasaki and S. Morita, "Two-Step Curing Reaction of Epoxy Resin Studied by Thermal Analysis and Infrared Spectroscopy," *Appl. Spectrosc.* **66**, 926-933 (2012).
268. H. Dau and K. Sauer, "Electric Field Effect on Chlorophyll Fluorescence and Its Relation to Photosystem II Charge Separation Reactions Studied by a Salt-Jump Technique," *Biochimica et Biophysica Acta (BBA) - Bioenergetics* **1098**, 49-60 (1991).
269. Y. Liu, "Magnetic Field Effects on Photosynthetic Reactions," Doctoral thesis (Leiden University, 2008).
270. H. P. S. B. Weber, T. Müller, J. Bochmann, M. Mücke, D. L. Moehring, and G. Rempe "Photon-Photon Entanglement with a Single Trapped Atom," *Phys. Rev. Lett.* **102**, 030501 (2009).
271. M. Burza, A. Gonoskov, G. Genoud, *et al.*, "Hollow Microspheres as Targets for Staged Laser-Driven Proton Acceleration," *New J. Phys.* **13**, 013030 (2011).
272. C. Heyl, J. Guedde, A. L'Huillier, and U. Hoefler, "High-Order Harmonic Generation with  $\mu$ J Laser Pulses at High Repetition Rates," *J. Phys. B: Atomic, Molecular and Opt. Phys.* **45**, 074020 (2012).
273. S. W. Hell, "Far-Field Optical Nanoscopy," *Science* **316**, 1153-1158 (2007).

274. R. J. Bouwens, G. D. Illingworth, P. A. Oesch, *et al.*, "Discovery of  $Z \sim 8$  Galaxies in the Hubble Ultra Deep Field from Ultra-Deep WFC3/IR Observations," *Astrophys. J. Lett.* **709**, L133 (2010).
275. K. Varju, P. Johnsson, J. Mauritsson, A. L. Huillier, and R. Lopez-Martens, "Physics of Attosecond Pulses Produced Via High Harmonic Generation," *Am. J. Phys.* **77**, 389-395 (2009).
276. P. W. Smith, "Mode-Locking of Lasers," *Proc. IEEE* **58**, 1342-1357 (1970).
277. S. Svanberg, J. Larsson, A. Persson, and C.-G. Wahlström, "Lund High-Power Laser Facility – Systems and First Results," *Physica Scripta* **49**, 187 (1994).
278. M. Lewenstein, P. Balcou, M. Y. Ivanov, A. L'huillier, and P. B. Corkum, "Theory of High-Harmonic Generation by Low-Frequency Laser Fields," *Phys. Rev. A* **49**, 2117-2132 (1994).
279. M. Sjöholm, P. Weibring, H. Edner, and S. Svanberg, "Atomic Mercury Flux Monitoring Using an Optical Parametric Oscillator Based Lidar System," *Opt. Expr.* **12**, 551-556 (2004).
280. D. Balthasar, "Color Matching by Using Tuple Matching," 402–407 in *International Conference on Image Analysis and Processing*, **1**, 2003).
281. M. Castelnovi, P. Musso, A. Sgorbissa, and R. Zaccaria, "Surveillance Robotics: Analyzing Scenes by Colors Analysis and Clustering," in *IEEE Internat. Symposium on Computational Intelligence in Robotics and Automation*, 2003).
282. M. S. Drew and J. Au, "Clustering of Compressed Illumination-Invariant Chromaticity Signatures for Efficient Video Summarization," *Image and Vision Computing* **21**, 705-716 (2003).
283. T.-W. Chen, "Fast Image Segmentation Based on K-Means Clustering with Histograms in HSV Color Space," (2008).
284. A. Kelber, A. Balkanius, and E. J. Warrant, "Colour Vision in Diurnal and Nocturnal Hawkmoths," *Integr. Comp. Biol.* **43**, 571–579 (2003).
285. E. Warrant, "Vision in the Dimmest Habitats on Earth," *J. Comp. Physiol. A Neuroethol. Sens. Neural. Behav. Physiol.* **190**, 765-789 (2004).
286. T. Svensson, M. Andersson, L. Rippe, J. Johansson, S. Folestad, and S. Andersson-Engels, "High Sensitivity Gas Spectroscopy of Porous, Highly Scattering Solids," *Opt. Lett.* **33**, 80-82 (2008).
287. K. S. Repasky, J. A. Shaw, R. Scheppelle, C. Melton, J. L. Carsten, and L. H. Spangler, "Optical Detection of Honeybees by Use of Wing-Beat Modulation of Scattered Laser Light for Locating Explosives and Land Mines," *Appl. Opt.* **45**, 1839-1843 (2006).
288. J. S. D.X. Hammer, M.O. Stone, H.G. Rylander III, A.J. Welch, "Infrared Spectral Sensitivity of *Melanophila Acuminata*," *J. Insect Physiol.* **47**, 1441–1450 (2001).
289. G. S. Bakken and A. R. Krochmal, "The Imaging Properties and Sensitivity of the Facial Pits of Pitvipers as Determined by Optical and Heat-Transfer Analysis," *J. Exp. Biol.* **210**, 2801-2810 (2007).
290. A. Runemark and M. Brydegaard, "Invited Review on Laser Applications in Ecological Entomology," *J. Ecol. Entomol.*, to appear (2013).
291. B. C. Regan, C. Julliot, B. Simmen, F. Vienot, P. Charles-Dominique, and J. D. Mollon, "Fruits, Foliage and the Evolution of Primate Colour Vision," *Philos. Trans. R. Soc. Lond. B Biol. Sci.* **356**, 229-283 (2001).
292. J. Carroll, "Photopigment Basis for Dichromatic Color Vision in the Horse," *J. Vision* **1**, 80-87 (2001).
293. O. Lind and A. Kelber, "Avian Colour Vision: Effects of Variation in Receptor Sensitivity and Noise Data on Model Predictions as Compared to Behavioural Results," *Vision Res.* **49**, 1939-1947 (2009).
294. E. R. Loew, L. J. Fleishman, R. G. Foster, and I. Provencio, "Visual Pigments and Oil Droplets in Diurnal Lizards: A Comparative Study of Caribbean Anoles," *J. Exp. Biol.* **205**, 927–938 (2002).
295. G. E. Hill and K. J. McGraw, *Bird Coloration, Volume 1: Mechanisms and Measurements* (Harvard University Press, 2006).
296. G. E. Hill and K. J. McGraw, *Bird Coloration, Volume 2: Function and Evolution*, (Harvard University Press, 2006).
297. R. L. Levien, "Eyeglasses with Spectral Color Shift," (United States Patent 1993).
298. E.-C. Yang and D. Osorio, "Spectral Sensitivities of Photoreceptors and Lamina Monopolar Cells in the Dragonfly, *Hemicordulia Tau*," *J. Comparative Physiol. A* **169**, 663-669 (1991).
299. J. Marshall, T. W. Cronin, and S. Kleinlogel, "Stomatopod Eye Structure and Function: A Review," *Arthropod Struct. Dev.* **36**, 420-448 (2007).
300. D. Osorio and M. Vorobyev, "A Review of the Evolution of Animal Colour Vision and Visual Communication Signals," *Vision Res.* **48**, 2042-2051 (2008).
301. E. A. Widder, M. I. Latz, P. J. Herring, and J. F. Case, "Far Red Bioluminescence from Two Deep-Sea Fishes," *Science* **225**, 512-514 (1984).
302. R. H. Douglas, J. C. Partridge, K. S. Dulai, D. M. Hunt, C. W. Mullineaux, and P. H. Hynninen, "Enhanced Retinal Longwave Sensitivity Using a Chlorophyll-Derived Photosensitizer in *Malacosteus Niger*, a Deep-Sea Dragon Fish with Far Red Bioluminescence," *Vision Res.* **39**, 2817–2832 (1999).
303. R. H. Douglas, C. W. Mullineaux, and J. C. Partridge, "Long-Wave Sensitivity in Deep-Sea Stomiid Dragonfish with Far-Red Bioluminescence: Evidence for a Dietary Origin of the Chlorophyll-Derived Retinal Photosensitizer of *Malacosteus Niger*," *Philos. Trans. R. Soc. Lond. B Biol. Sci.* **355**, 1269-1272 (2000).
304. M. Israelowitz, J.-A. Kwon, S. W. H. Rizvi, C. Gille, and H. P. von Schroeder, "Mechanism of Infrared Detection and Transduction by Beetle *Melanophila Acuminata* in Memory of Jerry Wolken," *J. Bionic Eng.* **8**, 129-139 (2011).

305. E. J. Warrant and N. A. Locket, "Vision in the Deep Sea," *Biol. Rev. Camb. Philos. Soc.* **79**, 671-712 (2004).
306. J. Brauers, N. Schulte, and T. Aach, "Multispectral Filter-Wheel Cameras: Geometric Distortion Model and Compensation Algorithms," *IEEE Trans. Image Processing* **17**, 2368-2380 (2008).
307. B. A. Spiering, "Multi Spectral Imaging System," (United States patent 1997).
308. F. Sigernes, D. A. Lorentzen, K. Heia, and T. Svenøe, "Multipurpose Spectral Imager," *Appl. Opt.* **39**, 3143-3153 (2000).
309. N. Gat, "Imaging Spectroscopy Using Tunable Filters: A Review," *Proc. SPIE* **4056**, 50-64 (2000).
310. J. Z. A. Gilerson, S. Hlaing, I. Ioannou, B. Gross, F. Moshary, and S. Ahmed, "Fluorescence Component in the Reflectance Spectra from Coastal Waters. II. Performance of Retrieval Algorithms," *Opt. Expr.* **16**, 2446-2460 (2008).
311. O. R. Scepanovic, Z. Volynskaya, C. R. Kong, L. H. Galindo, R. R. Dasari, and M. S. Feld, "A Multimodal Spectroscopy System for Real-Time Disease Diagnosis," *Rev. Sci. Instr.* **80**, 043103 (2009).
312. R. Reif, O. A' Amar, and I. J. Bigio, "Analytical Model of Light Reflectance for Extraction of the Optical Properties in Small Volumes of Turbid Media," *Appl. Opt.* **46**, 7317-7328 (2007).
313. M. G. Müller, I. Georgakoudi, Q. Zhang, J. Wu, and M. S. Feld, "Intrinsic Fluorescence Spectroscopy in Turbid Media: Disentangling Effects of Scattering and Absorption," *Appl. Opt.* **40**, 4633-4646 (2001).
314. "Scale of the Universe - Interactive Scale of the Universe Tool", retrieved 2012, <http://scaleofuniverse.com/>.
315. H. Kuze, H. Kinjo, Y. Sakurada, and N. Takeuchi, "Field-of-View Dependence of Lidar Signals by Use of Newtonian and Cassegrainian Telescopes," *Appl. Opt.* **37**, 3128-3132 (1998).
316. K. Stelmaszczyk, M. Dell'Aglio, S. Chudzynski, T. Stacewicz, and L. Wöste, "Analytical Function for Lidar Geometrical Compression Form-Factor Calculations," *Appl. Opt.* **44**, 1323-1331 (2005).
317. Z. Guan, P. Lundin, L. Mei, G. Somesfalean, and S. Svanberg, "Vertical Lidar Sounding of Atomic Mercury and Nitric Oxide In a major Chinese City," *Appl. Phys. B: Lasers and Opt.* **101**, 465-470 (2010).
318. A. Egner, S. Jakobs, and S. W. Hell, "Fast 100-nm Resolution Three-Dimensional Microscope Reveals Structural Plasticity of Mitochondria in Live Yeast," *PNAS* **99**, 3370-3375 (2002).
319. A. Glindemann, R. Abuter, F. Carbognani, *et al.*, "The VLT Interferometer," *Comptes Rendus de l'Académie des Sci. - Series IV - Phys.* **2**, 57-65 (2001).
320. P. J. Napier, D. S. Bagri, B. G. Clark, A. E. E. Rogers, J. D. Romney, A. R. Thompson, and R. C. Walker, "The Very Long-Base-Line Array," *Proc. IEEE* **82**, 658-672 (1994).
321. P. Gorenstein, "Grazing Incidence Telescopes for X-Ray Astronomy," *Opt. Eng.* **51** (2012).
322. H. V. Mudrakola, K. Zhang, and B. Cui, "Optically Resolving Individual Microtubules in Live Axons," *Structure (London, England)* **17**, 1433-1441 (2009).
323. M. Mirmehdi, X. Xie, and J. Suri, *Handbook of Texture Analysis* (Imperial College Press, London, UK, 2008).
324. M. G. Nichols, E. L. Hull, and T. H. Foster, "Design and Testing of a White-Light, Steady-State Diffuse Reflectance Spectrometer for Determination of Optical Properties of Highly Scattering Systems," *Appl. Opt.* **36**, 93-104 (1997).
325. A. Johansson, J. Axelsson, S. Andersson-Engels, and J. Swartling, "Realtime Light Dosimetry Software Tools for Interstitial Photodynamic Therapy of the Human Prostate," *Med. Phys.* **34**, 4309 (2007).
326. A. V. Klaus, V. L. Kulasekera, and V. Schawaroch, "Three-Dimensional Visualization of Insect Morphology Using Confocal Laser Scanning Microscopy," *J. Microsc.* **212**, 107-121 (2003).
327. P. J. Rodrigo and C. Pedersen, "Field Performance of an All-Semiconductor Laser Coherent Doppler Lidar," *Opt. Lett.* **37**, 2277-2279 (2012).
328. M. Gustafsson and M. Sebesta, "Refractometry of Microscopic Objects with Digital Holography," *Appl. Opt.* **43**, 4796-4801 (2004).
329. S. A. Boppart, "Optical Coherence Tomography: Technology and Applications for Neuroimaging," *Psychophysiology* **40**, 529-541 (2003).
330. G. P. Arumov, A. V. Bukharin, V. M. Linkin, *et al.*, "Compact Aerosol Lidar for Martian Atmosphere Monitoring According to NASA "Mars Surveyor Program '98"," in *6th Internat. Conference on Industrial Lasers and Laser Applications*, V. Y. Panchenko and V. S. Golubev, eds. (SPIE, Bellingham, 1999), pp. 494-500.
331. A. R. Bahrapour and A. A. Askari, "Fourier-Wavelet Regularized Deconvolution (ForWaRD) for Lidar Systems Based on TEA-CO<sub>2</sub> Laser," *Opt. Comm.* **257**, 97-111 (2006).
332. S. A. Combes, D. E. Rundle, J. M. Iwasaki, and J. D. Crall, "Linking Biomechanics and Ecology through Predator-Prey Interactions: Flight Performance of Dragonflies and Their Prey," *J. Exp. Biol.* **215**, 903-913 (2012).
333. T. Rodríguez, P. Sturm, P. Gargallo, *et al.*, "Photorealistic 3D Reconstruction from Handheld Cameras," *Machine Vision and Applications* **16**, 246-257 (2005).
334. E. H. Synge, "A Method of Investigating the Higher Atmosphere," *Philosophical Magazine* **9**, 1014-1020 (1930).

335. R. O. Prum, J. A. Cole, and R. H. Torres, "Blue Integumentary Structural Colours in Dragonflies (Odonata) are not Produced by Incoherent Tyndall Scattering," *J. Exp. Biol.* **207**, 3999-4009 (2004).
336. D. K. M. John G. Proakis, *Digital Signal Processing*, 4th Ed. ed., (Prentice Hall, 2006).
337. D. L. Flannery and J. L. Horner, "Fourier Optical Signal Processors," *Proc. IEEE* **77**, 1511-1527 (1989).
338. H. M. Shapiro, *Practical Flow Cytometry*, 4th ed., (Wiley-Liss, 2003).
339. T. A. Reichardt, S. E. Bisson, R. W. Crocker, and T. J. Kulp, "Analysis of Flow-Cytometer Scattering and Fluorescence Data to Identify Particle Mixtures," 69450R in *Optics and Photonics in Global Homeland Security IV*, (SPIE, **6945**, 2008).
340. A. Gogoi, L. J. Borthakur, A. Choudhury, G. A. Stanciu, and G. A. Ahmed, "Detector Array Incorporated Optical Scattering Instrument for Nephelometric Measurements on Small Particles," *Measurement Science and Technology* **20**, 095901 (2009).
341. H. Oltmann, J. Reimann, and S. Will, "Wide-Angle Light Scattering (WALS) for Soot Aggregate Characterization," *Combustion and Flame* **157**, 516-522 (2010).
342. W. H. Aughey and F. J. Baum, "Angular-Dependence Light Scattering-a High-Resolution Recording Instrument for the Angular Range 0.05-140°," *J. Opt. Soc. Am.* **44** (1954).
343. J. D. Watson and F. H. C. Crick, "Molecular Structure of Nucleic Acids - a Structure for Deoxyribose Nucleic Acid," *Nature* **171**, 737-738 (1953).
344. H. Tompkins and E. A. Irene, *Handbook of Ellipsometry*, (William Andrew, 2006).
345. H. Arwin, R. Magnusson, J. Landin, and K. Järrendahl, "Chirality-Induced Polarization Effects in the Cuticle of Scarab Beetles: 100 Years after Michelson," *Philos. Mag.* **92**, 1583-1599 (2012).
346. F. Chandezon, "Nord.Sud - Spectra 2009," *Reflète de la physique*, *Reveu de la Societé Française de Physique* (2009).
347. K. J. McGraw, "Multiple UV Reflectance Peaks in the Iridescent Neck Feathers of Pigeons," *Naturwissenschaften* **91**, 125-129 (2004).
348. D. J. Brink and N. G. v. d. Berg, "Structural Colours from the Feathers of the Bird *Bostrychia Hagedash*," *J. Phys. D: Appl. Phys.* **37**, 813-818 (2004).
349. S. M. Doucet, M. D. Shawkey, G. E. Hill, and R. Montgomerie, "Iridescent Plumage in Satin Bowerbirds: Structure, Mechanisms and Nanostructural Predictors of Individual Variation in Colour," *J. Exp. Biol.* **209**, 380-390 (2006).
350. E. Bard, G. Raisbeck, F. Yiou, and J. Jouzel, "Solar Irradiance During the Last 1200 Years Based on Cosmogenic Nuclides," *Tellus Series B-Chem. and Physical Meteorology* **52**, 985-992 (2000).
351. B. van Geel, O. M. Raspopov, H. Renssen, J. van der Plicht, V. A. Dergachev, and H. A. J. Meijer, "The Role of Solar Forcing Upon Climate Change," *Quaternary Science Reviews* **18**, 331-338 (1999).
352. V. F. Polcaro and A. Martocchia, "Supernovae Astrophysics from Middle Age Documents," in *Proc. the IAU Symp. 230*, (2005).
353. P. A. Rosen, S. Hensley, I. R. Joughin, F. K. Li, S. N. Madsen, E. Rodriguez, and R. M. Goldstein, "Synthetic Aperture Radar Interferometry," *Proc. IEEE* **88**, 333-382 (2000).
354. H. McNairn, C. Champagne, J. Shang, D. Holmström, and G. Reichert, "Integration of Optical and Synthetic Aperture Radar (SAR) Imagery for Delivering Operational Annual Crop Inventories," *Isprs J. Photogrammetry and Remote Sensing* **64**, 434-449 (2009).
355. J.-N. Juang, *Applied System Identification*, (Prentice Hall, 1993).
356. M. M. R. Isermann, *Identification of Dynamic Systems: An Introduction with Applications*, (Springer, 2010).
357. K. J. Keesman, *System Identification: An Introduction*, (Springer, 2011).
358. C. af Klinteberg, A. M. Enejder, I. Wang, S. Andersson-Engels, S. Svanberg, and K. Svanberg, "Kinetic Fluorescence Studies of 5-Aminolaevulinic Acid-Induced Protoporphyrin IX Accumulation in Basal Cell Carcinomas," *J. Photochem. Photobiol. B* **49**, 120-128 (1999).
359. H. Heyerdahl, I. Wang, D. L. Liu, *et al.*, "Pharmacokinetic Studies on 5-Aminolevulinic Acid-Induced Protoporphyrin IX Accumulation in Tumours and Normal Tissues," *Cancer Lett.* **112**, 225-231 (1997).
360. M. Shirmanova, E. Zagaynova, M. Sirotkina, *et al.*, "In Vivo Study of Photosensitizer Pharmacokinetics by Fluorescence Transillumination Imaging," *J. Biomed. Opt.* **15**, 048004 (2010).
361. R. R. Galigekere, M. B. Sørensen, R. Nayak, and P. J. Rao, "Method and Apparatus for *in Vitro* Analysis of the Physical Response of Blood-Vessels to Vaso-Active Agents," US 2011/0135171 A1 (United States Patent 2009).
362. J. Spigulis, A. Lihachev, and R. Erts, "Imaging of Laser-Excited Tissue Autofluorescence Bleaching Rates," *Appl. Opt.* **48**, D163-D168 (2009).
363. S. Takatani, P. W. Cheung, and E. A. Ernst, "A Noninvasive Tissue Reflectance Oximeter, an Instrument for Measurement of Tissue Hemoglobin Oxygen Saturation *in Vivo*," *Ann. Biomed. Eng.* **8**, 1-15 (1980).
364. R. Kern, N. Boeddeker, L. Dittmar, and M. Egelhaaf, "Blowfly Flight Characteristics are Shaped by Environmental Features and Controlled by Optic Flow Information," *J. Exp. Biol.* **215**, 2501-2514 (2012).
365. J. F. Windmill, J. Sœur, and D. Robert, "The Next Step in Cicada Audition: Measuring Pico-Mechanics in the Cicada's Ear," *J. Exp. Biol.* **212**, 4079-4083 (2009).

366. J. Casas, S. Bacher, J. Tautz, R. Meyhöfer, and D. Pierre, "Leaf Vibrations and Air Movements in a Leafminer–Parasitoid System," *Biological control* **11**, 147–153 (1998).
367. B. Ward, A. C. Baker, and V. F. Humphrey, "Nonlinear Propagation Applied to the Improvement of Resolution in Diagnostic Medical Ultrasound," *J. Acoust. Soc. Am.* **101**, 143-154 (1997).
368. D. H. Simpson, C. T. Chin, and P. N. Burns, "Pulse Inversion Doppler: A New Method for Detecting Nonlinear Echoes from Microbubble Contrast Agents," *IEEE Trans. Ultrasonics Ferroelectrics and Frequency Control* **46**, 372-382 (1999).
369. F. A. Duck, "Nonlinear Acoustics in Diagnostic Ultrasound," *Ultrasound Med. Biol.* **28**, 1-18 (2002).
370. T. Fujii and T. Fukuchi, *Laser Remote Sensing*, (CRC Press, 2005).
371. P. A. De Beule, C. Dunsby, N. P. Galletly, *et al.*, "A Hyperspectral Fluorescence Lifetime Probe for Skin Cancer Diagnosis," *Rev. Sci. Instr.* **78**, 123101 (2007).
372. T. Polivka, S. P. Balashov, P. Chabera, E. S. Imasheva, A. Yartsev, V. Sundstrom, and J. K. Lanyi, "Femtosecond Carotenoid to Retinal Energy Transfer in Xanthorhodopsin," *Biophysical J.* **96**, 2268-2277 (2009).
373. X. He, J. M. Dahlström, R. Rakowski, C. M. Heyl, A. Persson, J. Mauritsson, and A. L’Huillier, "Interference Effects in Two-Color High-Order Harmonic Generation," *Phys. Rev. A* **82**, 033410 (2010).
374. T. Remetter, P. Johnsson, J. Mauritsson, *et al.*, "Attosecond Electron Wave Packet Interferometry," *Nature Phys.* **2**, 323-326 (2006).
375. K. Vishwanath, B. Pogue, and M.-A. Mycek, "Quantitative Fluorescence Lifetime Spectroscopy in Turbid Media: Comparison of Theoretical, Experimental and Computational Methods," *Phys. Med. Biol.* **47**, 3387 (2002).
376. W. P. Hooper and G. M. Frick, "Lidar Detected Spike Returns," *J. Appl. Remote Sensing* **4** (2010).
377. R. Lawl, M. J. Plank, A. James, and J. L. Blanchard, "Size-Spectra Dynamics from Stochastic Predation and Growth of Individuals," *Ecol.* **90**, 802–811 (2009).
378. E. Benoît and M.-J. Rochet, "A Continuous Model of Biomass Size Spectra Governed by Predation and the Effects of Fishing on Them," *J. Theor. Biol.* **226**, 9-21 (2004).
379. S. Volker, "Hole-Burning Spectroscopy," *Ann. Rev. Phys. Chem.* **40**, 499-530 (1989).
380. M. Nilsson, L. Rippe, S. Kröll, R. Klieber, and D. Suter, "Hole-Burning Techniques for Isolation and Study of Individual Hyperfine Transitions in Inhomogeneously Broadened Solids Demonstrated in Pr<sup>3+</sup>:Y<sub>2</sub>SiO<sub>5</sub>," *Phys. Rev. B* **70**, 214116 (2004).
381. A. Wiedensohler, W. Birmili, A. Nowak, *et al.*, "Particle Mobility Size Spectrometers: Harmonization of Technical Standards and Data Structure to Facilitate High Quality Long-Term Observations of Atmospheric Particle Number Size Distributions," *Atmos. Meas. Tech. Discuss.* **3**, 5521-5587 (2010).
382. S. Tubasum, D. Thomsson, R. Cogdell, I. Scheblykin, and T. Pullerits, "Polarization Single Complex Imaging of Circular Photosynthetic Antenna," *Photosynth. Res.* **111**, 41-45 (2012).
383. J. Craven-Jones, M. W. Kudenov, Maryn G. Stapelbroek, and E. L. Dereniak, "Infrared Hyperspectral Imaging Polarimeter Using Birefringent Prisms," *Appl. Opt.* **50**, 1170-1185 (2011).
384. J. S. Tyo, D. L. Goldstein, D. B. Chenault, and J. A. Shaw, "Review of Passive Imaging Polarimetry for Remote Sensing Applications," *Appl. Opt.* **45**, 5453-5469 (2006).
385. S. Andersson-Engels, R. Berg, K. Svanberg, and S. Svanberg, "Multi-Colour Fluorescence Imaging in Connection with Photodynamic Therapy of  $\delta$ -amino Levulinic Acid (ALA) Sensitised Skin Malignancies," *Bioimaging* **3**, 134-143 (1995).
386. N. J. Pust and J. A. Shaw, "Dual-Field Imaging Polarimeter Using Liquid Crystal Variable Retarders," *Appl. Opt.* **45**, 5470-5478 (2006).
387. J. R. Wallace BA, *Modern Technique for Circular Dichroism and Synchrotron Radiation Circular Dichroism Spectroscopy*, (Amsterdam: IOS Press, 2009).
388. S. Breugnot and P. Clemenceau, "Modeling and Performances of a Polarization Active Imager at Lambda = 806 nm," *Opt. Eng.* **39**, 2681-2688 (2000).
389. R. Muheim, "Behavioural and Physiological Mechanisms of Polarized Light Sensitivity in Birds," *Proc. R. Soc. B* **366**, 763-771 (2011).
390. D. V. Gábor Horváth, *Polarized Light in Animal Vision: Polarization Patterns in Nature* (Springer, 2004).
391. I. Gusachenko, G. Latour, and M.-C. Schanne-Klein, "Polarization-Resolved Second Harmonic Microscopy in Anisotropic Thick Tissues," *Opt. Expr.* **18**, 19339-19352 (2010).
392. N. J. Pust and J. A. Shaw, "Digital All-Sky Polarization Imaging of Partly Cloudy Skies," *Appl. Opt.* **47**, 190-198 (2008).
393. S. Yoshioka and S. Kinoshita, "Direct Determination of the Refractive Index of Natural Multilayer Systems," *Phys. Rev. E* **83**, 051917 (2011).
394. H. Arwin, R. Magnusson, J. Landin, and K. Jarrendahl, "Chirality-Induced Polarization Effects in the Cuticle of Scarab Beetles: 100 Years after Michelson," *Philosophical Magazine* **92**, 1583-1599 (2012).
395. J. Karimi, M. Hassani-Kakhki, and M. M. Awal, "Identifying Thrips (*Insecta: Thysanoptera*) Using DNA Barcodes," *J. Cell and Molecular Research* **2**, 35-41 (2010).
396. J. P. Kratochvil and C. Smart, "Calibration of Light-Scattering Instruments Absolute Angular Intensity Measurements on Mie Scatterers," *J. Colloid Sci.* **20**, 875-892 (1965).

397. H. E. M. Alden, and S. Svanberg, "Remote Measurement of Atmospheric Mercury Using Differential Absorption Lidar," *Opt. Lett.* **7**, 221-223 (1982).
398. M. Andersson, R. Grönlund, L. Persson, M. Sjöholm, K. Svanberg, and S. Svanberg, "Laser Spectroscopy of Gas in Scattering Media at Scales Ranging from Kilometers to Millimeters," *Laser Phys.* **17**, 893-902 (2007).
399. J. I. Rodríguez-Fernández, C. J. B. D. C. C. Pasquini, K. M. G. d. Lima, and M. O. M. G. G. C. Arizaga, "Barcoding without DNA? Species Identification Using near Infrared Spectroscopy," *Zootaxa* **2933**, 46-54 (2011).
400. H. B. Manning, G. T. Kennedy, D. M. Owen, *et al.*, "A Compact, Multidimensional Spectrofluorometer Exploiting Supercontinuum Generation," *J. Biophot.* **1**, 494-505 (2008).
401. M. W. Kudenov, M. J. Escuti, E. L. Dereniak, and K. Oka, "White-Light Channeled Imaging Polarimeter Using Broadband Polarization Gratings," *Appl. Opt.* **50**, 2283-2293 (2011).
402. A. Runemark, K. Sagonas, and E. Svensson, "Dietary Niche Divergence Drives Changes in Morphology and Feeding Performance Among Mainland and Islet Lizard Population," (To appear).
403. J. S. Tyo, E. N. Pugh, and N. Engheta, "Colorimetric Representations for Use with Polarization-Difference Imaging of Objects in Scattering Media," *J. Opt. Soc. Am. A - Opt. Imag. Sci. Vision* **15**, 367-374 (1998).
404. M. Vedel, N. Lechocinski, and S. Breugnot, "Compact and Robust Linear Stokes Polarization Camera," *EPJ Web Conferences* **5**, 01005 (2010).
405. E. Stamatatos, "A Survey of Modern Authorship Attribution Methods," *J. Am. Soc. Information Sci. Technol.* **60**, 538-556 (2009).
406. D. Jurafsky and J. H. Martin, *Speech and Language Processing*, 2nd ed., (Pearson Prentice Hall, 2008).
407. T. W. Anderson, *An Introduction to Multivariate Statistical Analysis*, 3rd ed., Wiley Series in Probability and Statistics, (John Wiley, Hoboken, NJ, 2003).
408. A. C. Rechner, *Methods of Multivariate Analysis*, 2nd ed., (Wiley Interscience, New York, 2002).
409. K. R. Beebe and B. R. Kowalski, "An Introduction to Multivariate Calibration and Analysis," *Anal. Chem.* **59**, 1007A-1017A (1987).
410. T. J. Farrell and M. S. Patterson, "A Diffusion Theory Model of Spatially Resolved, Steady-State Diffuse Reflectance for the Noninvasive Determination of Tissue Optical Properties *in Vivo*," *Med. Phys.* **19**, 879-888 (1992).
411. J. Wu, M. S. Feld, and R. P. Rava, "Analytical Model for Extracting Intrinsic Fluorescence in Turbid Media," *Appl. Opt.* **32**, 3585-3595 (1993).
412. S. L. J. Craig M. Gardner, and Ashley J. Welch, "Fluorescence Spectroscopy of Tissue: Recovery of Intrinsic Fluorescence from Measured Fluorescence," *Appl. Opt.* **35**, 1780-1792 (1996).
413. A. Runemark, M. Brydegaard, and E. I. Svensson, "Predation Release Facilitates Island Gigantism in Lizards and Increases Population Divergence in Phenotypic Traits," to appear (2012).
414. R. Feltens, R. Gerner, S. Kalkhof, H. Groger-Arndt, and M. von Bergen, "Discrimination of Different Species from the Genus *Drosophila* by Intact Protein Profiling Using Matrix-Assisted Laser Desorption Ionization Mass Spectrometry," *BMC Evol. Biol.* **10**, 95 (2010).
415. M. Salman, "Optically Remote Sensing Methods for Insect Monitoring," Masters thesis (Lund University, Lund Reports on Atomic Physics, To appear).
416. O. E. Rhodes and R. K. Chesser, *Population Dynamics in Ecological Space and Time*, (University of Chicago Press, 1996).
417. R. Schoen, *Dynamic Population Models*, (Springer, 2007).
418. J. Pastor, *Mathematical Ecology of Populations and Ecosystems*, (Wiley-Blackwell, 2008).
419. H. R. Thieme, *Mathematics in Population Biology*, (Princeton Series in Theoretical and Computational Biology, Princeton University Press, 2003).
420. L. Moral and A. F. Pacheco, "Algebraic Approach to the Radioactive Decay Equations," *Am. J. Phys.* **71**, 684 (2003).
421. D. Yuan and W. Kernan, "Explicit Solutions for Exit-Only Radioactive Decay Chains," *J. Appl. Phys.* **101**, 094907 (2007).
422. W. Windig and B. Antalek, "Direct Exponential Curve Resolution Algorithm (DECRA) • a Novel Application of the Generalized Rank Annihilation Method for a Single Spectral Mixture Data Set with Exponentially Decaying Contribution Profiles," *Chemometr. Intell. Lab.* **37**, 241-254 (1997).
423. J. Sandsten, P. Weibring, H. Edner, and S. Svanberg, "Real-Time Gas-Correlation Imaging Employing Thermal Background Radiation," *Opt. Expr.* **6**, 92-103 (2000).
424. J. T. Zoueu, G. L. Loum, T. C. Haba, M. Brydegaard, and H. Menan, "Optical Microscope Based on Multispectral Imaging Applied to Plasmodium Diagnosis," *J. Appl. Sci.* **8**, 2711-2717 (2008).
425. B. K. Wilson, M. R. Behrend, M. P. Horning, and M. C. Hegg, "Detection of Malarial Byproduct Hemozoin Utilizing Its Unique Scattering Properties," *Opt. Expr.* **19**, 12190 (2011).
426. W. Becker, "Fluorescence Lifetime Imaging – Techniques and Applications," *J. Microsc.* **247**, 119-136 (2012).
427. F. Alves, C. Dullin, J. Napp, *et al.*, "Concept of a Selective Tumour Therapy and Its Evaluation by near-Infrared Fluorescence Imaging and Flat-Panel Volume Computed Tomography in Mice," *European J. Radiology* **70**, 286-293 (2009).

428. A. Svendsen, U. J. Lorenz, O. V. Boyarkin, and T. R. Rizzo, "A New Tandem Mass Spectrometer for Photofragment Spectroscopy of Cold, Gas-Phase Molecular Ions," *Rev. Sci. Instr.* **81**, 073107 (2010).
429. M. C. Benfield, P. Grosjean, P. F. Culverhouse, *et al.*, "Rapid Research on Automated Plankton Identification," *Oceanography* **20**, 172-187 (2007).
430. S. K. Jericho, J. Garcia-Sucerquia, W. B. Xu, M. H. Jericho, and H. J. Kreuzer, "Submersible Digital in-Line Holographic Microscope," *Rev. Sci. Instr.* **77** (2006).
431. R. S. Thorpe and M. Richard, "Evidence That Ultraviolet Markings are Associated with Patterns of Molecular Gene Flow," *PNAS* **98**, 3929-3934 (2001).
432. A. Runemark, B. Hansson, M. Ljungqvist, M. Brydegaard, and E. I. Svensson, "Has the Inbreeding Load for a Condition-Dependent Sexual Signalling Trait Been Purged in Insular Lizard Populations?," *Mol. Ecol.* (To appear).
433. T.-H. Chiou, A. R. Place, R. L. Caldwell, N. J. Marshall, and T. W. Cronin, "A Novel Function for a Carotenoid: Astaxanthin Used as a Polarizer for Visual Signalling in a Mantis Shrimp," *J. Exp. Biol.* **215**, 584-589 (2012).
434. Á. Egri, M. Blahó, G. Kriska, R. Farkas, M. Gyurkovszky, S. Ákesson, and G. Horváth, "Polarotactic Tabanids Find Striped Patterns with Brightness and/or Polarization Modulation Least Attractive: An Advantage of Zebra Stripes," *J. Exp. Biol.* **215**, 736-745 (2012).
435. R. C. Goris, Y. Atobe, M. Nakano, T. Hisajima, K. Funakoshi, and T. Kadota, "The Microvasculature of Python Pit Organs: Morphology and Blood Flow Microkinetics," *Microvascular Res.* **65**, 179-185 (2003).
436. L. M. Mathger and R. T. Hanlon, "Malleable Skin Coloration in Cephalopods: Selective Reflectance, Transmission and Absorbance of Light by Chromatophores and Iridophores," *Cell Tissue Res.* **329**, 179-186 (2007).
437. R. T. Hanlon, C. C. Chiao, L. M. Mathger, A. Barbosa, K. C. Buresch, and C. Chubb, "Cephalopod Dynamic Camouflage: Bridging the Continuum between Background Matching and Disruptive Coloration," *Proc. R. Soc. B* **364**, 429-437 (2009).
438. S. Johnsen and H. M. Sosik, "Cryptic Coloration and Mirrored Sides as Camouflage Strategies in near-Surface Pelagic Habitats: Implications for Foraging and Predator Avoidance," *Limnol. Oceanography* **48**, 1277-1288 (2003).

# PAPERS

**Simulation of multispectral X-ray imaging scenarios by  
Wien shift optical spectroscopy**

M. Brydegaard and S. Svanberg

*American Journal of Physics* **78**:170-175 (2010).

# Simulation of multispectral x-ray imaging scenarios by Wien shift optical spectroscopy

M. Brydegaard<sup>a)</sup> and S. Svanberg

Atomic Physics Division, Lund University, P.O. Box 118, SE-22 100 Lund, Sweden

(Received 22 December 2008; accepted 24 September 2009)

The acquisition of multispectral x-ray images and the treatment of such data are essential for understanding many devices that we encounter in everyday life. Examples include computerized tomography in hospitals and scanners at airports. X-ray devices remain impractical for undergraduate laboratories because of their considerable cost and the risk of exposure to ionizing radiation. One way to acquire spectral information and thus constituent-discriminating data in x-ray imaging is to alter the spectral contents of the illuminating x-ray source, which can be achieved by changing the x-ray tube voltage and thus energetically displacing the bremsstrahlung. A similar effect occurs in the emission from a black-body radiator in the optical and infrared regions when altering the temperature. We illustrate how to simulate the x-ray scenario with a webcam and an ordinary light bulb. Insight into how chemical and physical information regarding objects can be obtained in multispectral imaging supported by multivariate analysis is gained. © 2010 American Association of Physics Teachers.

[DOI: 10.1119/1.3248356]

## I. INTRODUCTION

The spectral contents in reflected light, that is, the colors of objects around us, helps us to distinguish objects and to determine their composition. X-ray spectra are particularly effective for determining the atomic composition using the characteristic lines, the energy of which is related to the nuclear charge.<sup>1</sup> For 2D and 3D x-ray images the bremsstrahlung from a metallic anode will yield a particular distribution of x-ray energies depending on the applied voltage. X-ray emission curves are shown in Fig. 1(a) for 10, 20, and 30 kV (adapted from Ref. 2), where the short wavelength cut-off moves to the left as the voltage is increased. Higher voltages are typically used in medical imaging.<sup>3</sup> If the x-ray attenuation coefficients have a different energy dependence, which is the case for bone, muscle, and blood<sup>4</sup> [Fig. 1(b)], and the illumination weights different parts of the attenuation curves differently, materials can be discriminated from each other. The bremsstrahlung [Fig. 1(a)] contains shorter wavelengths with increasing tube voltage, and thus the spectral weighting will be different. A multispectral image can be considered to consist of  $N$  “color” channels, which can be represented by an  $N$ -dimensional color space.<sup>5–7</sup> If object  $B$ , such as bone, has a different atomic composition from object  $M$ , such as muscle, the attenuation spectra are different as shown in Fig. 1(b), and the pixels or voxels of the two objects will be represented by swarms of data points separated in x-ray color space [Fig. 1(c)]. Projection of the values from  $B$  and  $M$  on a single axis might result in data overlap and prohibit distinction. For this reason we cannot distinguish blood from muscle in a traditional x-ray image that is taken with the bremsstrahlung distribution from the x-ray tube voltage. Similarly, we would not be able to distinguish toothpaste from explosives in a travel bag.

In our natural vision color space, the axes describe the contribution that the light from an object makes to each of our visual spectral channels: Red, green, and blue. Each axis represents the spectral response of a different type of receptor in the eye. For instance, the perceived reddish color from an object is given by

$$\text{red}_{\text{obj}} = \int_0^{\infty} E(\lambda)R_{\text{obj}}(\lambda)S_{\text{red}}(\lambda)d\lambda, \quad (1)$$

where  $\text{red}_{\text{obj}}$  is the perceived red color,  $E(\lambda)$  is the illumination emission spectrum,  $R_{\text{obj}}(\lambda)$  is the object reflectance spectrum,  $S_{\text{red}}(\lambda)$  is the spectral sensitivity of the red color channel, and  $\lambda$  is the wavelength.

We can provide spectral channels having either different  $E$  functions or different  $S$  functions because  $E$  and  $S$  enter Eq. (1) in an equivalent way. “What does the object look like when illuminated by red light?” This intriguing question is asked in certain everyday situations.

In multispectral reflectance imaging,<sup>8–11</sup> such as encountered in satellite earth resource imaging, a number of well-defined spectral bands are used for data recording. Present-day hyperspectral (imaging spectrometer) instruments have 128 or more spectral channels. If we use well-defined quasi-monochromatic spectral bands, the spectral recordings and subsequent image processing become conceptually simple because they relate to normal spectroscopy but with a large number of spatial points. Human vision or CCD color photography uses a small number of color channels, which are not so well defined. Clearly, spectral information can be obtained using broad and complex spectral distribution bands if they differ sufficiently from each other. Such “holistic” spectroscopy is well adapted for analysis using multivariate analysis techniques, such as principal component analysis.<sup>12–15</sup> A spectrum can be expanded into a number of principal component spectra, which are orthogonal to each other. Following this line of reasoning, x-ray multispectral imaging can be performed by using bremsstrahlung produced by three tube voltages  $U_1$ ,  $U_2$ , and  $U_3$  (which could be 30, 60, and 90 kV, corresponding to maximum photon energies of 30, 60, and 90 keV, respectively), providing measures from three generalized spectral channels<sup>5–7</sup> as shown in Fig. 1(c). Here the three axes in the spectral space represent illumination by the three tube voltages. The illumination spectra are quite different. Also we might choose to express the sensitivity  $S(\lambda)$  or the absorption spectrum as a function of tube voltage rather than wavelength.

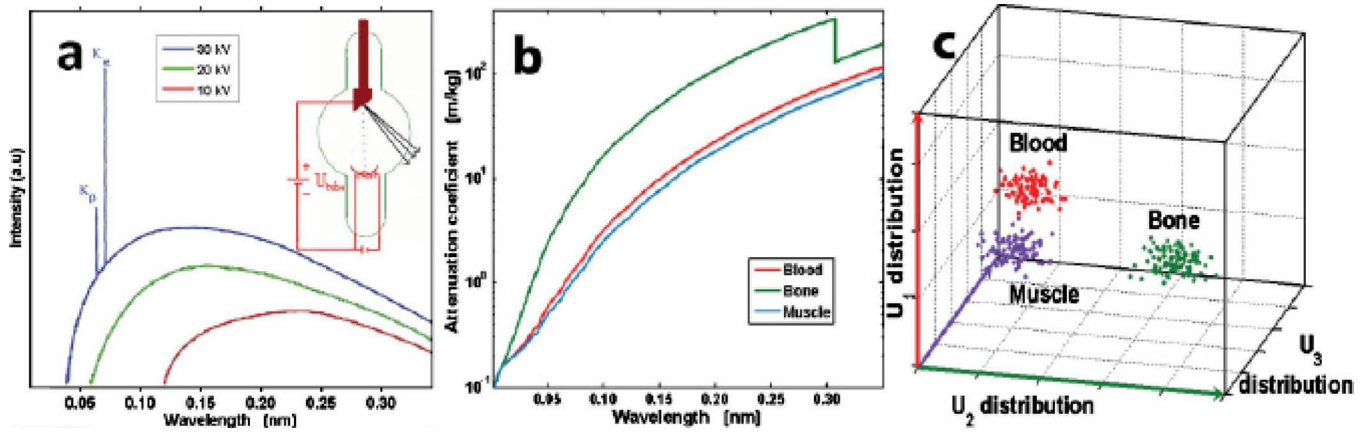


Fig. 1. (a) X-ray tube and three bremsstrahlung spectra generated by different tube voltages (adapted from Ref. 2). (b) X-ray attenuation spectra for different substances (data from Ref. 3). (c) Location of data points from several objects in an x-ray color space expanded by several tube voltages.

X-ray equipment is generally costly, and several safety issues have to be taken into account to minimize the exposure to unwanted ionizing radiation. These issues make it difficult to provide hands-on demonstrations in x-ray imaging, which is commonly encountered in medical diagnostics and security screening. One way to simulate the x-ray scenario is to take advantage of the Wien shift that blackbody radiators exhibit when their temperature changes. The conceptual similarity between bremsstrahlung and Planck radiation spectra is the theme of this paper.

The spectral content of a common filament bulb is given by the Planck distribution

$$E(\lambda, T) = \frac{2hc^2}{\lambda^5 \left( e^{\frac{hc}{\lambda kT}} - 1 \right)}, \quad (2)$$

where  $h$  is Planck's constant,  $c$  is the speed of light,  $k$  is Boltzmann's constant, and  $T$  is the radiator temperature.

A digital reflectance image in the light of a blackbody radiator is the product of the reflectance spectrum  $R(\lambda)$ ,  $E(\lambda, T)$ , and the sensitivity of the image chip  $S(\lambda)$  according to Eq. (1). The wavelength of the peak intensity,  $\lambda_{\max}$ , is given by Wien's displacement law,

$$\lambda_{\max}(T) = \frac{b}{T}, \quad (3)$$

where  $b$  is Wien's displacement constant. Integrating the Planck distribution over all wavelengths gives the total emitted intensity according to Stefan's law,

$$P_{\text{phot}} = \epsilon \sigma A T^4 \approx P_{\text{el}} = UI, \quad (4)$$

where  $P_{\text{phot}}$  is the radiated power,  $\epsilon$  is the emissivity,  $\sigma$  is the Stefan-Boltzmann's constant,  $A$  is the radiator area,  $P_{\text{el}}$  is the applied electrical power,  $U$  is the filament voltage, and  $I$  is the filament current. When imaging a blackbody illuminated scene, the temperature range of the blackbody will be limited by the lower emission for low temperatures and the filament melting point at high temperatures. The resistivity for metals depends almost linearly on temperature in the operational range of most blackbody emitters,

$$R = \frac{U}{I} \approx R_0 + r(T - T_0), \quad (5)$$

where  $R$  is the filament resistance,  $R_0$  the resistance at room temperature,  $r$  the thermal resistance coefficient, and  $T_0$  is the temperature of the room. Equation (6) to be introduced later, will be important for determining the absolute temperatures of blackbody emitters.

## II. EXPERIMENTAL SETUP

A schematic diagram of the experimental setup used for bremsstrahlung simulation employing a Planck radiator is shown in Fig. 2. A manually variable power supply (0–15  $V_{\text{dc}}$  and 2 A) is used to change the current to a 12 V and 3 W incandescent light bulb and thereby the temperature of the filament and the emitted spectrum. Images of the same scene are taken with different illumination temperatures. The voltage and current are measured for each image. The images are acquired using an ordinary webcam with a PixArt PAC207 imager. We also used another CMOS imager FillFactory IBIS5-A-1300 mounted in a Bessler camera. Both imagers are operated in black and white mode with the infrared blocking filters removed. Isolation from ambient light is provided by mounting the equipment onto the bottom of a bucket made of black plastic, and the bucket is placed upside down over the sample to be studied.

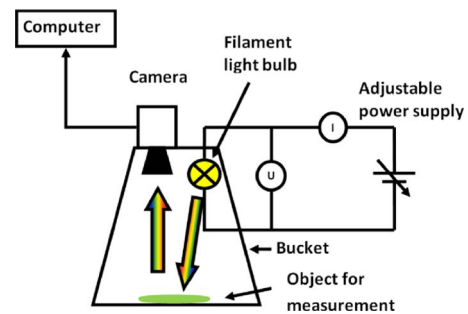


Fig. 2. Setup for Wien shift imaging. A bucket provides optical isolation for the experiment. Simultaneous recording of current and voltage provides an estimation of absolute temperatures.

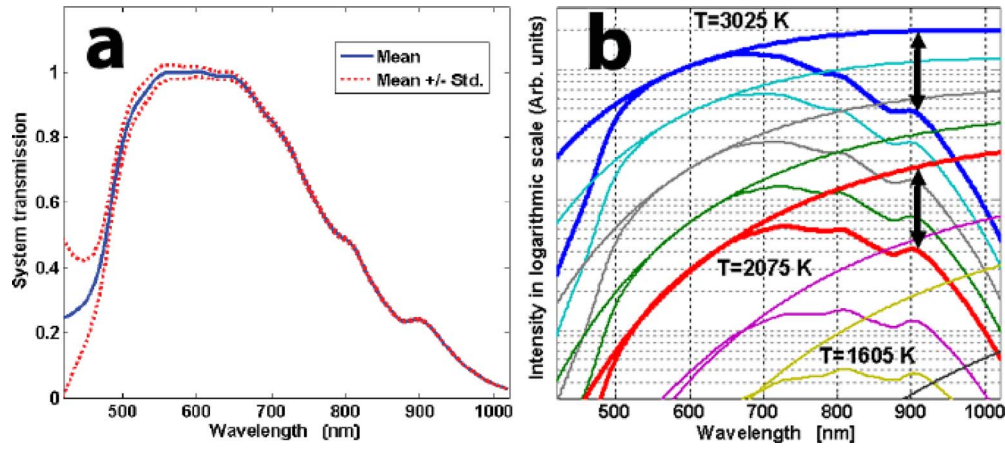


Fig. 3. (a) The absolute filament temperature is determined by minimizing the variance among the system transmission spectra, which are known to be the same. (b) Computed and actual filament emissions spectra on a log scale. (Equidistance at different temperatures is indicated by the arrows at a particular wavelength, showing that the system transmission measured for the two temperatures is the same—it is a system invariant.)

The total intensity will change considerably more than the spectral contents when varying the power. This fact is partly compensated by the automatic gain control of the camera, which adjusts the exposure time and gain. The Wien shift varies with  $P_{el}^{-1/4}$ , and thus the spectral content varies most for small  $P_{el}$ . If we represent a reflectance spectrum as a function of filament power, then because most of the information will come from small  $P_{el}$ , the current sweeping steps for small  $P_{el}$  should be the smallest.

### III. INSTRUMENT VERIFICATION

First the illumination source was characterized. The filament was swept over a range of temperatures while recording the voltage and current. The corresponding emission spectra  $W(n, \lambda)$  were recorded by a separate compact integrated spectrometer (Ocean Optics USB2000). To determine the absolute temperature of the filament, we need to know the coefficients in the expression  $T = p_1 R + p_2$ . A given temperature will correspond to a given theoretical emission spectrum. The actual emission will be the same or lower because the emitted power is decreased due to the emissivity being smaller than one and the bulk absorption of the concealing glass. The combined glass absorption spectrum and spectrometer sensitivity is unknown but is taken to be the same for each measurement. The thermal model parameters were found by minimizing the variance  $\sigma$ , among the spectral transfer functions of the system  $W/E$ , consisting of the emissivity, glass absorption, and the spectral sensitivity of the spectrometer [Fig. 3(a)]. We find  $p_1$  and  $p_2$  by numerically minimizing the value of  $Q$  defined by

$$Q(p_1, p_2) = \sum_{\lambda=400}^{1100} \sigma_n \left( \frac{W_n(\lambda)}{E(p_1 R_n + p_2, \lambda)} \right), \quad (6)$$

where  $E$  is the calculated Planck distribution,  $W_n$  is the measured distribution, and  $n$  labels the  $n$ th pair of measurements of  $W$  and  $R$ . The minimization is performed iteratively using MATLAB. Once the model parameters are determined, the measured spectra can be compared with the Planck distribution in Eq. (2), as shown in Fig. 3(b), where on the vertical logarithmic scale, the difference between the measured and computed spectral pair is independent of temperature as in-

dicated by the equally long arrows for two temperatures and a selected wavelength.

The ability to determine absolute temperatures and the unknown transfer function by only using the fact that the latter is constant is applicable in many spectroscopic applications and facilitates blackbody emitter-based calibration. For simplicity, all wavelengths are weighted equally, although their uncertainty is not equal.

The spectral sensitivity is related to the shifting of the peak emission according to Wien's displacement law with shifts toward the blue when the bulb voltage is increased. We note that the situation is conceptually very similar to the shift in the high-energy photon cut-off of bremsstrahlung when the applied voltage is increased [see Fig. 1(a)]. However, for a light bulb the temperature range is limited. The upper limit is the melting point of tungsten,  $T = 3695$  K (corresponding to the peak emission at 784 nm), and the lower limit comes from the detection limit of the camera. The spectral sensitivity of the camera limits the spectral range from 400 to 1100 nm.

To illustrate the system's capability of providing color information, four standard colored Schott glass filters [see Fig. 4(a)] were used in the system, and the filament temperature was swept from 1600 to 3000 K. The filters were placed on white paper, and the reflectance was calculated by subtracting the background and assuming total reflection for the white paper background. The detection system was checked for linearity. Figure 4(b) shows the case of a blue glass filter, BG38. When the filament is hot, the illumination contains a considerable amount of blue light, and the resulting signal [Eq. (1)] is large. When the temperature decreases, the illumination shifts toward the infrared and the blue content decreases because the transmitted light decreases and the signal decreases [see Fig. 4(c)]. We have plotted transmission versus the peak wavelength (inversely proportional to temperature) for the emission curve. This representation is unconventional because we usually represent transmission in terms of wavelength or energy. However, because the spectral resolution is poor, a better representation is obtained by using an integrative wavelength parameter such as the peak wavelength. Near the lowest temperatures and highest peak wavelengths, the filter becomes more transmissive again and the signal begins to rise. The behavior of the VG6 filter is simi-

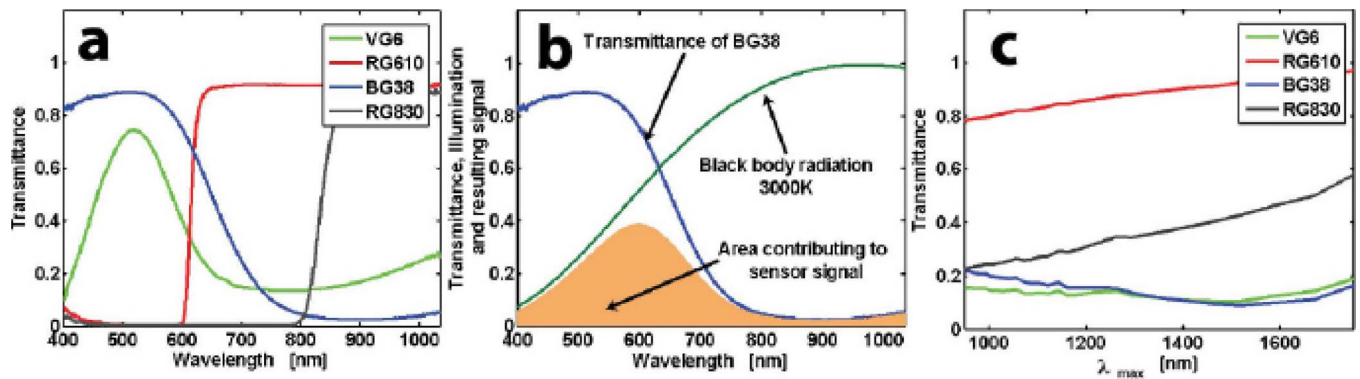


Fig. 4. (a) Transmission spectra of four commercial Schott colored glass filters expressed in wavelengths. (b) Illustration of transmitted light from a blue glass filter when illuminated by a 3000 K black-body; the shaded area represents the resulting signal received by the camera according to Eq. (1). (c) Transmitted light versus black-body peak radiation (inversely proportional to temperature), with each spectral value arising from a different temperature.

lar. For the RG610 and RG830 filters, the monotonically increasing transmittance values as the temperature decreases are shown in Fig. 4(c) and can easily be understood by considering the changing Planck distributions sampled over the sharp transmittance edges. For simplicity, the system transmission function was considered to be independent of wavelength in Fig. 4(b). This assumption has no influence on the curves in Fig. 4(c) because the system transmission cancels out when the filter transmission ratio is calculated using the white paper as a reference. The filter transmission corresponds to a filter of double thickness because light passes the filter twice. As for the x-ray attenuation curves shown in Fig. 1(b), the transmission curve in Fig. 4(c) cannot be described as a linear combination of the other curves. As noted in Sec. I, this observation is the key aspect in x-ray bremsstrahlung spectroscopy and imaging and in our analogous demonstration in the optical regime.

#### IV. IMAGING SPECTROSCOPY: LEAF OR FALSE LEAF?

With our demonstration of the feasibility of Wien shift spectroscopy, we now turn to multispectral imaging. A scenario including a leaf and a printed color picture of the same leaf was arranged. The picture was printed with a color laser printer. For a good laser printer we expect the appearance to the human eye to be close to the original. Several of our colleagues were unable to distinguish the false leaf from the real one at a distance of one meter. The picture of the leaf and the real leaf are shown in Fig. 5(a); it is very difficult to tell the difference between the two items when we are re-

stricted to the visible region. However, we have no information about the reflection properties in the near-infrared region not covered by human receptors. Vegetation is known to have a strong increase in reflectance starting at about 700 nm.

In separate spectral measurements (using the same Ocean Optics USB4000 spectrometer, an Oriel integrating sphere, and an Oriel XeHg short arc lamp), we found that the color picture exhibits a strong near-infrared reflectance but is displaced about 50 nm toward longer wavelengths [see Fig. 5(b)]. We also notice differences in the visible spectra; however we cannot distinguish spectra that give rise to the same contribution to our three spectral bands. It is expected that an infrared shift can be revealed by Wien shift imaging in the same way as we can distinguish the RG610 and RG830 filters in Fig. 4. The two-leaf arrangement was placed in our Wien shift imaging system. The temperature was swept in 26 steps from 1600 to 3000 K and images recorded.

To interpret the data we used linear decomposition. We briefly review the basic principles of principal component analysis,<sup>6,12–15</sup> also known as singular value decomposition. When working with spectroscopy and/or imaging, we usually acquire huge amounts of data. In most cases we are able to reduce the representation of a given set of spectra or a given set of images. If we were to measure the absorption at 1000 wavelengths of 100 cocktails made from blue Curaçao and red cranberry juice, we would realize that all measurements are a linear combination of the Curaçao and the cranberry spectra with given concentration coefficients. Thus we would be able to represent the 100 000 data points using only

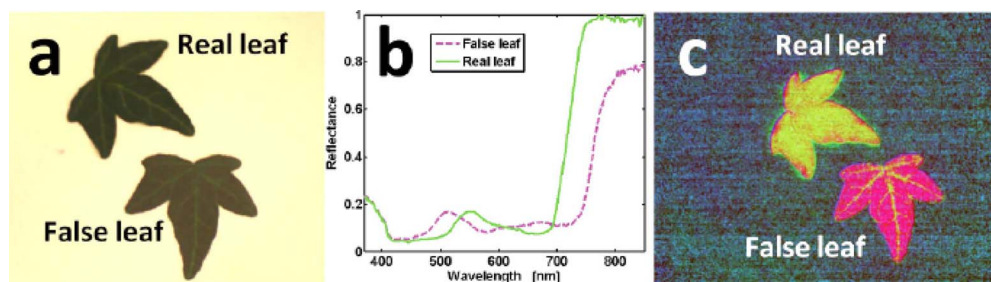


Fig. 5. (Color online) (a) Photograph of a real leaf placed next to a printout of the same leaf on white paper. (b) Reflectance spectra for the apparently similar real and false leaves. (c) The first three principal base images can be illustrated by a false color RGB picture, where a clear distinction between the leaves can be seen.

2000 points from the absorption spectra of Curaçao and cranberry plus the 200 linear coefficients specifying the concentration of each ingredient. In this case we would have reduced the data set without significant loss of information. Similar decomposition approaches can be applied to data sets of similar images such as x-ray images of a scene illuminated by distinct bremsstrahlung distributions. Principal component analysis does not require knowledge of the spectra of the components but provides the base vectors by analyzing the variance within the sample set. By decomposing and projecting onto principal components, we can describe each absorption spectrum or image with a few coefficients plus the corresponding auto generated principal components  $PC_\lambda$ ,

$$\mu_{n,\lambda} = k_{n,1}PC1_\lambda + k_{n,2}PC2_\lambda + k_{n,3}PC3_\lambda \dots, \quad (7)$$

where  $\mu_{n,\lambda}$  is the absorption coefficient for measurement  $n$  at wavelength  $\lambda$ ,  $k_{n,j}$  is the coefficient for reconstructing  $\mu_{n,\lambda}$  in terms of  $PC1_\lambda, \dots, PCj_\lambda$ ,  $PC1_\lambda$  is the mean spectrum for the complete data set,  $PC2_\lambda$  is the base spectrum describing the deviation of  $\mu_{1,\dots,N,\lambda}$  in the data set with respect to  $k_{n,1}PC1_\lambda$ ,  $PC3_\lambda$  is the base spectrum describing deviation of  $\mu_{1,\dots,N,\lambda}$  in the data set with respect to  $k_{n,1}PC1_\lambda + k_{n,2}PC2_\lambda$ , and so on.

In the spectral case the principal components are 1D vectors, which tell us in which regions spectral changes occur within the data set. We might think of principal component analysis applied to a set of spectra as recording each spectrum with a set of detectors with sensitivity bands defined by the principal components [see Eq. (1)] and giving rise to a color  $k_j$  because the mathematical operation is identical. In other words we see the spectra through principal component filters perfectly adapted to cover the variance within the data set.

In the imaging case the principal components are 2D base surfaces or 3D topographic base spaces that tell us which spatial regions in the image vary independently. Independently varying regions would be the case for multiple bands in a multispectral x-ray image of a bag containing different objects with different atomic compositions. By analyzing the residuals of the principal component analysis, it becomes clear that principal component analysis corresponds to a change in coordinates. If we represent 100 cocktails with 100 principal components, we would obtain a residual of zero. Luckily the principal components are sorted in order of decreasing significance, and by analyzing the drop in residuals depending on the chosen truncation, we can determine the number of independent spectra in the set. For the blue Curaçao and red cranberry cocktail, we would see a clear drop in compression residuals after the second component because there are only two ingredients in the sample set.

If we return to our acquired data set, we see that we are able to compress a series of pictures of the same scenario illuminated by different Planck distributions or different bremsstrahlung distributions in the same way as before. We also see that by constructing contrast functions, we are able to process the reduced data and turn the observations into meaningful information, such as detecting explosives in a bag or blood veins in a human body.

When we apply principal component analysis to the leaf pictures we ask, “Can we express the 26 pictures of the same scene illuminated by different Planck distributions as a scalar times one base picture?” If the scene contains substances with different spectral contents, the answer should be no [see Figs. 1(b), 4(c), and 5(b)]. The principal component analysis

residuals show a clear drop after the third component because there are three different spectral distributions in the picture due to the paper, leaf, and false leaf. We have reduced our data from 26 pictures to three pictures plus a  $26 \times 3$  matrix, thus roughly decreasing 26 million reflection measurements to 3 million. We also showed the ability of the system to access spectral information.

By presenting the first three principal component base images in a false color RGB representation, we emphasize the spectral difference between the leaves [Fig. 5(c)], illustrating our ability to make color and/or false color images using a black and white camera and illumination with a filament light bulb.

The method of presenting principal components in false color RGB images is useful for obtaining a quick overview of complicated data sets. In our case we applied it to a series of pictures with different illumination temperatures, but principal component analysis can be applied along any domain, such as time.<sup>16</sup>

## V. DISCUSSION AND CONCLUSIONS

A number of improvements to our setup can be made. In the first setup a linear film polarizer was used on the light source together with a perpendicular one in front of the camera to reject specular reflections and to ensure that the recorded light included multiple scattering in the sampled object. Because the polarizing filters perform poorly and become transparent in the infrared, this technique can be used only in combination with infrared insensitive cameras. To expand the sensitivity region the polarizers were removed, and nonspecular objects had to be imaged. Improvements can be obtained by using polarizers covering the entire spectral region. Other light sources can be applied, such as flash lamps, combined with rolling-shutter CMOS techniques.<sup>17</sup> Halogen lamps have been tested and give good results possibly due to their higher effective temperature.

## ACKNOWLEDGMENT

This work was supported by the Swedish Research Council through a Linnaeus Grant to the Lund Laser Centre.

<sup>a</sup>Electronic mail: mikkel.brydegaard@fysik.lth.se

<sup>1</sup>S. Svanberg, *Atomic and Molecular Spectroscopy: Basic Aspects and Practical Applications*, 4th ed. (Springer, Berlin, 2004).

<sup>2</sup>R. Jenkins, *X-ray Fluorescence Spectrometry*, 2nd ed. (Wiley, New York, 1999).

<sup>3</sup>E. E. Christensen, T. S. Curry, J. E. Dowdey, and R. C. Murry, *Christensen's Physics of Diagnostic Radiology*, 4th ed. (Lea & Febiger, Philadelphia, 1990).

<sup>4</sup>J. H. Hubbell, “Tables of x-ray mass attenuation coefficients and mass energy-absorption coefficients,” Ionizing Radiation Division, Physics Laboratory, National Institute of Standards and Technology, 1996.

<sup>5</sup>*Techniques and Application of Hyperspectral Image Analysis*, edited by H. F. Grahn and P. Geladi (Wiley, Hoboken, NJ, 2007).

<sup>6</sup>M. Brydegaard, Z. Guan, and S. Svanberg, “Broad-band multispectral microscope for imaging transmission spectroscopy employing array of light emitting diodes,” *Am. J. Phys.* **77**, 104–110 (2009).

<sup>7</sup>M. Brydegaard and S. Svanberg, “Contrast functions and spectral data handling,” in *Proceedings of the Optics and Laser Applications in Medicine and Environmental Monitoring for Sustainable Development*, edited by P. Buah-Bassuah (University of Cape Coast, Ghana, 2007), pp. 91–92.

<sup>8</sup>A. P. Cracknell and L. W. B. Hayes, *Introduction to Remote Sensing*, 2nd ed. (CRC, Boca Raton, FL, 2007).

<sup>9</sup>M. Borengasser, W. S. Hungate, and R. Watkins, *Hyperspectral Remote Sensing: Principles and Applications* (CRC, Boca Raton, FL, 2008).

- <sup>10</sup>A. K. Maini and V. Agrawal, *Satellite Technology: Principles and Applications* (Wiley, Chichester, 2007).
- <sup>11</sup>S. Svanberg, *Multi-Spectral Imaging—From Astronomy to Microscopy—From Radiowaves to Gamma Rays* (Springer-Verlag, Berlin) (to be published).
- <sup>12</sup>T. W. Anderson, *An Introduction to Multivariate Statistical Analysis*, 3rd ed. (Wiley, Hoboken, NJ, 2003).
- <sup>13</sup>A. C. Rechner, *Methods of Multivariate Analysis* (Wiley Interscience, New York, 2002).
- <sup>14</sup>K. R. Beebe and B. R. Kowalski, “An introduction to multivariate calibration and analysis,” *Anal. Chem.* **59**, 1007A–1017A (1987).
- <sup>15</sup>P. Weibring, T. Johansson, H. Edner, S. Svanberg, B. Sundnér, V. Raimondi, G. Cecchi, and L. Pantani, “Fluorescence lidar imaging of historical monuments,” *Appl. Opt.* **40**, 6111–6120 (2001), with color figures printed in “Fluorescence lidar imaging of historical monuments: Erratum,” *ibid.* **41**, 434–436 (2002).
- <sup>16</sup>E. M. C. Hillman and A. Moore, “All-optical anatomical co-registration for molecular imaging of small animals,” *Nat. Photonics* **1**, 526–529 (2007).
- <sup>17</sup>G. C. Holst and T. S. Lomheim, *CMOS/CCD Sensors and Camera Systems* (JCD, SPIE, Bellingham, WA, 2007).



Post Card Projector. Many students, having laboratory experience in image formation using a target lighted from behind, are surprised that an object brightly lit from the front will also produce an image. This is the basis for the post card projector, popular during the first portion of the 20th century. The post card is placed, upside down, in a holder at the back of the metal box. It is illuminated by two light bulbs (usually backed by reflectors), and the lens forms an upright image on the screen. Colored postcards were the vacation souvenir of the era and the grandparents of the modern digital vacation photograph. These two projectors are in the Greenslade Collection. (Photograph and Notes by Thomas B. Greenslade, Jr., Kenyon College)

## **Broad-band multi-spectral microscope for imaging transmission spectroscopy employing an array of light-emitting diodes (LEDs)**

M. Brydegaard, Z. Guan and S. Svanberg

*American Journal of Physics* 77:104-110 (2009).

# Broad-band multispectral microscope for imaging transmission spectroscopy employing an array of light-emitting diodes

Mikkel Brydegaard,<sup>a)</sup> Zuguang Guan, and Sune Svanberg  
*Atomic Physics Division, Lund University, P. O. Box 118, SE-221 00 Lund, Sweden*

(Received 30 April 2008; accepted 27 October 2008)

Optical spectral analysis and multispectral imaging provide powerful means for characterizing samples in a wide variety of applications and on many spatial scales. We present a simple implementation of these techniques in the context of microscopy. A modified commercial microscope equipped with a CMOS imaging detector, combined with an array of light emitting diodes with emission ranging from ultraviolet to near-infrared wavelengths, is described, and examples of information enhancement using multivariate analysis are presented. © 2009 American

*Association of Physics Teachers.*

[DOI: 10.1119/1.3027270]

## I. INTRODUCTION

The response to different wavelengths is characteristic of an object, and its optical reflectance spectrum (related to color) is important in identifying it. Color discrimination varies widely in biological and technological vision systems. Vision and color registration are illustrated in Fig. 1, as well as the corresponding interpretation methods. Humans have three broad color channels, while birds frequently have four, including ultra-violet (UV) sensitivity. The Mantis shrimp has 12 color channels. Clearly, the human visual perception makes quantification of the true spectral composition of an object difficult. In contrast, artificial vision systems (imagers) such as RGB (red-green-blue) cameras, satellite sensors, and spectrometers allow a much more precise quantification of the spectral properties, which are directly linked to the chemical composition of the object of interest. In spectroscopy the exact spatial origin of the emission is irrelevant; we only collect enough photons to record the spectral distribution (“fingerprint” or “signature”) of the material. If spectra are recorded in all spatial locations over the area studied, we obtain an image with distributed spectral fingerprints, a *multispectral image*. Such an image can be formed by sequentially recording the full spectra at adjacent points or by observing the entire object in a number of selected spectral bands. The number of independent spectral bands may vary from 1 in a black-and-white camera to 1024 or more in a modern spectrometer. Because digital data are provided by technological sensors, computer processing is used to interpret the data, frequently using multivariate analysis.

The purpose of this paper is to provide insight into the nature of digital multispectral imaging and to discuss an instrument suitable for projects in imaging spectroscopy. The power of multivariate analysis is demonstrated in the process. A simple and affordable implementation in terms of a microscope equipped with 13 quasi-monochromatic light-emitting diodes (LEDs) is presented.

Multispectral imaging allows us to extract physical and chemical information about an image scene. In contrast, normal image processing mostly focuses on the spatial properties of the image,<sup>1</sup> that is, on shapes. The applications of multispectral imaging range from astronomy to microscopy and cover the electromagnetic spectrum from gamma rays to radio waves.<sup>2</sup> Examples are the identification of possible cancer regions in medical imaging, delineating areas of for-

est decline in satellite images, and mapping areas containing a certain concentration of calcium ions in a fluorescence microscopy image.<sup>3-9</sup>

A relevant question for understanding our natural color perception and the potential for multispectral imaging is “What would the world look like and what information would we be able to see if we could manipulate the spectral sensitivity of our vision?” We are able to do so using various pieces of technological equipment as indicated in Fig. 1. The microscope discussed in this paper is one of many instruments providing imaging spectroscopy. Although the equipment used may vary widely, the general principles of multispectral imaging for extracting useful information are the same.<sup>2</sup>

Multivariate techniques<sup>10,11</sup> are well known in chemistry and are frequently referred to as chemometry.<sup>12</sup> In our case a given spectral distribution of a particular point in an object is approximated as a linear combination of a few base spectra (called principal components), in a way similar to the expansion of a wavefunction in a set of eigenfunctions. The base functions can be automatically generated by analyzing the variance in the ensemble of spectra from every pixel in the image. A pedagogical example of the use of the techniques in imaging spectroscopy can be found in Ref. 13. Multivariate techniques are provided in a MATLAB package,<sup>14</sup> and more specialized commercial programs are available.

In our demonstration of multispectral transmission imaging the spectral resolution arises from data acquired by multiplexing several LEDs,<sup>15</sup> which cover the visible range (400–700 nm) and extend into the UV and near infrared (NIR) regions. A commercial low-cost microscope equipped with a CMOS (complementary metal oxide semiconductor) imaging chip<sup>16</sup> was modified for multiple LED illumination, and the sensitivity spectrum of the CMOS device, which is well outside that of the human eye, is critically utilized.

## II. MULTISPECTRAL IMAGING AND MICROSCOPY

When light impinges on a sample as in transmission microscopy, the incident light intensity is split into a few parts. One part is reflected back toward the source, some light is refracted or scattered and results in a change in the angle of propagation, some light is absorbed by the molecules in the sample, and some light is transmitted. Also, part of the absorbed light might be reemitted as fluorescence light. These

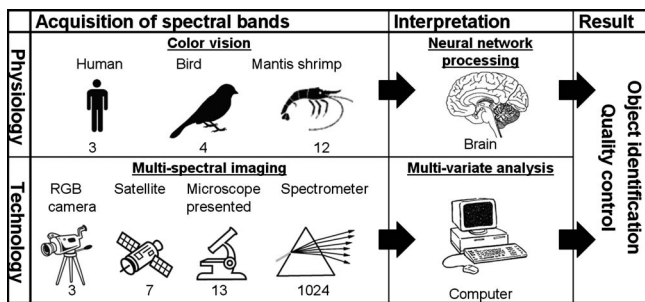


Fig. 1. Relation between color vision, multispectral imaging, multivariate analysis, and spectral bands of various species or spectral instruments (the digits refer to the number of spectral bands). The spatial resolution varies from megapixels in the RGB imager to a single pixel in a nonimaging point spectrometer.

phenomena are governed by Snell's law, the Fresnel equations, and the Beer-Lambert law (see, for example, Ref. 17). The transmittance  $T$  at a point is defined as the ratio between the transmitted intensity and the incident intensity on the illuminated side of the sample. When values for the transmittance are obtained at several wavelengths,  $T(\lambda)$ , we do transmission spectroscopy. When spectroscopy is done at several spatial locations, we obtain  $T(x, y, \lambda)$  and refer to multispectral transmission imaging. Similarly, absorption and reflection spectroscopy can be performed.

In normal transmission microscopy contrast arises partly from differences in the absorption properties of different parts of the sample and partly from spatial gradients in the refractive index. Absorption spectra and the influence of the refractive index are more likely to vary when a higher spectral resolution is available. Thus, increasing the number of spectral channels usually makes object identification easier. However, very high spectral resolution of absorption in the optical regime seldom leads to any additional information for solids and liquids, because the energy level structure is broad. The sharpest features are typically on the order of tens or even hundreds of nanometers in optical absorption spectra. In unaided transmission microscopy the naked eye perceives the three spectral bands of the corresponding cones of the human retina (in comparison to the thousands of spectral bands that commercial point spectrometers provide). Certain scenes appear without color, but clear spectral characteristics might be present in the UV or IR regions. UV vision is utilized by bees who can see color encodings of flower petals; these encodings are invisible to humans. Neither can we see the strong reflectance increase of green leaves in the near IR. We are unable to distinguish spectra even in the visible range. For example, filament and fluorescent light bulbs have different spectra, but both appear to be white to the human eye.

The contribution to the intensity  $u$  at a pixel for the color channel  $ch$  within a given spectral band is given by

$$u_{ch} = \int_0^{\infty} E(\lambda)T(\lambda)S_{ch}(\lambda)d\lambda, \quad (1)$$

with  $E$  the emission spectrum of the illumination,  $T$  the transmittance,  $S_{ch}$  the sensitivity spectrum or spectral band of the recording system in color channel  $ch$ , and  $\lambda$  the wavelength. Equation (1) expresses the fact that a response is

obtained only if the spectra of the illumination, transmittance, and detector sensitivity overlap.<sup>3,4</sup>

The same approach can be applied to all spectral instruments including color cameras and spectrometers; the main difference is that with a spectrometer the sensitivity bands are preferably narrow and ordered according to the wavelength, whereas in commercial color cameras the spectral channels are broad and overlapping in order to emulate the human eye. Natural vision channels are usually overlapping and can even have secondary sensitivity regions that require a brain to learn how to interpret the input from the visual channels. When constructing a spectral instrument we can change  $E$  and  $S$ , whereas  $T$  is unchanging and characterizes the sample. Because the order of multiplication is irrelevant,  $E$  and  $S$  are mathematically equivalent, which implies that we can either filter out certain wavelengths in the detector or equally well change the illumination spectrum. (In the time domain temporal resolution can be achieved either by using a short shutter time for continuous illumination, or by a short flash combined with an open shutter. In the latter case, as in the one considered by us, it is important that the background light be at a low level.) We can thus create a color picture by taking three black-and-white pictures of the same scene through three different color filters and combining the pictures. As we will see in the following, it makes no difference if we take three black-and-white pictures without color filters and sequentially use three differently color light sources illuminating the scene. In the first case we have a passive sensing method, and in the second case we use an active sensing method, where we need to be able to control the illumination spectrum. This approach is valid as long as fluorescence processes can be neglected.

The light intensity in multispectral images typically needs two spatial dimensions and one spectral dimension. For a color movie we would need four dimensions, with time the fourth dimension. Thus, the light intensity in a color movie is a function of four parameters:  $I(x, y, \lambda, t)$ . In contrast, the signal from a black-and-white CCD (charged coupled device) or a CMOS imaging chip is a function of only three parameters:  $I(x, y, t)$ .

Light levels are discretized in the detector by bits, space discretized by pixels, time by frames, and wavelength by color channels. The corresponding resolutions are dynamic resolution, spatial resolution, temporal resolution, and spectral resolution. When acquiring more dimensions than the imager possesses, sacrifices must be made in the resolution and/or the orthogonality of the dimensions. In commercial color cameras microscopic colored filters are placed in a regular pattern on the imaging chip so that some pixels become sensitive to one wavelength band and the neighboring pixels to another wavelength band. Spatial resolution is decreased because one color pixel consists of several original pixels. It is also clear that the pixel positions in space are not exactly the same for the different color channels, and thus the spectral dimension is not orthogonal to the spatial dimensions. In the example where a color picture was made by illuminating the scene with light from three differently colored light bulbs, it is understood that the pictures are taken at different times, and thus the spectral dimension is not orthogonal to the temporal dimension. In other acquisition systems such as the push-broom imager often used in hyperspectral satellites,<sup>3-5,18</sup> a spatial line is scanned where the colors in the individual elements on the line are dispersed by

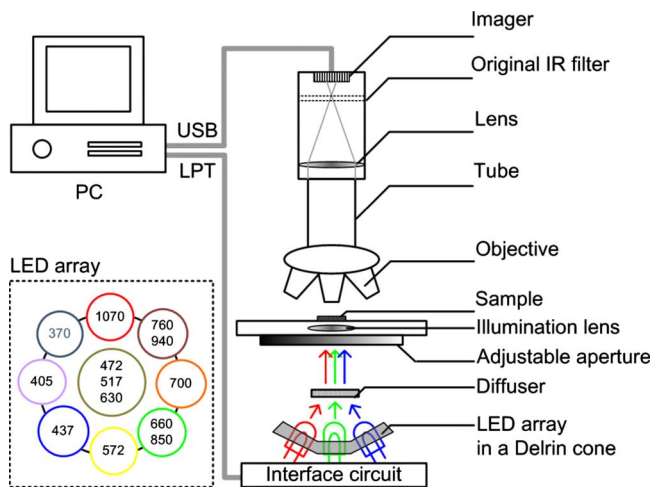


Fig. 2. Arrangement for multispectral transmission microscopy employing multiple LED illumination. Different wavelengths are emitted from a computer controlled LED array and the rays are combined by a diffuser. The light interacts with the sample differently for each wavelength, resulting in a unique picture for each wavelength.

a grating and imaged onto a matrix detector. In this case the spectral dimension is orthogonal to one of the spatial dimensions, but the remaining spatial dimension is not orthogonal to any of the others, including the temporal dimension. In this paper we will present a simple multispectral imaging system, based on the sequential multiplexing of illumination spectra.

### III. EQUIPMENT

We used a low-cost USB digital microscope available from [www.discoverthis.com](http://www.discoverthis.com). An overview of the system is shown in Fig. 2. It is a transmission microscope, providing magnifications of  $4\times$ ,  $10\times$ , and  $40\times$ , and is equipped with a CMOS imager with  $640 \times 480$  resolution. The imager is used in the black-and-white (gray-scale) mode. The microscope in its standard version is equipped with white-light LED illumination. We adapted this microscope for multispectral imaging by performing the steps discussed in the following. In principle, any conventional microscope can be used for the modifications described.

Most commercial CCD and CMOS imagers are used for visual applications although they also have sensitivity in the NIR spectral range. To suppress the influence from NIR light, visual digital imaging systems are equipped with an IR filter, cutting off the region outside human perception. In our application the NIR range is of great importance and is available more or less for free. Hence, it is important to remove the IR filter, which is located in the optical path in front of the imaging chip.

To achieve multispectral imaging we use multiple LEDs, which can be activated sequentially. We use nine LEDs, three of which have more than one emission wavelength (common anode, multiple cathode pins allowing sequential activation of individual diodes) to provide quasi-monochromatic illumination in 13 wavelength bands ranging from 370 to 1070 nm. The LEDs are Roithner LaserTechnik Models NS370L5RLO,  $\lambda=370$  nm; 3P4FCA,  $\lambda=405$  nm; B5-4RGB-CBA,  $\lambda=472, 517, 630$  nm; B5-433-20D,  $\lambda=572$  nm; LED 660/760-04A,  $\lambda=660, 850$  nm; ELD-700-

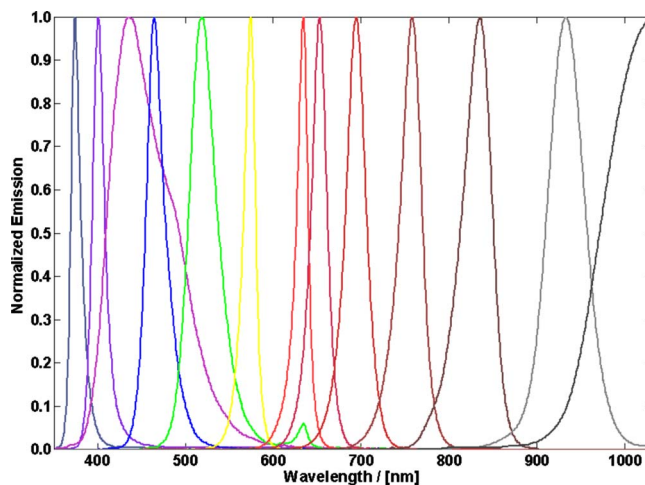


Fig. 3. Normalized spectral emissions of the different LED sources used in the multispectral microscope. Because illumination and sensitivity can be interchanged in spectroscopic instruments, we can consider the emissions as the spectral bands of the system.

524,  $\lambda=700$  nm; LED850/940-04A,  $\lambda=760, 940$  nm; LED1070-03,  $\lambda=1070$  nm; and Farnell TLHB5800,  $\lambda=437$  nm. The normalized spectral emission characteristics are given in Fig. 3, as measured separately with a compact Ocean Optics Model USB4000 spectrometer. The nine LEDs are mounted in a machined compact circular arrangement (diameter 32 mm) made of Delrin with eight LEDs on a circle (outer diameter 16.3 mm, inner diameter 13.3 mm); the ninth LED is placed in the center. They are arranged to centrally illuminate the same spot on the light diffuser plate of the microscope. The nine LEDs all have a 5.0 mm diameter epoxy casing and a divergence angle of  $20^\circ$ . The outer eight LEDs are tilted inward  $16^\circ$  in such a way that their optical axes meet 22 mm in front of each LED, where the optical diffuser is situated. The glass components in the microscope are fully transparent in the wavelength range covered by the LEDs. Detailed CAD drawings can be obtained upon request.

The LEDs are powered by an LM317 regulator with constant current of 30 mA. The LEDs are activated from four TTL signals from the parallel port of a computer used to control the equipment and process the images. The TTL signals are converted to VCC voltages by a quadruple LM324 operational amplifier. The binary addressing for the LEDs is decoded by a 4514 integrated circuit, which activates one output at a time as directed by the binary address. The decoded output opens individual BC547 transistors, which in turn activate the specified LED. The electronics fit on a board of dimensions  $\approx 5$  cm by  $\approx 10$  cm, which can be incorporated in the foot stand of the microscope. The power is supplied by a 12 V wall plug adapter. A detailed circuit schematic is available.

### IV. MEASUREMENTS AND IMAGE ANALYSIS

The objects to be studied are placed on the microscope table. For the lowest magnification setting,  $4\times$ , an object size of  $1260 \mu\text{m}$  times  $950 \mu\text{m}$  can be accommodated on the CMOS imaging chip. To illustrate the concepts of multispec-

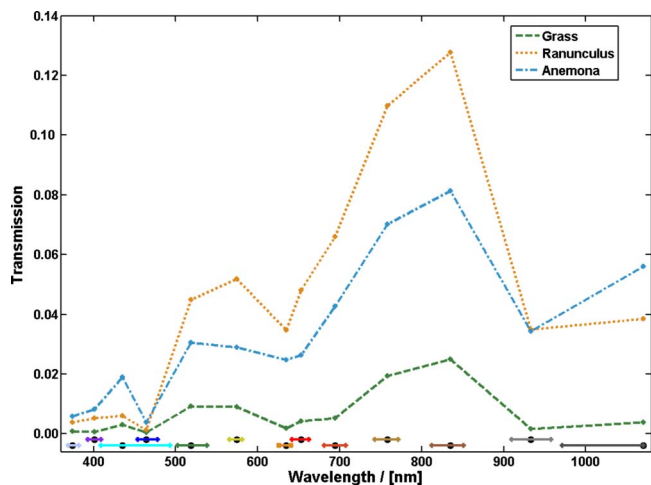


Fig. 4. Transmission spectra of a fresh leaf of grass, and for petals from *Ranunculus* and *Anemone*. Vegetation transmits considerably in the near infrared. The symbols in the lower part indicate  $\lambda_{\max}$  and FWHM for each spectral band.

tral imaging we have imaged a number of objects as described in the following. Biological samples were chosen, but the techniques are very general.

Chlorophyll in the chloroplasts of green vegetation has a strong absorption in the blue and red parts of the spectrum, with a somewhat weaker absorption in the green spectral range, causing vegetation to look green. What is not observed by the human eye is the strong transmission for NIR wavelengths beyond 700 nm. A leaf of *Poaceae* (grass) and petals from *Ranunculus* and *Anemone* (Nordic spring flowers) were studied. Pieces of the samples were placed in the same field of view with  $4\times$  magnification. A small piece of aluminum foil was also added. Two reference fields were selected in the image; one with no object, which was assumed to have 100% transmission, and one in the aluminum foil area with the assumption of 0% transmission. The transmission spectra were calculated and are shown in Fig. 4. The transmission increases dramatically for the invisible wavelengths from 700 to 760 nm. The purple *Anemone* has a transmission peak in the blue spectral region as well as substantial transmission at longer wavelengths including red. The *Ranunculus* features a high level of longer visible wavelengths, including yellow. The three fresh species also exhibit a strong absorption band due to water, centered around

980 nm. The fact that we acquire an entire spectrum for each of the spatial pixels by sequentially multiplexing the LEDs means that we can perform spectral identification of objects according to their transmission properties. For illustration we need an object with considerable spectral variance within the small field of view of the microscope.

A major difficulty for ecologists is to understand the visual perception of the environment by certain species, particularly because their spectral bands do not always correlate with our own. Physiological (natural) vision systems include complex photonics, such as polarization dependent multimode waveguides, interference filters, and spectral dispersing techniques.<sup>19</sup> In most cases spectral sensitivity is mainly due to a variety of receptors. For certain species receptors are combined with superimposed oil droplet color filters.<sup>20,21</sup> Spectral resolution varies in number from monochromatic to a dozen bands. Sensitivity ranges from 300 to 800 nm. Because the receptors and their accompanying droplets are spatially separated, it is expected that the effective sensitivity spectra can be retrieved with multispectral transmission microscopy.

A  $2\ \mu\text{m}$  thick cross-section of a budgerigar (*Melopsittacus undulatus*) retina was provided by the Vision Group in the Department of Cell and Organism Biology at Lund University. The sample was prepared with stabilizers and conserving agents and molded in epoxy. For other purposes the sample was contrast enhanced with methylene blue dye. The retinal sample was observed at  $40\times$  magnification as shown in Fig. 5(a). The multispectral images were acquired with refocusing in between changing the wavelength by sequentially activating the individual LEDs. The background was subtracted and a two-dimensional median filter was applied to remove “dead” pixels. Due to the large numerical aperture and the refocusing, the magnification changes considerably between the spectral acquisitions. This change was compensated by identifying “land marks” and performing spatial rectification transforms.<sup>1,22</sup> This procedure is time consuming whether the operation is done manually or by correlation techniques. It was observed that the methylene blue dye absorbs strongly between 550 and 700 nm [see Fig. 5(b)], which gives rise to a bluish tint, which is consistent with the well known spectrum for methylene blue. The larger brownish cells are rod cells used for monochromatic low-light level vision. The cones providing the budgerigar four spectral channels are considerably smaller in Fig. 5(a). The molecules responsible for the photoreception are highly unstable and

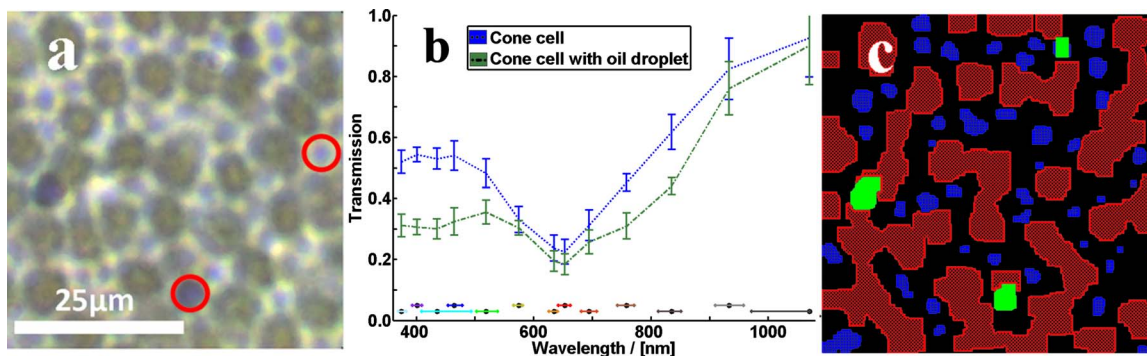


Fig. 5. (a) True color RGB picture of a cross section of budgerigar retina. (b) Spectra from two selected cone cells with and without oil droplet, such as those marked with small circles in (a). (c) Patterned answers from the three contrast functions; each pixel has been identified individually based on its spectral properties. Checker pattern (red) corresponds to rods, bright (green) to cones with oil droplet, and meshed patterns (blue) to plain cones.

photosensitive. Thus the procedure for analyzing these compounds requires darkroom dissection and immediate picture acquisition, which was not done for this paper. Also, the transmission through such samples is influenced by exposure time and light intensity, which makes analysis slightly more difficult. Nevertheless, the oil droplet filters are stable and can be analyzed. Two cones, with and without color filters, were spectrally probed as shown in Fig. 5(b).

The filter effect suppresses wavelengths below 500 nm, which suggests that this particular oil droplet is yellow.<sup>20,21</sup> As mentioned, budgerigars have four visual pigments, each with a superimposed oil droplet consisting of one out of four types. The purpose of these filters is believed to be to sharpen the sensitivity bands of the cone cells, although the spectral sensitivity is still limited to four spectral channels. It is well known that even very thin oil layers can absorb short wavelengths efficiently. Thus it is surprising that transmission only decreases by a factor of 2 in the short-wavelength range. The reason is that the simple optics of the microscope leads to substantial stray light, which gives rise to an offset in the transmission.

We will now demonstrate how the transmittance coefficients can be combined to answer a specific question of interest. As mentioned in Sec. I, we can approximate a spectrum as a linear combination of a few base spectra (principal components), thus representing the entire spectrum for each pixel (that is, the transmission coefficients for the 13 bands) by a reduced number of terms describing the projection of the pixel spectrum on the dominant principal components. We retain only the dominant projections necessary to describe the detectable independent spectra within the limitations of the noise present. The situation is similar to the case when the true spectral contents of a photographed object are projected onto the sensitivity curves in a commercial RGB digital camera [see Eq. (1)]. The only difference is that the principal components are sensitivity bands, perfectly matched to cover a complete spectral reconstruction in the picture (in contrast, the fixed RGB channels of the camera are present, even if there is no information, for example, in the red color channel for a particular scenario).

We now construct a *discrimination* or *contrast function*  $F$  by a multidimensional polynomial expansion in the principal components:  $F(PC1, PC2) = k_0 + k_1 PC1 + k_2 PC2 + k_3 (PC1 \times PC2)$ , which gives a reduced spectral representation (describing the amount of  $PC1, PC2, \dots$  in every measured pixel). We can find  $k$ 's such that  $F$  is close to one for pixels of the object of interest and close to zero for all others. A matrix formulation is used and solved by minimizing the least square residuals for a group of training pixels where the true answer is provided by an expert in the subject matter (in our case an animal physiologist marking the different cell types). The solution of such overdetermined systems of equations is well known from linear algebra. Setting a threshold in-between (for example,  $F > 0.7$ ) determines if the property is fulfilled (for example, a rod in our case). These procedures form the core of multivariate analysis as discussed in Refs. 10–14.

This approach is now applied to identify the specific oil types and to determine the spatial distribution of the oil. Because we are studying a slice that is only  $2 \mu\text{m}$  thick, droplets are not necessarily incorporated in the specimen slice used. Thus, only some of the cones will be associated with droplets. Three contrast functions were used for a spe-

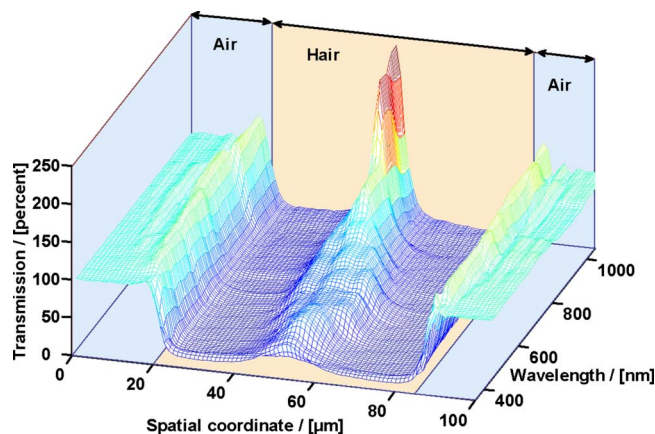


Fig. 6. Transmission cross section for a blond hair, represented in terms of one spatial and one spectral dimension. The hair acts as a cylindrical lens and focuses the light, causing the transmittance to pass 100% in the near infrared region, where absorption is low.

cific type of oil. As described, they are generated by reduction of data by a principal component analysis, followed by a multivariate polynomial model,<sup>23</sup> and eventually employing the binary morphological operations, erosion and dilation.<sup>1,22</sup> The spectrum for the rods [not shown in Fig. 5(b)] is useful for distinguishing them against the cones. The contrast functions answer the three questions: Is the pixel a rod? If not, is it a cone and, if so, does it carry an oil droplet superimposed? For these three cases we use the following representation: checker pattern (red) for rods, bright (green) for cones with oil droplet, and a meshed pattern (blue) for a plain cone, respectively. The result is shown in Fig. 5(c). We note that sometimes the droplet happen to be larger than the cone proper.

Human hairs have a typical diameter in the range 20–130  $\mu\text{m}$ , with blond hair thinner and black hair thicker. The color of hair is caused by two melanin pigments giving rise to brownish, blackish, and reddish variation. The appearance and characteristics of human hairs is discussed in Ref. 24. Several hair strands were spectrally analyzed.<sup>25</sup> Black and gray hair showed constant transmission in the visible region although at different levels, and transmission of brown hair curved upward for red light. Blond hair showed a linear transmission increase from 400 to 800 nm. Of special interest is the symmetry of hairs, which makes them behave like cylindrical lenses, adding further aspects useful for strand characterization. For closer study the blond hair was accommodated in the microscope using  $10\times$  magnification, and pictures were acquired sequentially for the different LEDs. The background signal was also recorded. Exposure times were adjusted for each spectral channel to exploit the dynamic range. Pictures were normalized by the exposure time, and the background was subtracted. The transmission as shown in Fig. 6 is calculated from the ratio between a region of interest on the object and a nonobscured reference field next to it. Note that refraction has a significant impact on the measurements. Transmission close to the borders of the hair is close to zero because of reflection losses due to the large incident angle. The defocusing caused by achromatic aberrations in the microscope lenses is observed and can be estimated from the steepness of the edges or the hair. We also note that the transmission in the IR region shown in Fig. 6 rises to more than 200% because of the focusing properties

of the hair strand, which is particularly transparent in this spectral region, thus allowing light from further out in the periphery to pile up in the middle. This effect strongly depends on the spectral focal shift. For the long wavelengths we start to see fringes next to the straw edge due to diffraction. Several spatial peaks are seen in the middle of the spectrum. These phenomena can be explained by the combined action of the Snel and Fresnel laws, and the special conditions around the Brewster angle. By further modeling of our relatively simple measurement situation, absolute values for both absorption and refraction index can be found. Thus, the phenomena accessible with a simple setup are very rich.

A detailed analysis of the absorptive and refractive phenomena we have discussed could have considerable use in forensic sciences and animal biology. The method provides further parameters to compare hairs from a crime scene. Hairs are present in various groups, for example, mammals, birds and insects, and contribute significantly to the visual differences between animals. Visual information takes up the largest computational power in the brain<sup>26</sup> in most animal species and is a crucial source for decision making in the search for food, predator avoidance, and reproduction. Because the spectral channels of many animals do not match those of humans,<sup>19,20</sup> a complete spectral analysis such as the one presented here is required for an accurate representation of hair appearance.

## V. DISCUSSION

We have shown how multispectral imaging can be demonstrated with simple and readily available equipment. Spectroscopy without spatial resolution was first illustrated for vegetation, resulting in 1D data. For the example of hair the 2D transmission data are arranged in one spatial and one spectral dimension. Full multispectral imaging uses spectral data for all spatial points, in our case recorded simultaneously for each illumination color. The data obtained after recording all available bands constitute 3D data, with two spatial and one spectral dimension. The hair cross section study produces data similar to push-broom scanning, frequently employed on a much larger scale in, for example, satellite imaging.<sup>3-5</sup> In our case one spatial dimension on the two-dimensional detector is used for line imaging, while the other one is used to analyze the dispersed light. The remaining spatial dimension is reconstructed by a sequential read out in the temporal dimension, taking advantage of the well defined movement of the satellite. For stationary objects sequential imaging through a set of pass-band filters can be made, producing spatially similar images which can then be co-processed. In such a setup the spectral dimension is created in the temporal domain. White-light illumination is normally used. Alternatively, as we have demonstrated, it is possible to illuminate small objects sequentially by narrow-band light sources, LEDs, which are commercially available in a range from 245 nm to 7  $\mu\text{m}$ . Thus, the spectral range is frequently limited by the detector rather than the source. Also, in the LED case the full intensity of the light source is utilized, while filtering of the reflected light (or the illumination white light) results in poorer efficiency because most of the light is wasted.

The low price of LEDs makes it economically advantageous to use narrow-band illumination of small objects rather than expensive narrow-band interference or tunable liquid crystal filters on the detection side. The cost of our

entire system, including LEDs, microscope, imager, and interface electronics is less than \$200. For the epoxy LEDs in our setup the brightest LED provides 17 mW of continuous power in the NIR and 4 mW in the UV.<sup>27</sup> Significantly increased peak output can be achieved in intermittent operation, because LEDs are primarily limited by the average heat dissipation.

The proof of principle measurements of leaf and petal spectra was done using the original PixArt PAC207 USB CMOS imager, included in the eyepiece of the microscope. The images had to be taken manually with the microscope because of a bug in the drivers, which inhibited automation of the acquisition. For later measurements a Sony ICX205AL imager installed in a Firewire camera was used for convenience.

An important issue with the current microscope is the achromatic aberration in the system. Few systems have a constant focus from UV to NIR. Thus different wavelengths focus on different depths in the sample. We refocused the microscope manually for the different LEDs. To automate the focusing a computer-controlled stepper motor could be used. Better solutions can be found by treating the image data in the spatial Fourier domain.

Recently, several efforts have been made to optically multiplex LEDs using advanced ray tracing and molded optics.<sup>28</sup> The aim is to join rays from several spatially distributed sources, losing as few photons as possible. Our system bases such multiplexing on the use of a diffusing plate, where several LEDs illuminate an almost identical spot from different angles. Ideally, light scatters in all directions, producing an even Lambertian-like distribution on the opposite site of the diffuser. Off-axis illumination influences the acquired picture in several ways. Light from a different direction will change the reflecting conditions for the many surfaces in the sample. Off-axis illumination will also cause features out of focus to be laterally translated in the picture. Therefore, the illumination profile should be as identical as possible for each wavelength to acquire the spectral properties in each pixel. The profile can be improved by using additional diffusers and apertures trading off the throughput. Uneven light distribution over the image can effectively be compensated by fitting low-order polynomial surfaces for each LED.

Fluorescence microscopy is possible but was not demonstrated here. Because fluorescence is a consequence of absorption, it is a powerful method to ensure that contrast arises from molecular absorption and less from refractive index gradients. Spectral information in fluorescence can be provided by different excitation sources or by a spectral analysis of the resulting fluorescence light. Thus, in principle we could provide an excitation-emission matrix in each pixel, multiplexing LEDs, and take advantage of the RGB filters in the color imager. Even LED-based fluorescent lifetime imaging could be performed with a pulsed LED employing the rolling-shutter exposure control of inexpensive CMOS imagers. Imaging in the temporal domain using LEDs has been demonstrated using more expensive equipment.<sup>29</sup>

In conclusion, we have demonstrated how a low cost setup can be used to illustrate the powerful concepts of multispectral imaging. We chose a microscopy implementation due to cost and educational aspects. The simple equipment suffers from certain deficiencies such as chromatic aberration and stray light and limitations in the available software drivers. Still it was possible to demonstrate advanced multispectral

concepts including multivariate analysis, providing many possibilities for quality inspections and object identification. Such techniques are now being pursued for diagnostics related to malaria.<sup>30</sup>

The simple case of transmission spectroscopy on grass leaves and flower petals and other specimens is suitable as undergraduate laboratory problems or classroom demonstrations. Multispectral image analysis can also be used for these simple cases or for pollen, spores, and biological cells. The study of human hair strands with all its intricacies regarding various optical phenomena is another example of a possible student project. The bird retina example illustrates that even emerging research in limited-resource environments can be pursued.

## ACKNOWLEDGMENTS

This work was supported by the Swedish Research Council through a Linnaeus grant to the Lund Laser Centre. The authors are very grateful to Olle Lind and Almut Kelber from the Vision Group, Department of Cell and Organism Biology, Lund University, for providing retina samples and for valuable discussions.

<sup>a)</sup>Electronic mail: mikkel.brydegaard@fysik.lth.se

<sup>1</sup>R. C. Gonzalez and R. E. Woods, *Digital Image Processing*, 3rd ed. (Pearson Prentice Hall, Upper Saddle River, NJ, 2008).

<sup>2</sup>S. Svanberg, *Multispectral Imaging-From Astronomy to Microscopy-From Radiowaves to Gammarays* (Springer Verlag, Berlin, 2009).

<sup>3</sup>A. P. Cracknell and L. W. B. Hayes, *Introduction to Remote Sensing*, 2nd ed. (CRC, Boca Raton, FL, 2007).

<sup>4</sup>M. Borengasser, W. S. Hungate, and R. Watkins, *Hyperspectral Remote Sensing: Principles and Applications* (CRC, Boca Raton, FL, 2008).

<sup>5</sup>A. K. Maini and V. Agrawal, *Satellite Technology: Principles and Applications* (Wiley, Chichester, 2007).

<sup>6</sup>E. Harrison, "Radiant information," *Sci. Am.* **297**(6), 78–83 (2007).

<sup>7</sup>D. B. Murphy, *Fundamentals of Light Microscopy and Electronic Imaging* (Wiley-Liss, New York, 2001).

<sup>8</sup>F. J. Kao and P. Török, *Optical Imaging and Microscopy: Techniques and Advanced Systems*, 2nd ed. (Springer Verlag, Berlin, 2007).

<sup>9</sup>J. R. Lakowicz, *Principles of Fluorescence Spectroscopy*, 3rd ed. (Springer, New York, 2006).

<sup>10</sup>T. W. Anderson, *An Introduction to Multivariate Statistical Analysis*, 3rd ed. (Wiley, Hoboken, NJ, 2003).

<sup>11</sup>A. C. Rechner, *Methods of Multivariate Analysis* (Wiley Interscience, New York, 2002).

<sup>12</sup>K. R. Beebe and B. R. Kowalski, "An introduction to multivariate calibration and analysis," *Anal. Chem.* **59**, 1007A–1017A (1987).

<sup>13</sup>P. Weibring, T. Johansson, H. Edner, S. Svanberg, B. Sundnér, V. Raimondi, G. Cecchi, and L. Pantani, "Fluorescence lidar imaging of historical monuments," *Appl. Opt.* **40**, 6111–6120 (2001); *ibid.* *Appl. Opt.* **41**, 434–436 (2002).

<sup>14</sup>MATLAB, Help files, The Mathworks.

<sup>15</sup>An early application of the use of LEDs in spectroscopy is demonstrated in P. H. Hauser, T. W. T. Rupasinghe, and N. E. Cates, "A multi-wavelength photometer based on light-emitting diodes," *Talanta* **42**, 605–612 (1995).

<sup>16</sup>G. C. Holst and T. S. Lomheim, *CMOS/CCD Sensors and Camera Systems* (JCD Publishing, SPIE, Bellingham, WA, 2007).

<sup>17</sup>E. Hecht, *Optics*, 4th ed. (Addison-Wesley, Reading, MA, 2002).

<sup>18</sup>C. H. Chen, *Image Processing for Remote Sensing* (CRC, Boca Raton, FL, 2008).

<sup>19</sup>E. J. Warrant and D. E. Nilsson, *Invertebrate Vision* (Cambridge U.P., Cambridge, 2006).

<sup>20</sup>T. H. Goldsmith, "What birds see," *Sci. Am.* **295**(1), 68–75 (2006).

<sup>21</sup>N. S. Hart and M. Vorobyev, "Modelling oil droplet absorption spectra and spectral sensitivities of bird cone photoreceptors," *J. Comp. Physiol., A* **191**, 381–392 (2005).

<sup>22</sup>MATLAB, Image Processing Toolbox, User's Guide, The Mathworks.

<sup>23</sup>M. Brydegaard and S. Svanberg, "Contrast functions and spectral data handling," in *Proceedings, Optics and Laser Applications in Medicine and Environmental Monitoring for Sustainable Development*, edited by P. Buah-Bassuah (University of Cape Coast, Ghana, 2007), pp. 91–92.

<sup>24</sup>R. R. Ogle and M. J. Fox, *Atlas of Human Hair Microscopic Characteristics* (CRC, Boca Raton, FL, 1999).

<sup>25</sup>M. Brydegaard, Z. G. Guan, and S. Svanberg, "Light-emitting diode (LED) based multispectral microscope for imaging transmission spectroscopy," *Lund Reports on Atomic Physics LRAP-395* (2008).

<sup>26</sup>H. Moravec, "When will computer hardware match the human brain?," *J. Evol. Techn.* **1**, 1–12 (1998).

<sup>27</sup>Roithner LaserTechnik GmbH (Austria), ([www.roithner-laser.com](http://www.roithner-laser.com)).

<sup>28</sup>B. Standish, "LEDs for bioanalytical and medical instruments," *Biophotonics Int.* **14**, 37–39 (2007).

<sup>29</sup>P. Herman, B. P. Maliwal, H. J. Lin, and J. R. Lakowicz, "Frequency-domain fluorescence microscopy with the LED as a light source," *J. Microsc.* **203**, 176–181 (2001).

<sup>30</sup>J. T. Zoueu, G. L. Loum, T. C. Haba, M. Brydegaard, and H. Menan, *J. Appl. Sci.* **8**, 2711–2717 (2008).

## PAPER III

### **Versatile multispectral microscope based on light emitting diodes**

M. Brydegaard, A. Merdasa, H. Jayaweera, J. Ålebring and S. Svanberg  
*Review of Scientific Instruments* **82**, 123106, (2011).

## Versatile multispectral microscope based on light emitting diodes

Mikkel Brydegaard, Aboma Merdasa, Hiran Jayaweera, Jens Ålebring, and Sune Svanberg

Citation: *Rev. Sci. Instrum.* **82**, 123106 (2011); doi: 10.1063/1.3660810

View online: <http://dx.doi.org/10.1063/1.3660810>

View Table of Contents: <http://rsi.aip.org/resource/1/RSINAK/v82/i12>

Published by the [American Institute of Physics](#).

---

### Related Articles

Design and analysis of multi-color confocal microscopy with a wavelength scanning detector  
*Rev. Sci. Instrum.* **83**, 053704 (2012)

Wavefront corrected light sheet microscopy in turbid media  
*Appl. Phys. Lett.* **100**, 191108 (2012)

Channelling optics for high quality imaging of sensory hair  
*Rev. Sci. Instrum.* **83**, 045001 (2012)

Total internal reflection fluorescence microscopy imaging-guided confocal single-molecule fluorescence spectroscopy  
*Rev. Sci. Instrum.* **83**, 013110 (2012)

A high accuracy femto-/picosecond laser damage test facility dedicated to the study of optical thin films  
*Rev. Sci. Instrum.* **83**, 013109 (2012)

---

### Additional information on *Rev. Sci. Instrum.*

Journal Homepage: <http://rsi.aip.org>

Journal Information: [http://rsi.aip.org/about/about\\_the\\_journal](http://rsi.aip.org/about/about_the_journal)

Top downloads: [http://rsi.aip.org/features/most\\_downloaded](http://rsi.aip.org/features/most_downloaded)

Information for Authors: <http://rsi.aip.org/authors>

## ADVERTISEMENT

**EMBEDDED  
PLANET**



Custom MicroTCA system integration.  
Embedded Planet and Schroff.  
Embedded Planet CPU with any DSP,  
FPGA, storage or power.  
Custom RTM or AMC designs.

[www.embeddedplanet.com](http://www.embeddedplanet.com)  
866.612.7865

**Schroff®**



## Versatile multispectral microscope based on light emitting diodes

Mikkel Brydegaard,<sup>1</sup> Aboma Merdasa,<sup>1,2</sup> Hiran Jayaweera,<sup>1,3</sup> Jens Ålebring,<sup>1</sup> and Sune Svanberg<sup>1</sup>

<sup>1</sup>*Division of Atomic Physics, Lund University, SE-221 00 Lund, Sweden*

<sup>2</sup>*ICFO, Institute of Photonic Sciences, Av. del Canal Olímpic, 08860 Barcelona, Spain*

<sup>3</sup>*Department of Physics, University of Colombo, Colombo 03, Sri Lanka*

(Received 2 April 2011; accepted 20 October 2011; published online 13 December 2011)

We describe the development of a novel multispectral microscope, based on light-emitting diodes, capable of acquiring megapixel images in thirteen spectral bands from the ultraviolet to the near infrared. The system captures images and spectra in transmittance, reflectance, and scattering modes. We present as examples of applications ground truth measurements for remote sensing and parasitology diagnostics. The system is a general purpose scientific instrument that could be used to develop dedicated simplified instruments with optimal bands and mode selection. © 2011 American Institute of Physics. [doi:10.1063/1.3660810]

### I. INTRODUCTION

Optical diagnostics involving optical spectroscopy is now applied in a vast range of research fields, including biomedicine, zoology, remote sensing, food sciences, and agriculture (see, e.g., Refs. 1 and 2). The backbone of advanced optical diagnostics involving photon transport usually starts by measuring the basic optical properties of the sample of interest, such as, its reflectance, transmission, absorption, scattering, or fluorescent yields.<sup>3,4</sup> These optical properties of the sample govern the extension of the interrogation volume in a variety samples on largely different scales; e.g., interstellar dust,<sup>5</sup> planetary atmospheres,<sup>6</sup> forest canopies,<sup>7</sup> living tissue,<sup>8</sup> bird plumage,<sup>9</sup> or photon migration within a single grain of rice.<sup>10</sup> Basic optical diagnostics often involves several steady-state measurements with an integrating sphere, e.g., total reflectance, total transmittance, and collimated transmittance.<sup>11</sup> Due to high requirements on radiance, broadband light is usually created with high-pressure xenon-mercury lamps, collimated into fibers, and then directed at the sample. After interaction with a sample of known thickness, the light propagation angle is measured in a number of angular intervals (discretized), representing total reflectance, transmittance, and collimated transmittance, and the light is collected and analyzed with multichannel spectrometers. For highly fluorescent samples, and when studying optical properties in the UV region, even the wavelength of the excitation light source must be selected (discretized) with an additional monochromator to separate reflectance from fluorescence.<sup>12</sup> The optical efficiency (photon economy) is usually poor in these setups, since light is lost every time the beam is divided. The area studied can be rather large, and the samples must be of a considerable size. Since the measurements are averaged spatially over the beam profile, it is impossible to describe the variation of properties within the sample. For example, a hole in the sample would increase the total transmittance in the same way as if the sample had been thinner or more transparent. The advantage of imaging spectroscopy is thus evident.

The stability of the spectrum produced by XeHg lamps is usually poor because of the turbulence caused by the extreme pressure and temperature, which makes calibration unreliable. In addition the relatively long acquisition time introduces uncertainties resulting from sample drying, or photobleaching and photokinetics, which may cause non-linear absorption and fluorescence.<sup>13</sup> A number of alternative methods exist, including time-resolved methods which are able to separate scattering and absorption phenomena,<sup>14,15</sup> and spatially resolved methods, where diffuse reflectance distributions are studied.<sup>16</sup> The acquisition time is usually long, the number of spectral bands is limited, and considerable sample volumes must be used for certain assumptions to be valid.

The recent development of light-emitting diodes (LEDs) as light sources<sup>17</sup> has afforded several advantages, including simplicity, reduced cost, and increasing emission yields every year. Stability has been improved<sup>18</sup> and modulation speed increased to the sub-nanosecond scale.<sup>19,20</sup> The light emitted from these devices currently ranges from 240 nm to 7  $\mu\text{m}$ .<sup>21</sup> Their use in diagnostic instrumentation implies a significant improvement in performance, due to the fact that spectroscopy can be performed in the illumination side, without losses due to wavelength selection, rather than on the detection side using lossy spectrometers or filters. The corresponding technology for acquiring multispectral images sequentially on the detection side would be imaging through costly interference filter wheels or tunable liquid crystal filters.

The recent development of complementary metal-oxide-semiconductor (CMOS) imagers<sup>22</sup> and industrial imagers for inspection provides millions of spatial light measurements. Also, they now include features such as fast triggering, synchronization, extended dynamic ranges, and the interesting feature of having no blooming, an intrinsic feature which allows measurements, even if parts of the image are saturated.

We present a LED-based multispectral microscope, which can be considered as an imaging spectrometer with improved photon economy, and reduced cost, capable of measuring the optical properties of samples with sizes ranging from few micrometers to a millimeter. The instrument

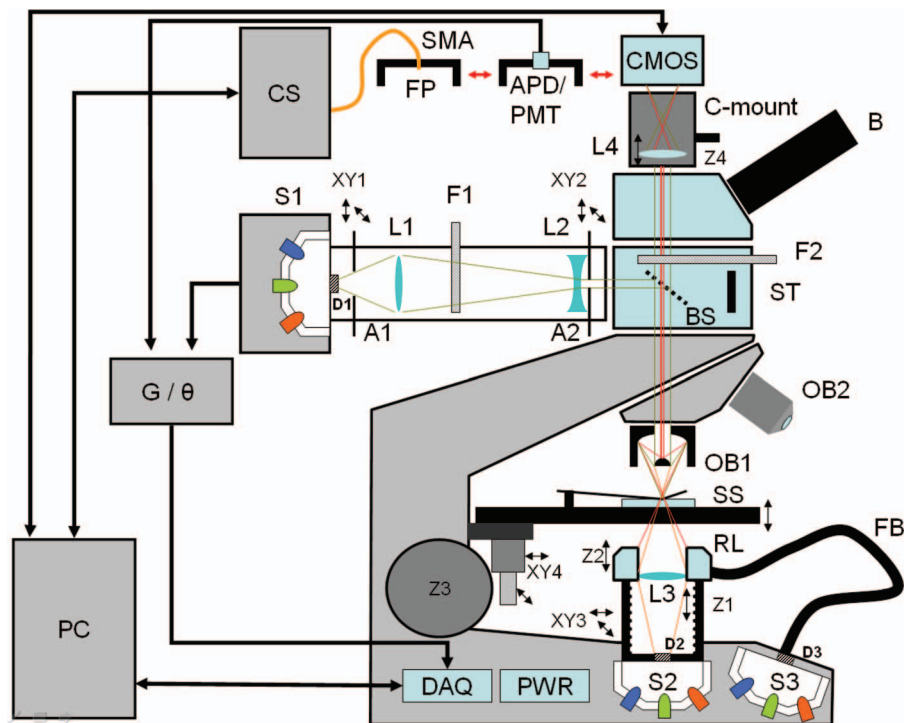


FIG. 1. (Color online) System overview. Three optical multiplexers, S1–S3, provide multispectral illumination from the UV to NIR region in reflectance, transmittance, and scattering mode, respectively. The light from the sample mounted on the sample stage, SS, is collected through a reflective objective OB1. Detection is generally performed by a monochromatic CMOS industrial camera. Alternatively, light can be detected by a compact fiber spectrometer, CS, e.g., for band calibration. Photodiodes or an APD can be used to study fast phenomena. Filter slots F1 and F2 can be used for various filters in polarization or fluorescence studies.

can be used to measure diffuse and specular reflectance, transmission, absorption, scattering, anisotropic scattering, and excitation-emission matrix fluorescence in 13 spectral bands ranging from 375 to 940 nm. Further, the instrument provides quantitative information on the consistency and spatial variation of the properties within the sample by use of a 5 megapixel CMOS camera.

## II. INSTRUMENT AND SYSTEM CONFIGURATION

### A. Optics

The instrument is based on a modified metallurgical microscope<sup>23–25</sup> (Brunel Microscopes Ltd. Model, SP80). The original filament light source for reflective imaging was removed. Three of the original lenses and achromats (OL1, OL2, and OL3) were removed, and three new LED multiplexing modules, S1, S2, and S3, were installed, two of them under the sample stage (SS). The modified microscope is shown schematically in Fig. 1.

The light sources, the LED multiplexing modules, are cylindrically symmetric cavities made of highly reflective white teflon, and serve to combine the rays from each LED.<sup>26</sup> For each module (S1, S2, and S3), the optical axes of each LED meet at a common point, where a 5 mm opal diffuser is located (D1, D2, D3, Edmunds Optics, NT46-162). The white teflon cavity enhances the throughput of the light transmitted through the transmissive opal diffusers. When the LEDs are switched on individually, a Lambertian-like source, which is independent of the incident angles, is achieved on the other

side of the diffusers. The LED multiplexing modules have slots for nine 5 mm LEDs; a central one surrounded by eight in a circle. By selecting one triple-band LED and two dual-band LEDs, a total of 13 spectral bands can be achieved ranging from 375 nm to 940 nm (Fig. 2). The LEDs were obtained from Roithner Laser Technik,<sup>21</sup> with details given in next paragraph. This roughly covers the spectral sensitivity range of CMOS imagers, which is also indicated in the figure. Beam centering (XY1) and collimation (XY2) of S1 are achieved by the adjustable apertures A1 and A2, and by the quartz lenses L1 and L2. Dispersive optical components in the instrument are made of quartz to reduce achromatic aberration and lens fluorescence in the illumination profiles towards the UV. Filter slot F1 enables polarizing or low-pass filters to be used for clean-up during fluorescence excitation of the light from S1. The beam from S1 is reflected to the interchangeable objectives OB1, OB2 by a broadband beam splitter. The direct transmission of the light from S1 is terminated on a black, non-fluorescent beam stop, ST. The beam divergence from S2 can be controlled by displacing the lens L3 (Edmund Optics, NT49-959) at the translation stage, Z1. Based on the setting of Z1, the lens L3 images the opal diffuser, D2, either on the sample or on the back of the secondary mirror of the Cassegrainian objective employed, OB1. The setting of Z1 therefore determines whether S2 produces light for scattering or transmission measurements. The light from S3 is fed into a fiber bundle and delivered to a ring light (RL) source (Edmund Optics, NT54-176), which illuminates the sample, at SS, symmetrically, but off-axis. In contrast, S1 and S2 illuminate SS on-axis. Centering of S2 and S3 is achieved using

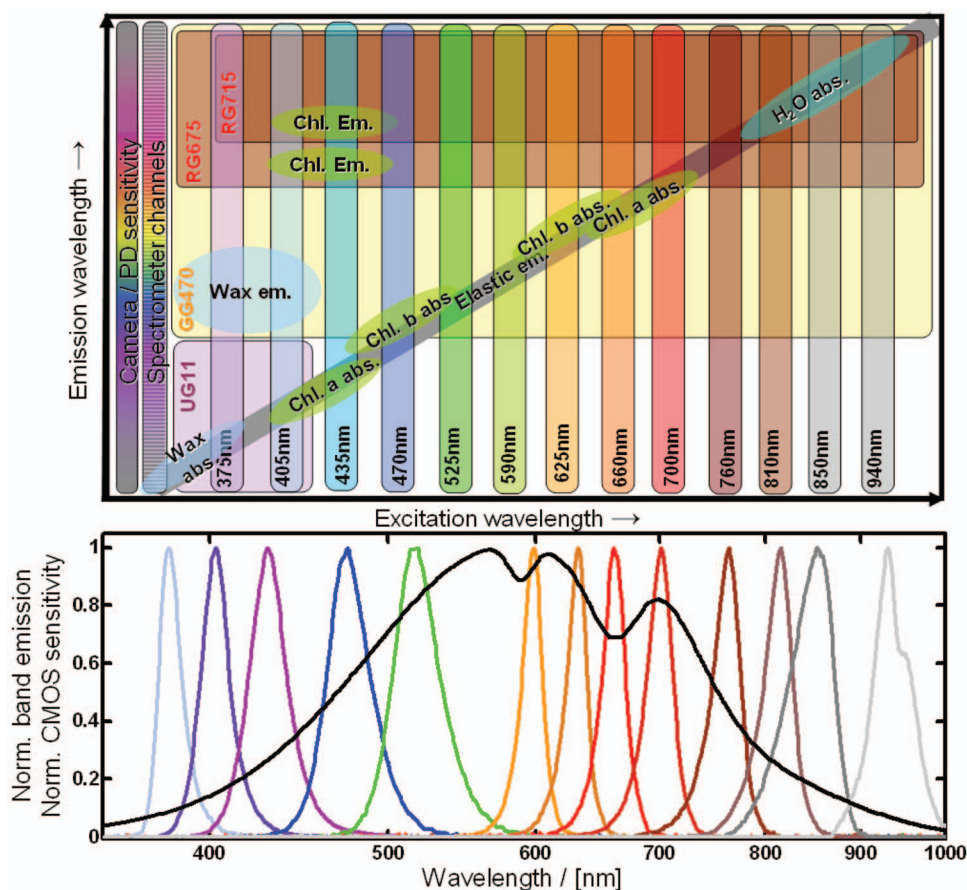


FIG. 2. (Color online) Upper panel: schematic spectral overview of the excitation emission matrix (EEM) with common botanical chromophores. Lower panel: Wavelength of LED emissions and the CMOS camera sensitivity (black curve).

the translation stage XY3. The incident angles from S3 on the sample can be tuned independently by the Z2 translation. In summary, S1–S3 provides monochromatic excitation illumination from the UV to near infrared (NIR) range, from three different angular lobes with respect to the observation lobe. Optical lobes in the instrument operating in different modes are shown in Fig. 3 and will be discussed below.

Particles exhibiting Mie scattering are known to scatter in a complicated angular pattern, which is not resolved by only three angular sectors/lobes. However, angular scans can be performed by translating at Z2, Fig. 1. Also, Mie scattering typically dominates for larger particle sizes in relation to the wavelength which are already spatially resolved by the imager. For smaller particles not spatially resolved, the angular distribution of Rayleigh scattering and emissions after multiple scattering events are considerably less structured, suggesting that a tri-modal measuring strategy is sufficient to describe the scattered distribution. Additional information regarding the number of scattering event can be gained by evaluating the degree of depolarization.

The objectives are either made of transmissive quartz, with low dispersion and long working distance (OB2), or have a Schmidt–Cassegrainian reflective design (OB1; Edmunds Optics, NT58-421) with zero chromatic aberration, numerical aperture  $NA = 0.28$ , focal length  $FL = 13.3$  mm, and working distance  $WD = 23.75$  mm. While traditional dispersive objectives provide a single on-axis angular sensitivity lobe, the

reflecting objective provides a bimodal, off-axis, and angular sensitivity lobe (Fig. 3). The resulting light from the sample, SS, is projected onto the angularly sensitive lobes and is collimated and propagated back through the beam splitter (BS). The light emitted from the sample passes the second filter slot, F2, where a polarizing filter can be inserted for studies of structural colors, or long-pass filters can be inserted to acquire the inelastic fluorescent elements of the excitation emission matrix (EEM). A full EEM showing the location of important botanical chromophores and the overlap with the instrument bands is presented in Fig. 2. A flip-in prism, P, enables the image to be seen in the visible bands through binoculars B; this facilitates sample adjustment and focusing. The emitted light is imaged directly on the CMOS imaging chip by the reflecting objective, OB1 (Fig. 1). The magnification is determined by the choice of objective and the adjustable distances Z3 and Z4. The camera in a 12 bit industrial class CMOS camera, 5 megapixels (Guppy-503B, Allied Vision Technology, with a MT9P031 sensor from Micron/Aptina). Additional adaptors enable a fiber probe, FB, connected to a compact spectrometer to be used instead of the imaging chip. This can be used for instrument calibration, for studies of detailed spectral features, and for the acquisition of detailed multi-wavelength-excitation fluorescence spectra. Alternatively, the detector can be replaced by a fast avalanche diode (APD) or a photomultiplier tube to record fast photokinetics and fluorescence lifetimes in the frequency domain. In this case, the current of the

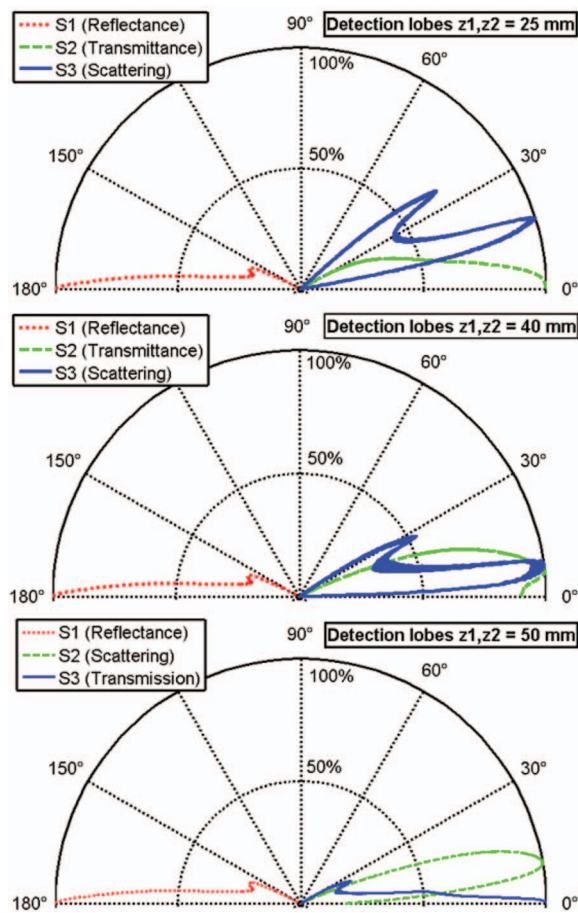


FIG. 3. (Color online) Angular discrimination for three settings of the sub-illumination translation stage ( $Z_1$  and  $Z_2$  in Fig. 1). Lobes are calculated using ray-tracing methods. The reflectance lobe from S1 remains constant, whereas S3 provides scattering and S2 provides transmittance for high settings/values of  $Z_1$  and  $Z_2$ . When the sub-illumination stage is lowered, light from the opal diffuser, D2, is imaged on the back of the secondary mirror of OB1, and light from the ring light enters the aperture directly. Thus, in this setting S2 provides scattering and S3 provides transmittance.

chosen source is swept over a range of radio frequencies, and the resulting demodulation and phase shifts are detected and recorded at low-frequencies (using, e.g., an AD8302 phase detector, Analog Devices).

## B. Electronics

The electronic circuit is controlled by a USB data acquisition board (DAQ, National Instruments, NI USB-6009) and enables multiplexing between different angular modes and different spectral bands. The LEDs are powered by adjustable constant-current sources (Fig. 4). The maximal currents allowed for the NIR sources are somewhat higher than the max current for the UV sources, because of the thermal limitations of LEDs. Since we have 39 sources, we can operate the LEDs in flash mode at currents exceeding the maximum recommendations for the continuous mode by allowing each source to cool between flashes (including a dark measurement). Being able to use higher power increases the signal-to-noise ratio (SNR). In this mode, the clock signal is provided by the camera used for synchronization. A security shut-off is included (in flash mode) in case the clock signal times out. Apart from

the DAQ controlling the current and the source, analog inputs allow the sources to be characterized in terms of voltage-current ( $U$ - $I$ ) curves. These curves provide information on the temperature of each source. Another interesting feature not presented in the schematics in Fig. 4 is that the circuit can be modified to reverse the voltage on the LEDs in order to use them as wavelength-selective detectors. This provides the opportunity for full EEM measurements on the samples. Detailed mechanical and circuit board drawings can be obtained from Ref. 27 and from the authors on request.

## C. Software

The equipment is controlled by LabVIEW software (National Instruments, NI). The user interface is shown in Fig. 5. The program controls camera exposure and gain, LED multiplexing and the current through the NI data acquisition board, DAQ. The graphical interface is constructed around a live preview picture from the camera for easy localization and focusing. Sliders are used to adjust the gain, exposure, and LED currents, while drop down menus are used to select the wavelength band and the angular mode, i.e., reflectance, transmission, or scattering. A live histogram enables the operator to adjust the settings to avoid saturation of the dynamic range. When the settings for a mode and a band have been chosen, they are added to a row in a measurement protocol. The columns of the table are: angular mode, wavelength, LED current, camera gain, exposure, pause between executing each row. Each row corresponds to the acquisition of one monochromatic image. When the whole protocol is executed, the program saves the images on the hard drive together with a copy of the measurement protocol.

Image analysis is performed in MATLAB (Mathworks), where the images are imported and arranged in multidimensional tensors. Calibration and filtering is pursued and analysis is performed according to the need of the studies.

## III. SYSTEM CHARACTERISTICS

### A. Optical discretization and calibration

As in any modern optical diagnostic method, the light properties are handled numerically by computers and therefore quantized, or otherwise expressed, discretized. The system can be characterized according to the domains listed in Table I.

Some experiments may require the discretization of polarization, inelastic effects such as fluorescence, or phase in interferometric setups. Below we will describe and characterize the multispectral microscope in the five domains listed above.

### B. Dynamic domain calibration and light intensity

In general, a multidimensional matrix or tensor,  $U$ , is obtained, containing matrix elements of intensity counts,  $u$ . By comparing the intensity counts before,  $U_0$ , and after interaction with a sample  $U_{sample}$ , a number of optical properties of the sample can be determined, and analyzed along each

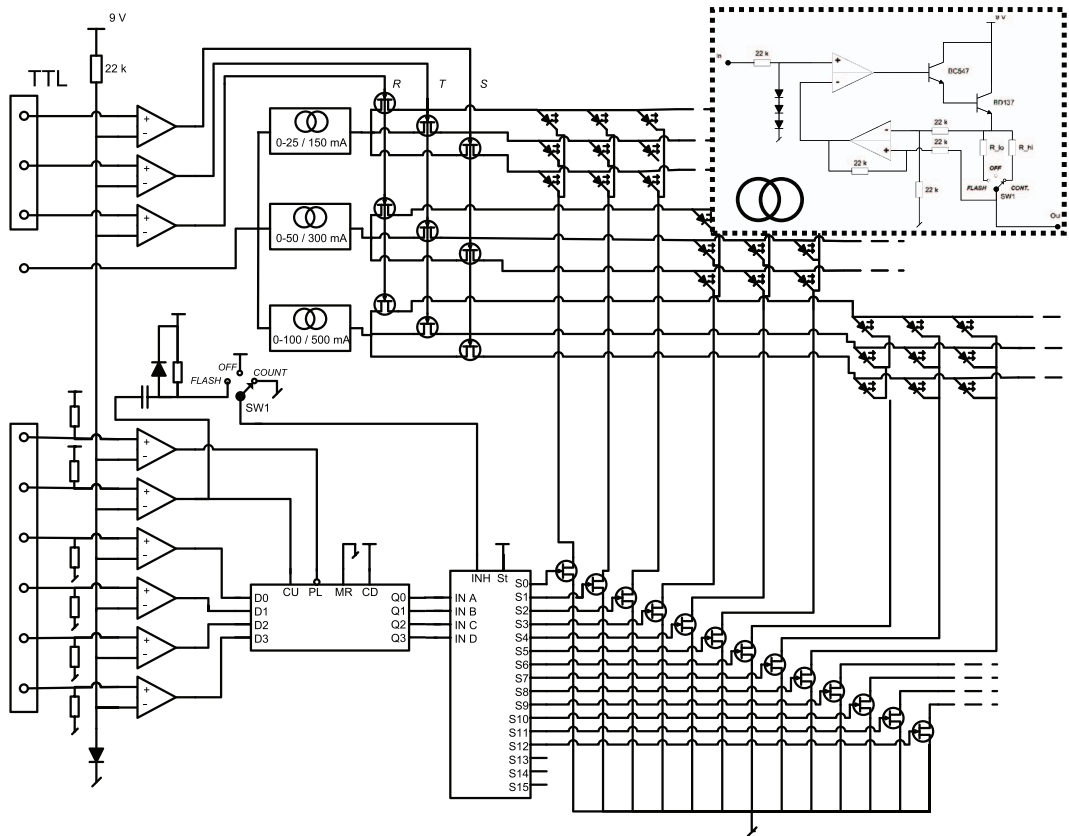


FIG. 4. Electronic schematic used for the multiplexing of sources. Inset: electronic scheme for the adjustable constant-current driver. UV and blue LEDs are driven with currents up to 25 mA, whereas the NIR LEDs can be driven with up to 100 mA.

domain. The dark tensor,  $U_{dark}$ , i.e., the contribution arising from the background and dark current in the detector, is subtracted from both these measurements. Since dark current varies with electronic gain, exposure time and instrument temperature, the measurement protocols for  $U_{dark}$ ,  $U_0$ , and  $U_{sample}$  should be identical. After dark current subtraction each element in the sample tensor is divided by the corresponding el-

ement in a bright reference image. This operation cancels out different emissive yields of the LEDs, electronic gains, and exposures for each band, and also the variation in the illumination intensity over the field of view (FOV):

$$\{T, R, S\} = \frac{U_{sample} - U_{dark}}{U_0 - U_{dark}}, \quad (1)$$

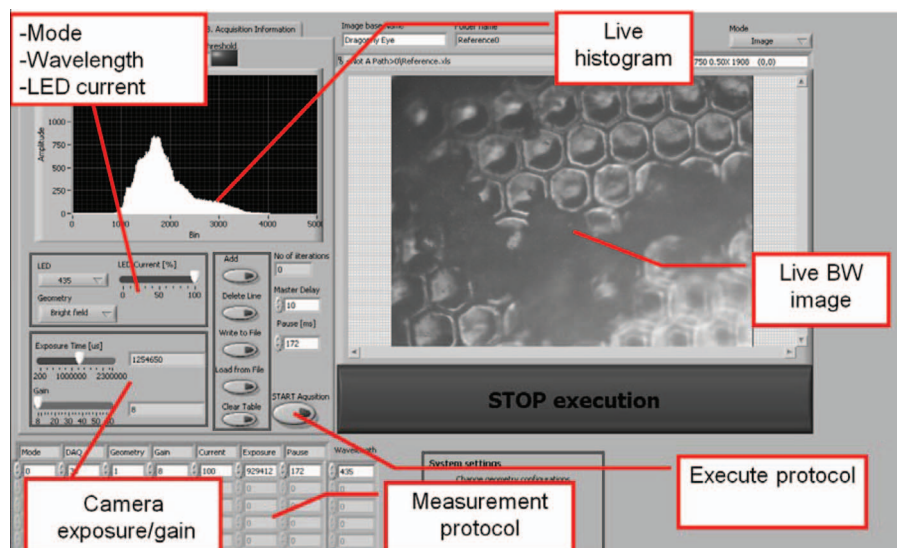


FIG. 5. (Color online) Graphical user interface (GUI) for controlling the LabView software. The GUI includes a live monochrome preview, live histogram, and settings can be made for the LEDs and camera. The settings can be added to a measurement protocol, which can then be executed automatically.

TABLE I. Discretization of different optical processes.

Subject to discretization	Light intensity	Spatial origin	Time	Light energy	Propagation
Domain	Dynamic	Spatial	Temporal	Spectral	Angular
Discretized by	Bits	Pixels	Frames	Spectral bands	Scattering lobes
Source constraint	Number of photons	Illumination beam profile	Exposure gate	Spectral linewidth	Beam divergence
Detector constraint	QE and SNR	Point spread function	Flash envelope	FWHM band sensitivity	Acceptance angle
Range	Full well and dynamic range	Field of view	Recording time	Spectral coverage	Numerical aperture
Quantity preserving initial condition	Bright reference	Specular, ballistic	Instant	Elastic	Ballistic
Phenomena causing changes in the property	Absorption, scattering	Photo-migration	Fluorescence, migration delay	Fluorescence, Raman, Doppler, harmonics, ionization	Refraction, reflection, Mie and Rayleigh scattering

where  $T$  is the transmittance,  $R$  is the reflectance,  $S$  is the scattering,  $U_{sample}$  is sample tensor,  $U_{dark}$  is dark tensor, and  $U_0$  is bright tensor. Details regarding calibration of each mode can be found in Table II.

The optical properties of the sample can be used to improve our fundamental understanding, alternatively  $T$ ,  $R$ , and  $S$  can be used in multivariate mathematics, and chemometric methods can predict special features of interest. Such analysis can be useful, e.g., for designing systems with optimal wavelengths for specific diagnostic tasks.

The CMOS imager used, gives rise to so-called “salt and pepper noise,” which implies that certain pixels are saturated and certain pixels are entirely black. This type of noise is static and cannot be removed by temporal averaging; instead a spatial 2D median filter removes this noise entirely. This operation decreases the spatial resolution slightly, but the spatial resolution of our system is mainly constrained by the optical resolution, and not by the spatial sampling of pixels.

### C. Spatial domain and field of view

In the spatial domain, the image of the object will be convoluted with the point spread function, PSF, well known from Fourier optics theory,

$$u_{pixel} = \int_{-\infty}^{\infty} \int_{-\infty}^{\infty} (E_{profile}(x, y) \text{PSF}_{pixel}(x, y)) \otimes I(x, y) dx dy, \quad (2)$$

TABLE II. Method of calibration for different sensitivity lobes.

Calibration of	Transmission	Reflectance	Scattering
Bright reference, $U_0$	Plain glass slide	Plain glass slide or opal diffuser	Lambertian opal diffuser
Dark reference, $U_{dark}$	LEDs off	Empty sample stage	Empty sample stage

where  $u_{pixel}$  is the contribution to the signal intensity in a given pixel,  $E_{profile}$  is the illumination profile,  $I$  is the intensity from the sample,  $\text{PSF}_{pixel}$  is the point spread function for a given pixel, and  $x, y$  is the spatial coordinates in the object plane.

The spatial confinement can either be provided by a narrow PSF and/or by a narrow scanning illumination profile as in confocal microscopy. As will be shown below, illumination and detection can be freely interchanged mathematically because of the fact that most optical processes are reciprocal and the same result is obtained when source and detector are swapped.<sup>28</sup> Equation (2) assumes a negligible amount of multiple scattering and photo-migration, which to some extent is valid in microscopic samples.

The CMOS imager has pixel sizes of  $2.2 \mu\text{m} \times 2.2 \mu\text{m}$  and an effective chip size of  $5.7 \text{mm} \times 4.3 \text{mm}$ . The finite reflective objective provides a magnification of 15 times, and thus the FOV is roughly  $380 \mu\text{m} \times 286 \mu\text{m}$ . Each pixel therefore has a square “footprint” of  $146 \text{nm} \times 146 \text{nm}$ . Other dispersive objectives with magnifications of  $4\times$  and  $10\times$  included with the original microscope provide a larger FOV, of up to one millimeter. The chromatic properties of these objectives are less convenient than for the reflecting objective; further they will themselves contribute a significant amount of reflectance, and thus consume a considerable amount of the dynamic range. Accurate spatial calibration can be achieved by placing objects with known dimensions in the object plane, e.g., micro-rulers.

The SNR in the dynamic domain can be traded off by spatial resolution by spatial averaging<sup>29,30</sup> where especially median filters are effective; see Sec. III B.

### D. Temporal domain

Consider the analogous effect of the temporal instrument function,

$$u_{frame} = \int_0^{\infty} (E(t)G_{frame}(t)) \otimes F(t) dt, \quad (3)$$

where  $u_{frame}$  is the contribution to the signal intensity from a time frame,  $E$  is the pulse envelope of illumination,  $G_{frame}$  is

the exposure time of the detector,  $F$  denotes the changes in the sample over time, and  $t$  is time.

Equation (3) states that a fast photograph of a changing process can be achieved either by a short camera exposure, or a short flash of illumination. The assumption made for Eq. (3) to be valid is that the photons should not be delayed by the sample. A delay could be caused by the fluorescence process; however, fluorescence is normally a weak phenomenon compared to elastic phenomena.

For a good SNR, exposure time varies between 0.02 and 2 s, and the acquisition of an entire dataset with 13 bands in transmission, reflection, and scattering typically takes 1 min. The same period is required to obtain the dark and bright references.

As in the spatial domain, the SNR in the dynamic domain can be improved at the expense of the temporal resolution. However, since a large fraction of the noise is static the spatial average is more effective.

### E. Spectral range domain

In general in LED spectroscopy it is more convenient to provide more spectral or angular modes by a plurality of LEDs rather than a plurality of detectors,<sup>26,31</sup> because of circuit simplicity and cost. The spectral bands are now defined by the sources rather than by the spectral discrimination on the detecting side (see Fig. 2). The result is equivalent, as is evident from Eq. (4), as long as there is no fluorescence:

$$u_{band} = \int_0^{\infty} E_{band}(\lambda) D(\lambda) O(\lambda) d\lambda, \quad (4)$$

where  $u_{band}$  is the contribution to the signal intensity from a given spectral band,  $E$  is the emission spectrum of the illumination,  $D$  is the detector sensitivity spectrum,  $O$  is the spectral property of the sample, and  $\lambda$  is the wavelength.

A C-mount to SMA adapter was used to connect the instrument to a fiber (see CS, SMA, FP, in Fig. 1) in order to characterize the system bands with a compact spectrometer (USB2000, Ocean Optics). The effective center wavelength,  $\lambda_{band\ center}$ , of a spectral band is given by the center of mass formula

$$\lambda_{band\ center} = \frac{\int_0^{\infty} (V_{band}(\lambda) - V_{dark}(\lambda)) D_{imager}(\lambda) \lambda d\lambda}{\int_0^{\infty} (V_{band}(\lambda) - V_{dark}(\lambda)) D_{spectrometer}(\lambda) d\lambda}, \quad (5)$$

where  $\lambda_{band\ center}$  is the effective center wavelength for a given band,  $V_{band}$  is the spectrometer recording at the image plane,  $V_{dark}$  is the dark spectrum,  $D_{imager}$  is the sensitivity spectrum of the imager (from manufacturer's datasheet), and  $D_{spectrometer}$  is the spectrometer sensitivity including fiber transmission.

The estimated bandwidth, full width at half maximum (FWHM), was compensated by detector sensitivity in a similar way. The measured characteristics of the LEDs used are given in Table III. Many of the sources are now available with an emissive yield several times higher.

TABLE III. Characteristics of LEDs used in the multispectral microscope.

Substrate	Part no.	$\lambda_{band}$ (nm)	FWHM (nm)	CW max power (mW)
AlGaP	NS375L_ERLM	380	12	26
AlGaP	LED405-33V	405	16	15
AlGaInP	LED435-12-30	430	23	20
InGaN	B5-4RGB-CBA	480	29	20
InGaN	B5-4RGB-CBA	525	34	10
AlGaInP	Y5CA5111P	600	17	55
AlGaInP	B5-4RGB-CBA	630	18	5
AlGaAs	LED660-850-04A	660	22	5
AlGaAs	ELD-700-524	700	25	10
AlGaAs	LED760-940-04A	760	29	15
AlGaAs	ELD-810-525	810	32	28
AlGaAs	LED660-850-04A	850	52	7
GaAs	LED760-940-04A	935	48	14

### F. Discretization of light propagation and estimation of angular sensitivity lobes

Several microscopic diagnostic methods are known, such as bright field microscopy, where transmitted light is observed from a thin sample slice; reflection (metallurgical) microscopy, where reflected light from opaque minerals or metallic parts is observed, and dark field microscopy in which the ballistic (non-scattered) light never reaches the detector, and only light scattered into the acceptance angle of the objective is detected. The last mentioned mode greatly enhances contrast in transparent biological samples, where organelles such as nuclei, cell membranes, and mitochondria show increased scattering. Since single scattering is most frequently observed in microscopic samples, the scattering distribution can be expected to have a strong dependence on wavelength, polarization, and size of the scatterer. The three well-known earlier mentioned methods in microscopy can all be summarized to a single consideration regarding the light propagation from the sample in respect to the prior incident propagation. For a given system we can consider a sensitivity lobe as being the spherical convolution between the acceptance of the objective and the angular distribution of illumination impinging on the FOV (See Fig. 3). If the sensitivity lobe covers the scattering angles,  $\theta$ , close to 0 the system can be used for transmittance measurements, which will be largely influenced by the absorption of the sample according to the Beer-Lambert law. A narrow lobe at  $\theta = 0$  implies collimated transmission, whereas a broad lobe implies a diffuse total transmittance measurement. If the system sensitivity lobe instead covers the scattering angles,  $\theta$ , close to 180°, the system will measure reflectance or backscattering. Such measurements will be greatly influenced by the refractive index of the sample, according to Fresnel's equations. A narrow sensitivity lobe at  $\theta = 180^\circ$  often implies a measurement of specular reflectance, whereas a broad lobe would imply a diffuse total reflectance measurement. Alternatively, diffuse reflectance can be measured by observing the depolarized backscatter with crossed polarizers. When the system sensitivity lobe covers  $\theta$  between 0 and 180°, we refer to a scattering measurement. The contribution here is described by Rayleigh and

Mie scattering theory. Any measurement involving a sample slide will suffer from a constraint inhibiting any effective system sensitivity lobe close to  $90^\circ$  in respect to the normal. Generally, the contribution to a lobe can be thought of as

$$u_{lobe} = \int_0^{180^\circ} \int_0^{360^\circ} (E_{\text{mod } e}(\theta, \phi) \otimes D(\theta, \phi)) S(\theta) \sin(\theta) d\phi d\theta, \quad (6)$$

where  $u_{lobe}$  is the contribution to signal intensity falling into a certain lobe,  $E$  is the angular distribution of incident illumination for a given mode,  $S$  is the scattering distribution of the sample,  $D$  is the detection lobe, fixed for the choice of objective,  $\theta$  is the relative scattering angle perpendicular to object plane, and  $\phi$ , is the relative scattering angle in object plane.

We note that although both illumination and acceptance lobes are cylindrically symmetric, and although the sample is non-ordered, the scattering angle projection on the object plane,  $\phi$ , is necessary for the 2D spherical convolution. The resulting effective system sensitivity lobes are still cylindrical and can be presented in a polar plot.

In an ideal case, the sensitivity lobes add up to a unit sphere. In practice, this is generally not achievable. From conservation of energy the following constraint for elastic light is obtained:

$$T + R + S + A \leq 1, \quad (7)$$

$T$ ,  $R$ , and  $S$  have been defined above, and  $A$  is the absorbance. Several approaches to derive basic optical properties such as the absorption coefficient,  $\mu_{\text{abs}}(\lambda)$ , the scattering coefficient,  $\mu_{\text{scat}}(\lambda)$ , anisotropic scattering,  $g$ , and refractive index,  $n$ , from a vector of contributions to several sensitivity lobes have been successfully applied.<sup>11</sup> Generally, the number of lobes should be at least as many as the number of unknown properties for such an inversion to work. Defining the sensitivity lobes of the instrument is essential as a first step towards quantitative dark-field microscopy, a topic which is currently untouched in general.

By translation of the sub illumination (Z1 together with Z2 in Fig. 1), several angular sensitivity lobes can be obtained with the system presented here. In the upper-most figure in Fig. 3 the optical multiplexer S2 in Fig. 1 accounts for the transmittance measurement, and S3 accounts for the scattering measurement. In the lower-most figure with a different translation of the sub illumination S2 accounts for the scattering, whereas S3 accounts for the transmittance measurement. The lobes in Fig. 3 are obtained by ray-tracing methodology using the FRED (Photon Engineering LLC) software package. The lobes are calculated using the reciprocity of optics, in which we can let the CMOS detector chip be acting as a light source in the ray-tracing simulation. By calculating the 2D convolution between the distribution of angular propagation on the FOV, from both the real light sources and from the imaginary rays from the detector source, we obtain the effective system sensitivity lobes. The lobes in Fig. 3 are cross-sections of the cylindrically symmetric lobes from the convolution. As in Fig. 2 each lobe was normalized to 100% responsivity.

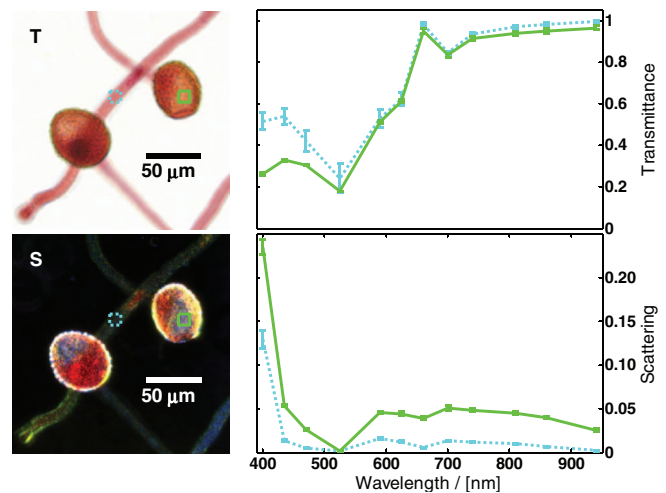


FIG. 6. (Color online) Microspectroscopy of pollen. The upper figures show transmittance, and the lower figures scattering. Proteins and waxes cause differential absorption in the blue and UV regions.

## IV. EXAMPLES OF AERAS OF APPLICATION

### A. Ground truth and bio-aerosol analysis for remote sensing and environmental monitoring

In the area of environmental monitoring and remote sensing, techniques such as light detection and ranging (LIDAR) and hyper-spectral imaging,<sup>2,32–37</sup> have proven efficient in analyzing various types of vegetation, atmospheric gases, and bio-aerosols.<sup>38–40</sup> The methods are known to be especially useful in combination with ground truth measurements, where the basic optical properties of the species of interest are investigated.<sup>41</sup> In Fig. 6, two pollen germinations were placed in the FOV. The picture to the upper left shows true color RGB (630 nm, 525 nm, 470 nm) transmission. The pollen tube seen as a pink fiber-like structure measures just  $10 \mu\text{m}$  in diameter. The pollen grain is considerably larger and appears as a sphere. In the lower left picture the same situation is shown in scattering imaging where the glass slide appears black. Two regions of interest (ROIs) were selected, one for the pollen tube and one for the pollen grain. The corresponding spectra are presented on the right. The error bars represent the variance within the ROIs. The pollen grain shows higher absorption in the violet region than the tube. The pollen grain is known to contain waxes and proteins which protect the genetic material. In scattering mode, the tubes appear mostly clear and transparent, whereas the grains have increased scattering and light is multiply scattered (whitish) due to the fractal elements of the grain. The spectral difference could provide a method for remote estimation of the grain/tube ratio useful in bio-aerosol measurements by differential absorption LIDAR (DIAL).<sup>39</sup>

Polarization analysis is a useful tool to investigate the spectral signatures of bio-aerosols. Two damselfly abdomens, one of each gender, (dried specimen) were placed in the instrument (Fig. 7). *Calopteryx splendens* is known to produce bluish and greenish colors by coherent scattering. Such structural colors would appear in the polarized reflectance, whereas they would vanish in the depolarized reflectance.

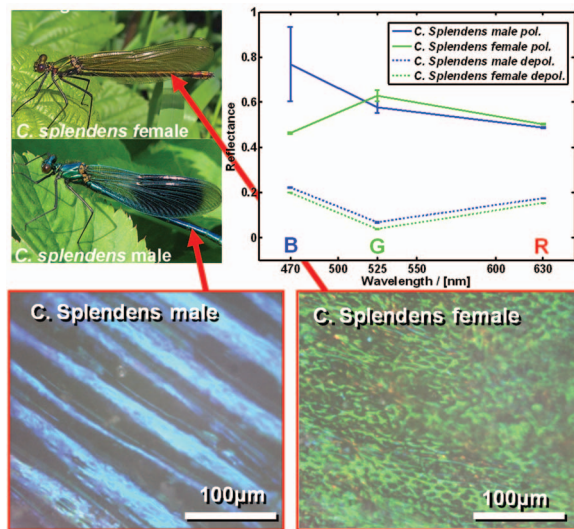


FIG. 7. (Color online) Demonstration of polarization effects in structural colors of a damselfly species. Note that the gender-specific spectral feature disappears in the depolarized reflectance—an inherent property of structural colors.

Spectral features based on differential absorption would be more prominent in depolarized reflectance since the specular part of reflectance would be removed. The RGB values for polarized and depolarized reflectance light were normalized to the polarized and depolarized reflectance from white paper, respectively. The dark reference must also be measured for each kind of polarized light because of the contribution from the beam stop, ST (see Fig. 1). Linear film polarizers (Edmunds Optics, NT45-667) for visible light (450–650 nm) were placed in filter positions F1 and F2. Three pieces of polarizers were cut out from a sheet, two identical and one perpendicular to the polarizing axis of the sheet. Polarization studies over a broader spectral range could be achieved with wire grid polarizers or Glan Thomson polarizers, but with a completely different cost.

Remote monitoring and classification of insects have so far been carried out for diverse purposes such as basic evolutionary ecology,<sup>41</sup> landmine detection,<sup>42</sup> and the evaluation of pest pheromone traps in agriculture.<sup>43</sup> Apart from use in insect studies,<sup>41</sup> the instrument has also been used to obtain supporting data for the remote sensing of birds.<sup>44</sup>

## B. Vegetation analysis in agriculture

Several commercial LED-based systems exist and are often used to measure leaf reflectance, transmittance, scattering, and chlorophyll fluorescence. Such measurements are related to the photon migration in forest canopies,<sup>38,45,46</sup> and multispectral satellite imaging is crucial in managing modern agriculture in terms of determining which crops are being grown, and foreseeing catastrophes such as drought or epidemics related to monocultures. The image on the left in Fig. 8 shows a composite image of a Chinese strawberry tree leaf (*Myricaceae Myrica rubra*). The sample has chlorophyll-filled patches with bright veins in between. Near-infrared (810 nm) transmission is shown as red, 810 nm scattering as green, and chlorophyll fluorescence at 700 nm is presented as blue. The fluorescence is induced with the 435 nm LED in reflectance mode and detected through a long-pass filter at 470 nm placed at F2 (See Fig. 1). In principle, multi-wavelength-excitation imaging could be performed without having to remove the long-pass filter.<sup>47</sup> Other parameters related to the condition of the plant can be extracted using photokinetics and the Kautsky process.<sup>48,49</sup> Such temporal characteristics have been used in gender classification for improved crop yield.<sup>50,51</sup> The decay curve on the right in Fig. 8 shows the decay of chlorophyll fluorescence associated with the entire image. In principle, a lifetime image could be generated, in which each pixel is color-coded according to the decay time; however, in this specimen there was no significant spatial variance of the decay times. The data were fitted to the following model:

$$F(t) = F_0 e^{-t/\tau} + F_b, \quad (8)$$

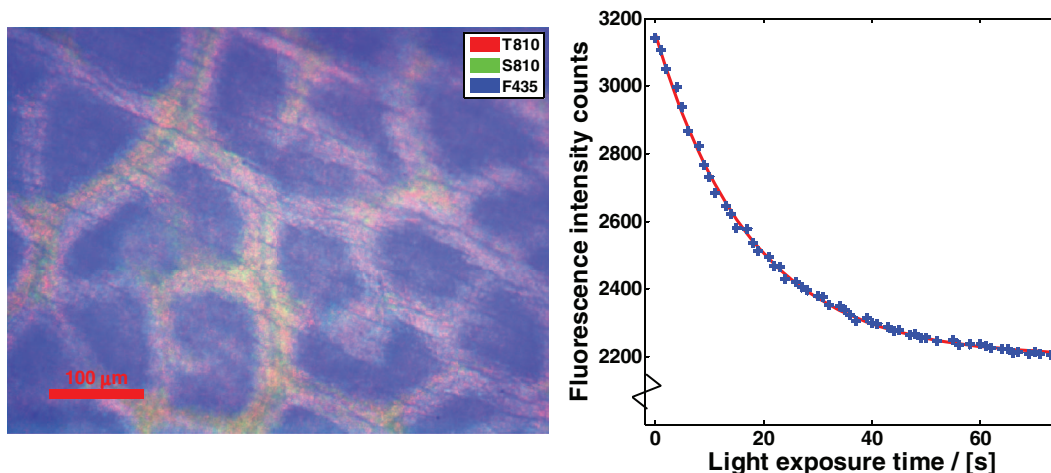


FIG. 8. (Color online) Left: composite image of a *Myricaceae Myrica rubra* leaf. The 810 nm transmittance is illustrated in red, the 810 nm scattering in green, and 435 nm-induced chlorophyll fluorescence at 700 nm is illustrated in blue. Right: the photochemical reaction of chlorophyll over time related to the Kautsky processes.

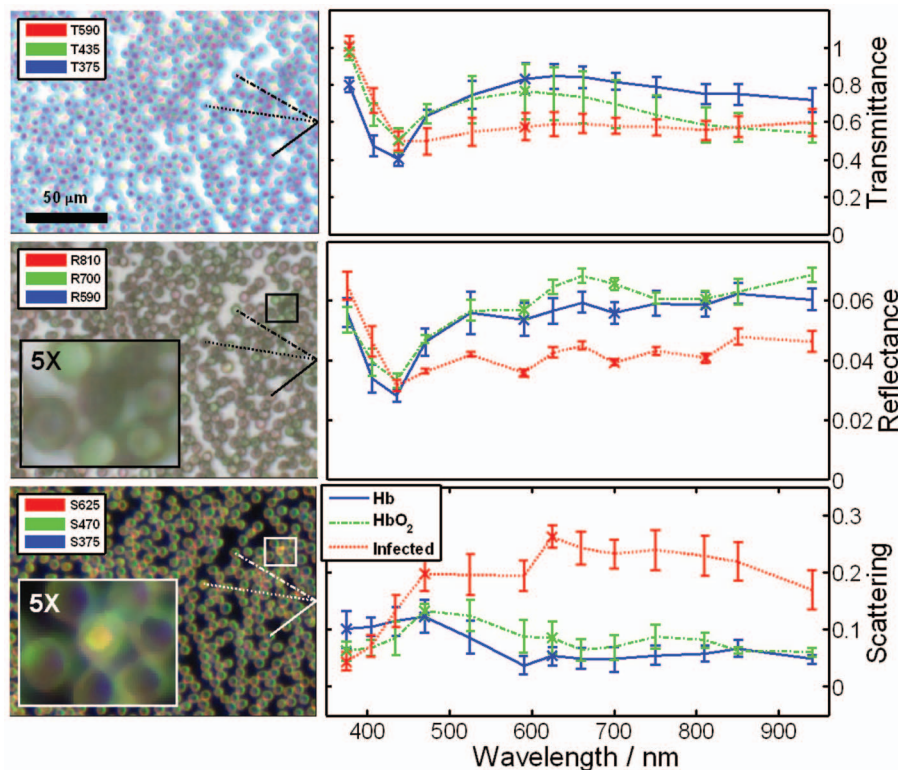


FIG. 9. (Color online) Top left: false color transmittance image of infected blood smear, 590 nm: red, 435 nm: green and 375 nm: blue. Top right: spectra from three ROIs: deoxygenated RBC, oxygenated RBC and a malaria-infected RBC. The error bars indicate within-cell variance. Middle left: false color reflectance image, 810 nm: red, 700 nm: green, 590 nm: blue. The inset shows a  $5\times$  zoom. Middle right: corresponding reflectance spectra. Bottom left: false color image of scattering, 625 nm: red, 470 nm: green, 375 nm: blue. The infected RBCs show increased scattering; see example in the  $5\times$  inset. Bottom right: corresponding scattering spectra.

where  $F$  denotes the fluorescence intensity counts,  $F_0$  denotes initial fluorescence intensity counts,  $F_b$  denotes convergent fluorescence intensity counts, and  $\tau$  is the time constant.

The intensity fell to  $F_b/(F_b + F_0) = 69\%$  of the initial value and the time constant was 17.7 s with the 95% confidence interval 17.2–18.2 s. The specimen was a couple of hours fresh and was studied at room temperature. In general, detailed analysis of photokinetics requires careful calibration of the absolute excitation power impinging on the sample.

### C. Malaria analysis in parasitological studies

The characteristics of *Plasmodium falciparum* parasites, causing malaria, are presented in Ref. 52. Detection of the parasites usually involve time-consuming staining, and the result relies to a great extent on the experience of the evaluating pathologist.<sup>27,53,54</sup> The delay in diagnosis often means that the patient does not return for care, while an inexperienced evaluator often results in a higher false-negative ratio. The scattering of light from single red blood cells (RBCs) or erythrocytes is described in<sup>55,56</sup>. One alternative to staining and manual evaluation is multispectral imaging<sup>27,54</sup> together with multivariate analysis.<sup>57–60</sup> Fig. 9 shows the results of analyzing a malaria infected blood smear in the instrument. The images are all filtered by a  $3 \times 3$  median filter. Different false-color pictures are presented in transmission, reflectance, and scattering mode in the left of the figure. The legend in each image shows which bands are displayed in the RGB image.

Three cells are selected, and their corresponding spectra are shown for each mode on the right. Error bars represent the variance within a ROI of  $\varnothing 3 \mu\text{m}$ . The RBCs are seen as  $7 \mu\text{m}$  diameter discs; the osmotic pressure causes them to either be inflated or donut shaped,<sup>61</sup> which affects the scattering distribution. The two selected healthy cells in Fig. 9 are both swollen RBCs. In the middle picture of Fig. 9 the reflectance shows a clear circle for the inflated RBCs and a circle with a dot in the middle for the donut-shaped RBCs. The absorption properties of hemoglobin change according to whether the RBC carries oxygen or not.<sup>62</sup> This feature is particularly visible in the red-NIR region around 700 nm, and this effect causes certain RBCs to appear green or pink in the false color reflectance image in Fig. 9. Since healthy human RBCs have no internal structure, scattering takes place mostly at the edges. Infected RBCs scatter significantly higher amount of red and NIR light, and they appear as “glowing” yellow cells in Fig. 9 (bottom left). These interesting results suggest that staining free detection could be improved by including spectrally resolved dark field mode microscopy.

The diffraction limit for the reflecting objective imaging at longest spectral band, 940 nm, corresponds to  $2 \mu\text{m}$  resolution. As can be seen in the zoom inserts, the  $7 \mu\text{m}$  RBCs are resolved close to the diffraction limit. The pixel size is, however, ten times smaller. Because of this oversampling the median filter can be applied to remove the salt and pepper noise essentially without any detrimental effect on the spatial resolution.

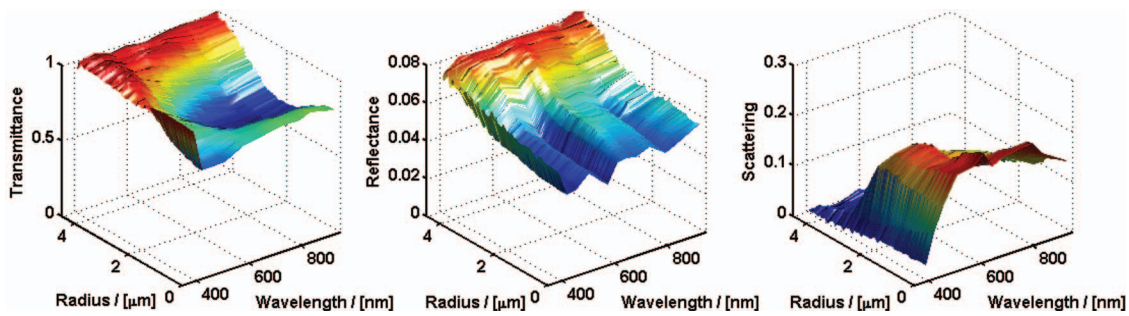


FIG. 10. (Color online) The radial dependence of the transmission, reflectance and scattering spectra from a single healthy red blood cell.

Since RBCs are cylindrically symmetric and align themselves parallel with the microscope slide in a blood smear, the optical properties can be studied as a function of the radius of the cell. Figure 10 shows three such surfaces for transmittance, reflectance, and scattering for a donut-shaped RBC. Healthy RBCs do not scatter red light at the centre due to lack of internal structures. Because of the topology of RBCs, both healthy and infected cells scatter light from the edges. Analysis of the spectral properties in relation to the radius of each cell in the FOV could provide further specificity, for example in healthy RBCs: red light should scatter from the edges but not from the center.

Because of the very large amount of data provided by the instrument, the equipment is especially suited for analyzing variance, both within a cell, between cells and between individuals. Spatial variance can be investigated either as shown above with error bars, or in multivariate analysis, singular value decomposition (SVD), and histograms in one,

two, three or more dimensions. All spectra in each spatial pixel in the scenario in Fig. 9 were concatenated (an operation that places transmittance, reflectance, and scattering vectors one after the other). The concatenated vectors were then decomposed by SVD, and from the eigenvalues it could be concluded that most of the variance within the dataset could be explained by just 3 principal spectral components, out of the total of 39 recorded in the 13 bands in 3 angular lobes. Following decomposition, the data are de-concatenated into transmittance, reflectance, and scattering. The weights of the first 3 components are shown in Fig. 11 (left). The new spectral components span up an optimized 3D color space, in which each pixel falls into a given position (see the black dot scatter plot in Fig. 11, right). By counting the number of observations per unit volume it is possible to construct a 3D histogram tensor. Such a 3D histogram is also illustrated in Fig. 11, right, with iso-surfaces encircling three orders of magnitude of count concentrations in the color space. If

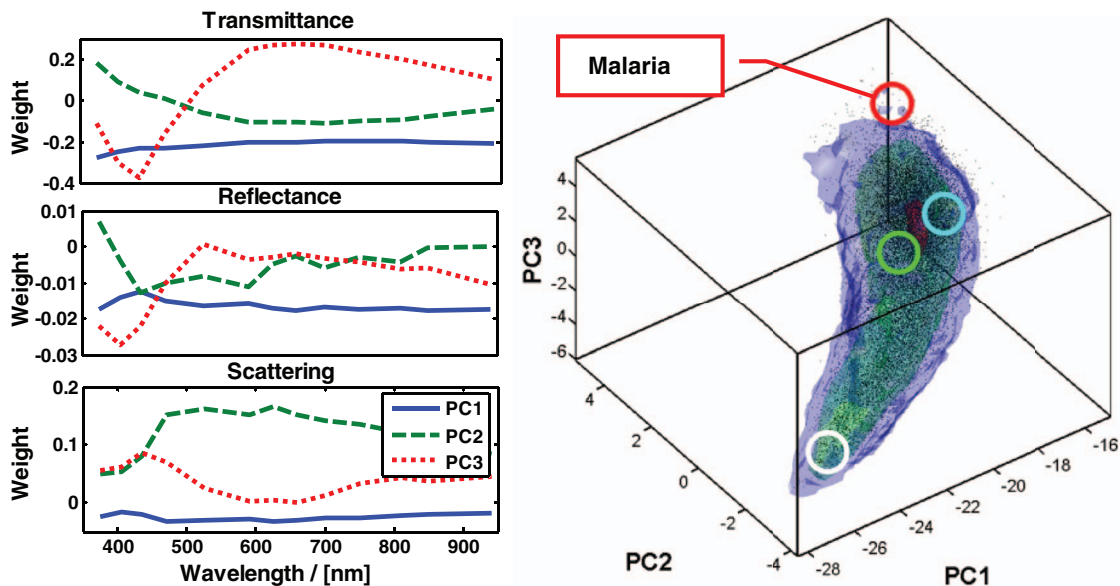


FIG. 11. (Color online) SVD evaluation of infected blood smear. Left: The three components accounting for 75% of the variance in the image. The spectra were concatenated prior to the SVD analysis; thus the components in the various modes are associated. Right: 3D scatter plot with iso-surfaces covering three magnitudes of the 3D probability histogram. The white circle at the bottom indicates the location of the pixels from an empty glass slide. Green and cyan circles in the center indicate the averaged location of the two healthy RBCs from Fig. 9. The core of the scatter plot indicated by a red isosurface, corresponds to the cell peripheries. The infected blood cell illustrated in Fig. 9 falls into the sparse region indicated by the red circle at the top of the figure.

a certain volume unit in the space can be associated with infected RBCs, the counts in that unit volume will relate linearly to the percentage of infected RBCs.

## V. COMMENTS ON THE CONSTRUCTION AND UTILIZATION OF THE INSTRUMENT

The powerful yet inexpensive instrument described in this paper is of great interest in many contexts, not least in solving problems in the Developing World. The assembly and testing of replicas of the described instrument was done during a two-week workshop at the Laser and Fiber Optical Centre, LAFOC, University of Cape Coast, UCC, Ghana. A total of nine units were constructed. The cost of materials for each instrument was approximately 5 000 €. The microscopes are now distributed among the participants from six institutes: LAFOC-UCC-Ghana; Laboratory of Instrumentation Image and Spectroscopy, National Polytechnic Institute of Yamoussoukro, Ivory Coast; Nuclear Laboratory, University of Cheikh Anta Diop of Dakar, Senegal; Department of Physics, University of Bamako, Mali; Department of Physics, University of Nairobi, Kenya; and Department of Instrumentation, University of Colombo, Sri Lanka. Contact details can be provided by the authors upon request. A web community has been established for sharing and discussing data and calibration methods, etc. So far short measurement campaigns have been conducted in Ivory Coast, Senegal, Mali, and Sweden.

## VI. SUMMARY AND CONCLUSION

We have described the design and calibration of a new general purpose multispectral microscope, capable of acquiring megapixel images of microscopic scenes from the UV to NIR, thus providing millions of transmittance, reflectance, and scattering spectra. We have discussed optical discrimination, and we have briefly described environmental sensing and parasitological applications. We have demonstrated polarization and fluorescence studies, and discussed a number of multivariate methods for data evaluation. In conclusion, the instrument described constitutes a powerful development platform for a multitude of applications. Since the presented instrument is mainly based on an imaging detector, the spatial resolution or optical sectioning does not compare to confocal methods<sup>63</sup> or super resolution methods.<sup>64,65</sup> Instead, the strength of this instrument should be found in the broad spectral range covered, the combination of plurality of angular modes and the cost and simplicity of the construction. The vast majority of other multispectral imagers are based on spectral discrimination on the detection side with considerable photon losses associated. Typically this is achieved by spatial scanning combined with costly diffraction gratings,<sup>63</sup> or more recently, by prism-grating-prism devices.<sup>66</sup> Alternatively, spectral discrimination can be achieved by temporal sequencing, like in the present study, but performed with tunable wavelength filters on the detection side.<sup>67</sup> Spectrally resolved transmission microscopy has previously been pursued commercially by traditional methods.<sup>25</sup> Especially the absorption of organic fibers in the UV has led to various applications in forensic science.

Multispectral fluorescence microscopy was pursued in Ref. 63 also by use of a diffracting spectrometer. Multi-spectral macro imaging by multiplexing of LEDs has been pursued commercially<sup>31</sup> in the VIS-NIR range; however, only considering reflectance and employing dispersive objectives.

## ACKNOWLEDGMENTS

This work was supported by a grant from the International Science Programme, Uppsala, Sweden, a direct grant from the Swedish Research Council and a Linnaeus grant to the Lund Laser Centre, and by the PIEp/IDRE consortium. The project was additionally supported by LAFOC, University of Cape Coast, Ghana, Laboratory of Instrumentation Image and Spectroscopy, National Polytechnic Institute of Yamoussoukro, Ivory Coast and the Nuclear Laboratory, Sheikh Anta Diop, Dakar, Senegal. We acknowledge the Botanical Gardens at Lund University for providing samples. We are also very grateful for the helpful collaboration of Ba Abdramen, Benjamin Anderson, Stefan Andersson-Engels, Paul Buah Bassuah, Amadou Coulibali, Jojo Moses Eghan, Ekou Kouassi, Zuguang Guan, Ernst v. Groningen, Menan Herve, Mbaye Mamadue, Ababacar Ndao, Anna Runemark, Ouattara Sie, Linnea Sjöholm, Pelle Steen, Salma Sylla, Amadou Wague, Maren Wellenreuther, and Jeremie Zoueu.

- <sup>1</sup>S. Svanberg, *Atomic and Molecular Spectroscopy* (Springer, Heidelberg Berlin 2004).
- <sup>2</sup>S. Svanberg, *Multi-spectral Imaging: From Astronomy to Microscopy—From Radiowaves to Gamma Rays* (Springer, Heidelberg Berlin, to be published).
- <sup>3</sup>V. Tuchin, *Tissue Optics: Light Scattering Methods and Instruments for Medical Diagnosis*, 2nd ed. (SPIE, Bellingham, 2007).
- <sup>4</sup>S. Jacques and B. Pogue, *J. Biomed. Opt.* **13**, 041302 (2008).
- <sup>5</sup>L. G. Henyey and J. L. Greenstein, *Astrophys. J.* **93**, 70 (1941).
- <sup>6</sup>Y. M. Timofeyev and A. V. Vassilev, *Theoretical Fundamentals of Atmospheric Optics* (Cambridge International Science Publishing, Cambridge, UK, 2008).
- <sup>7</sup>X. Li, A. H. Strahler, and C. E. Woodcock, *IEEE Trans Geosci. Remote Sens.* **33**, 466 (1995).
- <sup>8</sup>*Handbook of Biomedical Fluorescence*, edited by M. A. Mycek and B. W. Pogue (CRC, New York, 2003).
- <sup>9</sup>M. Brydegaard, P. Lundin, Z. Guan, A. Runemark, S. Åkesson, and S. Svanberg, *Appl. Opt.* **49**, 4531 (2010).
- <sup>10</sup>T. J. Bjärang at FOSS Analytical, U. S. patent 7,830,530 B2 (November 9, 2010).
- <sup>11</sup>A. M. K. Nilsson, C. Sturesson, D. L. Liu, and S. Andersson-Engels, *Appl. Opt.* **37**, 1256 (1998).
- <sup>12</sup>M. Kim, Y. Chen, S. Kang, I. Kim, A. Lefcourt, and M. Kim, *Appl. Spectrosc.* **60**, 1210 (2006).
- <sup>13</sup>M. Brydegaard, N. Haj-Hosseini, K. Wårdell, and S. Andersson-Engels, *IEEE Photon. J.* **3**, 407 (2011).
- <sup>14</sup>S. Fantini, M. A. Franceschini, J. B. Fishkin, B. Barbieri, and E. Gratton, *Appl. Opt.* **33**, 5204 (1994).
- <sup>15</sup>E. Gratton, S. Fantini, M. A. Franceschini, G. Gratton, and M. Fabiani, *Philos. Trans. R. Soc. London, Ser. B* **352**, 1354 (1997).
- <sup>16</sup>B. Yuan, S. A. Burgess, A. Iranmahboob, M. B. Bouchard, N. Lehrner, C. Bordier, and E. M. C. Hillman, *Rev. Sci. Instrum.* **80**, 043706 (2009).
- <sup>17</sup>E. F. Schubert, *Light-Emitting Diodes*, 2nd ed. (Cambridge University Press, Cambridge, England, 2006), p. 432.
- <sup>18</sup>R. W. Cole and J. N. Turner, *Microsc. Microanal.* **14**, 243 (2008).
- <sup>19</sup>P. Herman, B. P. Maliwal, H. J. Lin, and R. Lakowicz, *J. Microsc.* **203**, 176 (2001).
- <sup>20</sup>PicoQuant, 2011; see <http://www.picoquant.com>.
- <sup>21</sup>Roithner LaserTechnik GmbH Austria, 2011; see <http://www.roithner-laser.com>.
- <sup>22</sup>G. C. Holst and T. S. Lomheim *CMOS/CCD Sensors and Camera Systems* (SPIE, Bellingham, 2007), p. 355.

- <sup>23</sup>D. B. Murphy, *Fundamentals of Light Microscopy and Electronic Imaging* (Wiley, New York, 2001), p. 360.
- <sup>24</sup>F. J. Kao and P. Török, *Optical Imaging and Microscopy: Techniques and Advanced Systems*, 2nd ed. (Springer-Verlag, Berlin, 2007), p. 395.
- <sup>25</sup>Craic Technologies™, 2011; see <http://www.microspectra.com>.
- <sup>26</sup>M. Brydegaard, Z. Guan, and S. Svanberg, *Am. J. Phys.* **77**, 104 (2009).
- <sup>27</sup>A. Merdasa, "Lund Reports on Atomic Physics LRAP-415," M.S. thesis (Atomic Physics Division, Lund University, 2010).
- <sup>28</sup>E. Hecht, *Optics*, 4th ed. (Addison-Wesley, Reading, MA, 2002).
- <sup>29</sup>R. C. Gonzalez and R. E. Woods, *Digital Image Processing*, 3rd ed. (Pearson Prentice Hall, Upper Saddle River, NJ, 2008).
- <sup>30</sup>C. H. Chen, *Image Processing for Remote Sensing* (CRC, Boca Raton, FL, 2008).
- <sup>31</sup>Videometer A/S, 2011; see <http://www.videometer.com>.
- <sup>32</sup>S. Svanberg, "LIDAR," in *Handbook of Lasers and Optics*, edited by F. Träger (Springer, Heidelberg, 2007) p. 1031.
- <sup>33</sup>D. M. Winker, C. A. Hostetler, M. A. Vaughan, and A. H. Omar, PC-SCI-202.01 (NASA, 2006); see [www.calipso.larc.nasa.gov](http://www.calipso.larc.nasa.gov).
- <sup>34</sup>A. P. Cracknell and L. W. B. Hayes, *Introduction to Remote Sensing*, 2nd ed. (CRC, Boca Raton, FL, 2007).
- <sup>35</sup>M. Borengasser, W. S. Hungate, and R. Watkins, *Hyperspectral Remote Sensing: Principles and Applications* (CRC, Boca Raton, FL, 2008).
- <sup>36</sup>A. K. Maini and V. Agrawal, *Satellite Technology: Principles and Applications* (Wiley, Chichester, 2007).
- <sup>37</sup>F. M. Mims III, *Appl. Opt.* **31**, 6965 (1992).
- <sup>38</sup>A. Ounis, Z. G. Cerovic, I. Moya, and J. M. Briantais, *Remote Sens. Environ.* **76**, 33 (2001).
- <sup>39</sup>R. Grönlund, M. Sjöholm, P. Weibring, H. Edner, and S. Svanberg, *Atmos. Environ.* **39**, 7474 (2005).
- <sup>40</sup>J. R. Simard, G. Roy, P. Mathieu, V. Larochelle, J. McFee, and J. Ho, *IEEE Trans Geosci. Remote Sens.* **42**, 865 (2004).
- <sup>41</sup>Z. G. Guan, M. Brydegaard, P. Lundin, M. Wellenreuther, A. Runemark, E. I. Svensson, and S. Svanberg, *Appl. Opt.* **49**, 5133 (2010).
- <sup>42</sup>D. S. Hoffman, A. R. Nehrir, K. S. Repasky, J. A. Shaw, and J. L. Carlsten, *Appl. Opt.* **46**, 3007 (2007).
- <sup>43</sup>L. Mei, Z. G. Guan, H. J. Zhou, J. Lv, Z. R. Zhu, J. A. Cheng, F. J. Chen, C. Löfstedt, S. Svanberg, and G. Somesfalean, "Agricultural pest monitoring using fluorescence lidar techniques Feasibility study," *Appl. Phys. B: Lasers Optics* (in press).
- <sup>44</sup>P. Lundin, P. Samuelsson, S. Svanberg, A. Runemark, S. Åkesson, and M. Brydegaard, *Appl. Opt.* **50**, 3396 (2011).
- <sup>45</sup>R. Furfaro and B. D. Ganapola, *Transp. Theory Stat. Phys.* **36**, 107 (2007).
- <sup>46</sup>FORCE, A real-time optical solutions for sustainable agriculture, FORCE-A, Multiplex®2, 2007; see [www.force-a.eu](http://www.force-a.eu).
- <sup>47</sup>S. J. Hart and R. D. Jiji, *Analyst (Amsterdam)* **127**, 1693 (2002).
- <sup>48</sup>J. R. Lakowicz, *Principles of Fluorescence Spectroscopy*, 3rd ed. (Springer, Heidelberg, 2006), p. 725.
- <sup>49</sup>G. Agati, *Pure Appl. Opt.* **7**, 797 (1998).
- <sup>50</sup>S. Ek, B. Anderson, and S. Svanberg, *Spectrochim. Acta, Part B* **63**, 349 (2008).
- <sup>51</sup>B. Anderson, P. K. Buah-Bassuah, and J. P. Tetteh, *Winter College on Optics and Energy, International Centre for Theoretical Physics (ICTP)*, Trieste, Italy, 2010.
- <sup>52</sup>*Malaria: Drugs, Disease and Post-genomic Biology*, edited by D. Sullivan and S. Krishna (Springer, Heidelberg, 2010), p. 444.
- <sup>53</sup>World Health Organization, *Basic Malaria Microscopy Part I. Learner's Guide*, 2nd ed. (WHO Press, Geneva, Switzerland, 2010), p. 80.
- <sup>54</sup>J. T. Zoueu, G. L. Loum, T. C. Haba, M. Brydegaard, and H. Menan, *J. Appl. Sci.* **8**, 2711 (2008).
- <sup>55</sup>M. Hammer, D. Schweitzer, B. Michel, E. Thamm, and A. Kolb, *Appl. Opt.* **37**, 7410 (1998).
- <sup>56</sup>A. M. K. Nilsson, P. Alsholm, A. Karlsson, and S. Andersson-Engels, *Appl. Opt.* **37**, 2735 (1998).
- <sup>57</sup>T. W. Anderson, *An Introduction to Multivariate Statistical Analysis*, 3rd ed. (Wiley, Hoboken, NJ, 2003).
- <sup>58</sup>A. C. Rechner, *Methods of Multivariate Analysis* (Wiley, New York, 2002).
- <sup>59</sup>K. R. Beebe and B. R. Kowalski, *Anal. Chem.* **59**, 1007A (1987).
- <sup>60</sup>P. Weibring, T. Johansson, H. Edner, S. Svanberg, B. Sundnér, V. Raimondi, G. Cecchi, and L. Pantani, *Appl. Opt.* **40**, 6111 (2001); P. Weibring, T. Johansson, H. Edner, S. Svanberg, B. Sundnér, V. Raimondi, G. Cecchi, and L. Pantani, *ibid.* **41**, 434 (2002).
- <sup>61</sup>Y. Tan, D. Sun, J. Wang, and W. Huang, *IEEE Trans. Biomed. Eng.* **57**, 1816 (2010).
- <sup>62</sup>D. J. Faber, M. C. G. Aalders, E. G. Mik, B. A. Hooper, M. J. C. v. Gemert, and T. G. v. Leeuwen, *Phys. Rev. Lett.* **93**, 028102 (2004).
- <sup>63</sup>M. B. Sinclair, D. M. Haaland, J. A. Timlin, and H. D. T. Jones, *Appl. Opt.* **45**, 6283 (2006).
- <sup>64</sup>S. W. Hell, *Nat. Biotechnol.* **21**, 1347 (2003).
- <sup>65</sup>M. J. Rust, M. Bates, and X. Zhuang, *Nat. Methods* **3**, 793 (2006).
- <sup>66</sup>E. Herrala, J. T. Okkonen, T. S. Hyvarinen, M. Aikio, and J. Lammasniemi, *Proc. SPIE* **2248**, 33 (1994).
- <sup>67</sup>N. Gat, *Proc. SPIE* **4056**, 50 (2000).

## PAPER IV

### **Staining-free malaria diagnostic by multispectral and multimodality LED microscopy**

A. Merdasa, M. Brydegaard, S. Svanberg and J. T. Zoueu

*Submitted.*

# Staining-free malaria diagnostics by multispectral and multimodality light emitting diode microscopy

A. Merdasa<sup>1,2</sup>, M. Brydegaard<sup>1</sup>, S. Svanberg<sup>1,3</sup>, and J. T. Zoueu<sup>4</sup>

<sup>1</sup>Atomic Physics Division, Lund University, P. O. Box 118, SE-221 00 Lund, Sweden

<sup>2</sup>Department of Chemical Physics, Lund University, P. O. Box 124, SE-221 00 Lund, Sweden

<sup>3</sup>Center for Optical and Electromagnetic Research, South China Normal University, University City Campus, Guangzhou 500056, China

<sup>4</sup>Laboratoire d'Instrumentation Image et Spectroscopie, INP-HB, DFR-GEE, BP 1093 Yamoussoukro, Côte d'Ivoire

*We report an accurate optical differentiation technique between healthy and malaria infected erythrocytes by quasi simultaneous measurements of transmittance, reflectance and scattering properties of unstained blood smears using a multispectral and multimode light emitting diode (LED) microscope. We propose a technique for automated imaging, identification and counting of malaria infected erythrocytes for real-time and cost-effective parasitaemia diagnosis as an effective alternative to the manual screening of stained blood smears, now considered to be the “gold standard” in malaria diagnosis. We evaluate the performance of our algorithm against manual estimations of an expert and show a spectrally resolved increased scattering from malaria infected blood cells.*

## 1. Introduction

Malaria continues to ravage the developing world and remains one of the major world-health problems (WHO). Rapid, low-cost, easy-to-use and sensitive malaria diagnostic technologies are considered to be the effective alternatives to fight the overuse of drugs. When malaria infection is clinically suspected, subsequent overuse subsequently leads to the increase of drug resistance of the parasite, which is currently observed in the malaria abatement [1]; the precise identification of the malaria parasite and its staging, will definitely facilitate its treatment with appropriate drugs. Many efforts have been made in the technological development for rapid and quantitative diagnosis of malaria [2-5]. Several optical approaches have also been explored [6-9], focusing on the detection of the malaria pigment *hemozoin*, which is rest product resulting from bio-crystallisation of the toxic substance *free heme* released by the parasite in its food vacuole, and which is very characteristic for a malaria infection. These techniques often require expensive equipment and well-equipped laboratories which make them unrealistic on a large scale in malaria endemic areas [10]. Despite the increasing number of sophisticated technologies, Giemsa staining of thin and thick blood smears remains the “gold standard” for malaria diagnosis [11,12]. Due to the transparency of the infected erythrocytes (or red blood cells, RBCs), under bright field microscopy, a dye agent is required to enhance the visual contrast of the parasite and its various shapes for accurate identification. Fluorescence staining techniques can under optimum conditions detect 20-50 parasites/ $\mu$ L [11], but is rather time consuming and requires well-trained personnel; moreover, it requires manual examination using

high-power microscopy of typically hundred fields of the slide for providing a confident decision. In order to get precise results, the dye needs to be replaced between 2-3 times which are rarely fulfilled leading to inaccurate diagnosis and thereby to presumptive treatment [13]. Due to the high dependence on the laboratory staff operator it causes a number of false positive/negative smears. The disadvantage of fluorescence microscopy in malaria detection comes from the protocol of staining the blood smear and the manual examination of many fields to count, identify and interpret the slides. The highest sensitivity of this method is only reached by well-trained microscopists. The current optical techniques also include wide-field confocal polarization microscopy [14], laser desorption mass spectroscopy (LDMS) [15], third-harmonic generation imaging [16], and magneto-optical testing [17]. These techniques overcome some of the issues of specificity and sensitivity but are inappropriate for realistic employment in the developing parts of the world, since they likewise require expensive equipment and proper expertise. Another approach has been to develop antigen-based rapid diagnostic tests (RDTs), which can be self-administered outside the laboratory. There is contradicting information with regard to the sensitivity of antigen-based techniques [11] vs. microscopy [12], but the reports agree on the fact, that the cumulative costs for administering the test on a wide scale poses a monetary problem, since the cost of a test ranges between \$0.50-\$1.50. Since nearly 500 million cases of malaria are estimated on a yearly basis, all the above mentioned factors must be optimized in order to tackle the problem head on. An indirect problem caused by not being able to administer reliable tests is that common fever due to other infections is misinterpreted as

symptoms of malaria infection. As an effect, antimalarial drugs are used in cases where they are not needed which creates a risk that the parasite develops a resistance to the drugs [11].

An RBC is about 7  $\mu\text{m}$  in diameter and roughly 2  $\mu\text{m}$  thick [18, 19]. RBCs are unique from other cells in the body since they have no internal structure and can therefore deform quite easily, which is important for them to easily flow through small vessels and capillaries. Blood carries many signs of possible diseases and since haemoglobin is one of the strongest absorbers of light in the human body [19, 20, 21] there is a great motivation to use optical methods to explore potential for disease discovery. Some diseases, including malaria, will affect the cell morphology and their dynamic properties [22], which may be useful in diagnosing infections. Haemoglobin is the main constituent in the RBC and its optical properties have been well characterized over a broad spectral range [18, 23]. In the absorption spectrum there is a strong absorption band at 405 nm; the Soret band of haemoglobin. The scattering coefficient is dependent on the shape, orientation, and refractive-index distribution of the RBC since the scattering cross-section will vary across the disc-shaped RBC [12, 19, 24, 25]. The refractive index is related to the absorption coefficient through the Kramer-Kronig relation [26]. In a thin film on a microscopy slide there is ideally one layer of RBCs deposited, and single scattering by light can be assumed, whereas from a thick blood film having multiple layers of RBCs, multiple scattering is expected. Optical properties of whole blood have been studied extensively in relation to photo migration in the field of tissue optics [27]. Thin and thick films serve to extract different characteristics from a sample, where a thin smear is better for identifying the level of parasitaemia as well as the specificity, and a thick smear is better for detection since there are multiple layers and therefore more RBCs [10]. In the optical region, the type of scattering phenomenon is generally modelled with Mie scattering since the dimensions of an RBC is roughly one order of magnitude larger than the wavelength used to interrogate it [19,24]. However, when applying this scattering model, the RBC is assumed to be spherical, which in reality it is not. This becomes evident in the difference seen between the forward scattered and back scattered light where there is a strong angular dependence on the incident light [24,28]. Hemozoin, being the key substance in the existence of a malaria infection, has also been shown to exhibit strong backscattering at angles of roughly  $150^\circ$ - $160^\circ$  to the optical axis [12]. These factors will complicate the interpretation of the recorded scattered light, especially if RBCs do overlap in the blood smear [29], but this scattering phenomenon can also give clues as to how experiments can be conducted in

more clever ways to find better contrast between healthy and malaria infected samples, i.e. which angles to record the signal. Previous work shows that an increase in the plasma osmolarity (plasma concentration in whole blood) increases the absorption coefficient and at the same time decreases the scattering coefficient for red light at 632 nm. Similarly, the hematocrit level (% of RBCs in the blood) will independently affect the scattering and absorption properties [18].

In the present work we apply multispectral and multimodal LED microscopy to investigate modes of optimal contrast in thin blood smears by simultaneous differentiation between healthy and infected blood cells employing transmittance, reflectance, and scattering recording geometries. These recording geometries comprise what we from now on refer to as the angular modes of acquisition of the microscope. With this technique we overcome the transparency of an RBC seen in bright field microscopy since we are extending the spectrum of investigation to UV and IR. Optical spectra are extracted from individual blood cells in the multispectral images of all angular modes and show different characteristics between different blood cells. Advanced clustering algorithms are employed and the outcome is compared to the evaluation of an expert in the field. The proposed technique is based on inexpensive and realistic technology where contrast is created using nine sequentially selected illuminating LEDs with thirteen bands over a broad spectral range from UV to IR. The results presented in this paper are from a measurement campaign held at Laboratoire d'Instrumentation Image et Spectroscopie in Yamoussoukro, Ivory Coast in 2009.

## 2. Experimental Setup & Methods

### A. Sample Preparation

Blood samples were prepared and delivered from the local clinic in Yamoussoukro, Ivory Coast. Blood smears were prepared by putting a drop of blood on an empty microscope slide and carefully spreading it with another microscope slide. They were prepared by the physicians at the clinic where no further chemicals were added to the sample. The samples were imaged within a few hours after preparation, and the peripheral areas of the smear were observed since they exhibit a single layer of RBCs

### B. Imaging System

Images were acquired using a multi-mode, multispectral imaging system developed by our group and presented in [30]. In this system, nine LEDs were used to selectively illuminate the samples at thirteen different wavelengths ranging from ultraviolet (UV) to near infrared (NIR) (380 nm - 935 nm). The sample was illuminated in three

angular geometries thus providing transmittance, reflectance, and scattering information. Thus, in effect, the data from the sample were recorded in 39 different ways. An overview of the system specifically showing how the sample is illuminated in the three angular modes can be seen in Fig. 1. The effective detection regions of the system are also shown here.

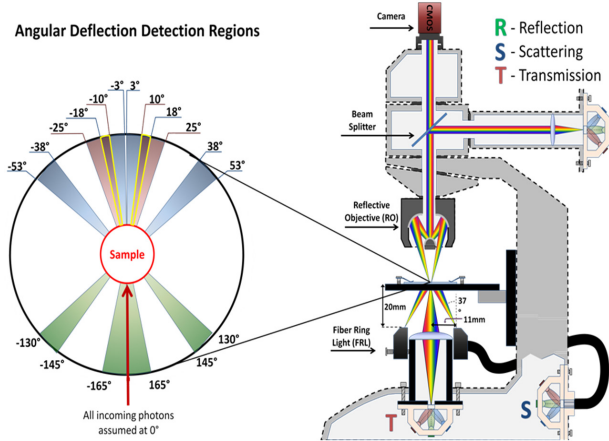


Fig. 1. Right: Overview of the imaging system showing a vertical cross-section of the microscope with arrangements for each angular mode (R, S, and T) indicated. In each illumination battery there are nine LEDs (with a total of thirteen bands each, only three LED drawn above) illuminating one and the same spot where an opal diffuser is placed in order to give an even distribution of light from each LED and remove angular dependence of the incident LED illumination. The rainbow of colours is a representation of a broad illumination range and the RGB colour for the LEDs is simply to indicate that each LED is quasi monochromatic and is not representative of the actual illumination from that specific location. Left: Diagram of angular lobes with an overlapping region indicated by yellow lines. The colour representation stands for the different detection regions for reflection (green), scattering (blue) and transmission (red). The angles represent the angles all incoming photons are deflected into and are independent of from which angular geometry they emerge.

The camera used was a 5MPix (2592 x 1944) monochromatic CMOS camera (Guppy-503B, Allied Vision Technology, with a MT9P031 sensor from Micron/Aptina) with individual pixel size of  $2.2 \mu\text{m} \times 2.2 \mu\text{m}$ , each having a 12-bit pixel depth. In order for the broad spectral range to be imaged at the fixed image plane of the imaging chip, dispersion was minimized by using quartz lenses and a reflecting objective (Edmund Optics, NT58-421) with 15X magnification and .28 NA, giving an estimated point spread function (PSF) range of  $.67 \mu\text{m} - 1.68 \mu\text{m}$  for the wavelength range used. The illumination to measure scattering was accomplished through a fiber-optic ring light (Edmund Optics, NT54-176) device (FRL) where the light emerges at the circumference of a circle which was placed at a certain distance below the sample. The fibers inside the ring are tilted inward so that the light field converges at the distance of the sample.

There are two important things to note regarding the ability of the system to collect light, and they are in regard to the reflecting objective and the FRL. The objective has a Cassegrainian type of telescope arrangement where essentially a concave and a convex mirror work in conjunction to magnify the light. In this configuration, the convex mirror surface is located directly on the optical axis and thus blocks part of the light in all angular modes (see Fig. 1). Regarding the FRL, light emerges at a tilt angle of  $37^\circ$  to the normal from the circumference of a circle having a diameter of 22 mm. Thus, changing the height of this source in relation to the sample will change the angle at which light impinges on the sample. This height was set at 20 mm during the experiment which provided the detection sensitivity regions demonstrated in Fig. 1. These aspects with regard to the objective and FRL should be taken into account when analyzing the scattered light from malaria samples. There is an overlap of detection regions between transmission and scattering indicated with yellow lines. These can be adjusted to overlap less by moving the FRL in the vertical direction; however, this was not realized at the time the measurements were made.

### C. Image Acquisition

The system was controlled from a PC using a custom-made program in LabVIEW™ (National Instruments, NI) where images were captured and saved in 16-bit unsigned integer images in TIFF format. For each illumination wavelength, a bright and a dark reference image was acquired but depending on which angular geometry was used, these recordings were done differently. For transmittance and reflectance measurements, the bright reference was an empty microscope slide placed in the object plane, whereas for scattering measurements an opal diffuser was used. Camera exposure times and gains were adjusted to give the highest intensities in the image without saturating the bright references. The dark reference images for transmittance and reflectance were taken by disconnecting the illumination current and using the same exposure times as for the bright references. For the scattering dark reference the opal diffuser was simply removed and acquisition parameters for the scattering bright references were applied. All acquisition parameters were set with the bright references and then the sample was placed in the object plane and imaged for all three angular geometries. It was of importance to acquire all sample images for all geometries consecutively, keeping the sample in the same location in order to be able to compare transmittance, reflectance and scattering properties of single RBCs.

#### D. Image Analysis

Once all images were taken and saved, they were analyzed using a customized algorithm in MatLab® (MathWorks Inc.). Initially, the background images were subtracted from all sample images. Then the normalization procedure was made differently for the three angular modes. For scattering, the dark reference image ( $\text{Im}_D$ ) was subtracted from the sample ( $\text{Im}_S$ ) and the bright ( $\text{Im}_B$ ) reference images. Then the sample image was divided by the bright reference image to obtain the normalized image ( $\text{Im}_{Norm}$ ) according to Eq. (1)

$$\text{Im}_{Norm} = \frac{\text{Im}_S - \text{Im}_D}{\text{Im}_B - \text{Im}_D} \quad (1)$$

For reflectance and transmittance, an algorithm was written to automatically find the regions in the sample image where there were no RBCs. A 2-dimensional polynomial fit was applied with the intensity values in these regions; thus, a virtual bright reference image was extracted from the sample image and Eq. (1) was used. In this flat field calibration, the intensity values given for each pixel were normalized with respect to the nearest empty region, which means the image is in effect not normalized to the microscope slide only, but to the regions free from RBCs. Normal human blood consists of 55% plasma (90% water and 10% proteins) and 45% cells [18, 23], which suggests that the normalization is made not only to the microscope slide but also to some plasma residue. Finally, to remove noise, a 2-D median filter was applied to the normalized images.

Following the normalization, the centers of all RBCs were manually selected in the entire image since we did not have a trained algorithm to find them automatically. Once the spectral fingerprints of infected cells have been determined, this step can be automated. For each RBC, the spectrum for reflectance, scattering and transmittance was extracted and concatenated into one vector having 39 elements (3 geometries x 13  $\lambda$ ). Spectra for 453 RBCs were extracted and Singular Value Decomposition (SVD) was used [31]. SVD is a multivariate technique where the data are transformed into a new hyper-dimensional coordinate system where variance is maximized along each dimension representing a specific variable. From the transformation of the original data having ( $\mathbf{M}_{n,\lambda}$  – where  $n$  represents a specific RBC out of a total number of  $N$  RBCs, and  $\lambda$  the wavelength), three arrays can be extracted, where base-spectra ( $\mathbf{V}_{\lambda,m}$  – where  $m$  represents the spectral component), eigenvalues ( $\mathbf{\Sigma}_{m,m}$ ) and linear coefficients ( $\mathbf{U}_{n,m}$ ) represent the original data according to Eq. (2),

$$\mathbf{M}_{n,\lambda} = \mathbf{U}_{n,m} \mathbf{\Sigma}_{m,m} \mathbf{V}_{\lambda,m}^* \quad (2)$$

The base spectra, also called loadings, are a new set of base functions of the original data which are all orthogonal to each other. Because of the orthogonality between all vectors within  $\mathbf{V}$ , they represent the original data much more efficiently where the first eigenvector,  $\Sigma_1$ , is the most significant,  $\Sigma_2$  being the second most significant, and so on. Therefore, the first base spectrum resembles the average of all original spectra for the RBCs over all wavelengths; naturally so since the average is the best summary of all data.  $\mathbf{\Sigma}$  contains the eigenvalues for each eigenvector representing the importance of each eigenvector in relation to the others. This allows for removal of the eigenvectors that provide no additional contrast.  $\mathbf{U}$ , also called scores, contains the linear coefficients for each RBC explaining how much of each eigenvector is required in order to recreate the original spectrum for that RBC. With this information, we can reduce our original data to represent the significant contrast with only a few eigenvectors rather than all contained in the original data by the removal of insignificant variables for the desired contrast. Adding more dimensions will not provide any additional contrast but only increases the noise and reduces the potential contrast of the outcome. In our case, each eigenvector represents one LED for a specific angular geometry, thus giving us 39 PCs (principal components). Not all illumination bands gave a strong contrast between the cells and this became evident using SVD.

Hierarchical clustering and dendrogram representation [32] were applied to summarize the interdistance of the SVD scores to see if there were any discrete clusters of data points in the new coordinate system and how related these were. The number of dimensions from the SVD analysis was truncated to 3; thus, the algorithm clustered all 453 data points into an equal number of clusters. The number of clusters was chosen to equal the number of dimensions because we essentially select to observe the data with a reduced number of observations (dimensions) [32]. If the number of clusters is greater, the observations would no longer be linearly independent and we would have to account for factors that are not observed from the reduced data. From each data point, a line is drawn to all the other data points in this new Euclidian space and the length determines how related they are. The shorter the line, the greater the chance that two points belong to the same cluster or that they are from two closely related clusters. This information is presented in a dendrogram, which gives an overview of how close the clusters are to each other in the Euclidean space. From this dendrogram, the RBC coordinates belonging to each group can be marked in the original image and the average spectra for all clusters can be extracted, plotted, and compared to each other.

### 3. Results

The results will be presented with the notion that we do not know which cells are infected and which are healthy. Rather, we will focus on finding the spectral differences between the RBCs through SVD and Hierarchical clustering. We do know that the sample is infected, but which RBCs belong to which category will be left for the discussion section.

#### *A. True-colour representation of single RBCs*

Measurements were taken at the following wavelengths: 380, 405, 430, 480, 525, 600, 630, 660, 700, 760, 810, 850, and 935 nm in transmittance, reflectance and scattering. Using MatLab®, true-colour representations of the sample were constructed by combining the normalized images taken at 630 nm (red), 525 nm (green), and 480 nm (blue) (Fig. 2). Thus, the images appear as if one would manually observe them through the microscope binocular under white light illumination. Fig. 2 shows the same region of the sample in all three angular modes. Since all measurements for the three angular modes were taken without moving the sample, one can compare the three modes in each pixel. However, the effective pixel-size is far below the diffraction limit set by the imaging system. This means one pixel is affected by a number of near-lying pixels and can therefore not be considered individually. However, evaluating the RBC as a whole one can argue that pixels from different parts of the RBC play different roles in the differentiation between healthy and infected cells. Therefore, malaria criteria should be applied on a pixel level but evaluated on a whole cell level; in Fig. 2 we can clearly see the RBCs to be distinctly separated. The following images show a cropped out region from the original image to better show the appearance of individual RBCs; however, all analysis was made on the full image containing 453 RBCs. It becomes evident from these true-colour representations that there are significant differences between RBCs in all three geometries, but for different reasons.

In Fig. 2a (reflection) we can see the expected red colour of the RBCs, but there is a clear distinction between the cells. Some cells appear slightly brownish whereas others appear redder. The contrast is most evident in Fig. 2b (scattering) where we can clearly see the RBCs seemingly having an internal structure. Those without internal structure appear to have hollow centers whereas those having something concrete inside scatter significantly. In the acquisition for scattering, the FRL is aligned so that in the absence of a sample, the majority of the light passes outside the aperture of the objective. Thus, when there is something in

the sample plane deflecting the light from its original path into the aperture of the objective, a signal is measured from what we define as zero; being the dark reference.

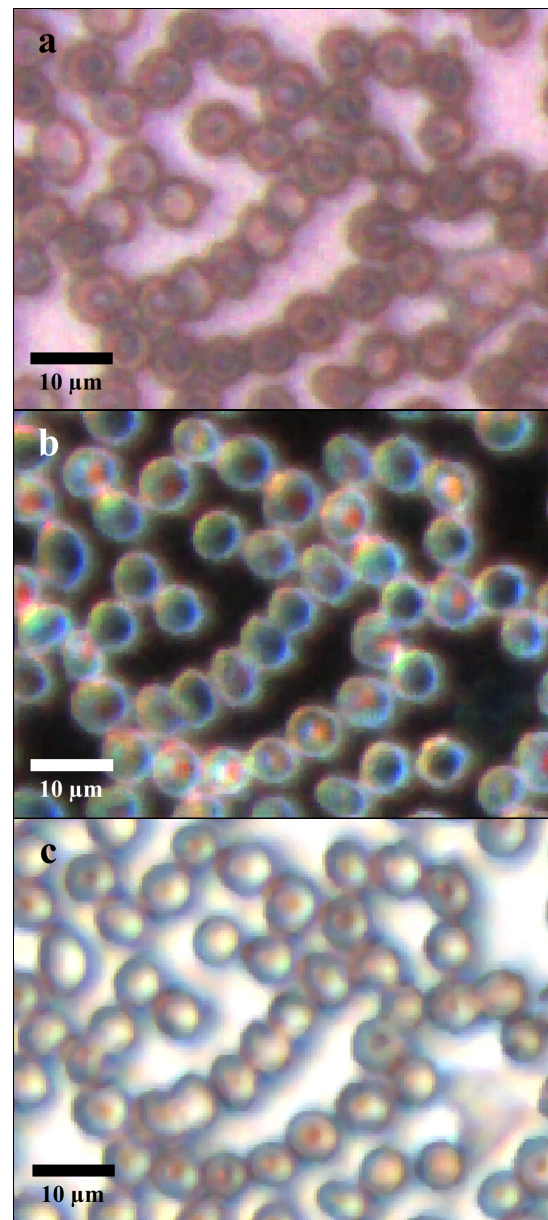


Fig. 2a-c. True-colour representation of the images taken for the three angular modes where we see spectral differences in all, but to different degrees. 2a (reflection) shows the decrease in reflection in some RBCs where the central region appears darker, which can be attributed to the typical doughnut-shape of RBCs. 2b (scattering) shows the largest contrast between the RBCs. 2c (transmission) shows some RBCs absorbing more light than others in a centralized region, thus appearing as darker spots. The central red dot is most clearly visible in the scattering geometry.

In Fig. 2c (transmission) the light passes through the RBCs and we can observe a reduced transmittance from some cells compared to others. There is an apparent darker region in the center of some RBCs which seems to slightly change from cell to cell. One reason why the cells appear white rather than red is because they have been

normalized to the regions free from cells. These regions contain blood plasma which has similar spectral characteristics as haemoglobin [23] and thus the RBCs appear white rather than red. In this aspect, the transmission sample would not appear as it does in Fig. 2c to the human eye. What is interesting is that Fig. 2a is also normalized to the region free from RBCs, but there is a larger contrast due to the scattering properties of RBCs where the back-scattered light is significantly stronger when the light is incident at an angle to the normal of the RBC surface [24], which according to Fig. 1 covers the photons that are deflected at angles between 35°-50° and 0°-15° from their incidence. We also see that the angular sensitivity regions for transmission lie close to the optical axis as these photons are not deflected far from it. This is another contributing reason to why higher intensities can be measured from the cells compared to the white reference (empty slide) as the forward scattering property of individual RBCs tends to increase the intensity when the angle of the incident light approaches the plane perpendicular to the optical axis [24].

Comparing all angular modes, we can see that the invisible characteristics in transmission become clearly visible in scattering. In general we see that the differences of the cells in each angular mode correlate well between the angular modes; the same RBC having a brown spot in Fig. 2c (transmission), appears browner in Fig. 2a (reflection), and has a red spot in the center of Fig. 2b (scattering). From the three images in Fig. 2 we can draw a conclusion that some RBCs have some sort of internal structure, which will be discussed further below. According to the life-cycle of the *p. falciparum* parasite, where during its trophozoite stage it enters the RBCs and grows within, we can expect to see the infected cells having some sort of internal structure [11]. We keep this in mind as we continue to apply statistical methods for all RBCs in all geometries and spectral bands.

### B. Singular Value Decomposition & Hierarchical clustering

Before any further analysis was made the spectra had to be collected from the RBCs. This was done by cropping out a region with a 3 pixel radius from the center of the RBC over which an average intensity was acquired at each spectral band. Thus, a spectrum for every RBC in each geometry was extracted at a resolution of 13 spectral bands from 380 nm to 935 nm. In order to perform the SVD analysis we had to concatenate the spectra from the three different geometries into one for each RBC, which is seen in Fig. 3a. In this plot we can see the general trend of how the spectral characteristics change throughout the three geometrical modes, but also the variance between the blood cells. In Fig. 3b we see the extracted

eigenvalues,  $\Sigma_m$ , once SVD has been applied. To determine where to truncate our data, we had to study the relevance of the signal of each  $\Sigma$  in comparison to what we define as noise; or rather, irrelevant information. The noise level was chosen from the apparent plateau in Fig. 3b, where a black line is interpolated through the plateau. Based on this noise level,  $\Sigma_1$  gives a signal-to-noise ratio of approx. 6:1,  $\Sigma_2$  approx. 3:1 and  $\Sigma_3$  slightly less than 2:1. We decided that this was the lowest we would go before adding another PC did not provide additional relevant information. Therefore, the first three  $\Sigma$  were used as indicated by the three red circles in Fig. 3b.

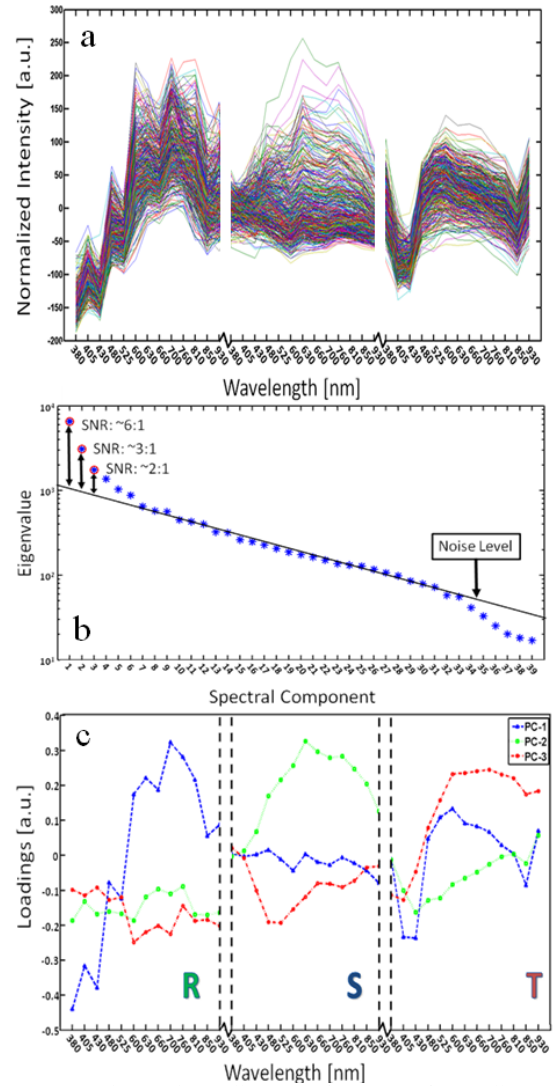


Fig. 3a shows the collection of spectra from all RBCs concatenated between the three angular modes. The rather large variance becomes evident. Fig. 3b shows the eigenvalues for each PC where the first three are considered to be most relevant as their SNR is 2:1 or higher. The noise level is indicated with a black line drawn through the apparent plateau. The y-scale is logarithmic. Fig. 3c shows the first three base spectra for all PCs and it is evident that the original data can be represented quite well with these curves. The spectra have been divided up in the angular modes.

In Fig. 3c the first three base-spectra are plotted in different colours and they are separated into their

respective angular geometry. Comparing Figs. 3a and 3c we see that from the first three base-spectra we can more or less describe all the original spectra for the RBCs in different linear combinations. How much of each eigenvector we use is indicated in  $U$  for each RBC and we recreate the original spectra from the reduced set of coordinates according to Eq. (2),

$$M_{n=1..N,\lambda=1..tr} = U_{n=1..N,s=1..tr} \sum_{s=1..tr,s=1..tr} V_{\lambda_{1..tr},s=1..tr}^* \quad (3)$$

where  $N$  represents the total number of RBCs ( $N=453$ ) and  $tr$  stands for the number of dimensions we decided to reduce the data to, which in our case is  $tr=3$ . Since we used only the three first eigenvectors, and the fact that they are orthogonal, it is easy to visualize the data points in a three dimensional space. However, we should keep in mind that since the different eigenvectors carry different weight, the scales will be different along each dimension. Each RBC is then represented as a point in a 3D histogram.

From the new coordinate system, the Euclidean distances between all points were calculated in order to determine which cluster they belong to. The relation between these three clusters is shown in the dendrogram in Fig. 4. On the y-axis the values represent the distance in the Euclidian space which was previously transformed with the SVD analysis; thus the values carry no units. Note that the colour coding is not related to Fig. 3 but rather to the spectra in Fig. 5. Overall we can see that clusters 1 and 2 are closer related to each other than cluster 3. From the 453 RBCs examined, 9 fell into cluster 1, 118 into cluster 2 and 326 into cluster 3. Also evident in the figure are several sub-clusters. We choose three clusters, but there is of course a possibility that there are more variables that differentiate RBCs. However, the three clusters seem to be significantly separated to motivate to compare them, and this should become more evident when examining their spectral characteristics in the following section.

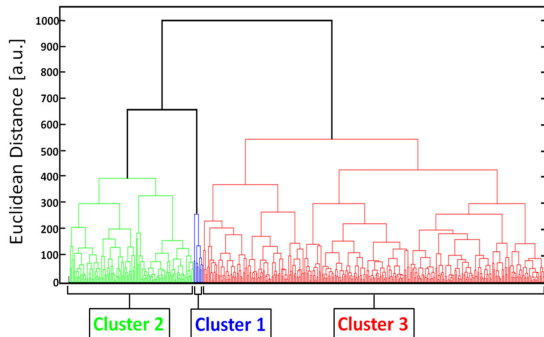


Fig. 4. Dendrogram representation of all the RBCs and their relation according to the reduced variables from the SVD analysis. The colour coding is kept for the next section where the spectra are shown for each cluster. The y-axis represents the Euclidean distance in the newly formed coordinate system and

therefore carries no units. In cluster 1 there are 108 RBCs, in cluster 2 there are 9 RBCs and in cluster 3 there are 326 RBCs.

### C. Individual RBC spectra in all angular modes

Tracing back the colour space coordinates for the data points in the clusters, we took the average spectrum for each cluster and plotted them separately for each angular geometry seen in Fig. 5. In all spectra we can see some differences between the different clusters, but some promote the contrast more than others. What becomes clear is the progression as we observe all three clusters. Cluster 1 has by far more RBCs than the other two, followed by cluster 2 and, finally, very few RBCs in cluster 3. Remembering the life-cycle of the malaria parasite we note that when it enters the RBC in its trophozoite stage it consumes haemoglobin. Then it makes sense that we can see a progression as RBCs would naturally be in different stages of infection; the longer the parasite has been occupying the RBC, the more its spectral characteristics would differ from a healthy RBC. In Fig. 5a (reflection) we would also expect to see a decrease in reflection due to the high absorption at the characteristic Soret absorption band of haemoglobin at 405 nm, but it seems to have shifted to around 430 nm. This can partially be explained by the scattering characteristics of RBCs which heavily depend on the shape and orientation of the cell as well as the angle of the incident light. There is a progression of increased reflectance moving from cluster 1 to cluster 3 as well as a general increase of reflectance from 480 nm up through 930 nm. In Fig. 5b (scattering) we see the largest contrast where all three clusters differ significantly from 480 nm and above, where cluster 1 and 2 seem to peak around 630 nm. It does make sense that the scattering geometry gives the strongest contrast because not only the parasite, but also the hemozoin that it expels, has structure providing contrast with regard to a healthy cell with only haemoglobin [27]. The changing of spectral characteristics is most apparent in scattering going from cluster 1 to cluster 3. Scattering significantly increases in each ascending cluster for all wavelengths above 430 nm. In Fig. 5c (transmission) we see the characteristic Soret absorption of haemoglobin clearly at 405 nm, which appears to be at more or less the same level in all clusters, with perhaps a slight increase in absorption for clusters 1 and 2. What is more apparent in transmission is the increased absorption over the spectral region 480 nm - 810 nm as we move toward cluster 3 from cluster 1. The increased absorption can be paralleled with the decreased reflectance comparing the clusters.

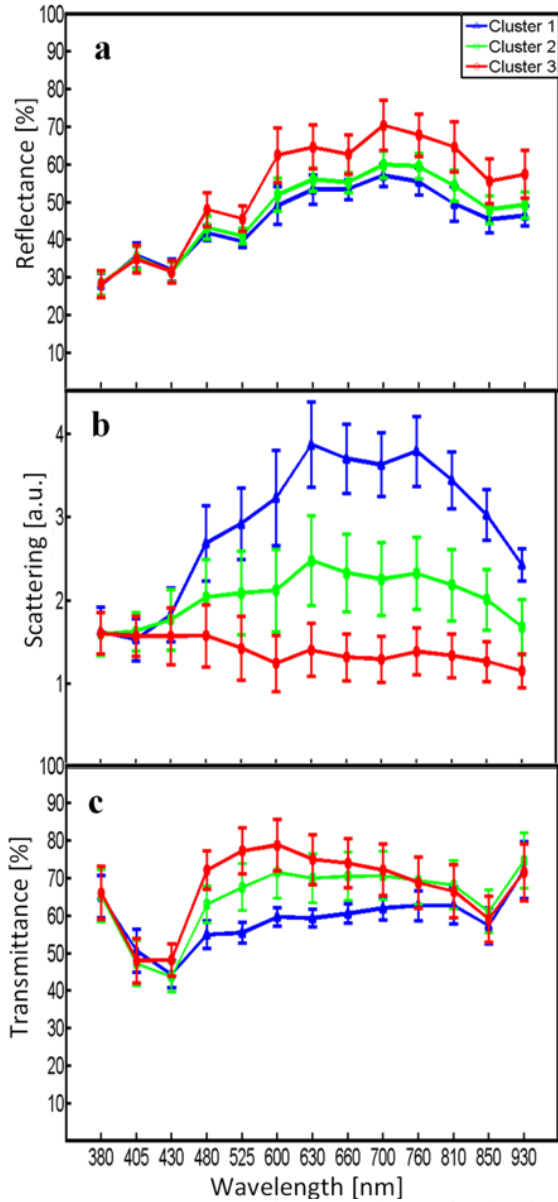


Fig. 5a-c. Average spectra for the 3 clusters for the three angular geometries. In all spectra we see contrast to some extent between the three clusters. 5a (reflectance) shows a progression from cluster 1 to cluster 3 of an increase in reflectance. 5b (scattering) exhibits the strongest contrast where the progression of increased scattering goes from cluster 3 to cluster 1. 5c (transmission) shows an increase in absorption from cluster 3 to cluster 1, which we can understand from 5a where we saw a decrease in reflectance in a similar fashion.

#### D. Mapping of cluster classifications onto RBCs

Once the three clusters were found, the respective coordinates were marked on the true-colour images to get a visual perception of how the different RBCs would appear to the human eye if observed directly through the binoculars of a microscope. Fig. 6 is the same as Fig. 4 but having all RBCs marked with their respective cluster where cluster 1 is represented with a blue triangle, cluster 2 with a green square, and cluster 3 with a red circle. Note that some RBCs are not marked at all since they were not counted in the original list

for reasons such as lying too close to a border or having an odd shape.

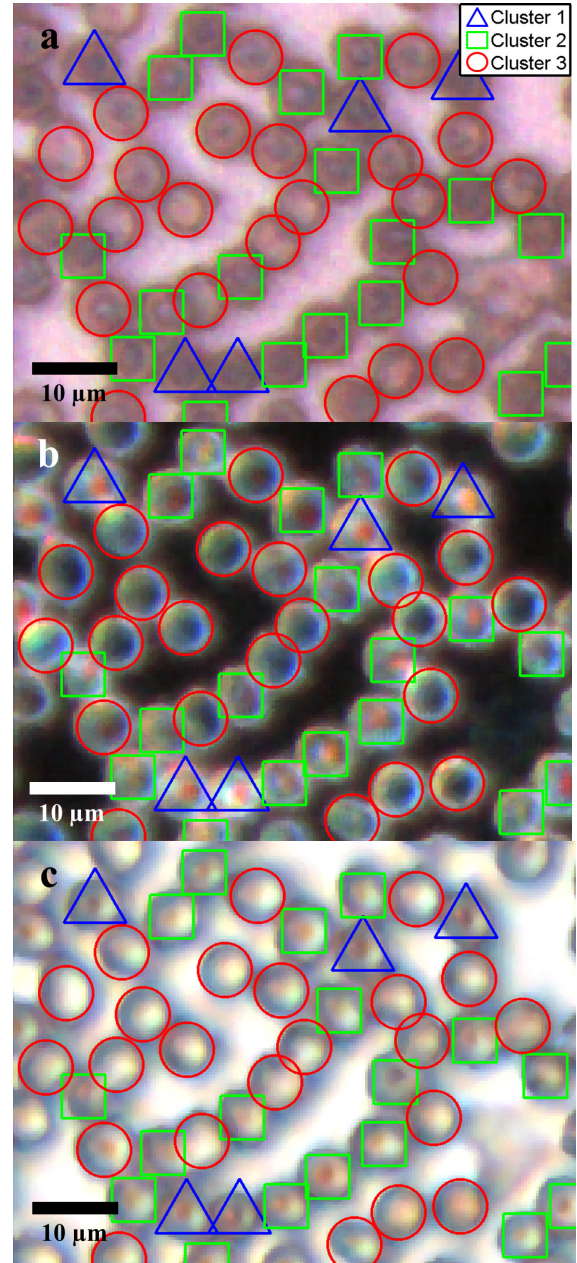


Fig. 6a-c. From the three different clusters marked in this true-colour image we see significant distinctions in all angular modes, where the largest is again seen in scattering. 6a (reflectance) only shows a small, but still significant variance between the different clusters. It is more evident in 6b (scattering) as well as 6c (transmission). Cluster 1 is clearly distinct from cluster 3 in 6b, which was already evident in Fig. 5b. Some of the markings are not centered, which is due to the initial selection not being exactly in the middle of the RBC, but due to the cropped out region being significantly smaller than the RBC, it should not play a significant role.

In Fig. 6a (reflection) we see a distinction in contrast between the clusters, but it is not as clear as in the other two angular modes. This we can understand from the results in Fig. 5a, where the reflectance spectra do not show large contrast

between the clusters. However, we can see significant differences between the general appearances of the RBCs belonging to the different clusters. RBCs belonging to clusters 1 and 2 seem to progressively get darker and browner compared to the RBCs in cluster 3. Fig. 6b (scattering) provides the largest contrast, as expected from the spectra in Fig. 5b. The red spots seen in the RBC centers are clearly visible in clusters 1 and 2 and clearly not in cluster 3. Comparing cluster 1 to cluster 2 there appears to be a slight difference in visibility of the red spot. The previously discussed progression of the spectra is most visible in Fig. 6b for scattering, where all RBCs belonging to cluster 1 have the brightest red spots in the center. There is also a number of RBCs belonging to cluster 2 having the bright spot but not as bright as the ones from cluster 1. All RBCs belonging to cluster 3 are lacking a red spot in the middle. From Fig. 6c (transmission) we see there are differences between the three clusters where there is an apparent brown spot in the center of the RBCs belonging to cluster 1 and 2, and not in cluster 3. Between cluster 1 and 2 we again see the slight difference in visibility of the spot in the center. The fact that the spot in the middle is brown in transmission and reflection and red in scattering is due to the different normalization procedure for the acquisition modes.

### E. Malaria expert evaluation

The blood smear was independently analysed visually by one of us (JTZ) who has considerable experience in malaria evaluation. For all studied RBCs he had to decide whether the RBC was infected or healthy. If he was uncertain to determine an infection he could also indicate that. Fig. 7 shows a chart with the corresponding classification. The results are presented cluster by cluster where the percentage represents how many of the RBCs in that cluster belong to each classification. Cluster 1 has 9 RBCs out of which 22.2 % are healthy, 44.5 % are infected and 33.3 % uncertain. Cluster 2 has 118 RBCs out of which 70.3 % are healthy, 5.1 % infected and 24.6 % uncertain. Cluster 3 has 324 RBCs out of which 93.8 % are healthy, 1.5 % infected and 4.7 % uncertain. This gives a total of 389 healthy and 15 infected RBCs with the certainty of the expert; thus, over the entire sample our expert confirms that 3.3 % are infected. Malaria parasitemia ranges depending on the severity of the infection as well as the age of the patient. The rate found from a study in 1995 was 1.6 % for children aged 1-4 and 5.5 % for patients of 15 years and up [33]. From this we can say that our results are acceptable. However, a proper procedure of first using our microscope and then directly staining the sample and applying a conventional counting method was not made. For this reason we cannot give any value of specificity

and sensitivity but rather conclude that our method gives promising results in good agreement with conventional methods. We can also infer from the chart that the percentage of infected cells decreases as well as the number of healthy cells increases from cluster 1 to 3. Although the number of RBCs in cluster 1 is significantly lower than cluster three, the majority of them are found to be infected. This is a strong indication that our routine can identify malaria infected blood cells without the use of staining.

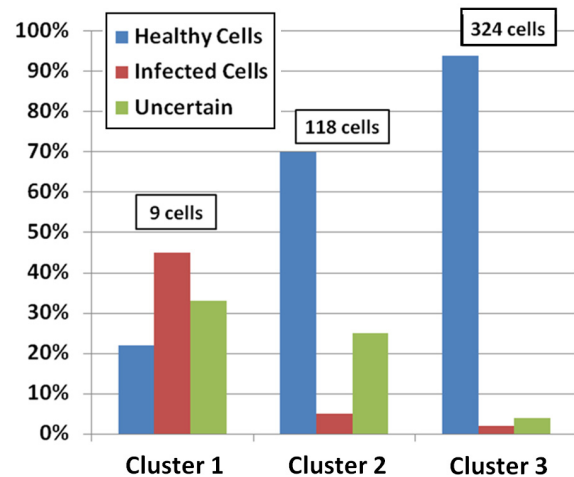


Fig. 7. A chart showing the distribution of healthy and infected cells for the different clusters analyzed by our malaria expert. In each cluster there is also a column indicating how many blood cells the expert could not properly distinguish. The trend becomes obvious as the number of infected cells strongly decreases as we go from cluster 1 to 3. Similarly, the number of healthy cells increases from cluster 1 to 3.

## 4. Discussion

We have presented a robust and automated approach based on the optical fingerprint of RBCs and multivariate analysis to differentiate infected RBCs from healthy in an unstained positive blood smear. This technique exploits the variation of the optical properties of the constituents of the RBCs. The normalization step provides a common basis for comparison between samples of different origins. Uninfected RBCs are essentially composed of haemoglobin and their spectra are expected to be dominated by the spectral fingerprint of oxy-hemoglobin, strongly characterized by the Soret band (414 nm) and their two additional bands at 541 nm and 576 nm, in transmission mode [34]. The various parasite stages (trophozoite, ring, schizont or gametocyte), the presence of hemozoin, or the decrease of hemoglobin concentration, show up in all three acquisition modes, therefore giving a strong indication when an infection is prevalent. Yulia *et al.* have published quasi-exhaustive optical fingerprints of all stages of the *plasmodium falciparum* as well as hemozoin spectra [35]. Hemozoin displays a particular absorption band at 630 nm and 660 nm. Wilson *et al.* have measured

an overall decrease of the scattering probability from UV to near infrared. Cluster 2 (Fig. 5) shows the general spectral behavior of the *plasmodium falciparum* parasite. Our approach is focused on the mean pixel value of the RBCs properties rather than specific plasmodium indicators. For this reason, the cluster 3 spectrum is examined in terms of average characteristics of the indicators above for the three modes. This spectral differentiation between healthy and infected RBCs is particularly observed by an increase in scattering, decrease in reflectance as well as a decrease in transmittance of infected RBCs compared to healthy ones. The visual differentiation of the RBCs in unstained blood smears is very hard because of possible confusion between the various shapes of the RBCs in the three modes, platelets or other residues stuck to the RBCs. The central valley of RBC (due to its biconcave shape) can exhibit an artificial increase of scattering and absorption and a decrease of reflection similar to that of the symptoms of infection. This visual confusion is solved by spectral analysis, and will be further examined. In order to extract values of specificity and sensitivity, our technique needs to be done in accordance with a laboratory conducting the conventional Giemsa-staining technique. The same areas of the blood smear should be viewed in both microscopes, where a proper staining procedure is conducted immediately after the multispectral microscope has been applied. Therefore we cannot draw any stronger conclusion than that our technique seems to agree well with the expert's visual analysis.

Although the development platform includes a camera for high resolution acquisition and a computer to analyze the data, we believe that hand-held devices using only LEDs and an objective in a battery-driven box can create visible contrast to the naked eye, since it mainly comes from the selective illumination and appropriate angular geometries; this is very realistic for the developing world especially since the contrast is instantly seen without having to prepare the sample through staining and the test can be administered without costs for biological test-strips. Using this technique with more samples and defining proper values for specificity and sensitivity, we can determine which LEDs in which angular geometry give the strongest contrast and from this create simple push-button devices which readily detect malaria within a few seconds. We base this conclusion on the fact that we have created contrast without the use of staining and by simply selectively illuminating the sample with different LEDs in different geometries, which can be readily recreated in a more convenient manner for the field.

Finally, we want to acknowledge that there are improvements to be made according to the above arguments. There are a number of factors that affect the optical properties of blood such as the

hematocrit level (volume fraction of cells within the whole blood volume), oxygenation of haemoglobin which leads to changes in absorption, osmolarity changes which affect the haemoglobin concentration and therefore indirectly changes the absorption of the RBCs. These are all discussed in reference [18]. However, as we are already seeing a strong contrast between what apparently are infected and healthy RBCs, this study should only increase the confidence in our results.

## 5. Acknowledgements

We would like to extend our gratitude to many parties being involved in bringing this research forward. The International Science Programme (ISP), Uppsala University, has been supporting this research by providing funds for building 6 additional microscopes that are today being employed in various parts of the developing world. ISP has also funded several workshops where this research was shared amongst participating students and professors of AFSIN (African Spectral and Imaging Network). Funding has also come from a direct grant from the Swedish Research Council and from a Linnaeus grant to the Lund Laser Centre (LLC). Much appreciation is extended to Jens Ålebring and Hiran Jayaweera for their contributions in the construction of the microscope.

## References

- [1] P.B. Bloland, M. Ettl, "Making malaria treatment policy in the face of drug resistance", *Annals of Tropical Medicine and Parasitology*, **93**(1), 5-23 (1999)
- [2] P.A. Wintstanelly, S.A. Ward, R.W. Snow, "Clinical status and implication of antimalarial drug resistance", *Microbes & Infection*, **4**(2), 157-164 (2002)
- [3] A. Moody, "Rapid diagnostic test for Malaria parasites", *Clinical Microbiology Review* **15**(1), 66-78 (2002)
- [4] C. Wongsrichanalai, M.J. Barcus, S. Muth, A. Sutamihardja, W.H. Wernsdorfer, "A review of malaria diagnostic tools: Microscopy and rapid diagnostic test (RDT)", *American Journal of Tropical Medicine & Hygiene*, **77**(6), 119-127 (2007)
- [5] C.K. Murray, R.A. Gasser Jr., A.J. Magill, R.S. Miller, "Update on rapid diagnostic testing for Malaria", *Clinical Microbiology Reviews*, **21**(1), 97-110 (2008)
- [6] W.G. Lee, Y-G. Kim, B.G. Chung, U. Demirci, A. Khademhosseini, "Nano/microfluids for diagnostic of infectious diseases in developing countries", *Advances Drug Deliver Reviews*, **62**(4-5), 449-457 (2010)
- [7] T. Hänscheid, E. Valadas, M.P. Grobusch, "Automated malaria diagnostics using pigment detection", *Parasitology Today*, **16**(12), 549-551 (2000)
- [8] S. Cho, S. Kim, Y. Kim, Y. Park, "Optical imaging techniques for the study of malaria", *Trends in Biotechnology*, **20**(2), 71-79 (2012)
- [9] F. Kawamoto, "Rapid diagnosis of malaria by fluorescence microscopy with light microscope and interference filter", *The Lancet*, **337**(8735), 200-202 (1991)
- [10] M.T. Makler, C.J. Palmer, A.L. Ager, "A review of practical techniques for the diagnosis of malaria", *Annals of Tropical Medicine & Parasitology* **92**, 419-433 (1998)

- [11] P.J. Guering, P. Olliaro, F. Nosten, P. Druilhe, R. Laxminarayan, F. Binka, W. L. Kilama, N. Ford, N. J. White, "Malaria: current status of control, diagnosis, treatment, and a proposed agenda for research and development", *The Lancet: Infectious Diseases* **Vol. 2**, 564-573 (2002)
- [12] B.K. Wilson, M.R. Behrend, M.P. Horning, M. C. Hegg, "Detection of malarial byproduct hemozoin utilizing its unique scattering properties", *Optics Express* **19**(13), 12190-12196 (2011)
- [13] D. Lenz, P.G. Kremsner, B. Lell, B. Biallas, M. Boettcher, B. Mordmüller, A.A. Adegnik, "Assessment of LED fluorescence microscopy for the diagnosis of *Plasmodium falciparum* infections in Gabon", *Malaria Journal* **10**:194 (2011)
- [14] M.C. Campbell, C.J. Cookson, J.M. Bueno, A. Seamann, M.L. Kislak, "Confocal polarimetry measurements of tissue infected with malaria", *OSA Technical Digest*, paper FThK1 (2007)
- [15] P.F. Scholl, D. Kongkasuriyachai, P.A. Demirev, A.B. Feldman, F.S. Lin, D.J. Sullivan Jr., N. Kumar, "Rapid detection of malaria infection in vivo by laser desorption mass spectrometry", *American Journal of Tropical Medicine & Hygiene* **71**(5), 546-551 (2004)
- [16] J.M. Bélisle, S. Constantino, M.L. Leimanis, M-J. Bellemare, D.S. Bohle, E. Georges, P. Wiseman, "Sensitive detection of malaria infection by third harmonic generation imaging", *Biophysical Journal* **94**(4), L26-L28 (2008)
- [17] P.F. Mens, R.J. Matelon, B.Y. Nour, D.M. Newman, H.D. Schalig, "Laboratory evaluation on the sensitivity and specificity of a novel and rapid detection method for malaria diagnosis based on magneto-optical technology (MOT)", *Malaria Journal* **9**:207 (2010)
- [18] A. Roggan, M. Friebe, K. Dörschel, A. Hahn, G. Müller, "Optical properties of circulating human blood in the wavelength range 400-2500 nm", *Journal of Biomedical Optics* **4**(1), 36-46 (1999).
- [19] M. Hammer, D. Schweitzer, B. Michel, E. Thamm, A. Kolb, "Single scattering by blood cells", *Applied Optics* **37**(31), 7410-7418 (1998)
- [20] E.K. Hanson, J. Ballantyne, "A blue spectral shift of the haemoglobin soret band correlates with the age (time since deposition) of dried bloodstains", *PLoS One* **5**(9), 12830-12840 (2010)
- [21] D.H. Tycko, M.H. Metz, E.A. Epstein, A. Grinbaum, "Flow-cytometric light scattering measurements of red blood cell volume and haemoglobin concentration", *Applied Optics* **24**(9), 1355-1365 (1985)
- [22] M.S. Amin, Y. Park, N. Lue, R.R. Dasari, M. Badizadegan, M.S. Feld, G. Popescu, "Microrheology of red blood cell membranes using dynamic scattering microscopy", *Optics Express* **15**(25), 17001-17009 (2007)
- [23] M. Meinke, G. Müller, J. Helfmann, M. Friebe, "Optical properties of platelets and blood plasma and their influence on the optical behavior of whole blood in the visible to near infrared wavelength range", *Journal of Biomedical Optics* **12**(1), 14024-14032 (2007)
- [24] A.M.K. Nilsson, P. Alsholm, A. Karlsson, S. Andersson-Engels, "T-matrix computations of light scattering by red blood cells", *Applied Optics* **37**(13), 2735-2748 (1998)
- [25] G.S. Noland, N. Briones, D.J. Sullivan Jr., "The shape and size of hemozoin crystals distinguishes diverse *Plasmodium* species", *Molecular and Biochemical Parasitology* **130**(2), 91-99 (2003)
- [26] D.J. Faber, "Oxygen saturation-dependent absorption and scattering of blood", *Physical Review Letters* **93**(2), 28102 (2004)
- [27] M. Friebe, A. Roggan, G. Müller, M. Meinke. "Determination of optical properties of human blood in the spectral range 250 to 1100 nm using Monte Carlo simulations with hematocrit-dependent effective scattering phase functions", *Journal of Biomedical Optics* **11**(3), 34021-34031 (2006)
- [28] G.A. Jamjoom, "Dark-field microscopy for detection of malaria in unstained blood films", *Journal of Clinical Microbiology* **17**(5), 717-721 (1983)
- [29] J. He, A. Karlsson, J. Swartling, S. Andersson-Engels, "Light scattering by multiple red blood cells", *J. Opt. Soc. Am. A* **21**(10), 1953-1961 (2003)
- [30] M. Brydegaard, A. Merdasa, H. Jayaweera, J. Ålebring, S. Svanberg, "Versatile multispectral microscope based on light emitting diodes", *Review of Scientific Instruments* **82**(12), 3660810-3660822 (2011)
- [31] G.H. Golub, C. Reinsch, "Handbook series linear algebra: singular value decomposition and least squares solutions", *Numerische Mathematik* **14**(5), 403-420 (1970)
- [32] A. Runemark, M. Wellenreuther, H. Jayaweera, S. Svanberg, M. Brydegaard, "Rare events in remote dark field spectroscopy: an ecological case study of insects", *Selected Topics in Quantum Electronics, IEEE Journal of PP*(99), 1 (2012)
- [33] S.P. Kachur, E. Nicolas, V. Jean-Francois, A. Benitez, P.B. Bloland, Y.S. Jean, D.L. Mount, T.K. Ruebush II, P.Nguyen-Dinh, "Prevalence of malaria parasitemia and accuracy of microscopic diagnosis in Haiti, October 1995", *Pan. Am. J. Public Health* **3**(1), 35-39 (1998).
- [34] B.K. Wilson, M.R. Behrend, M.P. Horning, M.C. Hegg, "Detection of malarial byproduct hemozoin utilizing its unique scattering properties", *Optics Express* **19**(13), 12190-12196 (2011)
- [35] Y.M. Serebrennikova, J. Patel, L.H. Garcia-Rubio, "Interpretation of the ultraviolet-visible spectra of malarial parasite *Plasmodium falciparum*", *Applied Optics* **49**(2/10), 180-188 (2010)

## PAPER V

**Chemometric approach to chromatic spatial variance.**

**Case study: Patchiness of the Skyros wall lizard**

M. Brydegaard, A. Runemark and R. Bro

*Journal of Chemometrics* **26**(6), 246-255 (2012).

# Chemometric approach to chromatic spatial variance. Case study: patchiness of the Skyros wall lizard

Mikkel Brydegaard<sup>a\*</sup>, Anna Runemark<sup>b</sup> and Rasmus Bro<sup>c</sup>

**In this paper, we demonstrate how to take advantage of the large number of spatial samples provided by commercial multispectral RGB imagers. We investigate the possibility to use various multidimensional histograms and probability distributions for decomposition and predictive models. We show how these methods can be used in an example using images of different Skyros wall lizards and demonstrate improved performance in prediction of color morph compared with traditional parameterization techniques of spatial variance. Copyright © 2012 John Wiley & Sons, Ltd.**

**Keywords:** ND histograms; SVD; multivariate regression; RGB; clustering; imaging; image summation; patchiness; spatial variance; texture analysis

## 1. INTRODUCTION

The recent large-scale commercialization of color charge-coupled devices (CCD) [1,2] and color complimentary metal-oxide semiconductor (CMOS) imagers has provided a widespread spectroscopic light-detecting component, which can be found in webcams, digital cameras, and mobile phones. Recent developments of color imagers combined with heavily increased computational power and parallel GPU processing [3] open new areas of spectroscopic opportunities worth exploring. Although the three spectral bands (red, green, and blue) mimicking the human eye physiology are few, broad, and overlapping and provide a rather poor spectral resolution in comparison to scientific spectrometers, the spatial resolution, in the range of megapixels, is far superior to the number of spectroscopic samples, which could be provided by any point spectrometer within any reasonable time frame. The tradeoffs between spectral, spatial, and temporal resolution is well known for spectroscopists, and it is generally hard to compromise [4]. Also, it is worth noting that sensitivity of a spectroscopic method cannot be obtained without confinement in all domains; dynamic, spectral, spatial, and temporal; see, for example, Table 1 in Reference [4].

In this paper, we will discuss a way to exploit data from RGB multispectral imagers providing a large numbers of spatial points but with poor spectral resolution. We will demonstrate how to take advantage of the spatial resolution, in a way, so that we can utilize more significant principal components than the number of spectral bands, which is generally not considered possible in traditional spectroscopic and chemometric applications.

The power of spectral decomposition known from chemometrics relates to the fact that spectral features from given chemical substances generally remain fixed on the wavelength axis, while the other axis relates to the concentration of the substance providing the spectral feature. This holds true for absorption, fluorescence emission, or other spectroscopic methods. Such optical spectral analysis is typically performed using spectrometers. The typical operation of polychromators consists

of conversion from spectral domain to spatial domain using dispersive gratings or prisms in combination with imaging of a slit onto a CCD detector [5]. Thus, the source for spectroscopic data is highly similar to image data, with the difference that in the first case, each vector element represents integration over a spectral band, whereas in the image, matrix element represents integration over a point spread function.

Applying the light particle model on the incident light, we can even claim that both spectroscopic and image data are histograms where the vector or matrix elements are counts of photons with a certain property, of wavelength or spatial origin, respectively. Another good analogy to this is gamma spectroscopy, where single photons are counted and sorted in a histogram according to their energy [6]. From this point of view, we can easily understand that histogram data with few photons, due to low light intensity or short exposure time, constitute noisy images or spectra, just as we need many two-dice rolls to produce a well-defined binomial distribution. We also understand that receiving a single photon with the energy of 589 nm, we have difficulty to determine the source. Only by analyzing the details of the variance of photon energies that we can determine whether the source is, for example, a sodium lamp, a yellow LED, a filament lamp, or sunlight, which might all have average photon energies of just 589 nm. The case where we can

\* Correspondence to: M. Brydegaard, Atomic Physics Division, Lund University, PO Box 118, SE-221 00 Lund, Sweden.  
E-mail: mikkel.brydegaard@fysik.lth.se

a M. Brydegaard  
Atomic Physics Division, Lund University, SE-221 00 Lund, Sweden

b A. Runemark  
Animal Ecology, Lund University, SE-221 00 Lund, Sweden

c R. Bro  
Department of Food Science, University of Copenhagen, Copenhagen, Denmark

distinguish between sources using the histogram of the variance rather than a single average value also occurs in the spatial domain; consider, for example, the spatially averaged reflectance spectra of a gray donkey and a zebra, which might be identical, even for a high-resolution spectrometer, whereas the spatial variances are completely different in the two cases.

In the discipline of chemometrics, it is also well known that spectroscopic data might have bins along several domains, corresponding to different properties of the photons. Such properties could be scattering angles [4] or both excitation and emission wavelengths as in excitation emission matrix (EEM) spectroscopy. Here, fluorescent light is collected and discretized both by excitation and emission wavelength [7]. This constitutes a 2D surface of intensities where a given substance gives rise to 2D spectral features at a specific position on the plane. The intensity height of the feature relates to the concentration of the given substance. In the case of the EEM, all data result from a single spatial sample. Histograms of higher dimensionality are even known from samples taken over time, for example, in flow cytometry where a few parameters, for example, total fluorescence, side and back scattering, are measured in thousands of samples per second [8,9]. Histogram of higher dimensionality could also be thought of as in the X-ray absorption fields in computerized tomography, where the counts correspond to the absorbed number of photons and the bins correspond to spatial voxels.

In this paper, we will demonstrate how to produce histograms of various dimensionalities from RGB imager data.

## 2. CASE STUDY: THE SKYROS WALL LIZARD

Here, we demonstrate this concept on the Skyros wall lizard, *Podarcis gaigeae*, a species that is polymorphic with respect to throat color [11]. The Skyros wall lizard is found only on the Greek island of Skyros (lat.: 38.50, long.: 24.34) and in its surrounding archipelago [10]. The throat color is likely to be determined by one co-dominant (both alleles are expressed because none is dominant over the other) gene with three different alleles (different varieties of the gene), orange (O), yellow (Y), and white (W) [11]. Because each lizard has two alleles, there are six possible throat color patterns, OO, OY, OW, YY, YW, and WW, where the individuals with two different color alleles (OY, OW, and YW) have patchy throats (Figure 1). The pigments involved in lizard throat pigmentation are carotenoids and pteridins [12,13]. Structural ultraviolet or bluish colors are also known to occur in certain reptile species [14]. For the particular species in this study, such colors were only present on the trunk (side) of the lizard [15]. In addition to the O, Y, and W signal colors, some *P. gaigeae* lizards also have small black eumelanin [12] spots on the throats

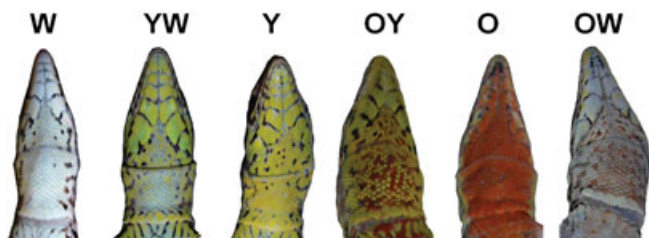


**Figure 1.** Examples of the six types of throat colorations found among the Skyros wall lizard.

(Figure 1). Whether the lizards have such black spots or not is independent of the signal color of the throat; there are specimens both with and without these black spots for all throat color types. In this system, using the mean color without taking the spatial variance into account would generate a continuous color distribution between the differently colored lizards, which would not capture the discrete presence/absence of the specific alleles. We here refer to the discussion between Vercken [16] and Cote [17] applying RGB imaging and point spectroscopy, respectively, on a similar system. The mean reflectance spectra of each of the six color morphs are presented in Figure 2. In this study, we will only briefly discuss the point spectroscopic measurements and focus on analysis of RGB images.

Classifying discrete throat color types ("color morphs") based on well-defined quantitative criteria would allow biologists to address a new set of questions regarding the physiology and behavior of these different color morphs. Color polymorphic species from many different taxa are widely used as model systems for addressing evolutionary questions [18,19]. Different color morphs have been shown to differ with respect to morphology [20], behavior [21], and life-history traits [22]. Certain morphs may also be favored by mate choice [21,23]. The Skyros wall lizard is an interesting model system for addressing evolutionary questions because of the presence of morphologically strongly diverged populations [23,24] on small islets separated by sea level rise only hundreds or thousands of years ago [25]. These populations have also diverged genetically [11] and behaviorally [26]. To be able to correctly determine frequency of different color morphs in these diverged populations of the Skyros wall lizard, as well as study whether different morphs differ morphologically, genetically, and behaviorally, a quantitative classification method that determines color morph affinity is necessary. Such a classification method would enable us to address new and exciting evolutionary questions.

## 3. MATERIALS AND METHODS

Skyros wall lizards were captured on the island of Skyros (Greece) and on islets in its surrounding archipelago during peak reproductive period (March–May) during 2007 and 2008. Lizards were caught in four mainland populations and three different islet

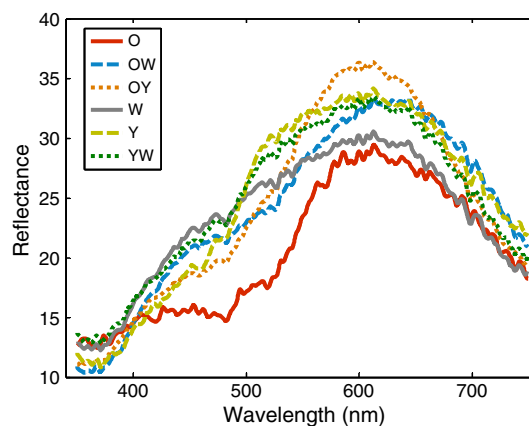


**Figure 2.** Mean reflectance spectra of the six groups classed by visual inspection of the biologist.

populations (Nyfi, Agios Fokas, Atsitsa, and Palamari on the main island and Lakonisi, Mesa Diavates, and Exo Diavates; see [11] for more details on sample locations), which differ with respect to morph frequency and body size. Animals were photographed with a trichromatic 6Mpix (DMC FX01, Panasonic corp. Osaka, Japan) RGB color camera in an optically isolated box using the built-in xenon flash (Figure 3). A white background reference was used for flat field calibration. Specular reflections were avoided with two crossed polarization filters on the illumination and objective, respectively (NT38-491, Edmund Optics Inc., New Jersey, USA). Animals from two of the islets (Lakonisi and Mesa Diavates) and two mainland populations (Nyfi and Agios Fokas) were brought into the lab and photographed there, whereas animals from Exo Diavates, Atsitsa, and Palamari were photographed in the field. Animals were individually marked through toe clipping.

Diffuse point reflectance spectroscopy was performed with a compact spectrometer and fiber optic probe in 45° configuration (USB4000, Ocean Optics Inc., Florida, USA). The measurements were white calibrated against a spectralon reference. The instrument provided diffuse reflectance from 350 to 750 nm (Figure 2).

Animals were cooled (e.g., to natural night time temperatures) for immobilization during the photographic sessions. In this paper, a total sample size of  $N_{\text{sample}}=272$  is used. The subset is 26 specimens of type O, 39 of type OW, 12 of type OY, 56 of type W, 45 of type Y, and 94 of type YW.

#### 4. ANALYSIS

We consider the signal  $I$  for a given pixel in a given wavelength band:

$$I_{x,y,ch} = \int_{\lambda=0}^{\infty} S_{ch}(\lambda)R_{x,y}(\lambda)E_{x,y}(\lambda)d\lambda \quad (1)$$

where  $I$  are the light intensity counts;  $x,y$  the spatial coordinates in the picture;  $ch$  the wavelength band red, green, or blue;  $S_{ch}$  the spectral sensitivity band for color band  $ch$ ;  $R$  the depolarized reflectance of depicted object;  $E$  the emission spectrum of white XeHg flash illumination; and  $\lambda$  the wavelength.

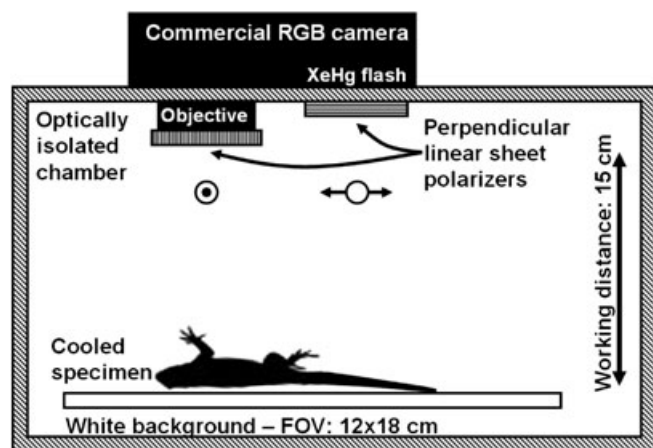


**Figure 3.** Setup for depolarized photography of specimens in controlled conditions.

Here,  $S_{ch}$  is the spectral response of each band often given in quantum yield in the datasheet of the imager chip. As seen in Eq. 1, it is understood that the signal  $I$  in a given pixel does not only depend on the reflectance  $R$  of the depicted object in point  $x,y$  but also on the illumination profile,  $E$ , and to great extent the geometry of the illumination source and the depicted scenario, that is, distances and surface orientations in each point. Because the specimens were photographed on a white background, we are able to approximate the illumination profile with a polynomial of the form

$$E_{x,y,ch} = k_{0,ch}x^0y^0 + k_{1,ch}x^0y^1 + k_{2,ch}x^1y^0 + k_{3,ch}x^1y^1 + k_{4,ch}x^0y^2 + k_{5,ch}x^2y^0 \quad (2)$$

where  $E$  are the approximated intensity counts of illumination profile and  $k$  the fit coefficients.

Here, the coefficients  $k_{0,ch} \dots k_{5,ch}$  are found by linear regression by using a training set only including the white background pixels. The empty background pixels were easily detectable by using an adaptive threshold based on the gravitation points on the gray-scale histogram of the images. Illumination profiles of each spectral band,  $ch$ , were individually fitted. No significant improvement was found by increasing the order of the polynomial and the cross-product terms. Provided the illumination profile, we are now able to approximate the absolute reflectance,  $R$ , for each spectral band,  $ch$ , in each pixel in  $x,y$ :

$$R_{x,y,ch} = \frac{I_{x,y,ch}}{E_{x,y,ch}} \quad (3)$$

This procedure removes a large fraction of the instrumentally induced variance in terms of shot-to-shot stability of the flash, and so on. The dark current could be assumed to be negligible. From the flat field calibrated image,  $R$ , a small region of interest (polygonal ROI) was cropped out from the throat of each specimen. The ROI selection was based on common fix points based on the intersection of certain scales. On average, 17,153 pixels were obtained from each specimen (std: 8664, min: 3076, max: 51,445). The large variance in ROI sizes is partly caused by the large size variation in the specimens caused by the pattern that lizards on the islets have larger body sizes [24], a phenomenon referred to as island gigantism in biology. The two spatial domains,  $x$  and  $y$ , were discarded, and the pixels from each ROI were organized in a matrix,  $RGB_{1 \dots N_{\text{pix}},ch}$ , regardless of their spatial origin. Here, the columns are the three spectral bands, red, green, and blue, and where the rows run from 1 to the number of pixels in the ROI,  $N_{\text{pix}}$ . Rows with pixels on the margins of the dynamical range (having either 0 or 1 in reflectance) were excluded from the analysis (less than 0.2%). This is carried out to avoid nonlinearity.

In this study, we will investigate the possibilities to increase the cluster prediction ability (of lizard colormorph classification) by the use of the spatial variance within the ROI. We will compare histograms/probability distributions of various dimensionalities to the crude parameterizations, spatial averaged RGB value,  $\mu_{RGB}$ , and the standard deviations,  $\sigma_{RGB}$ , defined as

$$\mu_{RGB} = \frac{\sum_{n=1}^{Npix} RGB_{n,ch}}{Npix}, \quad \sigma_{RGB} = \sqrt{\frac{\sum_{n=1}^{Npix} (RGB_{n,ch} - \mu_{RGB})^2}{Npix}} \quad (4)$$

$$\gamma_{RGB} = \frac{\sum_{n=1}^{Npix} (RGB_{n,ch} - \mu_{RGB})^3}{Npix \sigma_{RGB}^3}, \quad \beta_{RGB} = \frac{\sum_{n=1}^{Npix} (RGB_{n,ch} - \mu_{RGB})^4}{Npix \sigma_{RGB}^4}$$

where  $RGB$  is the  $Npix$ -by-3 matrix containing reflectance in red, green, and blue band from each pixel in the ROI;  $\mu_{RGB}$  the spatially averaged reflectance for red, green, and blue band;  $\sigma_{RGB}$  the standard deviation for reflectances in each spectral band;  $\gamma_{RGB}$  the skewness for reflectances in each spectral band; and  $\beta_{RGB}$  the kurtosis deviation for reflectances in each spectral band.

To estimate the discrete probability distribution, the three reflectances for each spectral band are discretized into a number of bins,  $NoB$ :

$$b_{m=1\dots NoB+1} = \frac{0, 1, 2, \dots, NoB}{NoB}, \quad 0 \leq b \leq 1 \quad (5)$$

where  $b$  is the vector defining the discrete bins and  $NoB$  the number of bins.

$$P1_{m=1\dots NoB, ch=1\dots 3} = \frac{\sum_{n=1}^{Npix} (b_{m1} \leq RGB_{n,ch} < b_{m1+1})}{Npix} \quad (6)$$

where  $P1_{1\dots NoB, ch}$  is the estimated probability distribution for reflectance in each band.

Here, the Boolean outcomes of the inequalities are interpreted as 0 or 1. Two examples of the three probability vectors,  $P1$ , can be observed in Figure 4 left. The upper left subfigure shows

distributions from a homogeneously colored specimen, type Y (Figure 1). The lower left subfigure shows the distribution for a patchy specimen, type OY (Figure 1). The multimodality is clear in the patchy case; however, in this parameterization of the variance, there is no information on the correlation between the three spectral bands. Chromaticity is, in general, a term describing the relative intensities between two of more spectral bands. The absolute reflectance variance is largely due to geometrical effects, and chromaticity is much more object specific. This is well known from a list of sciences such as remote sensing, light detection and ranging differential absorption LIDAR spectroscopy (LIDAR DIAL [27]), computer vision [9], chromatic bands in vision physiology [28], and image compression [29,30]. For this reason, it might be beneficial to discard the absolute reflectance values and only consider relative quantities between spectral bands, the so called chromaticity or spectral shapes. This will reduce dimensionality by one, and for the trichromatic RGB imager under consideration, this will reduce the RGB color space to a chromatic plane:

$$C_{1\dots Npix, c=1\dots 2} = \frac{RGB_{1\dots Npix, 1\dots 2}}{\sum_{ch=1}^3 RGB_{1\dots Npix, ch}}, \quad 0 < C < 1, \quad C_{n,1} + C_{n,2} < 1 \quad (7)$$

where  $C$  is the  $Npix$ -by-2 matrix with two chromatic components describing each pixel.

To be able to parameterize the correlation between the two chromatic components in  $C$ , we now expand the concept of histograms to two dimensions. Although this is carried out computationally, the step resembles the physical example of going from a linear 1D CCD detector to a 2D imaging CCD as discussed previously.

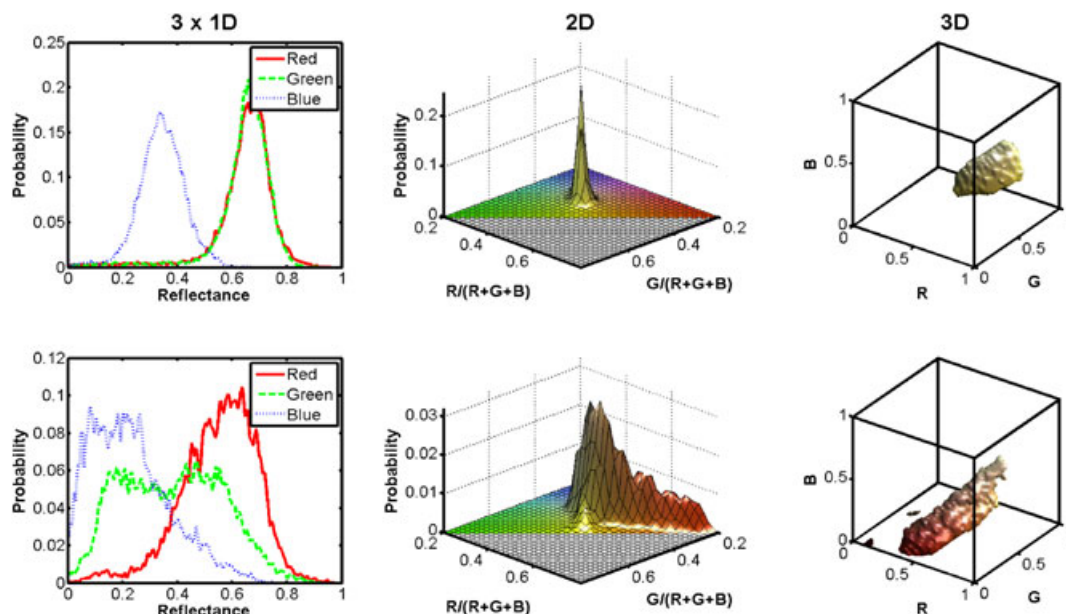


**Figure 4.** Upper row: reflectance distributions for a homogeneously colored type Y. Lower row: corresponding distributions for a patchy specimen, type OY. Left column: three 1D distributions for each spectral band. Middle column: 2D chromatic plane distributions color coded with corresponding colors for the two example specimen. Right column: iso-surfaces encapsulating probabilities higher than 1% in the 3D RGB color space of the two sample specimens. Surface is coded with corresponding color.

$$P2_{m1=1\dots NoB, m2=1\dots NoB} = \frac{\sum_{n=1}^{Npix} (b_{m1} < C_{n,1} < b_{m1+1}) \cap (b_{m2} < C_{n,2} < b_{m2+1})}{Npix} \quad (8)$$

where  $P2$  is the estimated probability distribution in the chromatic plane.

Two examples of the two-dimensional chromatic probability planes are shown in Figure 4 middle column. In the upper middle subfigure, the homogeneous specimen type Y (Figure 1) is illustrated. The plane is colored with the corresponding color hue regardless of the shade. The lower middle subfigure is an example from the patchy specimen type OY (Figure 1). Especially, note the difference on the axis: because the patchy specimen has a broader distribution, the peak probability is only one-tenth of the homogeneous case. The axis has been cropped because of it being unlikely to detect the most extreme colors.

We can further expand the concept of histograms and probability distributions to three dimensions and obtain probability fields, with some resemblance to quantum mechanics. A technical analogy would be to take the step from a 2D imaging CCD to a 3D tomography. In our case, such a probability distribution field would give us the probability of observing a pixel in a given position in the RGB color space. Although we already made certain arguments for discarding the absolute values, one argument for keeping the absolute reflectance is the fact that the combined effect of the dull features of melanin absorbance and the spectral behavior of the scattering coefficient tends to produce flat scaling of the visible reflectance without leaving any specific chromatic component. In addition, the low intensity counts for melanized scales would produce a large uncertainty in the determination of the chromatic components because of the low denominator in Eq. 7. The 3D probability distribution is estimated

$$P3_{m1,m2,m3} = \frac{\sum_{n=1}^{Npix} (b_{m1} < RGB_{n,1} < b_{m1+1}) \cap (b_{m2} < RGB_{n,2} < b_{m2+1}) \cap (b_{m3} < RGB_{n,3} < b_{m3+1})}{Npix} \quad (9)$$

where  $P3$  is the estimated probability distribution field in the RGB color space.

In practice, for this histogram as well as for the 1D and 2D case, the histogram is computed in a cumulative way using indexing (see pseudocode in Box 1). This greatly decreases the computational time required to produce the histogram.

Box 1. Example on pseudocode producing a 3D histogram, where RGB is an  $N$ -by-3 matrix where the elements are reflectance between zero and one,  $NoB$  is the number of bins.

```

RGB = 1 + round((NoB - 1) * RGB);
P3 = zeros(NoB, NoB, NoB);
for n = 1:Npix
    P3(RGB(n, 1), RGB(n, 2), RGB(n, 3)) = P3(RGB(n, 1),
    RGB(n, 2), RGB(n, 3)) + 1;
end
P3 = P3/Npix;

```

Two examples of probability fields are shown in Figure 4 right. With increasing dimensionality, it becomes more difficult to visualize the probability distributions. One way to visualize a full 3D tensor is to use iso-surfaces. In Figure 4 right, two such iso-surfaces are shown. They both encapsulate probabilities larger than 1%. The visualization obviously appears completely different for other thresholds. The upper right subfigure shows the homogeneous specimen type Y (Figure 1). The lower right subfigure shows the probability distribution in the RGB color space for the patchy specimen for type OY (Figure 1). The iso-surfaces are color coded according to the corresponding color in the RGB color space. The three upper and three lower subfigures in Figure 4 all originate from the same two specimens. It follows from the definition of all three probability distributions that

$$\sum_{m1=1}^{NoB} P1_{m1, ch} = 1, \sum_{m1=1}^{NoB} \sum_{m2=1}^{NoB} P2_{m1, m2} = 1, \sum_{m1=1}^{NoB} \sum_{m2=1}^{NoB} \sum_{m3=1}^{NoB} P3_{m1, m2, m3} = 1 \quad (10)$$

and further

$$P1_{m1, ch} \in \{0 \dots 1\}, P2_{m1, m2} \in \{0 \dots 1\}, P3_{m1, m2, m3} \in \{0 \dots 1\} \quad (11)$$

In order to perform a comparative study in terms of prediction ability for the probability distribution of various dimensionalities, we choose the number of bins in the following way: for the 1D case, we choose  $NoB = 254$  bins corresponding to the 256 gray levels, provided by the 8-bit imager, minus the first and the last elements, which were excluded. Because  $P1$  contains one probability vector for each of the three spectral bands, the 1D case gives us a number of total bins,  $NTB = 762$  elements for each sample. In the 2D case,  $P2$ , we choose  $NoB = 40$  bins. This gives

us a chromatic plane with 1600 elements; however, because the function space of  $C$  is only defined strictly on one side of the diagonal, the choice of 40 bins gives us  $NTB = 760$  elements, which can assume anything else than 0. In the 3D case,  $P3$ , we choose  $NoB = 9$ , which gives us  $NTB = 739$  cubic bins in the RGB color space.

The probability elements from the three histograms of various dimensionalities from all specimens were arranged in a matrix  $M_{1\dots N_{\text{sampl}}, 1\dots NTB}$ . Thus, the various dimensions are temporally discarded for the purpose of applying a truncated singular value decomposition (SVD) of the probability distribution for all 272 specimens:

$$U_{1\dots N_{\text{sampl}}, 1\dots tr} \Sigma_{1\dots tr, 1\dots tr} V_{1\dots NTB, 1\dots tr}^* \approx M_{1\dots N_{\text{sampl}}, 1\dots NTB} \quad (12)$$

where

$$U_{1\dots N_{\text{sampl}}, 1\dots tr} \Sigma_{1\dots tr, 1\dots tr} V_{1\dots NTB, 1\dots tr}^* - M_{1\dots N_{\text{sampl}}, 1\dots NTB} \rightarrow 0, \text{ when } tr \rightarrow NTB \quad (13)$$

where  $U_{1\dots N_{\text{sampl}}, 1\dots tr}$  are the coefficients for truncated representation,  $\Sigma_{1\dots N_{\text{sampl}}, 1\dots N_{\text{sampl}}}$  the diagonal matrix containing root of

eigenvalues,  $V_{1\dots NTB,1\dots tr}$  the eigenvectors, eigenplanes, or eigenfields, and  $tr$  the truncation.

The principal 1D, 2D, or 3D vectors, planes, or fields, respectively, are reconstructed after the decomposition. According to how rapid the eigenvalues decay, the SVD approximates the probability distribution from each specimen more or less efficiently. Thus, a truncated set of  $tr$  components summarizes the spatial chromatic variance. By definition, the columns of  $U$ ,  $\Sigma$ , and  $V$  are sorted in order of decreasing magnitude, which enables us to separate low-variance noise from information by truncating the representation after a given value. The SVD is traditionally applied on probability distributions that are physically produced by instruments like spectrometers [31,32] or imagers [33]. The main difference to this example is that we created the distribution computationally exploiting the spatial variance in an ROI.

In Figure 5, the first four eigenvector components from the 1D distributions are presented. The first component in the uppermost subfigure closely resembles the mean of the histogram for each spectral band for all samples. The successive components describe in more and more details the shape of the three distributions. By definition, the components are orthogonal to each other; however, it is worth noting that it is the concatenated vectors in  $M$  that are orthogonal and not necessarily the reconstructed components for spectral band; see, for example, the red distribution in components 3 and 4 in the lowermost subfigures.

In Figure 6, the first four eigenplane components from the 2D case are presented. In this 2D case, we have now expanded the set of 2D distribution in terms of principal component planes. Again, the coloring of the plane corresponds to the real chromatic value, regardless of the shade. The first component is, as

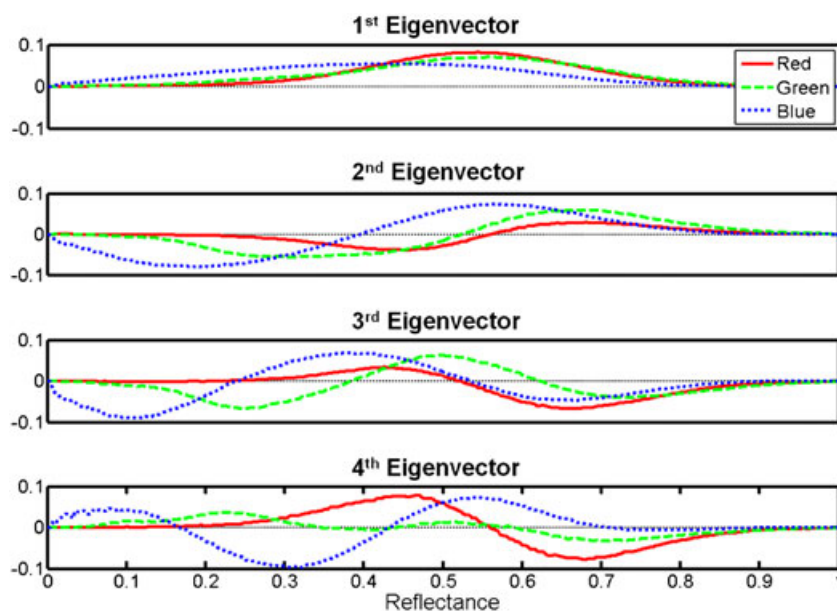


Figure 5. The first four eigenvector components of the concatenated 1D distributions.

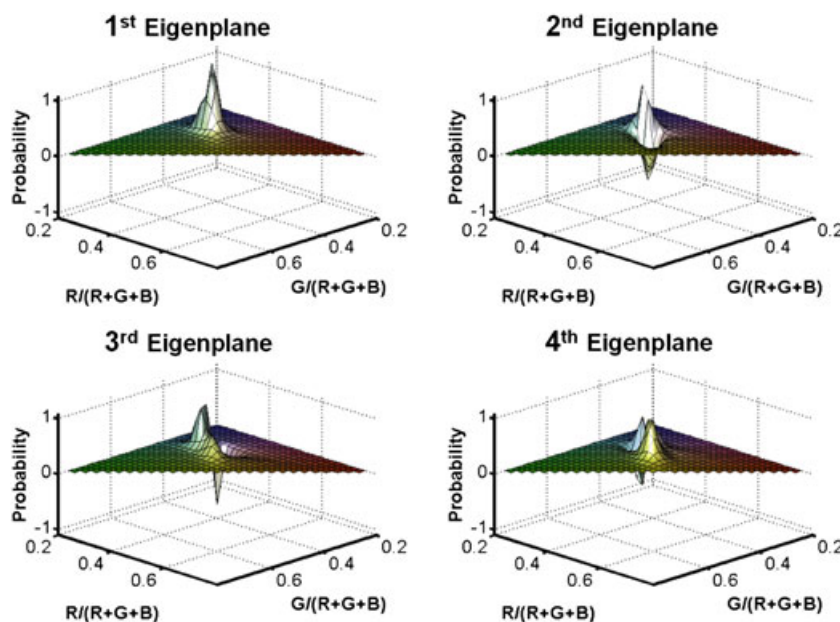


Figure 6. The first four eigenplane components of the 2D chromatic planes.

before, close to the mean distribution of all samples; the following components enable a number of ways to deform the distribution in increasing details. Note the orthogonality between the 2D distributions.

In the case of the 3D distributions, visualization is now additionally problematic because of the fact that the component eigenfields now have both positive and negative regions, as was the case also for lower dimensionality. In Figure 7, the first four eigenfield components are presented with iso-surfaces in such a way that the positive regions are encapsulated by red surfaces and the negative regions are encapsulated by blue surfaces. While the first few components merely imply slight shifts or broadening of the main mode, the higher-order components reveal the severe multimodality originating from the differently colored scales in some of the specimens.

The decay of eigenvalues for each case is presented in Figure 8. The faster the decay, the lesser components are required for an accurate approximation of the distribution of the various dimensionalities. In Figure 9, four comparative scatter plots are presented. In the upper left, the spatially averaged RGB reflectance is mapped out. In the remaining subfigures  $U_{n,1...3}$  is mapped out for the decomposed probability distributions of the various dimensionality. 3D scatter plots are generally difficult to read, but some condensation can be seen for the 2D and 3D case in the two lower figures.

In the following section, we will investigate the possibility of using a truncated representation of the histograms of various dimensionalities in order to improve prediction of the classes presented in Figure 1. For the prediction, we use a simple regression-based discriminant analysis finding the projection of maximum separation:

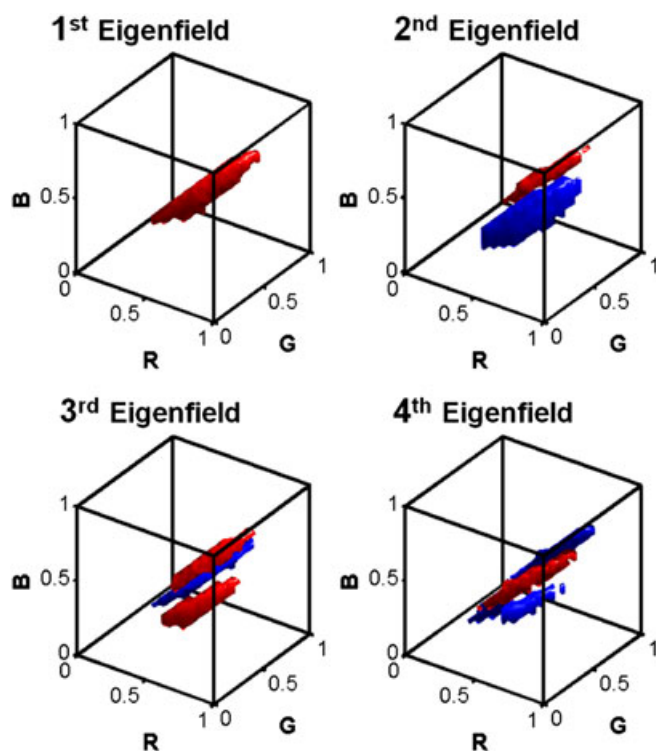


**Figure 7.** The first four eigenfield components distribution fields of the 3D distributions in the RGB color space. The red surface encapsulates the positive regions, and the blue surface encapsulates the negative regions of the fields.

$$\theta_{1...DOF,c=1...6} = (\Phi_{n \in \text{train}, 1...DOF} * \Phi_{n \in \text{train}, 1...DOF})^{-1} \Phi_{n \in \text{train}, 1...DOF} * Y_{n \in \text{train}, 1...6} \quad (14)$$

where  $\theta_{1...DOF,c=1...6}$  is the predictive linear discriminant function,  $DOF$  the degrees of freedom for the discriminant function,  $c$  the number indicating the classes presented in Figure 1,  $\text{train}$  the training set including all sample except one,  $\Phi_{n \in \text{train}, 1...DOF}$  the regressor for a given training set with  $DOF$  degrees of freedom, and  $Y_{n \in \text{train}, 1...6}$  the Boolean matrix with expert answers on each class in Figure 1.

This can be thought of as an optimal linear transform. The predicted class is estimated by simple matrix multiplication

$$\hat{Y}_{n \in \text{eval}, 1...6} = \Phi_{n \in \text{eval}, 1...DOF} \theta_{1...DOF, 1...6} \quad (15)$$

where  $\hat{Y}$  is the predicted class and  $\text{eval}$  the evaluation set consisting of one sample left out.

We also tried to use more standard classification approaches, and similar results were obtained (results not shown). Both training and prediction are carried out iteratively, leaving out the predicted sample from the training set according to a leave-one-out methodology. For comparison of the histograms,

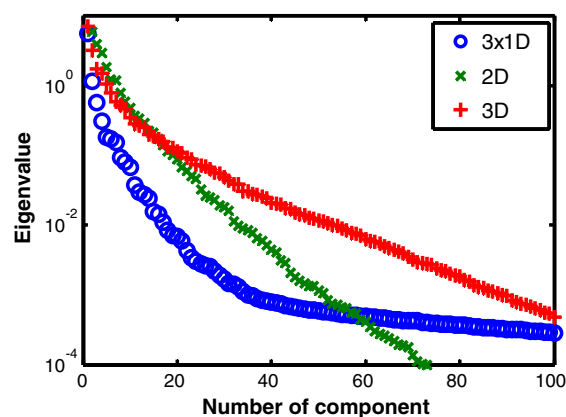


**Figure 8.** The decay of the eigenvalues for each case.

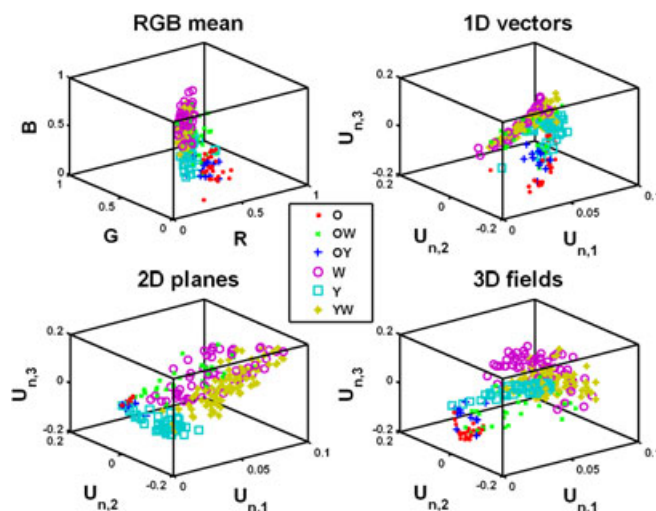


**Figure 9.** Upper left: Scatter plot of spatial mean RGB reflectance. Upper right and remaining subfigures: Scatter plot of the components associated with the first three eigenvectors, eigenplanes and eigenfields respectively.

we use two very simple models that only take the spatial mean,  $\mu_{RGB}$ , into consideration and another model that additionally considers the standard deviation  $\sigma_{RGB}$ . The regressors are

$$\begin{aligned} \Phi_{mean} &= [1 \quad \mu_{RGB}] \quad , \quad \Phi_{mean\&std} = [1 \quad \mu_{RGB} \quad \sigma_{RGB}] \quad (16) \\ \Phi_{mean\&std\&skew} &= [1 \quad \mu_{RGB} \quad \sigma_{RGB} \quad \gamma_{RGB}] \\ \Phi_{mean\&std\&skew\&kurtosis} &= [1 \quad \mu_{RGB} \quad \sigma_{RGB} \quad \gamma_{RGB} \quad \beta_{RGB}] \end{aligned}$$

The DOF are 4, 7, 10, and 13, respectively. The overall performance of the models is measured as the mean correlation between  $Y$  and  $\hat{Y}$  for every class. The performance when the spatial mean is used is 56%. When a standard deviation factor for each spectral band is included, the performance increases to 61%. When skewness and kurtosis are additionally included, the prediction performance became worse (Figure 10). This can be expected because of the fact that skewness and kurtosis fail to describe multimodal distributions. When a truncated set of the probability distribution of various dimensionalities is used, the regressor had the form

$$\Phi = [1 \quad U_{1\dots N_{\text{samp}}, 1\dots tr}] \quad (17)$$

Here, the  $DOF = tr + 1$ . For all three types of distribution, the truncation number was iteratively increased and the prediction performance evaluated. The result is shown with respect to the truncation number in Figure 10. For all three cases, the prediction performance first increases when the regressors have additional information. When higher components are included, noise and other irrelevant variation are introduced, and the performance drops again. For comparison, the performance of the two simple models is shown as straight lines. The equivalent DOF of the two simple models has been marked with black crosses. When the three 1D probability distributions are used, the performance is considerably lower for the equivalent DOF of both simple models. However, the three 1D distributions perform slightly better than the spatial average when eight vector components are included. For the decomposed 2D probability planes, the performance is better than both the simple models even for an equivalent number of DOF. The performance peaks at 12 principal components at

a performance of 75% after which there is no significant improvement.

In the case of the decomposed 3D probability fields, the prediction performance is also significantly better than for the simple models even for an equivalent DOF number. The peak performance at 71% with the use of 11 components is slightly lower than for the 2D case (Figure 10). This could be explained by the fact that absolute reflectance values are less stable than the ratios between the spectral bands. The reason for that is primarily that the backscattering in each pixel depends largely on the surface orientation, according to Fresnel's equations. This gives rise to linearly scaling of all three spectral bands because the refractive index can be assumed to be flat throughout the spectral range covered by the camera. Such scaling is canceled out in the 2D case (Eq. 7).

Because spatial information has been discarded so far, we investigated prediction improvement by including the spatial power spectrum from each spectral band. The spatial power spectra were calculated for each sample by a 2D fast Fourier transform (FFT). By following the FFT, the frequency contributions from the sharp edges of the polygonal ROIs were subtracted. The absolute FFT values were radially integrated, and mean values were binned on a logarithmic scale from spatial periods ranging from 10 mm to 100  $\mu\text{m}$ . We choose 10 bins on each spectral band in order to produce continuous spatial power spectra. The range is limited by the sizes of the ROIs and the image resolution. The spatial power spectra were normalized by the sum of the integrated spectra in order for the spatial power spectra to be comparable in magnitude to the various probability function (Eq. 10). The three power spectra were then concatenated and fed into the SVD compression either alone or concatenated with the various probability distributions. The steps following Eq. 12 were identical to previous ones. Predicting by a truncated representation of the spatial power spectra alone gives poorer performance than any other tested methods (Figure 10). Merging the spatial power spectra with the various probability distributions generally gives a minor (2%) improvement of prediction.

Because the peak performance for both 2D and 3D distribution includes as many as 12 components, we cannot exclude the possibility of even higher performance if the sample size was to be increased, especially because we only had 12 samples of type OY. When the performance of the classification of each type is analyzed individually, it can be seen that the group OY gives the lowest percentage of correctly classified individuals (Figure 11).

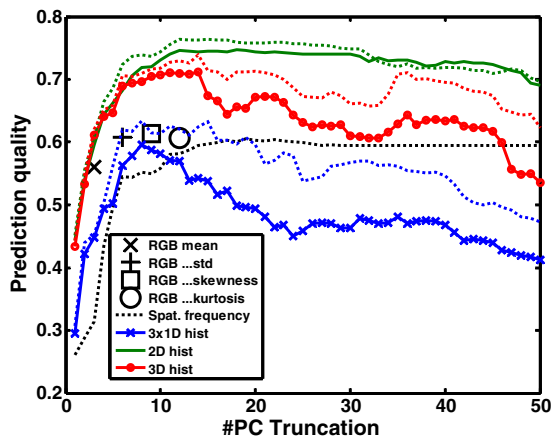


**Figure 10.** The prediction performance of various models as a function of truncation (degree of freedom minus one). The dotted lines represent the improvement by adding the spatial power spectra.

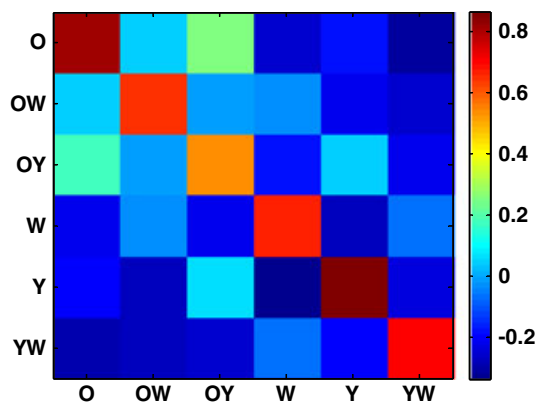


**Figure 11.** Performance and cross-correlations for the individual classing of the types also referred to as the confusion matrix. The worst performing group OY is also the one with least samples ( $N = 12$ ).

## 5. DISCUSSION

Here, we have shown that the use of multidimensional probability distributions can potentially increase prediction performance in comparison to spatially averaged values in certain scenarios. The use of SVD for approximation of the probability distributions of various dimensionalities can be expected not to be the optimal approach for factorization because the distribution modes would displace continuously in the color spaces with varying concentration of chromophores. Yet, the SVD provides a robust rough approximation that proves better than parameters such as the mean, the standard deviation, the skewness, and the kurtosis. The limited discrimination in the 3D scatter plots in Figure 9 can be understood considering that better performance is achieved with more than three components, which is also one of the main arguments in this study. Unfortunately, it is difficult to adequately visualize scatter plots of higher dimensionality.

Apart from the results presented in this paper, identical analysis was performed for a different binning choice where the bins increased exponentially with the dimensionality (constant discrimination on each spectral band). The results in Figure 10 were essentially the same, and the method is largely insensitive to the binning choice within these limits. Considering the classification problem, we also tested whether a second-order polynomial term in the regressors (Eq. 17) would improve the prediction performance, but this was not the case.

The method presented provides a complementary approach and inspiration to traditional image summation based on spatial frequencies, wavelet analysis, and spatial correlations in gray-scale images [34–38]. The multidimensional histogram introduced in this paper does not by itself consider the areal extension size of patches nor does it consider the inter-distance between patches. Variance is considered as long as it is resolved by the imaging system, whereas spatial variance averaged out within a single pixel would disappear. Therefore, the approach is intended for images with equal pixel size on the sample. The described methodology could be extended to include distance and size features. One approach to parameterize spatial features is to include the spatial power spectra for each band as briefly described in this paper. For ordered patterns, even the directional component can be considered apart from the radial integral used in this paper. Apart from the individual power spectra from each spectral band briefly considered in this paper, the cross-correlation between bands as a function of respective displacement could also be considered. As always, when the dimensionality and the number of total bins are increased, the probability estimates created by the finite number of pixels falling into each bins become increasingly uncertain. Visualization of probability distribution tensors of more than three dimensions is exceedingly difficult. Alternatively, methods treating the absolute position of all patches on the lizard throats fall under the category of image morphology. This approach would require more accurate information on the head orientation and sample geometry for each sample; also, it would require a large number of tediously manually selected landmarks on each sample. Such landmarks might be missing for some samples or difficult to select in practice. We cannot exclude the possibility that including some of the aforementioned features would further increase the specificity. However, according to our interpretation of the images and spatial power spectra, the individual throat scales are uniformly colored; they are randomly positioned (this is not the case for the sides and backs of the lizards where repeated

sequences of pigmented scales form stripes in some cases). Therefore, the only additional information captured by the employed spatial power spectra from the throats is the scale size. Scale size presumably scales with the body size, but there is no correlation between body size and color morph in this species. Considering the aforementioned statements, it can also be understood that the scale size is identical in each spectral band and that correlations between different spectral bands is already accurately parameterized by the multidimensional histograms presented in this paper because the scales are resolved by the imaging system.

The spectrometer measurements (Figure 2) are only briefly discussed in this paper. However, linear decomposition (SVD) of the log of reflectance, provided from the highly resolving spectrometer, confirmed that coloration is determined by at least five independent spectral components. For this reason, there is no reason to try to further reduce the number of spectral components provided by the RGB imager. On the contrary, improvement in prediction performance might be achieved by the use of a more advanced imager, for example, [39]. The throat coloration is mainly thought to be meant for intraspecies visual communication, and the plurality of spectral components encountered on the throat can partly be understood from the presumably tetrachromatic vision of the Skyros wall lizard [40].

The method presented in this paper is easily adoptable to image data with additional spectral bands and color spaces of higher dimensionality. Here, one would face problems with visualization, but the prediction could still be performed in an identical way. Although the bands in this case are all in the visible regime, the method would be applicable for specially chosen bands for a particular scenario. The method could prove important in image summation in, for example, summarizing microscopic tissue structures in histopathology [4], checking homogenization in quality inspection in food science [41,42], macroscopic skin structures in dermatology [43], or summarizing of combustion cells for prediction combustion engine efficiency [44].

The use of multidimensional probability distributions supports the existence of discrete throat color morphs in the Skyros wall lizard because the prediction performance is high, especially for morphs for which there are large sample sizes in the training set. The poor prediction performance for the OY morph stresses the importance of using adequate sample sizes when applying this method though. The identification of this polymorphism opens up for a new research agenda for the particular case of the morphs of the Skyros wall lizard, which is interesting because throat color morphs have proven useful for evolutionary studies in a wide range of lizard species [21,44–46]. More importantly, this provides a quantitative method for the classification of such throat color morphs from RGB images, which will prove useful in many biological systems. The method is not scale specific and could also be successfully applied to, for example, RGB pictures of habitats or even satellite pictures to identify, for example, certain types of vegetation.

## Acknowledgements

We thank Kostas Sagonas, Panagiotis Pafilis, and Efstratios Valakos and our helpful captains on Skyros for help during field work and Sune Svanberg for constructive comments on the manuscript. This study was partly supported by Swedish Research Council, a

Linnaeus grant to Lund Laser Center; IDRE-PIEp, a Swedish innovation initiative; the Royal Physiographic Society; Helge Ax:son Johnsons Foundation; Lars Hiertas Memory; and Långmanska Kulturfonden. All experimental procedures were in full compliance with Greek academic institution rules, as well as Greek national legislation on the scientific use and protection of wildlife.

## REFERENCES

1. Nobel Prize in Physics Year 2009, <http://nobelprize.org>, accessed 2012.
2. Holst GC, Lomheim TS. CMOS/CCD Sensors and Camera Systems, 2nd ed., SPIE Soc. Phot. Opt. Eng. 2011.
3. Sanders J, Kandrot E. CUDA by Example: An Introduction to General-Purpose GPU Programming, Addison-Wesley Professional, 2010.
4. Brydegaard M, Merdasa A, Jayaweera H, Ålebring J, Svanberg S. A multimode imaging spectrometer for angularly resolved optical diagnostics on the micro-scale Accepted in *Rev. Sci. Instr.* July 2011.
5. Svanberg S. *Atomic and Molecular Spectroscopy: Basic Aspects and Practical Applications* 4th ed. Springer: Berlin, 2004.
6. Gilmore G. *Practical Gamma-ray Spectroscopy* 2nd ed. Wiley: England, 2008.
7. Mycek MA, Pogue BW, Eds. *Handbook of Biomedical Fluorescence*. CRC: Boca Raton, FL, 2003.
8. Reichardt TA, Bisson SE, Crocker RW, Kulp TJ. Analysis of flow-cytometer scattering and fluorescence data to identify particle mixtures. 2008. *Proc. of SPIE* 2008; **6945**: 69450R-69450R-8.
9. Drew MS, Au J. Clustering of compressed illumination-invariant chromaticity signatures for efficient video summarization. *Image Vision Comput.* 2003; **21**: 705–716.
10. Arnold NE, Ovenden DW. *A Field Guide to the Reptiles and Amphibians of Britain and Europe* 2nd ed. Harper Collins Publishers: London, 2002.
11. Runemark A, Hansson B, Pafilis P, Valakos E, Svensson EI. Island biology and morphological divergence of the Skyros wall lizard *Podarcis gaigeae*: a combined role for local selection and genetic drift on color morph frequency divergence? *BMC Evol. Biol.* 2010; **10**(15): 269.
12. Macedonia JM, James S, Wittle LW, Clark DL. Skin pigments and coloration in the Jamaican radiation of *Anolis* lizards. *J. Herpetol.* 2000; **34**: 99–109.
13. Steffen JE, McGraw KJ. Contributions of pterin and carotenoid pigments to dewlap coloration in two anole species. *Comp. Biochem. Physiol. B Biochem. Mol. Biol.* 2007; **146**: 42–46.
14. Morrison RL, Rand MS, Frost-Mason SK. Cellular basis of color differences in three morphs of the lizard *Sceloporus undulatus erythrocheilus*. *Copeia* 1995; **1995**: 397–408.
15. Runemark A, Hansson B, Ljungqvist M, Brydegaard M, Svensson EI. Has the inbreeding load for a condition-dependent sexual signalling trait been purged in insular lizard populations? Submitted (To *Mol. Ecol.*).
16. Vercken E, Sinervo B, Clobert J. Colour variation in female common lizards: why we should speak of morphs, a reply to Cote et al. *J. Evol. Biol.* 2008; **21**: 1160–1164.
17. Cote J, Le Galliard J, Rossi J, Fitze P. Environmentally induced changes in carotenoid-based coloration of female lizards: a comment on Vercken et al. *J. Evol. Biol.* 2008; **21**: 1165–1172.
18. Gray SM, McKinnon JS. Linking color polymorphism maintenance and speciation. *Trends Ecol. Evol.* 2007; **22**: 71–79.
19. Roulin A. The evolution, maintenance and adaptive function of genetic colour polymorphism in birds. *Biol. Rev. (Cambridge)* 2004; **79**: 815–848.
20. Sinervo B, Miles DB, Frankino WA, Klukowski M, DeNardo DF. Testosterone, endurance, and Darwinian fitness: natural and sexual selection on the physiological bases of alternative male behaviors in side-blotched lizards. *Horm. Behav.* 2000; **38**: 222–233.
21. Sinervo B, Lively CM. The rock–paper–scissors game and the evolution of alternative male strategies. *Nature* 1996; **380**: 240–243.
22. Abbott J, Svensson EI. Phenotypic and genetic variation in emergence and development time of a trimorphic damselfly. *J. Evol. Biol.* 2005; **18**: 1464–1470.
23. Runemark A, Svensson EI. Female choice as a promoter of population divergence in male phenotypic characters? Evidence from a mainland-islet system. *Biol. J. Linn. Soc.* (in press) **169**(2).
24. Pafilis P, Meiri S, Fofopoulos J, Valakos E. Intraspecific competition and high food availability are associated with insular gigantism in a lizard. *Naturwissenschaften* 2009; **96**: 1107–1113.
25. Runemark A, Hey J, Hansson B, Svensson IE. Vicariance divergence and gene flow among islet populations of an endemic lizard. *Mol. Ecol.* 2012; **21**: 117–129.
26. Runemark A, Gabirot M, Svensson IE. Population divergence in chemical signals and the potential for premating isolation between islet- and mainland populations of the Skyros wall lizard, (*Podarcis gaigeae*). *J. Evol. Biol.* 2011; **24**: 795–809.
27. Edner H, Ragnarson P, Svanberg S, Wallinder E, Ferrara R, Maserti BE, Bargalgi R. Atmospheric mercury mapping in a cinnabar mining area. *Sci. Total Environ.* 1993; **133**: 1–15.
28. Warrant EM, ed. *Invertebrate Vision*. Cambridge U. Press: England, 2006.
29. Skodras A, Christopoulos C, Ebrahimi T. The JPEG 2000 still image compression standard. *IEEE Signal Process Mag.* 2001; **1053–5888**: 36–58.
30. Thyagarajan KS. *Still Image and Video Compression with MATLAB*. Wiley-IEEE Press: England, 2011.
31. Weibring P, Johansson T, Edner H, Svanberg S, Sundnér B, Raimondi V, Cecchi G, Pantani LB. Fluorescence lidar imaging of historical monuments. *Appl. Opt.* 2001; **40**: 6111–6120.
32. Weibring P, Johansson T, Edner H, Svanberg S, Sundnér B, Raimondi V, Cecchi G, Pantani LB. Fluorescence lidar imaging of historical monuments: erratum. *Appl. Opt.* 2002; **41**: 434–436.
33. Hillman EMC, Moore A. All-optical anatomical co-registration for molecular imaging of small animals. *Nat. Photonics* 2007; **1**: 526–529.
34. Kurz L, Hafed Bentefifa M. *Analysis of Variance in Statistical Image Processing*. Cambridge U. Press: England, 2006.
35. Geladi P, Grahn H. *Multivariate Image Analysis*. Ed. John Wiley & Sons Ltd: Chichester, England, 1996.
36. Prats-Montalbán JM, de Juan A, Ferrer A. Multivariate image analysis: a review with applications. *Chemometr. Intell. Lab.* 2011; **107**: 1–23.
37. Van de Wouwer G. Wavelets for Multiscale Texture Analysis, PhD Thesis, Department of Physics, University of Antwerp, Belgium, 1998.
38. Liu JJ, MacGregor JF. On the extraction of spectral and spatial information from images. *Chemometr. Intell. Lab.* 2007; **85**: 119–130.
39. Videometer A/S, <http://videometer.com>, accessed 2011.
40. Loew ER, Fleishman LJ, Foster RG, Provencio I. Visual pigments and oil droplets in diurnal lizards: a comparative study of Caribbean anoles. *J. Exp. Biol.* 2002; **205**: 927–938.
41. Yu H, MacGregor JF. Multivariate image analysis and regression for prediction of coating and distribution in the production of snack foods. *Chemometr. Intell. Lab.* 2003; **72**: 57–1.
42. Mei L, Lundin P, Brydegaard M, Gong S, Tang D, Somesfalean G, He S, Svanberg S. Tea classification and quality assessment using laser induced fluorescence and chemometric evaluation. *Appl. Opt.* 2012; **51**: 803–811.
43. Prats-Montalbán JM, Ferrer A, Bro R, Hancewicz T. Prediction of skin quality properties by different multivariate image analysis methodologies. *Intell. Lab.* 2009; **96**: 6–13.
44. Kohse-Höinghaus K, Barlowb RS, Aldén M, Wolfrum J. Combustion at the focus: laser diagnostics and control. *Proc. Combust. Institute* 2005; **30**: 89–123.
45. Olsson M, Healey M, Wapstra E, Schwartz T, Lebas N, Uller T. Mating system variation and morph fluctuations in a polymorphic lizard. *Mol. Ecol.* 2007; **16**: 5307–5315.
46. Huyghe K, Small M, Vanhooydonck B, Herrel A, Tadic Z, Van Damme R, Backeljau T. Genetic divergence among sympatric colour morphs of the Dalmatian wall lizard (*Podarcis melisellensis*). *Genetica (Dordrecht)* 2010; **138**: 387–393.

## PAPER VI

### **Tea classification and quality assessment using laser induced fluorescence and chemometric evaluation**

L. Mei, P. Lundin, M. Brydegaard, S. Gong, D. Tang,  
G. Somesfalean, S. He and S. Svanberg

*Applied Optics* **51**, 803-811, (2012).

# Tea classification and quality assessment using laser-induced fluorescence and chemometric evaluation

Liang Mei,<sup>1,2,3,\*</sup> Patrik Lundin,<sup>3</sup> Mikkel Brydegaard,<sup>3</sup> Shuying Gong,<sup>4</sup> Desong Tang,<sup>4</sup> Gabriel Somesfalean,<sup>1,2,3</sup> Sailing He,<sup>1,2</sup> and Sune Svanberg<sup>2,3</sup>

<sup>1</sup>Centre for Optical and Electromagnetic Research, Zhejiang University, Hangzhou 310058, China

<sup>2</sup>Joint Research Center of Photonics, Zhejiang University-Royal Institute of Technology-Lund University, Hangzhou 310058, China

<sup>3</sup>Division of Atomic Physics, Department of Physics, Lund University, SE-221 00 Lund, Sweden

<sup>4</sup>Tea Science Research Institute, College of Agriculture & Biotechnology, Zhejiang University, Hangzhou 310058, China

\*Corresponding author: meiliang@coer.zju.edu.cn

Received 15 June 2011; revised 2 December 2011; accepted 7 December 2011; posted 7 December 2011 (Doc. ID 149035); published 17 February 2012

Laser-induced fluorescence was used to evaluate the classification and quality of Chinese oolong teas and jasmine teas. The fluorescence of four different types of Chinese oolong teas—Guangdong oolong, North Fujian oolong, South Fujian oolong, and Taiwan oolong was recorded and singular value decomposition was used to describe the autofluorescence of the tea samples. Linear discriminant analysis was used to train a predictive chemometric model and a leave-one-out methodology was used to classify the types and evaluate the quality of the tea samples. The predicted classification of the oolong teas and the grade of the jasmine teas were estimated using this method. The agreement between the grades evaluated by the tea experts and by the chemometric model shows the potential of this technique to be used for practical assessment of tea grades. © 2012 Optical Society of America

OCIS codes: 300.2530, 120.0120.

## 1 Introduction

Tea is a popular beverage used throughout the world, especially in China where people started drinking tea thousands of years ago [1]. There are numerous scientific reports about the beneficial effects of tea on human health [2–4]. The quality of tea is dependent on many factors, such as the growing environment [5] and the processing technique [6,7]. Repeated or constant quality controls for the manufacturing in the tea plant facility are also of highest importance to ob-

tain a high standard tea. It is rather difficult for a nonspecialist to judge the quality of the tea on the market and there are also plenty of counterfeit teas which are of poor quality but still sold at high prices. Since a number of factors can influence the quality of tea, its assessment is a systematic and complicated process in which the integrated effect of color, aroma, taste as well as shape of the tea leaves should be considered. At present, the assessment of the tea quality is commonly made by sensory evaluation from tea experts, but this is unfortunately susceptible to influence of the environment and subjectivity. To make the evaluation more efficient and objective, several tea experts are usually summoned to assess the

tea quality [8]. Thus both for the customers and the tea industry, developing technologies to objectively assess tea quality and discriminate between different tea types is highly desired. Computer vision technology and electronic tongue techniques are gradually applied in the assessment of tea quality [9,10]. The computer vision technology is based on analyzing the shape and color of tea leaves, while the detailed chemical composition in tea is not considered. The electronic tongue is made up of a series of chemical sensors which analyze the raw tea material or brewed teas. In recent years, the near infrared spectroscopy technique (NIRS) has started to be applied to evaluate the quality of the dried tea [11–13]. The characteristics of the absorption spectrum in the near infrared spectral region could be used to assess the general quality or types of many kinds of tea, however the analysis model built for a certain type of tea may not be suitable for another type [14].

The laser-induced fluorescence (LIF) technology has been developed for almost half a century and is now widely used in, e.g., food chemistry [15], medical diagnosis [16–18], microscopy [19], and remote sensing [20–22], especially in plant investigation. By illuminating the leaves of the plant, the LIF techniques were also used to classify the plant types and species [23], study the plant constituents [24], and investigate nutrient deficiencies in corn [25]. Multi-spectral fluorescence imaging systems were also developed to investigate plant leaves [26] and food stuff [27]. To our knowledge, this paper describes the first application of LIF in the assessment of commercial tea grades and tea breed in the lab by shining a laser beam on tea leaves. For evaluation, singular value decomposition is used to describe the autofluorescence spectra of the tea samples and multivariate regression is used to predict the tea classification and quality with leave-one-out methodology.

The fluorescence signatures of teas have features characteristic for vegetation in general. Thus, a dominant aspect is the dual-peaked distribution, due to chlorophyll, in the near-IR region, with peaks around 690 nm and 735 nm [20]. Chlorophyll is the key pigment in photosynthesis and the fluorescence signals reflect chlorophyll contents as well as physiological stress factors [28,29]. The fluorescence distribution in the blue-green spectral region is due to a large number of components, such as tea polyphenols, flavonoid [30], and wax protecting for dehydration and UV exposure of the living plants. It should be noted that any oils or additives in tea treatment would also contribute to the fluorescence in the blue-green region. However, the tea types studied in this work are all natural without additives.

## 2 Materials and Methods

### A. Tea

Oolong and jasmine teas were investigated in the present work. The oolong tea samples are from different regions of China, and are provided by different

companies. The classification is assessed by tea experts through the color, shape, smell, taste, and the unique processing technique of the tea samples. The quality of the jasmine teas depends on the freshness and tenderness of the tea leaves and it is also affected by the white petals which are added into the tea during manufacturing. The jasmine tea samples used were provided by a specialized company. The tea qualities were determined by 2–3 company experts according to the Chinese National Standard for jasmine tea (GB/T 22292-2008).

### B. Experimental Setup

The LIF experimental setup is depicted in Fig. 1. The third harmonic (355 nm) of a Nd:YAG laser with an energy of 3 mJ/pulse at 20 Hz and an approximate pulse duration of 10 ns was used to induce fluorescence in the tea samples. The samples were placed on an anodized aluminum plate with negligible fluorescence. The emission from the tea samples was filtered by a long pass filter (Edmund Optics, L38, 380 nm, 2.6 mm thickness) before it was recorded with an optical multichannel analyzer (OMA) composed by a crossed Czerny–Turner grating spectrometer (ORIEL instruments, Model 77400) connected to an image-intensified and 10 ns time-gateable charged coupled device (ANDOR Technology, Model DH501-25U-01). The fluorescence measurements for each sample were performed five times in a so-called pseudoreplication procedure, where different sections of the sample were illuminated in each recording. The tea samples were kept in movement while being irradiated by 100 laser pulses per measurement. A halogen filament lamp (Oriel, Model No. 63355, wavelength range, 250–2500 nm) was used to calibrate the response curve of the OMA system. The wavelength scale of the OMA system was calibrated by a cadmium lamp and a HeNe laser at 632.8 nm. The spectral resolution is 6.5 nm. The spectrometer does not have any second-order rejection filters, but the influence of the second-order contribution in the 700–800 nm region is minor.

Standard red-green-blue (RGB) photographs of the tea samples were acquired by a Panasonic digital camera (DMC-FX01) in a flash mode inside an optically isolated box. Crossed polarizers were put in front of the flash lamp and the objective in order to obtain a depolarized reflective image. This ensures

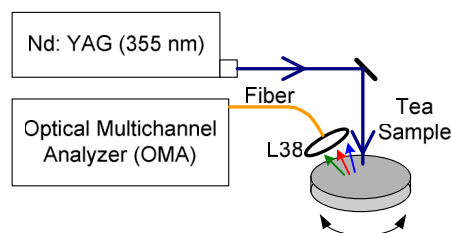


Fig. 1. (Color online) Laser-induced fluorescence setup, L38 (long pass filter at 380 nm). The tea samples were placed on a black metal sheet which was kept moving during each experiment.



Fig. 2. (Color online) Pictures of Guangdong (GD) teas: (a–e) correspond to Wudong Baiye Dancong (WBD), Dawuye (Autumn) (DA), Huangzhixiang Dancong (Spring) (HDS), Zhilanxiang Dancong (ZD), and Gongxiang Dancong (GD), respectively.

that specular reflexes are rejected and that image contrast is enhanced. The images are flat-field and white-calibrated by spatial interpolation, using a white paper included in parts of the photographs.

### C. Singular Value Decomposition

Singular value decomposition (SVD) is an orthogonal linear transformation applied on the recorded data, which is widely used in chemometry. The original data matrix is transformed into a new coordinate system, where the original data can be represented by a few principal components. The procedure facilitates the extraction of the important information and leads to substantial reduction of redundant data features.

Considering the fluorescence spectra of  $N$  samples being recorded by a spectrometer which has  $P$  spectral bands for one measurement, the whole data set can form a  $N$  row,  $P$  column matrix, which is denoted by  $\mathbf{S}$ . Its SVD gives

$$\mathbf{S} = \mathbf{U}_{1\dots N,1\dots N} \mathbf{\Sigma}_{1\dots N,1\dots P} \mathbf{V}_{1\dots P,1\dots P}^T, \quad (1)$$

where  $\mathbf{U}$  is the normalized eigenvector of matrix  $\mathbf{S}\mathbf{S}^T$  which indicates the contribution of each principal component to the sample,  $\mathbf{\Sigma}$  is the square root of the diagonal matrix of the eigenvalues of the matrices  $\mathbf{S}\mathbf{S}^T$  and  $\mathbf{S}^T\mathbf{S}$  which indicates the importance of the corresponding principal components,  $\mathbf{V}$  is the normalized eigenvector of the matrix  $\mathbf{S}^T\mathbf{S}$  which gives the principal components of the decomposition.

If the number of samples ( $N$ ) is much smaller than the number of data sampling points ( $P$ ), most of the principal components contribute insignificantly to the reconstitution of the original data. To compress the information, we therefore select only the most important principal components to represent the original data. The important components can be selected by a scree or elbow test [31]. The eigenvalues of the principal components ( $\mathbf{\Sigma}$ ) are plotted according to their size and the point where the slope of the size of the eigenvalues goes from “steep” to “flat” is found (this is often called the elbow). A truncation before the elbow is determined and is denoted by  $\text{tr}$ . The matrix  $\mathbf{S}$  can be approximately described as follows:

$$\mathbf{S} \approx \mathbf{U}_{1\dots N,1\dots \text{tr}} \mathbf{\Sigma}_{1\dots \text{tr},1\dots \text{tr}} \mathbf{V}_{1\dots P,1\dots \text{tr}}^T. \quad (2)$$

Here  $\mathbf{U}_{1\dots N,1\dots \text{tr}}$  and  $\mathbf{\Sigma}_{1\dots \text{tr},1\dots \text{tr}}$  are the first  $\text{tr}$  principal components of matrices  $\mathbf{U}$  and  $\mathbf{\Sigma}$ , respectively.

$\mathbf{V}_{1\dots P,1\dots \text{tr}}^T$  is the transpose of the first  $\text{tr}$  principal components of matrix  $\mathbf{V}$ .

### D. Linear Discriminant Analysis

In order to predict the classification or quality of the tea sample, we can establish a leave-one-out predictive model which describes how the principal components contribute to the classification or quality. In this predictive model, each sample is left out one by one and the rest are used to build the model. If the sample left out is denoted by  $i$  and the number of variables to be predicted is denoted by  $M$ , the prediction model can be described as follows:

$$\mathbf{Y}_{k=1,2\dots N,k\neq i;1\dots M} = \boldsymbol{\phi}_{k=1,2\dots N,k\neq i;0\dots \text{tr}} \boldsymbol{\theta}_{0\dots \text{tr};1\dots M}, \quad (3)$$

$$\boldsymbol{\phi}_{k,j} = \begin{cases} 1 & j = 0; \\ \mathbf{U}_{k,j} & j = 1, 2, \dots, \text{tr}; \end{cases} \quad k = 1, 2, \dots, N, k \neq i. \quad (4)$$

Here  $\mathbf{Y}_{k=1,2\dots N,k\neq i;1\dots M}$  is the predefined matrix of the classifications or qualities which are given by the tea experts,  $\mathbf{U}_{k,j}$  is the contribution of the  $j$ th principal component to the sample  $k$ ,  $\boldsymbol{\theta}_{0\dots \text{tr};1\dots M}$  is the linear coefficient matrix which needs to be solved by regression of Eq. (3). The matrix  $\boldsymbol{\phi}$  is referred to as the regressor and the bias in its first column ensures that zero quality or a negative classification does not necessarily imply that the sample cannot fluoresce. In classification, this kind of linear equation is referred to as linear discriminant analysis (LDA). The classification or quality of the tea sample which has been left out can be predicted as

$$\hat{\mathbf{Y}}_{1\dots M} = \boldsymbol{\phi}_{i;0\dots \text{tr}} \boldsymbol{\theta}_{0\dots \text{tr};1\dots M}. \quad (5)$$

By performing the predictive model for each sample, we can obtain the predicted classifications and

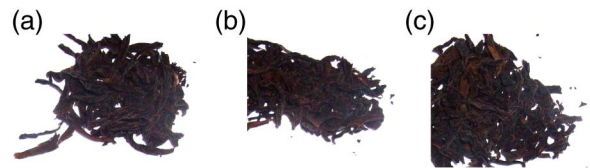


Fig. 3. (Color online) Pictures of north Fujian (N-FJ) oolong teas: (a–c) correspond to Shuixian (SX), Dahongpao (DHP), and Wuyi Rougui (superfine) (WRs), respectively.

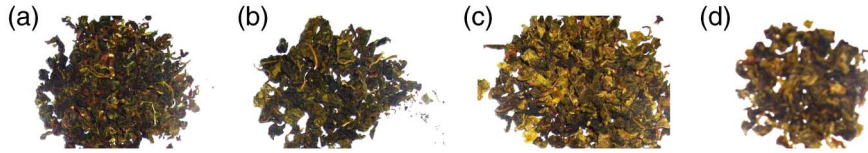


Fig. 4. (Color online) Pictures of south Fujian (S-FJ) teas: (a–d) correspond to Baiya Qilan (BQ), Yongchun Foshou (YF), Huangdan (HD), and Tieguanyin (TGY), respectively.

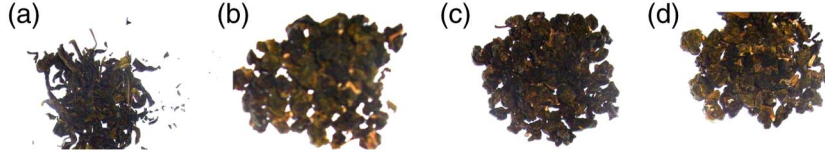


Fig. 5. (Color online) Pictures of the Taiwan (TW) teas: (a–d) correspond to Wenshan Baozhong (WB), Dayuling (DYL), Dongding Oolong (DDO), and Alishan Tea (ALS), respectively.

qualities while exploiting the sample size in the best possible way.

### 3. Results

#### A. Classification for Different Types of Oolong Tea

Sixteen oolong tea samples originating from different locations in China—Guangdong (GD, Fig. 2), North Fujian (N-FJ, Fig. 3), South Fujian (S-FJ, Fig. 4), and Taiwan (TW, Fig. 5), were used for the measurements. The names, types, and corresponding abbreviations of the 16 oolong tea samples are given in Table 1.

The GD and N-FJ teas have similar shapes and the color of the tea leaves is basically black. The S-FJ and TW teas are granulated, the leaf color of the TW teas is close to black while the leaf color of the S-FJ teas is a bit green. Through visual inspection by nonspecialists it is very difficult to distinguish between these similar tea leaves, while the fluorescence of the four types of teas is very different, something that can be used to classify the tea samples. The average fluorescence spectra of the five recordings for each tea sample are shown in Fig. 6. The spectra are normalized by the fluorescence intensity of the chlorophyll around 690 nm. The peak around 355 nm is the elastic scattering of the excited wavelength.

Since each sample was measured five times, 80 pseudoreplicated tea sample recordings were obtained. All the pseudoreplicated tea sample recordings were numbered from 1 to 80. The types of the tea samples are denoted as  $m = 1, 2, 3, 4$ , which represents GD, N-FJ, S-FJ, and TW, respectively. The predefined matrix for the classifications can be given as

$$Y_{n,m} = \begin{cases} 1 & n \in \text{type } m \\ 0 & n \notin \text{type } m \end{cases} \quad n = 1, 2, \dots, N. \quad (6)$$

In order to describe the quality of the classification, we define a discrimination index  $Q$  for each type according to Eq. (7).

$$Q_m = \frac{|\mu_{\hat{Y}_{n \in m}} - \mu_{\hat{Y}_{n \notin m}}|}{\sqrt{\sigma_{\hat{Y}_{n \in m}}^2 - \sigma_{\hat{Y}_{n \notin m}}^2}}. \quad (7)$$

Here  $\mu_{\hat{Y}_{n \in m}}$  and  $\mu_{\hat{Y}_{n \notin m}}$  are the mean output of the predictive classification algorithm for type  $m$ ,  $\sigma_{\hat{Y}_{n \in m}}^2$  and  $\sigma_{\hat{Y}_{n \notin m}}^2$  are the standard deviations corresponding to  $\mu_{\hat{Y}_{n \in m}}$  and  $\mu_{\hat{Y}_{n \notin m}}$ , respectively,  $Q_m$  is the discrimination index for type  $m$ .

The eigenvalues are presented in Fig. 7. According to the principle of an elbow test [31], the truncation value is determined as 9 ( $tr = 9$ ). As seen in this figure, the eigenvalues of the first three principal components are much higher than the others which mean that these components have much higher significance. The principal components used in the predictive model are given in Fig. 8. By evaluating Eq. (5) for each sample, we can obtain the predicted classifications and the discrimination indices, as shown in Fig. 9. The discrimination indices for the four different types of tea samples are 3.02, 7.37,

Table 1. Oolong Tea Names, Types, and Corresponding Abbreviations

Name	Type	Abbreviation
Wudong Baiye Dancong	GD	WBD
Dawuye (Autumn)		DA
Huangzhixiang Dancong (Spring)		HDS
Zhilanxiang Dancong		ZD
Gongxiang Dancong		GD
Shuixian	N-FJ	SX
Dahongpao		DHP
Wuyi Rougui (superfine)		WRs
Baiya Qilan	S-FJ	BQ
Yongchun Foshou		YF
Huangdan		HD
Tieguanyin		TGY
Wenshan Baozhong	TW	WB
Dayuling		DYL
Dongding Oolong		DDO
Alishan Tea		ALS

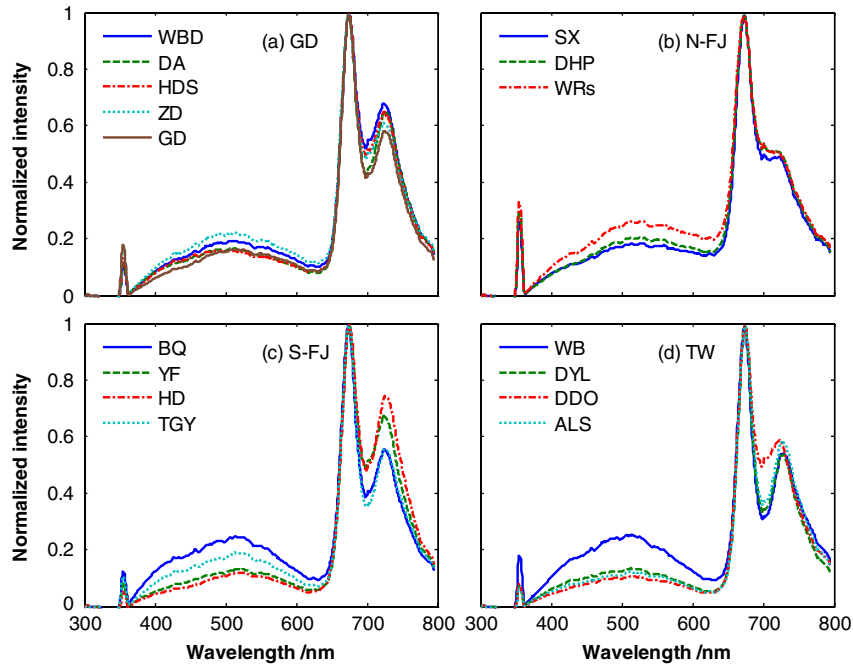


Fig. 6. (Color online) Oolong tea fluorescence: (a–d) correspond to the spectra of GD, N-FJ, S-FJ, and TW tea samples, respectively. The peak around 355 nm is the elastic scattering of the excited wavelength. The fluorescence peak in the near infrared region is due to chlorophyll.

2.45, and 2.86, respectively. It shows that both the Guangdong and the north Fujian oolong teas are very easy to classify from the other tea samples, while the tea samples from south Fujian and Taiwan would be somewhat more difficult to distinguish from the other.

#### B. Grade Assessment for Jasmine Teas

Jasmine tea is made of jasmine flowers and thus a few white petals can be observed in jasmine tea samples (Fig. 10). The grade cannot easily be assessed by only observing the color and texture of the jasmine tea, as the samples look very similar to each other. In the fluorescence experiment, ten jasmine tea samples were measured and each sample was again

measured five times by illuminating different sections of the tea samples with laser light, which gives 50 pseudo tea sample recordings. All the jasmine teas are denoted with different grades from 1 to 10 (1 being the best), which were assessed by the tea experts. The averaged experimental fluorescence spectra of the five recordings for each tea sample are shown in Fig. 11. According to the principle of the elbow test [31], the truncation can be determined as 3 ( $tr = 3$ ). The eigenvalues and the first three principal components of the fluorescence spectra are shown in Fig. 12. Only one parameter is used to describe the quality corresponding to the so-called grade. The predefined matrix can be described as

$$Y_{n_t} = n \quad n = 1, 2, \dots, 10, t = 1, 2, 3, 4, 5, \quad (8)$$

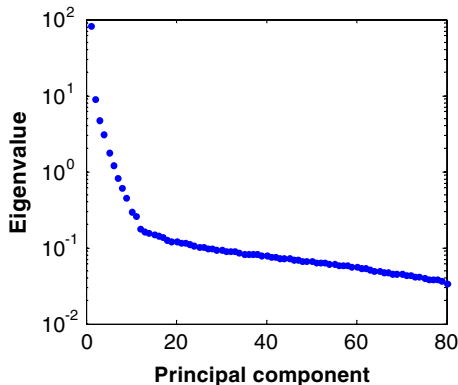


Fig. 7. (Color online) Eigenvalues of the principal components which represent the weight of each principal component. When data are projected on the first principal component, the signal to noise ratio, SNR, is as large as 1000:1.

where  $t$  is the measurement occasion. By evaluating Eq. (5), the predicted grade can be calculated. Since each sample has been measured five times, the predicted grades are also averaged five times, as shown in Fig. 13. The predicted grades do not have any upper or lower limitation and the deviation only means that the evaluated quality of the tea samples is lower or higher than the expert defined quality. As can be seen in Fig. 11, the fluorescence spectra of the three best samples (grade 1, 2, and 3) are almost overlapped in the near infrared region. This could be the main reason why these three samples are very difficult to discriminate, which also shows the limitation of the present fluorescence technique. However, it can be expected that by utilizing multiple excitation wavelengths, the quality of the three best tea

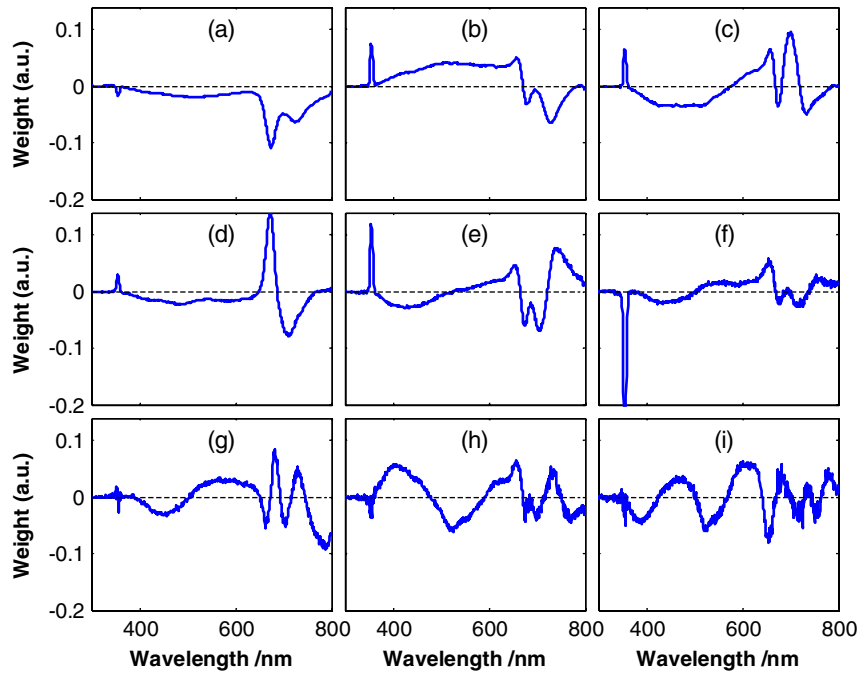


Fig. 8. (Color online) Principal components: (a–i) correspond to the first through ninth components, respectively.

samples could still be well separated. The prediction quality of the model can be described with the correlation between the predicted grade and the grade assessed by the experts. The corresponding correlation coefficient is in this case 0.986, which shows a very good prediction for tea grades. Because the experts do not evaluate the grade linearly, it is expected that the evaluated grades have some devia-

tion from the expert grades. This could be overcome by introducing a sigmoidal link function in the predictive model as known from neurology, where the nonlinear expert grade can be considered by the link function. From this point of view, the predicted grades are very reliable. The experimental results show the potential for using this technique for grade assessment of jasmine tea.

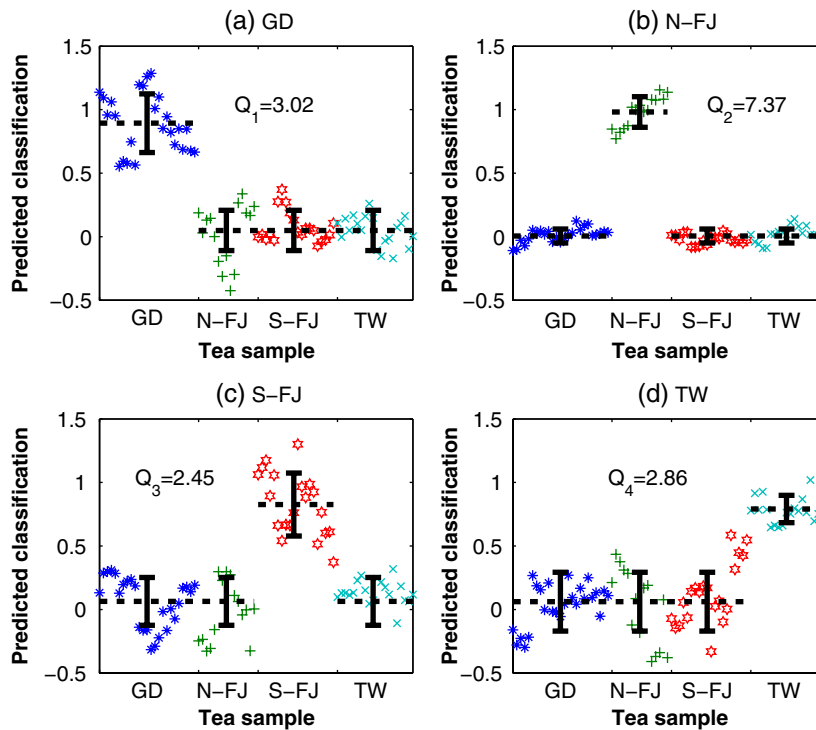


Fig. 9. (Color online) Predicted classifications for the oolong tea samples. The dotted lines are the mean predicted classification and the solid lines are the standard deviations corresponding to the mean predictive classification.  $Q_{1...4}$  is the discrimination index for each type of tea.



Fig. 10. (Color online) Jasmine tea pictures, (a–j) correspond to grade 1 to 10, respectively.

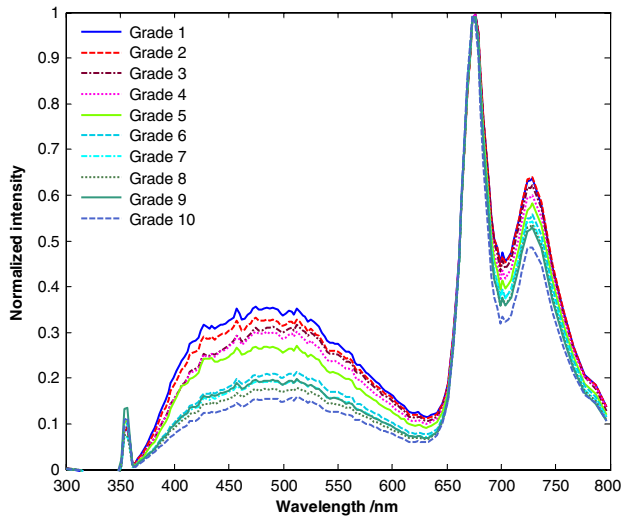


Fig. 11. (Color online) Fluorescence of jasmine teas. The fluorescence spectra have been averaged five times. The peak around 355 nm is the elastic scattering of the excited wavelength. The small peak around 710 nm is the second-order of the excitation wavelength. The weakness of this peak shows that the influence of the grating second-order spectrum in the 700–800 nm region is negligible. The fluorescence peak in the near infrared region is due to chlorophyll.

#### 4. Discussion

Our proof-of-principle measurements have demonstrated that the LIF technique in combination with the SVD and LDA evaluation methods can be used to accurately classify and evaluate tea samples. By set-

ting a proper truncation, tea classification and quality assessment can be well performed using this analytical tool. Because of an insufficient amount of tea samples, pseudoreplication was used to increase the sample size. This procedure might not be the optimal choice for prediction, but it still reflects the situation if the method should be applied commercially. More samples can further increase the accuracy and make the predicted results more reliable. The investigation of more samples will be the target for future work. By setting a proper threshold, tea samples which are difficult for experts to classify could be easily identified using this technique.

As we can see from the classification results of oolong tea samples, some of them are not easy to distinguish since we only use one wavelength to induce fluorescence which limits the information obtained from the tea leaves. The best three jasmine tea samples are also very difficult to discriminate due to their similar fluorescence spectra. However, this could be improved by using multiwavelength excitation. We note that the evaluation variability between experts is generally lower than the system error of the present technique. However, human senses are prone to be less accurate due to fatigue or subjectivity, which is not the case for a spectroscopic-based instrument. We can also analyze the spatial chromatic variance of the tea image to understand the texture of the tea leaves which could be helpful for classifying the types and judging the grade. Further, the laser source could be replaced by several inexpensive and robust light emitting diodes (e.g., Roithner

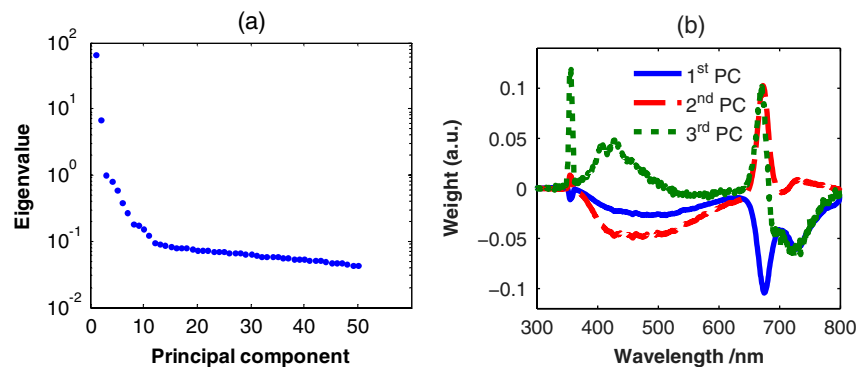


Fig. 12. (Color online) (a) Eigenvalues of the principal components, the first three eigenvalues represent most of the information; (b) the first three principal components.

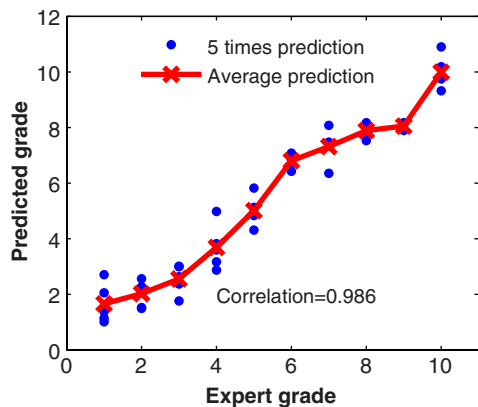


Fig. 13. (Color online) Grade assessment of jasmine tea samples (where grade 1 means the best quality). The correlation coefficient between the predicted and expert grades is 0.986.

LaserTechnik, 375 nm, 30 mW, CW) with different emitting wavelengths. Similarly, the OMA system can be simplified for the specific application by using a compact (e.g., Ocean Optics USB series) spectrometer and the computation equipment can also be made very compact. Thus, the whole system can be made realistic and powerful. In summary, the experts' results and our experimental evaluation agree well, illustrating that the LIF technique can be used to identify tea types and assess tea qualities in future real-world applications.

In the present work, we have not compared the performance of our technique with traditional techniques, e.g., NIRS. Actually, it is rather difficult to compare the general performance of these two techniques since their characteristics would be very different for various types of tea. A detailed comparison of these two techniques could be the topic of future work.

Further studies could involve safety aspects and improved tea preservation, where the influence of different packaging methods, external environmental factors (e.g., moisture, temperature, sunlight), and aging can be analyzed with the proposed technique and compared with conventional classification by human experts. The present technique gives a possibility for industrial applications through the development of a specific LIF-based instrument, to be used for initial screening of the raw material, online process control, and quality assessment.

This project was supported by a Swedish VR-SIDA Grant, by a Swedish Research Council direct grant, by a Linnaeus Research Grant to the Lund Laser Center, and by the Knut and Alice Wallenberg Foundation. Further, it was supported by a grant from the State Key Laboratory of Modern Optical Instrumentation.

## References

1. Y. Lu, *The Classic of Tea: Origins & Rituals*, Translated by F. R. Carpenter, ed. (Ecco Press, 1995).
2. G. V. Stagg and D. J. Millin, "The nutritional and therapeutic value of tea: a review," *J. Sci. Food Agric.* **26**, 1439–1459 (1975).

3. H. F. Stich, M. P. Rosin, and L. Bryson, "Inhibition of mutagenicity of a model nitrosation reaction by naturally occurring phenolics, coffee and tea," *Mutation Res.* **95**, 119–128 (1982).
4. H. N. Graham, M. E. Harbowy, and D. A. Balentine, "Tea: the plant and its manufacture; chemistry and consumption of the beverage," in *Caffeine*, G. A. Spiller, ed. (CRC Press, 1998), pp. 65–66.
5. P. O. Owuor, N. W. Francis, and K. N. Wilson, "Influence of region of production on relative clonal plain tea quality parameters in Kenya," *Food Chem.* **119**, 1168–1174 (2010).
6. P. O. Owuor and M. Obanda, "The effects of blending clonal leaf on black tea quality," *Food Chem.* **66**, 147–152 (1998).
7. P. O. Owuor and M. Obanda, "Comparative responses in plain black tea quality parameters of different tea clones to fermentation temperature and duration," *Food Chem.* **72**, 319–327 (2001).
8. Y. R. Liang, J. L. Lu, L. Y. Zhang, S. Wu, and Y. Wu, "Estimation of black tea quality by analysis of chemical composition and colour difference of tea infusions," *Food Chem.* **80**, 283–290 (2003).
9. Q. S. Cheng, S. Q. Jiang, and X. Y. Wang, "Discrimination of tea's quality level based on electronic tongue and pattern recognition," *Food Machinery* **24**, 124–126 (2008).
10. X. L. Li and Y. He, "Classification of tea grade by multi-spectral images and combined features," *Trans. Chin. Soc. Agric. Machinery* **40**, 113–118 (2009).
11. X. H. Gu, Y. Feng, and J. Tang, "Discrimination of tea varieties by mid-infrared spectroscopy combined with PLS," *J. Anal. Sci.* **24**, 131–135 (2008).
12. Z. Y. Niu, M. Y. Liu, and X. Lin, "Application of different near-infrared spectrometers in tea quality inspection," *Hubei Agric. Sci.* **48**, 2562–2565 (2009).
13. S. H. Yan, "Evaluation of the composition and sensory properties of tea using near infrared spectroscopy and principal component analysis," *J. Near Infrared Spectrosc.* **13**, 313–325 (2005).
14. J. Zhou, H. Cheng, and L. Y. Wang, "Recent advance on the application of near-infrared spectroscopy in tea," *J. Tea Sci.* **28**, 294–300 (2008).
15. J. P. Wold, R. Bro, A. Veberg, F. Lundby, A. N. Nilsen, and J. Moan, "Active photosensitizers in butter detected by fluorescence spectroscopy and multivariate curve resolution," *J. Agric. Food Chem.* **54**, 10197–10204 (2006).
16. S. Andersson-Engels, J. Johansson, U. Stenram, K. Svanberg, and S. Svanberg, "Time-resolved laser-induced fluorescence spectroscopy for enhanced demarcation of human atherosclerotic plaques," *J. Photochem. Photobiol. B* **4**, 363–369 (1990).
17. S. Montán, K. Svanberg, and S. Svanberg, "Multicolor imaging and contrast enhancement in cancer-tumor localization using laser-induced fluorescence in hematoporphyrin-derivative-bearing tissue," *Opt. Lett.* **10**, 56–58 (1985).
18. M. A. Mycek and W. P. Brian, *Handbook of Biomedical Fluorescence*, 1st ed. (CRC Press, 2003).
19. J. R. Lakowicz, "Multiphoton excitation and microscopy," in *Principles of Fluorescence Spectroscopy*, 3rd ed. (Springer, 2006), pp. 607–621.
20. S. Svanberg, "Fluorescence lidar monitoring of vegetation status," *Phys. Scr. T* **58**, 79–85 (1995).
21. V. Raimondi, G. Cecchi, L. Pantani, and R. Chiari, "Fluorescence lidar monitoring of historic buildings," *Appl. Opt.* **37**, 1089–1098 (1998).
22. S. Svanberg, "Fluorescence spectroscopy and imaging of lidar targets," in *Laser Remote Sensing*, T. Fujii and T. Fukuchi, eds. (CRC Press, 2005), pp. 433–467.
23. E. W. Chappelle, F. M. Wood, J. E. Mcmurtrey, and W. W. Newcomb, "Laser-induced fluorescence of green plants. 1. A technique for the remote detection of plant stress and species differentiation," *Appl. Opt.* **23**, 134–138 (1984).
24. M. Lang, F. Stober, and H. K. Lichtenthaler, "Fluorescence emission-spectra of plant-leaves and plant constituents," *Radiat. Environ. Biophys.* **30**, 333–347 (1991).

25. E. W. Chappelle, J. E. McMurtrey, F. M. Wood, and W. W. Newcomb, "Laser-induced fluorescence of green plants. 2. LIF caused by nutrient deficiencies in corn," *Appl. Opt.* **23**, 139–142 (1984).
26. M. S. Kim, J. E. McMurtrey, C. L. Mulchi, C. S. T. Daughtry, E. W. Chappelle, and Y. R. Chen, "Steady-state multispectral fluorescence imaging system for plant leaves," *Appl. Opt.* **40**, 157–166 (2001).
27. M. S. Kim, A. M. Lefcourt, and Y. R. Chen, "Multispectral laser-induced fluorescence imaging system for large biological samples," *Appl. Opt.* **42**, 3927–3934 (2003).
28. A. J. Hoff and J. Deisenhofer, "Photophysics of photosynthesis. Structure and spectroscopy of reaction centers of purple bacteria," *Phys. Rep.* **287**, 1–247 (1997).
29. H. K. Lichtenthaler and U. Rinderle, "The role of chlorophyll fluorescence in the detection of stress conditions in plants," *CRC Crit. Rev. Anal. Chem.* **19**, S29–S85 (1988).
30. D. A. Balentine, S. A. Wiseman, and L. C. Bouwens, "The chemistry of tea flavonoids," *Crit. Rev. Food Sci. Nutr.* **37**, 693–704 (1997).
31. I. T. Jolliffe, "Choosing a subset of principal components or variables," in *Principal Component Analysis*, 2nd ed. (Springer, 2002), pp. 115–118.

## PAPER VII

### **Photobleaching-insensitive fluorescence diagnostics in skin and brain tissue**

M. Brydegaard, N. Hosseini, K. Wårdell and S. Anderson-Engels  
*IEEE Journal Photonics* **3**, 407-421, (2010).



# Photobleaching-Insensitive Fluorescence Diagnostics in Skin and Brain Tissue

M. Brydegaard,<sup>1</sup> N. Haj-Hosseini,<sup>2</sup> K. Wårdell,<sup>2</sup> and S. Andersson-Engels<sup>1</sup>

<sup>1</sup>Department of Physics, Lund University, 221 00 Lund, Sweden

<sup>2</sup>Department of Biomedical Engineering, Linköping University, 581 85 Linköping, Sweden

DOI: 10.1109/JPHOT.2011.2141656  
1943-0655/\$26.00 ©2011 IEEE

Manuscript received March 1, 2011; revised April 3, 2011; accepted April 5, 2011. Date of publication April 11, 2011; date of current version May 6, 2011. This work was supported by a Swedish Research Council (VR) Linnaeus grant to the Lund Laser Center (LLC), the Swedish Foundation for Strategic Research (SSF), the VR Group under Grant No. 331-2006-7661, and a PIEp/IDRE Swedish innovation initiative grant. Corresponding author: M. Brydegaard (e-mail: Mikkel.Brydegaard@fysik.lth.se).

**Abstract:** In this paper, we investigate the possibility of using accurate prediction models for the prediction of protoporphyrin bleaching dynamics to achieve photobleaching-insensitive methods to improve the evaluation of data in an existing clinical fluorescence-guided resection technique. To simulate the scenario, measurements were carried out *in vivo* on skin of healthy volunteers using a compact fiber-based fluorescence spectroscopy system. We have developed an effective method for the parameterization of sequences of bleaching spectra. We analyze convergence and decay rates with respect to initial conditions and excitation irradiance. We also discuss the consequences and the potential for bleaching-insensitive measurements and their applicability in a few examples from *in vivo* open brain surgery.

**Index Terms:** Fluorescence-guided resection, FGR, 5-ALA, PpIX, protoporphyrin, photobleaching, laser-induced fluorescence spectroscopy, LIF, optical diagnostics, tissue optics, skin, brain, dynamic models, system identification, state space models.

## 1. Introduction

### 1.1. Background of Fluorescence-Guided Resection

Optical diagnostic methods are important tools in modern medicine due to their often noninvasive nature and due to their rapid evaluation possibilities [1]. In the area of open brain surgery, two such types of fluorescence-based methods are currently being developed to assist the surgeon in deciding which tissue to remove and which to spare. Both methods rely on the increased concentration of fluorescent tumor markers, e.g., protoporphyrin (PpIX) [2]–[7], in malignant tumors. Imaging systems incorporated into the surgeon's stereo microscope have been developed, in which the fluorescence intensity can be displayed in every point at the line of sight in the area of resection [8]–[10]. However, these types of methods have limited depth penetrating ability, and their use is restricted in subsurface regions or regions covered by fluids such as blood or flushing liquid. Another kind of method consists of a nonimaging, contact-point fiber probe [11]–[13] (see Fig. 1), allowing the surgeon to penetrate tumor tissue with the probe tip and proceed to underlying regions when the signal from the instrument confirms the presence of the tumor. These methods provide comparably extended depth information. The brain surgeon's task is extremely demanding, and any tool that can provide aid without causing additional concern or distraction is welcome. In terms of performance, both imaging and contact-fiber probe systems have advantages and disadvantages. Imaging systems

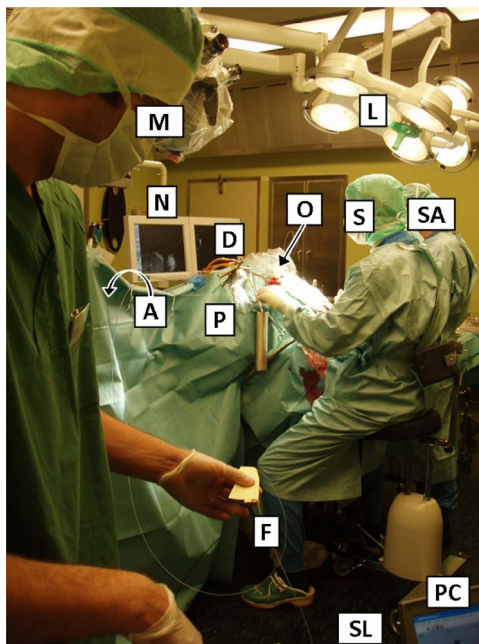


Fig. 1. Scene in the operation theater, demonstrating *in vivo* measurements during open brain surgery. (P) Patient, (S) surgeon, (SA) surgeon's assistant, (O) skull opening, (A) anesthetist and surveillance monitors, (L) surgical light system, (M) operating microscope, (N) displays showing offline MRI maps and navigation system, (D) flushing/ultrasonic tool drainage tubes, (F) fiber probe, (SL) box containing the spectrometer and laser, and (PC) controlling laptop.

are integrated into the operating microscope, while the steel rod fiber probe can be combined with the additional hand tools used by the surgeon, such as ultrasonic vacuum suction devices, scalpels, and navigation systems [14]. Both imaging and fiber-based systems must be compatible with the bright spotlights used in the operation theater (see Fig. 1). Further, the instruments have to be compatible with sterilization procedures. However, both types of systems suffer from the fact that the measurement of PpIX concentration influences the concentration itself due to photobleaching [15]–[23]. This can lead to inconsistency in the measurements. In a typical situation, in which the ratio between the PpIX and the tissue autofluorescence is used to determine whether to remove brain tissue or not, the criterion for removal might be met in one instance, while after bleaching, just a few seconds later, it might not be met in the same region. In this paper, we have investigated the possibility of improving the evaluation of a clinically used fiber-based method to achieve bleaching-insensitive methods. We used *in vivo* healthy skin measurements as a model for the process in a manner which resembles the actual clinical scenario. We then tested the applicability on a limited set of *in vivo* brain tumor data acquired during open brain surgery.

### 1.2. Dynamic Modeling

In the fluorescence measurements performed in this paper, the recorded fluorescence spectrum will depend on the fluorophore concentration in a complex way. First, we will develop a dynamic model to describe the evolution of the fluorescence spectrum when recording the fluorescence over a period of time from the same tissue location. This model describes the photobleaching process of the involved chromophores. Our ambition in this paper is to learn whether such dynamic model can be used to improve the consistency of the criterion for tissue resection under severe bleaching conditions. When light from the excitation fiber impinges on the tissue, it undergoes photomigration, and the energy is deposited in the interrogation volume in a manner governed by the absorption coefficients and scattering properties of the sample at the excitation wavelength [1]. The total absorption is the sum of all the absorbing constituent concentrations multiplied by their respective

absorption cross sections. The absorbed energy is then partly turned into heat, partly reemitted as fluorescence, and partly consumed to drive photochemically induced reactions. The last mentioned pathway can in turn lead to destruction of the particular molecules, which would alter the local absorption coefficient. This, in turn, will result in a change in the extension of the interrogation volume and the volume in which the excitation energy is deposited with time in a sequence of measurements. When a bleachable sensitizer is embedded in a presumably nonbleachable tissue matrix [24], this may lead to an increase in autofluorescence over time as the sensitizer bleaches out of the interrogation volume, hence quenching the excitation and emission of the autofluorescence to a lesser degree. This is known to have only a small effect on the tissue autofluorescence, but some studies suggest that autofluorescence increases during bleaching, e.g., [17], and another suggests a decrease [3], [24].

The fluorescent light emitted from each volume element eventually undergoes a second photon migration process and may be subject to emission quenching or re-absorption before reaching the detection fiber. The detected spectrum is thus perturbed by any absorber present within the emitted spectral range within the interrogation volume. To evaluate the spectral shape of the recorded fluorescence spectra, data can be reduced from the number of spectral bands in the spectrometer to the number of spectral components involved by using singular value decomposition (SVD, which is identical to principal component analysis (PCA), except that the mean is not subtracted in SVD) [25]–[30]. When decomposing the spectra from such a bleaching sequence with SVD, a truncation point can be determined from the spectral eigenvalues. The spectrum at any given time in the sequence can be described by a linear combination of the corresponding eigenvectors or base spectra. The loadings related to the concentrations of the involved substances (and, thus, their respective cross sections) can be expected to perturb the interrogation volume and the energy deposition; thus, the loadings can be considered as dynamical states. In the mathematical space defined by the concentration loadings, the time-evolution trajectory resulting from a bleaching sequence can be expected to be governed by a certain function of the concentration composition in the previous instance. Such trajectories can thus be described by a vector field, which can be obtained by performing system identification [31]–[36]. While we can expect at least as many dynamic states in the dynamic model as linearly independent base spectra, we cannot exclude the possibility of more hidden dynamic states. It is, however, generally accepted that the bleaching process of PpIX in tissue can be fairly well described by two dynamic states [24], [37]. Each absorber can either remain stable, be destroyed and go to a nonabsorbing state (increasing the fluorescence from deeper lying fluorophores), go to a nonfluorescing state, or turn into a new compound influencing the detected fluorescence in a new way [22], [37], [38]. All such behaviors are included in state space models used in control theory and robotics, the evolution of ecosystems, and chemical and nuclear chain decays [31]–[36]. Here, the dynamic states are expressed as a linear combination (the so-called system matrix or dynamic model) of the same dynamic states in the previous instance or instances. The diagonal elements of the system matrix correspond to individual exponential decays, whereas the coefficients off the diagonal represent the production or destruction of one dynamic state related to another dynamic state. While the tissue autofluorescence obviously does not bleach to a nonzero value within a reasonable time, it is less intuitive that the sensitizer concentration bleaches to anything else than to zero. However, several indications point toward such a behavior [39], [40]. Reasons for this behavior might be found in the bottleneck of dissolved oxygen in-flow to the interrogation volume, in diffusion into or production of PpIX inside the interrogation volume [41]. Other reasons may be found in the fact that the PpIX sensitizer can be found in different subcellular compartments with different ambient conditions, and bleaching only takes place in the simultaneous presence of dissolved oxygen and PpIX [42]. There are also indications of a fluorescent photoproduct from the destruction of PpIX [22], [37], [38], [41], [42].

While the concentration composition constantly changes along the trajectory in the state space [34], a few properties of such a trajectory remains constant and could hence be used for photobleaching-insensitive evaluation. These properties include the convergence composition point, which is reached either by solving the zero derivatives of the transfer function, or to extrapolating bleaching to infinity. The system dynamics and decay times found in the coefficients in

the system matrix of a state space model are also constant throughout the bleaching process. If any of these properties depends on the initial concentration composition, a bleaching-insensitive method could be achieved by applying dynamic models to the short bleaching sequences. Apart from the time-invariant transfer function, we can also expect time-dependent behavior in an *in vivo* scenario. Heart beats and breathing [43], [44] may give rise to slight variations in the optical return or diffusion properties, as well as any movement's of the surgeon's hand. Such difficulties could be overcome by optimizing the instrument for fast acquisition, rather than a plurality of spectral bands.

## 2. Methods and Data Set

### 2.1. Optical Touch Pointer

We have recently developed and presented a fiber-optic fluorescence spectrometer [13]. The system can be operated in either continuous or a modulated mode (for background subtraction). Excitation is achieved by a near-UV diode laser module emitting at 405 nm with a maximal power of 50 mW (Oxxius, Lannion, France). A spectrometer (EPP 2000, Stellarnet, Tampa, FL, USA) operating in the wavelength range of 240–850 nm with a resolution of 3 nm is coupled to the system to obtain the optical signal. The elastically back-scattered light from the tissue is rejected by a 3-mm long-pass, cutoff filter at 475 nm (Schott CG-GG-475-0.50-3, CVI Melles Griot, Albuquerque, NM, USA). A fiber-optic probe, in contact with the tissue at distal end, is connected to the laser source and the spectrometer. The probe consist of an excitation fiber in the center ( $\varnothing_{\text{core}} = 600 \mu\text{m}$ , NA = 0.37 in air) surrounded by nine collection fibers ( $\varnothing_{\text{core}} = 200 \mu\text{m}$ , NA = 0.22 in air). The technical description of the system and the method of use have been presented previously [13]. The modulation of the laser is synchronized by the spectrometer read out using the counter circuit in the data acquisition board (National Instruments, Inc., Austin, TX, USA).

### 2.2. Skin Measurements

The measurements were performed on four volunteers after obtaining permission from the local ethical committee (No. M139-07, and No. T83-09, *Regionala etikprövningsnämnden i Linköping*). Written informed consent was obtained from all participants. Methylaminolevulinat cream (METVIX<sup>®</sup> 160 mg/g, Photocure ASA, Norway) was applied topically in a 2–3-mm-thick layer over an area of roughly 3 cm<sup>2</sup> on the tape-stripped skin of the forearm, 4–6 hours prior to the measurements. The pharmacokinetics of PpIX is described in several studies [38], [45]–[49], and within the given time, the levels can be assumed saturated. During this interval the treated site was covered by a nontransparent plaster to avoid any light exposure. The arm was fixed, and the measurements were performed about 3 mm apart [see Fig. 2(a)] on a new site for each sequence. The probe was suspended in a gliding guide tube and the pressure on the skin can be assumed constant between sequences and test persons. The sequences were recorded in a darkened room. However, in between the measurements, the light was turned on.

The laser was adjusted to fiber tip continuous powers of 1, 2.5, 5, 7.5, and 10 mW (the average power for the modulated measurements is half that of the continuous ones). The irradiation was administered to an area of 0.28 mm<sup>2</sup>. In each measurement the recording was made until the PpIX peak at 635 nm was substantially photobleached [see Fig. 2(b)]. In some measurements, specifically those at higher laser power, the measurement was stopped earlier due to irritation of the skin. The integration time of the spectrometer was 200 ms, in continuous mode, and 100 ms, in the modulated mode, which was matched to the duration of laser-on/off time slots. In modulated mode, the sum of two consecutive spectra were stored. Thus, the sampling rate for continuous acquisition was 200 ms, and for modulated sequences, it was 400 ms since dark spectra were continuously recorded in the 1–0 ms laser off-time slots. Recordings were performed on both nontreated and ALA-treated skin on four individuals. In total, 129 sequences were recorded on ALA-treated skin were recorded, out of which 44 were in modulated mode and 85 in continuous mode. Further, 90 sequences were also recorded on nontreated skin, including 30 recorded in modulated mode and 60 in continuous mode.

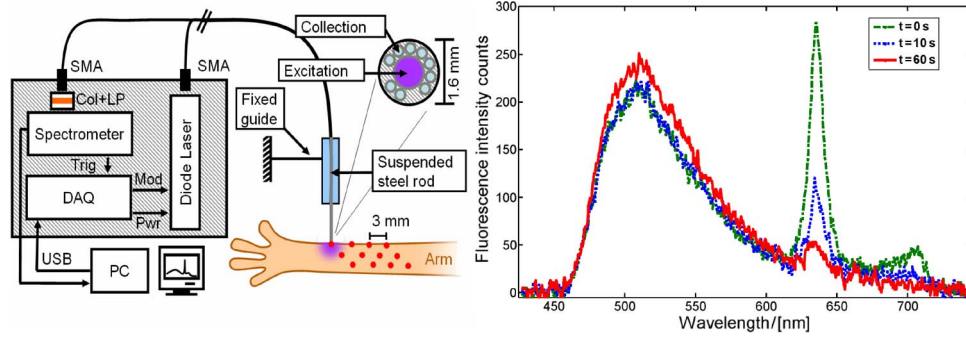


Fig. 2. (Left) Apparatus used to measure laser-induced fluorescence. (Right) Example of bleaching of ALA-treated skin excited by 7.5 mW of continuous 405-nm light. The green light distribution around 500 nm arises due to the tissue autofluorescence and increases slightly with time in this case. The red fluorescence at 635 nm arises from the photosensitizer, i.e., PpIX, and decreases with time of radiation. The signal is considerably different from those obtained in imaging systems due to photon migration [10].

### 2.3. Brain Measurements

The applicability of the method to a few examples of *in vivo* brain fluorescence measurement (Ethical Committee, No. M139-07) is also presented in this paper. ALA, 5 mg/kg diluted in orange juice, was administered orally approximately 3–4 hours before the measurements were initiated. Five sequences were recorded from the brain tumor tissue during tumor resection surgery, all from the same patient. The tumor was suspected to be a glioblastoma multiforme. Three of these recordings were performed in continuous mode in full operation theater light but with a shielding device covering the tissue in an approximately 10-mm vicinity from the probe. Three sequences were recorded in modulated mode with background subtraction. The excitation power was 5 mW and the integration time 500 ms in tumor tissue in both cases.

### 2.4. Data Processing and Analysis

Sequence data files were imported into Matlab (MathWorks Inc.) [30]. In the case of acquisition with modulated mode, the dark spectra were subtracted; in the case of the continuous mode, the dark current was estimated from the mean of the dark region blocked by the optical long-pass filter. The intensity counts were normalized to the exposure time (constant) and the varying laser powers. Time frames showing continuous bleaching sequences were handpicked after analyzing the total intensity over time. Thus, spectra obtained prior to skin contact and unsteady sequences were excluded. In total, 40 891 spectra were included, belonging to 219 bleaching sequences, including ALA-treated and non-ALA-treated regions, irradiated by different excitation powers. The spectra were organized in a single matrix  $M$ , the rows being the individual observations and columns representing the spectral bands.  $M$  was decomposed with SVD

$$M_{n=1..N,\lambda} = U_{n=1..N,s=1..N} \Sigma_{n=1..N,s=1..N} V_{\lambda,s=1..N}^* \quad (1)$$

Here,  $U$  is a matrix with rows representing individuals and columns corresponding to the content of each base spectrum.  $\Sigma$  is a diagonal matrix with eigenvalues representing the significance of each base spectrum in decreasing order.  $V$  is a matrix with rows representing spectral bands and columns corresponding to spectral components with decreasing significance. By analyzing the eigenvalues in a log scale plot the noise floor and numbers of significant components can be judged, and a truncation  $tr$  can be decided; thus, the entire data set can be expressed as

$$\hat{M}_{n=1..N,\lambda} = U_{n=1..N,s=1..tr} \Sigma_{s=1..tr,s=1..tr} V_{\lambda,s=1..tr}^* \quad (2)$$

Here,  $\hat{M}$  is the approximated matrix  $M$  using a truncated number of base spectra in  $V$ . The base spectra in the columns of  $V$  might not necessarily have a physical interpretation; we are, however, allowed to freely rotate the first  $tr$  components of  $V$  without introducing any loss of information, since a rotational matrix has a determinant of one. To give a meaningful name to spectral base components, we may choose to rotate the base vectors in  $V$  according to some preknowledge, e.g., spectral features at certain regions or features expected from treated or nontreated samples

$$B_{\lambda,s=1..tr} = R_{s=1..tr,s=1..tr} V_{\lambda,s=1..tr}. \quad (3)$$

Here,  $B$  is a matrix containing new meaningful base spectra in the columns, and  $R$  is a rotational matrix with rotational angles based on preknowledge. Quantities of the composition in terms of meaningful components can now be found by projection, that is, minimizing the least-square residual

$$Y_{n=1..N,s=1..tr} = \left( B_{\lambda,s=1..tr}^T B_{\lambda,s=1..tr} \right)^{-1} B_{\lambda,s=1..tr}^T M_{n=1..N,\lambda}. \quad (4)$$

In practice, these compositions can be rapidly calculated using the QR factorization algorithm [30]. If one spectral component can be assumed to be associated with the tissue/matrix autofluorescence, the composition can be normalized by that constituent, and dimensionless concentration-like quantities  $C$  are obtained:

$$C_{n=1..N,s=1..tr-1} = \frac{Y_{n=1..N,s=2..tr}}{Y_{n=1..N,s=auto\ matrix}}. \quad (5)$$

Such a dimensionless quantity could be the PpIX ratio typically used for resection criterion. In photokinetics, the spectral composition can be expressed in a sequence  $Y_{t,s=1..tr}$  or  $C_{t,s=1..tr}$ , which is retrieved from a (possibly changing) interrogation volume as a function of the spectral composition in the previous instance

$$Y_{t,s=1..tr} = Y_{t-1,s=1..tr} \theta_{s=1..tr,s=1..tr}. \quad (6)$$

Here,  $\theta$  is the system matrix of the dynamic model. The diagonal terms in  $\theta$  correspond to decay rates of simple single exponential decays. The terms off the diagonal in  $\theta$  represents the possibility of onecomponent turning into another detectable component. Several impositions can be set on  $\theta$  regarding strict stability theorems [31]–[35]; for example, the eigenvalues of the system matrix cannot be complex if it is assumed that there are no cycles in the photochemical reaction chain. Since all spectral components must necessarily converge to zero in the above model (seen by solving  $Y_t = Y_{t-1}, \theta \neq 1$ ), it is necessary to add a bias term to allow the model to converge to anything else than zero

$$Y_{t=1..T,s=1..tr} = \Phi_{t=0..T-1,d=1..DOF} \theta_{d=1..DOF,s=1..tr}, \quad \Phi = [1 \quad Y_{t=0..T-1,s=1..tr}]. \quad (7)$$

$DOF$  are the degrees of freedom in the dynamical model, and in this case,  $DOF = tr + 1$ . Obviously, such models can be expanded to any degree of complexity, including polynomial expansions and cross products of the columns in  $Y$ . They should, however, have a physical interpretation, and additional DOFs imply decreased stability, and poorer convergence, and an increase in the number of observations required to estimate a good model. A rough estimate of the dynamic model coefficients can be found by regression:

$$\hat{\theta}_{d=1..DOF,s=1..tr} = \left( \Phi_{t=0..T-1,d=1..DOF}^T \Phi_{t=0..T-1,d=1..DOF} \right)^{-1} \Phi_{t=0..T-1,d=1..DOF}^T Y_{t=1..T,s=1..tr}. \quad (8)$$

Again, this can be rapidly calculated by the QR factorization. This estimate can be used as an initial guess, and the dynamic model coefficients  $\hat{\theta}$  and initial conditions  $\hat{Y}_0$  can be refined by minimizing the

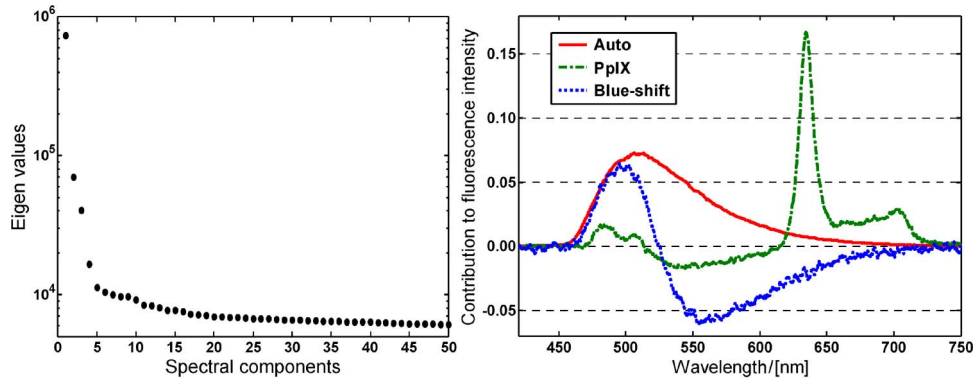


Fig. 3. (Left) Singular value decomposition reveals that all 40 891 spectra can be described as a linear function of four spectra. Note that components beyond the 50th have been omitted. (Right) Base spectra upon which the rest of the analysis is based. The base spectra from the SVD are rotated so that the first principal components match the autofluorescence constructed as the mean spectrum for non-ALA-treated skin.

squared residuals from prediction from time zero

$$\min_{\hat{Y}_0 \hat{\theta}} \left( \sum_{t=1..T} \sum_{s=1..tr} \left( Y_{t=1..T, s=1..tr} - \hat{Y}_{0, s=1..tr} \hat{\theta}_{d=1..DOF, s=1..tr}^{t=0..T} \right)^2 \right). \quad (9)$$

In our model, we refined the coefficient iteratively and numerically. The spectral composition at infinity was calculated as

$$\hat{Y}_{\infty, s=1..tr} = \hat{Y}_{0, tr=1..tr} \hat{\theta}_{d=1..DOF, s=1..tr}^{\infty}. \quad (10)$$

Several attempts were made to predict the initial PpIX ratio in  $Y_0$  from the dynamic parameters of the trajectory in  $\hat{\theta}$ . These attempts included biased hyperplane predictions using all coefficients in the dynamic model. Although the process is described by several dynamic states, the single exponential half life time was visualized briefly with respect to excitation power and initial conditions. This half life time is defined as the time from  $t = 0$  for a component to reach the mean of the initial quantity and the converged quantity.

### 3. Results and Discussion

The eigenvalues in the diagonal matrix  $\Sigma$ , which was obtained from the SVD, revealed that all 40 891 spectra could be described by just four base spectra [see Fig. 3(a)]. The fourth base spectrum was classified as spiky residuals from background lighting, which only occur in the continuous wave (CW) mode when there is no dark subtraction. The fifth to tenth components are electronic readout noise, fast sinus, and cosines in the entire spectrum, independent of light intensities, that also cover the area below the long-pass fluorescent filter. These electronic reflections or read out errors can also be observed in a logarithmic frequency domain power plot of the entire data.

The measurements were projected onto the three spectral components. For the components to be meaningful, the coordinate system was rotated as follows. The angles of the first rotation were determined in such a way that the first spectral component minimizes the residuals with respect to the mean spectrum for all non-ALA-treated measurements; this component is denoted tissue autofluorescence. The angles of the second rotation are found by maximizing the variance from 627 nm to 642 nm in the second component and is denoted PpIX. The remaining component is referred to as a blue-shift of the autofluorescence [see Fig. 3(b)]. Further, data were also projected on the spiky background residual from the CW mode and a flat bias. These two last-mentioned

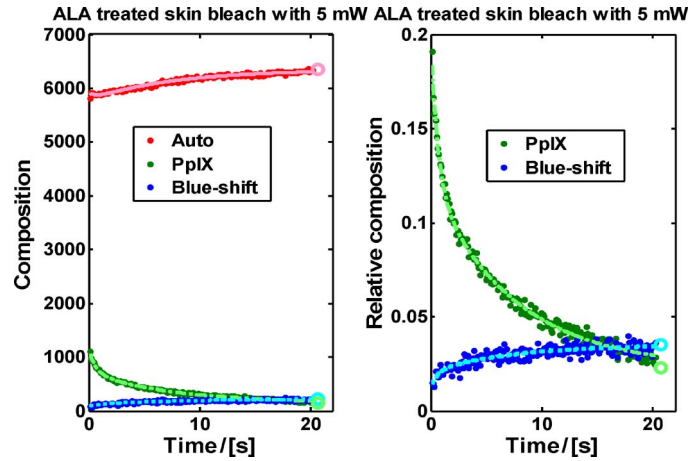


Fig. 4. Results for ALA-treated skin bleached with a power of 5 mW. (Left) Absolute fluorescence intensity expressed as counts as a function of time. In this particular sequence, the autofluorescence increases. (Right) Dimensionless values of the concentrations of PpIX and the blue-shift obtained by dividing them with the autofluorescence. The circles indicate convergence of each component; note that the convergence for the PpIX ratio is significantly different from zero. This particular sequence was recorded in continuous mode.

projections were later removed from data. Compression sequence residuals ( $M - \hat{M}$ ) were analyzed in the spectral domain and in the measurements from different individuals, and no systematic errors were found. The squared compression residuals were also analyzed in logarithmic histograms; obviously, sequences acquired at lower excitation power yielded larger relative residuals due to noise.

When the skin data are projected on the base components the composition can be plotted as a function of time [see Fig. 4(a)]. In this particular case, the autofluorescence increases slightly during bleaching. The average relative change in autofluorescence was not significant, being 0% for ALA-treated and  $-2\%$  for nontreated tissue, both with standard deviations of 8%. The large variance from sequence-to-sequence implies that some sequences show a relative change as large as  $\pm 20\%$ . ALA-treated tissue showed a weak significant negative power dependence of  $0.4\%/mW$  relative change, whereas nontreated tissue showed no power dependence. To convert the fluorescence intensity in terms of counts into normalized quantities related to concentration, the PpIX and the blue-shift counts were divided by the with autofluorescence counts [see Fig. 4(b)]. This operation cancels out several aspects related to the geometry of the interrogation volume. This operation can be compared with standard dimensionless evaluation methods in computer vision [50] or spectroscopy where, e.g., the Raman signal from water or nitrogen matrices is used for normalization [51], [52]. Tissue autofluorescence is arguably more arbitrary due to the complexity of the tissue matrix; however, in our data set, all the interrogation volumes could be described by the three components in Fig. 3(b).

We describe the evolution of the ratios by a 6-DOF model, as described above, and two initial conditions:  $PpIX_0$  and  $BlueShift_0$

$$\hat{C}_{t+1,s=1..2} = [1 \quad \hat{C}_{t,s=1..2}] \hat{\theta}_{d=1..3,s=1..2}. \quad (11)$$

It was noted that even the absolute values at any time can be reconstructed from a linear combination of these two time series. Thus, there are only two dynamic states, although three base spectra were found; this is in accordance with previous findings [23], [24], [37]. We refer to these dynamic states as the ‘‘PpIX ratio’’ and ‘‘Blue-shift ratio,’’ respectively. Models which did not converge, or models which converged but contained complex eigenvalues, were omitted, leaving 191 of 219 sequences. Several of the omitted sequences were short and noisy, and some were discontinuous due to movement during the measurement. In some of the sequences, fast periodic

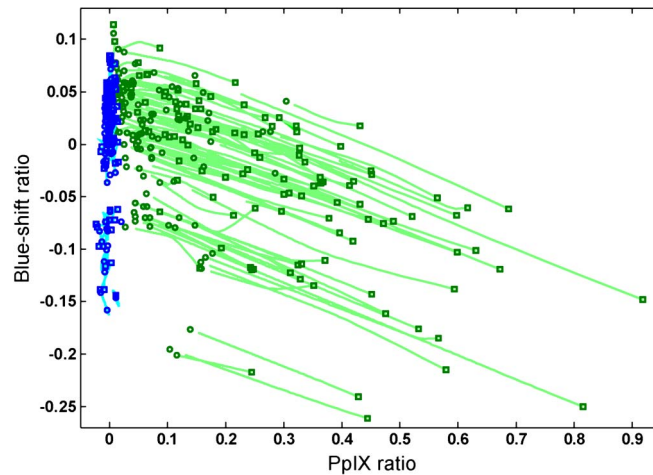


Fig. 5. Map of trajectories in state space. Squares indicate starting points, and circles are infinity extrapolated by solving for the derivative equaling zero. Green lines represent sequences from ALA-treated skin sample, and blue lines represent non-ALA-treated sequences.

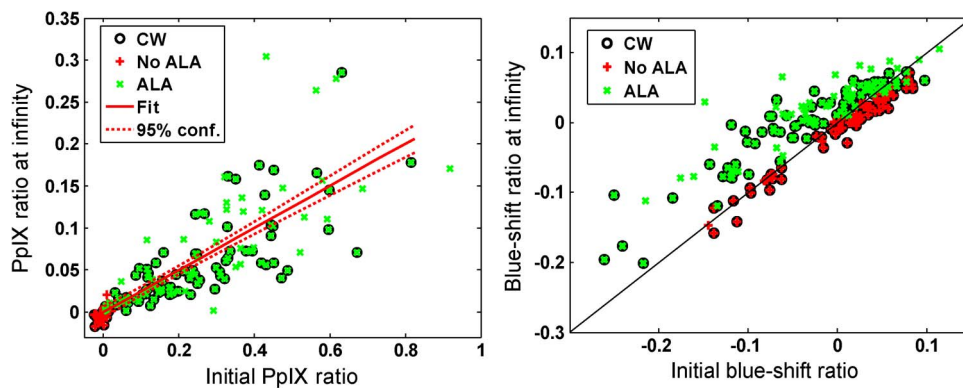


Fig. 6. (Left) The correlation between initial PpIX ratios and infinity extrapolated ratios is 0.83 ( $p$ -value  $10^{-50}$ ). This is promising with regard to estimating initial concentrations in terms of the constant infinity extrapolated properties. Green: ALA-treated tissue. Red: Nontreated tissue. Circles: Instrument operated in CW without dark subtraction. Crosses: Instrument operated in modulated mode. (Right) Infinite blue-shift ratio versus the initial blue-shift ratio. Green: ALA-treated sample. Red: Nontreated sample. Circles: Instrument operated in CW without dark subtraction. Initially, ALA-treated skin has lower blue-shift ratio than nontreated skin. After bleaching to infinity, ALA-treated skin has a higher blue-shift ratio than nontreated skin.

residuals were observed in the regime of heart beat frequency. Other slow time-dependent behaviors could arise from breathing [43], [44]. No systematic differences were found between the residuals and the squared residuals with respect to the early and late measurement points.

Considering the relative compositions of PpIX and blue-shift ratios, the state space trajectories can be mapped out in a plane, as illustrated in Fig. 5. It can be seen that the convergence points for ALA-treated samples (indicated by circles) are not located at a PpIX ratio of zero.

If we assume that each sequence starts with an entirely unbleached interrogation volume, we can plot the initial ratio of PpIX versus the ratio at infinity [see Fig. 6(a)]. The correlation coefficient was  $r = 0.83$  ( $p$ -value  $10^{-50}$ ). For the convenience of the reader, a straight line was fitted (slope  $0.25 \pm 0.024$  PpIX Inf/Init and intercept  $-0.00031 \pm 0.0065$  PpIX Inf, confidence 95%). The confidence interval is for the line fit. As can be seen from Fig. 6(a), confidence for new observation is dependent

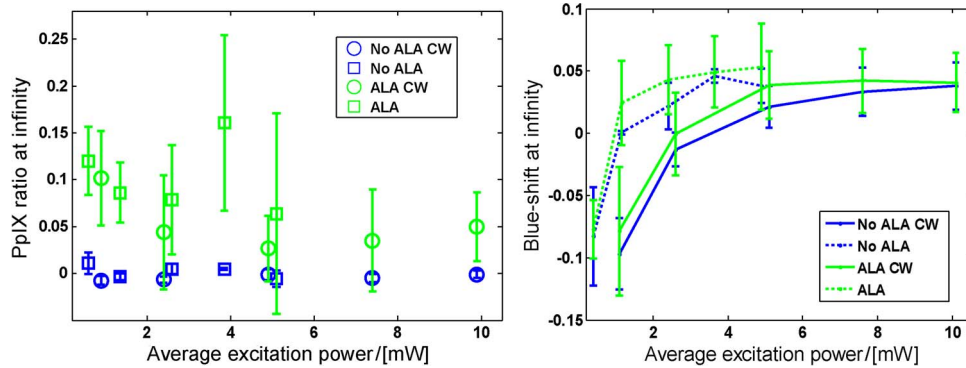


Fig. 7. (Left) PpIX ratio convergence is invariant with respect to excitation power. No significant difference between pulsed or CW. (Right) Higher excitation yields bluer convergence points. No significant difference between pulsed or CW, ALA, or no ALA.

on the initial value. Since the convergence point is independent of bleaching, this shows that the convergence point could potentially be used for bleaching-insensitive clinical evaluation.

We investigated whether the prediction of the initial PpIX ratio could be further improved by including the remaining parameters such as blue-shift convergence or decay times. These attempts included multivariate polynomial prediction models, which also include cross-product terms. No significant improvement was observed. We investigated the results in Fig. 6 in relation to whether the absolute autofluorescence increases or diminishes during bleaching, and no relation was found. When analyzing the blue-shift component in a similar manner, we observed that the blue-shift of ALA-treated tissue increased with bleaching, whereas nontreated tissue showed a slight red-shift [see Fig. 6(b)]. For the two aforementioned analyses, no systematic difference between the individuals was found.

To investigate whether the nonzero convergence concentration of PpIX arises from its production or in-flow in the interrogation volume, or whether it arises from PpIX trapped in the cell organelles, with inhibiting bleaching due to the low dissolved oxygen concentrations, we performed an excitation power analysis. Fig. 7(a) shows the PpIX ratio at infinity in relation to bleaching power. No significant power dependence could be seen. At very lower excitation powers, a slight increase in PpIX ratio convergence is observed, but this could equally well be explained by the noisy conditions. When applying the same analysis to the blue-shift ratio [see Fig. 7(b)], we observed that higher excitation powers yielded convergence points with a higher blue-shift. Similar results were obtained in [53].

No significant relation was found between the dynamic coefficients in the system matrix, i.e., the decay rates, and the initial PpIX ratio (in accordance with previous findings [23]). When performing excitation power analysis on the half life time of PpIX ratio, we observed a rather large variance between the different sequences. If we assume that the fluorescence bleaching half life time depends on the power according to  $t_{1/2} = k_0 + k_1/P$  ( $k_0$  implies constraints on the bleaching other than excitation flux), we observe that the decay rates saturates within the range of excitation powers used in clinical situations, which is typically 5 mW (see Fig. 8). This would suggest that in-flow of oxygen into the interrogation volume constrains the bleaching process, rather than excitation flux [18]. One considerable difference between continuous and modulated bleaching is the in-flow of, e.g., PpIX and oxygen during the dark time slots.

Several bleaching sequences from an open brain surgery situation were analyzed using SVD analysis, as described above. The eigenvalues revealed that spectra in the sequences could be effectively described by four base spectra; however, each sequence only required two components, namely, tissue autofluorescence and the PpIX signal. When rotating the coordinate system to minimize the PpIX imprint on the autofluorescence, the following two observations were made: The PpIX peak wavelength was slightly higher than for the skin (637 nm versus 634 nm for skin), and there was a change of the spectral knee shape in the region 650–700 associated with

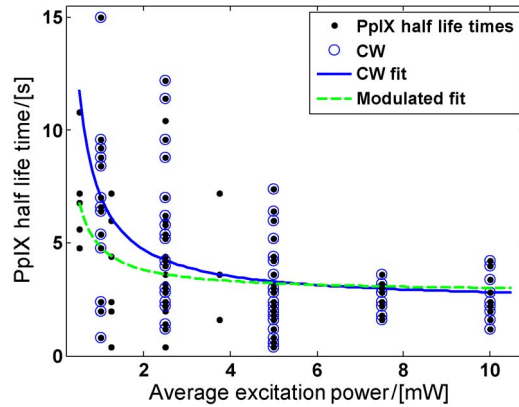


Fig. 8. Half life time of the PpIX ratio from the initial value to the final value. The data were fitted with the function  $t_{1/2} = k_0 + k_1/P$ . Such bottleneck behavior suggests that bleaching is limited by oxygen diffusion once the excitation light flux saturates.

TABLE 1

For short sequence lengths, noise and small bleaching degree are reflected in the 95% confidence bounds

Mode	PpIX ratio @ t=0	PpIX ratio @ t=inf	PpIX half life time / [s]
CW, 5mW	1.39 [1.37...1.40]	0.156 [-1.27...1.576]	48.69 [-16.23...113.6]
CW, 5mW	2.61 [2.58...2.64]	1.058 [-0.16...2.27]	71.1 [0.94...141.3]
CW, 5mW	2.24 [2.22...2.26]	0.713 [0.60...0.83]	18.27 [15.94...20.61]
Modulated, 2.5mW	1.53 [1.50...1.56]	0.403 [0.35...0.46]	12.63 [11.23...14.03]
Modulated, 2.5mW	1.39 [1.36-1.43]	0.530 [0.47...0.58]	6.964 [5.82...8.11]

photoproducts of PpIX [40]. A possible explanation for the shift could be different instrument temperatures or different scattering properties [54]. However, in continuous mode, it is difficult to distinguish this knee from the migrated red light from neighboring regions induced by the strong surgery theater lamp. The plurality of spectral components needed for the three different sequences on *in vivo* brain samples are mainly assigned different background conditions, as well as small spectral shifts of the PpIX signal in the order of 2 nm.

The temporal evolution of the PpIX ratio was in this case effectively explained by a single exponential with a bias or a state space model of the form

$$C_{t=1..T,s=1} = [1 \quad C_{t=0..T-1,s=1}] \theta_{d=1..2}. \quad (12)$$

One reason for this could be the fact that the strong theater lamp would induce a considerable bleaching of any fast bleaching component before the sequence could be recorded.

The magnitudes of the base components have been scaled to match those given above in this paper [see Fig. 3(b)], and thus, we can compare the convergence PpIX ratios directly. The details of the brain sequences are given in Table 1. We note that the convergence PpIX ratio is relatively high compared with those presented in, e.g., Fig. 6(a) (especially for the values with the better confidence intervals). This could be an indication of the applicability of the method presented, since the sequences of the brain samples were all measured on changes.

Fig. 9 presents an initial and a converged spectra. It should be noted that the interrogation volume is likely to have undergone bleaching prior to the recording due to the operating theater lamp.

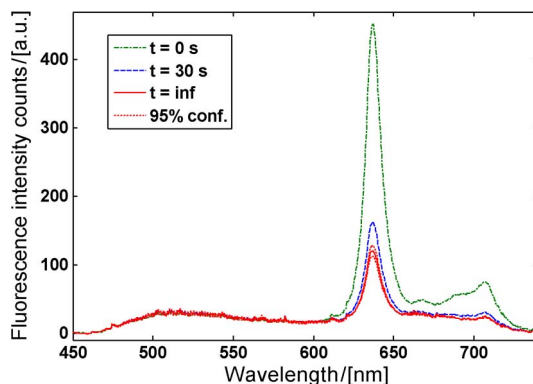


Fig. 9. Initial and infinity spectrum from an *in vivo* brain bleaching sequence.

There were no indications of PpIX bleaching photoproducts in the skin data, while the blue-shift increased during bleaching. However, bleaching features changing the spectral shape in the 650–700-nm range were observed in brain tissue (see Fig. 9). The photoproduct from PpIX bleaching has been observed previously in skin samples [22], [38]; one possible explanation is the difference that, in this paper, healthy skin was studied, whereas malignant skin was studied in [38]. Interestingly, the production of the photoproducts is dynamically locked to the destruction of PpIX; thus, PpIX and photoproducts will not be separated by the SVD analysis of a bleaching sequence; instead, the SVD will e.g., express a steady spectral component and a component representing both the reduction of PpIX and the increase in the photoproducts.

#### 4. Conclusion

Using data from ALA-treated and non-ALA-treated skin and brain tissue *in vivo*, we have shown that bleaching sequences from individual interrogation volumes can be effectively described by a small number of spectral components (three and two, respectively). We have also shown that we can accurately predict the spectra in time and extrapolate them to infinity. We observed an interesting correlation between the PpIX ratio after infinite bleaching and the initial PpIX ratio (related to the respective concentrations). In a clinical situation, this would allow us to obtain bleaching-insensitive quantities by recording short sequences instead of individual spectra. Within the power regime 0.35–3.5 W/cm<sup>2</sup>, the PpIX convergence ratio is independent of power, which indicates that the converged PpIX signal probably arises from organelles where oxygenation inhibits bleaching, rather than the in-flow or production of PpIX. A large spread in the bleaching half life times was observed; the PpIX half life time was found to be unrelated to the initial PpIX concentration. This is encouraging since the convergence point is easier to determine, whereas a half life time can only be determined for the limited time during which the sequence shows any significant bleaching.

The instrument used in this paper features a large number of spectral bands but rather low optical throughput and sampling frequency. The fact that the large data set can be described by very few spectral components suggests that sensitivity and modulation speed should be prioritized in future instruments at the expense of spectral resolution. This would greatly increase the signal-to-noise and signal-to-background (operating theater lamp) ratio. A second generation instrument is likely to be based on a set of dichroic beam splitters [16] and photomultiplier tubes (PMTs) or avalanche photodiodes (APDs), which would enable modulation in the kilohertz regime and compatibility with fluorescence lifetime acquisition [55]. It is well known that the fluorescence is largely influenced by re-absorption; thus, it is desirable to include a white light source for elastic reflectance, e.g., an InGaN+Ce:YAG LED [56]. Such a feature may further improve the prediction of the initial PpIX content and reduce some of the biological variance between different interrogation volumes caused by, e.g., re-absorbing chromophores and, not least, the different local oxygen levels (accessed by the absorbance of Hb and HbO). In this paper, the elastic scattered excitation light was rejected by

a long-pass filter. Detailed information on the change of the extension of the interrogation volume could be obtained by even considering the elastically scattered excitation light. We have shown how certain properties can be investigated by analyzing the bleaching dynamics with respect to the excitation power [39]; in this paper, the different powers were applied to different interrogation volumes. In future studies, it could be interesting to bleach the same interrogation volume by a plurality of excitation powers to investigate the properties related to intraorganellar PpIX, the diffusion of oxygen, and production and diffusion of PpIX.

## Acknowledgment

The authors acknowledge Prof. S. Svanberg for his valuable input. We also thank J. Richter, a neurosurgeon with the Department of Neurosurgery, Linköping University, for the opportunity to conduct measurements during surgeries. We also thank R. Johansson for his efforts related to the dynamical modeling.

## References

- [1] M. A. Mycek and B. W. Pogue, Eds., *Handbook of Biomedical Fluorescence*. Boca Raton, FL: CRC, 2003, p. 688.
- [2] J. Moan and Q. Peng, "An outline of the history of PDT," in *Photodynamic Therapy*, T. Patrice, Ed. Cambridge, U.K.: Roy. Soc. Chem., 2003, pp. 1–18.
- [3] C. af Klinteberg, "On the use of light for the characterization and treatment of malignant tumours," Ph.D. dissertation, Lund Univ., Lund, Sweden, 1999.
- [4] J. Moan, J. T. H. M. Van Den Akker, P. Juzenas, L. W. Ma, E. Angell-Petersen, Ø. B. Gasmar, and V. Iani, "On the basis for tumor selectivity in the 5-aminolevulinic acid-induced synthesis of protoporphyrin IX," *J. Porphyr. Phthalocya.*, vol. 5, no. 2, pp. 170–176, Feb. 2001.
- [5] A. Novotny and W. Stummer, "5-Aminolevulinic acid and the blood-brain barrier—A review," *Med. Laser Appl.*, vol. 18, no. 1, pp. 36–40, 2003.
- [6] W. Stummer, U. Pichlmeier, T. Mainel, O. D. Wiestler, F. Zanella, and H. Reulen, "Fluorescence-guided surgery with 5-aminolevulinic acid for resection of malignant glioma: A randomized controlled multicentre phase III trial," *Lancet Oncol.*, vol. 7, no. 5, pp. 392–401, May 2006.
- [7] S. Utsuki, H. Oka, S. Sato, S. Shimizu, S. Suzuki, Y. Tanizaki, K. Kondo, Y. Miyajima, and K. Fujii, "Histological examination of false positive tissue resection using 5-aminolevulinic acid-induced fluorescence guidance," *Neurol. Med. Chir. (Tokyo)*, vol. 47, no. 5, pp. 210–214, May 2007.
- [8] B. W. Pogue, S. L. Gibbs-Strauss, P. A. Valdés, K. S. Samkoe, D. W. Roberts, and K. D. Paulsen, "Review of neurosurgical fluorescence imaging methodologies," *IEEE J. Sel. Topics Quantum Electron.*, vol. 16, no. 3, pp. 493–505, May/Jun. 2010.
- [9] M. Hefti, G. von Campe, A. Siegner, H. Looser, and H. Landolt, "5-Aminolaevulinic acid-induced protoporphyrin IX fluorescence in high-grade glioma surgery," *Swiss Med. Wkly.*, vol. 138, no. 11/12, pp. 180–185, Mar. 2008.
- [10] M. A. Scott, C. Hopper, A. Sahota, R. Springett, B. W. McIlroy, S. G. Bown, and A. J. MacRobert, "Fluorescence photodiagnosics and photobleaching studies of cancerous lesions using ratio imaging and spectroscopic techniques," *Lasers Med. Sci.*, vol. 15, no. 1, pp. 63–72, 2000.
- [11] C. af Klinteberg, M. Andreasson, O. Sandström, S. Andersson-Engels, and S. Svanberg, "Compact medical fluorosensor for minimally invasive tissue characterization," *Rev. Sci. Instrum.*, vol. 76, no. 3, p. 034303, Mar. 2005.
- [12] M. A. Ilias, J. Richter, F. Westermark, M. Brantmark, S. Anderson-Engels, and K. Wårdell, "Evaluation of a fiber-optic fluorescence spectroscopy system to assist neurosurgical tumor resections," *Proc. SPIE*, vol. 6631, pp. 66310W-1–66310W-8, 2007.
- [13] N. Haj-Hosseini, J. Richter, S. Andersson-Engels, and K. Wårdell, "Optical touch pointer for fluorescence guided glioblastoma resection using 5-aminolevulinic acid," *Lasers Surg. Med.*, vol. 42, no. 1, pp. 9–14, Jan. 2010.
- [14] J. Richter, N. Haj-Hosseini, S. Anderson-Engels, and K. Wårdell, "Fluorescence spectroscopy measurements in ultrasonic navigated resection of malignant brain tumors," *Lasers Surg. Med.*, vol. 43, no. 1, pp. 8–14, Jan. 2011.
- [15] I. A. Boere, D. J. Robinson, H. S. de Bruijn, J. Boogert, H. W. Tilanus, H. J. C. M. Sterenborg, and R. W. F. de Bruin, "Monitoring in situ dosimetry and protoporphyrin IX fluorescence photobleaching in the normal rat esophagus during 5-aminolevulinic acid photodynamic therapy," *Photochem. Photobiol.*, vol. 78, no. 3, pp. 271–277, Sep. 2003.
- [16] B. W. Pogue, C. Sheng, X. Zhou, P. Hoopes, and T. Hasan, "Photobleaching-based dosimetry predicts deposited dose in ALA-PpIX PDT of rodent esophagus," *Photochem. Photobiol.*, vol. 83, no. 3, pp. 738–748, May/Jun. 2007.
- [17] N. Haj-Hosseini, J. Richter, S. Andersson-Engels, and K. Wårdell, "Photobleaching behavior of protoporphyrin IX during 5-aminolevulinic acid marked glioblastoma detection," *Proc. SPIE*, vol. 7161, p. 716131, 2009.
- [18] A. Curnow, B. W. McIlroy, M. J. Postle-Hacon, A. J. MacRobert, and S. G. Bown, "Light dose fractionation to enhance photodynamic therapy using 5-aminolevulinic acid in the normal rat colon," *Photochem. Photobiol.*, vol. 69, no. 1, pp. 71–76, Jan. 1999.
- [19] J. Moan, L. Ma, V. Iani, and A. Juzeniene, "Influence of light exposure on the kinetics of protoporphyrin IX formation in normal skin of hairless mice after application of 5-aminolevulinic acid methyl ester," *J. Invest. Dermatol.*, vol. 125, no. 5, pp. 1039–1044, Nov. 2005.
- [20] K. K. Wang, S. Mitra, and T. H. Foster, "A comprehensive mathematical model of microscopic dose deposition in photodynamic therapy," *Med. Phys.*, vol. 34, no. 1, pp. 282–293, Jan. 2007.

- [21] A. Orenstein, G. Kostenich, and Z. Malik, "The kinetics of protoporphyrin fluorescence during ALA-PDT in human malignant skin tumors," *Cancer Lett.*, vol. 120, no. 2, pp. 229–234, Dec. 1997.
- [22] J. C. Finlay, D. L. Conover, E. L. Hull, and T. H. Foster, "Porphyrin bleaching and PDT-induced spectral changes are irradiance dependent in ALA-sensitized normal rat skin *in vivo*," *Photochem. Photobiol.*, vol. 73, no. 1, pp. 54–63, Jan. 2001.
- [23] D. J. Robinson, H. S. de Bruijn, N. van der Veen, M. R. Stringer, S. B. Brown, and W. M. Star, "Fluorescence photobleaching of ALA-induced protoporphyrin IX during photodynamic therapy of normal hairless mouse skin: The effect of light dose and irradiance and the resulting biological effect," *Photochem. Photobiol.*, vol. 67, no. 1, pp. 140–149, Jan. 1998.
- [24] A. Lihachev and J. Spigulis, "Skin autofluorescence fading at 405/532 nm laser excitation," *IEEE Xplore*, 10.1109/NO, vol. 10, pp. 63–65, 2007.
- [25] T. W. Anderson, *An Introduction to Multivariate Statistical Analysis*, 3rd ed. Hoboken, NJ: Wiley, 2003.
- [26] A. C. Rechner, *Methods of Multivariate Analysis*. New York: Wiley Interscience, 2002.
- [27] K. R. Beebe and B. R. Kowalski, "An introduction to multivariate calibration and analysis," *Anal. Chem.*, vol. 59, pp. 1007A–1017A, 1987.
- [28] P. Weibring, T. Johansson, H. Edner, S. Svanberg, B. Sundnér, V. Raimondi, G. Cecchi, and L. Pantani, "Fluorescence lidar imaging of historical monuments," *Appl. Opt.*, vol. 40, no. 33, pp. 6111–6120, Nov. 2001.
- [29] P. Weibring, T. Johansson, H. Edner, S. Svanberg, B. Sundnér, V. Raimondi, G. Cecchi, and L. Pantani, "Fluorescence lidar imaging of historical monuments: Erratum," *Appl. Opt.*, vol. 41, no. 3, pp. 434–436, Jan. 2002.
- [30] MATLAB, Help files, The Mathworks.
- [31] L. Ljung, *System Identification: Theory for the User*, 2nd ed. Englewood Cliffs, NJ: Prentice-Hall, 1999, 672 p.
- [32] R. Isermann, *Identification of Dynamical Systems: An Introduction With Applications*, 1st ed. New York: Springer-Verlag, 2010, p. 550.
- [33] Y. Zhu, *Multivariable System Identification for Process Control*, 1st ed. Amsterdam, The Netherlands: Elsevier, 2001, 372 p.
- [34] R. Johansson, *System Modeling and Identification*. Englewood Cliffs, NJ: Prentice-Hall, 1993, p. 528.
- [35] S. Bittanti and G. Picci, Eds., *Identification, Adaptation, Learning: The Science of Learning Models from Data (NATO ASI Series/Computer and Systems Sciences)*, 1st ed. New York: Springer-Verlag, 1996, 552 p.
- [36] S. Dobre, T. Bastogne, M. Barberi-Heyob, D. Bechet, J. Didelon, and A. Richard, "System identification of the intracellular photoreaction process induced by photodynamic therapy," in *Proc. 16th Mediterranean Conf. Control Autom.*, Ajaccio, France, Jun. 2008, pp. 1729–1734.
- [37] J. C. Finlay, S. Mitra, M. S. Patterson, and T. H. Foster, "Photobleaching kinetics of Photofrin *in vivo* and in multicell tumour spheroids indicate two simultaneous bleaching mechanisms," *Phys. Med. Biol.*, vol. 49, no. 21, pp. 4837–4860, Nov. 2004.
- [38] C. af Klinteberg, A. M. K. Enejder, I. Wang, S. Andersson-Engels, S. Svanberg, and K. Svanberg, "Kinetic fluorescence studies of 5-aminolaevulinic acid-induced protoporphyrin IX accumulation in basal cell carcinomas," *J. Photochem. Photobiol. B: Biol.*, vol. 49, no. 2/3, pp. 120–128, Apr. 1999.
- [39] K. K. Wang, W. J. Cottrell, S. Mitra, A. R. Oseroff, and T. H. Foster, "Simulations of measured photobleaching kinetics in human basal cell carcinomas suggest blood flow reductions during ALA-PDT," *Lasers Surg. Med.*, vol. 41, no. 9, pp. 686–696, Nov. 2009.
- [40] W. J. Cottrell, A. D. Paquette, K. R. Keymel, T. H. Foster, and A. R. Oseroff, "Irradiance-dependent photobleaching and pain in delta-aminolevulinic acid-photodynamic therapy of superficial basal cell carcinomas," *Clin. Cancer Res.*, vol. 14, no. 14, pp. 4475–4483, Jul. 2008.
- [41] B. W. Pogue, C. Sheng, J. Benevides, D. Forcione, B. Puricelli, N. Nishioka, and T. Hasan, "Protoporphyrin IX fluorescence photobleaching increases with the use of fractionated irradiation in the esophagus," *J. Biomed. Opt.*, vol. 13, no. 3, p. 034009, May/June. 2008.
- [42] J. S. Dysart and M. S. Patterson, "Photobleaching kinetics, photoproduct formation, and dose estimation during ALA induced PpIX PDT of MLL cells under well oxygenated and hypoxic conditions," *Photochem. Photobiol. Sci.*, vol. 5, no. 1, pp. 73–81, 2006.
- [43] J. Spigulis, "Optical non-invasive monitoring of skin blood pulsations," *Appl. Opt.*, vol. 44, no. 10, pp. 1850–1857, Apr. 2005.
- [44] J. Spigulis, L. Gailite, A. Lihachev, and R. Erts, "Simultaneous recording of skin blood pulsations at different vascular depths by multi-wavelength photoplethysmography," *Appl. Opt.*, vol. 46, no. 10, pp. 1754–1759, Apr. 2007.
- [45] H. Heyerdahl, I. Wang, D. L. Liu, R. Berg, S. Anderson-Engels, Q. Peng, J. Moan, S. Svanberg, and K. Svanberg, "Pharmacokinetic studies on 5-aminolevulinic acid-induced protoporphyrin IX accumulation in tumours and normal tissues," *Cancer Lett.*, vol. 112, no. 2, pp. 225–231, Jan. 1997.
- [46] N. van der Veen, H. S. de Bruijn, R. J. W. Berg, and W. M. Star, "Kinetics and localisation of PpIX fluorescence after topical and systemic ALA application, observed in skin and skin tumours of UVB-treated mice," *Brit. J. Cancer*, vol. 73, no. 7, pp. 925–930, Apr. 1996.
- [47] M. Shirmanova, E. Zagaynova, M. Sirotkina, L. Snopova, I. Balalaeva, I. Krutova, N. Lekanova, I. Turchin, A. Orlova, and M. Kleshnin, "In vivo study of photosensitizer pharmacokinetics fluorescence transillumination imaging," *J. Biomed. Opt.*, vol. 15, no. 4, p. 048004, Jul./Aug. 2010.
- [48] J. Johansson, R. Berg, K. Svanberg, and S. Svanberg, "Laser-induced fluorescence studies of normal and malignant tumour tissue of rat following intravenous injection of  $\delta$ -amino levulinic acid," *Lasers Surg. Med.*, vol. 20, no. 3, pp. 272–279, 1997.
- [49] B. Kramer and K. Uberriegler, "In-vitro investigation of ALA-induced protoporphyrin IX," *J. Photochem. Photobiol. B: Biol.*, vol. 36, no. 2, pp. 121–126, Nov. 1996.
- [50] M. Drew and J. Au, "Clustering of compressed illumination-invariant chromaticity signatures for efficient video summarization," *Image Vis. Comput.*, vol. 21, no. 8, pp. 705–716, Aug. 2003.

- [51] F. E. Hoge and R. N. Swift, "Airborne simultaneous spectroscopic detection of laser-induced water Raman backscatter and fluorescence from chlorophyll a and other naturally occurring pigments," *Appl. Opt.*, vol. 20, no. 18, pp. 3197–3205, Sep. 1981.
- [52] D. N. Whiteman, S. H. Melfi, and R. A. Ferrare, "Raman LIDAR system for the measurement of water-vapor and aerosols in the Earth's atmosphere," *Appl. Opt.*, vol. 31, no. 16, pp. 3068–3082, Jun. 1992.
- [53] B. W. Pogue, J. D. Pitts, M. A. Mycek, R. D. Sloboda, C. M. Wilmot, J. F. Brandsema, and J. A. O'Hara, "In vivo NADH fluorescence monitoring as an assay for cellular damage in photodynamic therapy," *Photochem. Photobiol.*, vol. 74, no. 6, pp. 817–824, Dec. 2001.
- [54] J. Swartling, J. Svensson, D. Bengtsson, K. Terike, and S. Andersson-Engels, "Fluorescence spectra provide information on the depth of fluorescent lesions in tissue," *Appl. Opt.*, vol. 44, no. 10, pp. 1934–1941, Apr. 2005.
- [55] P. V. Butte, A. N. Mamelak, M. Nuno, S. I. Bannykh, K. L. Black, and L. Marcu, "Fluorescence lifetime spectroscopy for guided therapy of brain tumors," *NeuroImage (BMISPS)*, vol. 54, pp. 125–135, 2011.
- [56] M. Brydegaard, P. Lundin, Z. Guan, A. Runemark, S. Åkesson, and S. Svanberg, "Feasibility study: Fluorescence lidar for remote bird classification," *Appl. Opt.*, vol. 49, no. 24, pp. 4531–4544, Aug. 2010.

## PAPER VIII

### ***In vivo* measurements of diffuse reflectance and time-resolved autofluorescence emission spectra of basal cell carcinomas**

A.J. Thompson, M. Brydegaard Sørensen, S. Coda, G. Kennedy, R. Patalay, U. Waitong-Bramming, P.A.A. De Beule, M.A.A. Neil, S. Andersson-Engels, N. Bendsø, P.M. French, K. Svanberg and C. Dunsby

*Journal of Biophotonics* 5,240-254 (2012).

FULL ARTICLE

## ***In vivo* measurements of diffuse reflectance and time-resolved autofluorescence emission spectra of basal cell carcinomas**

Alex J. Thompson<sup>\*,1</sup>, Sergio Coda<sup>1,6</sup>, Mikkel Brydegaard Sørensen<sup>2</sup>, Gordon Kennedy<sup>1</sup>, Rakesh Patalay<sup>1,3</sup>, Ulrika Waitong-Brämning<sup>4</sup>, Pieter A. A. De Beule<sup>1</sup>, Mark A. A. Neil<sup>1</sup>, Stefan Andersson-Engels<sup>2</sup>, Niels Bendsøe<sup>5</sup>, Paul M. W. French<sup>1</sup>, Katarina Svanberg<sup>4</sup>, and Chris Dunsby<sup>\*,1</sup>

<sup>1</sup> Photonics Group, Department of Physics, Imperial College, Prince Consort Road, London, UK

<sup>2</sup> Atomic Physics Division, Lund University, Lund, Sweden

<sup>3</sup> Department of Dermatology, Imperial College Healthcare NHS Trust, London, UK

<sup>4</sup> Department of Oncology, Lund University Hospital, Lund, Sweden

<sup>5</sup> Department of Dermatology, Lund University Hospital, Lund, Sweden

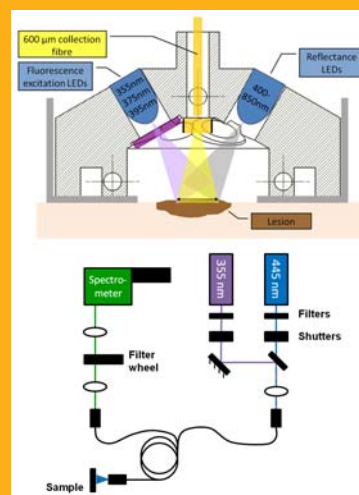
<sup>6</sup> Department of Gastroenterology, Imperial College Healthcare NHS Trust, London, UK

Received 18 November 2011, revised 23 December 2011, accepted 12 January 2012

Published online 6 February 2012

**Key words:** fluorescence, fluorescence lifetime, diffuse reflectance, skin cancer, spectrometer, fibre probe

We present a clinical investigation of diffuse reflectance and time-resolved autofluorescence spectra of skin cancer with an emphasis on basal cell carcinoma. A total of 25 patients were measured using a compact steady-state diffuse reflectance/fluorescence spectrometer and a fibre-optic-coupled multispectral time-resolved spectrofluorometer. Measurements were performed *in vivo* prior to surgical excision of the investigated region. Singular value decomposition was used to reduce the dimensionality of steady state diffuse reflectance and fluorescence spectra. Linear discriminant analysis was then applied to the measurements of basal cell carcinomas (BCCs) and used to predict the tissue disease state with a leave-one-out methodology. This approach was able to correctly diagnose 87% of the BCCs. With 445 nm excitation a decrease in the spectrally averaged fluorescence lifetime was observed between normal tissue and BCC lesions with a mean value of 886 ps. Furthermore, the fluorescence lifetime for BCCs was lower than that of the surrounding healthy tissue in all cases and statistical analysis of the data revealed that this decrease was significant ( $p = 0.002$ ).



Schematic diagrams of the two spectrometers showing the steady state spectrometer measurement head (top) and the optical layout of the time-resolved system (bottom).

\* Corresponding authors: e-mail: alex.thompson08@imperial.ac.uk, Phone: +44 207 594 1278, Fax: +44 (0)20 7594 7714; e-mail: christopher.dunsby@imperial.ac.uk, Phone: +44 207 594 7755, Fax: +44 (0)20 7594 7714

## 1. Introduction

Non-melanoma skin cancer (NMSC), which includes basal cell carcinoma (BCC) and squamous cell carcinoma (SCC), accounts for 90% of all skin malignancies and represents a significant health problem worldwide. Despite the extended survival prognosis of these diseases compared to malignant melanoma, their incidence is rising. In the UK and the USA respectively, there are approximately 100,000 and 1,000,000 new cases reported every year [1, 2]. Additionally, amongst white populations in Europe, the USA, Canada and Australia the average increase in NMSC has been between 3 and 8% per year since the 1960s [3, 4].

Although a number of novel imaging techniques have become available, there is still no gold standard for skin cancer imaging. Most incidences of skin cancer are diagnosed based on clinical history and visual inspection by a clinician. In many cases the diagnosis still remains unclear and a biopsy is required for confirmation. This is an invasive procedure requiring the removal of tissue from the patient which is both painful and scarring. The histopathological analysis of the sample is also expensive and time consuming and can result in the unnecessary excision of benign lesions [5]. A non-invasive method of assessment, capable of avoiding unnecessary biopsies, would therefore be desirable.

A number of optical techniques are being investigated for the detection and delineation of skin cancers owing to their potential to acquire non-invasive spectroscopic information and to image with sub-cellular resolution. Diffuse reflectance measurements [6] offer one potential source of optical contrast, and have been applied to detect skin cancer, e.g. [7]. Similarly, spectroscopy and imaging of polarized light have been used to study epithelial tissues [8, 9], including those involved in skin pathology [10]. Confocal reflectance microscopy provides high resolution images of tissue morphology and has been used to investigate skin lesions [11, 12], but this technique does not provide functional information about the tissue. Optical coherence tomography (OCT) [13] allows imaging at greater depths within tissue but, again, does not normally supply functional information. Raman spectroscopy can be used to obtain highly detailed spectroscopic information [14] but usually requires long data acquisition times and cannot be readily extended to provide a wide-field screening tool that can image fields of view of several centimetres.

Another opportunity for obtaining contrast between cancerous and normal tissue is to detect endogenous tissue autofluorescence. The principal contributors to skin autofluorescence for near-ultraviolet and blue excitation are reduced nicotinamide adenine dinucleotide (phosphate) (NAD(P)H), flavins, keratin, collagen and elastin [15, 16]. Changes in the fluorescence properties of these molecules can re-

port on altered metabolism, protein cross links, cell signalling and even disease state [15, 17–19]. In particular the fluorescence lifetime of endogenous fluorophores, which is relatively insensitive to fluorophore concentration and to signal attenuation by the sample, has been shown (both *ex vivo* and *in vivo*) to effectively differentiate between healthy and diseased tissue, for example in atherosclerotic plaques [20, 21] and in various types of cancer [22–31]. Accordingly, there is significant interest in the development of instruments that can measure the autofluorescence properties of skin for clinical diagnosis, e.g. [32–38]. This autofluorescence signal can be resolved with respect to a number of different parameters including excitation spectrum, emission spectrum and fluorescence lifetime.

Several studies have used measurements of steady-state fluorescence intensity or emission spectra to discriminate between normal and neoplastic tissue. Intensity measurements alone, however, are sensitive to variations in excitation efficiency and heterogeneous sample attenuation and so are difficult to compare between samples and patients. Spectrally-resolved ratiometric measurements can provide more quantitative readouts but their discrimination can be restricted by the broad overlapping fluorescence spectra of many tissue fluorophores [39]. Time-resolved fluorescence spectroscopy (TRFS) is also inherently ratiometric and thus provides additional quantitative measurement capabilities. For these reasons, a considerable amount of research has been carried out to investigate the potential of both time- and spectrally-resolved fluorescence measurements for diagnostic purposes.

Tissue autofluorescence can be excited using either one- or two-photon absorption. While two-photon fluorescence microscopy provides high resolution and permits depth resolved imaging, it is difficult to use such nonlinear excitation to achieve a wide-field imaging modality that can rapidly screen fields of view of many centimetres. Single photon excitation can enable such wide-field imaging and so it is important to determine which combination of spectroscopic parameters – e.g. excitation and detection wavelengths – provide the greatest contrast between normal tissue and (different) disease states.

Instruments developed to monitor both fluorescence lifetime and spectra of tissue include the work of Glanzmann et al. [40], Pitts et al. [41], de Beule et al. [42] and Sun et al. [43]. There are also systems capable of measuring other optical properties, such as diffuse reflectance, in addition to the fluorescence, e.g. [32, 33].

There have been several recent examples of the application of such instruments to skin including previous work by our group on *ex vivo* tissue that showed significant differences between the fluorescence lifetimes of healthy and diseased tissue in non-

melanoma skin cancer [24, 42]. In addition, Rajaram et al. studied non-melanoma skin cancer *in vivo* using a combination of diffuse reflectance and fluorescence spectroscopy [33], while Blackwell et al. used an instrument recording fluorescence decays in four spectral channels to compare the fluorescence signature of human skin from diabetic and non-diabetic test subjects *in vivo* [44].

In this paper we describe the application of both a time-resolved fluorescence spectrofluorometer and a compact instrument combining steady-state spectroscopy of diffuse reflected light and fluorescence to investigate the clinical diagnostic potential of autofluorescence and reflectance measurements of tissue. We report the results from an *in vivo* pilot study of skin cancer in 25 patients.

## 2. Materials and methods

### 2.1 Wide-field steady-state spectrometer (A)

The first instrument described here measures diffuse reflectance spectra and fluorescence spectra with three different excitation wavelengths. It is a compact and portable system controlled using software written in Matlab<sup>®</sup> (MathWorks<sup>TM</sup>) running on a laptop computer. The measurement head (Figure 1) is coupled to a small spectrometer (USB4000, cylindrical lens and second order rejection filter installed, Ocean Optics, The Netherlands) that provides 3 nm resolution and the whole system fits into a small ( $20 \times 15 \times 15$  cm) portable case.

The instrument incorporates seven continuous wave LED sources (Roithner Lasertechnik). A 430 nm LED, a white light LED (Blue + Ce:YAG conversion, 450–700 nm) and a dual near infrared LED (750 nm and 850 nm) are used for the reflect-

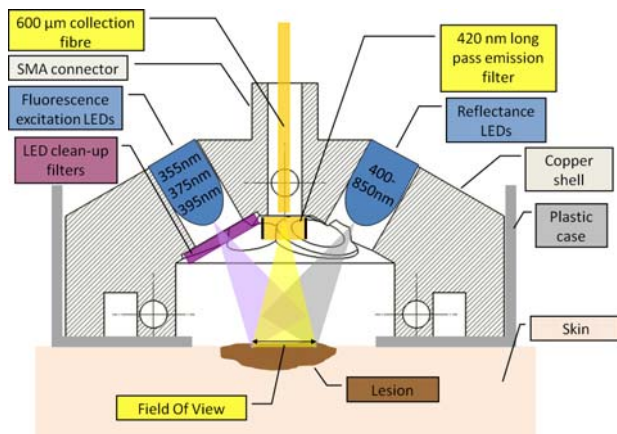


**Figure 1** (online color at: [www.biophotonics-journal.org](http://www.biophotonics-journal.org)) Cross-section through the measurement head of the wide-field steady state spectrometer (instrument A).

ance measurements while LEDs at 355, 375 and 395 nm provide excitation for the fluorescence measurements. The emission from the ultraviolet (UV) LEDs is passed through clean up filters (1 mm UG1 or UG11, Schott, Germany) and each source is directed toward the same central measurement site, where the illumination spot is elliptical with major and minor diameters of approximately 8 mm and 6 mm respectively. The angles of incidence and the use of non-contact optics in the system are designed to minimise specular reflections. We note that the fixed size of the illumination spot means that when measuring small lesions some unwanted signal may be acquired from the surrounding healthy tissue. In this study, however, the diameter of most lesions was similar to or greater than that of the illumination spot, hence, this did not present a significant problem.

For a typical measurement, the sample is illuminated by each source sequentially and the fluorescence or diffuse reflected light passes through a 420 nm long pass emission filter (3 mm GG420) and is collected by a 600  $\mu$ m diameter optical fibre that delivers the light to the spectrometer. The LEDs and filters are contained within a copper shell, and the thermal dependence of the emissive yield is compensated for by measuring the voltage-current characteristics of the LEDs. Dark spectra are recorded by switching off the sources and these are subtracted from the clinical measurements. The reflectance was calibrated with a 50% diffuse grey reference (Oriol Instruments, USA) and the fluorescence intensity counts were white calibrated with a filament source (Oriol Instruments, USA). A single reflectance spectrum over a broad spectral range can be generated by combining the data obtained with each of the four reflectance LEDs. In practice, however, differences in the LED beam profiles led to errors when combining the reflectance spectra. Therefore, the data presented in this paper consist solely of the reflectance measured using the white light LED.

In a single acquisition, the reflectance and fluorescence spectra are recorded at each excitation wavelength in sequence, requiring a total acquisition time of approximately 30 s when averaging over 5 measurements. Thus, a dataset consists of a diffuse white light reflectance spectrum and a fluorescence spectrum for each of the three excitation wavelengths [45]. A more complete description of the system can be found in the publication by Brydegaard et al. [46].

### 2.2 Time-resolved fibre-optic probe spectrofluorometer (B)

The time-resolved spectrometer (B) has been described previously [42, 45] and was configured as

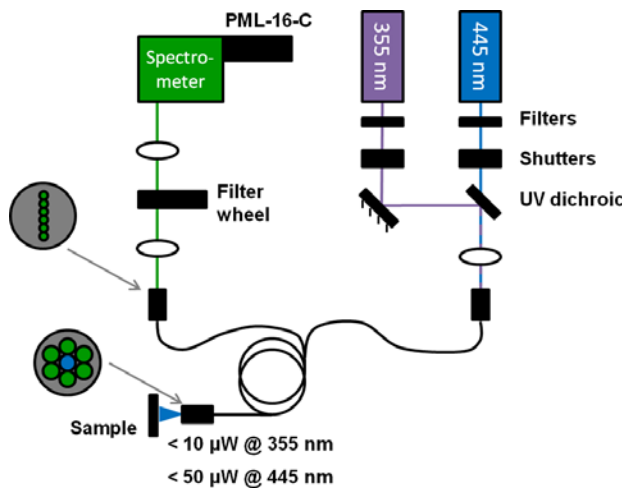


**Figure 2** (online color at: [www.biophotonics-journal.org](http://www.biophotonics-journal.org)) Experimental layout of the fluorescence lifetime fibre probe spectrofluorometer (instrument B).

shown in Figure 2. Two pulsed laser sources were used for excitation: a frequency tripled ultrafast Yb: glass fibre laser (UVPower355, Fianium Ltd., UK), which provided 10 ps pulses at 355 nm with a repetition rate of 37.1 MHz; and a diode laser (LDH-P-C-440B, PicoQuant GmbH, Germany), which emitted 50–150 ps pulses at 445 nm with an adjustable repetition rate of up to 40 MHz. This radiation was coupled into the excitation channel of a custom built fibre-optic probe (FiberTech Optica, Canada) that comprised seven multimode optical fibres with core diameters of 200  $\mu\text{m}$ . At the distal end of the probe, the fibres are arranged with the central excitation fibre surrounded by the six collection fibres (inset at bottom left of Figure 2) in order to provide a reasonable illumination and collection efficiency while maintaining a relatively small probe size. For the *in vivo* skin measurements the average power at the sample was limited to 10  $\mu\text{W}$  of UV and 50  $\mu\text{W}$  of blue light. Spectral bandpass filters were employed to narrow the emission of the laser diode (Z440/20 $\times$ , Chroma Technology, USA) and to ensure that none of the fundamental radiation (at 1.06  $\mu\text{m}$ ) from the Yb: glass fibre laser was transmitted to the sample (UG1, Schott, Germany). Computer controlled mechanical shutters in the two beam paths were used to switch between the two excitation sources. The output from the excitation optical fibre was directed onto the sample over an area of  $\sim 0.2 \text{ mm}^2$  and the resulting fluorescence was collected by the six multimode collection fibres. The output from these collection optical fibres was then imaged onto the input slit of a grating spectrometer (MS125 1/8 m, Lot-Oriel, UK), which was attached to a 16 channel multi-anode photomultiplier tube (PMT) detector (PML-16-C, Becker-Hickl GmbH, Germany). In the detection branch of the proximal end of the

bundle, the six collection fibres are positioned in a line (inset at middle left of Figure 2) in order to maximise the coupling into the input slit of the spectrograph. The PMT was linked to a computer with a time correlated single photon counting (TCSPC) card (SPC-730, Becker-Hickl GmbH, Germany) running custom written LabVIEW software that recorded fluorescence decay profiles in 16 spectral channels. A motorised filter wheel containing two emission filters (HQ 375 LP and E475 LP v2, Chroma Technology, USA) was also placed in the beam path between the fibre probe output and the spectrograph to ensure that no scattered excitation light reached the 16 channel detector. The whole system was mounted on a 60  $\times$  60  $\text{cm}^2$  optical breadboard to facilitate transportation and was fully enclosed for safe use in a clinical setting.

For each measurement we acquired 5 s of data using UV excitation followed by 5 s of data with blue excitation, and this cycle was repeated 3 times giving a total acquisition time of  $\sim 30$  s. The raw data obtained with this system thus comprised two sets of 16 spectrally resolved fluorescence decays – one for each excitation wavelength – with three identical measurements performed in all cases.

In order to properly analyse the raw data it is first necessary to determine the wavelength range collected by each PMT channel and to determine its relative sensitivity. The former was achieved by illuminating the distal end of the fibre probe with white light passed through a calibrated monochromator, which allowed the spectral centre and bandwidth of each detection channel to be determined. Secondly, the relative sensitivity of each channel was determined by recording the signal obtained from a calibrated white light source (LS-1-CAL, Ocean Optics, The Netherlands) and this information was then used to correct the intensity measured in each channel [42].

### 2.3 Experimental procedure: *in vivo* clinical measurements of skin cancer

Using the two systems described above, a total of 27 lesions on 25 patients (all of skin phototypes I–III) were investigated at Lund University Hospital prior to surgical excision of the measured region. Patients were assessed and recruited by the clinical team during outpatient clinics. The study was conducted with the approval of the local ethics committee and in accordance with the ethical principles of the Declaration of Helsinki. Each lesion was assigned a unique number for identification purposes and the characteristics of the lesions measured with each spectrometer are summarised in Table 1. We note that not

**Table 1** Summary of the skin lesions studied showing the histological diagnoses.

Lesion type (histological diagnosis)	Number of lesions	
	Instrument A	Instrument B
BCC	8	10
SCC	1	3
Benign naevus	2	2
Dysplastic naevus	1	1
Malignant melanoma	3	3
Actinic keratosis	3	3
Other	4	5
Number of lesions	22	27
Normal skin	23	27
Total measurements	45	54

all of the sites were measured with instrument A as its collection configuration meant that some lesions were unsuitable for measurement because their highly curved morphology made it difficult to correctly position the spectrometer.

Using the time-resolved system (B), two measurements were taken from the peri-lesional skin surrounding each lesion and between one and four measurements were performed on the lesion itself (depending on its size). With the steady state spectroscopy system (A), two measurements were made in each case: one on the lesion and one on the neighbouring tissue. Figure 3 shows images of two example lesions with the solid white circles showing the locations of the time-resolved fluorescence measurements and the dotted white circles indicating the regions at which the steady state spectrometer was applied. After the measurements had been performed, the entire region irradiated with instrument B was removed and sent for histopathology.

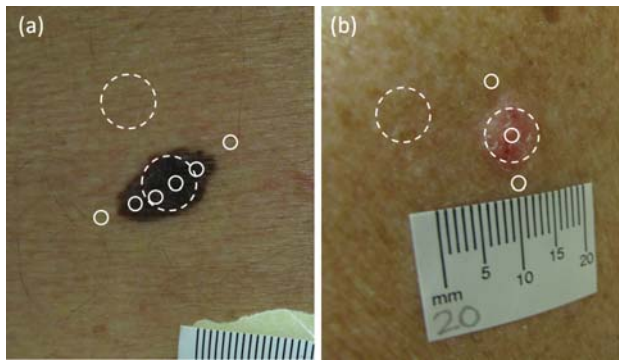


**Figure 3** (online color at: [www.biophotonics-journal.org](http://www.biophotonics-journal.org)) Example images showing where the fluorescence lifetime single-point measurements (solid circles) and the wide-field steady-state measurements (dotted circles) were performed. (a) Malignant melanoma of the back. (b) Nodular BCC of the left shoulder.

## 2.4 Data analysis

### 2.4.1 Fluorescence decay analysis

Autofluorescence from biological tissue normally exhibits a complex exponential decay profile due to the multitude of fluorophores present and their different states e.g. oxidised/reduced and free/protein bound. As only a limited number of photons are collected in each spectral channel, we chose to fit a double exponential model to the fluorescence decay curves recorded in each of the 16 spectral channels. This was performed according to Eq. (1), where  $\tau_1$  and  $\tau_2$  are the two lifetimes, and  $a_1$  and  $a_2$  are the two pre-exponential factors.

$$I(t) = a_1 \exp\left(\frac{-t}{\tau_1}\right) + a_2 \exp\left(\frac{-t}{\tau_2}\right) \quad (1)$$

From the decay parameters in Eq. (1), we calculate the mean fluorescence lifetime according to Eq. (2).

$$\tau_{\text{mean}} = \frac{a_1 \tau_1^2 + a_2 \tau_2^2}{a_1 \tau_1 + a_2 \tau_2} \quad (2)$$

The instrument response function (IRF) was determined by measuring a solution of the dye DASPI (2-(*p*-dimethylaminostyryl)-pyridylmethyl iodide, Radiant Dyes Laser Accessories GmbH, Germany) in water. DASPI is a fluorophore that has a fluorescence lifetime of less than 50 ps, which is significantly shorter than the response time of the PMT and so provides a good estimate of the IRF. As this measurement did not provide an IRF in all spectral channels, one representative spectral channel was selected and used for fitting all of the spectral channels. This approach is reasonable as the variation in the shape of the IRF between different spectral channels is low [47]. However, the temporal shift in the IRF between different spectral channels is significant and this was compensated for by introducing an adjustable temporal offset in each channel.

In order to summarise the fluorescence lifetime data, we calculated a spectrally averaged fluorescence lifetime by averaging the spectrally resolved mean lifetime values and weighting the data according to the fluorescence intensity in each channel. Hence, for each measurement site we obtained an intensity weighted average fluorescence lifetime. This approach was adopted as we observed very little variation in fluorescence lifetime with emission wavelength. The difference between these spectrally averaged mean lifetimes was then calculated for the normal and lesional tissue measured on each patient (i.e.  $\Delta\tau = \tau_{\text{lesion}} - \tau_{\text{normal}}$ ) and we note that investigating differences in fluorescence lifetime in this way

circumvents potential difficulties introduced by inter-patient variation in the measured lifetime values.

A statistical analysis was then performed on the calculated paired lifetime shifts,  $\Delta\tau$ , using the Wilcoxon signed rank test to determine if there were any significant differences between the healthy and diseased tissue. Lastly, we also calculated a mean emission wavelength from the time-resolved data at each measurement site and for each excitation wavelength. Again, we used these values to investigate whether there were significant differences between the healthy and diseased tissue.

### 2.4.2 Spectral data analysis – singular value decomposition (SVD) and linear discriminant analysis (LDA)

The spectral data obtained in this investigation comprised two fluorescence spectra from the time-resolved system (instrument B), excited at 355 and 445 nm, and one reflectance and three fluorescence spectra (excited at 355, 375 and 395 nm) from the steady state spectrometer (A). We compared the fluorescence spectra obtained with 355 nm excitation from both systems and confirmed that the measurements were consistent (data not shown). Our spectral analysis then focussed mainly on the data from spectrometer A as this provided more finely sampled spectra.

On inspection of the raw data it was clear that there was a large degree of inter-patient variation in the observed spectra. To illustrate this, we plotted the mean diffuse reflectance and fluorescence intensity for each disease type along with the standard deviation (see Section 3). Despite the inter-patient variability, there still appeared to be significant differences in the spectral signatures of healthy and diseased tissue. To quantify these differences we first used singular value decomposition (SVD) to break the acquired data down into a number of base spectral components [48, 49]. We then used the relative contributions of these components as input parameters for linear discriminant analysis (LDA) in order to predict the disease state of given measurement sites.

This approach is similar in concept to the use of SVD or principal component analysis (PCA) for feature selection followed by discriminant analysis for lesion classification, used in references [50–52]. We also note that a wide range of detailed model-based spectroscopic analysis approaches have been developed that allow physical optical parameters (such as reduced scattering and absorption coefficients, total haemoglobin concentration, scatterer size and density, blood oxygen saturation and native fluorophore

contributions) to be estimated from measured diffuse reflectance and fluorescence spectra, for example in references [32, 33, 53, 54]. However, in the present study we are only trying to establish whether differences exist between the different lesion types and so we restricted our analysis to spectral decomposition, rather than modelling the observed spectra from first principles. This approach is relatively simple and allows us to parameterise the measured spectra without making any assumptions about the constituent chromophores contained within the tissue.

In order to carry out this analysis, the numerical values describing the four spectra from the steady state system (A) were joined together (concatenated) to produce one ‘effective spectrum’ for each measurement site. We then generated a matrix,  $M$ , which contained the effective spectrum for every measured region, with each row representing a measurement site and each column representing a wavelength band. Software written in Matlab<sup>®</sup> (MathWorks<sup>TM</sup>) incorporating the inbuilt SVD function was then used to decompose  $M$  into its primary spectral components:

$$M_{n=1..N,\lambda} = U_{n=1..N,n=1..N} \Sigma_{n=1..N,n=1..N} V_{\lambda,n=1..N}^* \quad (3)$$

Here  $V$  is a matrix containing a new set of base spectral components (loadings) of the matrix,  $M$ .  $U$  is a matrix describing the relative contribution of each spectral component to the individual measurements (scores), while  $\Sigma$  is a diagonal matrix whose elements represent the overall significance of each base spectrum (the singular values). All three matrices are sorted in order of spectral significance. Thus, by plotting  $\Sigma$  on a log scale it is possible to find the number of components contributing to the effective spectra and, hence, decide upon a truncation ( $tr$ ) which will remove any redundant information (e.g. noise or the same chromophore measured in multiple bands) from the data. The matrix  $M$  can then be approximated as shown in Eq. (4).

$$M_{n=1..N,\lambda} \approx \hat{M}_{n=1..N,\lambda} \\ \approx U_{n=1..N,s=1..tr} \Sigma_{s=1..tr,s=1..tr} V_{\lambda,s=1..tr}^* \quad (4)$$

The truncated matrix,  $U$ , now contains only the scores of the most significant base spectral components for each measurement site. LDA was then used to generate a diagnostic model from all but one measurement site based on the corresponding histological diagnoses (i.e. BCC = 1, healthy = 0) and then to diagnose the remaining site. This was achieved with the Matlab<sup>®</sup> (MathWorks<sup>TM</sup>) software discussed above using the inbuilt LDA function (‘classify’). In order to ascertain the diagnostic potential of the spectral data, this leave-one-out methodology was undertaken for all the measured regions. We note that we only used the algorithm to differ-

entiate between BCCs and healthy tissue as we did not have enough measurements of other lesion types to produce reliable prediction algorithms.

In this analysis we examined the use of all spectra compared to the use of only some (e.g. just reflectance or reflectance and fluorescence excited at 375 nm) and we also looked at a variety of truncation values. Additionally, we investigated the effect of dividing each fluorescence spectrum by the reflectance prior to their use in the effective spectrum. This approach provides a partial compensation for re-absorption of the fluorescence emission and, hence, goes some way toward estimating the intrinsic fluorescence [15, 55]. Having found the approach with the best diagnostic accuracy (number of correct diagnoses/total number of measurements), we calculated the sensitivity and specificity that could be obtained using the spectral data.

### 3. Results

#### 3.1 Steady state spectral analysis

Figure 4 presents an example of the steady-state spectral data (instrument A) for a lesion that was subsequently diagnosed as a BCC. The graphs show a diffuse reflectance spectrum and three fluorescence spectra (one for each excitation wavelength) for the lesion and for adjacent ‘normal’ tissue. The instrument was calibrated as discussed in Section 2.1 and so the spectral intensities can be compared between sites.

It is clear from Figure 4 that there are spectral differences between the BCC and the adjacent normal tissue for the example shown. We note however, that there was considerable inter-patient variability in the acquired spectra, and to illustrate this we have plotted the mean reflectance spectra and mean fluorescence spectra (375 nm excitation) of healthy and diseased tissue measured from patients with BCCs (8 lesional and 7 healthy measurements) along with their associated standard deviations which provide an estimate of the inter-patient variability (see Figure 5).

From the results shown in Figure 5 it is clear that both the mean diffuse reflectance and the mean fluorescence with 375 nm excitation are lower for BCCs than they are on the surrounding healthy skin. This was also seen to be the case for the fluorescence spectra excited with 355 and 395 nm light. All of the recorded spectra exhibited a large degree of inter-patient variability and this is also clear in Figure 5 where the dotted curves indicate a spread of  $\pm 1$  standard deviation. We attribute this variability to inter-patient differences in factors such as skin

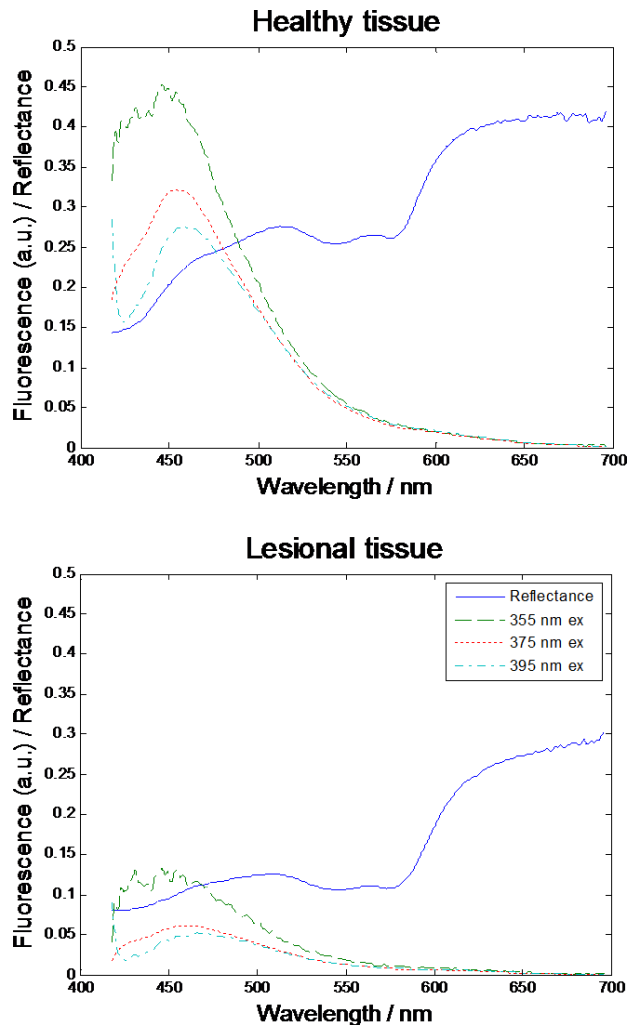


**Figure 4** (online color at: [www.biophotonics-journal.org](http://www.biophotonics-journal.org)) Example spectra from normal (upper) and lesional (lower) tissue with a histological diagnosis of BCC recorded using the steady-state spectrometer (A). Spectral intensities can be compared between sites due to the calibration of the instrument discussed in Section 2.1. Solid curve – diffuse reflectance spectrum, dashed curves – autofluorescence emission spectra at different excitation wavelengths (see key). Figure reproduced, with permission, from [45].

photo-type, level of sun exposure, age and the location of the measurement site on the body.

#### 3.2 SVD analysis of spectral data

As discussed in Section 2.4, we applied SVD to compress the diffuse reflectance and fluorescence spectra from all 15 BCC measurements made with the steady state spectrometer into a small number of base spectral components (as shown in Figure 6) in order to permit the subsequent use of LDA. We note that

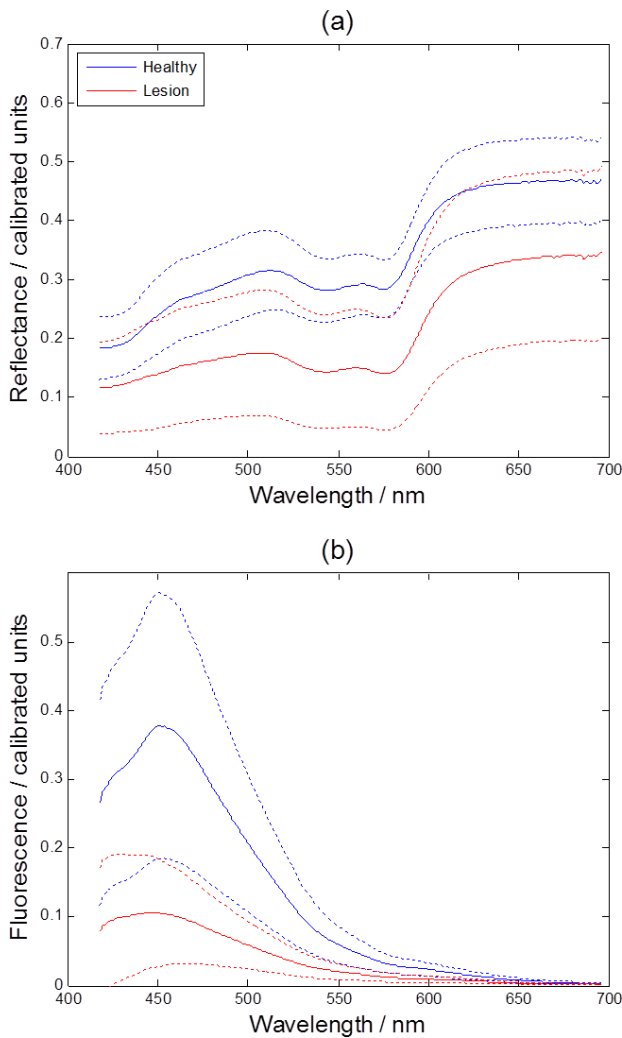


**Figure 5** (online color at: [www.biophotonics-journal.org](http://www.biophotonics-journal.org)) Graphs showing (a) mean diffuse reflectance (reproduced, with permission, from [45]) and (b) mean fluorescence with 375 nm excitation for all BCC measurement sites. Blue (upper) curves show data from healthy skin while the red (lower) curves represent the lesional measurements. Solid lines show the mean intensity values and the dotted lines give estimated confidence intervals of  $\pm 1$  standard deviation.

we tested different combinations of diffuse reflectance and fluorescence emission spectra, including ratios of fluorescence to diffuse reflectance spectra (i.e. estimates of the intrinsic fluorescence) in the effective spectrum. For BCCs, the best diagnostic accuracy was obtained when using the ratio of the 375 nm excited fluorescence spectrum to the diffuse reflectance. Hence, this data is displayed in Figure 6.

The singular values in  $\Sigma$  (Figure 6(a)) decrease steadily down to the noise floor and we observe that, after the 4<sup>th</sup> spectral component, there is a considerable drop in magnitude indicating that we may be

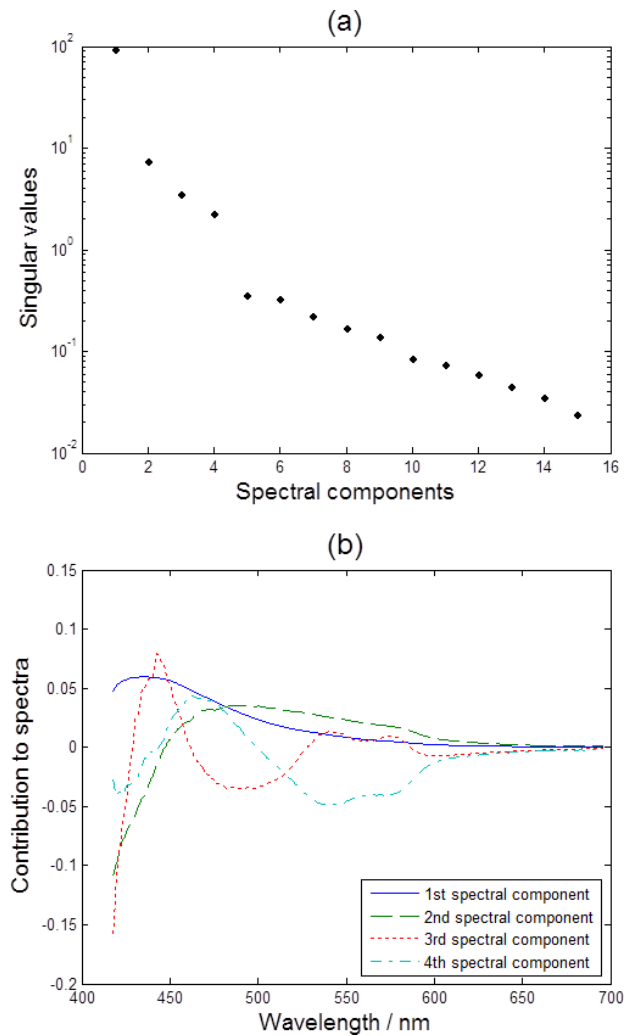


**Figure 6** (online color at: [www.biophotonics-journal.org](http://www.biophotonics-journal.org)) Output of SVD of the ratio of the fluorescence spectra (375 nm excitation) to the reflectance for all BCC measurement sites. (a) shows the significance (or singular values) of the individual spectral components while (b) shows the contributions of the first four spectral components to the fluorescence/reflectance ratio.

able to truncate the data here without a significant loss of information.

Figure 6(b) shows the contributions of the first four spectral components to the fluorescence/reflectance ratio. As is typical in SVD, the first component contains the dominant spectral features, which in this case has a form similar to a characteristic skin fluorescence spectrum. The remaining components indicate relative changes in either the fluorescence or the reflectance. In particular we can see that addition of the 3<sup>rd</sup> and 4<sup>th</sup> components will bring about changes in the contributions of the two haemoglobin absorption peaks at wavelengths of 540 and 575 nm.

As stated above, Figure 6(a) shows that truncation of the data after the 4<sup>th</sup> spectral component is reasonable due to the sudden drop in the magnitude of the singular values. For completeness, however, we tested many different truncation points when implementing LDA in order to find the one with the highest diagnostic accuracy. For BCCs alone, the optimum number of spectral components was indeed found to be four and the diagnostic accuracy, sensitivity and specificity obtained in this case were 87%, 100% and 71% respectively. This corresponded to just two false positive diagnoses in a total of 15 measurement sites (8 lesion, 7 normal) suggesting that SVD of fluorescence and reflectance spectra followed by LDA has the potential to aid the diagnosis of skin cancer.

Our future work will now involve the collection of more *in vivo* data such that we can investigate other lesion types (e.g. SCCs and malignant melanomas) on their own, as we have done for BCCs in this study. It would then not only be possible to look at the ability of the spectral data to classify a site as 'healthy' or 'unhealthy' but also its ability to classify a lesion in terms of its type.

### 3.3 Time-resolved autofluorescence measurements

As discussed in Section 2.4, the fluorescence emission spectra observed with instrument B were found to be in qualitative agreement with those measured using the steady state spectrometer (A). As the spectra acquired with instrument A have a higher spectral resolution and span a wider spectral range, we did not carry out a detailed analysis of the shape of the emission spectra acquired with the time-resolved instrument (B) but only calculated a mean emission wavelength for each measurement and here concentrate on the lifetime information.

We first quantified the intra-patient variability of the measured lifetime by comparing the values obtained from the two 'normal' peri-lesional sites on each patient (see Figure 3) and the differences in the spectrally averaged mean lifetime are shown in Figure 7. For both UV and blue excitation, the differences are evenly distributed about zero with mean values of  $-18$  and  $19$  ps respectively. Lesion 6 shows the largest difference in mean lifetime between the two normal sites for both excitation wavelengths and in each case the difference is greater than that observed in all other patients. We attribute this to the presence of scar tissue in the first peri-lesional measurement site. As an estimate of the error on the fluorescence lifetime, we also calculated the mean standard deviations of the normal tissue measure-

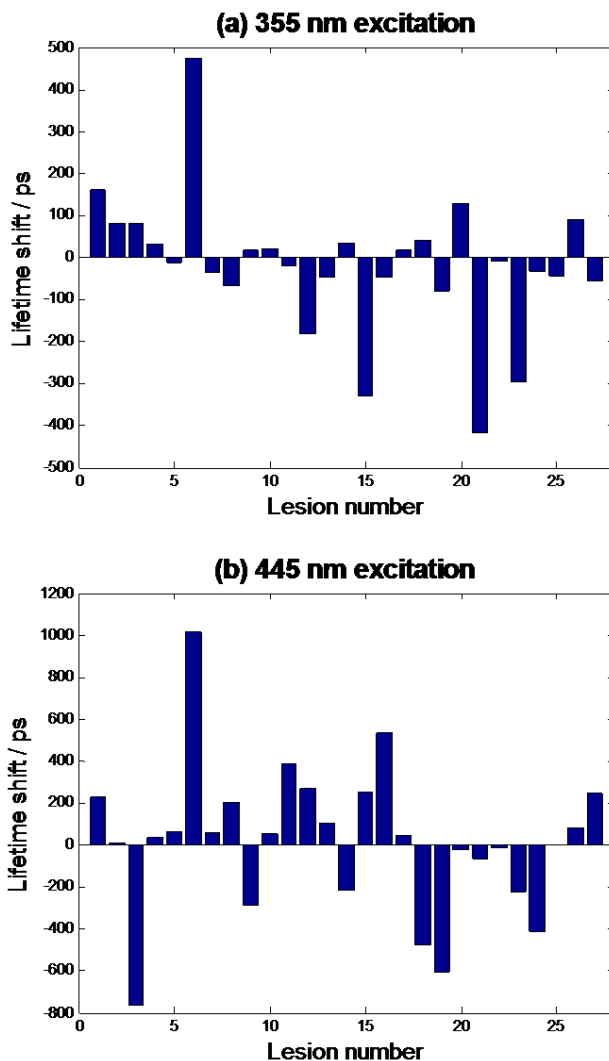


**Figure 7** (online color at: [www.biophotonics-journal.org](http://www.biophotonics-journal.org)) Graphs showing the lifetime shifts between the two measurements of the normal tissue surrounding each lesion (i.e.  $\Delta\tau = \tau_{\text{normal } 1} - \tau_{\text{normal } 2}$ ) for (a) UV and (b) blue excitation.

ments and these were found to be 75 ps with 355 nm excitation and 175 ps with 445 nm excitation.

Significant variations in the measured lifetimes were also observed between patients, and this is likely to be due to the factors discussed at the end of Section 3.1. However, we have chosen to investigate lifetime differences between the healthy and lesional tissue measured on individuals in order to circumvent the issue of inter-patient variability.

For BCCs, we then investigated the paired difference in fluorescence lifetime in each spectral channel between the healthy and diseased regions. First, it was observed that the fluorescence lifetime did not vary significantly with emission wavelength over the spectral range containing the peak fluorescent signal (425–540 nm for UV excitation and 475–550 nm for

blue excitation). The spectrally weighted healthy and lesional lifetimes, averaged across all BCC patients and including all spectral channels, were respectively  $2770 \pm 250$  ps and  $2880 \pm 409$  ps with UV excitation and  $3130 \pm 413$  ps and  $2240 \pm 480$  ps with blue excitation (where the Figures report the mean  $\pm$  one standard deviation). Similarly, the contrast observed in fluorescence lifetime did not vary substantially with emission wavelength (data not shown) and so we calculated a spectrally-integrated mean fluorescence lifetime for each measurement point for both UV and blue excitation, thus increasing the accuracy of the lifetime determination. Figure 8 shows the spectrally integrated mean lifetime shifts observed for patients diagnosed with BCC.

It is apparent from Figure 8 that there is no clear trend in the lifetime shifts of BCCs observed with

UV excitation (Figure 8(a)), while for blue (445 nm) excitation we can see that the fluorescence lifetime of BCCs is consistently lower than that of the surrounding peri-lesional skin. The mean lifetime decrease was calculated as 886 ps and the lifetime shifts observed in all but one case (lesion 1) were also seen to exceed our measurement of the mean intra-patient variability reported above (175 ps).

Finally, we calculated the mean emission wavelength for each BCC measurement site and for both excitation wavelengths. There was no significant difference in the mean emission wavelength between healthy skin and BCCs for either excitation wavelength (data not shown).

In general, the trends observed for BCCs were also seen to hold for all other lesion types. Therefore, in order to test for statistical significance, we performed Wilcoxon signed rank tests on the lifetime shifts for each individual lesion type and for all lesion types combined. For individual lesion types other than BCCs, there were not enough measurements for us to attribute statistical significance to the observed trends. For BCCs alone, however, we saw that with 445 nm excitation there was a consistent decrease in fluorescence lifetime (i.e.  $\tau_{\text{lesion}} < \tau_{\text{normal}}$ ) and that this was statistically significant with a  $p$ -value of 0.002. When investigating all the skin lesions included in this study as an ensemble (i.e. when considering all lesion types together) the same trend was observed, this time with a  $p$ -value of  $5.6 \times 10^{-6}$ .

To summarize, we have observed statistically significant differences between the fluorescence lifetime of healthy tissue and skin cancer when exciting with radiation centred at 445 nm. This is true when considering all of the skin lesions included in this study as an ensemble and when considering only the BCCs. Future work will involve the collection of more data so that it is possible to ascertain firstly whether this is true for more individual lesion types and, secondly, whether the fluorescence lifetime can be used to differentiate between different lesion types and not just between healthy and unhealthy tissue.

#### 4. Discussion

In this article we have described the application of two fibre-optic coupled spectrometers to an investigation of the optical signatures of skin cancer. The data from the two systems have been analysed separately in order to evaluate their potential for use in clinical diagnosis. We note that future work will involve the generation of a diagnostic model based on all three spectroscopic datasets, i.e. diffuse reflectance, fluorescence emission spectrum and fluorescence lifetime data. However, the diagnostic model

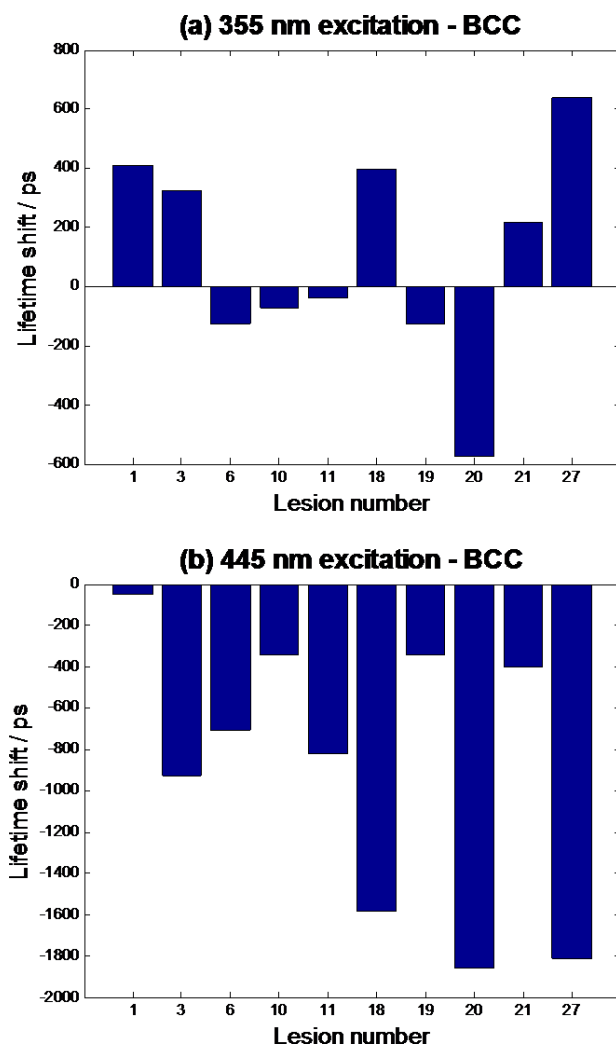


**Figure 8** (online color at: [www.biophotonics-journal.org](http://www.biophotonics-journal.org)) Graphs showing the lifetime shifts (i.e.  $\Delta\tau = \tau_{\text{lesion}} - \tau_{\text{normal}}$ ) for (a) UV and (b) blue excitation of all BCC lesions.

would then be based on a greater number of experimentally determined parameters and would require data collected over a greater number of patients than were available for this study.

The steady state data obtained with instrument A has shown firstly that the diffuse reflectance and fluorescence intensity excited at 355, 375 and 395 nm are lower in BCC lesions than they are on surrounding healthy tissue (see Figure 5). This observed difference is in agreement with the work of Rajaram et al. [33] who saw decreased diffuse reflectance and autofluorescence (with 337 nm excitation) from BCCs compared to the corresponding normal skin. Similarly Brancalion et al. reported reduced autofluorescence intensity in BCCs and SCCs, both *in vivo* (excitation at 350 nm) and in freshly resected frozen samples (360 nm excitation), which they attributed to a (histologically visible) loss of collagen and elastin [56].

In their work, Rajaram et al. chose to fit the observed spectra to models and, hence, were able to extract optical parameters of the tissue such as the absorption and scattering coefficients, haemoglobin concentration and the relative contributions of the constituent fluorophores. Using these parameters in a leave-one-out cross validation they were then able to diagnose BCCs with a sensitivity and specificity of 94% and 89% respectively [33]. We chose instead to decompose the recorded spectra into base spectral components using SVD. While this approach does not provide measurements of real optical properties, it does allow each measurement site to be characterised using a small number of parameters – i.e. the relative contributions (scores) from the few predominant spectral components. By using LDA in a leave-one-out protocol, we were able to diagnose BCCs and neighbouring healthy skin with a sensitivity and specificity of 100% and 71% respectively. This is similar to the result obtained by Rajaram et al. [33] but required no *a priori* knowledge of the constituent chromophores contained within the tissue under investigation.

The data acquired with instrument B shows that BCCs exhibit a statistically significant ( $p = 0.002$ ) decrease in their mean fluorescence lifetime relative to neighbouring healthy tissue when excited with 445 nm light (Figure 8). This result – and the observation that the fluorescence lifetime does not vary greatly with emission wavelength – are in accordance with previous *ex vivo* measurements made with the same system on freshly resected (<2 hours) tissue samples [42]. Given the small variation observed in fluorescence lifetime with emission wavelength, future studies could be carried out with a smaller number of detection channels. In addition, the absolute lifetime values observed *in vivo* are in reasonably good agreement with those seen *ex vivo* for both BCCs and normal skin using the blue exci-

tation source [42]. We also found that the mean fluorescence lifetime of BCCs was lower than that of the surrounding healthy skin in all patients and the shifts observed were greater than the mean intra-patient variation in 9 out of 10 cases. This indicates the future possibility of using time-resolved autofluorescence spectroscopy as a clinical diagnostic tool and suggests a potential sensitivity for BCC diagnosis of 90%.

When envisaging the design of such an optical system for diagnostic purposes, it is desirable to consider moving to an imaging modality rather than point spectroscopy, as this could potentially be used to rapidly screen multiple lesions in a short period of time. Much work has been done in this field including single- [56] and multi-photon imaging [57–60], fluorescence lifetime imaging [24] and also combinations of several non-linear imaging modalities [61–64]. Clearly imaging holds advantages over point spectroscopy in terms of the spatial resolution, the morphological information provided and the potential to rapidly identify margins. The point measurement systems presented in this paper, however, represent a significantly lower level of complexity and cost and are able to determine the fluorescence/reflectance spectral profiles and fluorescence lifetimes – information that is itself clinically useful – which may be used to guide the development of future imaging instrumentation. Of course, the cost of spectrometer B is higher than that of A but we note that it provides different functionality. Additionally, the recent demonstration of low cost fluorescence lifetime measurement circuitry, e.g. [65], suggests that the cost of spectrometer B could be significantly reduced.

## 5. Conclusions

A compact LED-based steady-state tissue spectrometer (A) and an ultrafast laser-based time-resolved spectrofluorometer coupled to a fibre optic probe (B) have been applied *in vivo* to a clinical investigation of skin cancer at Lund University Hospital. This study, which involved the investigation of 27 lesions, revealed clear differences between healthy and diseased tissue both in terms of spectral properties and autofluorescence lifetime (for excitation at 445 nm), indicating the potential of these instruments for clinical diagnostic purposes.

Singular value decomposition of steady state spectral data followed by linear discriminant analysis was shown to be a simple and useful tool for generating cancer prediction models which were able to diagnose BCCs with a sensitivity of 100% and a specificity of 71%. The mean autofluorescence lifetime of BCCs was shown to be lower than that of sur-

rounding healthy tissue ( $p = 0.002$ ) and the observed lifetime shifts were greater than the mean intra-patient variation in 90% of cases. Future work will involve increasing the number of lesions investigated such that it is possible to draw statistically significant conclusions for several more individual sub-classes of skin cancer such as squamous cell carcinomas and malignant melanomas.

**Acknowledgements** The authors gratefully acknowledge the funding for this work which was provided by the Engineering and Physical Sciences Research Council (EPSRC EP/F040202/1), the Photonics-4-Life European Network (FP7-ICT-2007-2, 224014) and the SKINSPEC-TION project (FP7-HEALTH-2007-A, 201577). Alex Thompson acknowledges an EPSRC funded Ph.D. studentship. Mikkel Brydegaard acknowledges funding through PIEp, a Swedish innovation initiative. Paul French acknowledges a Royal Society Wolfson Research Merit Award.

**Alex J. Thompson** received an M.Sci. degree in Physics from Durham University in 2008. He is currently pursuing a Ph.D. in the Photonics group of Imperial College London, UK. His research interests include the application of multidimensional fluorescence imaging and spectroscopy to the study and diagnosis of disease – specifically skin and gastro-intestinal cancer – as well as the use of adaptive optics to image through turbid media in microscopy and endomicroscopy.

**Sergio Coda** is a clinical research fellow between the Departments of Physics and Gastroenterology at Imperial College London. His research interests are focused on the development of novel endoscopic techniques including the application of Fluorescence Lifetime Imaging for label-free contrast of gastrointestinal disease. He received his Medical Degree in 2001 from La Sapienza University of Rome, Italy, and completed his Specialty training in General Surgery in 2007. He then pursued advanced training in therapeutic endoscopy at National Cancer Center Hospital of Tokyo, Japan.

**Mikkel Brydegaard Sørensen** obtained a Masters degree in electrical engineering with specialization in measurements and also control theory from Lund University, Sweden in 2007. He is currently pursuing a Ph.D. in Prof. Sune Svanberg's group: *Applied Molecular Spectroscopy and Remote Sensing*. His research topics include: biomedical and ecological applications of broad band elastic and inelastic optical spectroscopy, multivariate data analysis and innovation of realistic instrumentation for research in the developing world.

**Gordon Kennedy** received a B.Sc. in Applied Physics from Strathclyde University in 1988 and a Ph.D. in ultrafast laser physics from the University of St Andrews in 1993, where he remained as a postdoctoral research fellow until 1997. From 1997–2002 he was senior scientist at Diomed, a medical laser manufacturer. In 2002 he joined the Photonics Group in the Physics Department at Imperial College London working on adaptive optics for high resolution retinal imaging. His current research interests are in time-resolved biomedical imaging.

**Rakesh Patalay** graduated from University College London medical school in 1999. After practicing general internal medicine he trained as a dermatologist, working in several major teaching hospitals in the South East of England and London. He currently practices dermatology at Imperial College NHS Healthcare Trust. His current interests include using optical therapies for the treatment of acne and non-invasive imaging of the skin.

**Ulrika Waitong-Brämning** graduated with an M.D. at the University of Lund, Sweden, in 1996. In 2002 she started at the Department of Dermatology at Lund University Hospital at the skin/allergy research laboratory. In 2009 she took part in a collaboration between the Department of Dermatology and the Department of Oncology. This involved particular interest in the skin barrier function mainly measured with TEWL (transepidermal waterloss) in damaged skin or skin cancer and ways of evaluating treatments such as PDT (photodynamic therapy).

**Pieter A. A. De Beule** received an M.Sci. in Engineering Physics from UGent, Belgium (2003) and a Ph.D. in Physics (2008) for work on instrumentation for multi-dimensional fluorescence detection in the Photonics Group of Imperial College, UK. From 2007 to 2009 he was a senior physicist working at Smiths Detection, UK, on the development of novel gas sensing technologies. In 2009 he became a fellow of the International Iberian Nanotechnology Laboratory, Portugal, focusing on new instrumentation for optical imaging, being on secondment to the Laboratory of Cellular Dynamics at the Max Planck Institute for Biophysical Chemistry, Germany, and application of nanotechnology to environmental monitoring.

**Mark A. A. Neil** received a Ph.D. in Optical Information Processing at the University of Cambridge. In 1989 he moved to the Department of Engineering Science at Oxford University where he worked on holographic

and integrated optic components in photochromic materials and ferro-electric spatial light modulators as programmable phase devices for diffractive optics applications. Since 1996 he has also been working on advanced microscopy techniques and applications and is co-inventor of several techniques for realising optical sectioning in wide field microscopes. In 2002 he joined the Photonics Group in the Department of Physics at Imperial College London where he is currently a Professor.

**Stefan Andersson-Engels** is a physicist with a Ph.D. in Laser Spectroscopy for Biomedical Applications obtained in 1990. He is now, since more than 10 years ago, a professor at Lund University, Sweden, and is active in several research fields, including the development of interstitial photodynamic therapy of prostate cancer, optical spectroscopy to guide neurosurgery as well as in optical spectroscopy in pharmaceutical science.

**Niels Bendsoe** received the Physician Authorization (M.D. examination) in 1979, in 1985 he got both the Swedish and the Danish specialization in Dermatology and Venereology and in 2003 received his dissertation for Ph.D. in Medical Science; Dermatology and Venereology. He has been working at the Dermatology Clinic, Lund University Hospital since 1981 and is chief consulting dermatologist at the Lund University Hospital and the Department of Dermatology. He has been involved in the development of photodynamic therapy and tumour detection both in experimental studies as well as in the clinic.

**Paul M. W. French** received the B.Sc. Degree in Physics in 1983 and the Ph.D. degree in 1987 from Imperial College London. Much of his subsequent research career has been based at Imperial College London. In 1988 he was a visiting professor at the University of New Mexico and from 1990 to 1991 he worked on ultrafast all optical switching in optical fibres at AT&T Bell Laboratories, Holmdel, NJ. He is currently a Professor of Physics at Imperial College London and is Head of the Photonics Group. His current research includes a strong emphasis on fluorescence lifetime imaging for molecular biology, drug discovery and clinical applications. Prof. French is a Fellow of the Institute of Physics and the Optical Society of America and is the recipient of a Royal Society Wolfson Research Merit Award.

**Katarina Svanberg**, M.D. and Ph.D., is a chief consultant in Oncology and a professor of oncology at the Lund University Hospital. She is the director of the

Lund University Medical Centre and board member of the Lund Laser Centre, which is a European Large Scale Facility. During 2011 she is the president of the International Society for Optics and Photonics (SPIE). Her research fields include early tumour detection using various laser-based spectroscopic techniques, such as laser-induced fluorescence tissue characterization as well as photodynamic therapy in clinical and experimental use.

**Chris Dunsby** received an MSci. degree from Bristol University in 2000. In 2003 he received a Ph.D. from Imperial College, UK, in "Wide-field Coherence-gated Imaging Techniques Including Photorefractive Holography". He is now a joint lecturer between Photonics, Department of Physics and the Department of Histopathology, Division of Investigative Science at Imperial. His research interests are centred on the application of photonics and ultrafast laser technology to biomedical imaging and include multiphoton microscopy, multi-parameter fluorescence imaging and fluorescence lifetime imaging.

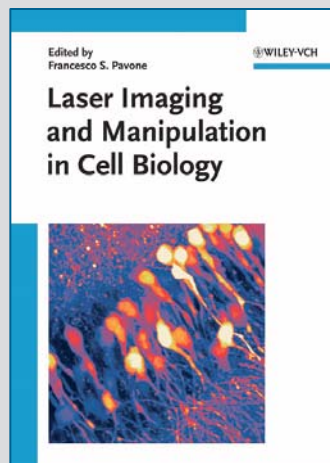
## References

- [1] Cancer Research UK, <http://info.cancerresearchuk.org/cancerstats/types/skin/#incidence> (2010).
- [2] American Cancer Society, [www.cancer.org](http://www.cancer.org) (2010).
- [3] T. L. Diepgen and V. Mahler, *Br. J. Dermatol.* **146**, 1–6 (2002).
- [4] M. Trakatelli, C. Ulrich, V. Del Marmol, S. Euvrard, E. Stockfleth, and D. Abeni, *Br. J. Dermatol.* **156**, 1–7 (2007).
- [5] M. Mogensen and G. B. Jemec, *Dermatol. Surg.* **33**(10), 1158–1174 (2007).
- [6] I. J. Bigio and J. R. Mourant, *Phys. Med. Biol.* **42**(5), 803–814 (1997).
- [7] R. Marchesini, N. Cascinelli, M. Brambilla, C. Clemente, L. Mascheroni, E. Pignoli, A. Testori, and D. R. Venturoli, *Photochem. Photobiol.* **55**, 515–522 (1992).
- [8] V. Backman, R. Gurjar, K. Badizadegan, L. Itzkan, R. R. Dasari, L. T. Perelman, and M. S. Feld, *IEEE J. Sel. Top. Quant. Electron.* **5**, 1019–1026 (1999).
- [9] S. L. Jacques, J. R. Roman, and K. Lee, *Lasers Surg. Med.* **26**(2), 119–129 (2000).
- [10] S. L. Jacques, J. C. Ramella-Roman, and K. Lee, *J. Biomed. Opt.* **7**(3), 329–340 (2002).
- [11] K. J. Busam, C. Charles, G. Lee, and A. C. Halpern, *Mod. Pathol.* **14**(9), 862–868 (2001).
- [12] S. Gonzalez and Z. Tannous, *J. Am. Acad. Dermatol.* **47**(6), 869–874 (2002).
- [13] D. Huang, E. A. Swanson, C. P. Lin, J. S. Schuman, W. G. Stinson, W. Chang, M. R. Hee, T. Flotte, K. Gregory, C. A. Puliafito, and J. G. Fujimoto, *Science* **254**(5035), 1178–1181 (1991).

- [14] P. J. Caspers, G. W. Lucassen, and G. J. Puppels, *Biophys. J.* **85**(1), 572–580 (2003).
- [15] M. Mycek and B. W. Pogue, *Handbook of Biomedical Fluorescence* (Marcel Dekker, New York, 2003).
- [16] R. R. Anderson and J. A. Parrish, *J. Invest. Dermatol.* **77**(1), 13–19 (1981).
- [17] M. C. Skala, K. M. Riching, D. K. Bird, A. Gendron-Fitzpatrick, J. Eickhoff, K. W. Eliceiri, P. J. Keely, and N. Ramanujam, *J. Biomed. Opt.* **12**(2), 024014 (2007).
- [18] D. R. Eyre, M. A. Paz, and P. M. Gallop, *Annu. Rev. Biochem.* **53**, 717–748 (1984).
- [19] L. Marcu, J. A. Jo, P. V. Butte, W. H. Yong, B. K. Pikul, K. L. Black, and R. C. Thompson, *Photochem. Photobiol.* **80**(1), 98–103 (2004).
- [20] L. Marcu, M. C. Fishbein, J. M. I. Maarek, and W. S. Grundfest, *Arterioscler. Thromb.* **21**(7), 1244–1250 (2001).
- [21] D. S. Elson, J. Requejo-Isidro, I. Munro, F. Reavell, J. Siegel, K. Suhling, P. Tadrous, R. Benninger, P. Lanigan, J. Mcginty, C. Talbot, B. Treanor, S. Webb, A. Sandison, A. Wallace, D. Davis, J. Lever, M. A. A. Neil, D. Phillips, G. W. Stamp, and P. M. W. French, *Photochem. Photobiol. Sci.* **3**(8), 795–801 (2004).
- [22] P. V. Butte, Q. Fang, J. A. Jo, W. H. Yong, B. K. Pikul, K. L. Black, and L. Marcu, *J. Biomed. Opt.* **15**(2), 027008 (2010).
- [23] P. V. Butte, B. K. Pikul, A. Hever, W. H. Yong, K. L. Black, and L. Marcu, *J. Biomed. Opt.* **10**(6), 064026 (2005).
- [24] N. P. Galletly, J. Mcginty, C. Dunsby, F. Teixeira, J. Requejo-Isidro, I. Munro, D. S. Elson, M. A. A. Neil, A. C. Chu, P. M. W. French, and G. W. Stamp, *Br. J. Dermatol.* **159**(1), 152–161 (2008).
- [25] J. Mcginty, N. P. Galletly, C. Dunsby, I. Munro, D. S. Elson, J. Requejo-Isidro, P. Cohen, R. Ahmad, A. Forsyth, A. V. Thillainayagam, M. A. A. Neil, P. M. W. French, and G. W. Stamp, *Biomed. Opt. Express* **1**(2), 627–640 (2010).
- [26] A. Pradhan, B. B. Das, K. M. Yoo, R. R. Alfano, J. Cleary, R. Prudente, and E. Celmer, *Proc. SPIE Conference* **1599**, 81–84 (1992).
- [27] C. Y. Wang, H. M. Chen, C. P. Chiang, C. You, and T. C. Hsiao, *Lasers Surg. Med.* **37**(1), 37–45 (2005).
- [28] M. Mycek, K. Schomacker, and N. Nishioka, *Gastroint. Endosc.* **48**(4), 390–394 (1998).
- [29] T. J. Pfefer, D. Y. Paithankar, J. M. Poneris, K. T. Schomacker, and N. S. Nishioka, *Lasers Surg. Med.* **32**(1), 10–16 (2003).
- [30] J. Leppert, J. Krajewski, S. R. Kantelhardt, S. Schlaffer, N. Petkus, E. Reusche, G. Huttmann, and A. Giese, *Neurosurgery* **58**(4), 759–767 (2006).
- [31] R. Cicchi, A. Crisci, A. Cosci, G. Nesi, D. Kapsokalyvas, S. Giancane, M. Carini, and F. S. Pavone, *Opt. Express* **18**(4), 3840–3849 (2010).
- [32] N. Rajaram, T. J. Aramil, K. Lee, J. S. Reichenberg, T. H. Nguyen, and J. W. Tunnell, *Appl. Opt.* **49**(2), 142–152 (2010).
- [33] N. Rajaram, J. S. Reichenberg, M. R. Migden, T. H. Nguyen, and J. W. Tunnell, *Lasers Surg. Med.* **42**(10), 716–727 (2010).
- [34] N. Kollias and G. Zonios, *Vib. Spectrosc.* **28**(1), 17–23 (2002).
- [35] W. Lohmann, M. Nilles, and R. H. Bodeker, *Naturwissenschaften*, **78**(10), 456–457 (1991).
- [36] W. Lohmann and E. Paul, *Naturwissenschaften*, **75**(4), 201–202 (1988).
- [37] M. Panjehpour, C. E. Julius, M. N. Phan, T. Vo-Dinh, and S. Overholt, *Lasers Surg. Med.* **31**(5), 367–373 (2002).
- [38] H. Sterenberg, M. Motamedi, R. F. Wagner, M. Duvic, S. Thomsen, and S. L. Jacques, *Lasers Med. Sci.* **9**(3), 191–201 (1994).
- [39] G. A. Wagnieres, W. M. Star, and B. C. Wilson, *Photochem. Photobiol.* **68**(5), 603–632 (1998).
- [40] T. Glanzmann, J. P. Ballini, H. Van Den Bergh, and G. Wagnieres, *Rev. Sci. Instrum.* **70**(10), 4067–4077 (1999).
- [41] J. D. Pitts and M. A. Mycek, *Rev. Sci. Instrum.* **72**(7), 3061–3072 (2001).
- [42] P. A. A. De Beule, C. Dunsby, N. P. Galletly, G. W. Stamp, A. C. Chu, U. Anand, P. Anand, C. D. Benham, A. Naylor, and P. M. W. French, *Rev. Sci. Instrum.* **78**(12), 123101 (2007).
- [43] Y. Sun, R. Liu, D. S. Elson, C. W. Hollars, J. A. Jo, J. Park, Y. Sun, and L. Marcu, *Opt. Lett.* **33**(6), 630–632 (2008).
- [44] J. Blackwell, K. M. Katika, L. Pilon, K. M. Dipple, S. R. Levin, and A. Nouvong, *J. Biomed. Opt.* **13**(1), 014004 (2008).
- [45] A. J. Thompson, H. B. Manning, M. Brydegaard, S. Coda, G. Kennedy, R. Patalay, U. Waitong-Brämning, P. A. A. De Beule, M. A. A. Neil, S. Andersson-Engels, Y. Itoh, N. Bendsøe, C. Dunsby, K. Svanberg, and P. M. W. French, *SPIE Photonics West Biomedical Optics Symposium*, 2011, San Francisco, CA, SPIE.
- [46] M. Brydegaard, P. Lundin, Z. Guan, A. Runemark, S. Akesson, and S. Svanberg, *Appl. Opt.* **49**(24), 4531–4544 (2010).
- [47] W. Becker, *User Manual – PML-16-C 16 Channel Detector Head for Time-Correlated Single Photon Counting* (Becker & Hickl GmbH, 2006).
- [48] M. Brydegaard, N. Haj-Hosseini, K. Wardell, and S. Andersson-Engels, *IEEE Photonics J.* **3**(3), 407–421 (2011).
- [49] P. Dewilde and E. Deprettere, *Singular Value Decomposition: an introduction*, in *SVD and Signal Processing: Algorithms, Applications and Architectures*, E. Deprettere (ed.) (Elsevier Science Publishers, Amsterdam, The Netherlands, 1988).
- [50] N. M. Marin, A. Milbourne, H. Rhodes, T. Ehlen, D. Miller, L. Benedet, R. Richards-Kortum, and M. Follen, *Gynecol. Oncol.* **99**(3, Suppl 1), S116–S120 (2005).
- [51] A. D. Ghanate, S. Kothiwale, S. P. Singh, D. Bertrand, and C. M. Krishna, *J. Biomed. Opt.* **16**(2), 025003 (2011).
- [52] E. N. Atkinson, M. F. Mitchell, N. Ramanujam, and R. Richards-Kortum, *J. Cell Biochem. Suppl.* **23**, 125–130 (1995).
- [53] C. R. Weber, R. A. Schwarz, E. N. Atkinson, D. D. Cox, C. Macaulay, M. Follen, and R. Richards-Kortum, *J. Biomed. Opt.* **13**(6), 064016 (2008).

- [54] T. J. Farrell, M. S. Patterson, and B. Wilson, *Med. Phys.* **19**(4), 879–988 (1992).
- [55] Q. Zhang, M. G. Muller, J. Wu, and M. S. Feld, *Opt. Lett.* **25**(19), 1451–1453 (2000).
- [56] L. Brancalione, A. J. Durkin, J. H. Tu, G. Menaker, J. D. Fallon, and N. Kollias, *Photochem. Photobiol.* **73**(2), 178–183 (2001).
- [57] E. Dimitrow, I. Riemann, A. Ehlers, M. J. Koehler, J. Norgauer, P. Elsner, K. Konig, and M. Kaatz, *Exp. Dermatol.* **18**(6), 509–515 (2009).
- [58] E. Dimitrow, M. Ziemer, M. J. Koehler, J. Norgauer, K. Konig, P. Elsner, and M. Kaatz, *J. Invest. Dermatol.* **129**(7), 1752–1758 (2009).
- [59] B. R. Masters, P. T. So, and E. Gratton, *Ann. N. Y. Acad. Sci.* **838**(1), 58–67 (1998).
- [60] J. Paoli, M. Smedh, A. M. Wennberg, and M. B. Ericson, *J. Invest. Dermatol.* **128**(5), 1248–1255 (2008).
- [61] R. Cicchi, S. Sestini, V. De Giorgi, D. Massi, T. Lotti, and F. S. Pavone, *J. Biophotonics* **1**(1), 62–73 (2008).
- [62] V. De Giorgi, D. Massi, S. Sestini, R. Cicchi, F. S. Pavone, and T. Lotti, *J. Eur. Acad. Dermatol. Venereol.* **23**(3), 314–316 (2009).
- [63] S. J. Lin, S. H. Jee, C. J. Kuo, R. J. Wu, W. C. Lin, J. S. Chen, Y. H. Liao, C. J. Hsu, T. F. Tsai, Y. F. Chen, and C. Y. Dong, *Opt. Lett.* **31**(18), 2756–2758 (2006).
- [64] R. Cicchi, D. Massi, S. Sestini, P. Carli, V. De Giorgi, T. Lotti, and F. S. Pavone, *Opt. Express*, **15**(16), 10135–10148 (2007).
- [65] R. A. Colyer, C. Lee, and E. Gratton, *Microsc. Res. Tech.* **71**(3), 201–213 (2008).

### +++ Suggested Reading +++ Suggested Reading +++ Suggested Reading +++



2010. XIV, 246 pages,  
71 figures, 3 in color.  
Hardcover.  
€ 99.– / £ 85.– / US\$ 135.–  
ISBN: 978-3-527-40929-7

Edited by *FRANCESCO S. PAVONE*

*European Laboratory for Non Linear Spectroscopy, and Department of Physics, University of Florence*

### Laser Imaging and Manipulation in Cell Biology

In 'Laser Imaging and Manipulation in Cell Biology', the editor has gathered a team of international experts to present the latest advances in the field of laser imaging and manipulation techniques. The result is broad coverage of the interactions with biological samples to perform novel optical manipulation operations, both on the cellular and tissue levels.

Of interest to physicists working and researching laser tissue mechanisms, cell biologists investigating new imaging and manipulation operation on the cellular level, medical doctors working with new laser therapies and diagnostic tools, as well as engineers developing new technologies in the field of optics and lasers.

Register now for the free  
**WILEY-VCH Newsletter!**  
[www.wiley-vch.de/home/pas](http://www.wiley-vch.de/home/pas)

WILEY-VCH • P.O. Box 10 11 61 • 69451 Weinheim, Germany  
Fax: +49 (0) 62 01 - 60 61 84  
e-mail: [service@wiley-vch.de](mailto:service@wiley-vch.de) • <http://www.wiley-vch.de>



## PAPER IX

### **Complete parameterization of temporally and spectrally resolved laser induced fluorescence data with applications in bio-photonics**

M. Brydegaard, A.J. Thompson, C. Dunsby, S. Andersson-Engels, N. Bendsø, K. Svanberg and S. Svanberg

*Manuscript in preparation.*

# Complete Parameterization of Temporally and Spectrally Resolved Laser Induced Fluorescence Data with Applications in Bio-Photonics

Mikkel Brydegaard,<sup>1,\*</sup> Alex Thompson,<sup>2</sup> Chris Dunsby<sup>2</sup>, Stefan Andersson-Engels<sup>1</sup>,  
Niels Bendsoe<sup>3</sup>, Katarina Svanberg<sup>4,5</sup> and Sune Svanberg<sup>1,5</sup>

<sup>1</sup>Physics Department, Lund University, P.O. Box 118, SE-221 00, Lund, Sweden

<sup>2</sup>Photonics Group, Physics Department, Imperial College London, London SW7 2AZ, UK

<sup>3</sup>Department of Dermatology, Lund University Hospital, SE-221 85 Lund, Sweden

<sup>4</sup>Department of Oncology, Lund University Hospital, SE-221 85 Lund, Sweden

<sup>5</sup>Center for Optical and Electromagnetic Research, South China Normal University, Guangzhou 510006, China

\*Corresponding author: [Mikkel.brydegaard@fysik.lth.se](mailto:Mikkel.brydegaard@fysik.lth.se)

*We present a dataset of spectrally and temporally resolved multi excitation fluorescence, recorded in vivo clinically. We demonstrate how data in the spectral and temporal domains are in certain ways coupled, and provide a method for integrated and effective parameterization for spectrally and time resolved fluorescence. This parameterization is based on linear algebra, matrix formulation and system identification. We demonstrate how to empirically extract single exponentially decaying components and provide rectified emission spectra without prior knowledge. We investigate the potential for improved cancer diagnostics according to the reduced parameters along the various domains.*

OCIS codes: 300.2530 Fluorescence, laser-induced, 300.6500 Spectroscopy, time-resolved 170.3650 Lifetime-based sensing, 170.6510 Spectroscopy, tissue diagnostics

## Introduction

### Outline

In this paper we briefly review the historical background of applied fluorescence spectroscopy in biomedicine, and we walk through the different approaches for dealing with emission quenching leading to time resolved fluorescence spectroscopy. We then briefly revise the parallel development of linear algebra and its application to population dynamics in ecology and nuclear physics, and, present an instrument capable of acquiring spectrally and temporally resolved fluorescence data as well as *in vivo* clinical datasets, both of which have earlier been presented. We then attend to the data evaluation issue and evaluate to what degree the temporal and spectral domains provide partly complementary information and how to systematically parameterize both domains with an integrated model. It is also shown how to further use this dynamic model for a unique rectification of the purely decaying fluorescence emissions from each transition. We demonstrate how to turn the arbitrary spectral components, which are typically obtained from singular value decomposition (SVD), similar to principal component analysis (PCA), into unique pure emissions from each transition. This will greatly increase the inter-comparability between future applied fluorescence studies. Our approach is entirely empirical, requires no *a priori* knowledge and offers a way to obtain the pure fluorescence components from fluorophores in their natural environment in complex biological matrixes. At the end of the paper we present the deduced parameters with respect to clinical oncological measurements.

### Historical background

During the 1980s and 1990s physicist started to explore new opportunities for biomedical electro-optical diagnostics with expectations of non-intrusive measurements and immediate evaluation. The new trends were permitted by the emerging technologies such as widely available personal computers for data interpretation, compact lasers at new wavelengths and the charged coupled devices (CCD). Mostly, varieties of optical fiber probes or imaging systems were developed<sup>1,2</sup>. Several successful applications based on the dominating chromophores such as oxy- and de-oxy-haemoglobin<sup>3,4</sup> were developed. In relation to this, the discipline of light transport in highly scattering media was established<sup>5-12</sup>. To extend the list of measurable endemic substances and tissue properties, the next natural step was the analysis of tissue autofluorescence<sup>1,13-18</sup> and the use of fluorescent sensitizers such as protoporphyrin nine, PpIX<sup>19,20</sup>. Since the fluorescence phenomenon is a secondary effect of absorption, the measured intensity of

inelastic photons is weaker by orders of magnitude in comparison to the elastic photons. For this reason it was quickly realized that acquired fluorescence data were heavily perturbed by the elastic properties of absorption and scattering at both the wavelength of excitation and the wavelength of emission. To proceed with absolute quantification of diverse fluorophores, methods for deriving the intrinsic fluorescence were developed. Many such efforts were based on measuring both elastic and inelastic properties, and then compensating the fluorescence signals for the elastic perturbations using knowledge from light transport in scattering media theory<sup>21-27</sup>. The fact that reflectance is governed by absorption, scattering, the anisotropic scattering factor and the refractive index once more led to an underdetermined system of equations with more unknowns than measurands, and even if the developed diffusion and Monte Carlo theories were advancing, it was hard to find practical application besides a rough approximation using ratio of the total escape of elastic and inelastic light<sup>28, 29</sup>. For this reason the instrumentation was extended to multiple fiber probes<sup>30</sup> and spatially resolved reflectance and fluorescence measurements<sup>31, 32</sup>. Other attempts were based on temporally resolving the fluorescence decays, arguing that lifetimes would be insensitive to the elastic properties and that they may provide additional information, e.g. on fluorophore environment. The instruments used were based either on the recording of a transient fluorescence following pulsed laser excitation<sup>27, 33, 34</sup>, on the phase delay in frequency domain methods<sup>35-38</sup> or on single photon counting using mode locked lasers<sup>39, 40</sup>. Some of the best performing instruments<sup>41</sup> draw on experience from atomic physics, where fluorescence lifetimes had been measured precisely in order to determine the absolute emission line strength of various elements<sup>42</sup>. Whereas the emission wavelengths were previously discretized in a large number of spectral bands, the fluorescence decays were in many cases collected in a broad band given by the sensitivity of the detector (photo multiplying tube PMT, or avalanche photodiode, APD)<sup>34</sup> or the intensified camera (ICCD)<sup>33, 43</sup>. It was quickly realized that the decay of the auto fluorescence of tissue could not be explained by a single exponential, but required a sum of several exponential functions. With some of the best performing systems scientists were able to fit up to three exponential decays, each with a different amplitude and lifetime<sup>41</sup>; however, the fitted coefficients were not necessarily unique. The fitting procedures turned out to be extremely ill-conditioned and numerically very sensitive to erroneously estimated background levels. The fact that the data from single photon counting instruments gives Poisson distributed intensities further complicated fitting with, e.g. least squares<sup>44</sup>. The reason why a sum of several exponential decays is necessary, is that electrons move not only between the ground state and one excited level, but several excited levels are involved. This should be obvious in tissue matrix where the optical absorption is due to several molecular constituents; however, even purely synthetic substances, such as elastin or collagen, also required several exponential decays for a fair representation<sup>41</sup>.

In parallel and independently of the optical community, the research in control theory, inherited from the rocketry earlier in the century, also experienced vast progress during the 1980s and 1990s. Whereas the discipline was previously based on analog electronics, microprocessors and computers could now be used for sophisticated control; especially linear algebra could now find real-time applications. The so-called state space models<sup>45</sup> were developed to describe the dynamics and interaction of populations of kinetic- and potential energy in robot joints. Advanced methods for creating such dynamical models from measured data were established in the discipline of system identification<sup>46-50</sup>. The progress was quickly welcomed in many other communities, for example, for example, multispecies population ecology<sup>51-54</sup>. Here the models could effectively describe the size of populations of interacting species in an ecosystem over time. Further, the entire stability theory could be imported directly, with crucial applications for predicting sustainability of ecosystems prior to their collapses. Such models were previously applied to describe populations of nuclear isotopes, their decay and their interaction in terms of mother and daughter activity<sup>55-59</sup>.

In optical spectroscopy only a few groups have started to adopt system identification approaches, e.g. in bleaching studies<sup>60, 61</sup>. Here the simple linear models are capable of describing complicated phenomena such as one chromophore bleaching out of the interrogation volume and ceasing to obscure underlying chromophores<sup>62</sup>, and the phenomenon of a fluorophore bleaching into another fluorescent rest product with a different spectral signature<sup>63-65</sup>. Phenomena like production or inflow into the interrogation volume<sup>66, 67</sup> can further be explained by adding a simple bias to the model. To our knowledge, the community of fluorescence lifetime spectroscopy, also having a great deal to do with electron population dynamics, has so far mainly disregarded the progress in linear algebra based dynamic models and system identification. Considering absorption as electrons migrating from the ground state population to the excited state population, and fluorescence as electrons migrating from excited state populations to lower lying states, one quickly realizes that several routes would produce emitted fluorescent light, where a sum of exponential decays would not reflect the actual electron population sizes. This would, for example, be the case if an excited state decays non-radiatively to a second state, which decays to the ground states radiatively. Initially, there would be no fluorescence since the intermediate state is empty. In the case of one excited state having two radiative decay routes with different spectral signatures, the depletion of the excited state would be governed by the total transition rate;

this could even occur in a complex biological matrix where one fluorophore pumps another fluorophore<sup>68</sup>. All such mechanisms can be described by a simple linear dynamic model. Even quantum interference<sup>69</sup> can be explained by the very same model.

In this paper we present an effective and systematic way of completely parameterizing both spectrally and temporally resolved fluorescence, obtained from the instrument presented in<sup>70, 71</sup>. Our approach is based on empirical observations of the information down to the given noise limits for the system rather than on theoretical assumptions, which might not be valid in a given practical situation or which might be underdetermined for the given signal to noise conditions. Using this method we evaluate to what extent the time- and spectral domain provide independent information in the data set analyzed, and how to evaluate the dynamic model in order to obtain the pure spectral signature of each decaying transition.

## **Materials and methods**

### ***Sample set***

A total of 25 patients participated in the measurement campaign in the dermatology clinic at Lund University Hospital. Together they had 27 body locations where lesions were suspected. At each location both the suspected lesion and the surrounding tissue were subject to several measurements. 120 measurements of fluorescence lifetime were made. Out of those, 45 measurements of steady state fluorescence and reflectance spectroscopy were also performed on the exact same locations for cross validation. Each suspected lesion is also associated with an immediate evaluation by the eye of the dermatologist, a subset of the lesions were subject to biopsies and histological evaluation. According to the final diagnosis, 10 locations were classified as basal cell carcinoma, 6 as squamous cell carcinoma, 4 as melanoma types, 3 as actinic keratosis, 3 as benign lesions, 1 as Kaposi's sarcoma, and 1 as pyogenic granuloma. Participating patients spanned the age 41-94 years, median age being 74 years. 76% were men, 88% were blue eyed Caucasians, 32% had smoked during their lifetime, 20% mentioned particular exposure to sunlight and 20% additionally suffered from diabetes. The clinical context of the measurements, the patient distribution as just described, and the data recorded are reported in an earlier, more clinically directed paper<sup>71</sup>.

### ***Instrument for spectrally and temporally resolved fluorescence***

The apparatus for measuring spectrally resolved *in-vivo* tissue auto-fluorescence was developed by the Biophotonics group, Imperial College, London. Details regarding the instrument can be found in<sup>70, 71</sup>. In summary, the instrument excites the tissue by either a frequency tripled Yb:Glass laser at 355 nm or a GaN diode laser at 445 nm, emitting ~10ps and ~100 ps pulses, respectively, with megahertz repetition rates. Excitation light is delivered by a 200  $\mu\text{m}$  non-contact fiber and collected by six fibers with the same diameter. The field of view is ~ $\varnothing$ 2 mm. After long-pass filtering, light is analyzed by a grating spectrometer with a 16 multi-element photomultiplier in single-photon counting mode. The obtained time resolution is approximately 200 ps within a time window of 16 ns. The two outermost spectral bands were omitted in this study because of poor performance, leaving us with 14 spectral bands. Hereafter, the spectrometer covered 390-570 nm with a spectral resolution of 14 nm. The photon arrivals were measured using time correlated single photon counting into 4096 time channels over an 18 ns temporal detection window. The excitation light was attenuated to a low average photon probability, in order to avoid pile-up. Because of different temporal response of each spectral band the lifetime curves are shifted in respect to each other in such way that the rise time points of half maximum matches each other in time. The first 500 ps immediately after the pulse were omitted from the analysis to avoid effects from the width of the excitation pulse: this left 2352 timeslots during a 14 ns window. The spectral decays were averaged three times, and the total acquisition time for both excitations acquiring was 30 s. The dark current was estimated from the pre-pulse period. The relative intensity scale was calibrated by using a filament lamp.

### ***Instrument for spectrally resolved steady state fluorescence and reflectance***

A simpler light emitting diode based instrument was used for cross-validation on the identical spots as above. The instrument acquires steady-state fluorescence excited at 355 nm, 375 nm, 395 nm and 405 nm, and also steady-state diffuse reflectance from 420-700 nm; for details see<sup>71</sup>. In this study only reflectance from this instrument is considered, and the spectra are further reduced to two parameters related to the content of melanin and hemoglobin for each lesion and for the adjacent healthy skin.

## RGB digital still photography

Close up macro images of each lesion and the surrounding were taken with a digital still camera. Precise location of each steady state and life time measurement were super-imposed on the pictures. The pictures and the super-imposed position were used to visually judge two Boolean values for the presence of melanin, hereafter referred to as ‘melanization’, and a red appearance due to increased haemoglobin, referred to as ‘haemoglobilization’.

## Theory and Data Analysis

### Time Resolved Fluorescence as a Dynamical System.

In optical spectroscopy the state electron populations are not measured themselves. However, when molecules are excited to an upper state it can be measured in terms of absorption and when they subsequently return to the ground state, it is possible to measure that as fluorescence. Because of the Boltzmann distribution, thermal equilibrium excited populations at room temperature are negligible in comparison to the population in the ground state. For this reason a tissue volume system brought out of equilibrium, e.g. by photoabsorption of an impinging UV laser pulse, will emit from the excited state with an intensity directly proportional to the population in the excited state. Part of the fluorescent light is transported to the surface of the tissue in a random walk manner, and is eventually received by the collecting optics, in our case a simple fiber tip.

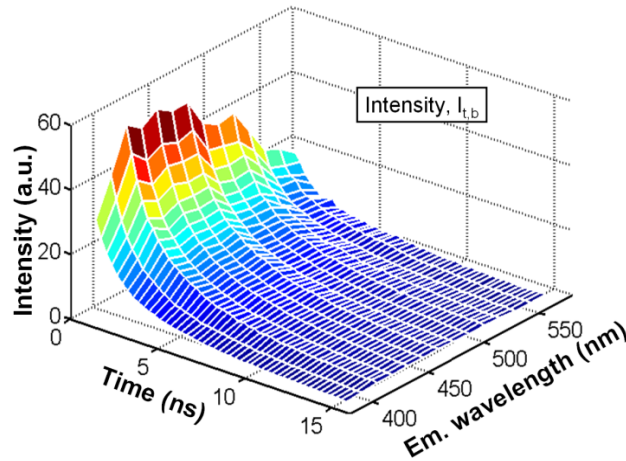


Fig. 1. Example of spectrally and temporally resolved fluorescence counts,  $I_{t,b,n}$ , from healthy tissue adjacent to a lesion on a patient suffering from Actinic Keratosis. Excitation wavelength: 355 nm.

Our time-resolved system provides a discrete fluorescent intensity count tensor,  $I_{t,b,n}$ , as a function of time after excitation and emission wavelength band for each of the 45 samples in the sample set. An example of a single acquisition is illustrated in Fig.1.

$I_{t,b,n}$	Photon counts compensated for dark current and the instruments spectral response curve, as a function of time, spectral emission and sample number
$t$	Timeslot index, in this study $t=1..2352$ , $\Delta_t=0.88..15.24$ ns
$\Delta_t$	Delay after pulse peak
$b$	Spectral band, in this study $b=1..14$
$\lambda_b$	Effective band wavelength, $\lambda_b=388..568$ nm
$n$	Sample number.

In biological solid-state molecules or tissue matrices the transitions are heavily perturbed and the emission bands are very broad and to a great extent overlapping. For this reason decomposition methods are required to estimate the strength of each line separately. Such methods could be linear projections or singular value decomposition (SVD). As already mentioned, the recorded fluorescence data are determined by the intrinsic fluorescence properties, but are also heavily perturbed by elastic light scattering in tissue. This means that it is a non-trivial task to project an acquired spectrum onto fluorescence spectra obtained from pure synthetic organic compounds. Furthermore, acquired fluorescence spectra will depend on the measurement geometry and might

change with the micro-environment of the fluorophore, e.g. pH or temperature. An empirical approach of facilitating fluorescence decomposition in a few base spectra is SVD<sup>72-75</sup>, where the observations are expanded in a number of base spectra sorted in descending significance. In this study we choose to temporally collapse the dimension of time and sample number, prior to SVD, in order to maintain a common base spectra set for all samples and times, and in this way we are able to do a comparative study. Following this decomposition we will be able to express our recorded fluorescence spectra from any sample at any time after excitation, as a linear combination of a reduced set of spectral components.

$$I_{b,m} = U_{m,s} \Sigma_{s,s} V'_{b,s} \quad (Eq.1)$$

$I_{m,b}$	Intensity counts compensated for background and spectral response
$m$	Running index of spectra including all time slots and samples, $m = 1..N*T$
$N$	Sample number, in this study $N=45$ for the 355 nm induced data and $N=220$ for the 445 nm induced data;
$T$	Number of time channels, in this study $T=2352$ after cropping
$U_{m,s}$	Compressed representation of data in terms of coefficients for linear mixing of new spectral components in $V_{b,s}$
$s$	Index of spectral component
$\Sigma_{s,s}$	Diagonal matrix singular values sorted in decreasing significance
$V_{b,s}$	Set of new spectral components in the basis of which data is expanded

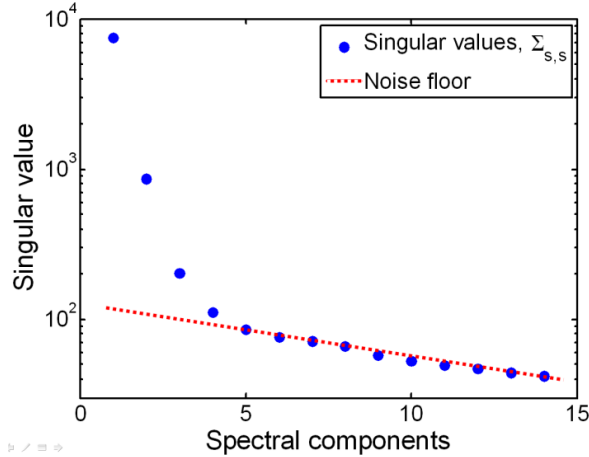


Fig. 2. Eigenvalues (squared spectral singular values) from decomposition of 355 nm induced fluorescence spectra from all patients. The Eigenvalues,  $S_{s,s}$ , show that spectra from any of the 45 samples at any given time after excitation can be accurately described by a linear combination of just three spectra. The SNR of the projection on the first spectral component is  $\sim 100:1$ , the SNR of projection on the second spectral components is  $\sim 10:1$  and SNR of the projection on the third component is  $\sim 1:1$ . Any attempts to extract additional spectral information are not meaningful.

Measurements of pure noise will produce exponentially decaying singular values, whereas information will cause the singular values to drop more rapidly. By analyzing the singular values on a logarithmic scale (Fig.2.) a spectral component truncation value,  $tr$ , can be determined; thus only the detected spectral components, within the given signal-to-noise ratio (SNR) of the system, are taken into consideration. In our case we demonstrate that we can accurately express the 355 nm induced fluorescence spectra from any of the 45 samples and at any time after excitation by a linear combination of just three components. Thus, we decided on the truncation value  $tr=3$  for the 355 nm induced dataset. For the 445 nm induced fluorescence we chose  $tr=2$ . When projecting the 355 nm induced data on those three components, the SNR for the projections are approximately 100:1, 10:1 and 1:1, respectively. Since our instrument is based on single-photon counting methodology, the SNR can be increased simply by increasing the acquisition time in order to assess smaller trace constituents. The fluorescence spectra for any sample at any delay time can now be expressed as:

$$I_{m,b} \approx U_{m,1..tr} \Sigma_{1..tr,1..tr} V'_{b,1..tr} \quad (Eq.2)$$

$tr$  Truncation number, in this study  $tr=3$  for the 355 nm excited data set, and  $tr=2$  for the 445 nm excited data set.

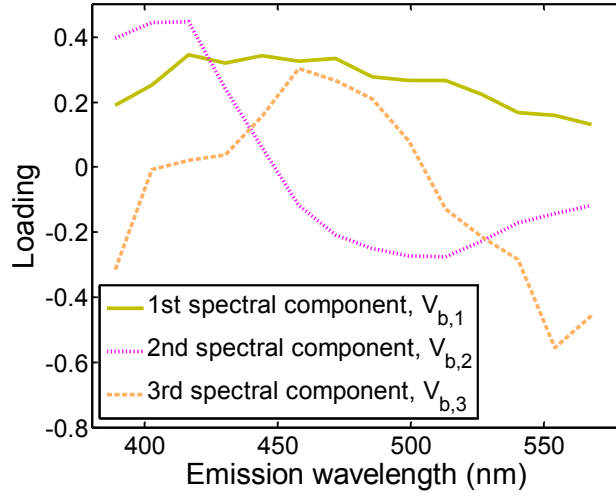


Fig. 3. First three spectral components computed by the SVD,  $V_{b,1..3}$ . The first spectral component, closely resembles the mean spectrum for all patients for all delay times. By definition the components are orthogonal and thus the second component yields negative loadings; however, when multiplied with their respective scores and summed, the results are strictly positive intensity counts. The spectral components are a linear transform of the true fluorescence signatures,  $F_{b,i,n}$ , of the involved fluorophores.

The three first spectral components are shown in Fig.3. The first spectral component,  $V_{b,1}$ , closely resembles the mean fluorescence from all samples and all delay times. As is common in SVD, the values of spectral components are both positive and negative, although  $I_{t,b}$  is strictly positive. The spectral components in  $V_{b,s}$  are related to the true fluorescence emissive yields,  $F_{b,s}$ , of the involved radiative transitions by a linear transformation:

$$F_{b,j,n} = V_{b,s} E_{s,j,n} \quad (Eq.3)$$

- $F_{b,j}$  Set of true fluorescence emissive yield spectra from each involved transition
- $E_{s,j}$  Linear transform of  $V_{s,s}$ , which produces  $F_{b,s}$
- $j$  Index,  $j=1..J$
- $J$  Number of energy populations

Eq. 3 is valid given the following assumptions:

- The numbers of spectral bands are larger than the number of involved radiative transitions.
- The spectral range covered is sufficiently broad to numerically allow orthogonalization of each transition.
- The probability of an emission spectrum from one transition being a linear combination of those from other transitions is negligible.

The latter assumption can be understood by the fact that two identical emission spectra implies two systems with identical sets of energy levels. Such two systems are identical in all respects and cannot produce two different lifetimes. The initially recorded intensities,  $I_{t,b,n}$ , can be expressed as a product between the population sizes,  $P_{j,t}$ , and the true emission spectra from each corresponding transition:

$$I_{t,b,n} = F_{b,1..J,n} P_{1..J,t,n} \quad (Eq.4)$$

$P_{j,t,n}$  Excited population size for transition  $j$  at time  $t$  for sample  $n$

As can be understood, the temporal evolution of the spectra can be entirely explained by the coefficients in  $U_{m,1..tr}$ . However, we introduce a new score matrix,  $C_{t,s,n}$ , explaining the composition in terms of the spectral components  $V_{b,s}$ . To maintain an equal SNR on the estimate of each spectral component we weight by  $\Sigma_{s,s}$ . Also we restore the original indexing including time slots and sample numbers,  $t$  and  $n$ .

$$C_{s,t,n} = (U_{m,s} \Sigma_{s,s})' \quad (Eq.5)$$

$C_{s,t,n}$  Scores explaining the composition in terms of the spectral components in  $V_{b,s}$ , at any given time,  $t$ , for any of the samples  $n$

Traditionally, fluorescence decays in a single emission band are explained by the sum of simple exponential decays:

$$I_{\Delta t} = \sum_j^J I_{0,j} e^{-\frac{\Delta t}{\tau_j}} \quad (\text{Eq.6})$$

$I_{0,j}$  Initial values after excitation  
 $\tau_j$  Fluorescent lifetimes

In discrete time slots the expression in Eq.6 can be written as:

$$I_t = \sum_j^J k_j I_{t,j} \quad (\text{Eq.7})$$

$I_{1..J}$  Initial condition  
 $k$  Coefficients describing the dynamics of the decay

Eq.7 describes the solution to any discrete linear differential equation. An equivalent differential form matrix formulation is:

$$\begin{aligned} \dot{\Phi}_{j,t} &= A_{j,j} \Phi_{j,t} \\ \dot{\Phi}_{j,t} &= \Phi_{j,t+1} - \Phi_{j,t} \\ \Phi_{j,t} &= \begin{bmatrix} I_{1..T-J} \\ I_{2..T-J+1} \\ \dots \\ I_{J..T} \end{bmatrix} \end{aligned} \quad (\text{Eq.8})$$

$$\Phi_{j,t} = \Phi_{j,t-1} + \dot{\Phi}_{j,t-1} = \Phi_{j,t-1} + A_{j,j} \Phi_{j,t-1} = e^{A_{j,j}t} \Phi_{j,1}$$

$\Phi_{j,t}$  Regressor, containing information on each dynamical state over time

$\dot{\Phi}_{j,t}$  Vector of discrete derivatives of intensity (forward derivative here, but choice is irrelevant as long as the same type is used in training and evaluation)

$A_{j,j}$  System matrix with  $J$  times  $J$  elements, constituting the vector field controlling the state space trajectory.

In the case of a purely diagonal  $A_{j,j}$  matrix the solution is once again a sum of independent exponential decays. By further introducing elements off the diagonal in  $A_{j,j}$ , we can additionally describe interaction between energy populations, for example, for example, mother and daughter activity as mentioned in the introduction. We now postulate that *the dynamical states are observable states and they are in fact the energy populations themselves*. Therefore they are also proportional to the emitted light from each population, with the assumption that each transition band emits a distinct spectral distribution. Thus

$$\dot{C}_{s,t,n} = A_{s,s,n} C_{s,t,n} \quad (\text{Eq.9})$$

Assuming that the initial condition is directly given by the initial measurement (which is not entirely true because of measurement uncertainty), a rough estimate of  $A_{j,j}$  can be found by least square regression:

$$\hat{A}_{j,j} = (\Phi_{j,t}' \Phi_{j,t})^{-1} \Phi_{j,t}' \dot{\Phi}_{j,t} \quad (\text{Eq.10})$$

Thus,

$$\hat{A}_{s,s,n} = (C_{s,t,n}' C_{s,t,n})^{-1} C_{s,t,n}' \dot{C}_{s,t,n} \quad (\text{Eq.11})$$

In practice, this Moore-Penrose pseudo-inverse is calculated by QR factorization, which is more computationally efficient than actual matrix inversion. The estimate of  $\hat{A}_{j,j,n}$  is later refined by a numerical gradient search method (Levenberg-Marquardt), which minimizes the squared residuals of the prediction from time zero by adjusting both the elements in  $\hat{A}_{j,j,n}$  and also the estimated initial condition  $\hat{C}_{s,1}$ . An example of a fitted dynamical vector field model  $\hat{A}_{j,j,n}$  is illustrated in Fig.4. The particular decay in this figure was chosen since this sample had a minimal third component, and thus we can approximately visualize the decay in a plane despite the fact that we expect three spectral components for the 355 nm induced data.

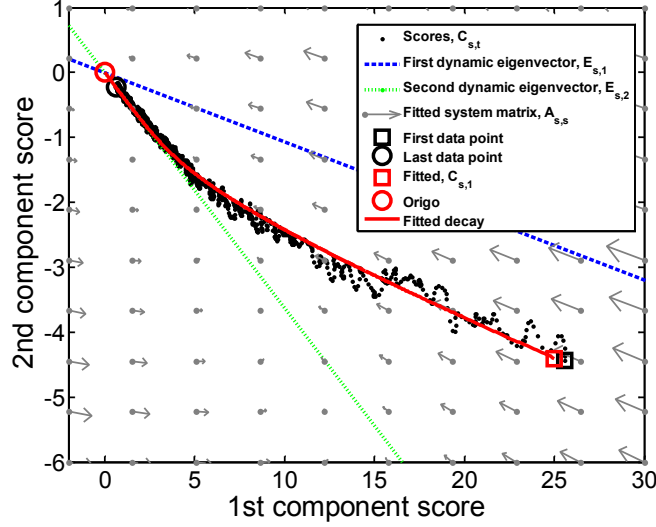


Fig. 4. When the scores,  $C_{s,t,n}$ , of both components are mapped out, the state space trajectory of the fluorescent decay can be seen. Since the decay is expanded on a set of arbitrary spectral components, which are a linear combination of the true fluorescent components, the coordinate system is a linear mapping of the state space trajectory of the true radiative transitions. The vector field,  $A_{s,s,n}$ , alone governs the dynamics of the decay. The two dynamic eigenvectors,  $E_{s,j,n}$ , of  $A_{s,s,n}$  are plotted as straight lines; these vectors can be used for rectification of the coordinate system, thus providing a coordinate system with the true radiative transitions on the axis. Due to conservation of energy the trajectory must necessarily converge to origo, which is also one of the three solutions to the state space model. These particular data are from a patient suffering from nodular basal cell cancer. This sample was chosen for visualization because of a minimal content of the third spectral component, enabling us to approximately visualize the trajectory and vector field in just two dimensions.

So far we have only stated, in Eq.3, that a linear mapping,  $E_{s,j,n}$ , exists, relating the arbitrary base spectra  $V_{b,s}$  from the SVD to the true emissions from each transaction, and that a corresponding linear mapping relates the arbitrary scores,  $C_{s,t}$ , from the SVD, to the true populations. In order to find this linear mapping,  $E_{s,j,n}$ , we apply Eigenvalue decomposition on the system matrix  $\hat{A}_{s,s,n}$  and simultaneously obtain the decay times as well as the linear mapping:

$$\hat{A}_{s,s,n} = E_{s,j,n} \Lambda_{j,j,n} E_{s,j,n}^{-1} \quad (\text{Eq.12})$$

$\Lambda_{j,j,n}$  Diagonal matrix containing the Eigenvalues of the system matrix

$E_{s,j,n}$  Corresponding set of Eigenvectors, also relating the purely decaying fluorescence components to the arbitrary coordinate system generated by the SVD; see Eq.3

Since any scalar product of the eigenvectors,  $E_{s,j,n}$ , solves the equation Eq.12, we choose the signs of the columns in  $E_{s,j,n}$  so that  $0 \leq E_{s,j,n}^{-1} C_{s,t,n}$ , and furthermore we choose a normalized vector length  $\sum_s^tr E_{s,j,n}^2 = 1^2 = 1$ . The only

function of this normalization is to balance to what extent a high fluorescence intensity is caused by a large population or a bright fluorescence quantum yield spectrum. For the purpose of uniqueness and consistency the Eigenvalues,  $\Lambda_{j,j,n}$ , are sorted in increasing magnitudes,  $\Lambda_{j,j,n} < \Lambda_{j+1,j+1,n}$ , and the correspondent Eigenvectors in

the columns of  $E_{s,j,n}$  are arranged in the same order. The diagonal elements in  $\Lambda_{j,j,n}$  are related to the lifetimes for the transitions,  $\tau_j$ , and the time resolution of the instrument as follows:

$$\tau_j = -\frac{\Delta t}{\Lambda_{j,j}} \quad (\text{Eq.13})$$

Thus,  $\tau_j < \tau_{j+1}$  and the first row in  $F_{b,j,n}$  will have the faster decay whereas the last row in  $F_{b,j,n}$  will have the slowest decay. By inserting Eq.12 in Eq.9 we obtain the statement:

$$\dot{C}_{s,t,n} = \hat{A}_{s,s,n} C_{s,t,n} = E_{s,j,n} \Lambda_{j,j,n} E_{s,j,n}^{-1} C_{s,t,n} \quad (\text{Eq.14})$$

We can express the strictly positive excited populations over time,  $P_{j,t,n}$ , as a linear combination of the arbitrary loadings from the SVD or the arbitrary dynamical states expressed in the coordinate system of the SVD:

$$P_{j,t,n} = E_{s,j,n}^{-1} C_{s,t,n} \geq 0 \quad (\text{Eq.15})$$

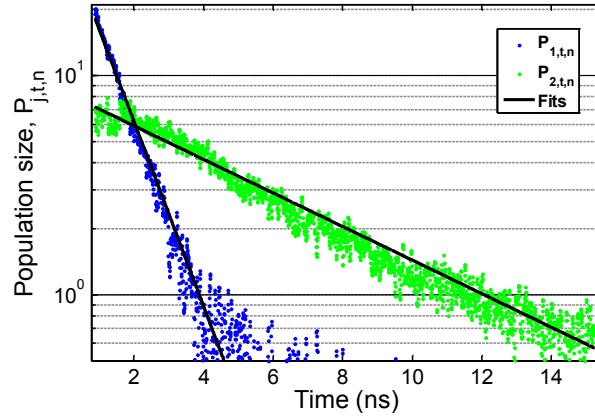


Fig. 5. When projecting the trajectories  $C_{s,t,n}$  on  $E_{s,j,n}$ , the populations sizes,  $P_{j,t,n}$ , are obtained. The exponential decays obtained are illustrated here as straight lines on a logarithmic scale.

Since we choose the signs of Eigenvectors,  $E_{s,j,n}$ , we can always have strictly positive population sizes. An example of populations  $P_{j,t,n}$  is shown in Fig.5; the sample is the same as the one presented in Fig.4. The corresponding rectified fluorescence emission signatures are derived according to Eq.3. The rectified transition emission spectra are shown in Fig.6. Insertion of Eq.15 in Eq. 14 gives:

$$\begin{aligned} \dot{C}_{s,t,n} &= E_{s,j,n} \Lambda_{j,j,n} P_{s,t,n} \rightarrow \\ E_{s,j,n}^{-1} \dot{C}_{s,t,n} &= E_{s,j,n}^{-1} E_{s,j,n} \Lambda_{j,j,n} P_{s,t,n} \rightarrow \\ \dot{P}_{s,t,n} &= \Lambda_{j,j,n} P_{s,t,n} \end{aligned} \quad (\text{Eq.16})$$

From this relation we can understand that the population dynamics can now be described by  $J$  independent exponential decays. Thus a complete description of  $I_{t,b,n}$  can uniquely be written:

$$I_{t,b,n} = F_{b,j,n} P_{j,1,n} e^{\frac{t\Delta t}{\Lambda_{j,j}}} \quad (\text{Eq.17})$$

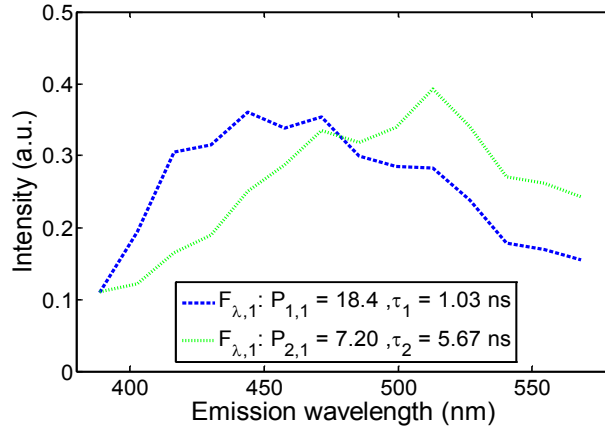


Fig. 6 Examples of rectified single decaying fluorescence spectral components obtained by transforming the arbitrary components from the SVD,  $V_{b,1,2}$ , by  $E_{s,j,n}$ .

The properties of the unique matrix decomposition presented in this study are that  $\Lambda_{j,j,n} < 0$  which implies strict system stability, which is obvious from the point of view of energy conservation. Also the Eigenvalues are real,  $\Lambda_{j,j,n} \in \mathfrak{R}^-$ , as long as there are no cycling energy routes or quantum interference. The fluorescence emissions,  $F_{b,j,n}$ , are independent of initial population after excitation,  $P_{j,1,n}$ , and can be determined as long as this is not zero. For decays of uncoupled populations, the rectified fluorescence components are strictly positive  $F_{b,j,n} > 0$ . The presented model is also capable of parameterizing cascade decays of coupled populations such as mother and daughter decays, but as can be understood from Eq.16, the estimated individual populations  $P_{j,1,n}$  are always decaying with a single exponential, which might not be the case of the actual populations. Therefore the coupled behavior is instead handled by the rectified fluorescence components,  $F_{b,j,n}$ , which for coupled can sometimes have negative parts. Although such coupled decays can be found naturally<sup>68</sup> they were not encountered in this study, and all rectified fluorescence spectra from all samples were positive definite. Mathematically, system matrixes,  $\hat{A}_{s,s,n}$ , can be constructed in such a way that the all Eigenvalues,  $\Lambda_{j,j,n}$ , are both negative and real, but the solution includes negative populations. Such dynamics are equally well explained by the presented model although they lack physical meaning, even in this case the elements in  $F_{b,j,n}$  are not necessarily positive definite. There is no inherent property of  $\hat{A}_{s,s,n}$  which assures positive definite solutions except the actual solution of all populations. Similar approaches in the field of nuclear science applied triangular system matrices. Such triangular matrices can be found by Schur matrix decomposition. However, the Schur decomposition is not unique, and further, since the system matrix is forced to be diagonal and thus with fewer degrees of freedom, the decomposition method necessarily requires the Eigenvectors to be orthogonal. Since physical emission spectra from each transition are in general not orthogonal such an approach does not solve the problem of indentifying emission in coupled systems.

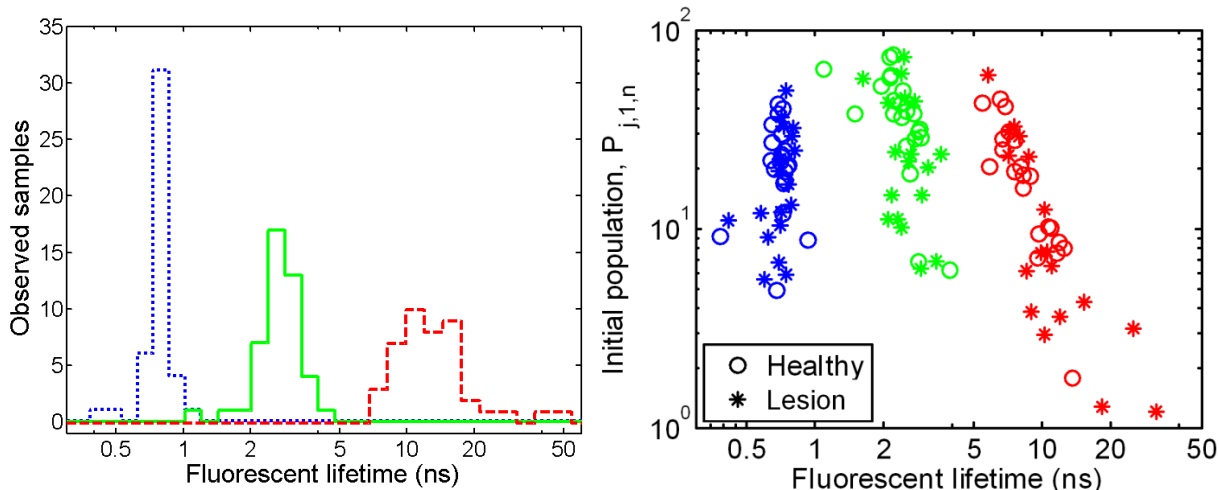


Fig. 7a: Histogram of the three parameterized lifetimes from 355 nm induced fluorescence. The histogram includes all measurements from healthy regions and lesions. 7b: The lifetimes of fluorescence components versus their initial populations. The scatter plot shows no discrepancy between healthy regions and lesions and mainly no systematic relation between initial population and lifetimes. When the intensities are low the lifetime estimate becomes uncertain; three data points with exceedingly low intensities are not shown in the figure.

## Statistical evaluation

### Cancer diagnostics aspects and benefits

Having factorized the highly dimensional data to a minimal representation, the parameter can be explored from several angles of approach. The fluorescence spectra induced by 355 nm light could for any patient and any decay time be explained by a linear combination of three spectral components ( $tr=3$ ). The three associated lifetimes,  $\tau$ , fall into three modes with median values of 0.7, 2.5 and 9.0 ns; see Fig. 7a. As in the previous analysis<sup>71</sup> there was no significant discrimination between lesions and healthy tissue at this excitation wavelength. Having said that lifetime spectroscopy is an intensity insensitive method, the lifetimes were analysed against the initial populations,  $P$ ; see Fig. 7b. The lifetimes were mainly uncorrelated to the initial population, but for samples with very low content of certain spectral components, implying low signal to noise of corresponding population, the lifetime becomes increasing uncertain in a seemingly systematic manner. In Fig. 7b three points are outside the plot, one very fast estimated lifetime and two very slow estimated lifetimes, all these samples had a very low initial population. Such data points would not appear if the SVD were to be applied individually on each sample.

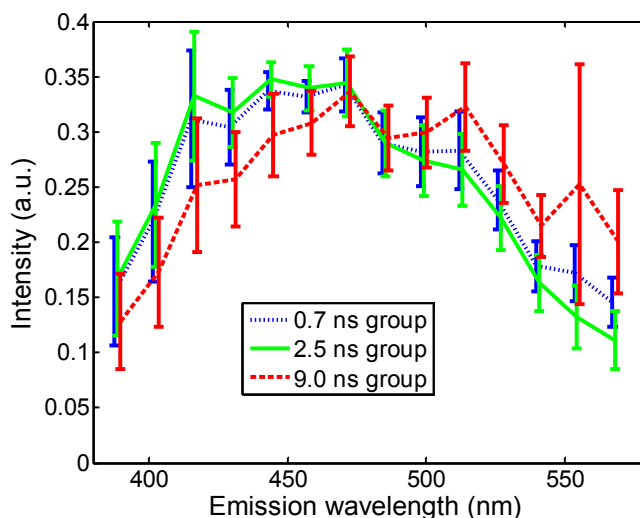


Fig. 8. Mean spectra of rectified spectral emission. The bars indicate biological variance within the dataset and are not indicators of the accuracy of the instrumentation or the parameterization method. The spectral components of the emission are to a great extent overlapping; however, the slowest component is the most red, while the medium fast component is the most blue.

The mean rectified emission spectra from each lifetime mode are presented in Fig.8. The error bars do not represent measurement or fitting error but biological variance among all measurements. The emissions are extensively overlapping and show large variance between the measurement spots. The medium fast mode showed the most bluish fluorescence whereas the slowest mode showed the most reddish fluorescence. The emission of each individual rectified spectrum was summarized by a gravitational point of the emission spectra. To investigate the spectral content in respect to the dynamic decay, the lifetimes were plotted against the center of mass emission; see Fig.9. As can be seen in the plot, the fluorescence lifetime is mainly independent of the emission wavelength. The very fast data point previously omitted can be seen at the bottom, and the two very slow lifetimes which were also excluded are seen in the top of the plot. As can be seen in Fig.7b these points have low intensities; therefore neither the lifetime of the center wavelength is reliable. These darkest data points are acquired from melanized regions and the fact that the center emission is displaced toward red is in accordance with the melanin absorption. Even in this analysis there was no discrimination between healthy and lesion tissue with excitation at 355 nm.

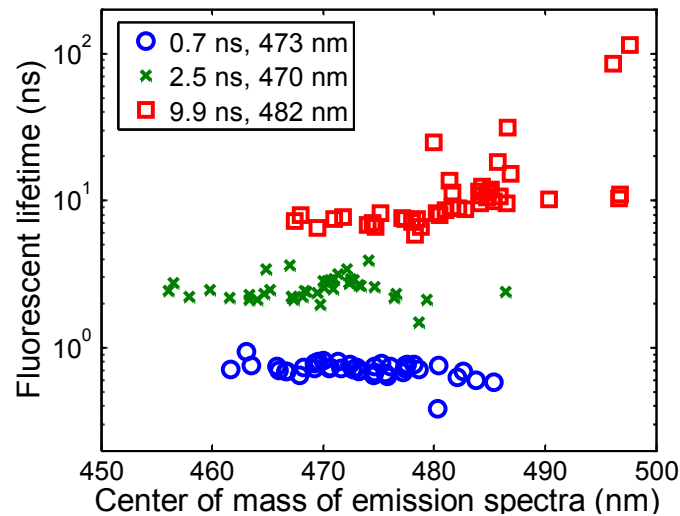


Fig. 9 Fluorescence lifetimes in respect to the center of emission wavelength. The two quantities are mainly unrelated. The data points from low intensities have uncertain lifetime parameterization; they also appear most red.

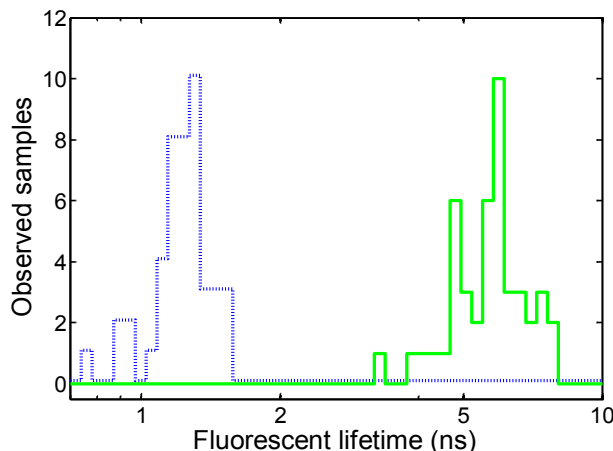


Fig. 10 Histogram of the two lifetimes obtained by 445 nm induced fluorescence.

As described previously<sup>71</sup>, the 445 nm induced fluorescence yields some discrimination between healthy and lesion tissue. We applied identical parametrization as used for the 355 nm data to the 445 nm induced data. With this excitation the fluorescence emission was only recorded in 7 spectral bands, due to the fixed wavelength scale of the spectrometer. The fluorescence spectra from any patient at any given time could be explained as a linear combination of just two spectral components ( $tr=2$ ). The lifetimes fell into to two modes - a fast decay around 1.2 ns and a slower decay at 5.7 ns; see Fig.10. The two lifetimes were plotted against a hemoglobin index obtained from

the steady-state diffuse reflectance spectrometer. The index was defined by the spectral shape similar to the normalized difference vegetation index as:

$$Haem = \frac{R_{\lambda_{on}} - R_{\lambda_{off}}}{R_{\lambda_{on}} + R_{\lambda_{off}}}, \quad 490nm < \lambda_{on} < 510nm, \quad 640nm < \lambda_{off} < 660nm$$

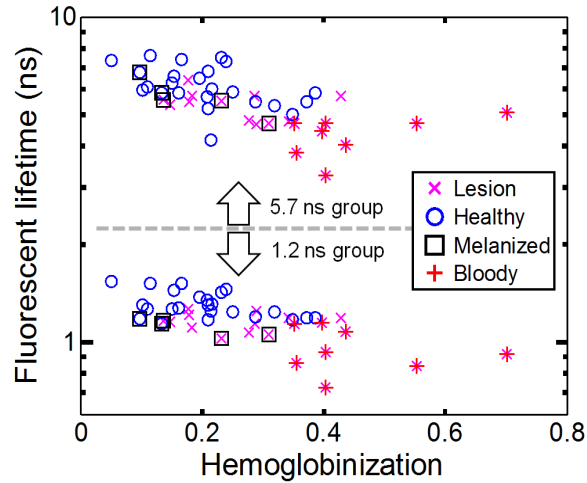


Fig. 11 Fluorescence lifetime decreases with increasing content of hemoglobin. The hemoglobin index is obtained by steady-state reflectance spectroscopy in accordance with the visual classification of reddish spots.

The data points were also visually classified from color photography in respect to melanization and hemaglobinzation. As can be seen in Fig.11, both the hemoglobin index from the reflectance and the visual classification are in accordance; also all data points classified with high hemoglobin content are lesions. The lifetimes show a weak correlation with the hemoglobin content with correlations coefficients of -0.6 for both lifetimes. This could suggest that lifetime based diagnostics could be influenced by the presence of blood. Similar analysis with the a melanization index did neither provide discrimination nor provided any obvious correlation.

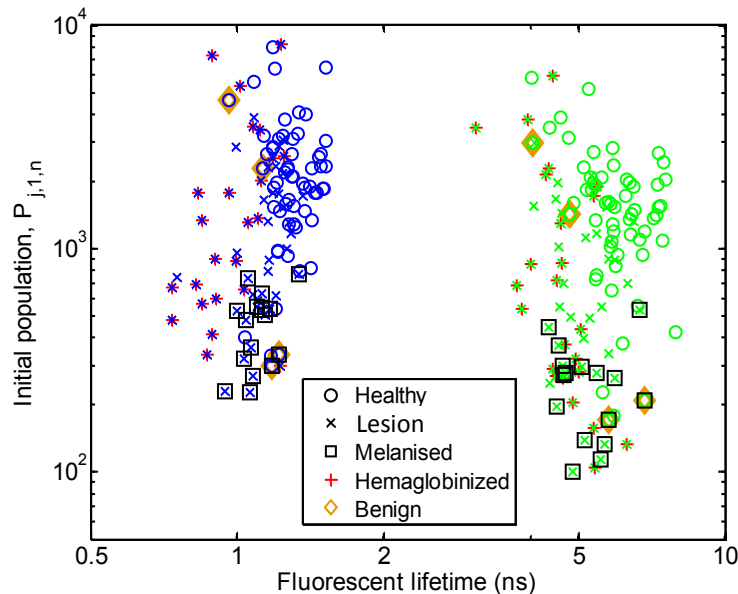


Fig. 12 Initial population and lifetimes of 445 nm induced fluorescence. As for the 355 nm induced fluorescence in Fig. 7b, the two quantities are mainly unrelated. Melanized samples decrease the initial population estimates, whereas hemoglobin decreases the lifetime estimates. Discrimination between healthy tissue and lesions is most apparent whenever the visual appearance also differs. The few examples of disagreement between the clinician and the histopathologist would also be misclassified by a method based on the evaluation of fluorescence lifetime.

As for the 355 nm induced fluorescence the initial populations or fluorescence intensities were analyzed in respect to the fluorescence lifetimes; see Fig.12. The data points classified as melanized mainly produce low intensities. The reddish data points show decreased lifetimes. A discrimination is seen between the healthy tissue and lesions which are either visually classed as melanized or hemoglobin containing. However, there is no obvious discrimination between the healthy data points and the data from lesions which were neither melanized nor reddish. Further, the few data points which were initially mistaken as lesions by the clinician, but which later were determined to be of benign nature by the histopathologist, are particularly intermingled with the lesion data points even in the lifetime analysis.

As suggested in many studies dealing with optical cancer diagnostics<sup>76</sup>, including our earlier evaluation<sup>71</sup>, the biological variance of optical properties between individuals is often larger than the within individual variance between healthy and lesion tissue. Therefore a cancer criterion based on differences between healthy and lesion tissue of the same patient is to be preferred rather than a criterion based on absolute optical properties. In Fig. 13 the two lifetimes for each lesion measurement are mapped out and connected by a line to the lifetimes of adjacent healthy tissue of the same individual. A strong correlation between the fast and slower lifetime is observed. Also the lesions consistently show shorter lifetimes with respect to the adjacent healthy tissue. This is in accordance with the previously reported<sup>71</sup> results with the same set of data points obtained with a single lifetime. In the previous evaluation<sup>71</sup> differentiation between malignant and healthy tissue was reported by lifetime shifts significantly deviating from zero. This was reported by taking the average of repeated decay measurements (up to 5) over the lesion and surrounding healthy tissue (2 measurements). Here we extend this analysis and consider all combinations of healthy-healthy and healthy-lesion measurements for single pairs of measurements without averaging.

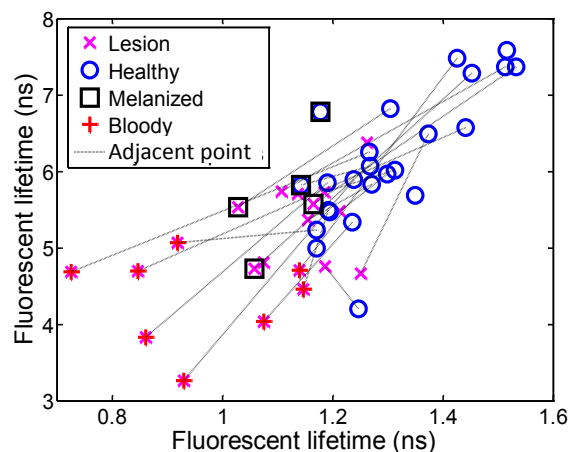


Fig. 13. When data points are evaluated in respect to the healthy adjacent tissue on the same individual, the lifetimes are consistently faster for the lesion. Thus, the lifetime change is significantly different from zero.

The 445 nm excited fluorescence from a total of 120 measurements, from 27 suspected lesional locations on 25 patients was parameterized according to the procedure above. The lifetime shift for both fluorescence decay components was calculated for all possible combinations within each location on the same individual. Only healthy-healthy and healthy-lesional pairs were considered. The results are shown in Fig.14; again a correlation between the fast and slow lifetime is seen. This implies that evaluation of a single crude lifetime would mainly lead to the same conclusion<sup>71</sup>. Unfortunately, the spread of the relative shift of the healthy-healthy is also very large and to great extend overlapping with the healthy-lesion lifetime changes. Further, nearly every single healthy-lesion shift which deviates significantly from the healthy-healthy shifts belongs to one the three categories: 1) Shifts involving a melanized spot, 2) Shifts involving a reddish spot, 3) Shifts involving a spot with was initially mistaken for a lesion by the clinician. The healthy-lesion shifts that do not belong to any of these categories entirely overlap with the healthy-healthy shifts. There may be a small shift in the centers of the clusters for healthy-healthy and non-bloody healthy-lesion points, although again the difference is not strong.

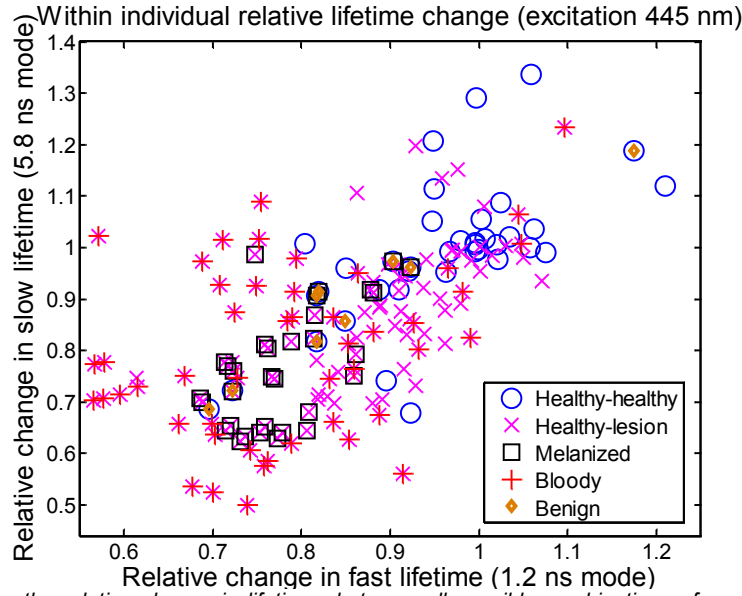


Fig. 14. When considering the relative change in lifetimes between all possible combinations of measurements from the same individuals the changes when a lesion is involved does not significantly differ from the change when no lesion is involved. Observation pairs involving a melanized, reddish or histopathologically determined benign spot have been marked accordingly. In particular, the lesions which do not differ visually can hardly be discriminated from the healthy ones.

## Discussion

We have briefly reviewed the historical background of optical instrumentation for tissue diagnostics leading to time resolved fluorescence instruments. Here the main arguments are insensitivity to absorption quenching of fluorescence excitation and emission, and also the sensitivity to the micro environment. We have used an ordinary chemometric approach to reduce a discrete spectrally and temporally resolved fluorescence decay surface into arbitrary temporal scores and spectral loading. We have then given the reason, based on causality, why, and shown empirically, that the dynamics of the scores can be explained by an ordinary first order linear differential equation. We have matrix formulated the problem and drawn parallel between electron population dynamics and population dynamics in robotics, ecology and nuclear physics. We have concluded that the decay rates must be a linear map of the dynamical states which are also the physical states in terms of population sizes. We further conclude that the scores are linear maps of the physical states and that the decay rates are therefore a linear map of the scores. We have shown empirically that when a sufficiently broad spectrum is recorded, the dynamical states are thus observable. The system identification approach is compatible with the existing foundation of population dynamics, and the matrix formulation and discrete manner is compatible with the discrete information from optical instrumentation in terms of spectral bands and time slots. We have shown how the initial guess of a system matrix describing the dynamic evolution of the spectra can be found in a robust manner through a simple regression; the estimated system matrix as well as the estimated initial condition can, in turn, be refined through numerical search. Alternatives to the latter could be weighting according to Poisson fits. We have then applied Eigenvalue decomposition to translate the arbitrary scores into electron populations and arbitrary loading into rectified single decaying fluorescence emission spectra. Thus, we have effectively provided an integrated minimal and unique parameterization of time and spectrally resolved fluorescence, which can be scientifically communicated in terms of 1) initial populations, 2) corresponding rectified fluorescence components and 3) associated decay times. We have shown empirically for the present data set that the temporal dynamics can equally well be described either by a linear map of  $J$  time instances in one spectral band (Eq.8) or, alternatively, by  $J$  spectral components in the single preceding time instance (Eq.9). Except for effects caused by absorption of excitation and emission in fluorescence spectroscopy, the spectrally and temporally information thus seems to be interchangeable. However, this does not imply that decomposing multiple spectral emissions or fitting multiple lifetimes is an equally well numerically conditioned inverse problem, nor have the same sensitivity to noise.

Although the instrumentation for lifetime resolved fluorescence is considerably more sophisticated than steady-state spectrally resolving equipment, there might be a numerical advantage and synergy of recording both simultaneously in terms of certainty and robustness of the parameterization. The method provided here is entirely

empirical and does not require any reference measurements or a *priori* knowledge regarding involved fluorophores and their properties. While other attempts of parameterization are based on continuous mathematics, normalization<sup>77</sup>, isometric points<sup>78</sup> and works for just two spectral components and do not consider multi species population dynamics<sup>79</sup>, the approach presented here resembles more methods in the chemometric community based linear algebra and matrix formulation<sup>80, 81</sup>. Such approaches can be generalized to include any number of populations, mainly limited by the signal to noise. Time-resolved multi-excitation-wavelength fluorescence and recording of the excitation emission matrix<sup>82</sup> can also be effectively reduced, primarily, e.g., by the PARAFAC<sup>83</sup> method, and secondarily by dynamical state space models as in this study. The presented time resolved factorization is equally powerful for slower processes in tissue optics such as photokinetic reactions<sup>84</sup> and bleaching processes<sup>67, 85-87</sup>. In this case a constant is added to the regressor allowing the system to converge to a value different than zero. The resulting parametrization in this case consists of an infinity spectrum and a set of purely exponential decaying spectral components.

The idea of a diagnostic criterion based on fluorescence lifetimes, in many ways resembles approaches evaluating spectral shapes or chromaticity in chemometry, remote sensing and machine vision<sup>88</sup>. It also resembles the idea behind polarimetric imaging<sup>89, 90</sup>. In all the three cases intensity insensitive methods decrease the variance of large absolute intensity variance and improve the classification performance. This result is, however, only reliable as long as the absolute intensities are well above the noise limit. In polarimetric imaging this issue is addressed by communicating the polarization parameters in a conical color space, where the polarization parameters degenerates when the intensity goes to zero<sup>90</sup>. Equivalently, a criterion based on lifetimes should converge to a single value when the absolute intensity goes to zero. Further, fluorescence lifetime quantities are not easy to integrate in traditional chemometric methods since they do not represent concentrations of the involved substances.

In terms of the potential for improved cancer diagnostics, no discrimination was found when inducing fluorescence with 355 nm light. As previously reported, the 445 nm induced fluorescence lifetimes yielded some discrimination, in particular when considering the relative shift in lifetimes when comparing healthy and lesion tissue from the same individual. The shift was significantly different from zero, but was not significantly different from the shift variance between healthy control spots. Further, a negative correlation was found between the blood content and the lifetimes, suggesting that spectral and lifetime measurements may provide complementary information. Even if lifetimes are insensitive to the emission re-absorption of blood, increased vascularization might change other parameters such as pH or oxygenation of the micro environment of the fluorophores. We found that lesions showing different lifetimes from the control group, were also visually distinct, either in terms of melanization or in terms of blood content. The few cases where benign or healthy tissue was initially mistaken for a lesion by the clinician would also be mistaken by this fluorescence lifetime approach. In the present study we thus find that the fluorescence lifetime monitoring does not necessarily provide any complementary information to spectral recordings.

### **Acknowledgement and funding**

We much appreciate financial support from the Photonics for Life (P4L) program by the European Union. Measurements were carried out with the ethical permit LU 335-98. We thank Lars Engström, Anders Robertsson and Can Xu for fruitful discussions regarding parameterization and discrete math.

### **References**

1. J. W. Feather, M. Hajizadeh-Saffar, G. Leslie, and J. B. Dawson, "A Portable Scanning Reflectance Spectrophotometer Using Visible Wavelengths for the Rapid Measurement of Skin Pigments," *Phys. Med. Biol.* **34**, 807-820 (1989).
2. R. Marchesini, S. Tomatis, C. Bartoli, *et al.*, "*In Vivo* Spectrophotometric Evaluation of Neoplastic and Non-Neoplastic Skin Pigmented Lesions. Iii. CCD Camera-Based Reflectance Imaging," *Photochem. Photobiol.* **62**, 151-154 (1995).
3. S. Takatani, P. W. Cheung, and E. A. Ernst, "A Noninvasive Tissue Reflectance Oximeter, an Instrument for Measurement of Tissue Hemoglobin Oxygen Saturation *in Vivo*," *Ann. Biomed. Eng.* **8**, 1-15 (1980).
4. D. Faber, M. Aalders, E. Mik, B. Hooper, M. van Gemert, and T. van Leeuwen, "Oxygen Saturation-Dependent Absorption and Scattering of Blood," *Phys. Rev. Lett.* **93** (2004).
5. R. A. J. Groenhuis, H. A. Ferwerda, and J. J. T. Bosch, "Scattering and Absorption of Turbid Materials Determined from Reflection Measurements. 1: Theory," *Appl. Opt.* **22**, 2456-2462 (1983).
6. M. S. Patterson, B. Chance, and B. C. Wilson, "Time Resolved Reflectance and Transmittance for the Non-Invasive Measurement of Tissue Optical Properties," *Appl. Opt.* **28**, 2331-2336 (1989).
7. L. Wang and S. L. Jacques, "Hybrid Model of Monte Carlo Simulation and Diffusion Theory for Light Reflectance by Turbid Media," *J. Opt. Soc. Am. A* **10**, 1746-1752 (1993).

8. S. Andersson-Engels, R. Berg, A. Persson, and S. Svanberg, "Multispectral Tissue Characterization with Time-Resolved Detection of Diffusely Scattered White Light," *Opt. Lett.* **18**, 1697-1699 (1993).
9. S. L. J. Craig M. Gardner, and Ashley J. Welch, "Fluorescence Spectroscopy of Tissue: Recovery of Intrinsic Fluorescence from Measured Fluorescence," *Appl. Opt.* **35**, 1780-1792 (1996).
10. M.-A. Mycek and B. W. Pogue, *Handbook of Biomedical Fluorescence*, p. 688 (CRC Press, 2003).
11. S. L. Jacques and B. W. Pogue, "Tutorial on Diffuse Light Transport," *J. Biomed. Opt.* **13**, 041302 (2008).
12. M. S. Patterson and B. W. Pogue, "Mathematical Model for Time-Resolved and Frequency-Domain Fluorescence Spectroscopy in Biological Tissues," *Appl. Opt.* **33**, 1963-1974 (1994).
13. B. C. Avraham Mayevsky, "Intracellular Oxidation Reduction State Measured in Situ by a Multichannel Fiber-Optic Surface Fluorometer," *Science* **217** (1982).
14. P. S. Andersson, S. Montán, and S. Svanberg, "Multispectral System for Medical Fluorescence Imaging," *IEEE J. Quant. Electr.* **23** (1987).
15. J. F. Brennan, G. I. Zonios, T. D. Wang, R. P. Rava, G. B. Hayes, R. R. Dasari, and M. S. Feld, "Portable Laser Spectrofluorimeter System for *in Vivo* Human Tissue Fluorescence Studies," *Appl. Spectrosc.* **47**, 2081-2086 (1993).
16. R. Richards-Kortum and E. Sevick-Muraca, "Quantitative Optical Spectroscopy for Tissue Diagnostics," *Ann. Rev. Phys. Chem.* **47**, 555 (1996).
17. A. F. Zuluaga, U. Utzinger, A. Durkin, *et al.*, "Fluorescence Excitation Emission Matrices of Human Tissue: A System for *in Vivo* Measurement and Method of Data Analysis," *Appl. Spectrosc.* **53**, 302-311 (1999).
18. N. Ramanujam, "Fluorescence Spectroscopy of Neoplastic and Non-Neoplastic Tissues," *Neoplasia* **2**, 89-117 (2000).
19. G. A. Wagnieres, W. M. Star, and B. C. Wilson, "*In Vivo* Fluorescence Spectroscopy and Imaging for Oncological Applications," *Photochem. Photobiol.* **68**, 603-632 (1998).
20. J. Moan and Q. Peng, *Photodynamic Therapy*, pp. 1-18 (Royal Soc. Chem., 2003).
21. J. Wu, M. S. Feld, and R. P. Rava, "Analytical Model for Extracting Intrinsic Fluorescence in Turbid Media," *Appl. Opt.* **32**, 3585-3595 (1993).
22. A. J. Durkin, S. Jaikumar, N. Ramanujam, and R. Richards-Kortum, "Relation between Fluorescence Spectra of Dilute and Turbid Samples," *Appl. Opt.* **33**, 414-423 (1994).
23. H. Zeng, C. MacAulay, D. I. McLean, and B. Palcic, "Spectroscopic and Microscopic Characteristics of Human Skin Autofluorescence Emission," *Photochem. Photobiol.* **61**, 639-645 (1995).
24. R. A. Zângaro, J. Landulfo Silveira, R. Manoharan, *et al.*, "Rapid Multiexcitation Fluorescence Spectroscopy System for *in Vivo* Tissue Diagnosis," *Appl. Opt.* **35**, 5211-5218 (1996).
25. N. N. Zhadin and R. R. Alfano, "Correction of the Internal Absorption Effect in Fluorescence Emission and Excitation Spectra from Absorption and Highly Scattering Media: Theory and Experiment," *J. Biomed. Opt.* **3**, 171-186 (1998).
26. I. Georgakoudi, B. C. Jacobson, J. Van Dam, *et al.*, "Fluorescence, Reflectance, and Light-Scattering Spectroscopy for Evaluating Dysplasia in Patients with Barrett's Esophagus," *Gastroenterology* **120**, 1620-1629 (2001).
27. C. af Klinteberg, M. Andreasson, O. Sandström, S. Andersson-Engels, and S. Svanberg, "Compact Medical Fluorosensor for Minimally Invasive Tissue Characterization," *Rev. Sci. Instr.* **76**, 034303 (2005).
28. Q. Zhang, M. G. Müller, J. Wu, and M. S. Feld, "Turbidity-Free Fluorescence Spectroscopy of Biological Tissue," *Opt. Lett.* **25**, 1451-1453 (2000).
29. M. G. Müller, I. Georgakoudi, Q. Zhang, J. Wu, and M. S. Feld, "Intrinsic Fluorescence Spectroscopy in Turbid Media: Disentangling Effects of Scattering and Absorption," *Appl. Opt.* **40** (2001).
30. M. G. Nichols, E. L. Hull, and T. H. Foster, "Design and Testing of a White-Light, Steady-State Diffuse Reflectance Spectrometer for Determination of Optical Properties of Highly Scattering Systems," *Appl. Opt.* **36**, 93-104 (1997).
31. A. Kienle, L. Lilge, M. S. Patterson, R. Hibst, R. Steiner, and B. C. Wilson, "Spatially Resolved Absolute Diffuse Reflectance Measurements for Noninvasive Determination of the Optical Scattering and Absorption Coefficients of Biological Tissue," *Appl. Opt.* **35**, 2304-2314 (1996).
32. B. Yuan, S. A. Burgess, A. Iranmahboob, M. B. Bouchard, N. Lehrer, C. Bordier, and E. M. C. Hillman, "A System for High-Resolution Depth-Resolved Optical Imaging of Fluorescence and Absorption Contrast," *Rev. Sci. Instr.* **80** (2009).
33. A. P. Rinaldo Cubeddu, P. Taroni, A. Torricelli, G. Valentini, F. Rinaldi, and E. Sorbellini, "Fluorescence Lifetime Imaging: An Application to the Detection of Skin Tumors," *IEEE JSTQE* **5**, 923-929 (1999).
34. K. Vishwanath, B. Pogue, and M.-A. Mycek, "Quantitative Fluorescence Lifetime Spectroscopy in Turbid Media: Comparison of Theoretical, Experimental and Computational Methods," *Phys. Med. Biol.* **47**, 3387 (2002).
35. P. T. C. S. Joshua B. Fishkin, Albert E. Cerussi, Sergio Fantini, Maria Angela Franceschini, and Enrico Gratton, "Frequency-Domain Method for Measuring Spectral Properties in Multiple-Scattering Media: Methemoglobin Absorption Spectrum in a Tissue-like Phantom," *Appl. Opt.* **34**, 1143- (1995).
36. E. Gratton, S. Fantini, M. A. Franceschini, G. Gratton, and M. Fabiani, "Measurements of Scattering and Absorption Changes in Muscle and Brain," *Proc. R. Soc. B* **352**, 727-735 (1997).
37. T. H. Pham, O. Coquoz, J. B. Fishkin, E. Anderson, and B. J. Tromberg, "Broad Bandwidth Frequency Domain Instrument for Quantitative Tissue Optical Spectroscopy," *Rev. Sci. Instr.* **71**, 2500 (2000).
38. L. O. S. Olivier Coquoz, and Bruce J. Tromberg, "Optical Property Measurements of Turbid Media in a Small-Volume Cuvette with Frequency-Domain Photon Migration," *Appl. Opt.* **40**, 6281-6291 (2001).
39. S. Andersson-Engels, J. Johansson, and S. Svanberg, "The Use of Time-Resolved Fluorescence for Diagnosis of Atherosclerotic Plaque and Malignant Tumours," *Spectrochimica Acta Part A: Molecular Spectrosc.* **46**, 1203-1210 (1990).
40. A. Pifferi, A. Torricelli, P. Taroni, D. Comelli, A. Bassi, and R. Cubeddu, "Fully Automated Time Domain Spectrometer for the Absorption and Scattering Characterization of Diffusive Media," *Rev. Sci. Instr.* **78**, 053103 (2007).
41. S. Andersson-Engels, A. Gustafson, J. Johansson, U. Stenram, K. Svanberg, and S. Svanberg, "Investigation of Possible Fluorophores in Human Atherosclerotic Plaque," *Lasers Life Sci.* **5**, 1-11 (1992).

42. J. Carlsson, L. Stuesson, and S. Svanberg, "Accurate Time-Resolved Laser Spectroscopy on Sputtered Metal Atoms," *Z. Phys. D - Atoms, Molecules and Clusters* **11**, 287-293 (1989).
43. S. Svanberg, *Atomic and Molecular Spectroscopy: Basic Aspects and Practical Applications*, 4th ed., Advanced Texts in Phys., p. 588 (Springer, Heibelberg, 2004).
44. C. Y. Fu, B. K. Ng, and S. G. Razul, "Fluorescence Lifetime Discrimination Using Expectation-Maximization Algorithm with Joint Deconvolution," *J. Biomed. Opt.* **14**, 064009 (2009).
45. R. L. W. II and D. A. Lawrence, *Linear State-Space Control Systems*, p. 480 (Wiley, 2007).
46. J.-N. Juang, *Applied System Identification* (Prentice Hall, 1993).
47. M. M. R. Isermann, *Identification of Dynamic Systems: An Introduction with Applications* (Springer, 2010).
48. K. J. Keesman, *System Identification: An Introduction* (Springer, 2011).
49. L. Ljung, *System Identification: Theory for the User*, 2nd ed., p. 672 (Prentice Hall, 1999).
50. Y. Zhu, *Multivariable System Identification for Process Control*, p. 372 (Elsevier Science, 2001).
51. O. E. Rhodes and R. K. Chesser, *Population Dynamics in Ecological Space and Time* (University of Chicago Press, 1996).
52. R. Schoen, *Dynamic Population Models*, p. 256 (Springer, 2007).
53. J. Pastor, *Mathematical Ecology of Populations and Ecosystems*, p. 344 (Wiley-Blackwell, 2008).
54. H. R. Thieme, *Mathematics in Population Biology*, p. 568 (Princeton Series in Theoretical and Computational Biology, Princeton University Press, 2003).
55. G. Ford, K. Wolfsberg, and B. Erdal, "Independent Yields of the Isomers of Xe133 and Xe135 for Neutron-Induced Fission of U233, U235, U238, and Amm242," *Phys. Rev. C* **30**, 195-213 (1984).
56. P. R. Pascholati, V. R. Vanin, and T. Kodama, "A Matricial Method to Obtain Sub-Barrier Fusion Cross Sections from Off-Line X-Ray Measurements," *Nucl. Instr. Meth. Phys. Res. Sect. A: Accelerators, Spectrometers, Detectors and Associated Equipment* **281**, 610-615 (1989).
57. L. Moral and A. F. Pacheco, "Algebraic Approach to the Radioactive Decay Equations," *Am. J. Phys.* **71**, 684 (2003).
58. D. Yuan and W. Kernan, "Explicit Solutions for Exit-Only Radioactive Decay Chains," *J. Appl. Phys.* **101**, 094907 (2007).
59. M. Amaku, P. R. Pascholati, and V. R. Vanin, "Decay Chain Differential Equations: Solution through Matrix Algebra," *Computer Phys. Comm.* **181**, 21-23 (2010).
60. S. Dobre, T. Bastogne, M. Barberi-Heyob, D. Bechet, J. Didelon, and A. Richard, "System Identification of the Intracellular Photoreaction Process Induced by Photodynamic Therapy," 1729-1734 in *Control and Automation, 2008 16th Mediterranean Conference on*, 2008).
61. M. Brydegaard, N. Haj-Hosseini, K. Wårdell, and S. Andersson-Engels, "Photobleaching-Insensitive Fluorescence Diagnostics in Skin and Brain Tissue," *IEEE Photonics J.* **3**, 407-421 (2011).
62. N. Haj-Hosseini, J. Richter, S. Andersson-Engels, and K. Wardell, "Photobleaching Behavior of Protoporphyrin IX During 5-Aminolevulinic Acid Marked Glioblastoma Detection," 716131 in (SPIE, **7161**, 2009).
63. C. af Klinteberg, A. M. Enejder, I. Wang, S. Andersson-Engels, S. Svanberg, and K. Svanberg, "Kinetic Fluorescence Studies of 5-Aminolaevulinic Acid-Induced Protoporphyrin IX Accumulation in Basal Cell Carcinomas," *J. Photochem. Photobiol. B* **49**, 120-128 (1999).
64. J. C. Finlay, D. L. Conover, E. L. Hull, and T. H. Foster, "Porphyrin Bleaching and PDT-Induced Spectral Changes Are Irradiance Dependent in ALA-Sensitized Normal Rat Skin in Vivo," *Photochem. Photobiol.* **73**, 54-63 (2001).
65. J. C. Finlay, S. Mitra, M. S. Patterson, and T. H. Foster, "Photobleaching Kinetics of Photofrin in Vivo and in Multicell Tumour Spheroids Indicate Two Simultaneous Bleaching Mechanisms," *Phys. Med. Biol.* **49**, 4837-4860 (2004).
66. W. J. Cottrell, A. D. Paquette, K. R. Keymel, T. H. Foster, and A. R. Oseroff, "Irradiance-Dependent Photobleaching and Pain in Delta-Aminolevulinic Acid-Photodynamic Therapy of Superficial Basal Cell Carcinomas," *Clin. Cancer Res.* **14**, 4475-4483 (2008).
67. K. K. Wang, W. J. Cottrell, S. Mitra, A. R. Oseroff, and T. H. Foster, "Simulations of Measured Photobleaching Kinetics in Human Basal Cell Carcinomas Suggest Blood Flow Reductions During ALA-PDT," *Lasers Surg. Med.* **41**, 686-696 (2009).
68. J. F. Jacobs, G. J. M. Koper, and W. N. J. Ursem, "UV Protective Coatings: A Botanical Approach," *Progr. Org. Coatings* **58**, 166-171 (2007).
69. H. Stolz, V. Langer, E. Schreiber, S. Permogorov, and W. von der Osten, "Picosecond Quantum-Beat Spectroscopy of Bound Excitons in Cds," *Phys. Rev. Lett.* **67**, 679-682 (1991).
70. P. A. De Beule, C. Dunsby, N. P. Galletly, *et al.*, "A Hyperspectral Fluorescence Lifetime Probe for Skin Cancer Diagnosis," *Rev. Sci. Instr.* **78**, 123101 (2007).
71. A. J. Thompson, S. Coda, M. B. Sorensen, *et al.*, "In Vivo Measurements of Diffuse Reflectance and Time-Resolved Autofluorescence Emission Spectra of Basal Cell Carcinomas," *J. Biophot.* **5**, 240-254 (2012).
72. A. C. Rechner, *Methods of Multivariate Analysis*, 2nd Ed. ed. (Wiley Interscience, New York, 2002).
73. T. W. Anderson, *An Introduction to Multivariate Statistical Analysis*, 3rd ed., Wiley Series in Probability and Statistics, p. 721 (John Wiley, Hoboken, NJ, 2003).
74. K. R. Beebe and B. R. Kowalski, "An Introduction to Multivariate Calibration and Analysis," *Anal. Chem.* **59**, 1007A-1017A (1987).
75. L. Eriksson, *Multi- and Megavariate Data Analysis. P. 1, Basic Principles and Applications*, 2., rev. and enl. ed., pp. xii, 425 s. (Umetrics Academy, Umeå, 2006).
76. S. Fantini and A. Sassaroli, "Near-Infrared Optical Mammography for Breast Cancer Detection with Intrinsic Contrast," *Ann. Biomed. Eng.* **40**, 398-407 (2012).
77. A. S. R. Koti and N. Periasamy, "Application of Time Resolved Area Normalized Emission Spectroscopy to Multicomponent Systems," *J. Chem. Phys.* **115**, 7094 (2001).
78. A. S. R. K. N. Periasamy, "Time Resolved Fluorescence Spectroscopy: Tres and Tranes," *Proc. Indian Nat. Sci. Acad.* **69A**, 41-48 (2003).
79. D. Chorvat, Jr. and A. Chorvatova, "Spectrally Resolved Time-Correlated Single Photon Counting: A Novel Approach for Characterization of Endogenous Fluorescence in Isolated Cardiac Myocytes," *Eur Biophys J* **36**, 73-83 (2006).

80. E. Sanchez, L. Scott Ramos, and B. R. Kowalski, "Generalized Rank Annihilation Method : I. Application to Liquid Chromatography—Diode Array Ultraviolet Detection Data," *J. Chromatography A* **385**, 151-164 (1987).
81. W. Windig and B. Antalek, "Direct Exponential Curve Resolution Algorithm (DECRA) • a Novel Application of the Generalized Rank Annihilation Method for a Single Spectral Mixture Data Set with Exponentially Decaying Contribution Profiles," *Chemometr. Intell. Lab.* **37**, 241-254 (1997).
82. H. B. Manning, G. T. Kennedy, D. M. Owen, *et al.*, "A Compact, Multidimensional Spectrofluorometer Exploiting Supercontinuum Generation," *J. Biophot.* **1**, 494-505 (2008).
83. R. Bro, "Parafac. Tutorial and Applications," *Chemometr. Intell. Lab.* **38**, 149-171 (1997).
84. A. Curnow, B. W. Mclroy, M. J. Postle-Hacon, A. J. MacRobert, and S. G. Bown, "Light Dose Fractionation to Enhance Photodynamic Therapy Using 5-Aminolevulinic Acid in the Normal Rat Colon," *Photochem. Photobiol.* **69**, 71-76 (1999).
85. A. Lihachev and J. Spigulis, "Skin Autofluorescence Fading at 405/532 nm Laser Excitation," *IEEE Xplore* **10**, 63-65 (2007).
86. J. Spigulis, A. Lihachev, and R. Erts, "Imaging of Laser-Excited Tissue Autofluorescence Bleaching Rates," *Appl. Opt.* **48**, D163-D168 (2009).
87. D. Jakovels and J. Spigulis, "Rgb Imaging of Laser-Excited Skin Autofluorescence Bleaching Rates," in *Laser Applications in Life Sci.*, M. Kinnunen and R. Myllyla, eds. (SPIE-Int Soc Optical Engineering, Bellingham, 2010).
88. M. S. Drew and J. Au, "Clustering of Compressed Illumination-Invariant Chromaticity Signatures for Efficient Video Summarization," *Image and Vision Computing* **21**, 705-716 (2003).
89. J. S. Tyo, E. N. Pugh, and N. Engheta, "Colorimetric Representations for Use with Polarization-Difference Imaging of Objects in Scattering Media," *J. Opt. Soc. Am. A-Opt. Imag. Sci. Vision* **15**, 367-374 (1998).
90. M. Vedel, N. Lechocinski, and S. Breugnot, "Compact and Robust Linear Stokes Polarization Camera," *EPJ Web Conferences* **5**, 01005 (2010).

**Insect monitoring with fluorescence lidar:**

**Feasibility study**

M. Brydegaard, Z. Guan, M. Wellenreuther, and S. Svanberg

*Applied Optics* **48**, 5668-5677, (2009).

# Insect monitoring with fluorescence lidar techniques: feasibility study

Mikkel Brydegaard,<sup>1,\*</sup> Zuguang Guan,<sup>1</sup> Maren Wellenreuther,<sup>2</sup> and Sune Svanberg<sup>1</sup>

<sup>1</sup>Atomic Physics Division, Lund University, P.O. Box 118, SE-221 00 Lund, Sweden

<sup>2</sup>Department of Ecology, Lund University, SE-223 62 Lund, Sweden

\*Corresponding author: mikkel.brydegaard@fysik.lth.se

Received 22 July 2009; revised 27 September 2009; accepted 27 September 2009;  
posted 28 September 2009 (Doc. ID 114651); published 12 October 2009

We investigate the possibilities of light detection and ranging (lidar) techniques to study migration of the damselfly species *Calopteryx splendens* and *C. virgo*. Laboratory and testing-range measurements at a distance of 60 m were performed using dried, mounted damselfly specimens. Laboratory measurements, including color photography in polarized light and spectroscopy of reflectance and induced fluorescence, reveal that damselflies exhibit reflectance and fluorescence properties that are closely tied to the generation of structural color. Lidar studies on *C. splendens* of both genders show that gender can be remotely determined, especially for specimens that were marked with Coumarin 102 and Rhodamine 6G dyes. The results obtained in this study will be useful for future field experiments, and provide guidelines for studying damselflies in their natural habitat using lidar to survey the air above the river surface. The findings will be applicable for many other insect species and should, therefore, bring new insights into migration and movement patterns of insects in general. © 2009 Optical Society of America

OCIS codes: 280.3640, 010.1100, 300.2530, 350.4238, 240.5698, 030.1670.

## 1. Introduction

### A. Background

Light detection and ranging (lidar) techniques have been developed for almost half a century and have since been widely used in, e.g., aerosol monitoring [1–6]. Stationary lidars and mobile systems have been employed with a wide variety of platforms, ranging from submarines, ships, trucks, cranes, airplanes, to satellites [7–10]. Aerosol studies typically involve vertical soundings or the generation of three-dimensional distribution maps. The data are usually obtained by time-resolved measurements of elastic backscattering using a limited number of laser frequencies. Even polarization of backscattered light can be analyzed to provide information regarding the number of scattering events and particle size distribution [10,11]. Apart from the strongly dominat-

ing elastic backscattering methods, three further lidar methods have been developed for detailed spectral analysis and classification of aerosols. These methods are based on (laser-induced fluorescence (LIF) spectroscopy [12–16], Raman spectroscopy [17], and laser-induced breakdown spectroscopy (LIBS) [18–22]). LIF methods have been employed in the past to distinguish between different types of pollen and aerosols that can potentially be used in biological warfare [16]. Raman lidar gives weak signals and has mostly been employed on water and nitrogen [17]. The LIBS method is more difficult to employ, but recent work has demonstrated assessment of aerosol salinity [22], following very early Russian work on cement particles [18]. Traditionally, aerosol particles are considered to be solid or liquid particles that can range from smoke, which has a particle size of a few nanometers, to friction particles and raindrops of several hundred micrometers in size. In addition to these advances, insects and even vertebrates, such as birds and bats, could potentially be detected using lidar techniques. In the past, bird

and insect monitoring and tracking have been extensively investigated using radar methodologies [23–26], including the classification of animals by multiband (matched) illumination [27,28]. Such applications of remote sensing techniques have important implications for local agriculture, as they allow pest forecasting. Reflectance signatures measured with multiband radar methods are typically given by interference arising from the structures of the reflecting object. However, similar advances in the use of lidar techniques have been slow, and until now, only a few studies have directly investigated the feasibility of lidar in insect and vertebrate monitoring. One example comes from a lidar study on honey bees in land mine detection [11]. That study measured backscattered light at a single wavelength and in two polarizations to detect bee echoes and to build up stochastic histograms to summarize the bee concentration in relation to the actual land mine locations. In addition, lidar sounding of fish demonstrated the possibility to detect moving live scatterers [29,30]. The bee study was followed up by investigations involving background rejection by wing beat modulation of reflected light [31,32]. Such an approach has also been used in the bird radar community [33], with the difference that the modulation frequencies are several magnitudes smaller.

## B. Motivation and Strategy

The present paper describes spectroscopic studies of two odonate species (Odonata: damselflies and dragonflies), the banded demoiselle *Calopteryx splendens* and the beautiful demoiselle *C. virgo* [34]. In particular, the main focus of this study was to test the feasibility of lidar for damselfly monitoring and study of movement patterns. Damselfly larvae are highly sensitive to water pollution and oxygen concentrations and have thus been used as biomarkers in the past [35]. Another important characteristic of damselflies is that, like all other insects, they are ectotherms and are particularly sensitive to changes in temperatures. Therefore, increasing ambient temperatures are expected to force insect species to shift their distributions by expanding into new geographic areas and by trying to escape from areas that become climatically unsuitable [36]. In Europe, many documented cases of range shifts among insects have been attributed directly to increasing temperatures [37]. For example, out of the 35 European butterfly species that were studied [38], 22 have shifted their ranges northward by 35–240 km over the last century, whereas only two have shifted south. There is also direct evidence that the species studied in the present work, *Calopteryx splendens* and *C. virgo*, are currently affected by climate change. In a recent study [39] Hickling *et al.* showed that 23 of the 24 temperate Odonata species in the United Kingdom, including the two *Calopteryx* species, significantly expanded their range size and northern range limit between 1960 and 1995. Together, these data strongly indicate that European

populations of these insects are currently moving northward.

Migration studies of insects are crucial for understanding the roles of gene flow in connecting population over a wide spatial scale [40,41], but progress in this area has been hampered by the difficulty of marking individuals. As a consequence, studies typically involve neighboring and low numbers of populations. Migration in insects is relatively difficult to study with traditional methods, such as radio transmitters or light loggers, because the size and weight of damselflies makes the attachment of the disproportionately large devices difficult. An alternative approach would be to mark neighboring populations with combinations of two or three different fluorescent dyes, such as Rhodamine variants, and then detect migrated marked individuals at a given population [42], by correlating the spectral fingerprint of each detected individual with the population of origin. Such dyes could either be sprayed or powdered on individual specimens or absorbed by the individual through the metabolic uptake of food or water (e.g., during the aquatic larval stage) [42–46]. A number of fluorescent dyes have already been used for freshwater tracking and environmental studies, and other dyes already exist due to detergents in wastewater [47]. Even with only a few appropriate and noninterfering dyes, a much larger number of site locations could be monitored simultaneously by using various nonparallel spectral combinations of the few dye types. This is especially true if the probability of detecting two individuals in a single voxel is small.

This paper presents optical spectroscopic features and the feasibility of damselfly monitoring using lidar and lidar LIF methods, and is organized in the following way. In Section 2 the general photophysical aspects of Odonata are discussed. Then, in Section 3, we develop strategies for the remote classification of the two damselfly species and the respective genders in order to produce species and gender selective three-dimensional distributions and behavioral studies over a temporal scale [48]. In particular, we demonstrate how to generate broadband “white” light by autofluorescence on the surface layers of *C. splendens* and *C. virgo* in order to detect how structural colors affect fluorescence. Such surface probed fluorescence studies have resemblance to those presented in [49]. In addition, laboratory and outdoor test range measurements are also described, including descriptions of methods for damselfly marking [42] to study migration of individuals between populations. For this we further investigate lidar LIF methods enhanced by fluorescent dye marking. In the latter case, individuals are marked with dye either by spraying or powdering dyes directly on the individual [46] or by adding dyes to the water, which is then incorporated into the body by the individual during the larval phase [50]. We further show how the structural imprint of the dye-enhanced fluorescence can be used for remote classification

of species and genders. Finally, in Section 4, we discuss the results and give suggestions for future work.

## 2. Damselfly Species Description and Relevant Photophysics

Photographs of *Calopteryx splendens* and *C. virgo* of both genders are shown in Fig. 1. The optical properties of the majority of insects are determined both by the chemical absorption imprint yielding “classical” colors, and structural colors, due to interference [51–58]. This becomes particularly clear when damselflies are observed in polarized light [58]. While common lidar methods like LIF lidar, differential absorption lidar (DIAL), and LIBS lidar commonly measure chemical colors, structural colors have never been measured in the lidar community, due to the fact that organized cells or organelles and layered structures on the nanoscale are required for the effect to be noteworthy. Even though ordinary cells might leave weak structural imprints in traditional reflectance, absorption, or fluorescent measurements [59,60], such effects are typically neglected. The main features of the reflectance of the damselfly abdomen can be explained by the arrangement of approximately 100 nm sized scattering nanospheres. (This is illustrated in Fig. 7(c) adopted from [61], to be discussed later.) This arrangement provides damselflies with their typical retroreflective properties, and an approximately 100 nm broad reflection band shifting from the blue to the green region, depending on the sizes of the nanospheres and on the angle of observation with respect to surface orientation and illumination. The nanosphere arrangement is situated just below the chitin cuticulum; the cuticulum can be more or less melanized [62]. Both chitin and melanin absorption peaks around 330 nm and both chitin and melanin produce broad fluorescence spectra covering the structural features in the blue and green region [63–65]. Further, certain Ordonates are known to have wax covered wings [66]. Botanical waxes are well studied in LIF lidar [67]. Typically, wax absorption increases dramatically below 355 nm and the maximum fluor-

escence yield is usually obtained around 330 nm excitation. Even waxes provide broad fluorescence spectra peaking in the blue region [68]. Reflectance can be further modified by absorbing ommochrome granules, which are situated beneath the scattering arrangement and prevent nonscattered light from being reemitted and, thus, strengthen the structural color. Furthermore ommochromes in certain Odonata species react to the temperature, regulating the temperature of the ectotherms by either migrating into the nanosphere region or contracting to a deeper lying layer, which increases reflectance. Such effects can be expected to alter even the fluorescence. The lowest of the six visual spectral bands typically found in Odonata [69] goes as far as 350 nm in the UV; thus, it is not unreasonable to expect the studied species to sexually signal via altered reflectance in this band. Vibrant structural colors are exhibited by the blue males of *C. splendens* and the green males of *C. virgo* [70]. Females of both species appear less colorful, with brown, green, and golden shadings. Males and females of the two *Calopteryx* species differ significantly in the absorption properties of their wings, due to differences in the amount of melanin. Males of *C. virgo* typically have over 90% of their wings melanized, whereas males of *C. splendens* have melanized patches covering about 50% of the wing surface [71–74]. Females of both species lack the melanized wing patches, but *C. virgo* females are brown, while *C. splendens* females are typically green [50].

## 3. Methods, Measurements, and Results

Optical measurements were performed under controlled conditions, both on a macro scale in the laboratory and on a 60 m lidar testing range. Measurements were taken in order to gain insights into the optical properties of the studied species and to develop realistic and practical methods for future field work.

### A. Laboratory Measurements

The reflective properties caused by the structural colors were investigated in detail in the laboratory. To confirm that the blue and green shades are indeed structural, two samples were photographed from a distance of 60 cm with a Sony F828 digital still red-green-blue (RGB) camera with a fixed visible linear polarizing laminated film (Edmund Optics) attached to the objective. The sample was illuminated by collimated light from a filament source (100 W Oriel, halogen-tungsten blackbody source) at an angle of 15°; see Fig. 2. For the experiment, two dried specimens (*C. splendens*, male and female) were fixed on a wire, and were photographed with parallel and perpendicular polarized illumination with respect to the polarizer on the camera objective. The photographs with maintained polarization reveal green, golden, and blue shades (Fig. 3), whereas the depolarized pictures are considerably darker and show mostly brown and reddish colors. For the convenience of the viewer, the intensities of the depolarized



Fig. 1. (Color online) Males of *C. virgo* have almost completely melanized wings, whereas males of *C. splendens* have melanized wing patches. The wings of *C. virgo* females are brown, while the wings of *C. splendens* females are typically green.

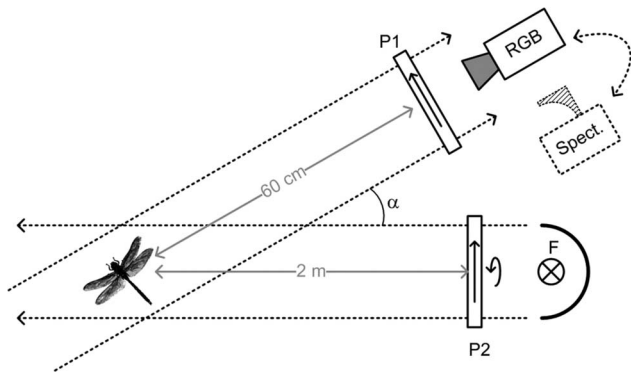


Fig. 2. Setup for color imaging and whole-body polarized reflectance studies. Samples are observed either with a color camera (RGB) or a spectrometer (Spect.) at low angle ( $\alpha = 15^\circ$ ) through a linear polarizer (P1). Collimated white illumination is provided by a tungsten filament lamp (F) which can be polarized in parallel or perpendicularly to P1 using P2.

photographs in Fig. 3 are multiplied by a factor of 5. Depolarized reflections originate mainly from the hairy parts of the specimens, more specifically, from multiple reflections of the four-folded wing and the abdomen tip. By subtracting the depolarized intensity from the polarized, we retain the pure structural color and, again, green, golden, and blue shades are observed. This finding is in contrast to the appearance of multiple-scattering biological samples, such as leaves or skin, where the structural color appears flat white, simply describing the refractive index of the sample (specular reflex). Following that, the samples were studied in a stereo microscope with a ring light configuration, and the results showed that the

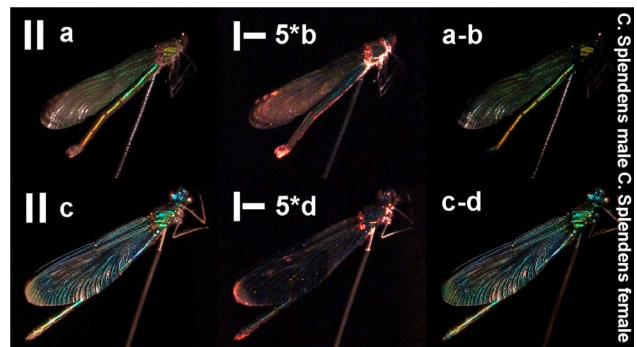


Fig. 3. (Color online) Photograph of damselflies in polarized light. Photographs a and c, indicated with  $\parallel$ , are photographed with parallel polarizers. Photographs b and d, indicated with  $\perp$ , show the depolarized light amplified by a factor of 5 to make it visible to the reader. Subtraction gives us the two figures to the outermost right, where structural colors remain.

structural blue and green shades were distributed over the entire body and wings, despite the fact that the effect to the naked eye was most obvious on the abdomen and thorax.

Studies of the whole-body reflectance were also performed by exchanging the RGB camera with a spectrometer (Ocean Optics USB4000) with an off-axis parabolic mirror telescope; see Fig. 2. Again, the spectral reflectance of the polarized and depolarized lights were measured for both specimens (*C. splendens* males and females); see Fig. 4. The depolarized reflectance is more than 1 magnitude smaller than the polarized, and the blue and green structural imprint disappears. The units are referenced to a  $\emptyset$  50 mm barium sulfate plug (approximately the size of

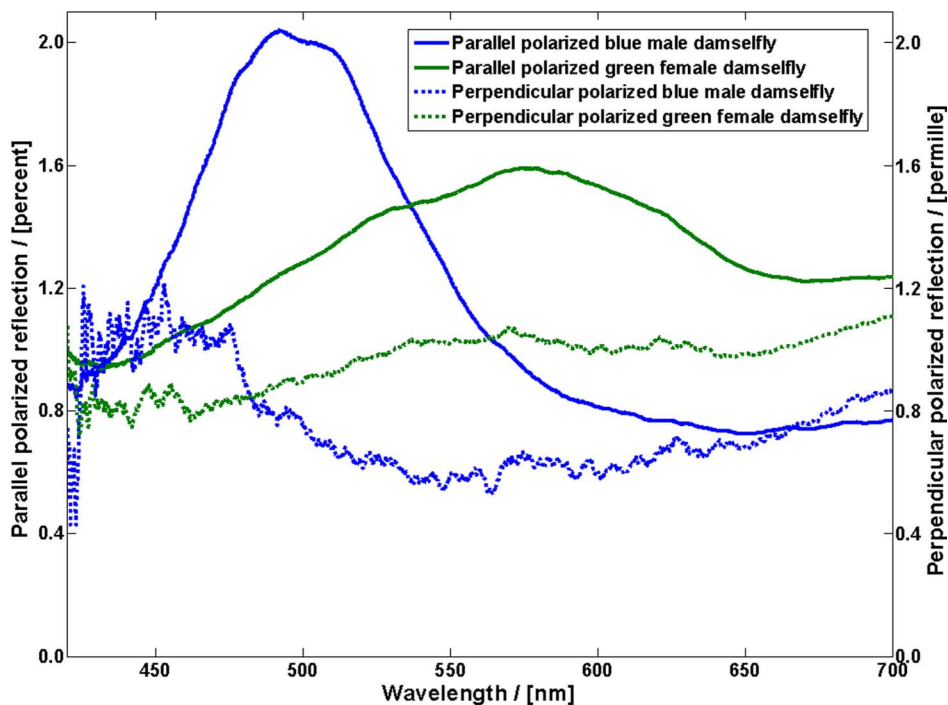


Fig. 4. (Color online) Polarized and depolarized whole-body reflectance measurements of *C. splendens* males and females. The blue and green reflectance features, respectively, disappear when polarizers are crossed. (Note the different scales.)

the specimen). The whole-body reflectances in Fig. 4 were also measured at a 15° angle with respect to the illumination. Further angular studies (data not presented here) reveal that the specimens have strong retroreflective properties, and that most light is reflected back directly toward the illumination. Also, the structural features are displaced to lower wavelengths when the angle between illumination and observation increases (shifts of the order of 50 nm were observed over 60°). This might have biological relevance, since the appearance to aquatic predators would be more bluish and match the sky, while the appearance to terrestrial predators would be slightly more greenish and match the vegetation.

Since broadband reflectance time-resolved lidar is labor intensive to perform, considering requirements for pulsed collimated sources, it would be considerably more realistic to perform LIF lidar. For this reason, the resemblance of reflectance and fluorescence was studied. It is well known that fluorescence spectroscopy cannot be performed without the influence of reflectance and transmission or considering photon migration spectroscopy. Thus, we can expect certain correlations between the two methods. Dried *C. splendens* specimens were measured at several spots using a bifurcated fiber probe; see Fig. 5. The illuminating fiber was connected to a diode laser at 375 nm (Power Technology Incorporated) or a white-light xenon flash (Ocean Optics, PX-2) for fluorescence and reflectance measurements, respectively. The collected light was detected in a spectrometer (Ocean Optics, USB4000) through a GG400 long-pass filter [75]. The sample and probe remained fixed at a 5 mm distance from the target in the fluorescence and reflectance measurements.

It is a general phenomenon that shorter excitation wavelengths are typically absorbed in the outer layers of biological samples [49,67] and autofluorescence from a number of biological compounds is usually produced with a small Stokes shift and with broad bluish–greenish fluorescence spectra. The measurements were performed at various spots on

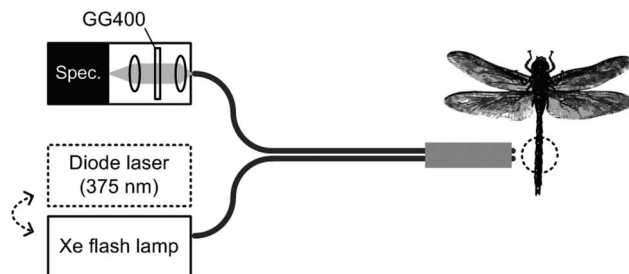


Fig. 5. Setup for fiber point measurements. Either a UV laser line or white light is passed into the bifurcated probe. The sample geometry is maintained constant between the measurements. A long-pass GG400 filter prevents blooming in the spectrometer (Spec.).

the specimens; however, not all data are presented here. Both laboratory and lidar test-range measurements suggest that bluish reflecting samples appear even more bluish under fluorescence, and greenish reflecting samples appear even more greenish under fluorescence; see Fig. 6. Our current understanding is that excitation light is absorbed in the outer layers of the cuticulus, either by wax, melanin, chitin, or in the scattering nanospheres themselves, producing broadband fluorescence light, which, in turn, is reflected by the underlying structural color-generating layers. In this way, the structural color enhances the blue or the green part of the fluorescence that is produced.

#### B. Lidar Test-Range Measurements

The Lund mobile lidar system, which is thoroughly described in [7] and displayed in Fig. 7, was used for remote measurements on damselflies. It is basically a coaxial system with a Ø 40 cm vertically looking telescope with the optical path folded by a roof-top scanning mirror. The repetition rate is 20 Hz. One laser transmitter is a Q-switched Nd:YAG laser, where the fundamental (1064 nm), the second-harmonic (532 nm), the third (355 nm), and the fourth-harmonic (266 nm) frequencies can be produced simultaneously. A second transmitter is a Nd:YAG-pumped optical parametric oscillator (OPO) system with wide

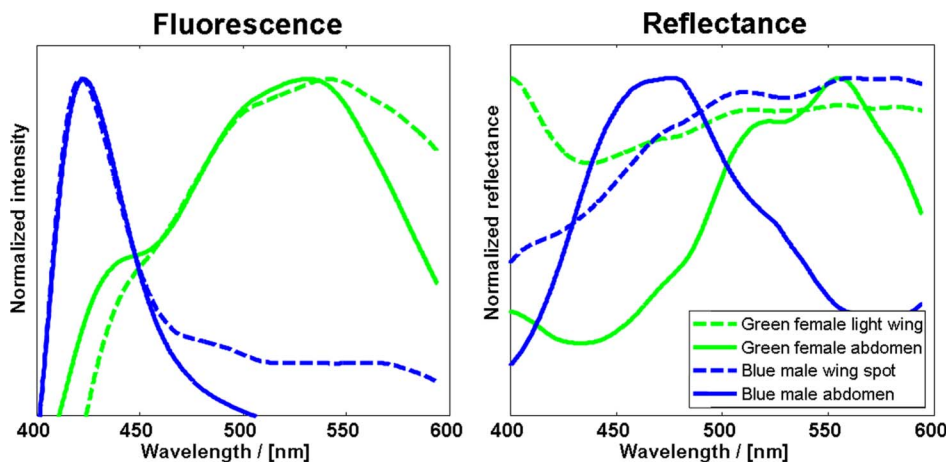


Fig. 6. (Color online) Comparison between reflectance and fluorescence spectra. In general, all measurements performed in this study suggest a positive correlation between fluorescence emission and reflectance.

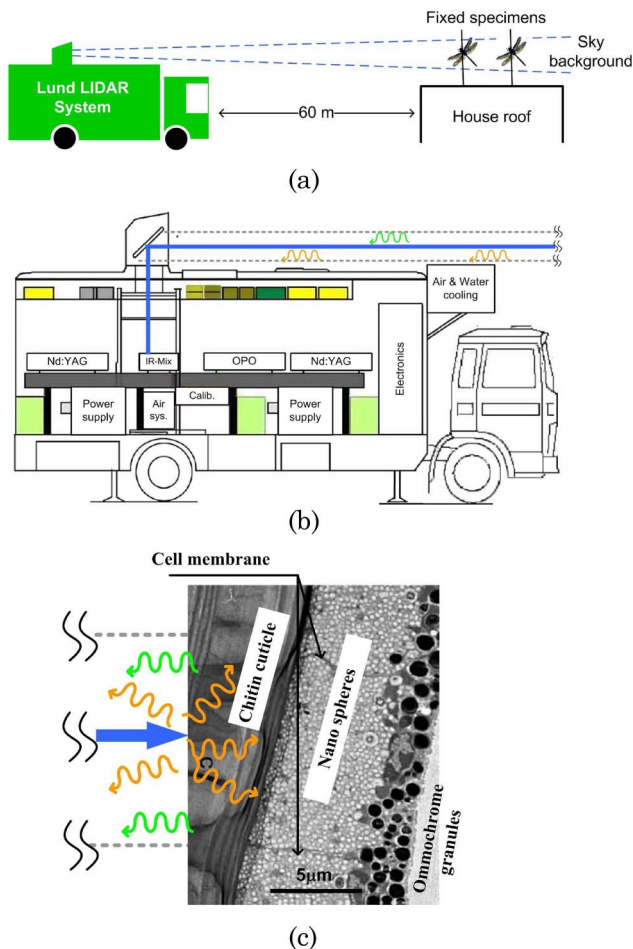


Fig. 7. (Color online) (a) Setup for test-range experiments. Insects were mounted on thin clean aluminum threads and were detected toward a bright sky background. (b) The versatile mobile lidar provides pulsed light continuously from 200 nm to 4  $\mu\text{m}$ . (c) The UV laser light induces broad fluorescent light in the wax or chitin, which is, in turn, partly reflected in the nanosphere array.

tunability, augmented by nonlinear wavelength-shifting techniques. In our initial experiments, we employed only the 355 and 266 nm radiation for demonstration. In the measurements, the pulse energies are limited to 25 and 10 mJ, respectively, for these two wavelengths. The FWHM of the laser pulse is approximately 15 ns, corresponding to about 2.25 m axial resolution. The spot size for the test-range measurements of targets at 60 m was approximately  $\varnothing$  10 cm. For the time-domain recording, a photomultiplier tube (PMT) (EMI 9816 QA) was used as the detector and an oscilloscope (Tektronix TDS544B) was used as the digitizer, sampling every 4 ns. The elastic signal was recorded through a 45° 355 nm dichroic mirror followed by a Schott UG11 filter to further suppress the background. Two fluorescence bands were recorded simultaneously by additional PMTs but will not be presented in this paper. For initial remote spectral analysis of LIF, an intensified fiber-coupled optical multiple channel analyzer (OMA) system is employed. With a 1 mm diameter fiber to transport light from the telescope focal plane to the spec-

trimeter, and using the fiber end as the “slit,” a spectral resolution of 14 nm was obtained. Detailed information of the OMA system can be found in [76]. Fluorescence with excitation at 355 nm was detected from the 60 m distant target through a 5 mm GG400 Schott filter, and fluorescence with excitation at 266 nm was detected through a 3 mm WG305 Schott filter; in each case the filters were used to suppress the overwhelming elastic signal while transmitting fluorescence at the lowest wavelengths as possible.

Elastic lidar returns from damselflies, which are mounted at 60 and 80 m distances, are shown in Fig. 8. Pulses at the third-harmonic Nd:YAG wavelength, 355 nm, were sent out after initial expansion into a 5 cm diameter beam, and echoes were collected with the lidar telescope. Elastic photons were selected with a dichroic 45° laser line mirror followed by a Schott UG11 high-pass glass filter. The signal was recorded by the PMT. Measurements were performed on two dried specimens of *C. splendens*, exposed to the expanded laser beam and with the gray sky as the background. The damselflies were held by thin aluminum wires (echoes from the wires were relatively small). The orientation and the position of the two specimens in the beam were heavily randomized by high wind speeds. Apart from the strong reflection from the window of the lidar system, both specimens are clearly resolved. The second echo is slightly weaker than the first. This might be explained by different orientation and positions in respect to the beam; also, the first specimen is partly shadowing both excitation and backscattered photons. Also, the trivial LIDAR signal falloff with range is at play.

Results from fluorescence measurements with the OMA system are shown in Fig. 9, for 355 and 266 nm excitation. Slight differences between the genders of *C. splendens* can be seen. The autofluorescence spectra were recorded at a 60 m distance at 355 nm excitation and in the lidar laboratory at 266 nm excitation (due to weather conditions). The insect specimens were the same, but the orientation was random as before. Beam sizes were  $\varnothing$  10 cm and 1 cm, respectively. A GG400 and a WG305 Schott long-pass filter

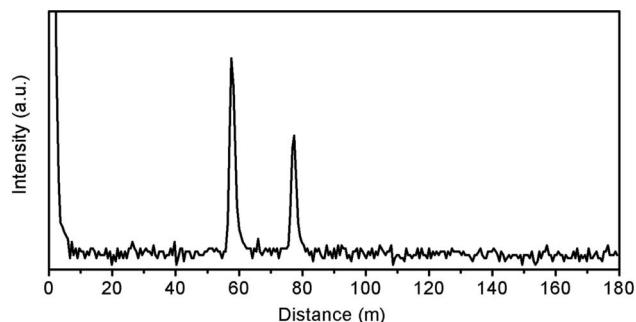


Fig. 8. Elastic lidar recording of mounted damselflies; the transmitted wavelength is 355 nm. Data are from a single laser pulse and the echoes arise from two fixed specimens (*C. splendens* female and male respectively) separated by 20 m. Fluorescence time series recording were also performed but are not presented in this paper.

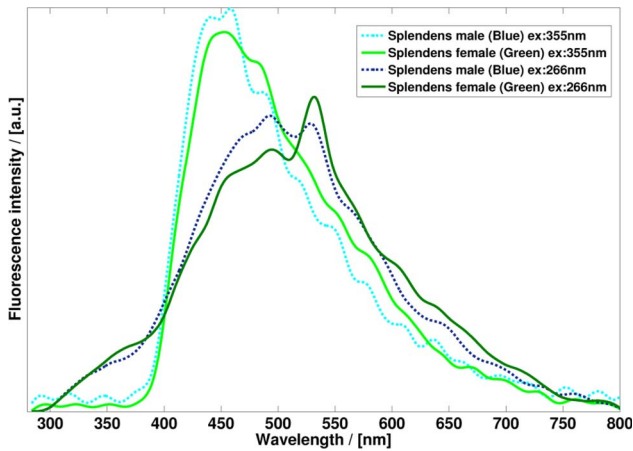


Fig. 9. (Color online) Normalized fluorescence spectra for 266 and 355 nm excitation; in both cases, imprints of the structural color are observed. Data from 20 laser shots were averaged.

were used, respectively. Emission spectra are broad and cover the region of 400–600 nm, where structural imprints are expected to occur. Emission spectra could be explained by previous measured spectra of both melanin and chitin. Even if the signal is weak, a slight difference between a blue and a green reflecting sample can be observed at both excitation wavelengths (Fig. 9). Both chitin and melanin absorption peak around 330 nm and the signal-to-noise ratio could probably be improved by moving to such an excitation wavelength.

Results of fluorescence lidar measurements on damselflies prepared with Coumarin 102 and Rhodamine 6G dye are shown in Fig. 10. In preparation for migration studies and population encoding experiments, dried specimens of both genders of *C. splendens* were sprayed with water solutions containing these dyes. Fluorescence spectra were measured at a 60 m distance with the same procedure as before. Apart from the obviously much stronger fluorescence signal from the two dyes, males and females with, respectively,

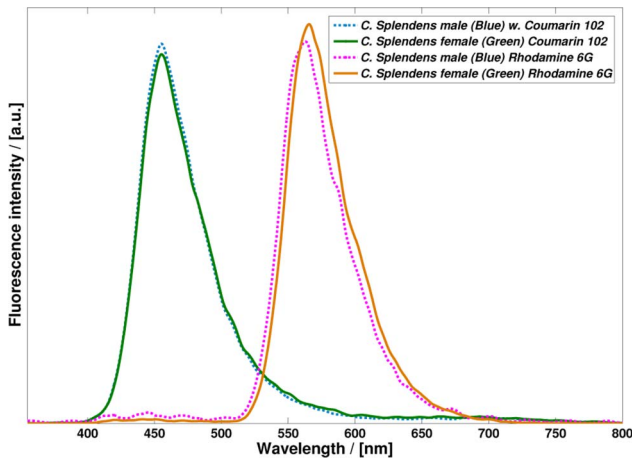


Fig. 10. (Color online) Fluorescence spectra for 355 nm excitation for dye-marked females and males of *C. splendens*. Strong dye fluorescence bands are seen with slight modifications due to structural colors. Data from 20 laser shots were averaged.

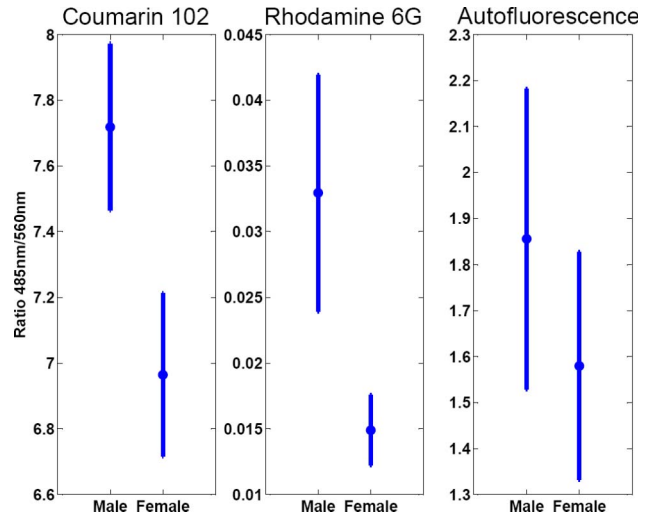


Fig. 11. *Calopteryx splendens* male/female contrast in autofluorescence and when using dye-enhanced fluorescence. Bars show standard deviation for a total of 20 shots. The overlap in autofluorescence is interpreted as lack of signal rather than lack of physical difference of the samples.

blue and green structural colors show distinct fluorescence spectra. This is in accordance with the view that the generated fluorescent light is reflected in the insect structures and, thus, the structural color imposes an imprint on the observed fluorescence.

Separation of male and female damselflies based on the measured ratio between two fluorescence intensities (at 485 and 560 nm, 25 nm FWHM, respectively) is illustrated in Fig. 11. In this case, we define the bands mathematically, with the spectra provided from the OMA, but such bands could easily be implemented using optical filters in front of PMTs with much higher sensitivity. When we take the ratio between the two bands, intensity units cancel, and the influence of all geometric effects due to sample orientation, position with respect to the laser beam, collection efficiencies, etc., cancel. We see a clear distinction between the *C. splendens* male and female specimens for the dyed samples. For the autofluorescence, the tendency is the same, but the contrast is poorer. This is mainly due to noisy signals rather than lack of physical differences.

#### 4. Discussion

We have performed a feasibility study to investigate the possibilities of lidar to study interpopulation migration and movement of the damselfly species *Calopteryx splendens* and *C. virgo*. Laboratory, as well as testing-range measurements, of dried, mounted specimens at distances of 60 to 80 m were performed. The damselflies exhibit reflectance and fluorescence properties that are closely tied to the generation of structural colors. Laboratory measurements, including color photography in polarized light and spectroscopy of reflectance and induced fluorescence, revealed these phenomena and an interesting connection between reflectance and fluorescence features. To our knowledge, we are the first group to acquire

structural colors using lidar. The number of *C. virgo* samples was limited as the dried samples are considerably fragile; hence, they quickly disintegrate in the measurement wind conditions. Laboratory measurements on *C. virgo* involving polarized color photographing and point reflectance/fluorescence were carried out. The results of these measurements also confirmed that the reflectance is indeed largely influenced by nanostructures and, as for *C. splendens*, the emitted fluorescence is positively correlated with the reflectance at the same wavelength region. Studies on lidar data of *C. splendens* of both genders showed that males and females can be remotely distinguished, especially for specimens that were marked with the dyes Coumarin 102 and Rhodamine 6G. The strength of the fluorescence signals (when studied with an optical multichannel analyzer connected to the lidar telescope) indicated that an arrangement of a small number of PMTs, each detecting a chosen spectral band, is advantageous for realistic single-shot recordings of flying insects. With such a setup, range-resolved recordings are obtained, which is advantageous compared to the gated spectrometer approach, where the time gate has to be preset. Such an approach is now being implemented in preparation for upcoming field experiments, where damselflies in their natural habitat will be studied with the lidar beam positioned at different heights over the river surface. Field studies have the potential to bring new insights into the migration, movement, and flying patterns of *Calopteryx* damselflies, and will provide guidelines for studies of other insect species. One concern when using LIF lidar at 266 nm is the transmission of the excitation light in the atmosphere; depending on varying conditions, ozone absorption and air scattering will attenuate the excitation pulse. Early work experience from previous field campaigns tells us that lidar returns can be detected in horizontal soundings at kilometer ranges even at 254 nm, where ozone absorbs the most [77,78]. The conditions might, however, not always be feasible. Alternative solutions for acquisition of structural colors by lidar might be found in multiband illumination with several laser lines, or with pulsed supercontinuum light sources [79,80]. However, the issues concerning eye safety in field settings would be much more severe than for the eye-safe UV used in, e.g., LIF lidar.

This work was supported by a Swedish Research Council project grant and by a Linnaeus grant to the Lund Laser Centre, Sweden. Fruitful discussions with and kind help from Patrik Lundin, Richard Prum, Joseph A. Shaw, Eric Warrant, Erik Svensson, Lisa Orr, and Can Xu are gratefully acknowledged.

## References

1. R. M. Measures, *Laser Remote Sensing: Fundamentals and Applications* (Wiley, 1984).
2. R. M. Measures, ed., *Laser Remote Chemical Analysis* (Wiley-Interscience, 1988).
3. M. Sigrist, ed., *Air Pollution Monitoring with Optical Techniques* (Wiley, 1993).
4. C. Weitkamp, ed., *LIDAR: Range-Resolved Optical Remote Sensing of the Atmosphere*, Springer Series in Optical Sciences (Springer, 2005).
5. T. Fujii and T. Fukuchi, eds., *Laser Remote Sensing* (CRC, 2005).
6. S. Svanberg, "LIDAR," in *Springer Handbook of Lasers and Optics* F. Träger, ed. (Springer, 2007), pp. 1031–1052.
7. P. Weibring, H. Edner, and S. Svanberg, "Versatile mobile lidar system for environmental monitoring," *Appl. Opt.* **42**, 3583–3594 (2003).
8. S. Harsdorf, M. Janssen, R. Reuter, B. Wachowic, and R. Willkomm, "Lidar as part of an ROV-based sensor network for the detection of chemical pollutants on the seafloor," in *Oceans '98 Conference Proceedings* (IEEE, 1998), Vol. 3, pp. 1250–1253.
9. M. Sowinska, B. Cunin, F. Heisel, and J. A. Miehe, "New UV-A laser-induced fluorescence imaging system for near-field remote sensing of vegetation: characteristics and performances," *Proc. SPIE* **3707**, 91–102 (1999).
10. D. M. Winker, C. A. Hostetler, M. A. Vaughan, and A. H. Omar, "Mission, Instrument, and Algorithms Overview," PC-SCI-202.01 (NASA, 2006), [www-calipso.larc.nasa.gov](http://www-calipso.larc.nasa.gov).
11. J. A. Shaw, N. L. Seldomridge, D. L. Dunkle, P. W. Nugent, L. H. Spangler, J. J. Bromenshank, C. B. Henderson, J. H. Churnside, and J. J. Wilson, "Polarization lidar measurements of honey bees in flight for locating land mines," *Opt. Express* **13**, 5853–5863 (2005).
12. S. Svanberg, "Laser fluorescence spectroscopy in environmental monitoring," in *Optoelectronics for Environmental Science*, S. Martellucci and A. N. Chester, eds. (Plenum 1990), pp. 15–27.
13. H. Edner, J. Johansson, S. Svanberg, and E. Wallinder, "Fluorescence lidar multicolor imaging of vegetation," *Appl. Opt.* **33**, 2471–2479 (1994).
14. P. Weibring, Th. Johansson, H. Edner, S. Svanberg, B. Sundnér, V. Raimondi, G. Cecchi, and L. Pantani, "Fluorescence lidar imaging of historical monuments," *Appl. Opt.* **40**, 6111–6120 (2001).
15. S. Svanberg, "Fluorescence spectroscopy and imaging of LIDAR targets," in *Laser Remote Sensing*, T. Fujii and T. Fukuchi eds. (CRC, 2005), Chap. 6.
16. Ø. Farsund, G. Rustad, I. Kåsen, and T. V. Haavardsholm, "Required spectral resolution for bioaerosol detection algorithms using standoff laser induced fluorescence measurements," *IEEE Sens. J.* **6** (2009).
17. D. N. Whiteman, S. H. Melfi, and R. A. Ferrare, "Raman LIDAR system for the measurement of water-vapor and aerosols in the earths atmosphere," *Appl. Opt.* **31**, 3068–3082 (1992).
18. V. E. Zuev, Y. D. Kopytin, V. A. Korolkov, M. E. Levitskii, M. F. Nebolsin, B. G. Sidorov, and N. P. Soldatkin, in *Proceedings of the 13th International Laser Radar Conference* (NASA Langley Research Center, 1986).
19. S. Palanco, J. M. Baena, and J. J. Laserna, "Open-path laser-induced plasma spectrometry for remote analytical measurements on solid surfaces," *Spectrochim. Acta B* **57**, 591–599 (2002).
20. K. Stelmaszczyk, P. Rohwetter, G. Méjean, J. Yu, E. Salmon, J. Kasparian, R. Ackermann, J.-P. Wolf, and L. Wöste, "Long-distance remote laser-induced breakdown using filamentation in air," *Appl. Phys. Lett.* **85**, 3977–3979 (2004).
21. R. Grönlund, M. Lundqvist, and S. Svanberg, "Remote imaging laser-induced breakdown spectroscopy and laser-induced fluorescence spectroscopy using nanosecond pulses from a mobile lidar system," *Appl. Spectrosc.* **60**, 853–859 (2006).
22. T. Fujii, N. Goto, M. Miki, T. Nayuki, and K. Nemoto, "Lidar measurement of constituents of microparticles in air by

- laser-induced breakdown spectroscopy using femtosecond terawatt laser pulses,” *Opt. Lett.* **31**, 3456–3458 (2006).
23. M. Skolnik, *Introduction to Radar Systems*, 3rd ed. (McGraw-Hill, 2002).
  24. J. C. Toomay and P. J. Hannen, *Radar Principles for the Non-Specialist*, 3rd ed. (SciTech, 2004).
  25. S. A. Gauthreaux Jr. and C. G. Belsler, “Radar ornithology and biological conservation,” *The Auk* **120**, 266–277 (2003).
  26. J. W. Chapman, D. R. Reynolds, and A. D. Smith, “Vertical-looking radar: a new tool for monitoring high-altitude insect migration,” *BioScience* **53**, 503–511 (2003).
  27. D. T. Gjessing, *Target Adaptive Matched Illumination Radar: Principles and Applications* (Institution of Engineering and Technology, 1986).
  28. S. P. Lohmeier, S. M. Sekelsky, J. M. Firda, G. A. Sadowy, and R. E. McIntosh, “Classification of particles in stratiform clouds using the 33 and 95 GHz polarimetric cloud profiling radar system (CPRS),” *IEEE Trans. Geosci. Remote Sens.* **35**, 256–270 (1997).
  29. K. Fredriksson, B. Galle, K. Nyström, S. Svanberg, and B. Öström, “Underwater laser-radar experiments for bathymetry and fish-school detection,” Göteborg Institute of Physics Reports GIPR-162 (Chalmers University of Technology, Göteborg, 1978).
  30. K. Fredriksson, B. Galle, K. Nyström, S. Svanberg, and B. Öström, “Marine laser probing: results of a field test,” Meddelanden från Havsfiskelaboratoriet No. 245 (Swedish Department of Fishery, Stockholm, 1979).
  31. K. S. Repasky, J. A. Shaw, R. Scheppele, C. Melton, J. L. Carsten, and L. H. Spangler, “Optical detection of honeybees by use of wing-beat modulation of scattered laser light for locating explosives and land mines,” *Appl. Opt.* **45**, 1839–1843 (2006).
  32. D. S. Hoffman, A. R. Nehrir, K. S. Repasky, J. A. Shaw, and J. L. Carlsten, “Range-resolved optical detection of honeybees by use of wing-beat modulation of scattered light for locating land mines,” *Appl. Opt.* **46**, 3007–3012 (2007).
  33. Von R. Bloch, B. Bruderer, and P. Steiner, “Flugverhalten nächtlich ziehender Vögel—Radardaten über den Zug verschiedener auf einem Alpenpass,” *Die Vodelwarte* **31**, 119–146 (1981).
  34. P. S. Corbet, *Behavior and Ecology of Odonata* (Harley, 1999).
  35. M. Campero, F. Ollevier, and R. Stoks, “Ecological relevance and sensitivity depending on the exposure time for two biomarkers,” *Environ. Toxicol.* **22**, 572–581 (2007).
  36. C. A. Deutsch, J. J. Tewksbury, R. B. Huey, K. S. Sheldon, C. K. Ghalambor, D. C. Haak, and P. R. Martin, “Impacts of climate warming on terrestrial ectotherms across latitude,” *Proc. Natl. Acad. Sci. USA* **105**, 6668–6672 (2008).
  37. C. Parmesan, “Ecological and evolutionary responses to recent climate change,” *Annu. Rev. Ecol. Syst.* **37**, 637–669 (2006).
  38. C. N. Parmesan, C. Ryrholm, C. Steganescu, J. K. Hill, C. D. Thomas, B. Descimon, B. Huntley, L. Kaila, J. Kullberg, T. Tammaru, W. J. Tennent, J. A. Thomas, and M. Warren, “Poleward shifts in geographical ranges of butterfly species associated with regional warming,” *Nature* **399**, 579–583 (1999).
  39. R. Hickling, D. B. Roy, J. K. Hill, and C. D. Thomas, “A northward shift of range margins in British Odonata,” *Glob. Change Biol.* **11**, 502–506 (2005).
  40. T. J. Case and M. L. Taper, “Interspecific competition, environmental gradients, gene flow, and the coevolution of species’ borders,” *Am. Nat.* **155**, 583–605 (2000).
  41. D. Garant, S. E. Forde, and A. P. Hendry, “The multifarious effects of dispersal and gene flow on contemporary adaptation,” *Funct. Ecol.* **21**, 434–443 (2007).
  42. J. R. Hagler and C. G. Jackson, “Methods for marking insects: current techniques and future prospects,” *Annu. Rev. Entomol.* **46**, 511–543 (2001).
  43. M. D. Ginzel and L. M. Hanks, “Evaluation of synthetic hydrocarbons for mark–recapture studies on the red milkweed beetle,” *Journal of chemical ecology* **28**, 1037–1043 (2002).
  44. R. W. Piper, “A novel technique for the individual marking of smaller insects,” *Entomol. Exper. Appl.* **106**, 155–157 (2003).
  45. A. E. A. Stephens, A. M. Barrington, V. A. Bush, N. M. Fletcher, V. Mitchell, and J. D. M. Suckling, “Evaluation of dyes for marking painted apple moths (*Teia anartoides* Walker, *Lep. Lymantriidae*) used in a sterile insect release program,” *Aust. J. Entomol.* **47**, 131–136 (2008).
  46. T. P. Gosden and E. I. Svensson, “Density-dependent male mating harassment, female resistance and male mimicry,” *Am. Nat.* **173**, 709–721 (2009).
  47. L. Celander, K. Fredriksson, B. Galle, and S. Svanberg, “Investigation of laser-induced fluorescence with applications to remote sensing of environmental parameters,” Göteborg Institute of Physics Reports GIPR-149 (Chalmers University of Technology, Göteborg 1978).
  48. T. D. Schultz, C. N. Anderson, and L. B. Symes, “The conspicuousness of colour cues in male pond damselflies depends on ambient light and visual system,” *Anim. Behav.* **76**, 1357–1364 (2008).
  49. H. Edner, J. Johansson, S. Svanberg, E. Wallinder, M. Bazzani, B. Breschi, G. Cecchi, L. Pantani, B. Radicati, V. Raimondi, D. Tirelli, G. Valmori, and P. Mazzinghi, “Laser-induced fluorescence monitoring of vegetation in Tuscany,” *EARSeL Adv. Remote Sens.* **1**, 119–130 (1992).
  50. G. Rüppel, D. Hilfert-Rüppel, G. Rehfeldt, and C. Schütte, *Die Prachtlibellen Europas*, Die neue Brehm-Bücherei Bd. 654 (Westarp Wissenschaften, 2005).
  51. Lord Rayleigh, “The iridescent colours of birds and insects,” *Proc. R. Soc. A Biol. Sci.* **128**, 624–641 (1930).
  52. M. Srinivasarao, “Nano-optics in the biological world: beetles, butterflies, birds, and moths,” *Chem. Rev.* **99**, 1935–1961 (1999).
  53. A. R. Parker and N. Martini, “Structural colour in animals—simple to complex optics,” *Opt. Laser Technol.* **38**, 315–322 (2006).
  54. S. Kinoshita, S. Yoshioka, Y. Fujii, and N. Okamoto, “Photophysics of structural color in the morpho butterflies,” *Forma* **17**, 103–121 (2002).
  55. P. Vukusic, J. R. Sambles, and C. R. Lawrence, “Structurally assisted blackness in butterfly scales,” *Proc. R. Soc. Biol. Sci.* **271**, 237–239 (2004).
  56. P. Vukusic, J. R. Sambles, C. R. Lawrence, and R. J. Wootton, “Now you see it—now you don’t,” *Nature* **410**, 36 (2001).
  57. I. R. Hooper, P. Vukusic, and R. J. Wootton, “Detailed optical study of the transparent wing membranes of the dragonfly *Aeshna cyanea*,” *Opt. Express* **14**, 4891–4897 (2006).
  58. J. A. Noyes, P. Vukusic, and I. R. Hooper, “Experimental method for reliably establishing the refractive index of buprestid beetle exocuticle,” *Opt. Express* **15**, 4351–4358 (2007).
  59. V. Backman, R. Gurjar, K. Badizadegan, I. Itzkan, R. R. Dasari, L. T. Perelman, and M. S. Feld, “Polarized light scattering spectroscopy for quantitative measurement of epithelial cellular structures *in situ*,” *IEEE J. Sel. Top. Quantum Electron.* **5**, 1019–1026 (1999).
  60. T. Wagner, S. Beirle, T. Deutschmann, M. Grzegorski, and U. Platt, “Satellite monitoring of different vegetation types by differential optical absorption spectroscopy (DOAS) in the red spectral range,” *Atmos. Chem. Phys.* **7**, 69–79 (2007).
  61. R. O. Prum, J. A. Cole, and R. H. Torres, “Blue integumentary structural colours in dragonflies (*Odonata*) are not produced by incoherent Tyndall scattering,” *J. Exp. Biol.* **207**, 3999–4009 (2004).

62. S. Fizeau-Braesch, "Pigments and color changes," *Annu. Rev. Entomol.* **17**, 403–424 (1972).
63. J. M. Gallas and M. Eisner, "Fluorescence of melanin—dependence upon excitation wavelength and concentration," *Photochem. Photobiol.* **45**, 595–600 (1987).
64. G. Luna-Bárcenas, B. Gonzalez-Campos, E. A. Elizalde-Peña, E. Vivaldo-Lima, J. F. Louvier-Hernández, Y. V. Vorobiev, and J. González-Hernández, "FEMO modelling of optical properties of natural biopolymers chitin and chitosan," *Phys. Stat. Sol.* **5**, 3736–3739 (2008).
65. L. Q. Wu, R. Ghodssi, Y. A. Elabd, and G. F. Payne, "Biomimetic pattern transfer," *Adv. Funct. Mater.* **15**, 189–195 (2005).
66. S. N. Gorba, A. Keselb, and J. Bergera, "Microsculpture of the wing surface in *Odonata*: evidence for cuticular wax covering," *Arthropod Struct. Dev.* **29**, 129–135 (2000).
67. A. Ounis, Z. G. Cerovic, J. M. Briantais, and I. Moya, "DE-FLIDAR: a new remote sensing instrument for estimation of epidermal UV absorption in leaves and canopies," in *Proceedings of European Association of Remote Sensing Laboratories (EARSeL)-SIG-Workshop LIDAR, Dresden/FRG (EARSeL, 2001)*, Vol. 1, pp. 196–204.
68. J. F. Jacobs, G. J. M. Koper, and W. N. J. Ursem, "UV protective coatings: a botanical approach," *Prog. Org. Coatings* **58**, 166–171 (2007).
69. E. Warrant, ed., *Invertebrate Vision* (Cambridge U. Press, 2006).
70. M. Wellereuther, M. Brydegaard, and E. Svensson are preparing a manuscript called "Role of female wing colour and male mate choice in premating isolation in allopatric and sympatric populations of damselflies".
71. G. De Marchi, "Precopulatory reproductive isolation and wing colour dimorphism in *Calopteryx splendens* females in southern Italy (*Zygoptera: Calopterygidae*)," *Odonatologica* **19**, 243–250 (1990).
72. M. J. Rantala, J. Koskimäki, J. Suhonen, J. Taskinen, and K. Tynkkynen, "Immunocompetence, developmental stability and wing spot size in *Calopteryx splendens*," *Proc. R. Soc. B* **267**, 2453–2457 (2000).
73. E. I. Svensson, L. Kristoffersen, K. Oskarsson, and S. Bensch, "Molecular population divergence and sexual selection on morphology in the banded demoiselle (*Calopteryx splendens*)," *Heredity* **93**, 423–433 (2004).
74. K. Tynkkynen, J. S. Kotiaho, M. Luojumäki, and J. Suhonen, "Interspecific territoriality in *Calopteryx* damselflies: the role of secondary sexual characters," *Anim. Behav.* **71**, 299–306 (2006).
75. U. Gustafsson, S. Pålsson, and S. Svanberg, "Compact fiber-optic fluorosensor using a continuous-wave violet diode laser and an integrated spectrometer," *Rev. Sci. Instrum.* **71**, 3004–3006 (2000).
76. C. af Klinteberg, M. Andreasson, O. Sandström, S. Andersson-Engels, and S. Svanberg, "Compact medical fluorosensor for minimally invasive tissue characterization," *Rev. Sci. Instrum.* **76**, 034303 (2005).
77. H. Edner, P. Ragnarson, S. Svanberg, E. Wallinder, R. Ferrara, B. E. Maserti, and R. Bargagli, "Atmospheric mercury mapping in a cinnabar mining area," *Sci. Total Environ.* **133** 1–15 (1993).
78. E. Wallinder, H. Edner, P. Ragnarson, and S. Svanberg, "Vertically sounding ozone LIDAR system based on a KrF excimer laser," *Phys. Scr.* **55**, 714–718 (1997).
79. C. af Klinteberg, A. Pifferi, S. Andersson-Engels, R. Cubeddu, and S. Svanberg, "In vivo absorption spectroscopy of tumor sensitizers using femtosecond white light," *Appl. Opt.* **44**, 2213–2220 (2005).
80. Ch. Abrahamsson, T. Svensson, S. Svanberg, S. Andersson-Engels, J. Johansson, and S. Folestad, "Time and wavelength resolved spectroscopy of turbid media using light continuum generated in a crystal fibre," *Opt. Express* **12**, 4103–4112 (2004).

## PAPER XI

### **Insect monitoring with fluorescence lidar techniques: Field experiments**

Z. G. Guan, M. Brydegaard, P. Lundin, M. Wellenreuther, A. Runemark,  
E.I. Svensson, and S. Svanberg  
*Applied Optics* **49**, 5133-5142, 2010.

# Insect monitoring with fluorescence lidar techniques: field experiments

Zuguang Guan,<sup>1,\*</sup> Mikkel Brydegaard,<sup>1</sup> Patrik Lundin,<sup>1</sup> Maren Wellenreuther,<sup>2</sup>  
Anna Runemark,<sup>2</sup> Erik I. Svensson,<sup>2</sup> and Sune Svanberg<sup>1</sup>

<sup>1</sup>Atomic Physics Division, Lund University, P.O. Box 118, SE-221 00 Lund, Sweden

<sup>2</sup>Department of Biology, Lund University, SE-223 62 Lund, Sweden

\*Corresponding author: zuguang.guan@fysik.lth.se

Received 9 June 2010; accepted 20 July 2010;  
posted 26 July 2010 (Doc. ID 129890); published 16 September 2010

Results from field experiments using a fluorescence lidar system to monitor movements of insects are reported. Measurements over a river surface were made at distances between 100 and 300 m, detecting, in particular, damselflies entering the 355 nm pulsed laser beam. The lidar system recorded the depolarized elastic backscattering and two broad bands of laser-induced fluorescence, with the separation wavelength at 500 nm. Captured species, dusted with characteristic fluorescent dye powders, could be followed spatially and temporally after release. Implications for ecological research are discussed. © 2010 Optical Society of America

OCIS codes: 280.3640, 300.2530.

## 1. Introduction

Lidar techniques have been developed for almost 50 years for atmospheric monitoring by analyzing the return echo from the aerosols distributed in the atmosphere [1–3]. The fluorescence lidar variety is useful in assessing phenomena in addition to those relying on elastic backscattering from aerosols. Because of the existence of alkali atoms and iron ions in an extremely low-pressure environment, fluorescence lidar is a unique technique for monitoring conditions in the upper atmosphere [3]. At a shorter range, the Swedish research group at Lund University, and others, have shown that remote targets within a few hundred meters can be analyzed successfully using laser-induced-fluorescence (LIF) spectroscopy [4]. Based on a well-developed mobile lidar system [5], the applications range from the optical diagnosis of historical monuments to the analysis of hydrological and vegetation targets. With the knowledge of measurements ranging from aerosols with sizes of less than 1  $\mu\text{m}$  to macro solid targets,

such as the Roman Colosseum [6], we are currently at the intermediate spatial scale by studying flying insects.

Monitoring insects and studying their movements is of great importance in biological research and environmental monitoring. For instance, damselfly larvae are highly sensitive to water pollution and dissolved oxygen concentrations and, thus, are used as biomarkers [7]. Like other ectotherms, damselflies are sensitive to ambient temperature, and many species have undergone a northward shift in their distribution due to global warming [8]. Dispersal studies of insects are also critical for understanding the role of dispersal between populations over wide spatial scales [9], which is important when developing conservation policies. The traditional method is limited to marking individuals with different dyes and then collecting individuals from neighboring populations [10]. Advanced remote detection techniques in this field have developed slowly. Pioneering work using elastic lidar to study honeybees for land mine detection has been reported [11–13].

Noticing the potential advances of LIF techniques in insect monitoring and the natural connection with the dye markers used for traditional tracing, we

demonstrated for what is believed to be the first time fluorescence lidar techniques for damselfly (*Calopteryx splendens* and *C. virgo*) monitoring at a distance of 60 m [14]. For initial remote spectral analysis of LIF, an intensified fiber-coupled optical multiple channel analyzer system [15] is employed. By averaging signals, even the autofluorescence from mounted dead damselflies was useful for distinguishing between species and sexes [14]. Importantly, damselflies dusted with different types of dye can be spatially resolved and distinguished from the fluorescence signature in a single lidar pulse. To further test the feasibility of such a technique, two weeks of field experiments were carried out in southern Sweden, where three geometrical arrangements were set up over a river surface [see Fig. 1(a)], and damselflies that were flying into the laser beam were detected and counted statistically. During the campaign, three groups of damselflies were dusted with dye powder and released into the natural environment. The fluorescence signatures in lidar signals reveal their presence, dispersal patterns, and activity in later measurements.

This paper is organized as follows. First, the fluorescence lidar equipment is introduced in Subsection 2.A, followed by a description, in Subsection 2.B, of the geographic setting of the field experiment where three lidar paths are set up. The selection and use of fluorescence dyes in the short-range test and in the field experiments are described in Subsection 2.C. Subsection 3.A shows a method used to distinguish three species of damselflies (dusted with different dyes) using their fluorescence signatures. In Subsection 3.B, the statistical results are presented and discussed in the spatial domain, as well as in the time domain, also taking weather conditions into account. In addition, the application of a method used to extract insect echoes out from the electronic perturbation is introduced in Subsection 3.C. Finally, we discuss the general applicability of the technique in biological systems and the biological implications of the findings.

## 2. Experimental Methods

### A. Lidar Equipment

The experimental facility is based on the Lund mobile lidar system [5], which is modified for the current study in important ways. The main equipment is presented in Fig. 1(b). The third harmonic (355 nm) of the Nd:YAG laser radiation is used with an energy of 40 mJ/pulse, and with a pulse width of 10 ns. After expanding to a beam diameter of 5 cm, the laser beam is transmitted by a mirror (40 cm × 56 cm) placed in a transmission dome, which can scan vertically and horizontally. A quartz window in the dome is used to protect the mirror from atmospheric dirt and dust. The elastic scattering and the fluorescence from the targets are reflected by the same mirror and collected by a telescope system with a diameter of 40 cm. The col-

lected light is distributed by several mirrors and is filtered, and then detected by three photomultipliers (PMTs). As shown in Fig. 1(b), the elastic scattering from the target is selected by a laser line mirror (LM) and recorded by PMT-1 in the time domain. A polarizer (P) is set at a crossed angle against the polarization state of the transmitted laser beam. Therefore, PMT-1 is sensitive only to depolarized backscattering, but blind to the copolarized echo from the target surface, and, hence, insensitive to the flying orientation of the insect in the laser beam. An extra-short-pass filter (SF) is used to suppress the fluorescence light from the target and background light from the sky thereafter. The fluorescence light passing

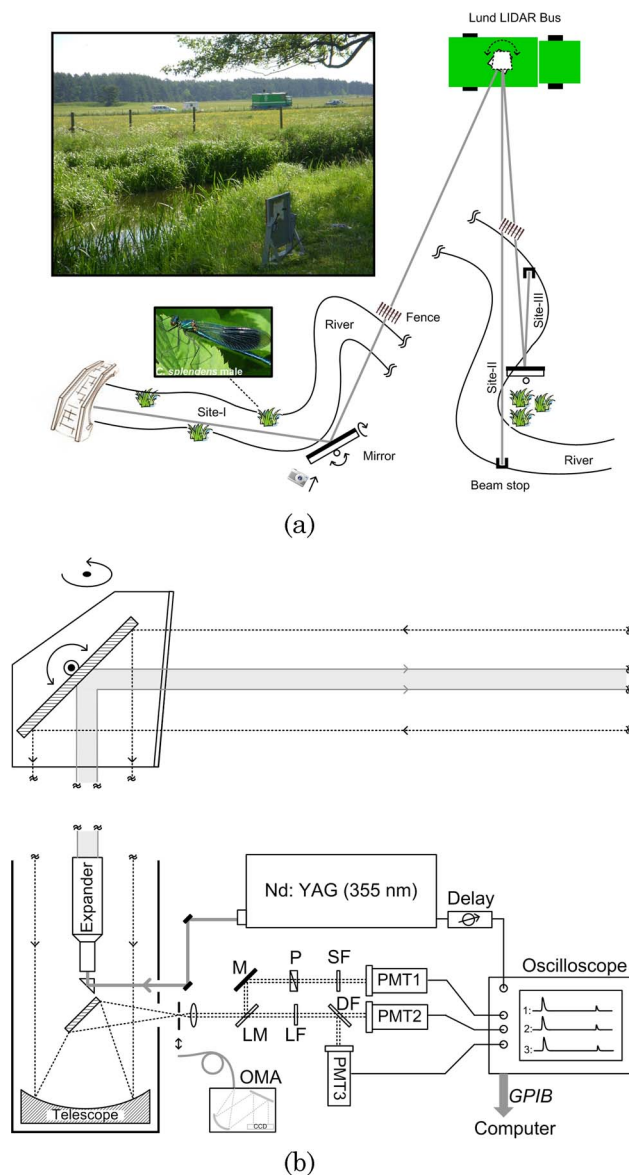


Fig. 1. (Color online) (a) Geographic diagram of the measurement locations. The inserted scenery picture is taken from the indicated position and direction; also shown is a male *C. splendens* damselfly. (b) Key equipment/components of the fluorescence lidar (PMT-1 is for detection of elastic scattering, while PMT-2 and PMT-3 are for yellow and blue bands of fluorescence, respectively).

through the LM is divided by a dichroic filter (DF) into two wavelength bands, blue (400–500 nm) and yellow (500–750 nm), and measured by PMT-3 and PMT-2, respectively. Before the DF, a long-pass filter (LF) is used to suppress the leakage of the elastic scattering through the LM. Three channels of signals from the PMTs are simultaneously recorded by a high-speed oscilloscope (Tektronix TDS544B), which samples every 8 ns. The start time of the sampling period is controllable by adding a tunable delay onto the synchronization trigger from the Nd:YAG laser. The recorded data are then read out through a GPIB connection by a computer in real time. The repetition rate of the whole system is limited to 10 Hz by communication speed, although the repetition rate of the laser system is 20 Hz. By using such a three-PMT system, both the elastic scattering and two bands of fluorescence can be analyzed in the time/spatial domain.

### B. Field Site

Insect measurements were performed with the Lund mobile lidar system at the Klingavälsån river, Veberöd (55°38' N, 13°29' E), in southern Sweden, during two weeks (1–7 and 24–30 June 2009); see Fig. 1(a). The vehicle was parked near the river, and the laser beam passed over a pasture enclosure, and was measuring in three different geometrical arrangements over the surface of the river. In the first week, the measurements were carried out at Site I, where the laser beam was folded by a plane mirror (~50 cm × 60 cm) in order to be close to the water surface, and then terminated below a bridge. The insects flying through the laser beam could be measured and analyzed in real time. In the second measurement week, the laser beam was moved to Sites II and III. At Site II, the laser beam followed a section of the river that included a peninsula and the beam was terminated by a black beam stop that was set up at the riverbank. Close to Site II, Site III was set up by folding the laser beam closer to the river surface, using the same plane mirror, but now mounted on the peninsula.

Single-pulse lidar echoes corresponding to three paths of the laser beam are shown in Fig. 2, correlated to a satellite image (obtained via the Google Earth tool) of the field. The backscattered signals from the static targets, including the quartz window (protecting the rooftop lidar mirror), a fence, the folding mirror, and the termination, are shown to be stable in all three bands during the long-term measurements. Ranges of interest are marked out in Fig. 2(a) and corresponding lidar echo signals are shown in Fig. 2(b). For instance, in Path I, the range between the mirror and the bridge, corresponding to Site I [compare with Fig. 1(a)], is from 186 to 260 m. Any small “blips” in between the fixed target echoes that show up in the elastic band are recorded by the system, and later counted as one detection in the histogram. The two fluorescence bands are basically used for analyzing dusted-and-released damselflies

in the second measurement week, since the auto-fluorescence from natural damselflies was too weak to be measured in a single pulse in daylight conditions, while the dye-induced fluorescence can easily be distinguished. From the static targets, we can see fluorescence signatures from the quartz window (due to the dust and dirt attached on the surface), but not (or very weakly) from the metal fence, while they saturate the PMTs at the black-painted terminations. We realized that the intensity of the fluorescence signal from the quartz window can be used for normalization, so that the instabilities of the fluorescence

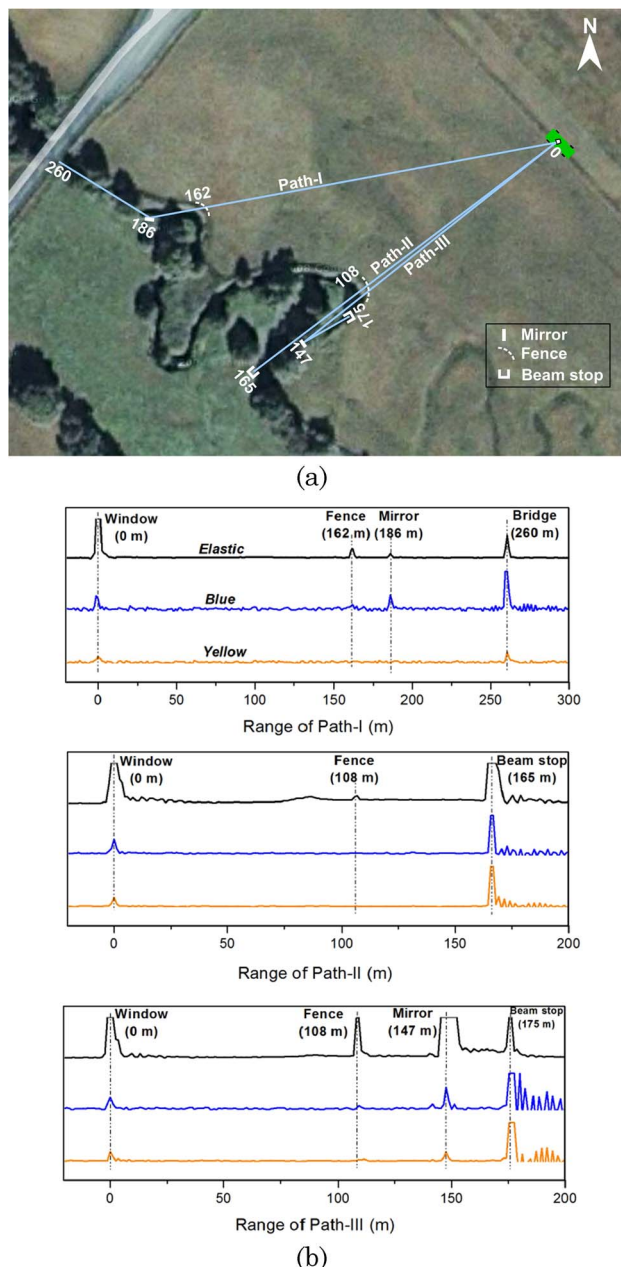


Fig. 2. (Color online) (a) Three lidar paths are shown on a satellite map; numbers indicate the lidar–target distances in meters; (b) lidar echoes from the static targets in Path I (top), Path II (middle), and Path III (bottom).

signals, depending on the laser power, PMT sensitivity, etc., can be compensated for.

### C. Application of Dyes

Before the field experiments, the performance of the lidar system was tested in Lund. Two dead *Calopterygidae* damselflies marked with different dyes (Coumarin 102 and Rhodamine 6G) were placed at different distances (60 and 80 m, respectively) within the laser path; see Fig. 3(a). The single-pulse reflection signal burst from the damselflies was then recorded by the three-PMT systems, as shown in Fig. 3(b). Obviously, the intensity (ratio) of the two fluorescence bands are different for the damselfly positioned at a closer distance, which is marked by Coumarin 102, a bluish dye, and the other one at a larger distance, marked by Rhodamine 6G, which is reddish. The fluorescence spectra of these two dyes for 355 nm excitation are shown in Fig. 10 of Ref. [14]. The above tests indicate that the fluorescence signature from a single lidar pulse is sufficient to distinguish damselflies marked with different dyes, which was encouraging for studying flying damselflies in their natural habitats.

In the later field experiments, three types of dye powder from Swada Inc. were used to dust three groups of captured damselflies belonging to the species *C. splendens* and *C. virgo*. Specifically, 43 *C. splendens* males were marked with Stellar green, 19 *C. splendens* females were marked with Comet blue, and 20 *C. virgo* males were marked with Nova red. It is worth mentioning that these dye powders are used regularly by biologists for dispersal and mating studies (see, e.g., [10]), and have been tested to not harm the insects. The fluorescence spectra for 355 nm excitation are shown in Fig. 4. With the cut-off wavelength of the dichroic filter, which distributes the light energy into two PMTs, at 500 nm, one can expect that the blue dye will mainly be seen by the

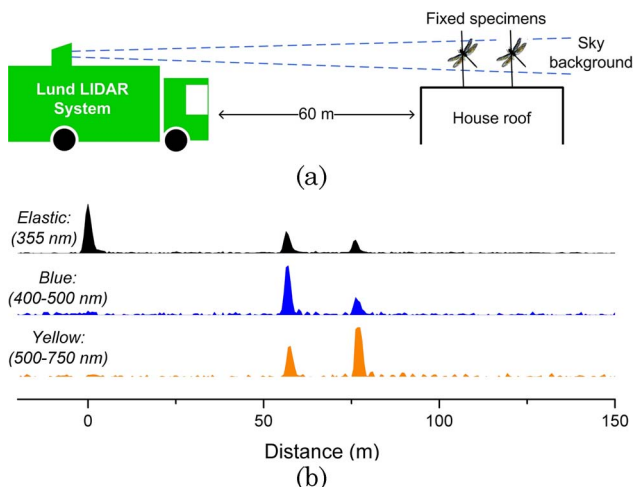


Fig. 3. (Color online) (a) Setup for the test-range measurements, and (b) range-resolved signals of the three channels, from two serially placed damselflies marked with different dyes (Coumarin 102 and Rhodamine 6G).

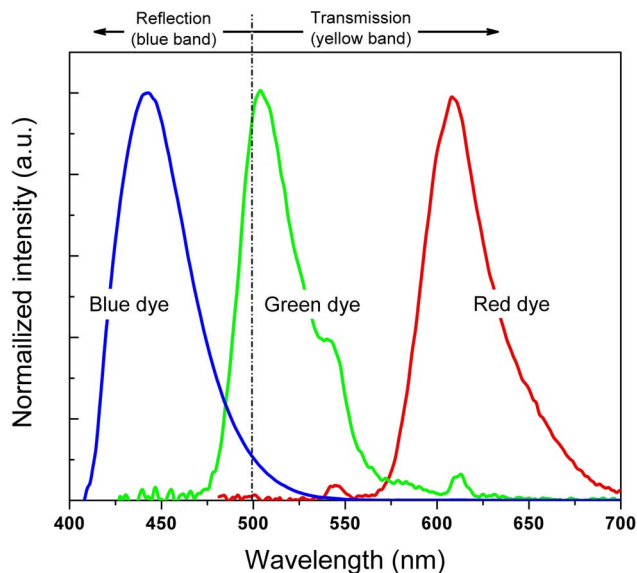


Fig. 4. (Color online) Fluorescence spectra of three dye powders used in the field experiments, with excitation wavelength at 355 nm. The dashed-dotted line indicates the cutoff wavelength of the dichroic filter.

blue-band PMT, while the red dye will be seen by the yellow-band PMT, and the green dye by both. Dusted damselflies were released at Site III during the measurement in the second week, 29 and 30 June 2009. They appear occasionally in the laser path together with unmarked damselflies, and are distinguished by the lidar system from them by the fluorescence signatures. Since the different species and sexes are dusted with different powders, information on species- and sex-specific habitat preferences and dispersal patterns can be obtained if a large enough number of insects is dusted and released. For calibrating the signals at the two fluorescence bands, glass tubes with the individual dyes are moved in and out of the laser beam (close to the fence) to get the standard fluorescence signatures. A detailed analysis of this procedure is given in Section 3.

## 3. Data Analysis

### A. Fluorescence Signature

The method of the fluorescence analysis of damselflies is described here. Figure 5(a) shows several examples of single-pulse lidar curves corresponding to different situations/events happening at Site III. The background consists of static signals (in the situation of no damselfly), and obvious “blips” (with the underlying area filled in) can be occasionally seen between the fence and the mirror (marked by light yellow shaded band), when damselflies fly into the laser beam. For the unmarked damselflies, the signals in the two fluorescence bands are not obvious due to the weak autofluorescence; however, the elastic backscattering is enough for statistical counting (see Subsection 3.B). For the dusted-and-released ones, the fluorescence signatures are clearly different for the three dye species. As expected, the blue

dye shows a stronger bluish fluorescence, while the red dye shows stronger fluorescence in the yellow band, and the green one shows a relatively equal intensity in both bands.

The echo signals corresponding to the damselflies observed in the two fluorescence bands are normalized to those arising from the quartz window at distance 0, before they are plotted in the scatter plot in Fig. 5(b). Here the echo energy is calculated by integrating the echo return intensity in the time domain. By doing so we obtain higher accuracy than by simply selecting the peak intensity, considering that the laser pulse width (10 ns) is comparable with the sampling temporal interval (8 ns). As mentioned above, the dye tubes were used for calibration. The normalized signals corresponding to these “standard” samples are first plotted in Fig. 5(b) as crossed marks, which separate clearly. The blue and red dyes occupy the upper-left and bottom-right areas, respectively, due to relatively strong bluish and yellowish fluorescence, while the green dye signals, with equal intensities in both bands, are situated in between. With such a calibration method, the signals corresponding to the dusted damselflies can be plotted into the same scatter plot and their respective dyes can be determined based on which area they are located in. The data from the field measurement of flying dusted-and-released damselflies are shown as round marks in the figure, and the three groups are well distinguished.

#### B. Statistical Analysis

Using the strategy described in Subsection 3.A, damselflies that appear in the laser beam were detected and statistically counted. The range-resolved results are shown in Fig. 6. For Site I, the data close to the mirror are disturbed by the riverbank vegetation moving in the wind. Many of the measured insects that were found close to the bridge were mosquitoes (according to visual observations), which cause weaker echoes than the damselflies. Mosquitoes and damselflies can thus be separated by adjusting the threshold for selecting echoes. The decay of the lidar curve with range ( $R$ ), following  $R^{-2}$ , has been considered when setting the threshold. Damselflies were mainly detected between 210 and 250 m. Three signal locations, indicating positions in which damselflies frequently appeared, were correlated with reed stands (preferred territories of damselflies [16]). For Site II, damselflies were mostly found around the peninsula, which was consistent with our visual observations. It is interesting to compare the results with Site III, where the peninsula was occupied by the mirror. During the measurements at Site III, we released three groups of damselflies near the fence on 29 and 30 June 2009. In later measurements, they are recorded, distinguished, and plotted in Fig. 6(c). The spatial distribution of the marked damselflies is comparable with that of the unmarked individuals.

Statistical analyses were also performed in the time domain. Figure 7 shows the result obtained at Site I, on 2 June 2009, together with the weather parameters. The damselflies were identified (shown in black) using the threshold method described above. The number of actively flying insects (including both mosquitoes and damselflies) decreased considerably as the temperature dropped and wind speed increased. The observed increase of damselflies in activity between 15:00 and 16:00 is probably

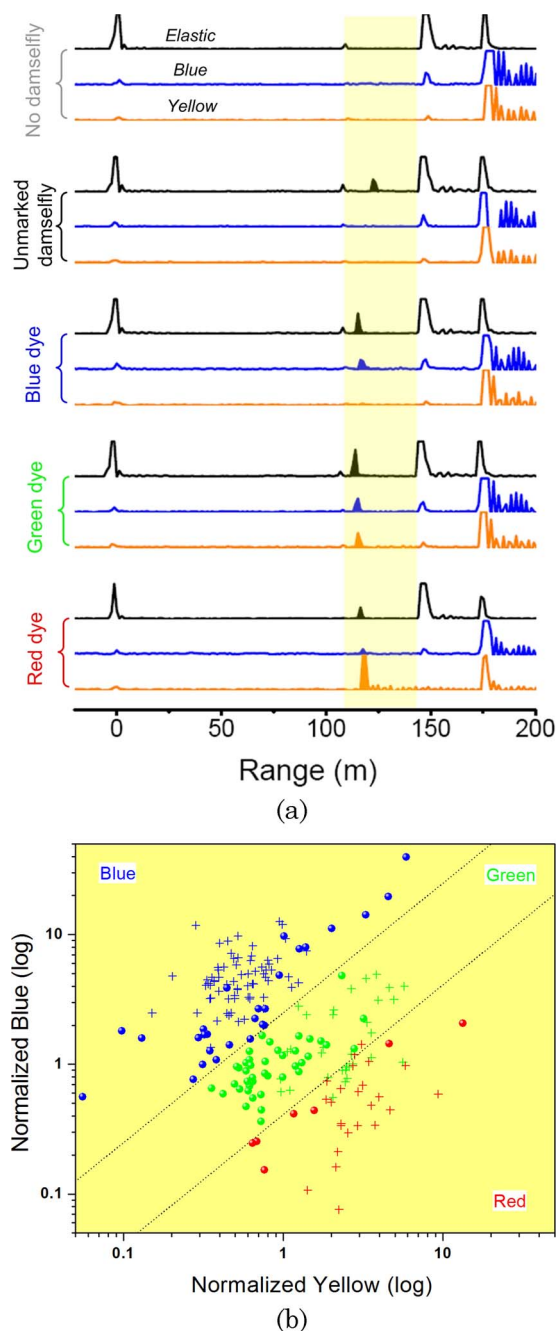


Fig. 5. (Color online) (a) Lidar signals showing different events at Site III, and (b) the scatter plot showing the fluorescence properties of three types of dyes; the crosses and the round marks indicate the calibrating dye tubes and the dusted damselflies, respectively.

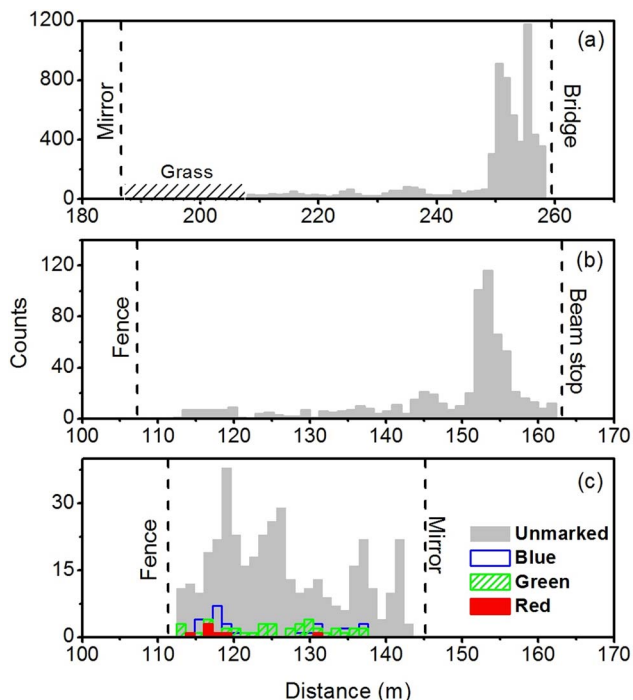


Fig. 6. (Color online) Spatial distributions of the flying damselflies at (a) Site I, (b) Site II, and (c) Site III. The colored histograms in (c) indicate dusted-and-released damselflies. The females marked with blue dye and males marked with green dye belong to the species *C. splendens*, whereas the males marked with red dye are *C. virgo*.

due to other environmental factors, such as increased Sun radiation due to local cloud movements. Results from the three consecutive measurement days at Site III, where dusted damselflies were released on 29 and 30 June 2009, are shown in Fig. 8. From the figure, it can be seen that several of the marked damselflies were alive on 30 June 2009, which corresponds to 1–2 days after they were originally marked.

### C. Perturbation Removal for Enhanced Damselfly Detection

One particular feature of insects in lidar data is their sudden temporal occurrence and disappearance, which is in great contrast to influences of perturbing static objects along the line of propagation of the light pulse. Such completely static features could, in principle, have been removed simply by subtracting an “empty” curve that contains only static information [such as the curves shown in Fig. 2(b)] from all measurements. In the real world, the strong reflections from the fence and the mirror in this case, can induce nonoptical features, e.g., oscillations caused by electronic reflections in the PMT cables or depletion of the charges in the dynodes. Such an unstable perturbation, together with a triggering uncertainty from the quasi-static features in the backscattering signal, makes the simple subtraction approach inapplicable, especially in the range closely after the mirror [see Fig. 5(a) from Site III], where the insect signals can be easily masked. Therefore, we investigated

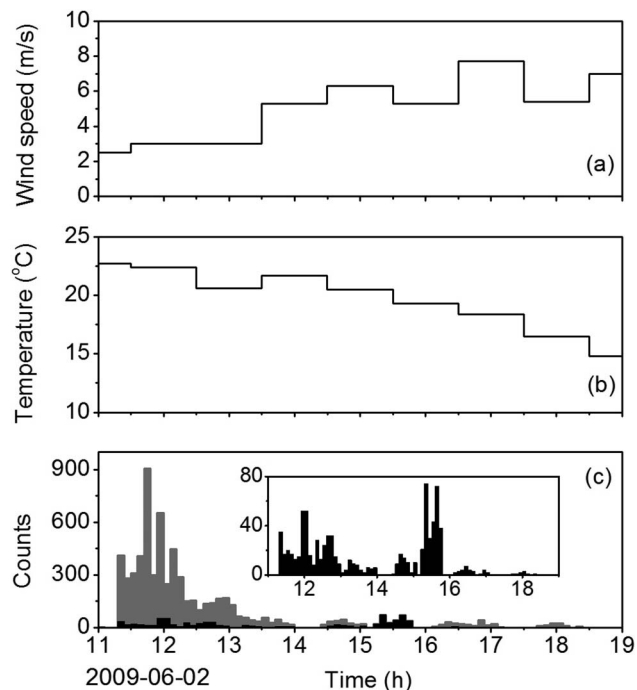


Fig. 7. (c) Measured counts of all insects (gray) and damselflies only (black) activity correlated to (a) the wind speed and (b) the temperature, at Site I. The inset of (c) shows the details of the histogram corresponding to damselflies.

the possibility of removing these quasi-static effects from the data by using the singular value decomposition (SVD) method [17]. SVD is generally not considered suitable for describing temporal phenomena; however, it can be applicable in some cases as a quick tool that requires no detailed information, as traditional input–output system identification methods would [18,19]. We successfully managed to describe the quasi-static background as a linear combination of three time series generated with SVD. As the insects only occur in about one out of a thousand shots, these events will be heavily suppressed by the data not involving a hit. The result of the removal can be seen in the example in Figs. 9(a) and 9(b). In this case, the insect echo is completely hidden in the ringing of the elastic PMT after the strong diffuse reflectance from the mirror [Fig. 9(a)]. While single pulses in any of the PMTs might be caused by “ghost photons” with intensity levels above the background,

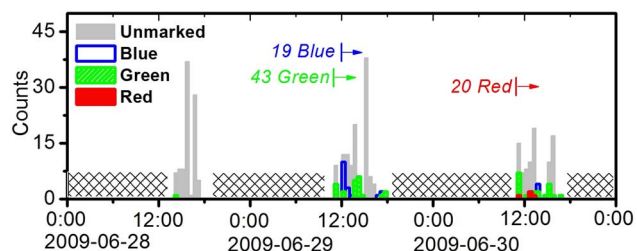


Fig. 8. (Color online) Three days of measurements at Site III. Gray and colored histograms indicate unmarked and dusted damselflies, respectively. Times for release of the dusted damselflies are marked. No measurements are performed during the periods marked by cross-hatching.

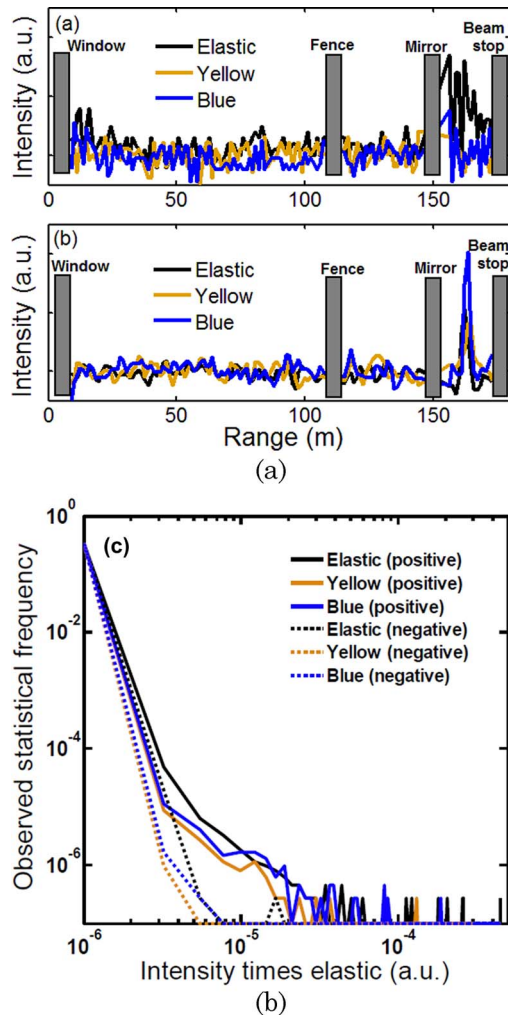


Fig. 9. (Color online) (a) Typical raw echo return after subtraction of “empty” curves (see the text). (b) Signal from the same shot after removing the quasi-static contribution from electronic oscillations, etc. The hit was detected on 29 June 2009, 11:35:27. (c) The insects give rise to a skewness in the intensity histogram. The dotted curves are the negative values. The separation indicates that the insects do, in fact, give an increased intensity return.

it is much less likely that such pulses occur simultaneously in two of the PMTs. One way to increase the contrast of true hits in respect to the ghost photons is to make use of the fuzzy logical AND operator, namely, to multiply the fluorescence signal by the elastic signal. This method is especially valid for marked damselflies that show obvious signals in fluorescence bands. After the removal of the quasi-static contribution, unbiased histograms can be produced on the returned fluorescent intensities times the elastic. In Fig. 9(c), we have produced such a histogram for the range between the fence and the mirror at Site III. The statistics are carried out on three time sections of totally 3 h on 29 and 30 June 2009. To study the insects in particular, the data containing information of road dust plumes from passing cars (discussed below) were excluded. The negative values generally represent the noise level; their amplitudes are plotted with dotted curves to compare with the

positive values plotted as solid curves. Clearly, the reflection signals from the insects produce much higher positive values compared with noise and, hence, induce a skewness in the histogram; see the mismatch between histograms in Fig. 9(c) corresponding to positive and negative values. Similar graphs were observed from the window to fence and the mirror to the termination stretch, although with less and more skewness, respectively. This is in accordance with the ecological *a priori* knowledge, with lower damselfly numbers at the closer range where the laser beam passes the pasture field, but a higher possibility of capturing the flying damselflies over the river surface at the farther range. The SVD method discussed above for quasi-static signature removal works consistently, and was applied successfully over several days of measurements. Figure 10 shows an example in which the removal method works on 25 s of data recorded in the afternoon of 29 July 2009. The three (elastic, blue, and yellow) bands of signals, with quasi-static features removed, are plotted as blue, green, and red, respectively, into a RGB false color map. All three channels are multiplied by the elastic channel to further enhance the contrast. Before the fence, a road dust plume induced by a passing car can be clearly seen on a zero background, thanks to the successful removal of the static/quasi-static features. Particularly, in the range between the mirror and the termination, where originally the insect echo was impossible to see before the removal operation, now clear information appears in different false colors due to different fluorescence performance. The green-dyed damselfly, with reflection signals in all three channels, shows as white in the map, while the natural (nondyed) one

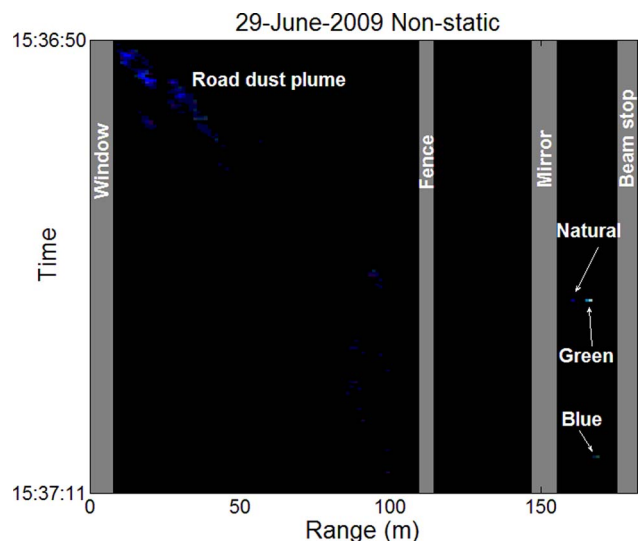


Fig. 10. (Color online) False color RGB representation of 25 s of lidar data with the quasi-static signal removed. Blue, elastic; green, blue fluorescence; red, yellow fluorescence. The inorganic road dust from a passing car gives rise to distributed elastic scattering signals, moving in the wind. The insect signatures appear only for a fraction of a second.

shows up as blue and the blue-dyed one shows up as cyan.

#### 4. Discussion

In this paper, we demonstrate the potential of lidar as a remote-sensing technique to model the spatial and temporal activity of *Calopteryx splendens* and *C. virgo* damselflies in the wild. Although several review articles on the potential of lidar in habitat modeling have appeared in the last few years, the number of applications on natural populations is low, and most of the studies until now have concentrated on bird habitats [20,21] rather than on birds themselves. In particular, we show that lidar can be applied to monitor unmarked damselflies in their natural habitats, and how the use of fluorescent dust helps to differentiate between damselfly sexes and species using a single lidar pulse. Applying such a computerized imaging setup on scales ranging from 100 m to a couple of kilometers will enable biologists to design new experiments and to address new and interesting questions regarding insect ecology, evolution, or optimal wing morphology. In addition, lidar monitoring is an efficient way to assess, for example, population sizes, lifetimes, and dispersal distances and rates, and such data are commonly needed for conservation planning.

Studying the ecological requirements and habitat use of invertebrates in a quantitative way is usually both time consuming and difficult. By using lidar, we show that quantitative data on the temperature and wind speed requirements of *C. splendens* and *C. virgo* can easily be collected during only a few days in the field. For ectotherms, like these damselflies, data on thermal tolerance ranges will be increasingly important in the face of global warming [22,23], since it might tell us about the prospects for local extinction or predict potential northward shifts in the distribution of species. In addition, we have estimated the type of vegetation and at which distances from the water the two species of damselflies occurred, and this adds additional important information about the environmental requirements of these species. Furthermore, the stationary nature of lidar allows the rapid assessment of temporal and spatial activities of individuals in a population. Data collection in such a setting would also be more objective, compared to commonly employed visual censuses by humans, which would increase comparability between sites and observers. Through the marking of different species and sexes with different types of fluorescent dyes, we could also estimate the dispersal patterns and rates of the marked damselflies, and study if habitat use is sex or species specific. This approach would also be useful for mark-recapture studies, a common technique for estimating population sizes where the recapture rate is usually the limiting factor.

From Fig. 6, a tendency for male *C. splendens* (marked by green powder) to be more dispersed along the river than *C. splendens* females and *C. virgo*

males can be seen. The difference in dispersion between males of the two species can be attributed to two factors. First, *C. virgo* males have been shown to be more aggressive than *C. splendens* males and are, thus, more dominant [24–26]. This difference in competitive ability is likely to result in the displacement of some *C. splendens* males from their preferred territories, and interspecific contests between males will also often lead to males of *C. splendens* being chased away by *C. virgo* males. Hence, *C. splendens* males might more often be actively displaced from their river territories than males of *C. virgo* and, hence, be in search for new territories. Second, male *C. splendens* commonly force copulations with females, while *C. virgo* males are more likely to perform a courtship display to initiate mating [27]. Forced copulations are being achieved by following flying females and then by forcing the females to bring up their abdomen to engage genitalia [28]. The chasing of females probably contributes to the wide dispersion of *C. splendens* males, thus further increasing the overall spread of males along a river. It should be noted from our result that *C. splendens* males were more dispersed along the river than females, contradicting previous findings, but this might be an artifact of the scale of different studies. A tendency for females to disperse greater distances than males has been observed in both *C. splendens* [29] and in the blue-tailed damselfly *Ischnura elegans* [30]. However, our study measured fine-scale dispersion patterns (scale of a few meters), while the two aforementioned studies investigated large-scale dispersion patterns (hundreds of meters), which were not measured in the current study. Thus, it is possible that the different results are caused by different scales at which the studies were conducted, and that small and large dispersion patterns differ between the sexes of *C. splendens*. In order to address this explicitly, more studies are needed to rigorously test this prediction. The finding that males prefer vegetated habitat near the water is consistent with previous studies on habitat use in these species [26,31]. Aquatic plants provide *C. splendens* males with good perching spots, and oviposition territory for females [32].

Biodiversity is diminishing at an accelerating pace [33], and, therefore, data on biodiversity and spatial distribution are urgently needed for conservation planning. However, the lack of taxonomists and funds precludes particularly the mapping of taxonomically diverse groups, such as invertebrates [21]. Therefore, management strategies mostly concentrate on charismatic vertebrates and only a few conspicuous invertebrates and ignore most other species [34]. However, the diversity of invertebrates is declining even more rapidly than that of plants and vertebrates [35], even though invertebrates are involved in important ecosystem functions, such as pollination and food webs. We thus clearly need better methods to rapidly, effectively, and cheaply assess the abundance and distribution of invertebrate species. The

results of our study are, therefore, encouraging and timely for future assessments of invertebrates.

## 5. Conclusions

Following proof-of-principle measurements [14], we have now performed successful real-world field experiments on insects *in vivo* and demonstrated the potential of the technique. Lidar provides simple but ecologically meaningful variables for a rapid extrapolation of activity, richness, and composition of insect assemblages across large areas. This enables conservationists to evaluate habitat over large areas and to define diversity hot spots, as well as to monitor changes in the distribution and abundance in response to environmental change. Low fluorescence yield of chitin at 355 nm excitation is a limitation when using nondyed species. However, improvement could be expected by employing, e.g., 266 nm (quadrupled Nd:YAG laser), or 308 nm (XeCl excimer laser) for a better match to the chitin absorption band. Further, the extended fluorescence band available then would also enhance the chance for classification without marking. We did not note any perturbation of the measured species when hit by 355 nm light; however, a shorter excitation wavelength would also be desirable to decrease such a possibility. Full sunlight measurement conditions were shown to be possible; clearly performance is improved for lower light levels. The fact that we estimate a probability rather than a concentration as in, e.g., aerosol lidar applications, implies that a large number of laser shots, in our case thousands of shots, are required to produce a good statistical distribution. Thus, the insect concentration should be considerable to produce a measurement in a limited time. This is particularly true if two-dimensional or three-dimensional mappings are desired.

With the experience gathered in the present work, it should be possible to perform lidar monitoring of insects of considerable impact on the ecology community.

The authors gratefully acknowledge the support from the Swedish Research Council through a project grant, and through a Linnaeus grant to the Lund Laser Centre. Further, we are grateful to the Knut and Alice Wallenberg Foundation for equipment grants.

## References

1. R. M. Measures, *Laser Remote Sensing: Fundamentals and Applications* (Wiley, 1984).
2. S. Svanberg, "LIDAR," in *Springer Handbook of Lasers and Optics*, F. Träger, ed. (Springer, 2007), pp. 1031–1052.
3. X. Chu and G. C. Papen, "Resonance fluorescence lidar," in *Laser Remote Sensing* T. Fujii and T. Fukuchi, eds. (CRC, 2005), Chap. 5, pp. 179–432.
4. S. Svanberg, "Fluorescence spectroscopy and imaging of lidar targets," in *Laser Remote Sensing* T. Fujii and T. Fukuchi, eds. (CRC, 2005), Chap. 6, pp. 433–468.
5. P. Weibring, H. Edner, and S. Svanberg, "Versatile mobile lidar system for environmental monitoring," *Appl. Opt.* **42**, 3583–3594 (2003).
6. L. Palombi, D. Lognoli, V. Raimondi, G. Cecchi, J. Hällström, K. Barup, C. Conti, R. Grönlund, A. Johansson, and S. Svanberg, "Hyperspectral fluorescence lidar imaging at the Colosseum, Rome: elucidating past conservation interventions," *Opt. Express* **16**, 6794–680 (2008).
7. M. Campero, F. Ollevier, and R. Stoks, "Ecological relevance and sensitivity depending on the exposure time for two biomarkers," *Environ. Toxicol.* **22**, 572–581 (2007).
8. R. Hickling, D. B. Roy, J. K. Hill, and C. D. Thomas, "A northward shift of range margins in British odonata," *Glob. Change Biol.* **11**, 502–506 (2005).
9. T. J. Case and M. L. Taper, "Interspecific competition, environmental gradients, gene flow, and the coevolution of species borders," *Am. Nat.* **155**, 583–605 (2000).
10. M. Joron and P. M. Brakefield, "Captivity masks inbreeding effects on male mating success in butterflies," *Nature* **424**, 191–194 (2003).
11. J. A. Shaw, N. L. Seldomridge, D. L. Dunkle, P. W. Nugent, L. H. Spangler, J. J. Bromenshank, C. B. Henderson, J. H. Churnside, and J. J. Wilson, "Polarization lidar measurements of honey bees in flight for locating land mines," *Opt. Express* **13**, 5853–5863 (2005).
12. K. S. Repasky, J. A. Shaw, R. Scheppele, C. Melton, J. L. Carsten, and L. H. Spangler, "Optical detection of honeybees by use of wing-beat modulation of scattered laser light for locating explosives and land mines," *Appl. Opt.* **45**, 1839–1843 (2006).
13. D. S. Hoffman, A. R. Nehrir, K. S. Repasky, J. A. Shaw, and J. L. Carsten, "Range-resolved optical detection of honeybees by use of wing-beat modulation of scattered light for locating land mines," *Appl. Opt.* **46**, 3007–3012 (2007).
14. M. Brydegaard, Z. G. Guan, M. Wellenreuther, and S. Svanberg, "Insect monitoring with fluorescence lidar techniques: feasibility study," *Appl. Opt.* **48**, 5668–5677 (2009).
15. C. af Klinteberg, M. Andreasson, O. Sandström, S. Andersson-Engels, and S. Svanberg, "Compact medical fluorosensor for minimally invasive tissue characterization," *Rev. Sci. Instrum.* **76**, 034303 (2005).
16. P. S. Corbet, *Dragonflies: Behavior and Ecology of Odonata Essex* (Harley, 1999).
17. E. Anderson, Z. Bai, C. Bischof, S. Blackford, J. Demmel, J. Dongarra, J. Du Croz, A. Greenbaum, S. Hammarling, A. McKenney, and D. Sorensen, *LAPACK User's Guide*, 3rd ed. (Society for Industrial and Applied Mathematics, 1999).
18. R. Johansson, *System Modeling and Identification* (Prentice Hall, 1993).
19. E. M. C. Hillman and A. Moore, "All-optical anatomical coregistration for molecular imaging of small animals using dynamic contrast," *Nat. Photon.* **1**, 526–530 (2007).
20. R. B. Bradbury, R. A. Hill, D. C. Mason, S. A. Hinsley, J. D. Wilson, H. Balzter, G. Q. A. Anderson, M. J. Wittingham, I. J. Davenport, and P. E. Bellamy, "Modeling relationships between birds and vegetation structure using airborne lidar data: a review with case studies from agricultural and woodland environments," *Ibis* **147**, 443–452 (2005).
21. K. T. Vierling, L. A. Vierling, W. A. Gould, S. Martinuzzi, and R. M. Clawges, "Lidar: Shedding new light on habitat characterization and modeling," *Front. Ecol. Environ.* **6**, 90–98 (2008).
22. C. N. Parmesan, "Climate and species' range," *Nature* **382**, 765–766 (1996).
23. C. N. Parmesan, C. Ryrholm, C. Steganescu, J. K. Hill, C. D. Thomas, B. Descimon, B. Huntley, L. Kaila, J. Kullberg, T. Tamaru, W. J. Tennent, J. A. Thomas, and M. Warren, "Poleward shifts in geographical ranges of butterfly species associated with regional warming," *Nature* **399**, 579–583 (1999).
24. K. Tynkkynen, M. J. Rantala, and J. Suhonen, "Interspecific aggression and character displacement in the damselfly *Calopteryx splendens*," *J. Evol. Biol.* **17**, 759–767 (2004).

25. K. Tynkkynen, J. S. Kotiaho, M. Luojumäki, and J. Suhonen, "Interspecific aggression causes negative selection on sexual characters," *Evolution* **59**, 1838–1843 (2005).
26. K. Tynkkynen, J. S. Kotiaho, M. Luojumäki, and J. Suhonen, "Interspecific territoriality in *Calopteryx* damselflies: the role of secondary sexual characters," *Anim. Behav.* **71**, 299–306 (2006).
27. G. Rüppe, D. Hilfert-Rüppe, G. Rehfeldt, and C. Schütte, *Die Prachtlibellen Europas* (Westarp Wissenschaften, 2005).
28. A. Cordero, "Forced copulations and female contact guarding at a high male density in a *Calopterygid* damselfly," *J. Insect Behav.* **12**, 27–37 (1999).
29. A. Chaput-Bardy, A. Gregoire, M. Baguette, A. Pagano, and J. Secondi, "Condition and phenotype-dependent dispersal in a damselfly, *Calopteryx splendens*," *PLoS ONE* **5**, e10694 (2010).
30. K. F. Conrad, K. H. Willson, K. Whitfield, I. F. Harvey, C. J. Thomas, and T. N. Sherratt, "Characteristics of dispersing *Ischnura elegans* and *Coenagrion puella* (odonata): age, sex, size morph and ectoparasitism," *Ecography* **25**, 439–445 (2002).
31. L. Ward and P. J. Mill, "Habitat factors influencing the presence of adult *Calopteryx splendens* (odonata: Zygoptera)," *Euro. J. Entomol.* **102**, 47–51 (2005).
32. D. W. Gibbons and D. Pain, "The influence of river flow rate on the breeding behaviour of calopteryx damselflies," *J. Anim. Ecol.* **61**, 283–289 (1992).
33. F. S. Chapin, E. S. Zavaleta, V. T. Eviner, R. L. Naylor, P. M. Vitousek, H. L. Reynolds, D. U. Hooper, S. Lavore, O. E. Sala, S. E. Hobbie, M. C. Mack, and S. Díaz, "Consequences of changing biodiversity," *Nature* **405**, 234–242 (2000).
34. P. M. Hammond, "Species inventory," in *Global Diversity Status of the Earth Living Resources*, B. Groombridge, ed. (Chapman and Hall, 1992), pp. 17–39.
35. J. A. Thomas, M. G. Telfer, D. B. Roy, C. D. Preston, J. J. D. Greenwood, J. Asher, R. Fox, R. T. Clarke, and J. H. Lawton, "Comparative losses of British butterflies, birds, and plants and the global extinction crisis," *Science* **303**, 1879–1881 (2004).

## PAPER XII

### **Rare events in remote dark field spectroscopy:**

#### **An ecological case study of insects**

A. Runemark, M. Wellenreuther, H. Jayaweera,

S. Svanberg and M. Brydegaard

*Journal of Selected Topics of Quantum Electronics,*

*Photonics for Environmental Sensing*, **18**, 1573-1582, 2011.

# Rare Events in Remote Dark-Field Spectroscopy: An Ecological Case Study of Insects

Anna Runemark, Maren Wellenreuther, Hiran H. E. Jayaweera, Sune Svanberg,  
and Mikkel Brydegaard, *Member, IEEE*

(Invited Paper)

**Abstract**—In this paper, a novel detection scheme for the monitoring of insect ecosystems is presented. Our method is based on the remote acquisition of passive sunlight scattering by two insect species. Procedures to identify rare events in remote dark-field spectroscopy are explained. We further demonstrate how to reduce the spectral representation, and how to discriminate between sexes, using a hierarchical clustering analysis. One-day cycle showing the temporal activities of the two sexes as well as data on activity patterns in relation to temperature and wind is presented. We also give a few examples of the potential use of the technique for studying interactions between sexes on a time scale of milliseconds.

**Index Terms**—*Calopteryx*, dark-field spectroscopy, ecosystems, entomology, insects, passive scattering spectroscopy, remote sensing.

## I. INTRODUCTION

THE application of modern spectroscopic methods to monitor several larger constituents of the atmosphere, such as birds and insects, has previously been demonstrated by our group. In earlier papers, we mainly focused on the use of Light Detection And Ranging (LIDAR) [1]–[5], and presented several approaches to insect marking experiments using laser-induced fluorescence. We are currently exploring several more compact and less expensive approaches. Here, we present dark-field spectroscopy, a monitoring method that does not require the marking of organisms. This enables the study of species that cannot be easily handled, or are difficult to capture. In addition, natural densities of organisms can be more accurately estimated with

Manuscript received September 6, 2011; revised November 24, 2011; accepted January 5, 2012. This work was supported in part by the Swedish Research Council through a direct grant and through a Linnaeus grant to the Lund Laser Center, University of Lund, Sweden, in part by the Royal Physiographic Society, in part by the Kullaberg Foundation, in part by the International Science Program ISP-SIDA, and in part by the Knut and Alice Wallenberg Foundation through a Linnaeus grant to CAnMove.

A. Runemark and M. Wellenreuther are with the Department of Biology, Lund University, Lund SE-221 00, Sweden (e-mail: Anna.Runemark@biol.lu.se; maren.wellenreuther@biol.lu.se).

H. H. E. Jayaweera is with the Centre for Instrument Development, University of Colombo, Colombo 00300, Sri Lanka (e-mail: hiran.jayaweera@sci.cmb.ac.lk).

S. Svanberg and M. Brydegaard are with the Applied Molecular Spectroscopy and Remote Sensing Group, Lund University, Lund SE-221 00, Sweden (e-mail: sune.svanberg@fysik.lth.se; mikkel.brydegaard@fysik.lth.se).

Color versions of one or more of the figures in this paper are available online at <http://ieeexplore.ieee.org>.

Digital Object Identifier 10.1109/JSTQE.2012.2184528

the current approach, because no population subsets need to be measured, but instead, whole population samples within designate areas can be investigated. Traditionally, manual counts have been used to quantify the numbers of individuals of different species of damselflies and to study the temporal activity patterns and interactions between species. However, manual observations are time consuming, and simultaneous monitoring of long river stretches over long time periods is laborious. In addition, interactions between damselflies on short time scales are easily missed during manual counts. The presented inexpensive method may, therefore, enable biologists to address new questions regarding temporal activity patterns in relation to weather conditions, like in this study, or other ecological variables.

## II. BACKGROUND

### A. Model Organism

The river Klingavälsån in southern Sweden is occupied by two closely related, ecologically similar [6] and coexisting populations of damselfly species: *Calopteryx splendens* and *C. virgo*. For this reason, this location provides an excellent place to test new methods that can detect and identify both different species and the sexes of these damselflies by making use of their slightly different scattering spectra. Damselflies are excellent biomarkers, since they have both an aquatic larval phase and a terrestrial adult phase, and thus can be used as indicators of both water and terrestrial habitat quality. Calopterygid damselflies are particularly suited as biomarkers because they inhabit flowing rivers with clean water and are sensitive to low oxygen conditions [6], [7]. In addition to being suitable biomarkers for habitat quality, damselflies are also sensitive to temperature changes [8], and *C. splendens* and *C. virgo* are predicted to shift their ranges northward in response to the global warming [9]. Simple quantitative monitoring of damselflies can, therefore, be useful both for investigations of freshwater and terrestrial ecosystem quality, and for the study of the effects of changing climatic conditions. In this study, we monitor flying damselflies in their adult, terrestrial phase, which lasts for a few weeks during the summer months.

### B. Spectral Appearance

*C. spp.* are diurnal and have striking blue and green–brown colored bodies. These colors are created by a combination of structural metallic colors arising from coherent scattering from

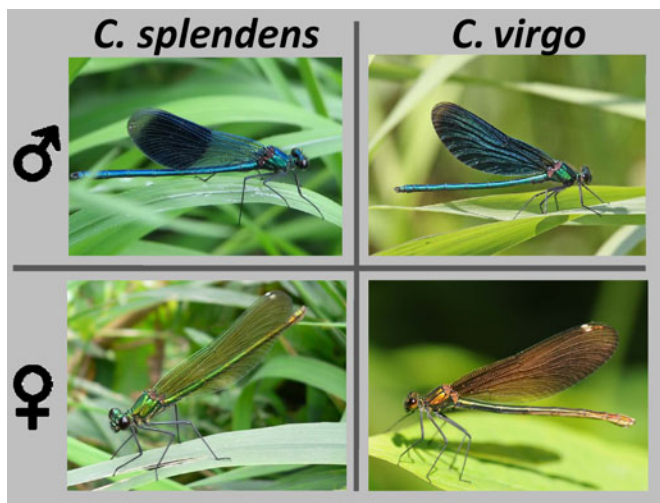


Fig. 1. Study organisms. (Left) A male and a female of the banded damselfly *C. splendens* are shown. (Right) A male and a female of the blue damselfly *C. virgo* are shown.

prevalent spatial frequencies in a nanoarrangement of organelles and chromophores [10]; see Fig. 1. Although the phenomenon is structural, the spectral features show no iridescence due to the spherical symmetry of the nanoarrays [10]. Females of *C. splendens* are greenish, whereas *C. virgo* females are more brownish. Females of both species have wing colors similar to their body [3], see Fig. 1. In contrast, males of both species have a blue body, and conspicuously melanised wings. *C. virgo* males have melanised wing-spots covering most of the wing (~90%), whereas *C. splendens* males have wing-spots, which cover around half of the wing [3], see Fig. 1. The differences in coloration between the sexes and species could be the result of sexual selection, and since males have higher variance in reproductive success, they are expected to be under stronger sexual selection [11]. The conspicuous dark body and wing color of males can be more easily spotted than the color of females (against the vegetation background), and the melanised wing patches of the males have also proven important for species recognition in coexisting populations [12]. Newly emerged and not fully hardened specimens [6] show increased specular reflectance, and can be distinguished by their glittering appearance from more mature individuals that have a hardened exoskeleton [13]. The habitat area studied in this study is the air volume above the river surface, and this area is generally not utilized by newly emerged individuals but typically exclusively by adult sexually mature damselfly individuals.

### C. Visual System

Several dragonfly species have been found to have up to six spectral classes of photoreceptors (spectral bands) covering the range 330–650 nm [14]. Although no such studies have been performed on damselflies so far, dragonflies and damselflies are sister taxa and hence likely to have similar visual systems. Damselflies have compound eyes and have a rather poor spatial resolution compared to humans, but an extremely wide field of view, and a fast temporal response. Another interesting aspect of the damselfly visual system is the ability to detect polarized

light, a feature which is common in insects, and in particular in species living over the water surface. The ability to detect polarized light has several implications both for the perception of structural colors and for horizon estimation during flight navigation.

## III. MATERIAL AND METHODS

### A. River System With Two Coexisting Damselfly Species

The river site in the Klingavälsån nature reserve (latitude 55.63°, longitude 13.54°) harbors a population consisting of both *C. splendens* and *C. virgo* damselflies. These damselfly populations have been extensively studied as model organisms for sexual selection, species recognition, and predation [15]–[17]. Studies of damselfly distribution and activity patterns have also been performed with fluorescence LIDAR in this population [4].

In order to compare the developed method to traditionally employed methods, manual counts of damselflies along the same stretch as used in the dark-field spectroscopy study were performed. These counts were performed every 30 min. Species and sex of all damselflies above the river surface was estimated and recorded. A synchronized digital still camera was used to take photographs for cross validation, and additional observations were recorded manually in a log book.

### B. Equipment and Optical Setup

The one-day experiment was carried out using instruments placed in an astronomical tent-dome observatory (Omegon, approximately  $\varnothing$  3 m). The dome was placed under the shade of an oak tree to minimize variation in instrument temperature. Further, the dome provided protection from the resident cattle. Power was provided by a 2-kW portable gasoline generator which had to be refueled three times during the day of the experiment. A weather station was installed on a 3-m pole 40 m from the dome, clear of the oak canopy. Light received from a 95-m-long observational path was collected by a  $\varnothing$  203 mm Newtonian telescope (Bresser, Location T, Fig. 2), focal length 800 mm, installed on a motorized equatorial GoTo mount (LXD75 Meade; the position was kept fixed during this experiment). The telescope's field of view (FOV, see details in Table I) was directed toward a 1 m cubic box of black anodized aluminum 95 m straight north from the dome (see Fig. 2, location B). We refer to this as the black termination; in the ideal case, the termination is entirely dark in which the only contribution to the light intensity received by the telescope would be the scattering from atmospheric constituent in the stretch T–B (see Fig. 2). The first 55 m of the FOV was over grassland and the remaining 40 m was over the river Klingavälsån. The FOV descended roughly from 4 m to less than 0.5 m over the river surface. Most of the FOV was illuminated throughout the day. The focusing and overlap of the FOV with the black termination was performed with an imager in the focal plane, after which the telescope was locked in position and alignment. The imager was removed and a 1-mm UV fiber (Edmunds Optics) was instead installed at the same place as the image of the black box in the focal plane of

TABLE I  
 VARIABLES AND ABBREVIATIONS

Short form	Explanation	Comments
FOV	Field of view	Roughly 95 m long, 4m <sup>3</sup> air volume
$I_{Vis}$	Intensity counts in the region 400-680 nm	Ranges from 0-65536 (16bit), includes dark current, imperfect termination, atmospheric scatter, insects scatter
$I_{Stat}$	Quasi-static intensity,	Includes dark current, imperfect termination, atmospheric scatter
$I_{BC}$	Background corrected intensity counts	Includes insects scatter, centered around zero with a considerable skewness
FWHM	Full width half maximum	Given by the fix slit width of the spectrometer
$I_0$	Time dependent intensity impinging on the FOV by which the trigger threshold is weighted	This function compensates for the increased light at noon
$A, W, D$	Model parameters for $I_0$	Fitted from white calibration events
$TST$	True sun time	Time corrected for summer time and longitude
SNR	Signal to noise ratio	Estimated from the noise floor of the Eigenvalues
$Act$	Insect activity	Measured in counts/hm <sup>3</sup>
$v$	Horizontal wind speed	Measured m/s approximately 5 m over the river surface
$T$	Local temperature	Measured in Kelvin
$T_{max}, T_{act}$	Model parameters for thermal dependence	
$k_{\phi}, k_v$	Model parameters for flight preferences	Fitted individually for both sexes using the slow time statistics
DOF	Degrees of freedom for statistical models	
VIS	Visible region	400-680 nm in this study
UV	Ultraviolet region	300-400 nm in this study
NIR	Near infrared region	700-1100 nm in this study
SVD	Singular Value Decomposition	Method for removing spectral redundancy
QR	QR factorization	A rapid method for solving the least square problem in linear algebra
CW	Continuous wave	
LD	Laser diode	
PMT	Photo multiplying tube	
APD	Avalanche photo diode	

the telescope. The FOV at termination was  $\phi$  120 mm, and the total air volume monitored was roughly 4 m<sup>3</sup>. The other end of the optical fiber was fed to a compact spectrometer (Ocean Optics, USB4000). The spectrometer had a cylindrical lens and higher order rejection filters installed. The slit width was 100  $\mu$ m yielding 4-nm resolution full-width at half-maximum. The spectral region covers 345–1040 nm. The integration time was set to 20 ms throughout the experiment, and thus, 50 spectra were recorded per second. The data were stored by two laptop computers: one logging the data from the weather station and another one storing the data from the spectrometer on an

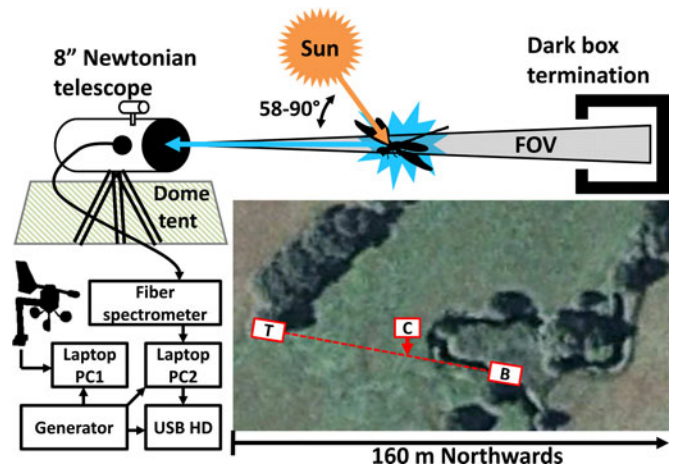


Fig. 2. Setup for the experiment. T: Newtonian telescope, C: calibration site, B: dark box termination. Light is collected by a 1-mm UV fiber in the focal plane of the telescope and fed to a compact spectrometer. Distance from the telescope to termination was 95 m of which the first 55 m covers the grassland and the remaining 40 m covers the river Klingavälsån.

external USB terabyte storage device. The cost of all equipment was roughly US\$ 5k, two magnitudes lower than in [1]–[5]. The spectrometer records a dark spectrum of the black termination unless something within the FOV scatters the sunlight into the telescope. The sunlight impinges on the FOV at roughly 58° at noon and at roughly 90° at 6 A.M. and P.M. However, the total atmospheric air mass prior to the intersection with the FOV was larger in the morning and evening. The experiment was carried out on the July 3, with clear sky during the whole day. Recording started at 6:31 A.M. and finished at 5:25 P.M. All times stated throughout this paper are true sun times (TST), corrected for summer time settings, and the longitude between the study site and Greenwich. In order to estimate the intensity and spectral profile of the illumination impinging on the FOV, standardized  $\phi$  30 mm pieces of white polystyrene foam were dropped through the FOV every hour. Precaution was taken so that the shadow of the operator did not disturb the white calibration. The calibration was performed at location C shown in Fig. 2.

#### IV. DATA PROCESSING AND ANALYSIS

##### A. Temporal Detection of Rare Events

Initially, the intensity counts from each spectrum were averaged within the visible range 400–680 nm. The NIR region was omitted in order to avoid vegetation-induced bias. The intensity vector  $I_{Vis}$  over time was filtered with a median filter with a time window of 2 s (101 samples); see Fig. 3. The filtered vector represents the static intensity counts  $I_{Stat}$  that arise due to three factors: from the dark-current (instrument temperature dependent), from the nonperfect black termination, and from atmospheric scattering in the FOV, which can change during the day. The static background vector is subtracted from the intensity vector, so that a background corrected intensity vector is obtained,  $I_{BC}$ .

A threshold is then used to detect all rare events that are caused by insects intersecting the FOV. Since the intensity impinging  $I_0$  on the FOV changes during the day, the threshold is weighted

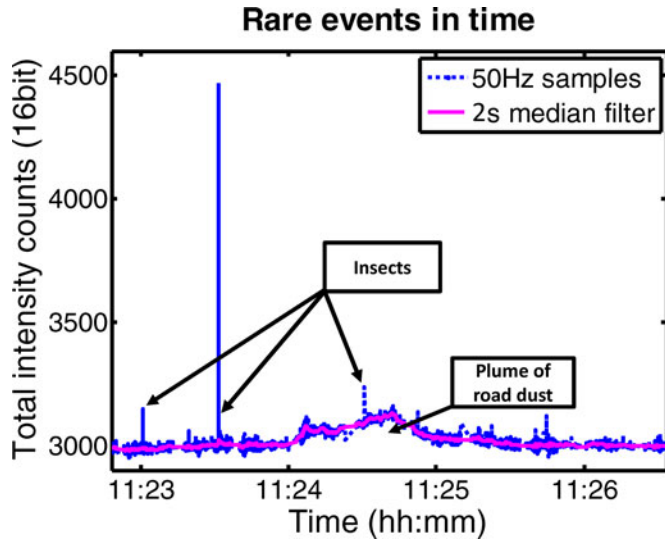


Fig. 3. Total scattered intensity over time, in the visible range, sampled at 50 Hz and with a 2-s broad median filter applied to the same signal, which is used to estimate the static signal. The positive fast spikes are caused by insects. Typically, the specimen passes the FOV in less than 50 ms. For comparison, the slow increase of scattering between 11:24 and 11:25 arose from a wide dust plume that was caused by a tractor driving upwind.

by  $I_0$ . We describe the time-dependent  $I_0$  as follows:

$$I_0(\text{TST}) = A \left( \frac{1 - \cos((\pi/12)\text{TST})}{2} \right)^W + D. \quad (1)$$

The parameters  $A$ ,  $W$ , and  $D$ , were fitted to  $I_{BC}$  for white reference events carried out throughout the day.  $A$  represents the light intensity and instrument sensitivity,  $D$  represents a bias, and  $W$  changes the waveform of the daily cycle. By plotting the skewness of  $I_{BC}$  on a histogram (see Fig. 4), the noise level can be estimated from the negative values of  $I_{BC}$ , and a level where the positive spikes can be identified with a negligible risk of including a false positive. The time-dependent threshold was scaled by this level. 1526 000 spectra were recorded during the day; and 3613 of these spectra were identified to belong to scattering events caused by insects given the specified threshold. When merging consecutive scattered spectra, the number of insect events passing the FOV was 1285. The average chance of detecting an insect for each acquisition was thus  $2.4 \times 10^{-3}$ , and if we assume no interactions between insects, then the risk for pile-ups would be  $5.6 \times 10^{-6}$  which is negligible; however, such an assumption is arguable. As can be seen in Fig. 4, a large number of events were also caused by insects below the threshold. These can also be identified when observing  $I_{BC}$  over time. They could be caused by smaller insects, which could potentially be prey species upon which the damselflies are feeding [6]. These events are omitted from this study, since their signal-to-noise ratio (SNR) would be too low for spectral analyses.

### B. Spectral Processing

The full spectra from the triggered events were extracted from the data files, and the neighboring static spectra were subtracted

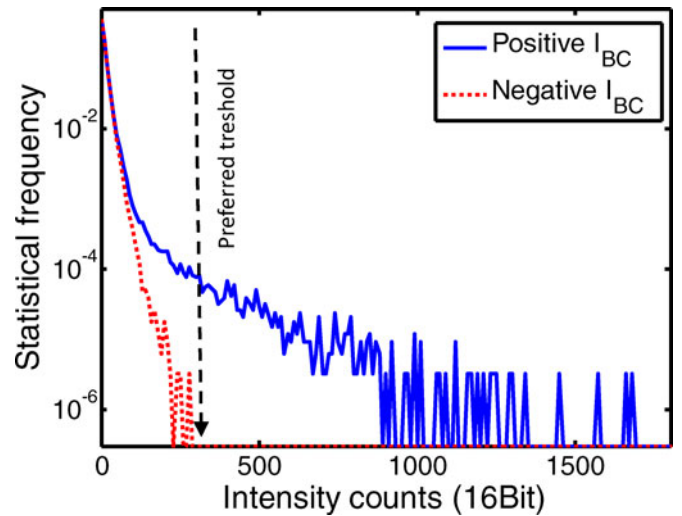


Fig. 4. Statistical frequency per sample in the late afternoon around 4:13 P.M. TST. The negative part has been flipped into a positive one for comparison. The obvious skewness arises from the rare events caused by insect intersecting the FOV. The negative observations show the noise levels and were used to set the threshold in order to avoid false triggering.

in such a way that dark current, imperfect dark termination, and slow atmospheric scattering were rejected so that only the scattering contribution was considered. In order to compensate for the spectral profile of the sun's emission, the spectral throughput of the atmosphere, the telescope, the fiber, and the sensitivity of the spectrometer, all scattering spectra were divided by the scattering spectrum from standardized white polystyrene foam pieces. The part of the spectra with reasonably good intensity (380–900 nm) was decomposed linearly using singular value decomposition (SVD) [18]–[21]. The singular values showed unambiguously that all scattering events during the entire day could be explained as a linear combination of six base spectra (see Fig. 5); thus, we are able to represent each spectra with six variables rather than one for each for the original 2664 spectral bands. A 6-D color space was expanded by this set of orthogonal base spectra and the scores were weighted by the singular values to maintain equal SNR on each axis. Because the absolute scattered intensity is likely to vary with the FOV-specimen-overlap and the cross section with the orientation and wing beat phase, the six scores were divided by the first principal component score. This kind of autonormalization leaves us with a spectral shape for improved spectral classification [22]. Further, since the first axis always becomes 1, we can reduce the dimensionality of our representation by 1, and thus we can now describe the spectral shape of each event in a 5-D color space.

### C. Unsupervised Clustering and Classification

After redundant information was removed with SVD, the Euclidean distances, in the 5-D color space, between each event and all other events were calculated, and the distances were fed into a hierarchical cluster analysis considering the furthest distance (see Fig. 6) [23]. The number of clusters should be at least as many as the spectral truncation number; otherwise, the spectral components would not be independent. However, the

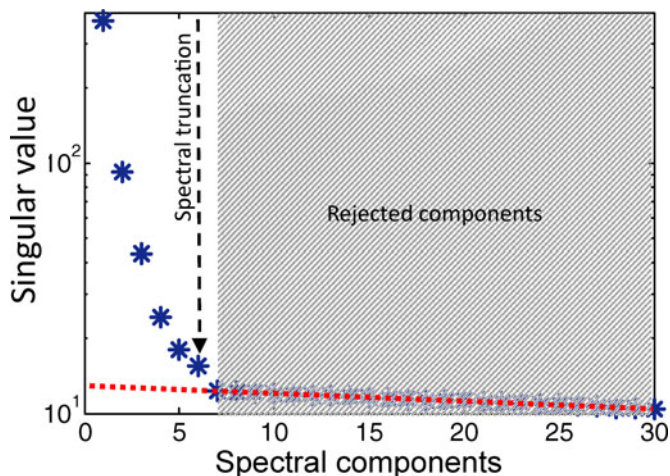


Fig. 5. When decomposing the spectra of the 2664 spectral bands of the 3613 events, the singular values suggest a remarkably clear truncation point after six spectral components. The red dashed line indicates the noise floor. Projection of data onto the first component gives an SNR of 30:1, whereas projection onto the sixth component only yields an SNR of 2:1.

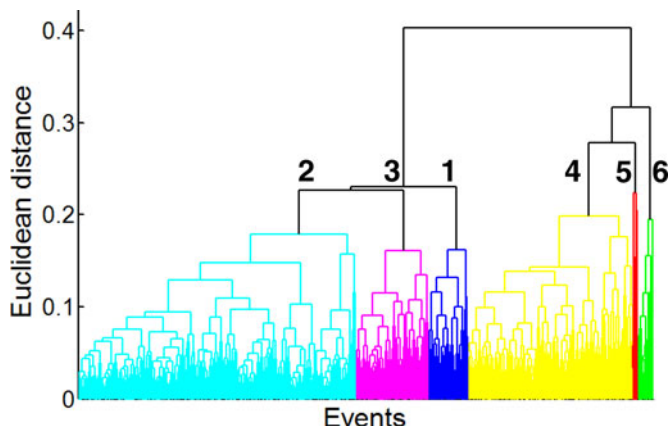


Fig. 6. Euclidean distance between each event represented in the 5-D color space is fed into a hierarchical cluster analysis. This dendrogram shows how similar the 3613 events are to each other. The first six branches were interpreted.

number of clusters can be larger than the number of spectral components. This would be the case if several clusters share the same chromophores, but in different discrete concentrations [1], [2]. The four groups of damselflies (males and females of *C. splendens* and *C. virgo*) share the same melanin pigment, but are differently melanised in discrete quantities [3], [24]. The most prominent signature, however, arises from the structural phenomenon and this does not decompose linearly because the center wavelength and feature width relate to the size and ordering of the nanostructures, respectively, rather than to specific spectral transition energy. Another spectral component, which is unrelated to the damselflies, arises from light reflected off the surrounding vegetation and carries the imprint of the chlorophyll absorption. This feature is mainly characterized by the steep slope at 700 nm. This component can be expected to be much stronger in events detected over grassland (the first 55 m of the FOV) in comparison to events detected over the river (the last

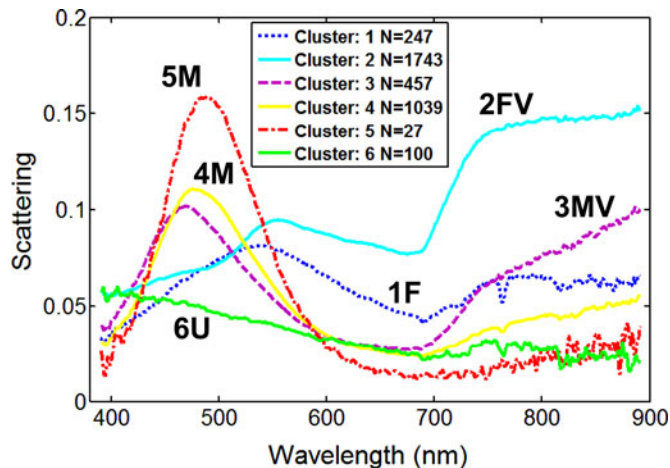


Fig. 7. Mean scattering spectra of each cluster. A scattering coefficient of 1 corresponds to the scatter from a white calibration polystyrene foam piece. M: male, F: female, V: vegetation imprint, U: uncertain. The spectra were interpreted as follows: 1F: female, 2FV: female with vegetation imprint, 3MV: male with vegetation imprint, 4M: male, 5M: male, 6U: uncertain.

40 m of FOV). Since this component reflects in any event, the effect would be a multiplication by two of any original discrete clusters, i.e., each cluster with and without a vegetation imprint.

We interpreted the first six branches of the hierarchical tree by plotting the cluster centroid spectra. The centroid spectra were calculated as the mean of all spectra assigned to a particular cluster (see Fig. 7). Clusters 3–5 show characteristic blue features, which are unlikely to arise from anything else natural other than the nanoarrays of damselfly males. The blue feature has close resemblance to the laboratory reference measurements in [3]. We are uncertain, however, whether the several peak positions (see clusters 3–5 in Fig. 7) relate to natural variance, the age of the individual, or perhaps the fact that two species are present at the site. Cluster 3 shows a significant imprint of vegetation, whereas clusters 4 and 5 can be assumed to be associated with males flying over the river surface. Clusters 1 and 2 can be associated with damselfly females. The green spectral feature at 550 nm could potentially be of importance for crypsis when the damselflies sit in the vegetation. This feature is less intense and broader than for males, as previously shown in laboratory measurement [3]. Cluster 2 carries a significantly larger vegetation imprint than cluster 1; and for this reason cluster 1 is associated with females flying over the river and cluster 2 is associated with females flying over the grassland. To further strengthen the statements made earlier, we can attend to a small detail in the centroid spectra presented in Fig. 7. The oxygen absorption band at 760 nm is a Fraunhofer line from the earth’s atmosphere. The oxygen path length from the detector to the insect compared to several kilometers’ path length prior to the incidence on the FOV is basically insignificant; however, the steady-state fluorescence of vegetation fills up this Fraunhofer line [25]. The white calibration was performed over grassland; thus, the oxygen line is not present in the two clusters that carry vegetation imprint, namely clusters 2 and 3. In cluster 1, which contains events over the river, the lack of vegetation

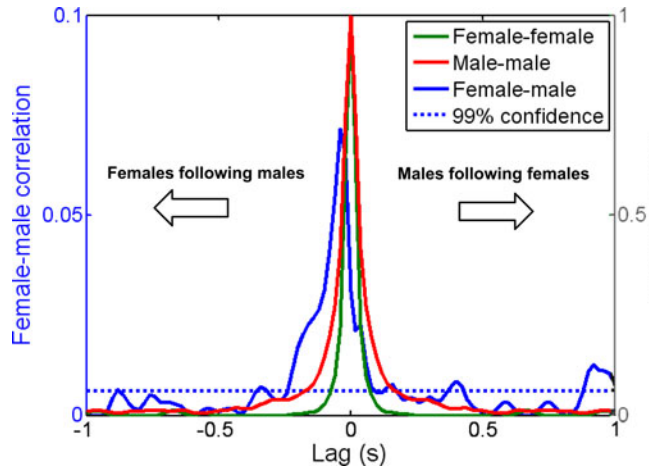


Fig. 8. Males classed to clusters 4M and 5M were cross-correlated with the females classed to cluster 1F. Positive lags on the female–male correlation correspond to males being spotted after a female spotting. The dashed confidence line is valid for the female–male correlation. Note the different scales on the Y-axis.

fluorescence at 760 nm leaves a minor dip around 760 nm. Cluster 6 is presumably related to the darker male damselflies that are characterized by a less prominent structural feature; however, we prefer to refer to this cluster as uncertain. The centroid spectra presented in Fig. 7 can be thought of as attractors in the 5-D color space, and each recorded scattering spectrum would fall into the cluster which it resembles the most. By analyzing consecutive scatter spectra, the consistency could be assessed. It was found that 80% of all consecutive scatter spectra were classed to the same cluster, and 93% were classed to the same sex.

## V. BIOLOGICAL RESULTS

### A. Interactions Between Sexes

A common idea is that males chase females when they arrive at the river for reproduction [6]. If we interpret “chasing” as two insects sharing the same trajectory in space, where the second insect is somewhat delayed behind the first, then there should be an increased chance of spotting a male when a female is detected if this hypothesis is true. To test this, we estimated the time-dependent correlation [26], [27] between the females classed to cluster 1F and the males classed to clusters 4M and 5M (see Fig. 8). The symmetric female autocorrelation is plotted with a green line for reference. This autocorrelation shows the duration of the scattering events arising when the female damselflies intersect the FOV. The male autocorrelation is plotted with a red line. From the width of the male autocorrelation, it can be seen that males stay longer in the FOV. In addition, the shapes of the female autocorrelation and male autocorrelation differ. While the autocorrelation at 0.5 is 54 ms for females and 70 ms for males, at 0.1 the difference in width of the autocorrelations has increased considerably to 120 and 248 ms for females and males, respectively. This could potentially be due to the territorial behavior of the males, which causes them to patrol and/or engage in territorial male–male interactions with

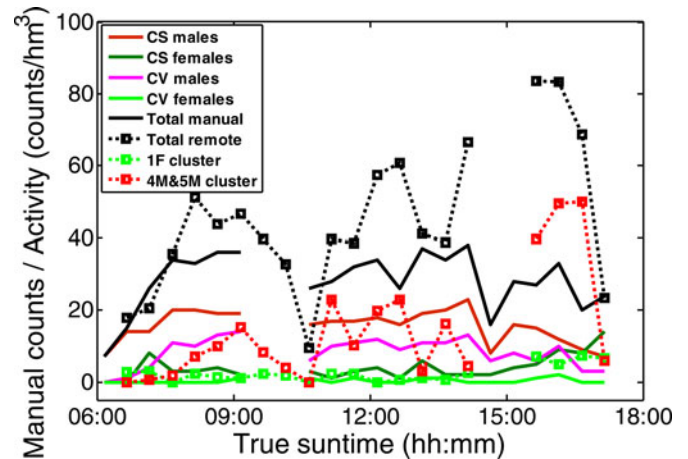


Fig. 9. Manual counts of free flying damselfly individuals of both sexes and species over the river surface (solid lines) versus automated estimates of the activity throughout the day (dashed lines). Note how the female activity increases toward the end of the day for both manual counts and the automated method.

con- and heterospecifics [28]. Alternatively, their flight patterns could differ with respect to the monitored path, e.g., the case of males mainly flying along the river. To our surprise, we find a female–male cross correlation, where females appear in the FOV approximately 100 ms after males have passed. This is likely the result of precopulatory tandems between males and females, rather than females chasing males. In such tandems, males grab females by the thorax with their clasping organs. When flying, clasped females are then connected to the males in such a way that they have to fly behind the males and hence pass the FOV after the males. We also find a much weaker, but still significant, correlation where males follow females, however. This less-well-defined increase in males that enter the FOV approximately 1 s after females have passed supports the prediction that females flying over the river are chased by males. The dashed confidence line at the bottom of the plot shows the 99% confidence limits of the female–male long-term cross correlations for the entire day. This type of analysis, with inspiration from digital signal processing [29] and system identification in robotics [30], is not possible with manual observations because of the poor time resolution, large uncertainty, and short observation duration. Clearly, a longer recording time would improve the accuracy of these types of correlations.

### B. Activity Patterns in Relation to Time, Temperature, and Wind Speed

The activity (in terms of number of damselflies in the FOV per hour per cubic meter) is similar to that estimated by manual censuses (see Fig. 9). The relative proportions of male and female damselflies are also consistent (see Fig. 9), which supports that the clusters have been correctly classified. The damselfly densities are also suitable for analyses of patterns on a much slower time scale than shown in Fig. 8. The activity of the two sexes can, for example, be analyzed with respect to the TST, wind and temperature (see Fig. 10).

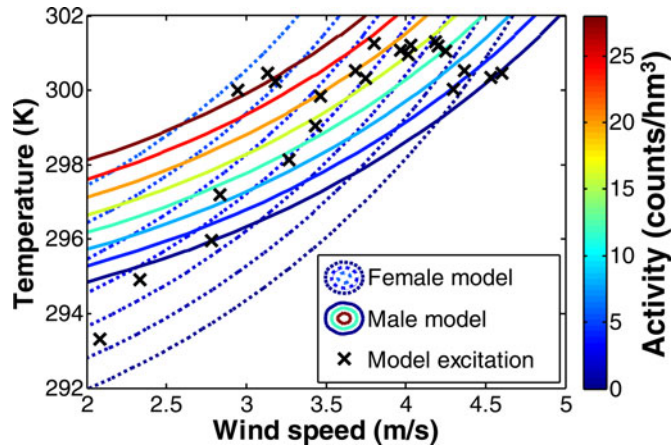


Fig. 10. Contour lines of flight preferences of both sexes based on computerized measurements. Female observations are plotted with dashed lines, while male observations are plotted with solid lines. As in Fig. 8, the absolute activity of the females is lower than that of the males, implying that they do not reach the top levels of activity, due to a lower number of females flying over the water surface.

In general, the activity of organisms with respect to temperature can be described by the shape

$$\text{Act}(T) = \text{Act}_0 \sqrt{T_{\max} - T} e^{-T_\alpha / T - T_{\text{act}}} \quad (2)$$

where  $\text{Act}$  is the activity in counts per hour cubic meter,  $T$  is the environmental temperature,  $\text{Act}_0$  is the general activity related to other circumstances than temperature,  $T_{\max}$  is the maximum temperature at which the organism can be active,  $T_{\text{act}}$  is the minimal temperature at which the organism can be active, and  $T_\alpha$  is the thermal sensitivity. This model is, however, hard to excite<sup>1</sup> outside a laboratory environment where the temperatures cannot be manipulated over the entire range. Instead, we apply a simple and more robust second-order polynomial thermal relation with one less degree of freedom (DOF). We also include a term allowing the flight preferences to depend on wind speed. Because the gradient of such a relation must necessarily be continuous and zero at zero wind speed, only even polynomial terms of the Taylor expansion of the wind parameter can be included

$$\text{Act}(T, v) = k_0 + k_{T1}T + k_{T2}T^2 + k_v v^2. \quad (3)$$

Here,  $v$  is wind speed in meters per second and  $k$ s are model parameters found by multidimensional regression with the QR factorization. Clearly, the accuracy, model excitation, details, and DOFs of the model can be increased if longer recordings are performed. We have not included an analysis of wind direction with respect to the orientation of the FOV in this study, even if this could have implications for the observations.

## VI. DISCUSSION AND OUTLOOK

The idea of this study is not to provide highly accurate data on the focal species,<sup>2</sup> but rather to explore new opportunities for using automated and modern electro-optics and spectral

<sup>1</sup>In system identification, *model excitation* implies the region for which the model can be trained.

<sup>2</sup>In biology, the *focal species* refers to the species described in the study.

classification in ecological monitoring. We have successfully demonstrated remote insect classification using an inexpensive, portable, and passive setup. One clear advantage of spectral identification in comparison to spatial image identification is that spectra do not become blurred when the sample is not in the focal plane of the telescope, and it does not produce a fast moving induce motion blur as is does in the spatial domain [31]. Clearly, the accuracy and reliability of the analysis of ecological events would benefit from longer recording times to improve statistical power.

The setup enabled us to successfully identify the two damselfly species to sex from their dark-field scattering differences. Since the classification presented in this study is unsupervised and we only had reference scattering spectra for the two sexes of *C. splendens* [3], we choose not to interpret more than the first six branches in the dendrogram in Fig. 6. For this reason, we cannot exclude the possibility that a refined analysis of the lower branches would enable us to discriminate between the two species. Although the coloration of the abdomen is fairly similar in the two species, the melanization of wings differs considerably (see Fig. 1). The proportions of males and females as well as the damselfly densities that were measured with our setup were generally consistent with the manual counts (see Fig. 9). This suggests that the setup used in this study does obtain reliable counts and activity patterns that can be used instead of the more laborious and time-consuming manual techniques. In addition to this, our measurements clearly showed a vegetation signature in the spectra of the categories 2FV and 3MV (see Fig. 7). These groups are probably made up of damselflies that were flying above vegetation rather than over the river. Obtaining these habitat measures (e.g., river versus grassland habitats) simultaneously with the damselfly counts is a particularly promising part of this method, because it allows, in addition to population monitoring, ecological insights into the lifestyle, activity patterns, and possible interactions between individuals.

Another biologically interesting result is the correlation between males and females (see Fig. 8). Females are more likely to be found at a well-defined and very short time behind males. This phenomenon is most likely caused by precopulatory tandems, in which the male has clasped the female. We also see a lower and less-well-defined signal of males following behind females at approximately ten times longer lag time. This implies that males chasing females typically appear at ten body length distance after the females. In the courtship interactions, males are commonly observed chasing the females during manual counts, and our results suggest that a common chasing distance is approximately ten damselfly body lengths. More information on the flight distances, directions of the chase in relation to the telescope, and flight speed would be needed to draw any further conclusions from these data. Nevertheless, although more fine-tuning is needed, we have shown that it is possible to study the interactions between insects over very short time scales. This technique can be applied to study both interactions within and between sexes of the same species, such as territorial behaviors and chasing of potential mates, and to study interactions between species, for example predator-prey interactions. Finally, both males and females were more active at higher temperatures

(e.g., activity increased from 292 to 302 K which was the highest temperature during the experimental period) and in lower wind speeds (activity was highest at 2 m/s, which was the lowest wind speed during the experimental period, and activities clearly decreased toward wind speeds of 5 m/s). Interestingly, there was a slight difference in the temperature dependence of different sexes where females were more active at slightly lower temperatures whereas males remained more active at slightly higher wind speeds (see Fig. 10).

Although the measurements with this experimental setup were rather successful, a number of improvements could be carried out: first, the analysis would benefit from an improved SNR. The components used in this experiment were simply the ones available in our laboratories and were not necessarily the optimal choice for the experiment. Given the SNR, the broad spectral features, and the necessity for a fast sampling, a slit width should be chosen that allows an increase of light. The SNR could further be improved by choosing a detector and grating blazing angle for optimal sensitivity around 400 nm. This would allow exploitation of the 300–400 nm region, where several interesting features could be expected (for example, absorption of chitin below 330 nm and UV features visible to the focal species and their bird predators). In the present experiment, the blaze was optimized for NIR, and the obtained signal was too weak for the UV region, even if plenty of sunlight can be found in this region. Thermoelectrically cooled compact spectrometers would further improve the SNR. Even compact multichannel photo multiplying tube (PMT) spectrometers could be considered [32]; however, the costs are considerable, the channels are few, and they typically do not include higher order rejection filters, which is necessary for such experiments. An improved SNR would also allow the detection and monitoring of smaller insects, and, for example, the interaction between predator and prey insects could also be studied. While the damselflies in this study have rather slow and chaotic wing beats, detection of other species might benefit from even faster sampling rates toward kilohertz [33], [34]. For studies of this kind, PMTs or avalanche photo diodes (APDs) should be used.

An improved black termination with improved shielding from the sunlight incident from all angles throughout the day would further make the interpretation easier and cancel out some uncertainty. Also, the white calibration could be made more consistent; one way would be to use a white sphere on a motorized swinging axis, so that the timing and intersection with the FOV are identical during each calibration event. Reference measurements of several groups of species and sexes could also be performed for improved interpretation of the centroid spectra.

For long-term unsupervised recordings, several issues should be addressed. A more robust telescope mount is necessary; also the entire setup would need a box or shed for weather protection. A CMOS RGB all-sky-imager should be included to monitor the sky in relation to the illumination of the FOV, which might be uneven on a partially cloudy day. The USB storage device should preferably be powered by laptops, so that the recordings are not interrupted by power cuts. The generator should preferably be exchanged with a solar panel.

A number of problems and questions still remain unsolved. Those are the estimation of the sample-FOV overlap, estimations of range to the events, and direction of flight with respect to the wind direction. Also, discrimination between the two species would be desirable to allow the more detailed investigation of the interactions and general ecology of them. One of the most interesting techniques involves the marking of individuals without recapture, such as those previously carried out with active fluorescence LIDAR [4], [5]. These studies allow the estimation of insect dispersal and lifetimes. This was not pursued in this study, but is likely to work well in the passive mode.

Although we describe purely passive sensing in this paper, there might be several benefits of intermittently employing an inexpensive continuous wave laser diode (LD), available from 405–980 nm up to 1 W power [35]. The method could still be noninvasive and nonperturbing if an NIR LD is used. Potential benefits could include the possibility to estimate the distance by  $1/r^2$  attenuation, and to estimate the sample-FOV overlap. The latter could be solved by painting the termination with a special fluorophore responding to that laser line with a given signature. Then, any obstruction of the beam would cause a decrease in that spectral component. Rare earths would produce very specific signatures, and could be used for various encoding strategies. Even fluorescent marking experiments, without range resolution, could be performed.

## VII. CONCLUSION

We have presented a simple, compact, inexpensive, and portable setup for remote insect classification. In contrast to earlier LIDAR-based studies [1]–[5], this setup can easily be employed by biologists. In this study, we have also provided an outline of how data from such a setup can be analyzed, and have given some tentative ideas that could be addressed with such data. We presented quantitative measures of temporal variations in damselfly activities during a day cycle, and related activities to temperature and wind speed. Moreover, phenomena were presented on a fast (millisecond) time scale, which has not been possible to estimate previously. Finally, we have discussed possible improvements and perspectives for future studies.

## REFERENCES

- [1] M. Brydegaard, P. Lundin, Z. G. Guan, A. Runemark, S. Åkesson, and S. Svanberg, "Feasibility study: Fluorescence lidar for remote bird classification," *Appl. Opt.*, vol. 49, pp. 4531–4544, 2010.
- [2] P. Lundin, P. Samuelsson, S. Svanberg, A. Runemark, S. Åkesson, and M. Brydegaard, "Remote nocturnal bird classification by spectroscopy in extended wavelength ranges," *Appl. Opt.*, vol. 50, pp. 3396–3411, 2011.
- [3] M. Brydegaard, Z. Guan, M. Wellenreuther, and S. Svanberg, "Insect monitoring with fluorescence lidar techniques: Feasibility study," *Appl. Opt.*, vol. 48, pp. 5668–5677, 2009.
- [4] Z. Guan, M. Brydegaard, P. Lundin, M. Wellenreuther, A. Runemark, E. I. Svensson, and Sune Svanberg, "Insect monitoring with fluorescence lidar techniques: Field experiments," *Appl. Opt.*, vol. 49, pp. 5133–5142, 2010.
- [5] L. Mei, Z. Guan, J. Lv, C. Löfstedt, H. Zhou, F. Chen, Z. Zhu, J. Cheng, S. Svanberg, and G. Somesfalean, "Agricultural pest monitoring using fluorescence lidar techniques: Feasibility study," *Appl. Phys. B*, Nov. 2011. Available: <http://www.springerlink.com/content/337766p1452x1k27/http://adsabs.harvard.edu/abs/2011ApPhB.tmp..885M>

- [6] G. Rüppele, D. Hilfert-Rüppele, G. Rehfeldt, and C. Schütte, *Die Prachtlibellen Europas*. Die neue Brehm-Bücherei Bd. 654, Westarp Wissenschaften, Hohenwarsleben, 2005.
- [7] R. Zahner, "Über die Bindung der mitteleuropäischen Calopteryx-Arten. (Odonata, Zygoptera) an den Lebensraum des strömenden Wassers. 2. Der Anteil der Imagines an der Biotopenbildung," *Int. Rev. Gesamte Hydrobiol.*, vol. 45, pp. 101–123, 1960.
- [8] R. Hickling, D. B. Roy, J. K. Hill, and C. D. Thomas, "A northward shift of range margins in British Odonata," *Glob. Chan. Biol.*, vol. 11, pp. 502–506, 2005.
- [9] M. Wellenreuther, K. Tynkkynen, and E. I. Svensson, "Simulating range expansion: Male mate choice and loss of premating isolation in damselflies," *Evolution*, vol. 64, pp. 242–252, 2010.
- [10] R. O. Prum, J. A. Cole, and R. H. Torres, "Blue integumentary structural colours in dragonflies (Odonata) are not produced by incoherent Tyndall scattering," *J. Exp. Biol.*, vol. 207, pp. 3999–4009, 2004.
- [11] M. J. Wade, "Sexual selection and variance in reproductive success," *Amer. Nat.*, vol. 114, pp. 742–747, 1979.
- [12] E. I. Svensson, F. Eroukhmanoff, and M. Friberg, "Effects of natural and sexual selection on adaptive population divergence and premating isolation in a damselfly," *Evolution*, vol. 60, pp. 1242–1253, 2006.
- [13] E. I. Svensson, F. Eroukhmanoff, K. Karlsson, A. Runemark, and A. Brodin, "A role for learning in population divergence in mate preferences," *Evolution*, vol. 64, pp. 3101–3113, 2010.
- [14] E. Warrant, Ed., *Invertebrate Vision*. Cambridge, U.K: Cambridge Univ. Press, 2006.
- [15] E. I. Svensson, K. Karlsson, M. Friberg, and F. Eroukhmanoff, "Gender differences in species recognition and the evolution of sexual isolation," *Curr. Biol.*, vol. 17, pp. 1943–1947, 2007.
- [16] E. I. Svensson and M. Friberg, "Selective predation on wing morphology in sympatric damselflies," *Amer. Nat.*, vol. 170, pp. 101–112, 2007.
- [17] M. Wellenreuther, E. Vercken, and E. I. Svensson, "A role of ecology in male mate discrimination of immigrant females?" *Biol. J. Linn. Soc.*, vol. 100, pp. 506–518, 2010.
- [18] A. C. Rechner, *Methods of Multivariate Analysis*. New York: Wiley Interscience, 2002.
- [19] T. W. Anderson, *An Introduction to Multivariate Statistical Analysis*, 3rd ed. Hoboken, NJ: Wiley, 2003.
- [20] P. Weibring, T. Johansson, H. Edner, S. Svanberg, B. Sundnér, V. Raimondi, G. Cecchi, and L. Pantani, "Fluorescence lidar imaging of historical monuments," *Appl. Opt.*, vol. 40, pp. 6111–6120, 2001.
- [21] P. Weibring, T. Johansson, H. Edner, S. Svanberg, B. Sundnér, V. Raimondi, G. Cecchi, and L. Pantani, "Fluorescence lidar imaging of historical monuments: Erratum," *Appl. Opt.*, vol. 41, pp. 434–436, 2002.
- [22] D. Balthasar, "Color matching by using tuple matching," in *Proc. Int. Conf. Image Analysis Process.*, Oct. 2003, pp. 402–407.
- [23] B. S. Everitt, S. Landau, M. Leese, and D. Stahl, *Cluster Analysis*, 5th ed. Hoboken, NJ: Wiley, 2011, p. 346.
- [24] M. Brydegaard, A. Runemark, and R. Bro, "Chemometric approach to chromatic spatial variance. Case study: Patchiness of the skyros wall lizard," *J. Chemometr.*, Nov. 2011.
- [25] I. Moya, L. Camenen, S. Evain, Y. Goulas, Z. G. Cerovic, G. Latouche, J. Flexas, and A. Ounis, "A new instrument for passive remote sensing: Measurements of sunlight-induced chlorophyll fluorescence," *Remote Sens. Environ.*, vol. 91, pp. 186–197, 2004.
- [26] L. Ljung, *System Identification: Theory for the User*, 2nd ed. Englewood Cliffs, NJ: Prentice-Hall, 1999, p. 672.
- [27] R. Isermann, *Identification of Dynamical Systems: An Introduction With Applications*, 1st ed. New York: Springer-Verlag, 2010, p. 550.
- [28] K. Tynkkynen, J. S. Kotiaho, M. Luojumäki, and J. Suhonen, "Interspecific territoriality in Calopteryx damselflies: The role of secondary sexual characters," *Anim. Behav.*, vol. 71, pp. 299–306, 2006.
- [29] S. Mitra, *Digital Signal Processing*, 3rd ed. New York: McGraw-Hill, 2005, p. 896.
- [30] R. Johansson, *System Modeling and Identification*. Englewood Cliffs, NJ: Prentice-Hall, 1993, p. 528.
- [31] M. Brydegaard, A. Merdasa, H. Jayaweera, J. Ålebringer, and S. Svanberg, "Versatile multi-spectral microscope based on light emitting diodes," *Rev. Sci. Int.*, vol. 82, p. 123106, 2011. Available: [http://rsi.aip.org/resource/1/rsinak/v82/i12/p123106\\_s1?isAuthorized=no](http://rsi.aip.org/resource/1/rsinak/v82/i12/p123106_s1?isAuthorized=no)
- [32] A. Thompson, H. Manning, M. Brydegaard, S. Coda, G. Kennedy, R. Patalay, U. Waitong-Braemming, P. De Beule, M. Neil, S. Andersson-Engel, Y. Itoh, N. Bendsøe, C. Dunsby, K. Svanberg, and P. French, "Hyperspectral fluorescence lifetime fibre probe spectroscopy for use in the study and diagnosis of osteoarthritis and skin cancer," *Proc. SPIE*, vol. 7895, p. 78950G, 2011.
- [33] K. S. Repasky, J. A. Shaw, R. Scheppele, C. Melton, J. L. Carsten, and L. H. Spangler, "Optical detection of honeybees by use of wing-beat modulation of scattered laser light for locating explosives and land mines," *Appl. Opt.*, vol. 45, pp. 1839–1843, 2006.
- [34] C. S. Hoffman, A. R. Nehrir, K. S. Repasky, J. A. Shaw, and J. L. Carsten, "Range-resolved optical detection of honeybees by use of wing-beat modulation of scattered light for locating land mines," *Appl. Opt.*, vol. 46, pp. 3007–3012, 2007.
- [35] Laserpointer distributor (2011). [Online]. Available: [www.o-like.com](http://www.o-like.com)



**Anna Runemark** was born in 1982 in Karlskrona, Sweden. She received the M.S. degree in biology from Uppsala University, Uppsala, Sweden, in 2006. The master's thesis was a minor field study, which was financially supported by a grant from the Swedish International Development cooperation Agency, and supervised by Prof. M. Björklund. Since 2007, she has been working toward the Ph.D. degree in evolutionary ecology at Lund University, Lund, Sweden, under the supervision of Prof. E. Svensson.

Her major research interests include evolutionary processes in fragmented populations, e.g., "Island biology and morphological divergence of the Skyros wall lizard *Podarcis gaigeae*: A combined role for local selection and genetic drift on color morph frequency divergence?" (*BMC Evolutionary Biology*, 2010), and prezygotic speciation mechanisms, see, for example, "Population divergence in chemical signals and the potential for premating isolation between islet- and mainland populations of the Skyros wall lizard" (*Podarcis gaigeae*) (*Journal of Evolutionary Biology*, 2011) and "A role for learning in population divergence of mate preferences" (*Evolution*, 2010). She has also been involved in an interdisciplinary collaboration with Prof. S. Svanberg's research group, which has resulted in three publications on ecological monitoring applications of LIDAR published in *Applied Optics*.

Ms. Runemark is a member of the European Society for Evolutionary Biology and has been reviewing for *Evolution*, *American Naturalist*, *Biological Journal of the Linnean Society*, *Animal Behavior*, *Journal of Avian Biology*, and *BMC Biology Notes*.



**Maren Wellenreuther** was born in 1976 in Göttingen, Germany. She undertook undergraduate studies from the University of Göttingen, Göttingen. She received the M.Sc. degree in 2001 from the University of Hamburg, Hamburg, Germany, within the field of marine science. In 1998, she received a one-year research grant from the German Academic Exchange Service (DAAD) to conduct research at the University of Adelaide, Australia, on predator-prey relationships. She started the Ph.D. degree with K. Clements, in 2001, on ecological speciation in a sympatric group of marine fish at the University of Auckland, Auckland, New Zealand, which was completed in 2007. The Ph.D. research was funded by a Top Achiever Doctoral Scholarship.

In 2007, she started a postdoctoral fellowship, funded by the Swedish Research Council, with Prof. E. Svensson at Lund University, Lund, Sweden, to study "the interplay between interspecific interactions, sexual isolation and gene flow in the dynamics of species ranges: the evolution of wing coloration in calopterygid damselflies." She is currently a Marie-Curie Postdoctoral Fellow at Lund University and is involved in "Mapping genotypes to phenotypes: development of a linkage map and mapping of colour polymorphisms in *Ischnura elegans* (Odonata)" with Prof. B. Hansson and Prof. E. Svensson. Her previous and current research interests involve the study of speciation using ecological and molecular tools, and include investigations of species distribution patterns, mate choice, sexual and natural selection, gene flow, and the interplay between phenotypes and genotypes in species formation. Three representative and recent publications are given as follows: "The role of ecology on the molecular diversity and population structure in a coenagrionid damselfly" (*PLoS ONE*, 2011), "Simulating range expansion: Male species recognition and loss of premating isolation in damselflies" (*Evolution*, 2010), and "The role of ecology in male mate discrimination of immigrant females" (*Biological Journal of the Linnean Society*, 2010).

Dr. Wellenreuther has, among others, reviewed for the following journals: *Behavioural Ecology*, *Animal Cognition*, *Evolutionary Ecology*, *Evolutionary Research*, *Journal of Fish Biology*, *Ecography*, *MEPS*, *PLoS ONE*, *Proceedings of the Royal Society B*, *Molecular Ecology*, *Journal of Evolutionary Biology*, *OIKOS*, *Evolution*, and *Animal Ecology*.



**Hiran H. E. Jayaweera** was born in 1980 in Matara, Sri Lanka. He received the B.S. degree in physics from the University of Colombo, Colombo, Sri Lanka, in 2004 with the specialty in microcontrollers and embedded systems. He is currently working toward the Ph.D. degree at the Centre for Instrument Development, University of Colombo. The work here is related to monitoring agricultural products with nondestructive tests.

In 2006 and 2009, he received fellowships from the International Science Programs of Uppsala University to visit Prof. S. Svanberg's research group to work in gas in scattering media absorption spectroscopy (GASMAS) and LED-induced fluorescence and reflection spectroscopy with application to biological materials. He was a Teaching Assistant and Assistant Lecturer at the University of Colombo. He teaches mathematics and physics to school kids who are the victims of the war in Sri Lanka. He has been teaching development of low-cost embedded systems for the undergraduates of the University of Colombo and general public in Sri Lanka. During his internship in Japan, he was involved in the research on photoluminance on quantum dots in the Itho Group of Keio University. He is active in an African research network for spectroscopy and imaging where he contributed with electronics and programming teaching in Ghana and Mali.

Mr. Jayaweera is a member of the Institute of Physics, Sri Lanka; the Young Scientist Federation, Sri Lanka; and the Sri Lanka Association for Advancement of Science.



**Mikkel Brydegaard** (M'11) was born in 1980 in Copenhagen, Denmark. He studied in a number of countries ranging from Venezuela to Romania. He received the Master of Electrical Engineering in 2007 from Lund University, Lund, Sweden, with specialty in measurements and control theory. He is currently working toward the Ph.D. degree in Lund University in Prof. S. Svanberg's group *Applied molecular spectroscopy and remote sensing*. Here, he is involved in broadband elastic and inelastic spectroscopy with applications in medicine, food science, and ecology.

He was a Teacher of Electronics in technical formation in Peru. He teaches ultrasound physics during internship in an Indian university. He filed more than five patent applications on instrumentation. He is teaching optical spectroscopy and imaging on request of the Swedish Government Program for Capacity Building (ISP-SIDA) in Ghana, Senegal, and Mali, for ICTP, Trieste, Italy, and for the Puya Raimondi Foundation, Lima, Peru. His special interests include realistic LED-based instrumentation, e.g., "Versatile multispectral microscope based on light emitting diodes" (*Review of Scientific Instrument*, 2011) and also novel applications of LIDAR, e.g., "Remote nocturnal bird classification by spectroscopy in extended wavelength ranges" (*Applied Optics*, 2011).

Mr. Brydegaard was appointed to a Board Member of the Interdivisional Group of Physics for Development (IGPD-EPS) 2010. He is a reviewer of the *Journal of Applied Optics* and *Journal of Physics*.



**Sune Svanberg** was born in 1943 in Trollhättan, Sweden. He received the Ph.D. degree in physics from Gothenburg University, Gothenburg, Sweden, in 1972.

He has been a Professor of physics at Lund University, Lund, Sweden, since 1980. During 1980–2009, he was the Head of the Atomic Physics Division and during 1996–2010, he was the Director of the Lund Laser Center. He is also the Coordinator of a long-term Linnaeus grant from the Swedish Research Council to the Lund Laser Center. He is an Honorary

Doctor/Professor at Lund, Liège, Lima, Riga, Chanchuen, Harbin, Hangzhou, and the Chinese Academy of Sciences. His research interests include atomic physics, high-power laser matter interaction, combustion diagnostics, environmental monitoring, and biophotonics.

Dr. Svanberg is a Fellow of the American Physical Society, the Optical Society of America, and the European Optical Society.

## PAPER XIII

### **Feasibility study: Fluorescence lidar for remote bird classification**

M. Brydegaard, P. Lundin, Z.G. Guan, A. Runemark

S. Åkesson and S. Svanberg

*Applied Optics* **49**, 4531-4544, 2010.

# Feasibility study: fluorescence lidar for remote bird classification

Mikkel Brydegaard,<sup>1,\*</sup> Patrik Lundin,<sup>1</sup> Zuguang Guan,<sup>1</sup> Anna Runemark,<sup>2</sup>  
Susanne Åkesson,<sup>2</sup> and Sune Svanberg<sup>1</sup>

<sup>1</sup>Atomic Physics Division, Lund University, P.O. Box 118, SE-221 00 Lund, Sweden

<sup>2</sup>Animal Ecology Division, Lund University, Sölvegatan 37, SE-223 62 Lund, Sweden

\*Corresponding author: mikkel.brydegaard@fysik.lth.se

Received 15 March 2010; revised 1 June 2010; accepted 25 June 2010;  
posted 16 July 2010 (Doc. ID 125454); published 13 August 2010

We present a method for remote classification of birds based on eye-safe fluorescence lidar techniques. Mechanisms of quenching are discussed. Plumage reflectance is related to plumage fluorescence. Laboratory measurements on reflectance and fluorescence are presented, as well as test-range measurements. Also we present examples of birds' in-flight lidar returns. The methods are suitable for studies of night migrating species and high-altitude classification with implications for the detailed understanding of bird migration and global virus spread. © 2010 Optical Society of America

OCIS codes: 010.3640, 300.2530, 280.1100.

## 1. Introduction

Birds, with their highly mobile lifestyle, have been able to successfully colonize new geographic areas and thereby have extended their breeding ranges to include most habitats of all continents [1]. At certain times of the year, millions of birds depart on migration flights across continents and seas. Many of these migration flights are performed at night, hidden from our eyes. Some birds have adapted to perform long migration flights across vast inhospitable areas, such as the Saharan desert and the Mediterranean Sea during their migrations between their summer breeding grounds in Northern Europe, and areas where they spend the winter in tropical Africa [2,3]. A large proportion of migratory songbirds fly at night and at high altitudes (>500 m) between these remote destinations [4,5]. By flying at night, the flight will potentially be less disturbed by turbulent wind conditions compared to daytime [6], and the birds will reduce the risk of being taken by predators [7]. Furthermore, by migrating at night, the birds can maximize the time spent on feeding during daytime [2,8].

## 2. Existing Methods

The intensity of migration, flight altitude, and directions of nocturnal bird migration flights have been studied by using a number of remote sensing methods, such as surveillance and tracking radars [9–14], ceilometers [15,16], infrared (IR) cameras [13,17], as well as lunar obscuration [18,19]. The surveillance and tracking radars and IR cameras enable the observer to get a relatively good estimate of the height distributions and numbers of birds passing overhead, while the ceilometer providing the same type of data is very limited in range (applicable altitude range is from a few meters to about 200 m) [15,16] and is not able to cover dominating flight altitudes under natural conditions. Moon watching (i.e., lunar obscuration) gives more crude estimates of directions and altitude ranges, but can be useful when there are limited possibilities to use major equipment (i.e., surveillance and tracking radar) because a pair of binoculars is all that is needed for observations, and large areas can be covered with many observation sites [20,21]. So far, it has not been possible to identify the species observed with the moon watching or the other methods. In some areas, migrating birds might even be confused with nocturnal insects and

mammalian migrants, such as bats, since some of the species explore the same time interval for migration.

All remote methods used so far to record nocturnal migration in free-flying birds have been limited by not being able to reveal what species have been observed. With a few exceptions, like the common swift (*Apus apus*), which has a very characteristic wing-beat pattern during flight and which can be identified by a tracking radar [22,23], most birds migrating at night and at high altitude will have to pass unidentified, as the flight speed and wing-beat frequency for birds of the same size range is similar, making only classifications of a few size groups possible by using tracking radar [24]. Another confounding factor is the altitude at which the birds migrate, which often exceeds 500 m during normal migration flights across the landscape [4,5,25]. For example, soaring birds normally occur up to a few thousand meters [26], making it difficult to visually identify the species, not only at night, but also during the day. To study the special adaptations for nocturnal as well as diurnal flight, the timing of migration for different age and sex classes of birds and the passage relative to topography, winds, and weather parameters, it would be of great interest to identify the individual birds down to the species, but also—when possible—to sex and age level. In this paper, we examine the possibility of using a fluorescence (light detection and ranging (lidar) system to identify the species of birds, on the basis of their size, plumage characteristics, and spectral features from their plumage.

### 3. Lidar Technique

Lidar techniques have been successively developed following the invention of the laser 50 years ago, but even a search-light-based variety was tested before that (for overviews of the field see, e.g., [27,28]). In a lidar system, an intense and short-duration laser pulse is transmitted into the atmosphere, and light, as scattered from objects or aerosol particles, returns to a receiving telescope placed adjacent to the transmitter. The optical return is converted to an electronic signal in a photomultiplier tube (PMT) and is recorded in a transient recorder/digital oscilloscope. Range resolution is obtained from the time-of-flight information (a fixed target 150 m in front of the system yields an echo after 1  $\mu$ s), and the best resolving ability is limited by the pulse duration (a 7 ns pulse yields an echo half-width of 1 m; nonoptimal electronics prolong the echo). Apart from ranging applications yielding target distance, elastic backscattering from aerosols can yield information on their distribution and properties. Distributions of pollutant gases with sharp absorptive imprints can be obtained with the differential absorption lidar (DIAL) variety of the technique, where the laser source is intermittently tuned between an absorbed and a nonabsorbed wavelength. The laser light can also induce fluorescence, which is utilized in fluorescence lidars. In particular, this is being exploited in long-range systems, where meteorite-produced alkali atoms and

iron ions in the upper atmosphere are monitored. At closer range, broadband fluorescence in solid targets can be induced, as discussed in, e.g., [27]. Applications include characterization of oil spills at sea, algal blooms, vegetation, and building facades (cultural heritage). In the zoological realm, lidar techniques have also been employed for studies of fish (see [29] and references therein), honeybees [30,31], and damselflies [32,33]. The present project on bird fluorescence lidar emerged out of the damselfly studies performed in our group.

### 4. Motivation

There are a number of bird flight and migration phenomena that would be of great interest to study if it were possible to identify the species (and age and sex) of the birds migrating at night and at high altitude during the day. For instance, more general questions related to selection of time of migration and flight directions relative to winds and topography, as well as the altitude of migration, could be studied for migrants with different morphology and flight adaptations. Comparative studies of bird migration could be performed at different geographic areas and during different times of the year. It would also be possible to study the composition of bird migrants for a given area, how their migration flight behavior might differ between species, and how the bird movements might lead to the spread of bird-borne diseases, such as avian flu and avian malaria, tick-borne diseases, and seeds [1,34].

### 5. Bird–Light Interaction

In the ultraviolet, visible, and near-IR (UV–VIS–NIR), plumage reflectance arises from microstructures of the barbs and leaflike barbule sheets, which range in thickness down to a couple of micrometers, with the even smaller barbicel hooks attached [see common wood pigeon *Columba palumbus* feather in Fig. 1(a)]. The barbules are neatly arranged, overlapping, and generally there is no line of sight through a single feather. The many air–solid interfaces between feather structures in the hollow feathers and in vacuoles cause the incident light to be reflected and transmitted according to Snell's law and the Fresnel equations. On the macroscopic scale, the many dispersion events cause incident light to behave diffusively, as is known from the theories of multiple scattering, photomigration, and tissue optics [35,36], and it eventually leaves the plumage to reach the observer. After such migration, light loses information regarding polarization and coherence; for this reason, this contribution to the total reflectance is referred to as incoherent scattering.

Along the migrated path, the light can be absorbed by chromophores that are embedded in the  $\beta$ -keratin matrix [37,38], which is the main constituent in feather structures [39]. The refractive index in the visible range is typically 1.55 [40]. The absorption of both  $\beta$ -keratin and the mammalian-occurring  $\alpha$ -keratin increases slowly from 400 to 300 nm,

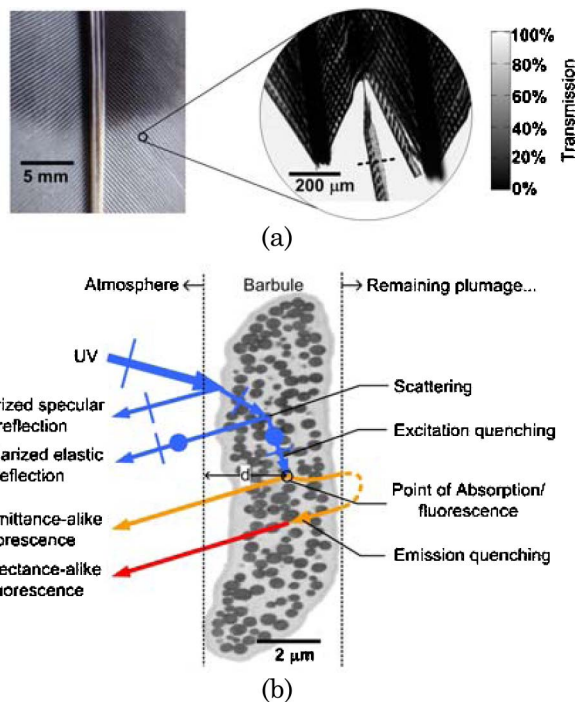


Fig. 1. (Color online) (a) Left, typical feather from pigeon; the melanin concentration is higher in the top part. Barbs are connected to the central trunk. Right, transmittance image at 590 nm; the barbules are attached to the two barbs and are neatly arranged, covering each other. A single barbule dangling from its barbicels transmits roughly half of the light. (b) When a UV laser pulse impinges on the plumage, a polarized specular angle-dependent elastic echo returns. After internal scattering events, polarization is lost and the echo is emitted omnidirectionally. Part of the excitation light will be quenched by the melanin granules with low fluorescent yield; remaining UV light is absorbed in the keratin matrix and produces broad emission. Emitted light will, in turn, be quenched by present chromophores on its way to the surface. The shorter the wavelength, the shorter the mean absorption depth,  $d$ , the less excitation quenching, and the more fluorescence resembles reflectance. See Eq. (1). Transmission electron image (TEM) (with permission from M. D. Shawkey [76]). The darker embedded spots arise from melanin granules.

increases dramatically below 300 nm, and peaks at 280 nm [41]. The most common chromophores are the black eumelanins and the reddish pheomelanin, which have dull spectral features with a monotonically increasing absorption toward lower wavelengths, and produce black, grayish, and brownish colors, whereas the second most common class of chromophores is carotenoids, which exhibit relatively sharp and characteristic spectral features and give rise to yellow, orange, and red colors ([37], Chaps. 5, 6). In certain taxa, chromophores such as pterins, porphyrins, and psittacofulvins can also be found ([37], Chap. 8). The number of chromophores used for bird–bird communication is not expected to be much higher than the number of spectral bands in the focal species [42]. The spectral features used in communication are also expected to appear in the full region covered by the available spectral bands of the focal species [42]. Birds have four spectral bands, ranging from approximately 350 to 700 nm [43]. This

range includes a UV band, which is not visible to the human eye, as well as light visible to humans; however, the remaining spectral bands are not positioned identically to those of humans. It is worthwhile to recall that the color space of birds is typically of higher dimensionality than ours, which complicates bird studies considerably [38].

In addition to the absorption taking place in the keratin matrix and the embedded chromophore granules, the reflectance of the feathers also depends on the presence of oils and waxes with a slightly lower refractive index. The large majority of birds secrete a preen oil, consisting mainly of diesters, from the uropygial gland [44]. Such grease films are typically less than 100 nm in thickness (thus thinner than the evanescence field), and transparent in the region of 350–700 nm. However, they do typically exhibit strong absorption below 320 nm [45].

Blue, UV reflecting, and iridescent plumages are typically based on constructive interference. Reflectance of such plumages will depend strongly on the angles of illumination and observation with respect to the surface orientation [46]. Structural color is typically produced by repetitive structures; that is, dominant spatial frequencies of changing refractive index along the optical axis in nanostructures in the feathers [37], Chap. 7, [47]. Such nanostructures can consist of ordered arrays of air-filled vacuoles or melanin granules. Structural effects alter the ratio between reflected and transmitted light from a single nanoarray. For effective structural colors, chromophores are required to prevent transmitted light from escaping the plumage after multiple scattering in the underlying plumage [Fig. 1(b), bobolink, *Dolichonyx oryzivorus*]. Because a structural color occurs because of interference, the effect cannot be described either by diffusion theory or by the Monte Carlo simulation commonly applied in tissue optics. For this reason, the structural contribution to the total reflectance is referred to as coherent scattering.

When considering laser-induced fluorescence (LIF) in birds for remote classification, the natural choice of excitation wavelength would be 266 nm, considering the bird eye-safety issue of using 355 nm excitation, as is common in remote LIF setups. Bird reflectance at 266 nm is not well studied because it is well below the UV sensitivity bands of any animal [48]. Preen oils and waxes and keratins increase heavily in absorption below 320 nm and produce a considerable broad bluish fluorescence, peaking around 400 (for botanical waxes) [49] and 380 nm ( $\alpha$ -keratin) [50]. In certain more rare taxa, including parrots, by using porphyrins as chromophores we can expect high fluorescence yield and relatively sharp and characteristic spectral features. Even if not directly pumped at 266 nm, the fluorescence emission from keratin might serve as an indirect pump for porphyrins. Fluorescence yields of melanins and carotenoids are low in comparison to those of greases and keratin. Embedded melanin granules are, however, expected to quench both excitation and

emission from keratin fluorescence. For this reason, we can expect to be able to classify birds by quantifying both eumelanin and pheomelanin content by spectrally analyzing the fluorescent emission from plumage, even if the fluorophores are identical for most feathers.

A typical effect in fluorescence spectroscopy is that the interrogation volume becomes more superficial the lower the excitation wavelength is [51]. The scattering coefficient is roughly  $600\text{ cm}^{-1}$  in solid keratin without granules or vacuoles, and the absorption cross section of solid keratin at  $266\text{ nm}$  is roughly  $2400\text{ cm}^{-1}$  [41]. This implies that half of the light is deposited in the outermost  $2\text{ }\mu\text{m}$  in solid keratin, corresponding to the thickness of a single barbule. The preen wax coatings have absorption coefficients of the same order of magnitude but are typically not thicker than  $100\text{ nm}$ . Melanins have a cross section that is roughly a factor of 10 higher than that of keratin at  $266\text{ nm}$  [52] and reach volumetric fill factors of up to 50% [53]. Because of the high scattering coefficient and absorption cross section at  $266\text{ nm}$ , we can expect most of the excitation energy in the outermost  $1\text{ }\mu\text{m}$  of the plumage. The resulting fluorescence light is created omnidirectionally in the interrogation volume. One part is quenched (reabsorbed) by the chromophores upon leaving the volume before reaching the surface, and the other part, propagating inward, is reflected in the plumage before reaching the observer [Fig. 1(b)]. For this reason, we can expect the fluorescence to be highly correlated with reflectance as long as the dominant fluorophores involved are the same from sample to sample and their emission covers the region where the chromophores absorb. We refer to this method as *on-target white-light generation*, which allows us to measure reflectance, including structural features [32], in the UV–VIS region with LIF lidar without risk of blinding the sample species.

Temporal delays in fluorescence from plumage might arise from the excited state lifetimes. The lifetime of keratin is  $1.4\text{ ns}$  and of melanin is  $2.2\text{ ns}$  [54]. Scattering lifetimes are expected to be at least 1 order of magnitude faster, where most visible photons have left the plumage after  $100\text{ ps}$ , corresponding to a  $3\text{ cm}$  path.

There is a great spatial variance in plumage colors in birds. The color can vary even within a single feather and barbule [37,38], and birds often differ in coloration between different body parts. Sexual dichromatism, where the sexes have different color patterns, is also common in birds [55]. Seasonal variation [56–58] and molt [59] are also known to affect plumage color, and some bird species also have a different nuptial plumage. In addition, color can be condition dependent, especially for carotenoid-based colors [60].

Museum specimens have been shown to accurately represent the coloration of wild birds [45], but some of the substances used for preservation can change

the reflectance spectra of the plumage, although the frequency of damaged skins is very low [61].

In the thermal-IR region between  $2.5$  and  $25\text{ }\mu\text{m}$ , plumage emissivity is approximately 80%, regardless of the chromophores. The plumage provides isolation and has been demonstrated to maintain large temperature gradients. Down is known to have exceptionally low transmittance in the mid- and thermal-IR region [62]. Down and feathers exhibit several strong features in the whole region and have a remarkable point close to  $5.8\text{ }\mu\text{m}$  where scattering disappears and the plumage becomes completely transparent due to Christiansen's effect [63,64]. While IR features do not reflect the chromophores, there seem to be several structural imprints in the mid-IR within the atmospheric windows on both sides of the  $\text{CO}_2$  band from  $3.5$  to  $5.5\text{ }\mu\text{m}$ . Such structural features might be species specific and feasible for passive remote classification (measurements not presented here). Further out in the radio frequency (RF) region, the reflectance or radar cross section (RCS) is governed by the entire naked body structure of the bird. As for optical structural colors, the RF reflectance is highly dependent on the illumination and observation angles and is often measured as a spherical function in relation to the bird pitch and roll orientation, which can be estimated from the flight trajectory. The spherical RCS function depends on the polarization with respect to the body orientation of the bird. The elastic return can be expected to be partly depolarized according to the linear depolarization ratio for the given wavelength in any of the regions: RF, IR, VIS, and UV. Spectral reflectance features in the RF appear when the wavelength matches the dominant features of the body from the angle of observation, with a maximum around  $10\text{ cm}$  [65]. Finally, the phase in the wing-beat cycle will change the properties of fluorescence, emissivity, and reflectance in the UV, VIS, IR and RF.

## 6. Proposed Strategy

We propose the use of LIF lidar to acquire additional parameters for classification of nighttime migrating birds. We plan to use  $266\text{ nm}$ , the fourth harmonic of a commercial pulsed Nd:YAG laser, as excitation because this wavelength is eye safe for birds [66]. The UV light will induce broadband whitish light in the plumage, which, in turn, will be partially reabsorbed (quenched) by the chromophores present and eventually be detected through a telescope. For the purpose of consistency of the geometry, vertical sounding should be performed to induce the fluorescence on the chest. For a field test, a main focus will be on migration points where the hit probability is high. Also, for upcoming field studies, the methods are planned to be integrated with IR and RF instrumentation, which provides additional information regarding trajectories and wing beats.

## 7. Methods and Setup

We will now describe the materials, techniques, and equipment used in our measurements. Twenty-four bird samples were borrowed from the Lund Zoological Museum. The samples were selected in terms of being representative species, genders, and ages that could potentially be sighted during summertime in Sweden. Several of the same or similar species with several genders without sexual dimorphism yielded similar results and are not included in this paper. The more interesting samples presented throughout this paper are presented in Table 1. Most samples are less than 100 years old, are well conserved in plastic envelopes in catalog loggers, and have not been exhibited.

### A. Point Measurements

Samples were air dusted and measured with a point fiber probe operating in reflectance and fluorescence modes [Fig. 2(a)]. The museum skins can be assumed to accurately reproduce the reflectance of living samples. Considering that no new fluorophores have been observed [46,61] and considering the principle

of conservation of energy, we can derive that, if reflectance remains the same in the range of keratin excitation and emission, then the fluorescence signature cannot change significantly. The plumage is illuminated angled at 30° to the surface normal in order to reject the specular reflection. Although this geometry slightly diminishes structural imprints, the effect could still be observed. In the spectroscopic measurements, we used light-emitting diode (LED) illumination switched among a 255 nm AlGaIn/GaN LED (255UVTOP); 355, 375, and 395 nm AlGaIn LEDs (NS355L-5RLO, NS375L-ERLM, RLU395-8-30); and a 450–700 nm InGaIn + Ce:YAG LED (5W4HCA-H30, Roithner-Lasertechnik). The current was kept constant by a LM317 regulator and the internal temperature was estimated from the current–voltage characteristics to compensate for the temperature-conversion-efficiency dependence. The sample geometry is identical between the reflectance and the 355 nm excited fluorescence measurements. Light is collected in a 600 μm UV fiber and fed to a compact spectrometer (Ocean Optics, USB4000). The reflectance and the fluorescence at 355 nm excitation

Table 1. Latin Names, Popular Names, Apparent Color and Sex of All Samples Presented in Figures Throughout This Paper<sup>a</sup>

Latin Species Name	Trivial Name	Color/Body Part	Sex	Comments	Figure	Symbol
<i>Acrocephalus arundinaceus</i>	Great reed warbler	Brown/back		Adult	3 and 4	
		Beige/side		Adult	12	
<i>Acrocephalus s. scirpaceus</i>	Reed warbler	Light brown/chest	Female	Adult	3–6	
		Brown/back	Female	Adult	5 and 6	
		Brown/side	Female	Adult	11	
<i>Columba palumbus</i>	Common wood pigeon	Gray/feather		Adult	1	
<i>Corvus monedula</i>	Jackdaw	Dark gray/front	Female	Adult	11	
<i>Corvus f. frugilegus</i>	Rook	Black/chest	Female	Adult	3 and 4	
		Black/side	Female	Adult	12	
<i>Dolichonyx oryzivorus</i>	Bobolink	Black/feather		Adapted from [76]	1	
<i>Erithacus r. rubicula</i>	European robin	Red/chest	Male	Adult	3–6	
		Front	Male	Adult	11	
<i>Larus michahellis</i>	Yellow-legged gull	Entire bird		Adult	2	
<i>Motacilla a. alba</i>	White wagtail	Light gray/chest	Male	Adult	3 and 4	
		Gray/back	Male	Adult	5 and 6	
		White/forehead	Male	Adult	5 and 6	
		Gray/groin	Male	Adult	5 and 6	
		Black/chest part	Male	Adult	5 and 6	
		Yellow/chest	Male	Adult	3–7	
<i>Parus caeruleus</i>	Blue tit	Blue/head	Male	Adult	3 and 4	
		Blue/tail	Male	Adult	5 and 6	
		Blue/side	Male	Adult	11	
		Black-irid./chest	Male	Adult	5 and 6	
<i>Sturnus v. vulgaris</i>	European starling	Many birds/side	M/F	Juveniles, in flight	8	
		Black-irid./side	Male	Adult	10	
		Black-irid./side		After autumn molt	11 and 12	
<i>Saxicola rubetra</i>	Whinchat	Orange/chest	Male	Adult	3 and 4	
<i>Sylvia atricapilla</i>	European blackcap	White/chest	Male	Adult	3 and 4	
		Gray/side	Male	Adult	12	

<sup>a</sup>Samples giving rise to similar reading have been omitted for the convenience of the reader. Museum samples were selected to be representative of their kind. The choice of species was based on the expectation for sightings in the season and habitat where the lidar was stationed.

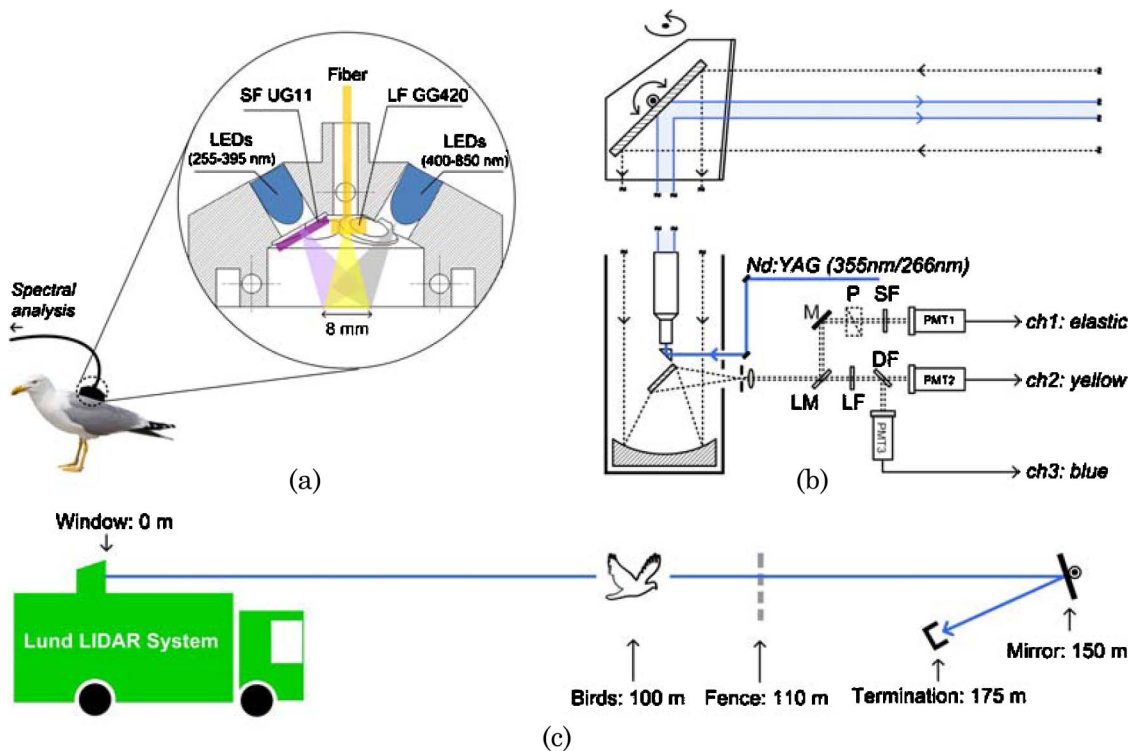


Fig. 2. (Color online) (a) Ground truth measurements were performed with a compact combined reflectance and fluorescence sensor. Various excitation wavelengths for fluorescence, as well as broadband light for elastic measurement, is provided by a selection of LEDs. (b) The Lund mobile lidar system was emitting at 266 and 355 nm in this study. A two degrees of freedom scanning mirror allows the beam direction to be controlled. The returning light is collected by a 40 cm telescope. The return can be discretized according to polarization and wavelength with a number of PMTs. (c) In-flight European starlings were recorded at an 85 m distance during another experiment on damselfly dispersal [33].

are filtered with a 5 mm thick long-pass filter (GG420, Schott), which suppresses the excitation. The excitation spectrum at 355 nm is cleaned up with a 1 mm excitation filter (UG11, Schott). The reflectance is calculated using a flat 50% gray reference (Oriol) and the fluorescence at 355 nm excitation is white-light calibrated against a blackbody reference (Oriol). The fluorescence induced by 255 nm radiation is observed directly without any spectral filters; it is not white-light calibrated, but spectra can be compared relatively.

Fluorescence lifetimes were measured on a number of samples, including eumelanized, pheomelanized, carotenoid, and structural colored plumage. The instrument is a multi-excitation, multi-emission, single-photon counting system developed by the Photonics Group, Department of Physics, at Imperial College London [67]. The plumage was excited by mode-locked lasers at 355 and 435 nm with a repetition rate of 37 MHz. The resulting fluorescence is detected in 16 bands in the range of approximately 385–600 nm. Time-resolved fluorescence instruments are typically developed to measure characteristics that are independent of reabsorption, which otherwise influences the fluorescence spectra.

Initial total transmittance measurements in the range of 2–25  $\mu\text{m}$  have been conducted with a Fourier transform spectrometer (ATI Mattson, Infinity series

FTIR). The results will not be discussed further in this paper.

## B. Lidar Measurement

The lidar facility for the experiments is based on the Lund mobile lidar system [68]. The main equipment is presented in Fig. 2(b). The third (355 nm) and fourth (266 nm) harmonics of a Nd:YAG laser radiation with energy of around 40 and 6 mJ/pulse, respectively, and with pulse width around 15 and 4 ns, respectively, were used for excitation. After expanding into a beam diameter of about 5 cm, the laser beam is transmitted by a horizontally and vertically scanning mirror with a size of  $\sim 40 \text{ cm} \times 56 \text{ cm}$  and mounted in a rooftop dome. A quartz window is used to protect the dome from dirt and dust in the atmosphere. The elastic scattering and the fluorescence from the targets are reflected by the same mirror and collected by a telescope system with a diameter of 40 cm. The collected light is distributed by a number of mirrors and filters to three PMTs for analysis. As shown in Fig. 2(b), the elastic scattering from the target is filtered out by a laser line mirror (LM) and recorded by PMT 1 in the time domain. A polarizer (P) is set at a crossed angle against the polarization state of the transmitted laser and, therefore, PMT 1 is only sensitive to depolarized backscattering. An additional short-pass filter (SF) is used to further suppress the fluorescence light

Table 2. Optical Component List for the Three-PMT System

Components	Excitation	
	355 nm	266 nm
Laser line mirror (LM)	45° 355 nm	45° 266 nm
Polarizer (P)	Film polarizer	none
Short-pass filter (SF)	UG11—1 mm	UG11—1 mm
Long-pass filter (LF)	GG400—5 mm	WG305—3 mm
Dichroic filter (DF)	Edmund Blue/Yellow	Edmund Blue/Yellow

from the target and background light from the sky. On the other hand, the fluorescence light transparent through the LM is divided by a dichroic filter (DF) into two wavelength bands (blue and yellow) and measured by PMT 2 and PMT 3, respectively. Before the DF, a long-pass filter (LF) is used to suppress the leakage of the elastic scattering through the LM. The list of the optical components mentioned above is shown in Table 2 for different excitation wavelengths. The three channels of signals from the PMTs are simultaneously recorded by a high-speed oscilloscope (Tektronix TDS544B), which samples every 8 ns. The recorded data are read out through a GPIB connection by a computer in real time. However, the repetition rate of the whole system is limited to 10 Hz by the communication speed, although the laser system is running at 20 Hz. By using such a three-PMT system, both the elastic scattering and the two bands of fluorescence signals can be analyzed in the time/spatial domain.

The field experiments were originally arranged for studying the migration of damselflies. Details will be found in a forthcoming publication [33]. As shown in Fig. 2(c), geometrically there is a metal fence at ~110 m away from the lidar bus, and a mirror at ~150 m is used to fold the laser beam for possible measurements at a longer distance over the surface of a river. Finally, a termination is set at ~175 m distance. During the damselfly measurements, by accident a group of starlings flew into the laser beam at a distance of ~100 m and were recorded by our system. This observation stimulated us to obtain the 24 bird samples from the Lund University Zoological Museum to measure them at the same place in the field (where the natural birds were encountered). It is worthwhile to mention that the weather conditions were sunny during the measurements. The illumination from sunlight can be easily quantified by analyzing the background intensities at the two fluorescence channels.

### 8. Analysis

#### A. Point Measurements

Reflectance spectra of nine particularly characteristic samples of special interest are presented on a logarithmic scale in Fig. 3. White, gray, and black varieties resulting from different eumelanin contents are observed with flat reflectance curves at different levels. Brownish, orange, and reddish pheomelanin-containing feathers bend and attenu-

ate reflectance toward the blue, as, for example, the orange chest of a whinchat (*Saxicola rubetra*). A yellow feather from a blue tit (*Parus caeruleus*) shows the characteristic double absorption dip of a carotenoid, while tail feathers with structurally generated blue shades from the same bird show a monotonic increase in reflectance toward the blue. In the 355 nm excited fluorescence in Fig. 4, white, gray, and black feathers maintain the same shape, but are scaled differently. For the brown, orange, and reddish pheomelanin feathers, the slope toward the red is different, indicating that the plumage is indeed redder even in fluorescence. In the case of the yellow carotenoid (lutein) feather, again, the double absorption dip can be observed, but this time in fluorescence quenching. The blue feather is harder to interpret in this measurement. The low values might indicate that even excitation light at 355 nm is reflected rather than absorbed and consequently reemitted as fluorescence.

The fluorescence measurements with 255 nm excitation were performed in a similar geometry as the previous measurements. These measurements are

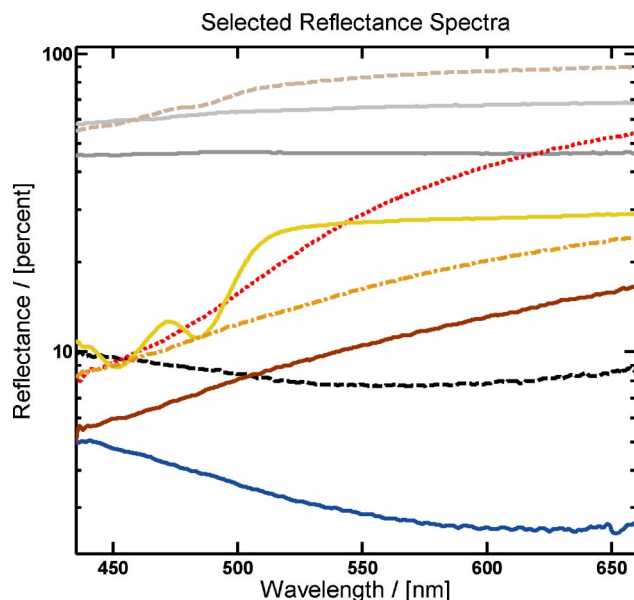


Fig. 3. (Color online) Reflectance spectra, curves colored according to appearance to humans. From top: light brown, reed warbler; white, white wagtail head; light gray, white wagtail chest; red, European robin; yellow, blue tit (note the sharp feature of the carotenoid lutein); orange, whinchat; brown, reed warbler; black, rook; and structural blue, blue tit.

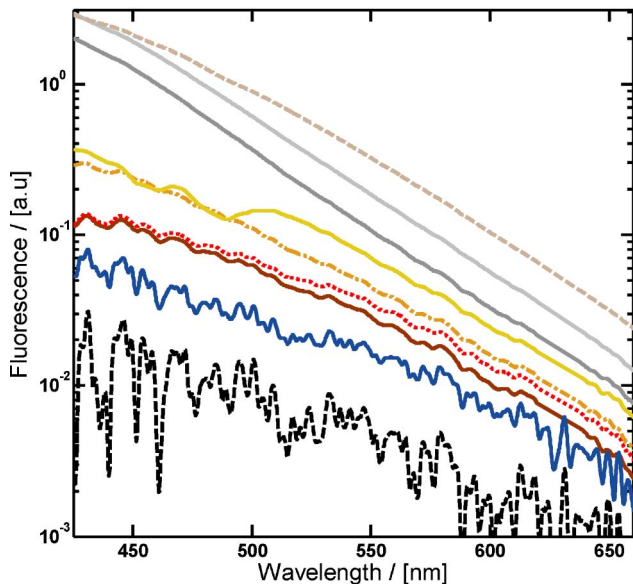


Fig. 4. (Color online) Fluorescence spectra excited at 355 nm, curves colored according to appearance to humans. From top: light brown, reed warbler; white, white wagtail head; light gray, white wagtail chest; yellow, blue tit; orange, whinchat; red, European robin; brown, great reed warbler; structural blue, blue tit; and black, rook.

presented on a logarithmic scale in Fig. 5. The curves are not white-light calibrated but can be compared in between. All the spectra have been normalized on the elastic light around 255 nm, even if we can expect the absolute reflectance to vary at 255 nm due to melanin variations. As in the previous measurement, white, gray, and black eumelanized plumages maintain the same shapes but they are scaled differently. Brown and reddish pheomelanized plumages are shifted to-

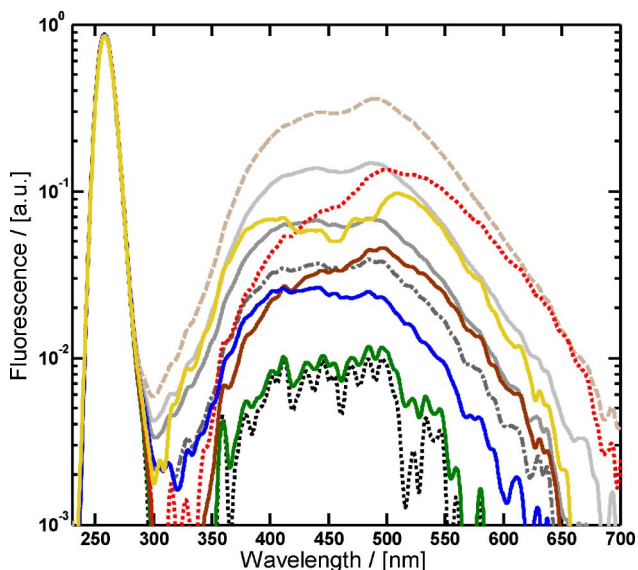


Fig. 5. (Color online) Fluorescence spectra excited at 255 nm, selected examples; curves colored according to appearance to humans. From top: light brown, reed warbler; white, white wagtail head; red, European robin; yellow, blue tit; light gray, white wagtail chest; brown, reed warbler; gray, white wagtail; structural blue, blue tit; black iridescent, European starling; and black, rook.

ward the red. The blue plumage is shifted toward the blue; thus, we conclude that even structural colors are positively correlated with the fluorescence, from which we understand that the interrogation volume of the fluorescence measurement is more superficial than the nanostructures causing the blue reflectance. The double absorption peak of the carotenoid is observed in the yellow feathers from the blue tit.

Even if we can expect somewhat lower sensitivity on the spectrometer at 255 nm, we notice that the fluorescence is considerable in comparison to the elastic light for the bright feathers. This is a major problem and might to some extent invalidate all elastic reflectance work performed with deuterium lamps in the avian and reptilian community, because using a broadband light source sums along the columns of the emission excitation matrix (EEM) (Fig. 6); thus, such reflectance measurements require the sample to have negligible fluorescence, which obviously might not always be the case.

The 14 spectra, out of which the more interesting ones were presented in Fig. 5, including varieties of eumelanized and pheomelanized plumages, a carotenoid, and a structural blue plumage, were analyzed using singular value decomposition (SVD) [69,70]. From the eigenvalues, we could read that 81% of the variance could be explained by the first principal component, 91% including the second, and 96% including the third one. The first component represents

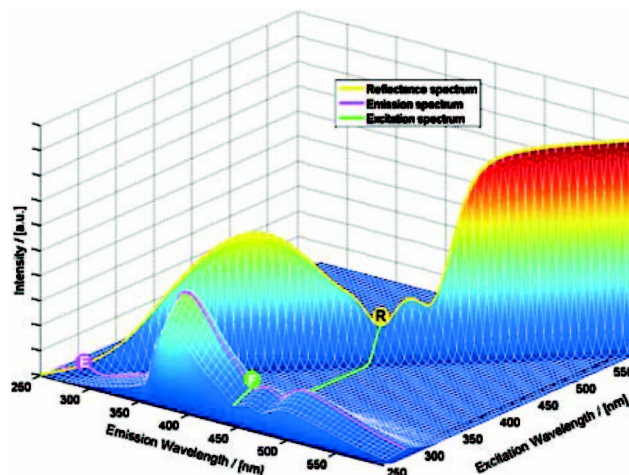


Fig. 6. Correlations in the EEM for a yellow-chested blue tit, with fluorescence exaggerated for demonstration purposes. The elastic diagonal (yellow curve, R) shows the reflectance of solid keratin with a carotenoid absorption dip. The fluorescence emission spectrum at 266 nm excitation (purple curve, E) shows the imprint of the absorbing carotenoid. Traditional methods for reflectance in ornithology sum all excitation elements (green curve, F) and assume fluorescence to be negligible. In ornithological LIF lidar, we can expect a fluorescence element  $F(\lambda_{ex}, \lambda_{em})$  to be negatively correlated with the reflectance  $E(\lambda_{ex})$ ; this explains why the structural blue plumage with high UV reflectance appears dark in fluorescence in Figs. 4 and 5. This is known as excitation quenching. In contrast,  $F(\lambda_{ex}, \lambda_{em})$  can be expected to be positively correlated with the reflectance  $R(\lambda_{em})$  due to emission quenching; this explains why red reflecting plumage appear even redder in fluorescence. Data extracted and remodeled from [37], Chap. 5, pp. 40, 49.

total keratin fluorescence and describes eumelanized plumages; the second component represents a redshift of the fluorescence and manages to describe pheomelanized plumages and also the blue structural color with negative loadings. This can be understood when comparing the dark brown and blue reflectance spectra in Fig. 3. The relatively sharp features caused by the carotenoid can only be accounted for when including a third principal component. Estimating the number of independent spectral components and localizing them in the spectral domain is crucial for designing spectral bands of a system for remote discrimination. According to this analysis, the optimal band choice for discriminating eumelanized, pheomelanized, and blue structural plumages is B1, 370–485, and B2, 485–600 nm. Including the carotenoid, the band choices should rather be B1, 370–420; B2, 420–500; and B3, 500–600 nm. In addition, a polarized or depolarized elastic band at 266 nm, B0, for estimating the beam–bird overlap on lidar hits is valuable; in this case, the different atmospheric attenuation of the returning elastic light should be considered, and the elastic returned energy would correlate with the amount of total energy deposited in the plumage. By dividing the returned energies in the remaining bands with this estimate, the scenario-dependent variance could be reduced. Because the specular reflectance might be highly dependent on the surface orientation, using depolarized elastic scattering could further contribute to confinement in the color space.

When normalizing with the elastic band and projecting the spectra on total fluorescence (first principal component from the SVD analysis) and redshift base spectra (second principal component from the above SVD analysis), the two-dimensional (2D) scatterplot presented in Fig. 7 is obtained. Plumage with different reflective characteristics can easily be separated, even in fluorescence. Clusters from plumage with similar reflective characteristics are more likely

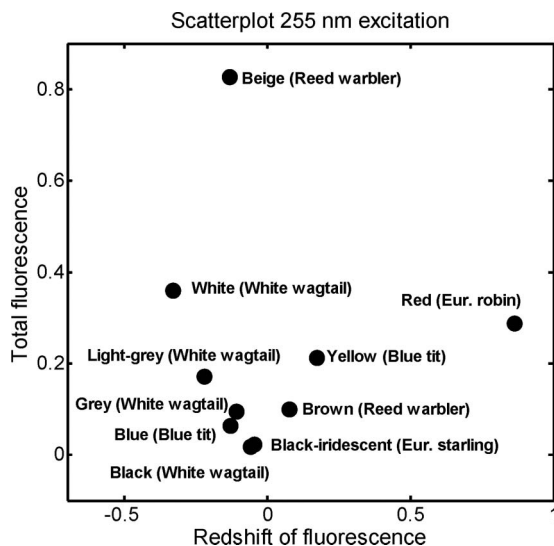


Fig. 7. Scatterplot of first and second principal components from Fig. 5.

to overlap in the scatterplot. The overlap in these scatterplots will eventually determine the success of remote classification. Obviously, overlaps are less likely in color spaces of higher dimensionality, but such scatterplots tend to be difficult to present on flat paper. Also, no improvement in discrimination can be expected by adding more spectral bands than the number of significant chromophores with independent spectral components involved. In Fig. 7, we notice the great spatial variance of measurements from different regions on the same sample, in a complete hit lidar situation, the acquired fluorescent signature is spatially averaged over the entire body; thus a gray bird might give identical echo as a black- and white-spotted bird; see for, example the different body parts of the white wagtail (*Motacilla alba*).

From the time-resolved data not presented in this paper, we could indeed conclude that the lifetime decays hold no information regarding the embedded chromophores, confirming our understanding of the quenching processes. Two spectral components were found in the decay; the lifetime at 390 nm was approximately 1.0 ns, whereas the lifetime was 1.6 ns at 580 nm.

To conclude this section, we propose the relation between plumage reflectance and fluorescence:

$$\frac{R_{\text{sample}}(\lambda)}{R_{\text{white}}(\lambda)} = (1 - \text{exq}(\lambda_{\text{ex}})) \frac{F_{\text{sample}}(\lambda_{\text{em}})}{F_{\text{white}}(\lambda_{\text{em}})}, \quad (1)$$

where  $R_{\text{sample}}(\lambda)$  is the diffuse reflectance,  $R_{\text{white}}(\lambda)$  is the diffuse reflectance of white plumage,  $F_{\text{sample}}(\lambda_{\text{em}})$  is the fluorescence spectrum,  $F_{\text{white}}(\lambda_{\text{em}})$  is the fluorescence of white plumage, and  $\text{exq}(\lambda_{\text{ex}})$  is the probability of embedded chromophores quenching the excitation.

Empiric results not presented in this paper show that  $\text{exq}$  is of the order of 20% at 355 nm excitation and that  $\text{exq}$  diminishes as the excitation wavelength decreases; thus, the lower the excitation wavelength, the more superficial the absorption field [shorter  $d$  in Fig. 1(b)] and the more resemblance to reflectance. A number of refinements can be done to the model—these include a bias taking into account the missing first specular reflection in the fluorescence ratio since the light is internally generated; however, this effect is compromised by the fact that the fluorescence is created omnidirectionally, whereas the superficial light in the elastic measurement would still remember its initial propagation in the very superficial layers. It is reasonable to presume dull dependency of the refractive index and dull exponential spectral effect due to differences in migrated path lengths; however, most such refinements of the models and estimation of additional parameters are numerically ill-conditioned with the dull features of the melanins.

## B. Remote Lidar Measurements

To explore the feasibility of using lidar to locate and distinguish between bird species, measurements

were done in the field, both on birds in flight and on museum specimens. The investigations were done with 266 and 355 nm excitation.

Figure 8 shows an example of a lidar return signal from a starling in flight obtained at a distance of  $\sim 100$  m. The signal is time/distance resolved in one elastic, E, reflectance channel at 355 nm, one fluorescence channel ranging from 400 to 500 nm, denoted blue fluorescence, B in figures, and one channel ranging from 500 to 750 nm and denoted yellow fluorescence, Y in figures. Further, a linear polarizer on the elastic channel allows either polarized or depolarized light to be detected. The reflection from the weather protecting quartz window in the dome [see Fig. 2(b)] is clearly seen in the elastic channel, while almost no fluorescence is observed. This observation shows that the leakage/filter fluorescence between the elastic and the fluorescence channels is small and any signal in the latter channels will indeed be fluorescence. At a distance of  $\sim 100$  m, all three channels show strong signals from a bird, demonstrating a broad fluorescence emission in both the blue and the yellow wavelength range. Direct intermediate comparison between the signals in the different channels is, however, not meaningful because of arbitrary gain settings. Shortly after 110 m, the reflection from a nonfluorescent metal fence wire is seen. Again, only the elastic channel is giving an output.

The possibility of distinguishing between different species with lidar was further investigated by recording the return signal in a similar way as for the starlings *in vivo*, but for the same museum birds that were investigated with laboratory point measurements. The birds were each put in and out of the lidar beam pathway in a fluctuating manner to simulate birds passing through the field of view of our system.

Since the lidar return is discretized in three spectral bands, we are able to overview the entire data set with a red-green-blue (RGB) representation. Figure 9 shows a RGB color image of all data acquired in a small time period, during which a museum bird was moved in and out of the beam several times. Elastic

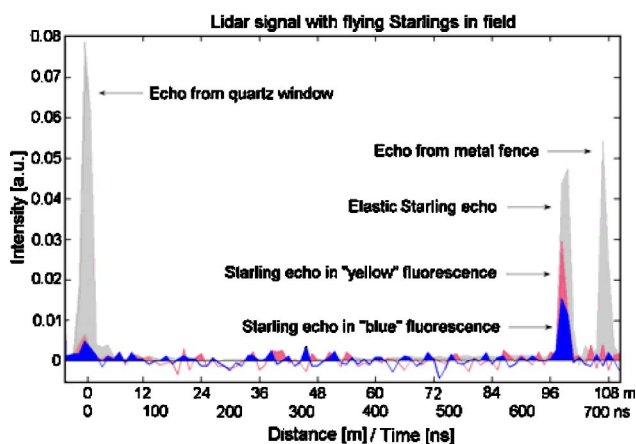


Fig. 8. (Color online) Single-shot echo from starling in flight. Elastic echoes arise from quartz window and metal fence. The relative areas under the European starling echo can be used for classification purpose.

signals at 355 nm are shown in blue, fluorescence between 400 and 500 nm in green, and fluorescence between 500 and 750 nm in red. The first blue line is the stationary elastic signal from the quartz window. As the bird is moved into the beam, all channels show increased return signals at the corresponding distance marked in the figure. Consequently, both the elastic signal from the folding mirror and the return signals from all channels at the position of the termination go down, since the incident energy was reduced from the earlier impact. These observations are presented more quantitatively in Fig. 10, where the echo energy (fast-time integral of intensity return), being a measure on the total recorded signal from the bird, the termination point, and the background light level (refer to regions in Fig. 9.) for each laser pulse, is exposed as a function of time.

It is essential to have a measure of how much light was illuminating the bird, i.e., the bird-beam overlap, to be able to quantize the fluorescence strength, not least when considering species classification. The bird-beam overlap has to be found for each laser pulse producing the fluorescent return. One approach is to normalize the fluorescence with the elastic signal, as in Fig. 5; however, the elastic reflectance, including the specular reflectance, might be highly dependent on the surface orientation of the plumage. Another approach to estimate the bird-beam overlap is to estimate the energy drop from later returns. In Figs. 9 and 10 middle, we observe how the obstruction of the bird is decreasing the signal from any light that is reflected or generated behind the bird. The amount to which these signals are affected is a measure of the overlap between the beam and the bird. The termination point in the case of vertical measurements could, for example, be a cloud base. Another similar possibility is to observe the decrease of the total backscattered atmospheric signal from air and aerosols behind the bird. Both these are examples of active techniques to quantify the

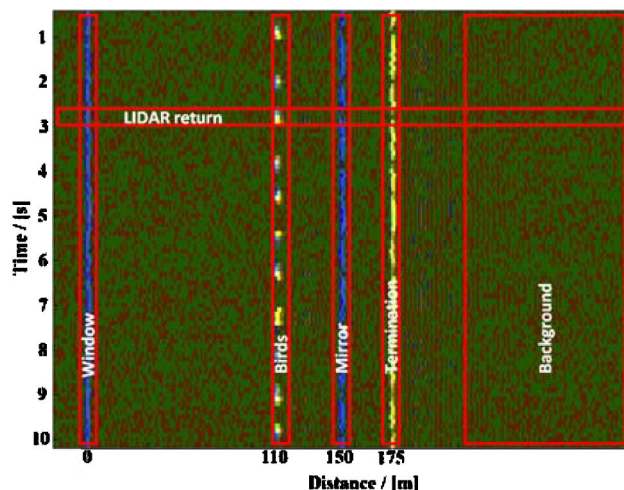


Fig. 9. (Color online) False color RGB representation or T-scan of complete lidar data acquired during 10 s. Blue, elastic; green, blue fluorescence; red, yellow fluorescence. Regions of interest are marked.

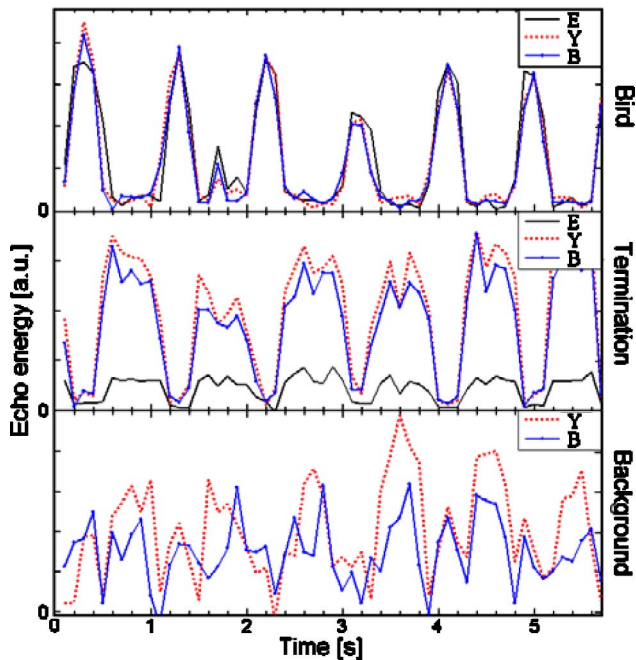


Fig. 10. (Color online) Intensity of the three cross sections marked in Fig. 9 plotted versus time. Notice the interplay, which allows estimating bird–beam overlap and also simultaneous determination of active fluorescence and passive reflectance.

bird–beam overlap. We also observe that the background light level after pulse termination is affected by the presence of a bird in the field of view; this can be explained by the amount of sunlight reflected in the plumage and into the telescope during the 1 ms the recording is done. This suggests that, not only do we acquire blue and yellow laser-induced fluorescence, but even blue and yellow passive reflectance simultaneously. In the case of the black European starling in Fig. 10, we observe an anticorrelation, meaning that the starling plumage is darker than our termination point. This could even be accomplished in vertical soundings with a cloud layer termination or the blue sky.

In earlier studies [33], as well as in this study, we have noticed one particular characteristic of zoological lidar; while clouds and dust plumes appear as distributed backscatters with a relatively slow time dependency matching the wind speeds, insects and birds in nature appear as sudden blips, giving rise to a much larger echo confined in spatial range as well as in temporal occurrence. The range confinement matches the lifetime of the matrix, typically around 1 ns if resolved by the system. The temporal confinement matches the overlap of the flight trajectory and the point spread function of the system. With our system we typically observed temporal occurrence in the order of a fifth of a second. This very unique feature simplifies separating the species echo from a quasi static background such as moving clouds.

The normalized fluorescence from the *in vivo* starlings and the museum samples were analyzed to explore the feasibility of remote species classification. The echo energy for the time/range resolved

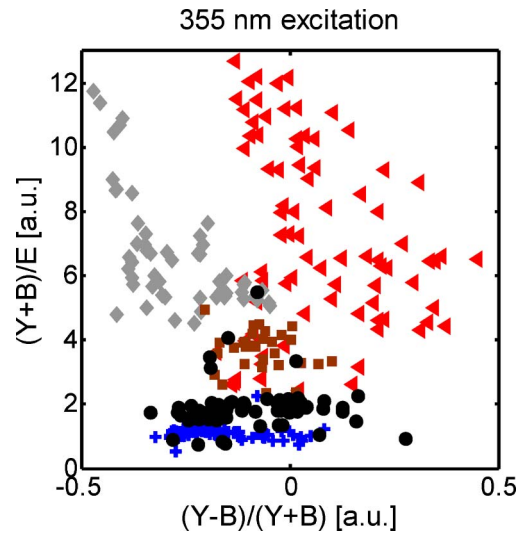


Fig. 11. (Color online) Scatterplot showing selected species with 355 nm excitation; total normalized fluorescence on the Y axis and redshift on the X axis. Dots are colored according to the human visual perception. From upper left: brown, reed warbler; red, European robin; black, European starling; black, rook; and blue, blue tit.

return signals were analyzed and intercompared. Figures 11 and 12 show the results of two such comparisons. Figure 11 is a 2D scatterplot obtained from measurements done in the field with 355 nm illumination. Each point in the plot corresponds to the reflection and fluorescence from a single laser pulse. As in Fig. 7, the vertical axis shows total fluorescence, while the horizontal axis represents the redshift. The five birds represented in the figure are a European robin (*Erithacus rubecula*), a blue tit, a reed warbler (*Acrocephalus scirpaceus*), a European starling (*Sturnus vulgaris*), and a jackdaw (*Corvus monedula*).

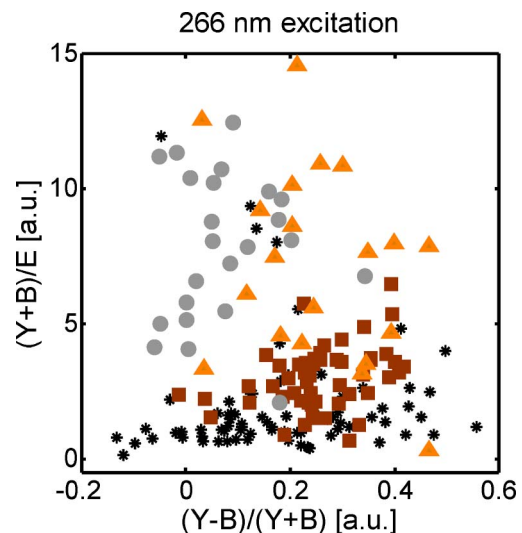


Fig. 12. (Color online) Scatterplot showing selected species with 266 nm excitation; total fluorescence on the Y axis and redshift on the X axis. Dots are colored according to the human visual perception. From upper left: gray, European blackcap; beige, reed warbler; black, European starling; and black, rook.

The scatterplot in Fig. 11 shows promising results, indicating that it, in fact, is possible to separate different species of birds with the help of a multichannel fluorescence lidar. The five different species of birds tend to gather at different positions in the plot, illustrating the variation in fluorescence between them. The European robin, which has a clear red belly, tends to go to the right side of the plot and also shows a relatively strong fluorescence compared to the other birds. Another species that fluoresce much is the reed warbler, which, on the other hand, has a hue more shifted toward the blue. In the center of the plot, the points from the somewhat darker starling gather with less strong fluorescence. The fluorescence color is as expected between the red robin and the more grayish great reed warbler. The jackdaw also shows a low fluorescence, which goes well with the fact that it is dark gray and black. It can also be observed that the blue tit shows a very low ratio between fluorescence and elastic reflection. The reason for this, as is revealed by the point fluorescence measurements in Fig. 4, is that the fluorescence is indeed very low for the bird at this wavelength. Because the reflectance for the blue feathers is high, the denominator in the  $y$  axis becomes large, while, at the same time, there is little light left to generate fluorescence.

Figure 12 is a similar scatterplot obtained from rooftop measurements at the test range in Lund [33] with 266 nm excitation. The four birds presented are a great reed warbler (*Acrocephalus arundinaceus*), a European black cap (*Sylvia atricapilla*), a European starling, and a rook (*Corvus frugilegus*).

The measurements done with 266 nm excitation were performed with a much lower output power from the laser than the ones with 355 nm excitation. This fact and other ones made the signals weaker, and the resulting scatterplot is not as clear as the one for 355 nm excitation. Still, some separation can be distinguished in the backscattering and fluorescence. As an example, the black rook shows low fluorescence, the relatively dark starling somewhat more, while the generally brighter European black cap and great reed warbler fluoresce more. One might discern that the European black cap is more shifted to the blue than the great reed warbler.

## 9. Discussion, Conclusions, and Perspectives

We have demonstrated eye-safe remote measurements of chromophore concentration and structural colors in plumages on distances of 100 m. From earlier experiences with elastic DIAL lidar on atomic mercury, at 254 nm, and the equally well-suited wavelengths of 308 and 313 nm for ozone monitoring [71,72], we know that returns from a solid target could be acquired from a single shot in a couple of kilometers. For several shots averaged, even the upper biosphere at 10 km is accessible [73]. In fluorescence lidar, which is an inelastic spectroscopic method, the UV light is only attenuated by the atmosphere one way, in contrast to elastic methods. We have explained the mechanisms relating the reflectance to the fluorescence of plumages.

We cannot expect to classify species with the same or similar plumage reflectance, nor would we be able to classify birds with the same or similar spatial average reflectance, e.g., a gray pigeon and a black-and-white wagtail, in a single shot. At the 266 nm experiments, our laser system was not running optimally and our output power was further limited by the damage threshold of the general purpose scanning mirror, which does not reflect optimally at 266 nm. In vertical sounding, we would avoid this issue and the cross section of an in-flight bird in vertical sounding would obviously be larger. The other main limitation of our method is that plenty of continuous background light is binned by the broad fluorescence channels. For this reason, we can expect the method to perform much better at night. We have demonstrated that a refined analysis of the background signal carries information on the passive Sun-induced reflectance or transmittance (depending on the geometry). For this reason, it might be of interest to track the Moon with the lidar during the night, compromising background levels for simultaneous passive transmission spectroscopy.

In terms of improved bird classification, not much information would be gained by more than four spectral bands. However, we suspect that large improvements could be achieved by fusing fluorescence lidar with radar or thermal-imaging methods. While excellent in acquiring chemical information, the big disadvantage of this type of stochastic lidar, in comparison to, e.g., DIAL lidar, is the fact that we do not get a measurement for certain in each shot. Thermal-IR imaging seems incapable of acquiring properties of the chromophores; on the other hand, it can easily acquire an entire night sky in real time. If a dedicated system was to be developed, the thermal image could be used for lidar tracking, providing complete sky coverage and several shots for each migrating bird. Of special interest is the fact that indexing the fluorescence return in the phase of the wing-beat cycle should provide clues on the spatial variation on the bird. Such a system would probably take a couple of years to develop, even if an existing commercial lidar solution could be suitable [74,75]. Eventually, ornithological preknowledge of the limited number of expected migrant species would help in the classification process.

From an ornithological point of view, several experiments of interest could be performed. These would include nighttime classification, and high-altitude classification at migration points for purposes of counting and migration statistics. Typical migration points in Scandinavia would be geographic northward-pointing tips in the spring, such as Skagen, Kullaberg, and Andøya, and southward pointing confinements in the autumn, e.g., Falsterbo and Ottenby at the southern point of the island of Öland in the Baltic Sea. At locations of capture sites at bird observatories, such as Anacapri, Italy, comparisons can be made to the species of migrants

captured during different parts of the migration seasons. Observations could be related to morphological traits and weather conditions for more profound physiological studies. Other experiments could consist of marking without recapturing studies. This would be achieved by attaching fluorescing material, e.g., nylon strings or rings to the captured species. The string could be fluorescence encoded with effective fluorophore mixtures that clearly separate in clusters in the color spaces. The markings could consist of gender, age, or breeding habitat, which would be registered at the position of the lidar. We see several new applications of lidar to nocturnal bird migration studies and observations of free-flying birds, and we intend to perform further tests in real field situations in the near future.

We acknowledge the Knut and Alice Wallenberg Foundation for their support throughout the development of lidar techniques in Lund. *Ex vivo* specimens were borrowed with the kind collaboration by the Zoological Museum, Lund. We thank the Chris Dunsby group, Photonics, at the Department of Physics, Imperial College London, for time-resolved fluorescence measurements. Thanks to Matthew D. Shawkey for kind permission to reproduce a TEM micrograph in Fig. 1(b). We acknowledge Kullabergsfonden for future support of field campaigns. This is a report from Lund Laser Centre (LLC) and the Centre for Animal Movement Research (CANMove) supported by Linnaeus grants from the Swedish Research Council and Lund University.

## References

1. I. Newton, *The Migration Ecology of Birds* (Academic, 2008).
2. T. Alerstam and Å. Lindström, "Optimal bird migration: the relative importance of time, energy and safety," in *Bird Migration: Physiology and Ecophysiology*, E. Gewinner, ed. (Springer-Verlag, 1990), pp. 331–351.
3. T. Alerstam, A. Hedenström, and S. Åkesson, "Long-distance migration: evolution and determinants," *Oikos* **103**, 247–260 (2003).
4. B. Bruderer and F. Liechti, "Höhe und Richtung von Tag- und Nachtzug im Herbst über Südwestdeutschland," *Ornitol. Beob.* **95**, 113–128 (1998).
5. S. Zehnder, S. Åkesson, F. Liechti, and B. Bruderer, "Nocturnal autumn bird migration at Falsterbo, South Sweden," *J. Avian Biol.* **32**, 239–248 (2001).
6. P. Kerlinger and F. R. Moore, "Atmospheric structure and avian migration," in *Current Ornithology*, D. M. Power, ed. (Plenum, 1989), Vol. 6, pp. 109–141.
7. Å. Lindström, "The role of predation risk in stopover habitat selection in migrating bramblings, *Fringilla montifringilla*," *Behav. Ecol.* **1**, 102–106 (1990).
8. S. Åkesson and A. Hedenström, "How migrants get there: migratory performance and orientation," *BioScience* **57**, 123–133 (2007).
9. M. B. Casement, "Migration across the Mediterranean observed by radar," *Ibis* **108**, 461–491 (1966).
10. J. L. F. Parslow, "The migration of passerine night migrants across the English channel studied by radar," *Ibis* **111**, 48–79 (1969).
11. D. H. W. Adams, "Radar observations of bird migration in Cyprus," *Ibis* **104**, 133–146 (1962).
12. T. Alerstam, "Nocturnal migration of Thrushes *Turdus*-Spp in Southern Sweden," *Oikos* **27**, 457–475 (1976).
13. B. Bruderer and F. Liechti, "Quantification of bird migration—different means compared," in *Proceedings of the Bird Strike Committee, Europe* (1994), Vol. 22, pp. 243–254.
14. T. Alerstam, J. Bäckman, G. A. Gudmundsson, A. Hedenström, S. S. Henningsson, H. Karlsson, M. Rosén, and R. Strandberg, "A polar system of intercontinental bird migration," *Proc. R. Soc. London Ser. B* **274**, 2523–2530 (2007).
15. S. A. Gauthreaux, Jr., "A portable ceilometer technique for studying low level nocturnal migration," *Bird Banding* **40**, 309–320 (1969).
16. S. Åkesson, "Coastal migration and wind drift compensation in nocturnal passerine migrants," *Ornis Scand.* **24**, 87–94 (1993).
17. S. Zehnder, S. Åkesson, F. Liechti, and B. Bruderer, "Seasonal and diurnal patterns of nocturnal bird migration at Falsterbo, South Sweden," *J. Avian Biol.* **32**, 239–248 (2001).
18. F. Liechti, D. Peter, R. Lardelli, and B. Bruderer, "Herbstlicher Vogelzug im Alpenraum nach Mond-Beobachtungen—Topographie und Wind beeinflussen den Zugverlauf," *Ornitol. Beob.* **93**, 131–152 (1996).
19. F. Liechti, "Calibrating the moon-watching method—changes and limits," *Avian Ecol. Beh.* **7**, 27–41 (2001).
20. F. Liechti, D. Peter, R. Lardelli, and B. Bruderer, "The Alps, an obstacle for nocturnal broad front migration—a survey based on moon-watching," *J. Ornithol.* **137**, 337–356 (1996).
21. P. H. Zehndijev and F. Liechti, "A quantitative estimate of the spatial and temporal distribution of nocturnal bird migration in south-eastern Europe—a coordinated moon-watching study," *Avian Sci.* **3**, 37–45 (2003).
22. B. Bruderer and E. Weitnauer, "Radar observations of the migration and night flights of the swift *Apus-Apus*," *Rev. Suisse Zool.* **79**, 1190–1200 (1972).
23. J. Bäckman and T. Alerstam, "Confronting the winds: Orientation and flight behaviour of roosting swifts, *Apus apus*," *Proc. R. Soc. London Ser. B* **268**, 1081–1087 (2001).
24. T. Alerstam, M. Rosén, J. Bäckman, P. G. P. Ericson, and O. Hellgren, "Flight speeds among bird species: allometric and phylogenetic effects," *PLoS Biol.* **5**, e197 (2007).
25. F. Liechti, B. Bruderer, and H. Papproth, "Quantification of nocturnal bird migration by moonwatching: comparison with radar and infrared observations," *J. Field Ornithol.* **66**, 457–468 (1995).
26. C. J. Pennycuik, "Soaring behavior and performance of some East African birds observed from a motor glider," *Ibis* **114**, 178–218 (1972).
27. S. Svanberg, "Fluorescence spectroscopy and imaging of LIDAR targets," in *Laser Remote Sensing*, T. Fujii and T. Fukuchi, eds. (CRC Press, 2005).
28. S. Svanberg, "LIDAR," in *Springer Handbook of Lasers and Optics* F. Träger, ed. (Springer, 2007), pp. 1031–1052.
29. S. Svanberg, "Laser fluorescence spectroscopy in environmental monitoring," in *Optoelectronics for Environmental Science*, S. Martellucci and A. N. Chester, eds. (Plenum, 1990).
30. K. S. Repasky, J. A. Shaw, R. Scheppele, C. Melton, J. L. Carsten, and L. H. Spangler, "Optical detection of honeybees by use of wing-beat modulation of scattered laser light for locating explosives and land mines," *Appl. Opt.* **45**, 1839–1843 (2006).
31. D. S. Hoffman, A. R. Nehrir, K. S. Repasky, J. A. Shaw, and J. L. Carsten, "Range-resolved optical detection of honeybees by use of wing-beat modulation of scattered light for locating land mines," *Appl. Opt.* **46**, 3007–3012 (2007).
32. M. Brydegaard, Z. G. Guan, M. Wellenreuther, and S. Svanberg, "Insect monitoring with fluorescence lidar techniques: feasibility study," *Appl. Opt.* **48**, 5668–5677 (2009).
33. Z. G. Guan, M. Brydegaard, P. Lundin, M. Wellenreuther, A. Runemark, E. Svensson, S. Åkesson, and S. Svanberg,

- “Fluorescence lidar for studies of movements of insects and birds,” in *Proceedings of the 25th International Laser Radar Conference ILRC25* (2010).
34. H. Dingle, *Migration: The Biology of Life on the Move* (Oxford U. Press, 1996).
  35. S. Jaques and B. Pogue, “Tutorial on diffuse light transport,” *J. Biomed. Opt.* **13**, 041302 (2008).
  36. V. Tuchin, “Tissue optics,” in *Light Scattering and Instruments for Medical Diagnosis*, 2nd ed. (SPIE Press, 2007).
  37. G. E. Hill and K. J. McGraw, eds., *Bird Coloration Volume 1: Mechanisms and Measurements* (Harvard U. Press, 2006).
  38. G. E. Hill and K. J. McGraw, eds., *Bird Coloration Volume 2: Function and Evolution* (Harvard U. Press, 2006).
  39. L. Pauling and R. B. Corey, “The structure of feather rachis keratin,” *Proc. Natl. Acad. Sci. USA* **37**, 256–261 (1951).
  40. D. J. Brink and N. G. van der Berg, “Structural colours from the feathers of the bird *Bostrychia hagedash*,” *J. Phys. D* **37**, 813–818 (2004).
  41. E. G. Bendit and D. Ross, “A technique for obtaining the ultraviolet absorption spectrum of solid keratin,” *Appl. Spectrosc.* **15**, 103–105 (1961).
  42. D. Osorio and M. Vorobyev, “A review of the evolution of animal colour vision and visual communication signals,” *Vision Res.* **48**, 2042–2051 (2008).
  43. A. T. Bennett and M. Thery, “Avian color vision and coloration: multidisciplinary evolutionary biology,” *Am. Nat.* **169**, S1–S6 (2007).
  44. J. Reneerkens and P. Korsten, “Plumage reflectance is not affected by preen wax composition in red knots *Calidris canutus*,” *J. Avian Biol.* **35**, 405–409 (2004).
  45. S. M. Doucet and G. E. Hill, “Do museum specimens accurately represent wild birds? A case study of carotenoid, melanin, and structural colours in long-tailed manakins *Chiroxiphia linearis*,” *J. Avian Biol.* **40**, 146–156 (2009).
  46. D. Osorio and A. Ham, “Spectral reflectance and directional properties of structural coloration in bird plumage,” *J. Exp. Biol.* **205**, 2017–2027 (2002).
  47. R. O. Prum, E. R. Dufresne, T. Quinn, and K. Waters, “Development of colour-producing beta-keratin nanostructures in avian feather barbs,” *J. R. Soc. Interface* **6**, S253–S265 (2009).
  48. E. Warrant and D. E. Nilsson, eds. *Invertebrate Vision* (Cambridge U. Press, 2006).
  49. J. F. Jacobs, G. J. M. Koper, and W. N. J. Ursem, “UV protective coatings: a botanical approach,” *Prog. Org. Coatings* **58**, 166–171 (2007).
  50. A. M. Pena, M. Strupler, T. Boulesteix, and M. C. Schanne-Klein, “Spectroscopic analysis of keratin endogenous signal for skin multiphoton microscopy,” *Opt. Express* **13**, 6268–6274 (2005).
  51. A. Ounis, Z. G. Cerovic, J. M. Briantais, and I. Moya, “DE-FLIDAR: a new remote sensing instrument for estimation of epidermal UV absorption in leaves and canopies,” in *Proceedings of European Association of Remote Sensing Laboratories (EARSeL)-SIG-Workshop LIDAR* (EARSeL, 2000), Vol. 1, pp. 196–204.
  52. G. B. Altshuler, K. Ilyasovand, C. V. Prikhodko, “Optical properties of human hair,” *Tech. Phys. Lett.* **21**, 216–218 (1995).
  53. S. Jacques, “Origins of tissue optical properties in the UVA, visible and NIR regions,” in *TOPS on Advances in Optical Imaging and Photon Migration II* (Optical Society of America, 1996), pp. 364–367.
  54. A. Ehlers, I. Riemann, M. Stark, and K. König, “Multiphoton fluorescence lifetime imaging of human hair,” *Microsc. Res. Tech.* **70**, 154–161 (2007).
  55. J. K. Armenta, P. O. Dunn, and L. A. Whittingham, “Quantifying avian sexual dichromatism: a comparison of methods,” *J. Exp. Biol.* **211**, 2423–2430 (2008).
  56. J. Ornborg, S. Andersson, S. C. Griffith, and B. C. Sheldon, “Seasonal changes in a ultraviolet structural colour signal in blue tits, *Parus caeruleus*,” *Biol. J. Linn. Soc.* **76**, 237–245 (2002).
  57. K. J. McGraw and G. E. Hill, “Plumage color as a dynamic trait: carotenoid pigmentation of male house finches (*Carpodacus mexicanus*) fades during the breeding season,” *Can. J. Zool.* **82**, 734–738 (2004).
  58. K. Delhey, A. Peters, A. Johnsen, and B. Kempenaers, “Seasonal changes in blue tit crown color: do they signal individual quality?,” *Behav. Ecol.* **17**, 790–798 (2006).
  59. E. J. Willoughby, M. Murphy, and H. L. Gorton, “Molt, plumage abrasion, and color change in Lawrence’s Goldfinch,” *Wilson Bull.* **114**, 380–392 (2002).
  60. A. Peters, K. Delhey, S. Andersson, H. van Noordwijk, and M. I. Foerschler, “Condition-dependence of multiple carotenoid-based plumage traits: an experimental study,” *Funct. Ecol.* **22**, 831–839 (2008).
  61. G. Pohland and P. Mullen, “Preservation agents influence UV-coloration of plumage in museum bird skins,” *J. Ornithol.* **147**, 464–467 (2006).
  62. X. Wan, J. Fan, and H. Wu, “Measurement of thermal radiative properties of penguin down and other fibrous materials using FTIR,” *Polym. Test.* **28**, 673–679 (2009).
  63. C. J. Dove, A. M. Rijke, X. Wang, and L. S. Andrews, “Infrared analysis of contour feathers—the conservation of body heat radiation in birds,” *J. Therm. Biol.* **32**, 42–46 (2007).
  64. S. C. V. Raman, “The theory of the Christiansen experiment,” *Proc. Indian Acad. Sci.* **A29**, 381–390 (1949).
  65. G. P. Kulemin, *Millimeter Wave Radar Targets and Clutter* (Artech House, 2003).
  66. I. C. Cuthill, J. C. Partridge, A. T. D. Bennett, S. C. Church, N. S. Hart, and S. Hunt, “Ultraviolet vision in birds,” *Adv. Study Behav.* **29**, 159–214 (2000).
  67. P. A. A. de Beule, C. Dunsby, N. P. Galletly, G. W. Stamp, A. C. Chu, U. Anand, P. Anand, C. D. Benham, A. Naylor, and P. M. W. French, “A hyperspectral fluorescence lifetime probe for skin cancer diagnosis,” *Rev. Sci. Instrum.* **78**, 123101 (2007).
  68. P. Weibring, H. Edner, and S. Svanberg, “Versatile mobile lidar system for environmental monitoring,” *Appl. Opt.* **42**, 3583–3594 (2003).
  69. P. Weibring, T. Johansson, H. Edner, S. Svanberg, B. Sundnér, V. Raimondi, G. Cecchi, and L. Pantani, “Fluorescence lidar imaging of historical monuments,” *Appl. Opt.* **40**, 6111–6120 (2001).
  70. P. Weibring, T. Johansson, H. Edner, S. Svanberg, B. Sundnér, V. Raimondi, G. Cecchi, and L. Pantani, “Fluorescence lidar imaging of historical monuments: erratum,” *Appl. Opt.* **41**, 434–436 (2002).
  71. E. Wallinder, H. Edner, P. Ragnarson, and S. Svanberg, “Vertically sounding ozone LIDAR system based on a KrF excimer laser,” *Phys. Scr.* **55**, 714–718 (1997).
  72. H. Edner, P. Ragnarson, S. Svanberg, E. Wallinder, R. Ferrara, B. E. Maserti, and R. Bargagli, “Atmospheric mercury mapping in a cinnabar mining area,” *Sci. Total Environ.* **133**, 1–15 (1993).
  73. U. P. Hoppe, G. H. Hansen, and W. Eriksen, “ALOMAR—Ground-based monitoring of stratospheric ozone and related atmospheric parameters,” in *27th International Symposium on Remote Sensing of Environment* (1998), pp. 244–247.
  74. Kipp & Zonen, Delft, the Netherlands (2010), [www.kippzonen.com](http://www.kippzonen.com).
  75. Alternatively Optech Inc., Kiln, Miss., USA (2010), [www.optech.com](http://www.optech.com).
  76. M. D. Shawkey, M. E. Hauber, L. K. Estep, and G. E. Hill, “Evolutionary transitions and mechanisms,” *J. R. Soc. Interface* **3**, 777–786 (2006).

## PAPER XIV

### **Remote nocturnal bird classification by spectroscopy in extended wavelength ranges**

P. Lundin, P. Samuelsson, S. Svanberg, A. Runemark,  
S. Åkesson and M. Brydegaard  
*Applied Optics*, **50**, 3396-3411, 2011.

# Remote nocturnal bird classification by spectroscopy in extended wavelength ranges

Patrik Lundin,<sup>1,\*</sup> Per Samuelsson,<sup>1</sup> Sune Svanberg,<sup>1</sup> Anna Runemark,<sup>2</sup> Susanne Åkesson,<sup>2</sup> and Mikkel Brydegaard<sup>1</sup>

<sup>1</sup>Atomic Physics Division, Lund University, P.O. Box 118, SE-221 00 Lund, Sweden

<sup>2</sup>Animal Ecology Division, Lund University, Sölvegatan 37, SE-223 62 Lund, Sweden

\*Corresponding author: patrik.lundin@fysik.lth.se

Received 4 January 2011; revised 13 May 2011; accepted 18 May 2011;  
posted 23 May 2011 (Doc. ID 140381); published 1 July 2011

We present optical methods at a wide range of wavelengths for remote classification of birds. The proposed methods include eye-safe fluorescence and depolarization lidar techniques, passive scattering spectroscopy, and infrared (IR) spectroscopy. In this paper we refine our previously presented method of remotely classifying birds with the help of laser-induced  $\beta$ -keratin fluorescence. Phenomena of excitation quenching are studied in the laboratory and are theoretically discussed in detail. It is shown how the ordered microstructures in bird feathers induce structural “colors” in the IR region with wavelengths of around 3–6  $\mu\text{m}$ . We show that transmittance in this region depends on the angle of incidence of the transmitted light in a species-specific way and that the transmittance exhibits a close correlation to the spatial periodicity in the arrangement of the feather barbules. We present a method by which the microstructure of feathers can be monitored in a remote fashion by utilization of thermal radiation and the wing beating of the bird. © 2011 Optical Society of America

*OCIS codes:* 170.1420, 280.3640, 300.2530, 300.6340, 280.4991.

## 1. Introduction

Migratory birds, which are highly adapted to manage long flights, cross seas and deserts on their long-distance migrations [1–3]. A great majority of songbirds, although most birds are diurnal, migrate at night [4,5]. During the night they will meet less turbulent wind conditions [6], lower predation rates [7], and they have the possibility to use the daytime for foraging [1,2]. A large proportion of migration also occurs at high altitudes (>500 m) [4]. Because our own perception and classification of birds is based primarily on visual information, studies of nocturnal bird migration are challenging.

There are a number of migration phenomena into which we cannot get insights from the currently

applied monitoring techniques. Techniques that enable identification of individual species during these conditions would let biologists address questions regarding, e.g., the timing of migration and flight directions in relation to winds and topography. Comparative studies of species composition between time, sites, and years could be performed, and migration routes of individual species could be monitored. Insight into flight patterns of different species is crucial for the understanding of how wing morphology and physiological adaptations affect decisions on strategies and timing of migration. Detailed analyses of the aerodynamics of bird flight have been extensively pursued using advanced laser methods in a wind tunnel setting; see, e.g., [8]. Knowledge of migration routes and timing of the migration of individual species would also improve our understanding of how and when bird-borne diseases such as avian flu, avian malaria, and tick-borne diseases

are expected to be spread, as well as how seeds will be dispersed [3,4,9].

In addition to identifying new species, automatic monitoring techniques not requiring continuous surveillance from field assistants would allow for more efficient studies during daytime and for species migrating at high altitudes. Scattering spectroscopy of a well-defined section of the sky would allow for a more quantitative evaluation with time-resolved data on the number of passing birds. Such an approach could be a good complement to existing manual observation techniques and enable biologists to address questions such as how densities of different species vary during the day and with the ambient conditions. In addition to species identification, classification of sexes, age classes, and ultimately estimation of the condition of individual birds, often reflected in the plumage, would be desirable.

The undoubtedly most traditional way to study birds and bird migration is visual observation with the aid of a pair of binoculars or a telescope, where the light from the Sun is used as light source and the bird can be identified based on appearance and plumage characteristics. The size, shape, and reflectance spectrum (color) of the bird, filtered through the human visual system, provide information about position, flight direction and species of the bird. As long as the light level is high enough and the distance short enough, this approach is very powerful. However, during the night and at longer distances, other approaches are needed.

In the discipline of remote sensing, information is retrieved from far distances. Typically, the methods rely on several regions of the electromagnetic spectrum, e.g., radio frequency (RF), infrared (IR), visible (VIS), and ultraviolet (UV) to transfer the information. Both active backscattering geometries, passive scattering, obscuration, and thermal emission schemes exist. Previously, a number of such methods have been applied to study the nocturnal migration of birds. Tracking and surveillance radars [10–15], IR cameras [5,15], ceilometers [16,17], and lunar obscuration [18,19] have been applied to study the flight altitudes and flight directions of night migrating birds as well as the number of migrants passing. A couple of studies [20,21] designed to compare different methods have drawn conclusions on the advantages and disadvantages of the tested existing methods. Detection of migrating birds from their calls has also been applied [22,23]. The call counts were significantly correlated with radar counts, but a great deal of the variation in vocalization counts remains unexplained, suggesting that factors other than bird density might influence call counts [22]. Although many migratory songbirds produce different flight calls [23], these calls might not enable identification of all species, and fluctuations in call frequencies due to variables other than bird densities might also confuse estimates from this method. Another way to study migratory routes and behavior of birds is to mount archival light loggers (geolocators)

[24] or global positioning system loggers [25] on individual birds. These methods give very informative data but are costly and require capture and recapture of specific individuals. Furthermore, geolocators do not enable detailed studies of the flight behavior of birds relative to topography because the precision of the positional information is limited.

Although existing methods have proven valuable for detection of nocturnal migrants, no method has so far enabled general determination of the species of birds. Information on wing-beat frequency and flight speed from tracking radar makes it possible to group migrants into size groups, because wing-beat frequency and flight speed are similar for birds with similar body sizes [26]. Only a very limited number of species with very characteristic wing-beat frequencies, for example, the common swift *Apus apus*, can be identified by tracking radar [27,28].

While bird coloration in the human visual spectrum and more recently also in the UV region above 300 nm has been studied extensively [29,30], little is known about the plumage properties in the deeper UV, parts of the near-IR (NIR) and mid-IR (MIR), information which might not be relevant for classical bird–bird interaction studies, but might still prove valuable for remote sensing purposes. In the present study we explore three new optical schemes using a broad range of the electromagnetic spectrum, including deep-UV, the full bird-VIS range, NIR, and MIR with the purpose of detection and species identification of night migrating birds. We present the most interesting results from each of the techniques and demonstrate several new opportunities.

## 2. Materials and Methods

The methods used, including light detection and ranging (lidar), IR studies, and passive reflectance, were partly pursued at Lund University. Both reference measurements and some of the test-range lidar measurements were performed in the university laser laboratories. In addition, field studies were made at a field site at the Kullaberg nature reserve close to Mölle in the southwest of Sweden (N 56° 18', E 12° 26'). The site is situated on a northwest-pointing peninsula that is a main migration point during the spring migration. Kullaberg is a protected area, and at this location many nocturnal passerine migrants usually pass, arriving from Denmark in the west to southwest after a short sea crossing in the spring and continuing toward breeding areas in the north to northeast. The lidar was strategically positioned near the outermost point of the peninsula, which should give the opportunity to test the technique on any birds passing by. The near-coastal site would enable us to test the lidar technique on coastal birds and locally foraging swallows and martins. For an overview of the field site, see Fig. 1. The work was performed with general ethical permits (nos. M172-06 and M204-06).



Fig. 1. (Color online) Photographic setup overview of the field site at Kullaberg and its location in Sweden. The site has the coordinates N 56° 18', E 12° 26'. Shown are the locations of the lidar equipment, the center dome in which the IR cameras were installed, the east dome with the passive telescope, and a weather station. Also shown are two directions in which different lidar measurements were performed.

#### A. Elastic and Inelastic Reference Measurements at Multiple Excitation Wavelengths

To understand what phenomena to expect in long-range experiments during lidar measurements in the field, effects of, e.g., excitation quenching were studied in detail in the laboratory. The spectral absorption properties of  $\beta$ -keratin are very important, e.g., when choosing the laser source for fluorescence studies. The reflectance and fluorescence at different excitation wavelengths were therefore studied in the following way: a number of museum samples of different bird species containing a diversity of pigments including eumelanin, pheomelanin, various carotenoids, as well as exhibiting structural colors were analyzed using a combined fluoresceins similar to that presented in [31]; modified with an extension further down in the UV and without a GG420 long-pass filter. Moreover, the sensor now also included LEDs with emission at 250 and 300 nm (Roithner Laser, UVTOP250 and UVTOP300). Reflectances for the plumage of the sample birds were obtained from 240 to 740 nm.

All observed reflectance spectra were naturally limited by the reflectance of pure  $\beta$ -keratin (white belly of an adult herring gull, *Larus argentatus*). The observed reflectance of pure  $\beta$ -keratin plumage can accurately be described by a (biased Gompertz) function of the form presented in Eq. (1):

$$R_{\text{keratin}}(\lambda) = A \cdot \exp\left(-\exp\left(\frac{\lambda - \lambda_0}{d}\right)\right) + S, \quad (1)$$

where  $R$  is the reflectance;  $A$  is a value between zero and one (minus  $S$ ), in our case 68%;  $\lambda$  is the wavelength valid between 240 and 740 nm;  $\lambda_0$  is the rise position equal to 365 nm;  $d$  is a measure of the steepness, in this case with the value 63 nm; and  $S$  is the specular reflection of roughly 4%.

The value of  $S$  greatly depends on the illumination and observation angles as well as the orientation of the feather barbules.  $A$  represents the reflectance at NIR and is a result of the incident photons escaping the field-of-view (FOV) of the detector; thus, it is unrelated to the absorption of  $\beta$ -keratin.  $A$  can be expected to vary considerably between different schemes for reflection measurements [32].

To verify the relation between plumage reflectance and fluorescence, presented in Eq. 1 in [31], the relative elastic light as well as fluorescence emissions generated from several excitation wavelengths were evaluated for a variety of pigments. The relation is highly sensitive to errors in the dark spectrum estimation, and any offset will cause the spectrum to tilt slightly in one or the other way. In a case study, we review the golden oriole (*Oriolus oriolus*), pigmented by the carotenoid lutein. The plumage of the bird was excited with three wavelengths, 266, 308, and 355 nm—all important in the lidar community—and the relative fluorescence shapes were measured.

#### B. Lidar

In a previous paper [31], we introduced laser-induced fluorescence (LIF) lidar to bird studies. We have demonstrated that remote retrieval of chemical information by measuring the chromophore composition from bird fluorescence spectra is a feasible alternative for remote classification of migrating birds. In that paper we discussed in detail various optical phenomena in feathers, such as scattering, absorption, fluorescence, polarization, and interference effects. The phenomena were experimentally studied in laboratory setups; fluorescence and reflectance studies were also performed in a remote fashion, both on museum bird samples and on live European starlings (*Sturnus vulgaris*) in the field [31].

The lidar technique, employing pulsed laser light sent out into the atmosphere, has, ever since the laser's invention, successfully been used in different forms. Examples of standard applications are the mapping of aerosols [33], clouds [34], temperature [35], and wind speed [36] in the atmosphere. Lidar is also used for gas concentration measurements [37–39] and fluorescence studies of, e.g., aerosols [40] and hard targets such as buildings, water compounds, and plants [41,42]. The technique is well documented, and overviews can be found in e.g., [43,44]. Lidar techniques have previously been successfully used for studying the presence and density of birds and diversity of bird species communities in relation to vegetation structure [45–47]. However, with the exception of our feasibility study [31], lidar has so far not been developed for species classification of birds migrating at night. In the present study we have improved the performance of the lidar setup, and we have also performed a detailed investigation of excitation quenching mechanisms and elastic depolarizing ratios.

The Lund University lidar system used has, in general, been extensively described in several

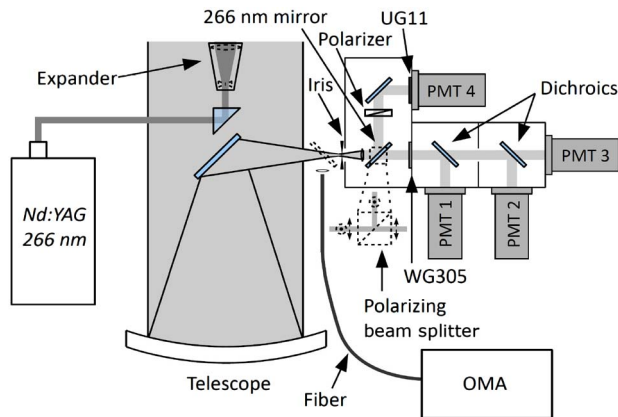


Fig. 2. (Color online) Schematic overview of the fluorescence and polarizing lidar system. The light from the laser is expanded and variably diverged before it is sent out vertically or in other inclinations. The returning light is focused onto the detector system with a 40 cm diameter telescope. Here it is separated into different spectral bands or two polarization directions, or it is sent through a fiber to an OMA.

previous papers (e.g., [48]) and the bird fluorescence lidar variety in an earlier version in [31]. Some important changes have, however, been implemented to improve the bird classification potential, and the most important features of the fluorescence lidar system are therefore presented in Fig. 2. The main improvements of the system are the implementation of one more fluorescence channel and the use of the more suitable, bird eye-safe, excitation wavelength, 266 nm.

Light pulses with a duration of around 4 ns, a wavelength of 266 nm, and pulse energies of around 10 mJ, are obtained by generating the fourth harmonic of a Q-switched Nd:YAG laser (Spectra Physics, Model PRO-200). The light is transmitted into the sky after passing through a Galilean quartz lens expander with the purpose to expand and (variably) set the divergence of the laser beam. The light can be transmitted vertically without any further optics (a tilt-angle quartz window can still be used for weather protection); alternatively, it can be sent out horizontally or with an angle of inclination between  $-10^\circ$  to  $+55^\circ$  with  $0.011^\circ$  angular resolution with the help of a motor-controlled folding mirror ( $40\text{ cm} \times 70\text{ cm}$ ), also providing the possibility of horizontal angular scanning ( $360^\circ$ ,  $0.0035^\circ$  resolution).

When light illuminates a bird, part of that light will be reflected, specularly or after several scattering events within the plumage, and part of it will be absorbed, and thus has the possibility to induce fluorescence. A small fraction of the fluorescence and reflected light will return to the lidar and can be focused onto the detecting system by a 40 cm diameter Newtonian telescope. The light passes through a variable aperture, used to control the FOV of the telescope. It is especially important to match the illumination profile and telescope FOV during daytime fluorescence studies when spectrally broad retrieval channels are usually employed. The background

light levels from the scattered sunlight can, under these conditions, heavily compete with the LIF signal, even if the necessary high voltage for the photomultipliers is time gated. Depending on the studies, there are several possible ways to analyze the lidar return. We have in these studies used three different approaches. An image-intensified optical multichannel analyzer (OMA) can record the full spectrum of the light, or a system with a polarizing beam splitter can separate the light into its polarized and depolarized components. The approach mainly used is, however, a four-channel time-resolving detector scheme separating the light into one depolarized elastic laser line channel and three broad wavelength bands, utilizing dichroic beam splitters; see Fig. 2.

### 1. Optical Multichannel Analyzer Lidar

With the OMA (crossed Czerny–Turner grating spectrometer ORIEL instruments, Model 77400, connected to an image intensified and down to 10 ns time gateable charge-coupled device, ANDOR Technology, Model DH501-25U-01), the full spectrum of the fluorescence from around 300 to 600 nm can be obtained (the range is limited by the second-order diffraction). However, the  $\beta$ -keratin fluorescence intensity rapidly decreases around 600 nm, and not much light is therefore expected at longer wavelengths. The OMA was employed by letting the light, instead of passing through the iris in Fig. 2, be focused into an optical fiber connected to the spectrometer. Even intensified, the sensitivity of the spectrometer is low compared to that of PMTs, and thus this approach is unfavorable in a single-shot situation, which is to be expected when no tracking is utilized and a bird passes by at migrating speed. The OMA system is however very suitable to perform laboratory studies with museum birds when signal averaging can be utilized. This setup was thus used at a docking position of the mobile laboratory in Lund, where light was transmitted to a rooftop some 80 m away, where museum sample birds were positioned, to record the full spectra of their bellies. The laser beam had a spot size diameter of around 6 cm at this distance, and the return collection efficiency of the fiber-coupled spectrometer was optimized by transmitting the 266 nm laser light, and simultaneous to that, sending continuous light from a high-pressure Hg(Xe) arc discharge lamp (Newport, Model 71226) backward through the collecting fiber and overlapping the corresponding spots. The fiber had a diameter of 1 mm, which, together with the focal length of the telescope of 1 m, gives a rough estimate of its collection angle of 1 mrad, equal to a spot size of 8 cm at a distance of 80 m—thus reasonably well matched to the spot size of the laser beam. The fiber was then moved to the spectrometer, and spectra were recorded and averaged for 250 shots for each bird.

## 2. Multiphotomultiplier Fluorescence Lidar

With four photomultiplier tubes (PMTs) and a system with long-pass filters and dichroic beam splitters, as described in Fig. 2, the returning light can be separated into the depolarized elastic component at 266 nm (separated with a 266 nm HR laser line mirror, VM-TIM UVFS HR > 99.5% at 266 nm, passing through a polarizing cube beam splitter and a UG11 short-pass filter, and recorded with a PMT Model 4816QA/234, Products for Research, Inc.) and three fluorescence bands (split with “UV-Blue” and “Blue-Green” dichroic plate beam splitters from Edmund Optics and recorded with PMT Model 9558/81 from Products for Research, Inc., Model RFI/B-217 from Thorn EMI-GENCOM, Inc., and Model 9558/81/265 from Products for Research, Inc., respectively). The light passes a WG305 long-pass filter before reaching the fluorescence detectors. The chosen fluorescence bands were: UV (around 305–410 nm), blue (around 410–515 nm) and green–yellow (around 515–570 nm) ranges, respectively. The signals were filtered with a 125 MHz low-pass filter to avoid undersampling the short (~4 ns) bird returns, recorded with a high-speed oscilloscope (Tektronix, Model TDS 544A, maximum 1 GS/s), and stored in a computer via a GPIB connection. The overall collecting speed was 10 Hz, limited by the data readout time, even if the laser repetition rate was 20 Hz. With these relatively broad bands, it is possible to collect enough light in a single shot to get a good signal-to-noise ratio but at the same time get enough spectral discrimination for bird classification. At nighttime, this multi-PMT system was used in a vertical transmitting fashion, sending out light pulses continuously and waiting for bird hits to occur. An automatic software program recorded the lidar returns for later analysis. Using time-gated high-voltage supplies to the PMTs would allow for fluorescence studies even during daytime. This was, however, not achieved during the campaign.

Unexpectedly and unfortunately, the number of birds migrating over the field site was low during the campaign. Therefore, to show an example of a multi-PMT recording of a live bird, such were collected and released at release sites some distance away from the lidar; see Fig. 1. The laser beam was pointed in a direction through which the birds were expected to fly.

## 3. Depolarization Lidar

The fraction of light illuminated on the bird that is reflected or backscattered with a different polarization direction could possibly provide species specific information. This information can be connected to the previously described laboratory reflectance measurements as the depolarization fraction is highly dependent on the total reflectivity. To explore how the depolarization fraction depends, e.g., on the abundance of pigments in the plumage, and the possible potential of depolarization lidar, measurements were performed remotely on the bellies of eight specimens

of museum bird samples (gray heron, *Ardea cinerea*; herring gull, *Larus argentatus*; chattering lory, *Lorius garrulus*; rook, *Corvus frugilegus*; pallid harrier, *Circus macrourus*; red ibis, *Eudocimus ruber*; barn owl, *Tyto alba guttata*; and sparrow-hawk, *Accipiter nisus*) at a distance of 85 m.

UV light was sent out from the laser, and the 1 mrad divergence resulted in an illumination spot just under 10 cm in diameter on the belly of the birds. The returning light was split into its depolarized and copolarized parts and detected with two separate PMTs. When depolarization studies are performed, the 266 nm HR mirror is switched to a polarizing cube beam splitter (VM-TIM,  $R_{II} > 99\%$ ,  $T_{\perp} > 90\%$ ), separating the light into a depolarized component and one with preserved polarization direction. A specular reflection, where the light has not been multiply scattered inside the plumage of the bird, should keep its polarization status better than the deeper penetrating light that will lose its polarization information to a larger extent. Furthermore, if the excitation light is significantly absorbed by any present pigment, relative to the absorption in the pure  $\beta$ -keratin matrix, this will reduce the depolarized emission and thereby induce differences between species with more or less of such pigments. In the field, depolarization measurements can be performed during daytime without suffering from the high background light-level, because an interference filter can be employed to block all light except for the narrow elastic laser line.

To establish that it is indeed realistic to obtain the depolarization ratio (DPR) from flying birds as well, measurements were also performed on barn swallows in the field at the site at Kullaberg. The birds were flying at distances between 50 to 200 m from the lidar equipment, over the sea, and close to a cliff. To be able to reach the position of the birds, the beam was transmitted horizontally. Because of this transmission geometry, the angle and part on the birds that was illuminated varied heavily upon, e.g., the flight direction. The results can therefore not be directly compared to reference measurements, which are all taken on the bellies of the birds. However, the possibility of measuring the depolarization from a single shot on a flying bird is demonstrated. In a migration study, for which the lidar would be vertically oriented, measuring birds from below, the illumination would most likely be exclusively straight from beneath which would result in a much more consistent angle of illumination.

### C. Infrared Imaging

We also present experimental studies in the MIR region and a novel scheme for passive remote classification in MIR. IR imaging has previously been applied to study nocturnal migration [5,15], but so far studies have focused on detection of migrants and little attention has been given to the spectral domain details of thermal emission from birds.

Colors arising from interference effects, rather than solely from pure spectral differential absorption, are commonly present in various objects in nature [49]. The periodic structures in some materials, with dominant spatial frequencies, induce interference effects, transmitting some colors and reflecting others. The presence of structural colors in insects and bird plumage has been extensively studied, and it has been known long since that some colors are produced by dominant spatial frequencies in refractive index variations rather than by differentially absorbing chemical pigments [49,50]. Bluish and greenish structural colors with wavelengths around 400–550 nm have been correlated with spatial frequencies from transmission electron microscopy (TEM) on nanosized arrays, typically containing sub-micrometer features [49]. Based on the information that bird feather barbules [the secondary branches of the rachis (trunk), considering that a feather is constructed by the main rachis, barbs, barbules, and hamuli] are well ordered with thicknesses in the order of  $2\ \mu\text{m}$ , thus about ten times larger than the structures inducing colors in the blue-green region, one might expect additional structural signatures in the MIR at wavelengths around  $4\ \mu\text{m}$ . Studies in the two atmospheric windows, on either side of a  $\text{CO}_2$  absorption band in the  $3\text{--}5\ \mu\text{m}$  region could therefore provide valuable information. To our knowledge, no studies of the structural bird “colors” in the MIR-thermal IR range have been performed so far. Here we present a novel MIR-based method capable of remotely retrieving information on the microstructure of the plumage.

Further, structural colors are known to often shift upward and downward in the spectral domain depending on the angle of observation with respect to illumination and the ordered matrix [30]. This can be explained geometrically as the effective distances (or spatial frequencies) depend on the angle of observation. If, e.g., the wings of a bird, constituting a substantial part of the area seen from beneath, are considered, the observer angle of view with respect to some feather structures will depend on the wing cycle phase. Observing (tracking) a bird over a complete wing cycle (preferably several) could then result in, e.g., a periodic shift of the MIR wavelength of maximum transmittance of body heat radiation. The features of such shift over time (amplitude, frequency, and bias) could, provide detailed information about the feather microstructures. The ability to retrieve information on the microscopic level over far distances by spectral analysis of the thermal emission could be thought of as remote microscopy. The information is, however, a statistical spatial average.

The potential for spectroscopy in the IR region was studied on sample feathers in the laboratory. Feathers from the outer (dorsal) side of the wings of seven different museum bird species were fixed in reversal film slide mounts. Each slide mount was then fixed to a rotation stage so that the feather could be rotated around the base trunk. For angles of incidence

ranging from  $-45^\circ$  to  $+45^\circ$  in increments of  $5^\circ$  (zero degrees corresponding to normal incidence), the transmittances of the feathers were measured in the range between  $2.5$  and  $25\ \mu\text{m}$  using a Fourier transform IR (FTIR) spectrometer (ATI Mattson, Model Infinity AR60). In general, the spectra will change according to all three rotations in space, very similarly to what is encountered in crystallography (see, e.g., [51]). The IR source was located on the ventral side of the feather.

To find a connection between the transmittance properties and the spatial structure of the feathers, a transmission microscope (Brunel Microscopes, Ltd., Model SP80, with an AVT Guppy-503 B/C CMOS camera, 810 nm LED illumination) was used to study the features of a number of feathers.

To further explore the feasibility of using the possible spectral information in the IR region, we consider a realistic case. The high metabolism of the flying bird results in an internal body temperature of around  $41^\circ\text{C}$  and causes thermal radiation to be emitted and filtered through the feathers in the bird plumage, as well as through atmospheric absorption. The radiation can then be detected with IR cameras with different detection bands selected by optical filters, preferably on each side of the  $\text{CO}_2$  absorption band at around  $4.3\ \mu\text{m}$ . Laboratory measurements show that the relative amount of radiation from the bird in each of these bands will differ depending on the transmittance properties of the plumages of different bird species. The relative contribution to each band in the two atmospheric transmittance windows was simulated for a number of birds based on the results from the laboratory spectrometer measurements. The simulation was done by integrating the product of blackbody emission, transmittance for plumage and atmosphere, the normalized detector responsivity of InSb, and optimal transmittance filters for each band. Further, this was done as a function of incidence angle, as described above, to investigate if different birds show any differences in wing-beat-induced dependence on the transmittance.

#### D. Passive Scattering Measurements

Telescopes have long since been used within the bird research community, but for enhanced visual observation without automation. We implement a telescope connected to a spectrometer for automatic recording and storage of events of spectral intensity change when birds pass through the FOV of the telescope. The sudden difference in the otherwise semi-static spectrum from the sky is recorded, providing information about the coloration of the bird. The same approach can be implemented in moonlight obscuration (so-called moon watching). A Newtonian telescope with an 8" aperture and 800 mm focal length (Bresser) mounted on an equatorial motorized stage (Messier Model LXD75 GoTo) was installed in the southeast dome of the location at Kullaberg, as indicated in Fig. 1. Clear view to the horizon was achieved in all directions except toward the east.

In the daytime, the telescope was directed toward the star Polaris; thus, in this mode we always had the Sun roughly perpendicular to the optical axis of the telescope. At nighttime, the moon was tracked using the motorized stage included in the telescope setup. In the focal plane of the telescope, a 1000  $\mu\text{m}$  diameter UV collection fiber (Edmund Optics) was installed feeding the light to a compact spectrometer (Ocean Optics, USB4000). In the daytime we employed a spectrometer slit width of 25  $\mu\text{m}$ , yielding 1.5 nm resolution, and at nighttime a 100  $\mu\text{m}$  slit, yielding 6 nm spectral resolution. Cylindrical lenses and second-order rejection filters were installed on the spectrometers. The light was detected by uncooled CCDs. In the daytime we were able to exploit the dynamical range by sample rates of 50 Hz, while in the moon tracking mode at nighttime, we achieved a 100 Hz sample rate, however, with a lower spectral resolution.

### 3. Analysis and Results

#### A. Elastic and Inelastic Reference Measurements at Multiple Excitation Wavelengths

The results of the reflectance measurements for the different bird species are shown in Fig. 3. Of particular interest in laser-based remote sensing of airborne  $\beta$ -keratin are certain laser lines. A 95% light absorption by  $\beta$ -keratin can be expected at 266 nm (quadrupled Nd:YAG radiation found in many lidar systems) and some 85% at 308 nm (XeCl excimer lasers typically used in ozone lidars). Although not very powerful, nitrogen lasers emitting at 337 nm might be used where roughly 75% of the light would be absorbed; however, several bird corneas and lenses start to become transparent at 337 nm, thus this choice could be harmful. The tripled Nd:YAG

line at 355 nm is potentially harmful for most bird vision systems, but could be applied for bats or scenarios with limited species involved. Some 65% absorption can be expected at 355 nm. Continuous wave emitting diode lasers at 375 and 405 nm might be used for small-scale experiments without range resolution with some 50% and 40% energy deposition, respectively. The three last-mentioned choices would, however, largely influence the birds and, further, many of the pigments would not be covered within the fluorescence emission range.

Reflectance at 266 nm is dominated by the specular contribution and is therefore highly dependent on the orientation of the feather structures. Because the reflectance is low, the relative accuracy is poor. Because the reference sensor was originally designed for nonordered samples and because of the cylindrically symmetric geometry [31], the reflectances at the various wavelength regions are difficult to combine. With respect to lidar measurements, this fact suggests that the depolarized elastic part is preferred in terms of normalizing the fluorescence. Within the group of diversely reflecting species, all of the reflectance data at 266 nm were nicely described by a  $\beta$ -distribution with mean of 34 per thousand and variance of 0.3 per thousand. Only a weak correlation between 266 nm and the reflectance at 308 nm of 33% was found, and 40% with 355 nm. Possibly the correlations are higher if the specular reflectance is rejected by observing only the depolarized contribution. The reflectance at 308 nm correlated 75% with the reflectance at 355 nm. Thus, normalizing fluorescence with the elastic signal at this excitation wavelength is slightly less favorable in terms of stability.

The data from the fluorescence measurements are not included here, but the combined case study measurements of reflectance and fluorescence at three excitation wavelengths for the golden oriole are presented in the bottom part of Fig. 3. The dark currents for each spectrum were compensated for so that the part of the spectrum between 550 and 650 nm that is not affected by lutein chromophores remains flat. The ratio spectra (see Eq. 1 in [31]) were scaled to match the elastic ratio for the unpigmented part. The double absorption dip of lutein indicates that greater contrast, between the spectral part affected by the chromophore and the unaffected part, is achieved for the lower excitation wavelength. We further note that the contrast in the 266 nm excited fluorescence ratio is better than that for the relative elastic light. This could be explained by the fact that the light is produced internally in the  $\beta$ -keratin matrix; thus, there is no specular contribution, which typically worsens the contrast in the elastic reflectance case.

A surprising result from the fluorescence measurements was that the gray heron showed even stronger fluorescence intensity in the UV than the unpigmented white herring gull. The same results were found from the lidar OMA measurements (results described in next section) and the bird was therefore

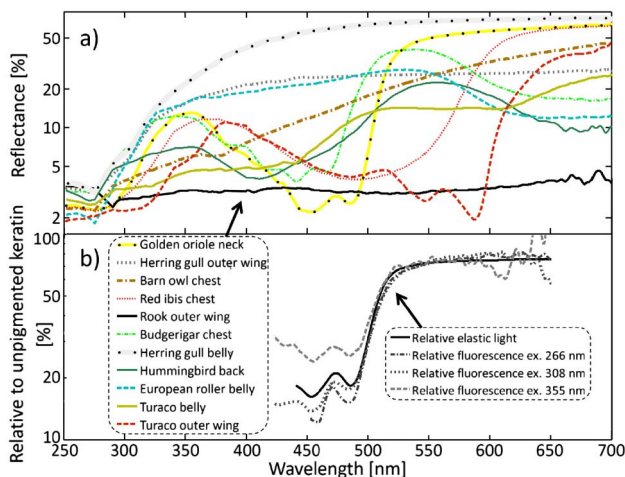


Fig. 3. (Color online) a) Reflectance spectra for different birds at locations specified in the legend. All of the birds are specified elsewhere except for the budgerigar, the hummingbird, and the turaco with Latin names *Melopsittacus undulatus*, *Colibri thalassinus*, and *Tauraco erythrolophus*, respectively. b) Fluorescence spectra ratios for the golden oriole. The fluorescence is given relative to unpigmented  $\beta$ -keratin. Excitation at 266, 308, and 355 nm.

investigated in more detail. It was seen that the chest showed spotwise higher reflectance than unpigmented  $\beta$ -keratin in the region 240 nm–340 nm. Consequently, even the fluorescence induced by 266 nm is higher in that region.

## B. Lidar

### 1. Optical Multichannel Analyzer Lidar

The lidar fluorescence returns from six museum bird samples were recorded, and their spectra averaged over 250 shots. The raw spectra of the birds are shown in Fig. 4a). Included in the figure is also the overall spectral transmittance for the bands that were chosen for the multi-PMT setup. The bands are chosen to maximize the classification possibility based on differences in spectra between birds. The natural way to choose the positions of the bands would be to match the visual bands of the birds. In these experiments we have, however, limited ourselves to three fluorescence bands. The positions of these bands are matching reasonably with the visual bands of the birds. The UV band goes from 305 to 410 nm while, as an example, the starling's (*Sturnus vulgaris*) UV band is centered at 362 nm; the blue

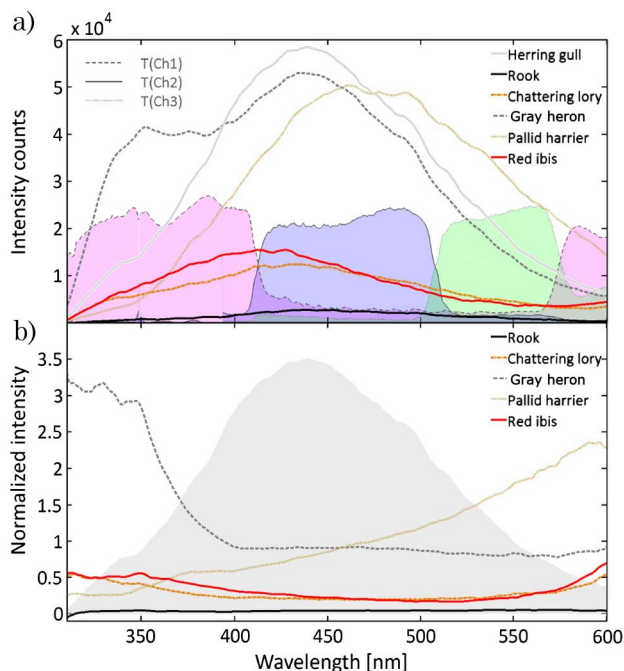


Fig. 4. (Color online) Fluorescence spectra from six birds as remotely obtained by the optical multichannel system. a) The spectra are averaged over 250 shots and smoothed with a 20-channel floating average. Included in the figure is also the overall spectral transmittance in each channel. In these curves are included the transmittance through all optics after the telescope but not the quantum efficiency of the PMTs. What can be noticed is that the UV channel also has some transmittance in the yellow region. However, the lower quantum efficiency of the PMT in this region, in combination with the low emission from  $\beta$ -keratin here, makes the contribution from this region to the total signal small. b) The same spectra divided with the herring gull spectrum.

band is between 410 and 515 nm while the starling's two middle bands are centered at 449 and 504 nm, respectively; the green band is from 515 to 570 nm and the corresponding band of the bird is centered at 563 nm [52]. The white plumage from the herring gull belly was chosen as a reference, due to its general lack of pigments. In order to more clearly reveal differences between the birds, their spectra are divided with the one from the herring gull, as shown in Fig. 4b). From previous studies, [31], we know that the fluorescence color is, in general, well correlated with the reflectance color and the same conclusion can be drawn from Fig. 4. The UV light of the laser induces fluorescence in the  $\beta$ -keratin in the feathers. This actual fluorescence spectrum does not vary much between birds, but when this “white” light is filtered through the plumage, it gets a bird-specific fingerprint through reabsorption. It can be mentioned that the black rook, absorbing much of the fluorescence, shows a very low light level throughout the spectrum. The red ibis and chattering lory, which are both red, show very similar and quite weak fluorescence spectra with a tendency of increased intensity toward the red side of the spectrum. The light-brown pallid harrier belly is also shifted toward the red compared to the herring gull. The increase of its spectrum, however, starts at lower wavelengths, which, combined with our higher visual sensitivity in the green region, makes this bird look brown and not red (what we see is, of course, reflectance, but we here assume that the fluorescence and reflectance are well correlated). The gray heron shows strong signal to the red, but its very strong signal in the UV was especially remarkable.

### 2. Multiphotomultiplier Fluorescence Lidar

The performance of the multi-PMT setup was determined by pursuing measurements on the same museum sample birds as the ones in the OMA section, but now on a single-shot basis. For each shot, the lidar returns in the four channels were recorded with the oscilloscope and saved through a LabView (National Instruments) interface. The echo return powers were automatically calculated with the help of a scheme that (i) sorts out the files containing bird echoes, (ii) finds the distance in that return at which the bird is considered to be, and (iii) calculates the echo power from the bird in each channel by integrating the signal from the full bird return. The last step is needed because the trigger jitter and the impulse response of the PMTs might differ slightly between channels. The peak-height alone could therefore be misleading or inaccurate. In Fig. 5, the information obtained is presented in an isosurface histogram plot. Here the different birds will end up at different positions in this three-dimensional (3D) color space constructed with the echo power of the three fluorescence channels normalized to the depolarized elastic channel as the axes. The 3D space is divided into  $20 \times 20 \times 20$  cubic bins, and, depending on the echo power

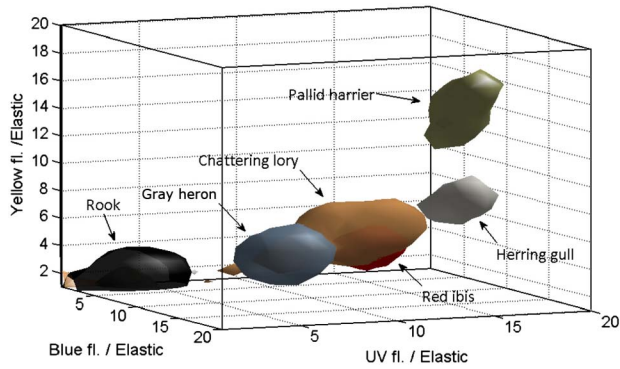


Fig. 5. (Color online) Isosurface 3D histogram plot for the fluorescence return from different birds. Depending on the fluorescence spectrum, different birds gather at different locations in the 3D space made from the three fluorescence channels normalized with the depolarized elastic channel.

in each channel, every lidar return will end up in one of these cubes, creating a 3D histogram field. The 3D histogram produces a probability distribution. A measurement at a later stage of an unknown species can be indexed in the histogram, and the probability for the unknown sample to belong to a certain species is given by its position in the color space. A surface with a certain confidence level, in the presented case 70%, is drawn in the histogram, meaning that a bird of the corresponding species would, with 70% probability, end up within this surface. The tendency of the echoes from the different birds to cluster at different places in this grid is clear. This implies that there is a potential for remote bird classification. The measurements are performed on one single individual of each species. Some larger spread could be expected if many individuals were included. On the other hand, further improvements of the system, e.g., using four fluorescence bands matching the vision bands of the birds, could compensate for this increased variation.

Fluorescence signals were also recorded of the live released birds, and an example of that is shown in Fig. 6. The example bird is a lesser whitethroat (*Sylvia curruca*), and the data are recorded at a distance of 80 m from the lidar.

### 3. Depolarization Lidar

The DPR is defined in Eq. (2):

$$\text{DPR} = \frac{I_{\perp}}{I_{\perp} + I_{\parallel}}, \quad (2)$$

where  $I_{\parallel}$  is the copolarized intensity and  $I_{\perp}$  is the depolarized intensity. In our case we have used the integrated echo power, as described in the previous section, as a measure of the return energies. As the two polarizations are recorded with different detectors and in different detector geometries, the signals have to be calibrated in order to get a quantitative axis for the DPR. In these measurements, we have calibrated the system by including a measurement

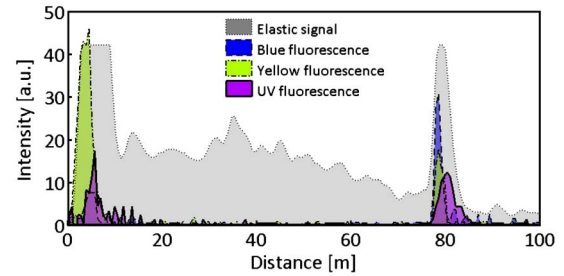


Fig. 6. (Color online) Lidar signals in the depolarized elastic and the three fluorescence channels during a released bird event (for the geometry, see Fig. 1). The bird is a lesser whitethroat released at 23:34, 28 May.

on a reference polystyrene plate with the well-known DPR. Included is also a measurement on a plate of diffuse aluminum, which should have a low DPR as long as the system does not suffer from interchannel leakage.

The results of the measurements on the museum birds are shown in Table 1. The mean DPRs with standard deviations are shown.

In Fig. 7, examples of lidar returns from a flying barn swallow (*Hirundo rustica*) and the museum gray heron are shown. In this case, the barn swallow was flying at a distance of 150 m. The signals in this specific example are low due to a partial hit. However, the strength in the two polarizations could still be compared. Pure hits on flying barn swallows also occurred with strong resulting signals, however, at closer range.

During the depolarization measurements on the barn swallows, a considerable amount of hits occurred, for which the position along the axis of the laser beam was recorded, as well as the time for the event. Histograms in the time and space of lidar signals can effectively be used to, e.g., map out preferred locations and flying times. This can then be correlated with, e.g., wind data or other conditions of interest. In Fig. 8, example histograms of the distance from the lidar equipment to the birds, and the time of the bird hit, are shown for recordings during the time 17:55 to 18:33 on 25 May 2010. A threshold taking into account the static backscatter light and the range-dependent signal strength was employed to recognize rare events of reflections from birds. This threshold was, in this case, set with quite a margin to make sure that all hits shown in the histogram are from birds and not from, e.g., smaller insects [53], which could also be seen as smaller events.

### C. Infrared Imaging

Examples of the IR transmittance spectra of feathers from three museum bird species: a blackbird, *Turdus merula*, the sparrow-hawk, and the pallid harrier at normal incidence are shown in Fig. 9, in addition to the spectral detectivity profiles of three different IR semiconductor detectors, as well as the atmospheric transmittance in the region. The lower transmittances at around 3.0, 6.1, and 6.5  $\mu\text{m}$  in the feather spectra are caused by  $\beta$ -keratin absorption. The peak

**Table 1. Remotely Measured DPRs at 266 nm Reflectance for a Gray Heron (*Ardea Cinerea*), Sparrow-Hawk (*Accipiter Nisus*), Red Ibis (*Eudocimus Ruber*), Chattering Lory (*Lorius Garrulus*), Barn Owl (*Tyto Alba Guttata*), Herring Gull (*Larus Argentatus*), Pallid Harrier (*Circus Macrourus*), Styrofoam, and Aluminum**

Species	Gray Heron	Sparrow-Hawk	Red Ibis	Chattering Lory	Barn Owl	Herring Gull	Rook	Pallid Harrier	Styrofoam	Aluminum
Mean DPR [-]	0.354	0.332	0.301	0.286	0.270	0.262	0.255	0.255	0.302	0.054
Standard deviation	0.008	0.037	0.017	0.018	0.012	0.009	0.019	0.011	0.007	0.010

at the  $5.9\ \mu\text{m}$  wavelength is due to the Christiansen effect, which occurs when the refractive index of air coincides with that of  $\beta$ -keratin [54]. This occurs on the lower wavelength slope of  $\beta$ -keratin absorption due to the Kramers–Kronig relation. The spectral position of a transmittance peak within the region  $4.0$  to  $5.5\ \mu\text{m}$  was found to be dependent on both bird species and the angle of incidence of the transmitted light. Plumage iridescence (i.e., the shift of wavelength of peak reflectance—or in this case transmittance—under an altered angle of observation, due to structural interference) has been studied in depth in the optical regime [29], and the result from our measurements shows that an analogous effect exists in the MIR. In the VIS region of the spectrum, iridescence is usually related to thin-film interference caused by sub-micrometer-scale structures inside feather barbules [29]. These are sometimes rather larger in size than the wavelength of peak reflectance, in which case the optical phenomenon is caused by higher order reflectance peaks with the zero-order peak in the NIR [29]. In order to investigate what is causing the observed peak shift in the MIR region, a feather from a herring gull was stretched in total 40% laterally and perpendicular to the trunk (approximately increasing the barb separation in the same way) in 15 steps, and the spectral transmittance was measured at each increment. The results (not presented here) show a shift of peak

transmittance from the  $4.2$  to  $4.5\ \mu\text{m}$  wavelength. Assuming that barbules or barbules are only rotated or shifted, not deformed in the process, this result shows that the MIR iridescence is not caused within individual barbules/barbules/hamuli but rather by the feather (or the  $\beta$ -keratin–air matrix) as a whole. The barbules, which are organized in a laminar fashion, constitute the majority of the interrogation area, and they also have a thickness that is of the same order of magnitude as the wavelengths.

In [55] it is shown analytically that the intensity of light scattered into a vector  $k$  in a medium consisting of quasi-ordered cylindrical fibers suspended in a medium of different refractive index, is proportional to the inverse of the Fourier frequency spectrum of the variation in refractive index along  $k$ . This result has been successfully applied in a number of cases to predict the reflectance spectra of feathers [56]. In [56], the variation in refractive index was estimated from the two-dimensional (2D) spatial Fourier spectra of TEM micrographs of cross-sectional slices of barbules. In the present study, we are instead exploiting the fact that the barbules are organized like Venetian blinds, which suggests that even for normally incident light, there is still some photon transport laterally in the feather, and thus the lateral spatial frequency of the barbules can be expected to influence the resulting reflectance spectra and by extension the transmittance spectra of the feathers. The fact that the sizes (or separations) in one of the spatial dimensions are usually well correlated to the sizes in the other two suggests that the spatial lateral frequency should be correlated with the one normal to the surface. In this way, we can expect

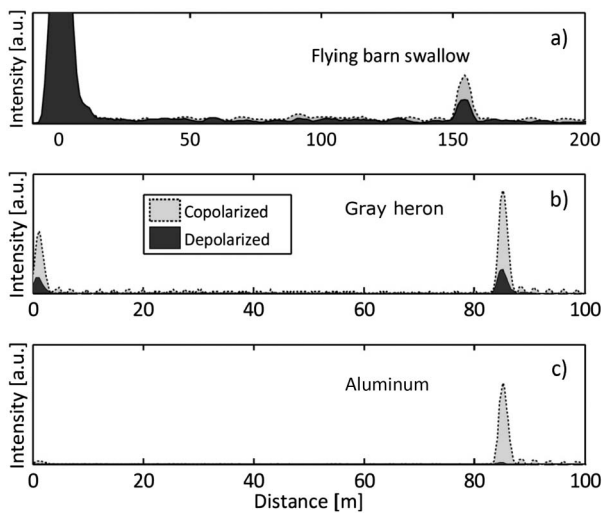


**Fig. 7. Lidar returns in a copolarized (dotted curve, light gray) and a depolarized (solid curve, dark gray) channel for a) flying barn swallow, b) museum sample gray heron, and c) aluminum plate.**

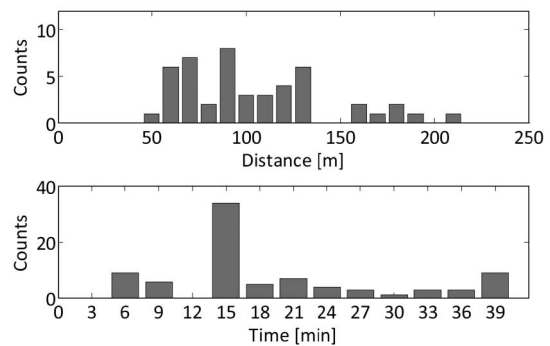


**Fig. 8. Histograms over the lidar return distributions in time and space for flying barn swallows recorded during a time span of 38 min. The direction in which the recordings are done is marked “Path North” in Fig. 1.**

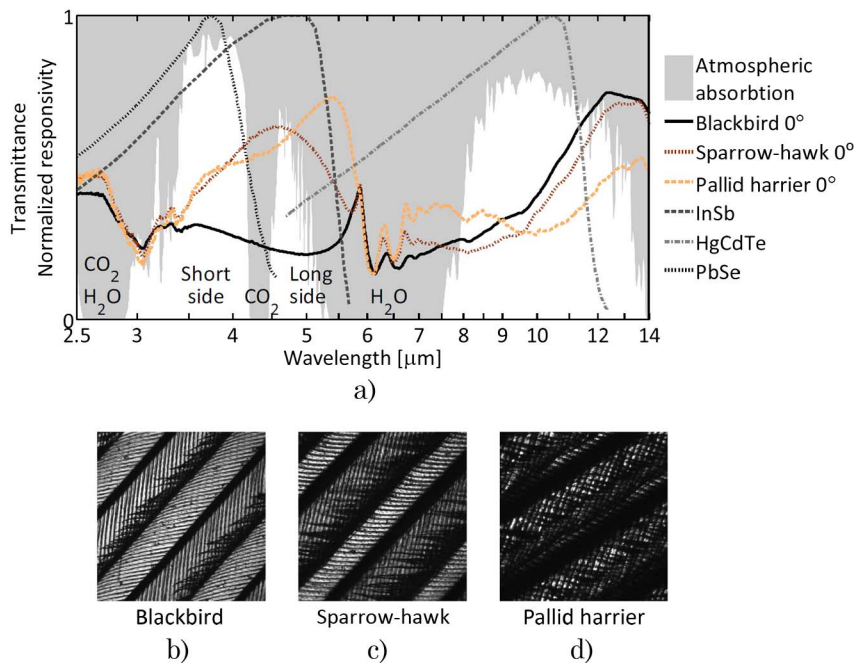


Fig. 9. (Color online) a) Spectral overview of structural MIR effects. The transmittance of three bird feathers at normal incidence shows significantly different spectral features in the wavelength region 3.5–5.5  $\mu\text{m}$ . For demonstration purposes, the feather transmittance spectra have been normalized to the Christiansen peak at 5.9  $\mu\text{m}$  wavelength and the transmittance dip at around 6.1  $\mu\text{m}$ , due to  $\beta$ -keratin absorption. Gray areas denote atmospheric absorption with the primary responsible species indicated. Also shown is the normalized responsivity of three different semiconductor detector materials. Below, sections of the micrographs used for spatial frequency analysis, showing barbules attached to opposite side of the barbs of the same b) blackbird, c) sparrow-hawk, and d) pallid harrier feathers.

that the spectra should be correlated to the measured lateral spatial frequency, even without lateral photon transport.

The spatial frequencies of the distal barbules of a number of sample feathers were estimated by the 2D FFT of light micrographs of the feathers, and the mean barbule periodicities in the plane of the feather surfaces were found as the reciprocal of the spatial frequency peaks (the azimuthal average was used to find the spatial frequency). The resulting inter-

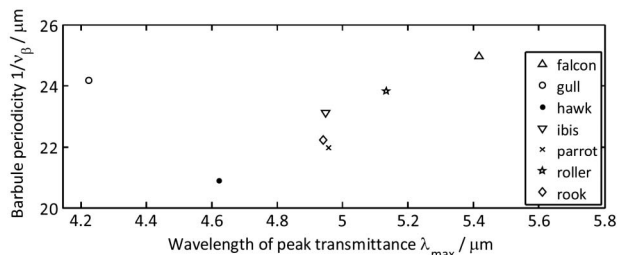


Fig. 10. Correlation between the periodicity of the distal barbule separation and the wavelength of peak transmittance for different bird feathers. It must be stressed that there is a significant uncertainty regarding both the wavelength of peak transmittance as well as barbule periodicity. The keratin absorption bands near 3 and 6  $\mu\text{m}$ , as well as the tail of the Christiansen peak, will affect the transmittance spectrum of keratin, resulting in a shift of the wavelength of maximum transmittance that would result from interference alone. Along the other axis, the measured interbarbule distances depend both on the location on the feather, and can be expected to further deviate for different feathers on the same individual bird.

barbule distances were then correlated to the wavelengths of peak transmittance for normally incident light for each feather, obtained from the Fourier transform spectrometer measurements. The result of this approach is presented in Fig. 10. A subset of six of the seven feathers measured with the microscope (the pallid harrier, the herring gull, the sparrow-hawk, the red ibis, the chattering lory, a European roller, *Coracias garrulus*, and the rook) exhibits a linear relationship between interbarbule spatial periodicity and peak transmittance wavelength with a correlation coefficient equal to 0.96 along one direction and 0.74 along the other (corresponding to directions perpendicular to barbules attached to opposite side of the barbs). This result further reinforces the evidence that the observed MIR interference effects are due to structural features caused by the feather microstructure, and it also suggests a way to remotely retrieve microscopic information from the plumage.

Because the wavelength range with a large variance in the feather spectra falls mostly within the atmospheric window between 3 and 5.5  $\mu\text{m}$ , the ratio between the signals from two spectral bands to either side of the  $\text{CO}_2$  absorption band at 4.3  $\mu\text{m}$  would be a candidate for remote classification. Species-dependent time modulation of the signal due to wing-beat patterns introduces another discriminating factor.

The proposed passive method for bird classification utilizes the metabolism of the bird as an IR

source, with an intensity distribution assumed to be that of a blackbody, and the cold sky as background. Spectral emissivity within an atmospheric window is low by definition, and the radiation emitted along the atmospheric path can therefore be neglected. Observations at elevation angles close to vertical will minimize the atmospheric path length and radiance. The choice of wavelength region also means that the resulting atmospheric scattering will be low compared to shorter wavelengths, further increasing the signal-to-noise ratio.

In a simplified model, the detector signal from light transmitted in a spectral band,  $b$ , is given by Eq. (3):

$$L_b = \int L(\lambda)\mathcal{T}(\lambda)S_b(\lambda)d\lambda, \quad (3)$$

where  $\lambda$  is the wavelength,  $L(\lambda)$  is the spectral radiance of the source,  $\mathcal{T}(\lambda)$  is the atmospheric transmittance along the path between the source and detector, and  $S_b(\lambda)$  is the combined transmittance of the optical filters and normalized detector responsivity. However, reflected radiation from the Earth might contribute substantially to the total detected signal in a practical case. The ratio between the radiance in the atmospheric transmittance bands at the short and long sides of the CO<sub>2</sub> absorption (denoted “Short side” and “Long side” in Fig. 9) depends on the angle of incidence of the transmitted light through the feather, or equivalently, the angle of observation of the bird’s wings, given by Eq. (4). This angle-dependent ratio is shown for three different species of birds in Fig. 11:

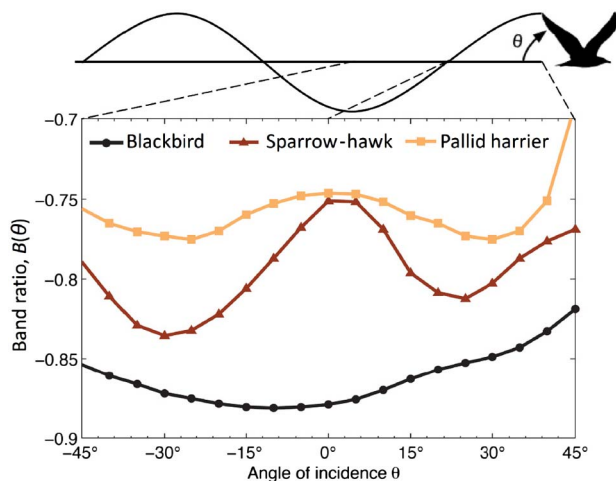


Fig. 11. (Color online) Calculated ratio between long and short (wavelength) spectral bands (relative slope) for blackbird, sparrow-hawk, and pallid harrier feathers. Ideal bandpass filters were used for calculations, defined as having spectral transmittance equal to 1 for wavelengths  $\lambda$  in the interval  $I$ , and 0 otherwise, where  $I$  was chosen as 2.7 to 4.3  $\mu\text{m}$  for the short-wavelength band, and 4.3 to 5.5  $\mu\text{m}$  for the long-wavelength band, corresponding to the two atmospheric windows on either side of the CO<sub>2</sub> absorption band at around 4.3  $\mu\text{m}$ .

$$B = \frac{L_{\text{long}} - L_{\text{short}}}{L_{\text{long}} + L_{\text{short}}}. \quad (4)$$

The ratio,  $B$ , is calculated from the blackbody spectrum as given by Planck’s law with absolute temperature  $T = 315$  K, detector responsivity of indium antimonide (InSb), and experimental feather transmittance spectra as measured using FTIR for angles of incidence,  $\theta$ , between  $-45^\circ$  and  $+45^\circ$ , when rotated around the trunk. The results show a distinct difference in shape between the three species—a fact that could hopefully be used in a live situation.

#### D. Passive Scattering Measurements

On 26 May 2010, 1,592,000 passive sky spectra were collected from 12:54:56 to 19:24:29. The data were loaded into MATLAB software (MathWorks). Darkness was presumed in the range 180 nm–260 nm, and this range constituted to a dark current estimation, which was subtracted from the data. To overview the data, we applied singular value decomposition (SVD). In total, eight significant spectral components were found. After rotation of the coordinate system from the SVD, one component could be associated with the temperature of the spectrometer, changing over the day. This component showed up as a derivative of the Fraunhofer lines and thus implies a shift of the spectrum due to the mechanical deformation internally in the spectrometer. After correcting data for the instrument temperature by rejecting the corresponding component, also the cosine of the true Sun time of the day could be accurately predicted independently of passing clouds. This was done by a simple hyperplane model. The spectral component accounting for the true Sun time showed reciprocal wavelength dependence and can be assumed to correspond to the total air mass in the light path. In principle, we can reject the time component as well and maintain a constant static Sun spectrum over the day. However, the rare events are likely to be influenced by the time of day anyhow, because the birds cannot be considered as spherical particles and because of the interruption of the static geometry.

The total intensity of each spectrum was calculated and analyzed with the Fourier transform. A distribution with a slight increase of 30% was observed around 3.3 Hz; this could be the mechanical eigenfrequency of the telescope. The increase was compensated for by a damping filter. The relative slope of the intensity was calculated and observed in a histogram—the very sudden changes caused by passing birds could easily be detected by employing a threshold. Several smaller events could be detected by lowering the threshold, but a refined analysis of the spectra from these events is not meaningful due to the close-lying noise levels. In the time frame of these measurements, we detected 16 rather large events. Typically, each event was resolved by two to four spectra, recorded with a time separation of 0.02 s. Most events, except for the one presented in Fig. 12, showed up as sudden drops in the static

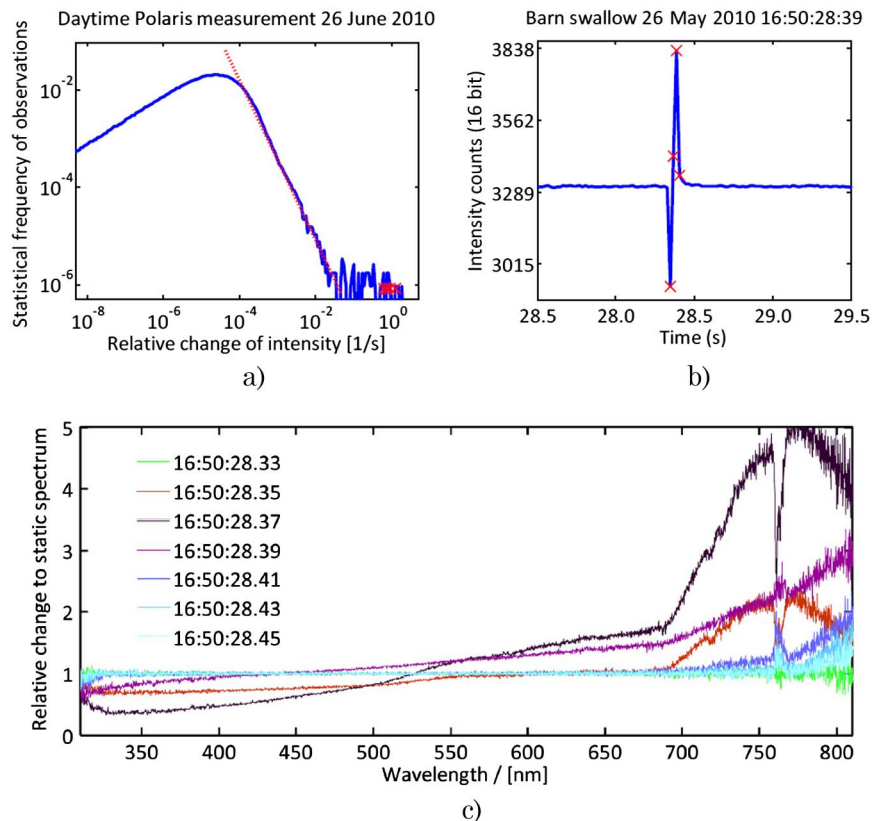


Fig. 12. (Color online) a) Histogram of relative slopes in total intensity enables us to determine a threshold for rare events. Crosses mark the events detected in Fig. 12b). b) Change in total collected mean intensity when a barn swallow passes by at 16:50 on 26 May 2010. c) Spectral intensity change relative to the static sky spectrum during the same event as in b).

intensity, resulting from an obscuration of the “sky” radiation. When analyzed in the spectral domain, the events were normalized with the quasi-static spectra at the time of the event. Most event spectra showed a flat ratio in the UV and VIS from 350 to 700 nm. Two of the events showed an intensity rise at around 550 nm. Both of these events arose from barn swallows passing roughly 30 m over the telescope, and thus features are presumed to be associated with their red pheomelanized throat. The events occurring at clear sky show an increase in the NIR just after 700 nm. This is interpreted as the vegetation-covered ground illuminating the birds from below (vegetation reflection is known to dramatically increase above 700 nm [57]). The increase in the NIR did not apply to the oxygen A band around 760 nm, a terrestrial Fraunhofer line of much interest in remote sensing of Sun-induced vegetation fluorescence (see, e.g., [58]). In a few spectra, the intensity in the 760 nm band was larger than in the remaining IR spectra; this could be caused by direct reflection of the sunlight in the bird, with the implication that the path length Sun–bird–telescope is smaller than the mean Sun–atmosphere–telescope path length when looking toward Polaris. Although no species-specific information can be expected in the NIR due to the lack of spectral bands in bird vision and therefore also chromophores in the plumage, reflectance of ground vegetation and information from Fraunhofer

lines, such as the oxygen band around 760 nm, could provide clues on the geometry of the event, altitude, and surface orientation. A better understanding of this would, however, require a larger sample number and altitude span of the recorded flying birds.

Although we applied a similar analysis to the data obtained by moon tracking where samples with the highest slopes were investigated, we unfortunately did not find any significant events there.

#### 4. Discussion, Conclusions, and Perspectives

The isosurface histogram exemplified in Fig. 5 was obtained with the multi-PMT setup on museum birds with the wings kept along the sides. In a live situation, a single shot would illuminate the bird in some part of its wing cycle, and the result might vary accordingly. The dependence on wing-beat phase could provide an additional source of information for species with varying pigmentation over the body, including the underwing coverts and primaries, where we could expect some sort of “doughnut” trajectory to arise in the color space. This fact could be exploited in the same way as proposed for the IR imaging, utilizing a tracking system. In a realistic situation, detection of the IR signal could be achieved by separating MIR light from the lidar telescope into the two bands using a dichroic beam splitter. Making one of these a quadrant detector would allow for bird tracking by feeding the differential signals of opposite

quadrants back to the motors controlling the elevation and horizontal angle of the folding mirror. If no opportunity for tracking is forthcoming, the information from the IR detection could still allow for indexing the lidar hit with regard to the phase of the wing cycle.

In our case, we present a color space with the normalized contributions to each spectral band. In principle, with profound calibration, the space could be linearly transformed into a concentration space with, e.g., eumelanin, pheomelanin, and lutein absorbance on the axes.

It should be noted that during lidar measurements, a large divergence of the beam will increase the probability of illuminating a bird, but, at the same time, the amount of light in each hit, and thus the signal-to-noise ratio, will unavoidably also decrease. The divergence has, therefore, to be decided depending on the current conditions. If tracking is employed, the divergence could be kept small.

Laboratory reflectance studies show that the reflectance at 266 nm is low and dominated by the specular reflection. It is also clear that the reflectance does not vary much between species, and we can conclude that the exact value is unstable and depends heavily on geometry effects, such as illumination angle. This tells us that the depolarized signal is preferred for normalization due to its better stability and independence of such effects. These results also go well in hand with the remote depolarization measurements performed with the lidar. The results from these show an insignificant difference between species, and as an example, the black rook and the herring gull, completely different in terms of abundance of chromophores, show similar DPRs. From this we can conclude that the DPR at 266 nm is probably not a good candidate for classification, but also that the excitation quenching by chromophores is insignificant at a wavelength of 266 nm. The larger differences of reflectance between the birds at longer wavelengths could possibly be utilized for species-dependent DPRs there.

The gray heron is a wetland bird feeding on fish and amphibians by frozen posture hiding at water edges and slow walking through the water in lakes and rivers. The male gray heron, as many other heron species, carries longer feathers on the back and breast, which are used in displays during the mating season. It is likely that the reflection characteristics of these feathers on the breast have evolved as an adaptation to foraging (camouflage) or mate choice, which in the latter case has been shown for several other bird species, including, e.g., the blue tit [59]. This could be one explanation to the high-UV reflectance observed for this bird.

The measurements of wing cycle dependence of the IR signals have been limited to single feathers, and a simplified wing model has been applied, where the wing feathers are aligned parallel to the air flow. Extrapolation to a more realistic situation is not trivial. However, symmetry around 0° incidence in

the band ratio implies that the total signal from feathers (wings) with opposite orientations will aggregate rather than average out. Further, the highly inelastic MIR-photon migration through plumage could potentially enhance structural features in the outermost layers. It should be noted, that apart from the spectral changes, wing beating will also contribute to a prominent (and trivial) intensity modulation as the wing cross section observed from ground level varies.

Three IR transmittance spectra at normal incidence are presented, which represent natural spectral fingerprints that may be shared by a number of birds. The general shape of the spectra is defined by the  $\beta$ -keratin absorption profile, which is essentially identical for all feathers, with the angular-dependent interference profile superimposed, whose central maximum at normal incidence, and the angular dependence of the same is dependent on bird species. As mentioned previously, this is likely due to the geometry of the barbules, and possibly the inclination of these with regard to the feather surface. The surface normal defining the plane of this effective optical surface of the feather may be determined, e.g., using reflectance measurements by scanning the angle in two axes and finding the maximum reflected intensity; our current equipment does not allow this. Full classification based on MIR spectral data alone is not realistic, because several birds may exhibit similar spectral fingerprints, but in the context of LIF lidar providing chemical information, the additional MIR information gained on the microstructure compliments LIF in a natural way. Because the effects thus incorporated have a wide spectral origin, from deep UV to MIR, they are likely to be the result of different physical phenomena, which indicates a large classification possibility. Reflectance measurements with active transmitters in the MIR would be an obvious complement to the transmittance spectra. Further, polarization analysis may shed more light on the cause of the interference effects.

The ability to perform remote IR analysis of live birds will likely depend on the degree to which the order of the feather structure is maintained in the plumage, as opposed to in single feathers. In contrast to VIS iridescent colors, the photon transport in the deeper lying plumage can be expected to be highly inelastic and could reinforce the structural signatures. Absolute wing-beat phase information is accurately predicted from the theoretical peak transmittance wavelength waveform, which provides important information for the LIF measurements in order to aid determination of which part of the bird that is being sampled.

The passive scattering studies correspond to a minimal portable setup, requiring only a telescope, a compact spectrometer and a laptop, thus making it ideal as a standalone method. However, similar signals could be retrieved for free in a lidar setup [31]. We have proposed a feasible method for instrument calibration and rare event detection based on the

relative slope of intensity change, and demonstrated spectral features associated with atmospheric path length and gases, subillumination from vegetation, and embedded chromophores on the birds. More statistics and larger altitude span are needed to draw conclusions regarding the Fraunhofer lines and the possibility for altitude determination of the passing birds.

Our findings imply three new feasible methods for remote classification of night-migrating and high-altitude flying birds. To date, little is known about the migration ecology of specific night-migrating species due to that current techniques do not allow species level identification, apart from a few exceptions. Applying the techniques described above could add information that enables biologists to identify some species and thus to address an entirely new set of questions for studies of the migration and flight adaptations of these species. Important insights in timing of migration, flight directions in relation to winds and topography, as well as monitoring of passing species could be accomplished. Such information is crucial for understanding basic biology, such as how wing morphology affects flight patterns during migration. Questions of more general interest, such as where and when different species that are hosts to diseases such as avian flu and tick-borne diseases are migrating, could also be resolved using such information [3,4,9]. Further development of these techniques to be more practically applicable in field situations could be a fruitful approach for exciting advantages in bird migration research.

We would like to acknowledge the Knut and Alice Wallenberg Foundation for their support throughout the development of lidar techniques in Lund. We would like to thank Kungliga Fysiografiska Sällskapet in Lund (Kullabergsfonden) for financial support of field campaigns. This is a report from the Lund Laser Centre (LLC) and the Centre for Animal Movement Research (CAnMove: 349-2007-8690) supported by Linnaeus grants from the Swedish Research Council and Lund University. *Ex vivo* specimens were borrowed with the kind collaboration by the Zoological Museum, Lund University, while live birds used in release studies were kindly provided by Falsterbo Bird Observatory. We thank the Kullaberg Natural Park, Naturum, and the Kullen cafeteria for their hospitality. We would also like to express gratitude to Zuguang Guan, Jan Skacel, and Matthias Burza for important assistance. We are also grateful to reviewers for valuable suggestions that helped to improve the quality of the work.

## References

1. S. Åkesson and A. Hedenström, "How migrants get there: migratory performance and orientation," *BioScience* **57**, 123–133 (2007).
2. T. Alerstam and Å. Lindström, "Optimal bird migration: the relative importance of time, energy and safety," in *Bird Migration: Physiology and Ecophysiology*, E. Gewinner, ed. (Springer-Verlag, 1990), pp. 331–351.

3. T. Alerstam, A. Hedenström, and S. Åkesson, "Long-distance migration: evolution and determinants," *Oikos* **103**, 247–260 (2003).
4. B. Bruderer and F. Liechti, "Intensität, Höhe und Richtung von Tag- und Nachtzug im Herbst über Südwestdeutschland," *Ornithol. Beob.* **95**, 113–128 (1998).
5. S. Zehnder, S. Åkesson, F. Liechti, and B. Bruderer, "Nocturnal autumn bird migration at Falsterbo, south Sweden," *J. Avian Biol.* **32**, 239–248 (2001).
6. P. Kerlinger and F. R. Moore, *Atmospheric Structure and Avian Migration* (Plenum, 1989).
7. Å. Lindström, "The role of predation risk in stopover habitat selection in migrating bramblings, *Fringilla montifringilla*," *Behav. Ecol.* **1**, 24–35 (1990).
8. P. Henningsson, G. Spedding, and A. Hedenstrom, "Vortex wake and flight kinematics of a swift in cruising flight in a wind tunnel," *J. Exp. Biol.* **211**, 717–730 (2008).
9. I. Newton, *The Migration Ecology of Birds* (Academic, 2008).
10. D. W. H. Adams, "Radar observations of bird migration in Cyprus," *Ibis* **104**, 133–146 (1962).
11. T. Alerstam, "Nocturnal migration of thrushes (*Turdus* spp.) in southern Sweden," *Oikos* **27**, 457–475 (1976).
12. T. Alerstam, J. Bäckman, G. A. Gudmundsson, A. Hedenström, S. S. Henningsson, H. Karlsson, M. Rosén, and R. Strandberg, "A polar system of intercontinental bird migration," *Proc. R. Soc. B* **274**, 2523–2530 (2007).
13. M. B. Casement, "Migration across the Mediterranean observed by radar," *Ibis* **108**, 461–491 (1966).
14. J. L. F. Parslow, "The migration of passerine night migrants across the English Channel studied by radar," *Ibis* **111**, 48–79 (1969).
15. B. Bruderer and F. Liechti, "Quantification of bird migration—different means compared," in *Proceedings of the Bird Strike Committee, Europe*, Vol. 22 (Bird Strike Committee Europe, 1994), pp. 243–254.
16. S. Åkesson, "Coastal migration and wind drift compensation in nocturnal passerine migrants," *Ornis Scand.* **24**, 87–94 (1993).
17. S. A. Gauthreaux, Jr., "A portable ceilometer technique for studying low level nocturnal migration," *Bird Banding* **40**, 309–320 (1969).
18. F. Liechti, "Calibrating the moon-watching method—changes and limits," *Avian Ecol. Beh.* **7**, 27–41 (2001).
19. F. Liechti, D. Peter, R. Lardelli, and B. Bruderer, "Herbstlicher Vogelzug im Alpenraum nach Mond-beobachtungen—Topographie und Wind beeinflussen den Zugverlauf," *Ornithol. Beob.* **93**, 131–152 (1996).
20. S. A. Gauthreaux and J. W. Livingston, "Monitoring bird migration with a fixed-beam radar and a thermal-imaging camera," *J. Field Ornithol.* **77**, 319–328 (2006).
21. F. Liechti, B. Bruderer, and H. Paproth, "Quantification of nocturnal bird migration by moonwatching: comparison with radar and infrared observations," *J. Field Ornithol.* **66**, 457–468 (1995).
22. A. Farnsworth, S. A. Gauthreaux, Jr., and D. van Blaricom, "A comparison of nocturnal call counts of migrating birds and reflectivity measurements on Doppler radar," *J. Avian Biol.* **35**, 365–369 (2004).
23. A. Farnsworth and I. J. Lovette, "Evolution of nocturnal flight calls in migrating wood-warblers: apparent lack of morphological constraints," *J. Avian Biol.* **36**, 337–347 (2005).
24. B. J. Stutchbury, S. A. Tarof, T. Done, E. Gow, P. M. Kramer, J. Tautin, J. W. Fox, and V. Afanasyev, "Tracking long-distance songbird migration by using geolocators," *Science* **323**, 896–896 (2009).
25. J. Meade, D. Biro, and T. Guilford, "Homing pigeons develop local route stereotypy," *Proc. R. Soc. B* **272**, 17–23 (2005).

26. T. Alerstam, M. Rosén, J. Bäckman, P. G. Ericson, and O. Hellgren, "Flight speeds among bird species: allometric and phylogenetic effects," *PLoS Biol.* **5**, 1656–1662 (2007).
27. J. Bäckman and T. Alerstam, "Confronting the winds: orientation and flight behaviour of roosting swifts, *Apus apus*," *Proc. R. Soc. B* **268**, 1081–1087 (2001).
28. B. Bruderer and E. Weitnauer, "Radarbeobachtungen über Zug und Nachtflüge des Mauerseglers (*Apus Apus*)," *Rev. Suisse Zool.* **79**, 1190–1200 (1972).
29. G. E. Hill and K. J. McGraw, *Bird Coloration, Mechanisms and Measurements*, Vol. 1 (Harvard University Press, 2006).
30. H. Noh, S. F. Liew, V. Saranathan, S. G. J. Mochrie, R. O. Prum, E. R. Dufresne, and H. Cao, "How noniridescent colors are generated by quasi-ordered structures of bird feathers," *Adv. Mat.* **22**, 2871–288 (2010).
31. M. Brydegaard, P. Lundin, Z. G. Guan, A. Runemark, S. Åkesson, and S. Svanberg, "Feasibility study: fluorescence lidar for remote bird classification," *Appl. Opt.* **49**, 4531–4544 (2010).
32. M. A. Mycek and B. W. Pogue, eds., *Handbook of Biomedical Fluorescence* (CRC Press, 2003).
33. N. Takeuchi, "Elastic lidar measurement of the troposphere," in *Laser Remote Sensing*, T. Fujii and T. Fukuchi, eds. (CRC Press, 2005), pp. 63–122.
34. C. M. R. Platt, J. C. Scott, and A. C. Dilley, "Remote sounding of high clouds. part VI: optical properties of mid-latitude and tropical cirrus," *J. Atmos. Sci.* **44**, 729–747 (1987).
35. R. G. Strauch, V. E. Derr, and R. E. Cupp, "Atmospheric temperature measurement using Raman backscatter," *Appl. Opt.* **10**, 2665–2669 (1971).
36. G. Benedetti-Michelangeli, F. Gongeduti, and G. Fiocco, "Measurement of aerosol motion and wind velocity in the lower troposphere by Doppler optical radar," *J. Atmos. Sci.* **29**, 906–910 (1972).
37. R. Grönlund, M. Sjöholm, P. Weibring, H. Edner, and S. Svanberg, "Elemental mercury emissions from chlor-alkali plants measured by lidar techniques," *Atmos. Environ.* **39**, 7474–7480 (2005).
38. N. Menyuk, D. K. Killinger, and W. E. DeFeo, "Remote sensing of NO using a differential lidar," *Appl. Opt.* **19**, 3282–3286 (1980).
39. Z. G. Guan, P. Lundin, L. Mei, G. Somesfalean, and S. Svanberg, "Vertical lidar sounding of atomic mercury and nitric oxide in a major Chinese city," *Appl. Phys. B* **101**, 465–470 (2010).
40. J. Gelbwachs and M. Birnbaum, "Fluorescence of atmospheric aerosols and lidar implications," *Appl. Opt.* **12**, 2442–2447 (1973).
41. P. Weibring, T. Johansson, H. Edner, S. Svanberg, B. Sundnér, V. Raimondi, G. Cecchi, and L. Pantani, "Fluorescence lidar imaging of historical monuments," *Appl. Opt.* **40**, 6111–6120 (2001).
42. A. Ounis, Z. G. Cerovic, J. M. Briantais, and I. Moya, "DE-FLIDAR: a new remote sensing instrument for estimation of epidermal UV absorption in leaves and canopies," in *Proceedings of the European Association of Remote Sensing Laboratories (EARSeL)-SIGWorkshop LIDAR*, Vol. 1 (EARSeL, 2000), pp. 196–204.
43. S. Svanberg, "LIDAR," in *Springer Handbook of Lasers and Optics*, F. Träger, ed. (Springer-Verlag, 2007), pp. 1031–1052.
44. T. Fujii and T. Fukuchi, eds., *Laser Remote Sensing* (CRC Press, 2005).
45. R. B. Bradbury, R. A. Hill, D. C. Mason, S. A. Hinsley, J. D. Wilson, H. Balzter, G. Q. A. Anderson, M. J. Whittingham, I. J. Davenport, and P. E. Bellamy, "Modelling relationships between birds and vegetation structure using airborne lidar data: a review with case studies from agricultural and woodland environments," *Ibis* **147**, 443–452 (2005).
46. R. Clawges, K. Vierling, L. Vierling, and E. Rowell, "The use of airborne lidar to assess avian species diversity, density, and occurrence in a pine/aspen forest," *Remote Sens. Environ.* **112**, 2064–2073 (2008).
47. N. E. Seavy, J. H. Viers, and J. K. Wood, "Riparian bird response to vegetation structure: a multiscale analysis using lidar measurements of canopy height," *Ecol. Appl.* **19**, 1848–1857 (2009).
48. P. Weibring, H. Edner, and S. Svanberg, "Versatile mobile lidar system for environmental monitoring," *Appl. Opt.* **42**, 3583–3594 (2003).
49. R. O. Prum, "Anatomy, physics and evolution of structural colors," in *Bird Coloration, Mechanisms and Measurements*, G. E. Hill and K. J. McGraw, eds., Vol. 1 (Harvard University Press, 2006), pp. 295–354.
50. M. Srinivasarau, "Nano-optics in the biological world," *Chem. Rev.* **99**, 1935–1961 (1999).
51. C. Giacobazzo, H. L. Monaco, G. Artioli, D. Viterbo, G. Ferraris, G. Gilli, G. Zanotti, and M. Catti, *Fundamentals of Crystallography* (Oxford University Press, 2002).
52. N. S. Hart, J. C. Partridge, and I. C. Cuthill, "Visual pigments, cone oil droplets and cone photoreceptor distribution in the European starling (*Sturnus vulgaris*)," *J. Exp. Biol.* **201**, 1433–1446 (1998).
53. Z. G. Guan, M. Brydegaard, P. Lundin, M. Wellenreuther, A. Runemark, E. I. Svensson, and S. Svanberg, "Insect monitoring with fluorescence lidar techniques: field experiments," *Appl. Opt.* **49**, 5133–5142 (2010).
54. C.V. Raman, "The theory of the Christiansen experiment," *Proc. Indian Acad. Sci.* **A29**, 381–390 (1949).
55. G. B. Benedek, "Theory of transparency of the eye," *Appl. Opt.* **10**, 459–473 (1971).
56. R. O. Prum and R. H. Torres, "A Fourier tool for the analysis of coherent light scattering by bio-optical nanostructures," *Integr. Comp. Biol.* **43**, 591–602 (2003).
57. S. Svanberg, *Atomic and Molecular Spectroscopy—Basic Aspects and Practical Applications*, 4th ed. (Springer-Verlag, 2004).
58. U. Rascher, B. Gioli, and F. Miglietta, "FLEX—fluorescence explorer: a remote sensing approach to quantify spatio-temporal variations of photosynthetic efficiency from space," *Photosynth. Res.* **91**, 293–294 (2007).
59. S. Hunt, A. T. Bennett, I. C. Cuthill, and R. Griffiths, "Blue tits are ultraviolet tits," *Proc. R. Soc. Lond. B* **265**, 451–455 (1998).

## PAPER XV

### **On the exploitation of mid-infrared iridescence of plumage for remote classification of nocturnal migrating birds**

M. Brydegaard, P. Samuelsson, M.W. Kudenov and S. Svanberg  
*Submitted.*

# On the Exploitation of Mid-Infrared Iridescence of Plumage for Remote Classification of Nocturnal Migrating Birds.

M. Brydegaard<sup>1\*</sup>, P. Samuelsson,<sup>1</sup> M. W. Kudenov<sup>2</sup> and S. Svanberg,<sup>1</sup>

<sup>1</sup>Atomic Physics Division, Lund University, P.O. Box 118, SE-221 00 Lund, Sweden

<sup>2</sup>College of Optical Science, University of Arizona, 1630 E. University Blvd. 94, Tucson, AZ 85721, USA

\*Corresponding author: [mikkel.brydegaard@fysik.lth.se](mailto:mikkel.brydegaard@fysik.lth.se)

**A challenging task in ornithology lies in identifying high altitude nocturnal migrating bird species and genders. While the current approaches including RADAR, lunar obscuration and single band thermal imaging provide means for detection, a more detailed spectral or polarimetric analysis of light has the potential for retrieval of additional information whereby the species and sex could be determined. In this paper we explore remote classification opportunities provided by iridescent features within feathers in the mid-infrared region. Our approach first involves characterizing the microstructural features of the feather using rotation and straining, and a scheme for their remote detection is proposed by correlating these microstructural changes to spectral and polarimetric effects. Furthermore, we simulate the spectral signature of the entire bird using a model, which demonstrates how classification would be achieved. Finally, we apply infrared hyperspectral polarization imaging showing that the net iridescent effect persists for the bird as a whole.**

*OCIS codes: 010.0280 Remote sensing and sensors, 010.3640 Lidar, 280.1100 Aerosol detection, 300.6340 Spectroscopy, infrared, 310.6628 Sub-wavelength structures, nanostructures.*

## Identifying nocturnal migrating birds

### *Background and motivation*

Birds are one of the less abundant constituents of the atmosphere; however, they can be found inhabiting ecosystems ranging from the Arctic to Antarctica. Birds can be found throughout the biosphere from 500 m below sea level (e.g. the Emperor penguin)<sup>1</sup> to more than 12 km above sea level (e.g., the Rüppel's vulture)<sup>2</sup>. The wingspan ranges two orders of magnitudes from 64 mm (Bee hummingbird) to 3.5 m (Wandering albatross). Birds contain the largest number of species among vertebrates, counting roughly ten thousands species, where the appearance of each species additionally varies with the gender, the juvenile/adult stage, season, and nutrition. Apart from their daily routines, certain bird species can undertake long migratory flights traveling up to 74.000 km per year (Sooty Shearwaters)<sup>3</sup>. As such, migrating birds are, to a great extent responsible for the global gene flow, not only transporting their own genetic material but also that of plant seeds, parasites, bacteria and viruses. For this reason the migratory flight of birds is not only a concern of the migrants themselves, but also a concern for agriculture and for the health of humans and domestic animals.

Monitoring of bird movement is presently mostly performed by capture and marking with rings, RF-ID tags, radio transmitters, sun loggers or GPS devices. However, monitoring of unmarked individuals remains exceedingly challenging due to the fact that the majority of species choose to migrate during night at a typical altitude of several kilometers. The options available to detect these migrants include lunar obscuration<sup>4</sup>, thermal imaging<sup>5, 6</sup> and RADAR<sup>5-7</sup>. The information retrieved includes altitude, directional heading, wing beat frequency and shape of silhouette. Unfortunately, these parameters only provide a limited ability to discriminate between the various species. In previous work we have demonstrated the additional ability of fluorescence LIDAR to remotely retrieve chemical information related to the various chromophores<sup>8, 9</sup> found in bird coloration<sup>10, 11</sup>. State of the art fluorescence LIDARs have also recently been developed in relation to bio warfare aerosol monitoring<sup>12-15</sup>. In the present paper we will demonstrate how additional information, related to the microstructure of bird plumage, can be retrieved from far distances. The main components in feather structure, in order of decreasing size, consist of a rachis (or the central trunk), with attached barbs, which in turn have attached barbules. Although the

barbules are the smallest of the mentioned features, they have the largest contribution to the feather cross sectional area due to their numbers. The arrangement of the barbules can be thought of as Venetian blinds. Glimpses of the complexity of feather microstructure are found in several electron microscopy studies<sup>16-22</sup>. Furthermore, micro-structural discrimination has been successfully demonstrated for identifying the species and gender of birds<sup>18, 19</sup>. Therefore, adding new and complimentary dimensions to the retrieved parameter space will, together with ornithologist expertise, further reduce the group of possible species and genders in a classification problem.

## Infrared properties of feathers

### Spectroscopy

Following the discovery of an additional ultraviolet band and spectral-band narrowing in most avian visual systems, the visible and ultraviolet properties of plumage have been investigated for many species during the last century<sup>10, 11</sup>. However, the infrared region (0.7-25  $\mu\text{m}$ ) has, to a great extent, been left untouched. The near infrared (NIR) region (0.7-1.1  $\mu\text{m}$ ), visible to the silicon (Si) detectors, contains weak absorption signatures from eu- and pheo-melanin. We have previously also demonstrated large chlorophyll imprint in the spectral signature of birds due to reflected sub-illumination when flying daytime over vegetation<sup>9</sup>. The behavior of the Fraunhofer A terrestrial oxygen line at 760 nm reflected in birds was preliminarily investigated in<sup>23</sup>.

Iridescence refers to scenarios where the spectral shape of the reflectance from objects changes considerably depending on the angle of observation or illumination<sup>24</sup>. Visible iridescent features have been shown to extend out to the near infrared region<sup>25</sup>. In the InGaAs detector domain (0.9-2.4  $\mu\text{m}$ ) we have now briefly explored transmittance properties of single feathers and whole wings. The feathers included samples colored both by carotenoids and by eu- and pheo-melanin. Spectral transmittance was measured using a compact spectrometer (StellarNet,

model EPP2000 NIR InGaAs) in the range 0.9-1.7  $\mu\text{m}$ ; however, all samples showed an entirely flat transmittance and with no obvious angular dependence.

Beyond 1.7  $\mu\text{m}$ , we measured the transmittance of several wing feathers from a number of bird species using an FTIR instrument (ATI Mattson, Infinity AR60) in the spectral region 2-25  $\mu\text{m}$ . Details regarding the samples are summarized in Table 1. Single feathers were mounted in window-free transparency slide frames, which were in turn attached to a rotation stage. This enabled each feather to be rotated around the central trunk (rachis). The transmittance was then measured between  $-50^\circ$  and  $+50^\circ$  in  $5^\circ$  increments, with zero degrees corresponding to normal incidence. The resulting spectra at normal incidence from four selected species are depicted in Fig. 1. A common broad keratin absorption feature can be observed around 3  $\mu\text{m}$ , whereas the four spectra show substantial differences in shape in the MIR region (Mid-infrared 3-5  $\mu\text{m}$ ) for the different species. A sharp peak, due to the Christiansen effect, is observed at 6  $\mu\text{m}$ ; we will discuss this effect within the next section. It should be mentioned that, for wavelength exceeding 10  $\mu\text{m}$ , feathers will increasingly transmit as the thickness of the barbules (2  $\mu\text{m}$ ) approaches the sub-wavelength thin film regime<sup>26</sup>.

Examples of the angular dependence of the MIR transmission are shown in Fig. 2ab, which depicts the cases for a Turaco feather and a European Roller feather. When the angle of incidence is increased from normal, it can be seen that the center of mass of MIR transmittance experiences a red or blue shift for the Turaco and European Roller, respectively. For larger angles the distinct behavior becomes more complex. We remind the reader that *absorptive* spectral features have a similar influence on reflectance and transmittance; while *structural* features have an opposing effect on reflectance and transmittance.

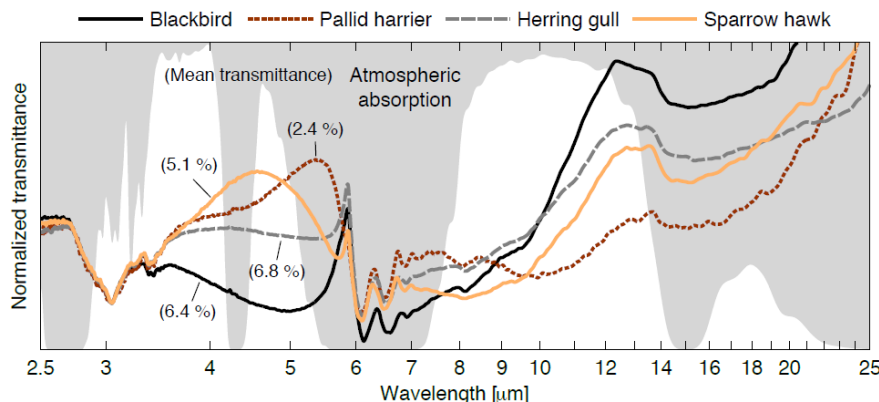


Fig. 1: Four different examples of transmission spectra from four different species. The spectra are measured from single feathers at normal incidence. The atmospheric transmission is superimposed. At 3  $\mu\text{m}$  an absorption band of keratin is seen. The 4-5  $\mu\text{m}$  is heavily influenced by structural features. The sharp features around 6  $\mu\text{m}$  arises in relation to the Christiansen effect. From 10  $\mu\text{m}$  and upward the transmission can be expected to increase according to the thin film approximation.

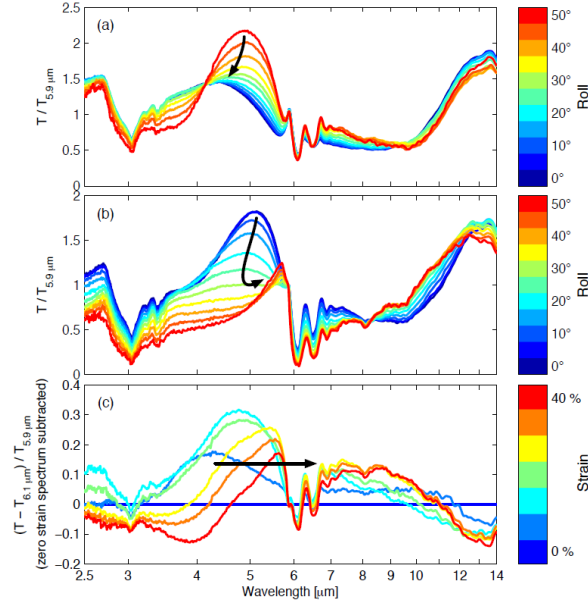


Fig. 2a: A feather from a European Roller illustrates that the center-of-mass of the MIR transmittance displaces to shorter wavelengths with increasing roll. 2b: In contrast a feather from a Turaco illustrates that the center of mass of the MIR transmittance displaces to longer wavelengths with increasing roll. 2c: Transmission spectra from a single herring gull feather when undergoing increased strain. The zero-strain spectrum has been subtracted. The experiment verifies that many of the spectral features are indeed structural. It also gives an idea of the spectral width of the structural feature.

In addition to the angular measurements, the transmittance of a Herring gull feather, was analyzed, for normal incidence illumination, while applying an incremental planar strain to the feather. The strain was oriented perpendicularly to the central rachis. Spectra were recorded from 0 to 40 percent strain. The applied strain alters the relative angle between the rachis and the barbs, as well as the angle between the barbs and the barbules. While the barbules are hooked together, their surface normal is expected to twist such that the inter barbule distance changes with the strain of the feather. The resulting spectra, with the baseline (i.e. 0% strain) spectrum subtracted are shown in Fig. 2c. The measurement illustrates that (1) the center of mass of the MIR transmittance is redshifted for increasing strain; and that (2) structural changes influence the transmission of the feather for wavelengths spanning 2-12  $\mu\text{m}$ . If we assume that the spectral transmittance feature is influenced solely by the spatial distribution of the barbules, then we would expect a 6  $\mu\text{m}$  spectral feature at full strain. However, keratin absorption and the Christiansen peak limit the amount of information available in this region. Furthermore, 6  $\mu\text{m}$  is within an opaque region of the atmospheric transmission<sup>27</sup>. The tension applied to the feathers during down-strokes and up-strokes, can be expected to vary

considerably during the wing beat cycle. Therefore we can expect the spectral signature of birds to vary during the wing beat cycle, solely due to the fact that the wing feathers experiences different strain.

### The Christiansen effect

The Christiansen effect, named after the doctoral supervisor of Niels Bohr, arises in two-compound matrixes at the spectral point where the refractive indices of the two constituents intersect<sup>28</sup>. The index matching causes scattering to vanish, and the light at this wavelength is transmitted ballistically through the matrix. The effect has been discussed occasionally in relation to atmospheric particles such as mineral dust<sup>29-31</sup>, ice crystals<sup>32-36</sup> and water droplets<sup>33</sup>. One interesting exploitation of this effect, in relation to atmospheric scatterers, would be the possibility of undistorted imaging through clouds. The effect was also observed in larger bioaerosols such as insects<sup>37</sup> and birds<sup>38, 39</sup>. The bird aspects were published by a group investigating heat radiation transfer in penguin down and plumage. The authors suggested a reciprocal extrapolation of the refractive index of keratin to the point of intersection with the refractive index of air. From our understanding, the phenomenon is slightly more complicated since the refractive index couples with the absorption through the Kramers-Kronig relations<sup>40</sup>. The derivative like relation implies that the refractive index is higher on the long-wavelength flank of an absorption band,  $\mu_a(\lambda)$ , and lower on the short-wavelength flank, as portrayed in Fig. 3. Since the coupling between absorption and refractive index increases linearly with  $\lambda$ , Christiansen effects in air-solid matrixes are typically found in the infrared region<sup>29-33, 35, 36, 41, 42</sup>. The change in refractive index will cause the scattering coefficient,  $\mu_s(\lambda)$ , to significantly deviate<sup>43</sup> from the usual  $\mu_s(\lambda) = b \lambda^{-a}$  behavior claimed in tissue optics<sup>44</sup>. Instead, the scattering coefficient would experience two minima on the short wavelength slope of the absorption band of the solid constituent; namely at the two spectral points,  $\lambda_0$  and  $\lambda_1$ , where the refractive index of the solid intersects the refractive index of air, and index matching is achieved (See Fig. 3). On the longer wavelength slope of the absorption band the large difference in refractive index instead leads to increased scattering. When adding  $\mu_a(\lambda)$  and  $\mu_s(\lambda)$  to obtain the total attenuation coefficient for the ballistic light ( $\mu_{att}(\lambda) = \mu_a(\lambda) + \mu_s(\lambda)$ ), the scattering minimum closest to the absorption maximum is to some extent cancelled out, whereas the scattering minimum furthest away from the absorption maximum leaves a prominent dip in the total attenuation coefficient (See Fig. 3). Since the Christiansen effect takes place on the slope of the absorption feature, the attenuation

dips are slightly displaced towards shorter wavelengths with respect to the scattering dips at the Christiansen wavelengths,  $\lambda_{Chr}$  (See Fig. 3). When feeding the attenuation coefficient,  $\mu_{att(\lambda)}$ , to the Beer-Lambert law, a sharp pronounced transmission peak is seen followed by smaller transmission peak. The effect is easily seen in downy feathers, but it can also be observed in single feathers. Here, the Christiansen effect is most pronounced for the Blackbird and Herring gull in Fig. 1 around  $6 \mu\text{m}$ . Similar features can be seen throughout Fig. 2. Imaging a bird at  $\lambda_{Chr}$  would result in a nude bird picture. Unfortunately, it would only work over very short distances since the atmosphere is opaque in this region. Furthermore, because this effect occurs close to an absorption band in the solid, scatter-free ballistic imaging is only achieved at expense of poor transmission. This dilemma resembles problems with other attempts to achieve scatter-free imaging by means of absorption<sup>45, 46</sup>.

It is noteworthy that there are two different scenarios when the Christiansen effect occurs. In our case, the refractive index of  $\beta$ -keratin decreases to that of air in the shorter flank of the solid absorption feature. The other possibility is that the refractive index of gas increases to that of the solid on the longer flank of, for instance, a strong gas atomic absorption line<sup>47, 48</sup>. Although this might be a challenging achievement, it would certainly provide interesting applications and implication for optical analysis and imaging inclusions in fibrous and porous materials<sup>49-51</sup>.

### Spectral broadening and interference filtering of black bodies

When considering thermal emission from a body, where the outermost layer is a microstructure giving rise to interference effects, the layer will to a greater extent transmit some spectral regions while reflecting other spectral regions inwards. It is noteworthy, that the inwards reflected photons are likely to be absorbed and reemitted with a new Planck profile - at this time including the spectral regions which previously escaped. This means that light would be given additional chances of escaping in the regions where the microstructure transmits thanks to the spectral broadening taking place during the photon migration in the thermal regime; see Fig. 4. An analogy to such broadening is also known from thick plasma emissions, e.g. around the mercury 254 nm line in a high-pressure mercury lamp.

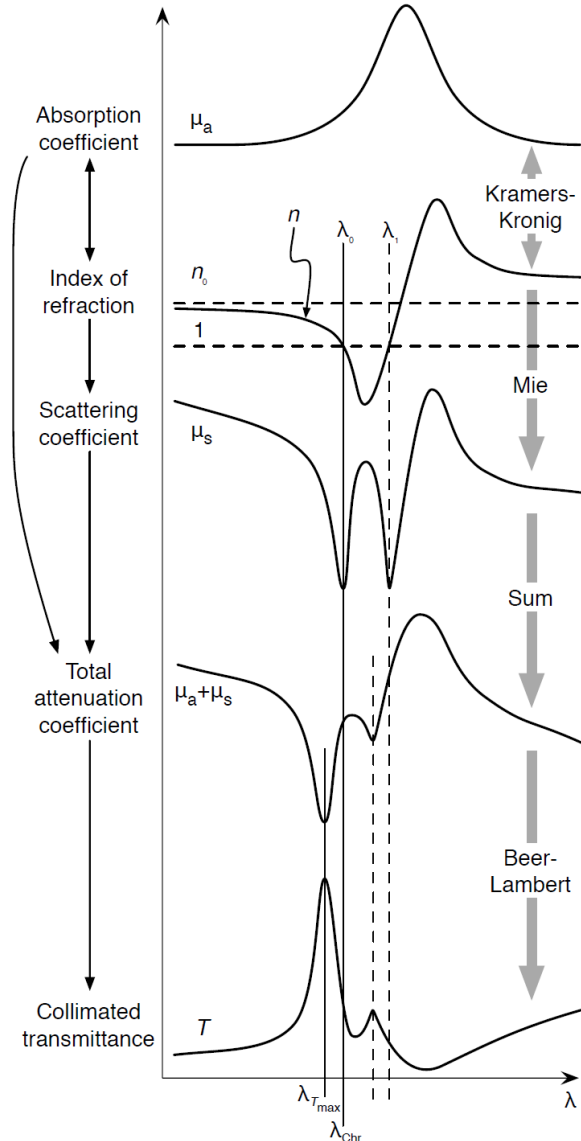


Fig. 3: Sketch showing related properties and phenomena in the spectral domain. From above: A MIR absorption feature given by  $\mu_a$  will be complimented by a deviation in refractive index,  $n$ , in respect to the refractive index far from the absorptive feature,  $n_0$  (causality and the Kramer-Kronig relation). If the deviation exceeds the difference to the refractive index of the surrounding media (in our case air) index matching will occur at two wavelengths,  $\lambda_{Chr0}$  and  $\lambda_{Chr1}$ , leading to the Christiansen effect. The index matching will cause Mie scattering,  $\mu_s$ , to vanish at two wavelengths; also the scattering coefficient will be increased on the long side slope of the absorption feature. When considering the coefficient for total attenuation of ballistic light,  $\mu_{att} = \mu_a + \mu_s$ , an attenuation minimum,  $\lambda_{Tmax}$ , results at a slightly shorter wavelength than  $\lambda_{Chr0}$ . When measuring the ballistic transmission, the effects will generate a sharp transmittance peak followed by a smaller peak. Notice the resemblance to, e.g. the Blackbird spectrum in Fig.1.

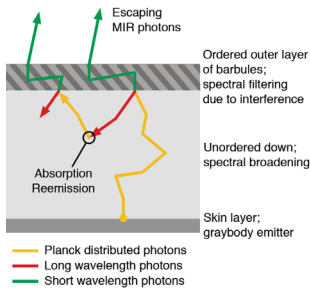


Fig. 4: Photo migration in the thermal regime can be expected to be highly inelastic. Thermal emission from a structured body where interference phenomena occur at the surface can be expected to show spectrally enhanced emission due to the fact that the light reflected inwards will be absorbed and reemitted with a new Planck distribution. Thus it will have renewed chances of escaping in the band transmitted by the structure.

### Near infrared microscopy

From the feather spectroscopy results it can be concluded that the spatial properties at the micrometer scale are closely related to the transmittance properties at the corresponding wavelength scale. In order to confirm and assess the nature of this spatial-spectral correspondence, and to allow comparison to the spectroscopic results, we proceeded to develop a parameterization of the spatial distribution of the barbules within each feather. The feathers used in the transmittance measurement were imaged using the microscope described in<sup>52</sup>. The instrument was used in wide field transmission mode at 810 nm; see Fig. 5a. For each image, the 2D spatial power spectrum was computed using the fast Fourier transform (2D FFT); see Fig. 5b. Subsequently, a polar transformation was applied to the 2D spatial power spectrum, resulting in a 2D matrix images with power densities according to their orientation (See Fig. 5c) and a given spatial frequency. By applying the polar transform, the principal orientations with maximal spatial power densities could be found using a peak detection algorithm. In this way, two principal orientations were observed for each feather - see Fig. 5d - corresponding to angles perpendicular to distal and proximal barbule orientations. The two principal orientations are also shown as arrows in the lower right corner of Fig. 5a for reference. By indexing these orientations into the polar transform of the 2D power spectrum and finding the maximum within the region corresponding to 10-40  $\mu\text{m}$ , a direct measure of the mean barbule distance over the imaged region was established; see Fig. 5e. The particular example shown in Fig. 5 is for a feather from a Sparrow hawk. The parameterizations of all the samples are presented in Table 1.

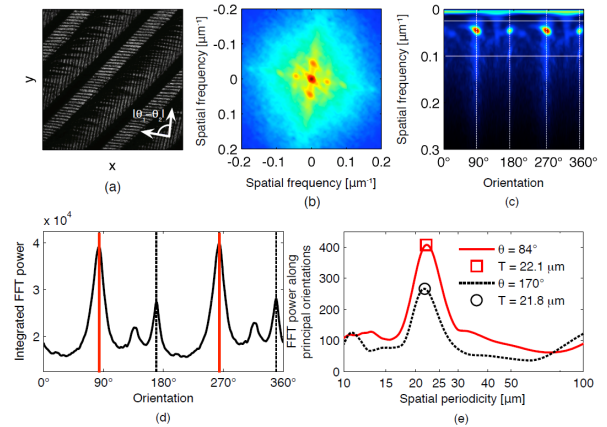


Fig. 5: Steps of the parameterization of dominant spatial frequencies in the  $x$ - $y$  domain. 5a: Transmission microscopy image at 810 nm of barbules structures from Sparrow hawk feather. 5b: The corresponding 2D spatial Fourier power spectrum. 5c: Polar spatial transform of the 2D spatial power spectrum. 5d: Extracted dominant orientations from polar transform. 5e: Extracted dominant features in radial spatial power spectrum from the dominant orientations. The two dominant orientations are also showed for reference in the lower right corner of Fig. 5a.

Table 1

Latin species name	Trivial name	Color / body part	$ \theta_1 - \theta_2 $ ( $^\circ$ )	$T_1$ ( $\mu\text{m}$ )	$T_2$ ( $\mu\text{m}$ )	Figure
<i>Turdus merula</i>	Blackbird	Black/side	$73.0 \pm 1.5$	$18.0 \pm 0.9$	$16.9 \pm 1.7$	1, 7, 8
<i>Circus macrourus</i>	Pallid harrier	Grey/side	$45.5 \pm 15.5^*$	$24.6 \pm 1.0$	$22.4 \pm 5.1^*$	1, 7, 8
<i>Larus argentatus</i>	Herring gull	White/side	$64.6 \pm 1.7$	$20.9 \pm 1.0$	$21.9 \pm 0.4$	1, 2
<i>Accipiter nisus</i>	Sparrow hawk	Brown/side	$84.9 \pm 3.6$	$23.2 \pm 2.6$	$22.4 \pm 2.4$	1, 5, 7, 8
<i>Lorius garrulus</i>	Chattering lory	Red/side	$55.5 \pm 2.5$	$20.8 \pm 0.9$	$17.6 \pm 0.8$	7, 8
<i>Coracias garrulus</i>	European roller	Cyan/side	$66.8 \pm 2.3$	$21.6 \pm 1.0$	$21.6 \pm 1.0$	2,
<i>Corvus frugilegus</i>	Rook	Black/side	$47.2 \pm 32.6^*$	$18.7 \pm 1.9$	$23.0 \pm 11.4^*$	7, 8
<i>Tauraco porphyreoleop</i>	Turaco	Blue/side	$59.9 \pm 2.2$	$20.9 \pm 0.7$	$19.0 \pm 0.6$	2, 7, 8
<i>Anas platyrhynchos</i>	Male mallard	Belly	No microscopy	No microscopy	No microscopy	9, 10, 11, 12

\* Large standard deviation since only one barbule orientation and corresponding periodicity could be reliably determined.

### Proposed remote assessment of microscopic information

#### Remote microscopy

In the times of the newly introduced super-resolution microscopy<sup>53, 54</sup> much effort is invested discussing novel ways to break Ernst Karl Abbe's diffraction resolution limit dating back from 1874. Although the criterion still mainly holds true for image formation in the X-Y domain, it does not imply that statistical information regarding much smaller structures cannot be acquired even with the hopeless numerical apertures for the case of telescopes. One of the most widely known examples is the retrieval of atomic composition of stars over light years distance in astronomy. Here, information on the picometer sized atoms can be concluded by analysis of the emitted light in the spectral domain<sup>55</sup>. Similarly,

multispectral molecular imaging has widespread applications in remote sensing and earth observation of, for example, the nanometer sized chlorophyll molecule inferred by satellites orbiting at hundreds of kilometers altitude<sup>56</sup>. Even in the case of aerosols, several hundreds of nanometers in size, precise size distributions can be estimated from kilometers distance, e.g., by multi-frequency- or broad-band LIDARs<sup>57, 58</sup> - this thanks to the size dependent scattering properties of the tiny particles. Remote aerosol particle size estimation has even been demonstrated by analysis of the Christiansen effect<sup>29, 33</sup> (See special paragraph above). One example of assessing the microstructure information in a solid is the satellite based age estimation of snow<sup>59</sup>. Although entirely white in the visible regime, its infrared incoherent reflectance is dominated by the strong absorption of ice. While the absorption spectrum of ice is time invariant, its reflectance is time dependent. This is because the reflectance is governed by the absorption weighted by the interrogation path-length, which is scaled by the scattering coefficient. As the microstructure of the snow collapses over time, the scattering coefficient decreases and the interrogated path length increases, this consequently leads to an augmented absorption imprint in the reflectance. In this way snow can be studied on a microscopic level from a distance of hundreds of kilometers.

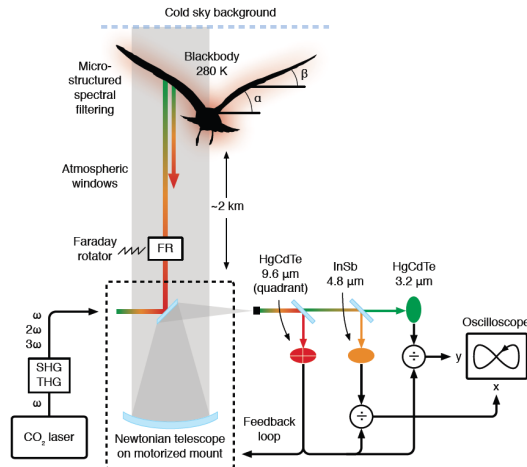


Fig. 6: Proposed implementation of remote microscopy for classification of night migrating birds at high altitude. Active illumination could be achieved by frequency doubling and tripling of a pulsed CO<sub>2</sub> laser, a Faraday rotator could be used to scan the polarization in respect to the orientation of the microstructure in the plumage. The reflected or passively emitted light is collected by a motorized Newtonian telescope. A dichroic beam splitter directs the thermal radiation to a quadrant detector used for feedback to the tracking telescope. The MIR is further separated in long- and short-wavelength radiation. The normalized emissions produce species characteristic Lissajous-like figures according to the feather microstructure.

When attending the coherent part of the reflectance, interference phenomena arise due to

dominant spatial frequencies, not the least in quasi-ordered biological matrices<sup>60</sup>. Such structures create a variety of optical phenomena including structural colors<sup>20, 61-66</sup>, multiple-beam interference, thin film effects<sup>67-69</sup> and diffraction. Although the level of ordering is not as high as in crystallography<sup>66, 70</sup>, the aforementioned optical phenomena can create dominant features in the spectral reflectance. Structurally generated colors can either be non-iridescent, as is the case for spherically symmetric dominant spatial frequencies, or they can be iridescent when the dominating spatial frequency depends on the spatial orientation. Iridescent spectral features are heavily tabooed in the remote sensing community due to the fact that the contribution to the reflectance is highly problematic and to a great extent spoils the pedagogical message of linear decomposition and spectral classification. Even if iridescent features are unfeasible to exploit in most remote sensing scenarios, there is one exception - the inherent angular scanning case of aerosol particles referred to as birds<sup>9</sup> and insects<sup>69</sup> during their natural wing beat cycle.

### Possible optical schemes

Inferring information about the feather microstructure of nocturnal migrants at high altitude would require the measurement of one or more wing beat cycles. For this purpose, the setup should preferably employ tracking by using a quadrant detector. Such detectors have been extensively developed in relation to air warfare in both mid- and thermal infrared regions; e.g.<sup>71, 72</sup>. To optically resolve a typical passerine migrant at a wavelength of 10 μm, with a wingspan of 10 cm flying at 2 km altitude (this will be the model migrant for the following estimations), it would require a telescope aperture of at least 20 cm and f/6. Such telescopes are commercially available, e.g. for amateur astronomy purposes, e.g.<sup>73</sup> (Conversely, detailed thermal image formation of migrants would require a much larger telescope). Applying the lens formula for such telescope, the aforementioned migrant would result in a spot in the order of 60 μm, well below available quadrant detector sizes<sup>71</sup>. The second concern is the photon collection efficiency in order to sample fast enough. The smallest of birds have wing beat frequencies of 50 Hz, implying that the Nyquist minimal sampling frequency should be at least 100 Hz. For a detailed representation of the waveform, also including the harmonic frequencies produced by iridescent features, the sampling frequency should reasonably be on the order of 1 kHz.

Passive detection schemes would rely on the photon emission rate of the bird and on the reflected sub-illumination from the earth. The metabolism of

migrating birds generates in the order of  $2W$ <sup>74, 75</sup>. Approximately 80% of this is dissipated by convection, 10% by evaporation, and 10% is irradiated. However, only a fraction (20%) of the power is emitted within the atmospheric windows, and only half of that fraction is radiated downwards. Thus, metabolism thermal emission delivers roughly 20 mW. Wings, constituting the largest optical cross section, can be assumed to be at ambient temperature<sup>76, 77</sup>. Using Stefan-Boltzmann's law, an estimate of downward emitted power is in the order of 600 mW. The exposure to upwelling illumination from earth on the bird is approximately 400 mW<sup>78</sup>. In comparison, it is exposed to 10 W of sunlight during daytime. Considering an emissivity of 0.95<sup>77</sup>, the reflected upwelling radiation is in the order of 20 mW. For all above mentioned thermal emissions the mid-infrared emission only constitutes roughly 6%, and the remaining 94% is emitted in the thermal window. Another passive scheme for consideration is the lunar obscuration<sup>4</sup>, where the iridescent feature is assessed in transmission. However, this would expose the bird to only 25  $\mu W$  of moonlight. From this 2% is emitted in the mid-infrared, 0.5% in the thermal window and the remaining 97% at shorter wavelengths. Additionally, full body transmittance which is dominated by light seeping through the wings, is more than one order of magnitude less than the reflectance. Therefore we can conclude that the transmitted moon light is always negligible in comparison to the other contributions. Emission powers are summarized in Table 2. All emitted powers from the bird can be directly compared and would, in both passive and active schemes, experience the same spherical attenuation over the 2 km altitude where the only essential gain factor is the aperture of the telescope.

Table 2.

Contribution to down welling radiation from a 10x10 cm bird	Mid-infrared, 3-5 $\mu m$	Thermal infrared, 8-14 $\mu m$
Planck emission	36 mW	560 mW
Reflected upwelling radiation	1 mW	19 mW
Radiated metabolism	1 mW	19 mW
Transmitted moon light	1 nW	300 pW

Active schemes would employ a pulsed mid-infrared laser. Both mid- and thermal infrared lasers are eye safe because of the opaqueness of water in the cornea<sup>79</sup>. Therefore, the major power limitation arises from possibly overheating of the bird. It is considered that one reason for most migrants to choose high altitude nocturnal migration is to avoid overheating<sup>75</sup>. Thus, exposing a bird to an equivalent of 10W of sunlight could clearly disturb the bird.

Assuming 1 W average exposure implies  $100 W/m^2$ . Using a typical LIDAR beam divergence of 1 mrad for a bird flying at an altitude of 2 km limits the laser source to 400 W. Assuming a 5% reflectance yields 50 mW of returned power. Since this is on the same order of magnitude as the Planck emission, according to Table 2, there is no reason to illuminate the bird with a continuous wave laser, since no signal increase would result, only possible disturbance of the bird. With a pulsed laser emitting 400 mJ pulses of 10 ns width at 1 kHz repetition (the required sampling frequency) the peak power impinging on the bird would be 100 kW, yielding several orders of magnitude improvement over the passive methods. Even slower repetition rates could be considered by indexing the measurements over several wing beat cycles using the phase from the passive thermal infrared modulation.

Following these considerations, the only commercially available sources candidates are pulsed CO<sub>2</sub> lasers<sup>80</sup> (not considering the military grade chemical deuterium fluoride lasers<sup>81</sup> at 3.8  $\mu m$ ). CO<sub>2</sub> lasers can be constructed with average powers up to 100 kW<sup>82</sup>. Pulsed or mode locked CO<sub>2</sub> lasers emit microsecond<sup>82</sup>, nanosecond<sup>83-87</sup> or picosecond pulses<sup>88</sup>. CO<sub>2</sub> lasers emit the fundamental frequency at 10.6  $\mu m$  or 9.6  $\mu m$ , which in turn can be doubled and tripled with efficiencies of the order of 6% and 2%, respectively<sup>84</sup>. The harmonics at 4.8  $\mu m$  and 3.2  $\mu m$  fall into the mid infrared atmospheric windows. The major components including fast InSb and HgCdTe detectors for LIDAR based on the CO<sub>2</sub> laser harmonics are presented in<sup>89-92</sup>. LIDAR schemes for remote microstructural assessment would be based on the emission of the fundamental thermal infrared line (for normalization purpose) and one or two harmonic frequencies. An additional advantage of active illumination is the control of polarization in respect to the orientation of the microfibers on the bird. By introducing a Faraday rotator prior to the emission of the laser beam an additional dimension is added to the recorded parameter space. Mid infrared (MIR) Faraday rotators are commercially available for Q-switched lasers; see e.g.<sup>93</sup>. Our proposed realization of remote microscopy for bird classification is shown in Fig. 6. Such system have close resemblance to military systems referred to as infrared search and tracking (IRST) systems<sup>94, 95</sup>; another scheme for dual band detection was previously developed in our research group<sup>96</sup>.

### The wing-beat cycle in a mid-infrared color space

We have previously demonstrated the possibility of the iridescence to produce harmonics of the spectral modulation during wingbeats<sup>9, 97</sup>. In the same paper, we also argued that improved classification can be expected by taking into account the full trajectory in an appropriate color space produced during the wing beat cycle. To illustrate this we have simulated the infrared signatures sampled in a few realistic spectral bands, for example the ones produced by a CO<sub>2</sub> laser and its corresponding harmonics. To do this, we used the FTIR data from the angular scans of several species. Although our instrument operates in transmission mode, structural colors are present in both transmission and reflection. Therefore, we can expect similar behavior in either modality. The following examples are not meant as a precise reference look-up table for bird classification, but as a way to visualize the complex concept of classification based on color space trajectories. We apply the body symmetry and consider only one side of the bird. We divided the wing into two foldable segments. The angle of each segment, with respect to nadir, is denoted  $\alpha$  and  $\beta$ ; see Fig. 6. We relate  $\alpha$  and  $\beta$  to the phase in the wing beat cycle,  $\varphi$ , as follows:

$$\alpha(\varphi) = A \frac{(+1 - 4\sin(\varphi) - 2\cos(\varphi) + \cos(2\varphi))}{4} \quad \text{Eq. 1}$$

$$\beta(\varphi) = A \frac{(-1 - 4\sin(\varphi) + 2\cos(\varphi) - \cos(2\varphi))}{4}$$

Here,  $\alpha$  and  $\beta$  is the angle of the outer and inner segment in respect to nadir in degrees.  $A$  is the amplitude of the of wing flapping in degrees, we use  $A = 35^\circ$ ,  $\varphi$  is the phase in the wing beat cycle in degrees,  $\varphi = 0$  correspond to the point in time when the bird will have the largest cross section in a zenith observation. Equation 1 represents a simplified model for wing flapping, where the wings are straight on the down strokes and partly folded on the upstrokes. We combine the two segments of outer and inner wings into a single signature  $S$ .

$$S(\lambda, \varphi) = T(\lambda, \alpha(\varphi))\cos(\alpha(\varphi)) + T(\lambda, \beta(\varphi))\cos(\beta(\varphi)) \quad \text{Eq.2}$$

Here,  $T$  is the measured spectral transmittance for the feather. Whereas the absolute infrared emission or reflectance from a bird will mainly correspond to the optical cross section, MIR iridescence would produce oscillations even in the ratios between two or more spectral bands. To demonstrate the concept, we simulated the ratio between the signature,  $S$ , on a common CO<sub>2</sub> laser line and the second harmonic. Both lines are within atmospheric transparency.

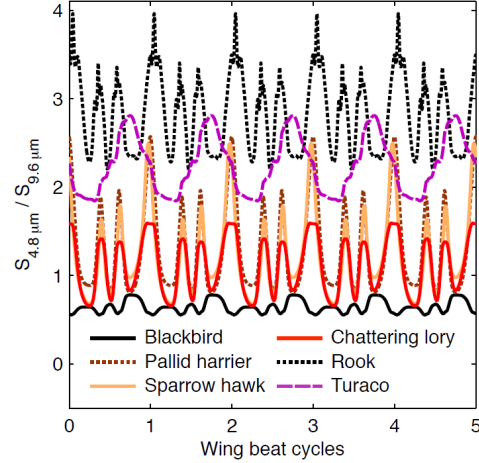


Fig. 7: A simple ratio between the signatures at 4.8  $\mu\text{m}$  and 9.6  $\mu\text{m}$  produces distinct waveforms for several species as a function of wing beats. Note the different biases, amplitudes, phases and harmonics.

The ratios for several birds are shown over five wing beats in Fig. 7. It is quickly realized that each waveform has a different bias, amplitude, harmonic content and phase. Note, that the phase is actually known since  $\varphi=0$  is the time when the optical cross-section and absolute signal is largest (during the down strokes). The aforementioned waveform parameters expand a multidimensional space that forms the basis for species classification and clustering.

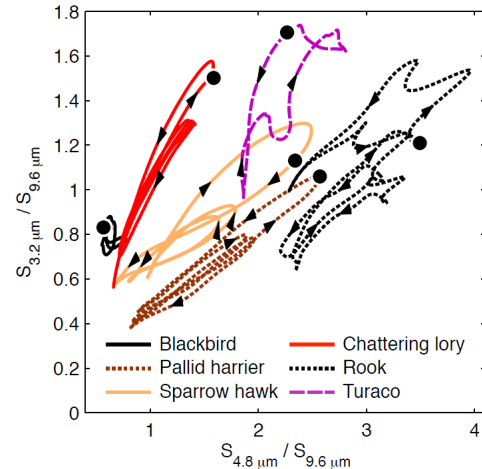


Fig. 8: Three spectral channels will allow classification based on detailed trajectories in a 2D color space resulting from the wing beat cycle. Here the normalized signature at 3.2  $\mu\text{m}$  is plotted against the normalized signature at 4.8  $\mu\text{m}$ . Trajectories for six species are plotted for comparison. The filled circles correspond to  $\varphi = 0$ , when the birds have their largest zenith cross section. The arrows show the direction of movement during the wing beat cycle. Note how the different species shows different trajectories in terms of position, modulation size, shape, phase and direction.

If we instead consider a system with three spectral bands, as illustrated in Fig. 6, we would obtain two

normalized ratios and the wing beat cycles will produce circulatory trajectories within a 2D color space. In Fig. 8 we have plotted such trajectories for several distinct species. While this graph is based on a transmittance signature and several rough approximations, similar measurements can be expected from a reflective detection scheme resembling that of Fig. 6. The trajectories in Fig. 8 produce different offset positions, shapes, modulation depths, and starting points. Furthermore, both clockwise and counter clockwise trajectories are found within different sub loops. Note the large modulations, on both ratios along the axis, demonstrating the considerable magnitude of the structural effects. The simulated data in Fig. 8 illustrate the advanced concept of species classification based on color space trajectories.

### Hyper spectral reflectance imaging of a whole bird

So far we have demonstrated iridescent features in the MIR for single feathers in transmittance. In order for these features to be feasible in a remote scenario the features would need to be present in reflectance for the bird as a whole. The spectral features and the angular dependence of adjacent feathers will need to add constructively, in order for an effective spectral modulation to arise from the wing beat cycle. To demonstrate this, we performed MIR hyper spectral imaging of a female mallard (*Anas platyrhynchos*) in reflectance mode using an instrument described in <sup>98-100</sup>. The sensor is an FTIR based imaging spectrometer operating from 1.4  $\mu\text{m}$  to 5  $\mu\text{m}$ . Apart from acquiring a continuous reflectance spectrum in every pixel, it also acquires all four Stokes parameters [ $s_0$   $s_1$   $s_2$   $s_3$ ], thus providing

a detailed description of the polarization after the light interacts with the sample. The sample was illuminated by an unpolarized filament tungsten lamp. The absolute reflectance,  $R$ , was estimated by normalizing with a known reference with flat reflectance throughout the spectral range of the instrument.

$$R_{x,y,\lambda,\Theta} = \frac{S_{0,x,y,\lambda,\Theta}}{S_{0,\{x,y\} \in \text{white},\lambda,\Theta}} \quad \text{Eq.3}$$

Here,  $x,y$  is the spatial coordinate in the image,  $\lambda$  is the MIR wavelength,  $\Theta$  is the roll of the bird. The degree of linear polarization,  $DOLP$ , is calculated

$$DOLP_{x,y,\lambda,\Theta} = \frac{\sqrt{S_{1,x,y,\lambda,\Theta}^2 + S_{2,x,y,\lambda,\Theta}^2}}{S_{0,x,y,\lambda,\Theta}} \quad \text{Eq.4}$$

and the orientation of the polarization is calculated

$$\Psi_{x,y,\lambda,\theta} = \tan^{-1} \left( \frac{S_{2,x,y,\lambda,\theta}}{S_{1,x,y,\lambda,\theta}} \right) \quad \text{Eq.5}$$

False-color MIR reflectance images for are presented for five different angles of roll in Fig. 9. Intensity normalized images are presented beneath. Note the mirrored coloration for the images for the negative rolls. The whole body reflectance,  $WBR$ , as a function of wing-nadir angle,  $\alpha$ , was estimated by matching either side of the bird with the other side for the negative roll angle:

$$WBR_{x,y,\lambda,\alpha} = \frac{R_{0,\{x,y\} \in \text{right},\lambda,\Theta} + R_{0,\{x,y\} \in \text{left},\lambda,-\Theta}}{2} \quad \text{Eq.6}$$

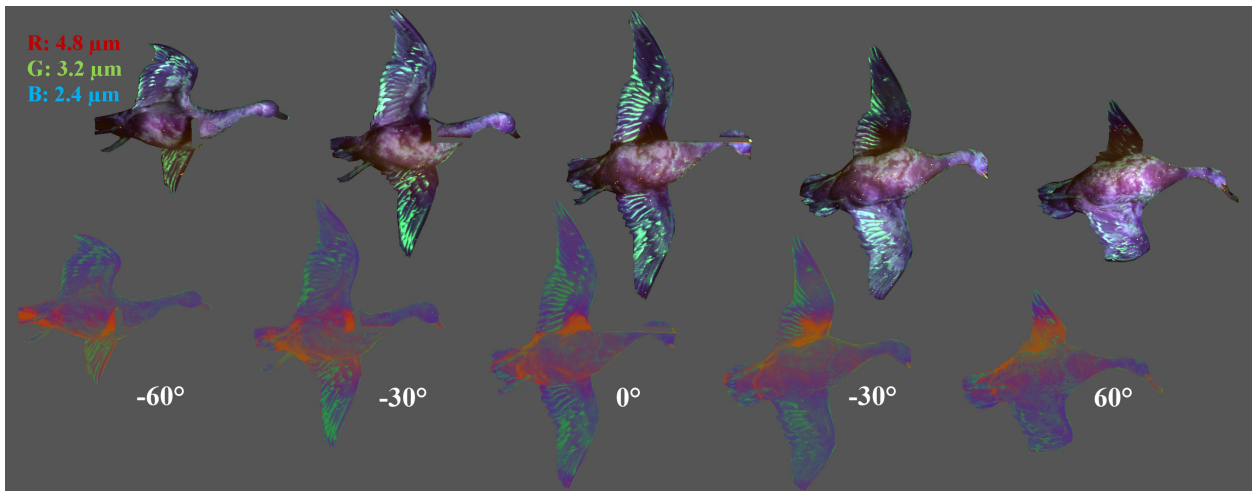


Fig. 9: False color RGB images of whole bird (ex-vivo male Mallard conserved specimen) rotated in five roll angles. Reflectance at three harmonic lines for the  $\text{CO}_2$  laser: 4.8  $\mu\text{m}$ , 3.2  $\mu\text{m}$  and 2.4  $\mu\text{m}$  is presented in the red, green and blue channel, respectively. Note the mirrored coloration between the first and the last figure.



Fig. 10: De-polarized, diagonal polarized and cross-polarized intensities mapped in a false color RGB. The male Mallard is rotated in 0°, 15°, 30° and 45°.

The whole body spectral reflectance signatures as a function of  $\alpha$  are presented in Fig. 11. The atmospheric transmission windows are superimposed. The arrows indicates the positions of three harmonics of the CO<sub>2</sub> laser.

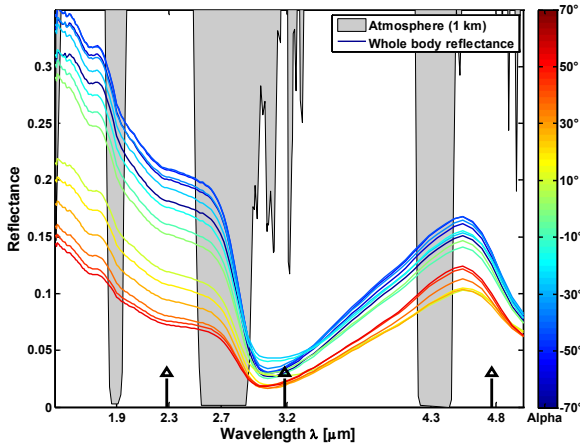


Fig. 11: Absolute whole body MIR reflectance for the female Mallard as function of the wing-nadir angle,  $\alpha$ .

To verify iridescence we introduce a term called redshift,  $RS$ , between two spectral bands, which we would be able to measure remotely with the setup presented in Fig. 6.

$$RS_{\lambda_L, \lambda_S, \alpha} = \frac{WBR_{\lambda_L, \alpha} - WBR_{\lambda_S, \alpha}}{WBR_{\lambda_L, \alpha} + WBR_{\lambda_S, \alpha}}, \quad \lambda_S < \lambda_L, \quad -1 \leq RS_{\lambda_L, \lambda_S, \alpha} \leq 1 \quad \text{Eq.7}$$

The measurable whole-body red-shift for three combinations of CO<sub>2</sub> laser harmonics are presented in Fig. 12a. The shift is plotted against wing-nadir angle,  $\alpha$ ; see Fig. 6. Depending on the band choice different relations are observed. In Fig. 12b. we have related  $\alpha$  to the wing-beat phase  $\phi$  through Eq. 1. Thus we can present the waveform we would expect to measure *in vivo* remotely. While some band choices show modest modulation of 10% depth, the band ratio between 4.8  $\mu\text{m}$  and 2.4  $\mu\text{m}$  flips sign and modulates 20% of the full range. For a comparison to

the visible regime it can be noted that the corresponding contrast between a yellow lemon and a green Granny Smith apple is 10%. As shown in Fig. 7 and Fig. 8., waveforms from other species and genders can be expected to be completely different.

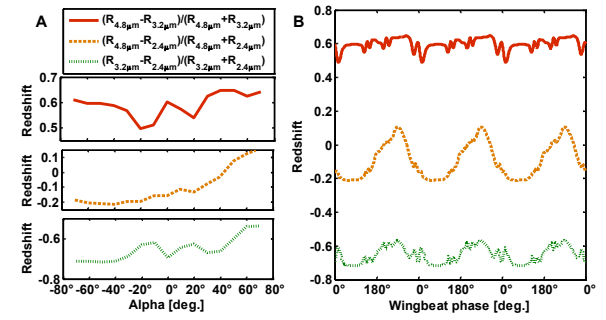


Fig. 12a: When spatially integrating the entire bird a pronounced spectral modulation persists. When considering the angular dependence of the spectral signature ratio, the redshift shows symmetric and asymmetric behaviors depending on the choice of bands. Fig. 12b: MIR multiband observation of the bird during flight would produce detailed waveforms. The ones presented here are ratios between reflectances at three different CO<sub>2</sub> laser harmonics. The relation between Fig. 12a and Fig. 12b is Eq. 1.

### Polarization reflectance imaging of a whole bird

We attempted to extract all four Stokes parameters from the measurement performed with the spectrally resolving FTIR polarimetric instrument<sup>98</sup> as a function of roll angles; however, the signal to noise ration did not permit any conclusions. We then limited us to perform a single broad band analysis using a simpler setup. In this setup the bird was illuminated through a wire grid linear polarizer and imaged in the MIR in terms of a cross-polarized, diagonal-polarized and co-polarized signal. These three intensities are displayed as in red, green and blue channel respectively in Fig.10. The DOLP obviously changes with the roll, but different parts of the wing also shows different DOLP, finally the belly also mainly shows different DOLP.

## Conclusion and perspectives

While visible iridescent colors are known from few selected species (the neck of pigeons is a well known example<sup>68</sup>), we have here demonstrated that most species have shimmering, iridescent colors in the MIR. We have presented significantly different MIR signatures for a list of species. We have discussed the different effects affecting the signature in the different infrared spectral regions. By means of rotation and stretching we have assigned microstructural effects to be responsible for some of those effects. We have provided a more detailed description of the Christiansen effect in feathers and plumage than previously suggested in literature. We have also speculated in how thermal spectral broadening could potentially enhance structural features in the infrared region. We have made a crude comparison of the magnitude of the phenomena contributing to the infrared signature of birds. We have given the background discussion for the basis of remote microscopy and we have proposed both a passive and an active optical detection scheme for remote retrieval of microstructural information from plumage of nocturnal migrating birds, which provide complementary information to that based on previously introduced methods such as RADAR, LIF LIDAR or lunar occultation. We have simulated signals similar to what we expect from such a setup, and we discussed how classification could be achieved in the multidimensional parameter space, expanded by wing beat waveform parameters or 2D trajectories. Finally, we have demonstrated that the structural effect from single feathers persists and interferes constructively for birds as a whole. Several aspects, such as detection limits, signal-noise ratios, the metabolic heat, the real-time wing flapping and aerodynamic strain applied to the feathers are difficult to evaluate for *ex-vivo* static specimens. However, we now consider having the proofs that the concepts are applicable, and that we can motivate a future construction of the proposed scheme for spectrally resolved MIR monitoring at strategic topographical locations, where the nocturnal bird migration is intense during spring or autumn (for example peninsula coastlines or mountain ridges). Synergetic monitoring with techniques such as RADAR<sup>7</sup>, fluorescence LIDAR<sup>9</sup> or operational aerosol LIDAR networks<sup>101</sup> would further improve the classification ability. More laboratory measurements would also be beneficial in terms of species statistics and especially gaining information on the MIR polarization, which is closely tied to structural features, could only briefly be explored in this study. Since the microstructure can be expected to a preference in orientation, both the

polarization state of both illumination and detection should preferably be controlled<sup>102</sup>.

The exploitation of iridescence in combination with wing beat scanning for species identification also has a great potential for insects<sup>69, 103</sup>. As small insects are too small to be individually detected by RADAR wavelengths, this technique may be even more valuable for understanding patterns of migration and dispersal in this field; however, wing beat frequencies are an order of magnitudes higher for insects than for birds. Remote insect classification would have great potential to enhance our understanding of the spread of for instance vector born diseases and distribution of pollinators and agricultural pests<sup>104</sup>. Further, our group has previously demonstrated how remote electro-optical classification can shed light on fast interactions, for example between sexes of damselflies<sup>105</sup>, and that it also has great potential for studying predator-prey interactions. In summary, we foresee a new exciting era of infrared spectroscopy applied to field biology promising new ways of looking at previously inaccessible scenarios.

## Acknowledgement

In this study several strong efforts were done to demonstrate the discussed effects in real-time, in field and *in vivo*. Unfortunately, none of these attempts produced any presentable data due to instrumental limitations. We want to sincerely thank Patrik Lundin for helping out during the field campaign<sup>9</sup>. We want to thank Anna Runemark for assistance during the field campaign and for providing *in vivo* zebra finches from a remote field station during a blizzard in her late pregnancy. We want to thank Susanne Åkesson for introducing us to the fascinating world of birds, for attempts of *in vivo* release studies and for facilitating *in vivo* measurements. We thank Jonas Sandsten for help with dual band IR imaging equipment. We thank Eustace Dereniak for collaboration and measurements performed in his lab. We want to thank Johan Stein and the Department of Building Physics, Lund University, for lending of infrared equipment. We are grateful for assistance by the staff of the Zoological museum in Lund, in providing *ex vivo* bird- and feather samples. We much appreciate the financial support from the Kullaberg Foundation and the Swedish Research Council through a direct grant and a Linnaeus grant to the Lund Laser Centre. Animal handling was done in accordance with ethical permit M204-06.

## References

1. A. Ancel, G. L. Kooyman, P. J. Ponganis, J. P. Gendner, J. Lignon, and X. Mestre, "Foraging Behaviour of Emperor Penguins as a Resource Detector in Winter and Summer," *Nature* **360**, 336–339 (1992).
2. R. C. Laybourne, "Collision between a Vulture and an Aircraft at an Altitude of 37,000 Feet," *The Wilson Bulletin* (Wilson Ornithological Society) **86**, 461–462 (1974).
3. S. A. Shaffer, Y. Tremblay, H. Weimerskirch, *et al.*, "Migratory Shearwaters Integrate Oceanic Resources across the Pacific Ocean in an Endless Summer," *PNAS* **103**, 12799-12802 (2006).
4. P. H. Zehntindijev and F. Liechti, "A Quantitative Estimate of the Spatial and Temporal Distribution of Nocturnal Bird Migration in South-Eastern Europe - a Coordinated Moon-Watching Study," *Avian Sci* **3**, 37-45 (2003).
5. F. Liechti and B. Bruderer, "Quantification of Nocturnal Bird Migration by Moonwatching: Comparison with Radar and Infrared Observations," *J. Field Ornithol.* **66**, 457-468 (1995).
6. S. A. Gauthreaux and J. W. Livingston, "Monitoring Bird Migration with a Fixed-Beam Radar and a Thermal-Imaging Camera," *J. Field Ornithol.* **77**, 319-328 (2006).
7. T. Alerstam, J. Backman, G. A. Gudmundsson, *et al.*, "A Polar System of Intercontinental Bird Migration," *Proc. R. Soc. B* **274**, 2523-2530 (2007).
8. M. Brydegaard, P. Lundin, Z. G. Guan, A. Runemark, S. Åkesson, and S. Svanberg, "Feasibility Study: Fluorescence Lidar for Remote Bird Classification," *Appl. Opt.* **49**, 1-15 (2010).
9. P. Lundin, P. Samuelson, S. Svanberg, A. Runemark, S. Åkesson, and M. Brydegaard, "Remote Nocturnal Bird Classification by Spectroscopy in Extended Wavelength Ranges," *Appl. Opt.* **50** (2011).
10. G. E. Hill and K. J. McGraw, *Bird Coloration, Volume 1: Mechanisms and Measurements* (Harvard University Press, 2006).
11. G. E. Hill and K. J. McGraw, *Bird Coloration, Volume 2: Function and Evolution*, (Harvard University Press, 2006).
12. A. Boreysho, A. Savin, A. Morozov, M. Konyaev, and K. Konovalov, "Remote Detection and Recognition of Bio-Aerosols by Laser-Induced Fluorescence Lidar: Practical Implementation and Field Tests," *Proc. SPIE* **6733**, 673305-673305-673305 (2007).
13. R. J. Hopkins, S. J. Barrington, M. J. Castle, *et al.*, "UV-LIF Lidar for Standoff BW Aerosol Detection," *Proc. SPIE* **7484**, 748409-748409-748411 (2009).
14. Z. Mierczyk, K. Kopczyski, M. Zygmunt, *et al.*, "Fluorescence/Depolarization Lidar for Mid-Range Stand-Off Detection of Biological Agents," 80371J-80371J-80379 (2011).
15. T. Y. He, F. Gao, S. Stani, D. Veberi, K. Bergant, A. Dolan, and X. Q. Song, "Scanning Mobile Lidar for Aerosol Tracking and Biological Aerosol Identification," *Proc. SPIE* **7832**, 78320U-78320U-78326 (2010).
16. F.-M. Lei, Y.-H. Qu, Y.-L. Gan, A. Gebauer, and M. Kaiser, "The Feather Microstructure of Passerine Sparrows in China," *J. Ornithology* **143**, 205-212 (2002).
17. R. O. Prum, "Evolution of the Morphological Innovations of Feathers," *J. Exp. Zool. B Mol. Dev. Evol.* **304**, 570-579 (2005).
18. L. C. Straker, M. A. Raposo, and M. Attias, "*Spina Cortica* and *Tapetum Spinosus*, Two New Microstructures of Flight Feathers: Description, Function and Distribution in Modern Birds," *J. Struct. Biol.* **162**, 301-311 (2008).
19. E. Lee, M. Aoyama, and S. Sugita, "Microstructure of the Feather in Japanese Jungle Crows (*Corvus Macrorhynchos*) with Distinguishing Gender Differences," *Anat. Sci. Int.* **84**, 141-147 (2009).
20. M. D. Shawkey, V. Saranathan, H. Pálsdóttir, J. Crum, M. H. Ellisman, M. Auer, and R. O. Prum, "Electron Tomography, Three-Dimensional Fourier Analysis and Colour Prediction of a Three-Dimensional Amorphous Biophotonic Nanostructure," *J. R. Soc. Interface* **6**, 213-220 (2009).
21. E. O. Fadeeva and O. F. Chernova, "Peculiarities of the Contour Feather Microstructure in the Cordovidae Family," *Biol. Bulletin* **38**, 369-378 (2011).
22. T. Bachmann and H. Wagner, "The Three-Dimensional Shape of Serrations at Barn Owl Wings: Towards a Typical Natural Serration as a Role Model for Biomimetic Applications," *J. Anat.* **219**, 192-202 (2011).
23. P. Lundin, M. Brydegaard, L. Cocola, A. Runemark, S. Åkesson, and S. Svanberg, "Passive Unmanned Sky Spectroscopy for Remote Bird Classification," in *Conference on Remote Sensing for Agriculture, Ecosystems, and Hydrology XIII/18th Internat. Symposium on Remote* (SPIE-Int Soc Optical Engineering Prague, Czech Republic, 2011), pp. 81740J-81740J-81711.
24. D. Osorio and A. D. Ham, "Spectral Reflectance and Directional Properties of Structural Coloration in Bird Plumage," *J. Exp. Biol.* **205**, 2017-2027 (2002).
25. D. J. Brink and N. G. v. d. Berg, "Structural Colours from the Feathers of the Bird *Bostrychia Hagedash*," *J. Phys. D: Appl. Phys.* **37**, 813-818 (2004).
26. R. S. Sennett and G. D. Scott, "The Structure of Evaporated Metal Films and Their Optical Properties," *J. Opt. Soc. Am.* **40**, 203-210 (1950).
27. E. E. Bell, L. Eisner, J. Young, and R. A. Oetjen, "Spectral Radiance of Sky and Terrain at Wavelengths between 1 and 20 Microns. II. Sky Measurements," *J. Opt.Soc.Am.* **50**, 1313-1317 (1960).
28. C. Christiansen, "Untersuchungen über die Optischen Eigenschaften von Fein Verteilten Körpern," *Ann. Phys. Chem.* **23**, **24**, 293-306,439-446 (1884,1885).
29. H. R. Carlon, "Christiansen Effect in IR Spectra of Soil-Derived Atmospheric Dusts," *Appl. Opt.* **18** (1979).
30. M. J. Pollard, P. R. Griffiths, and K. Nishikida, "Investigation of the Christiansen Effect in the Mid-Infrared Region for Airborne Particles," *Appl. Spectrosc.* **61**, 860 (2007).
31. M. M. Hedman, P. D. Nicholson, M. R. Showalter, *et al.*, "The Christiansen Effect in Saturn's Narrow Dusty Rings and the Spectral Identification of Clumps in the F Ring," *Icarus* **215**, 695-711 (2011).
32. W. P. Arnott, Y. Y. Dong, and J. Hallett, "Extinction Efficiency in the Infrared (2–18 μm) of Laboratory Ice Clouds: Observations of Scattering Minima in the Christiansen Bands of Ice," *Appl. Opt.* **34**, 341-551 (1995).
33. W. P. Arnott, C. Schmitt, Y. Liu, and J. Hallett, "Droplet Size Spectra and Water-Vapor Concentration of Laboratory Water Clouds: Inversion of Fourier Transform Infrared (500–5000 cm<sup>-1</sup>) Optical-Depth Measurement," *Appl. Opt.* **36**, 5205-5216 (1997).
34. P. Yang, B.-C. Gao, B. A. Baum, *et al.*, "Radiative Properties of Cirrus Clouds in the Infrared (8–13 μm) Spectral Region," *J. Quantitative Spectrosc. & Radiative Transfer* **70**, 473-504 (2001).

35. P. Yang, "Spectral Signature of Ice Clouds in the Far-Infrared Region: Single-Scattering Calculations and Radiative Sensitivity Study," *J. Geophys. Research* **108**, 4569 (2003).
36. H.-L. Huang, P. Yang, H. Wei, B. A. Baum, Y. Hu, P. Antonelli, and S. A. Ackerman, "Inference of Ice Cloud Properties from High Spectral Resolution Infrared Observations," *IEEE Trans. Geosci. Remote Sens.* **42**, 842 (2004).
37. M. J. Smith and R. T. Carl, "Applications of Microspectroscopy in the near-Infrared Region," *Appl. Spectrosc.* **43**, 865-873 (1989).
38. C. J. Dove, A. M. Rijke, X. Wang, and L. S. Andrews, "Infrared Analysis of Contour Feathers - the Conservation of Body Heat Radiation in Birds," *J. Therm. Biol.* **32**, 42-46 (2007).
39. X. Wan, J. Fan, and H. Wu, "Measurement of Thermal Radiative Properties of Penguin Down and Other Fibrous Materials Using FTIR," *Polymer Testing* **28**, 673-679 (2009).
40. V. Lucarini, K.-E. Peiponen, J. J. Saarinen, and E. M. Vartiainen, *Kramers-Kronig Relations in Optical Materials Research*, (Springer, Berlin, Heidelberg, 2005).
41. C. G. Schmitt, "Infrared Emission (500-2000  $\text{cm}^{-1}$ ) of Laboratory Ice Clouds," (University of Nevada, 1998).
42. M. Franz, B. M. Fischer, and M. Walther, "The Christiansen Effect in Terahertz Time-Domain Spectra of Coarse-Grained Powders," *Appl. Phys. Lett.* **92**, 021107 (2008).
43. D. Faber, M. Aalders, E. Mik, B. Hooper, M. van Gemert, and T. van Leeuwen, "Oxygen Saturation-Dependent Absorption and Scattering of Blood," *Phys. Rev. Lett.* **93** (2004).
44. S. L. Jacques and B. W. Pogue, "Tutorial on Diffuse Light Transport," *J. Biomed. Opt.* **13**, 041302 (2008).
45. K. M. Yoo, F. Liu, and R. R. Alfano, "Imaging through a Scattering Wall Using Absorption," *Opt. Lett.* **16**, 1068-1070 (1991).
46. Z.-W. Z. K. M. Yoo, S. A. Ahmed, and R. R. Alfano, "Imaging Objects Hidden in Scattering Media Using a Fluorescence-Absorption Technique," *Opt. Lett.* **16**, 1252-1254 (1991).
47. R. Grönlund, M. Sjöholm, P. Weibring, H. Edner, and S. Svanberg, "Elemental Mercury Emissions from Chlor-Alkali Plants Measured by Lidar Techniques," *Atmospheric Environ.* **39**, 7474-7480 (2005).
48. U. Gustafsson, J. Alnis, and S. Svanberg, "Atomic Spectroscopy with Violet Laser Diodes," *Am. J. Phys.* **68**, 660-664 (2000).
49. M. Sjöholm, G. Somesfalean, J. Alnis, S. Andersson-Engels, and S. Svanberg, "Analysis of Gas Dispersed in Scattering Media," *Opt. Lett.* **26**, 16-18 (2001).
50. S. Svanberg, *Atomic and Molecular Spectroscopy: Basic Aspects and Practical Applications*, 4th ed., (Springer, Heidelberg, 2004).
51. M. Andersson, R. Grönlund, L. Persson, M. Sjöholm, K. Svanberg, and S. Svanberg, "Laser Spectroscopy of Gas in Scattering Media at Scales Ranging from Kilometers to Millimeters," *Laser Phys.* **17**, 893-902 (2007).
52. M. Brydegaard, A. Merdasa, H. Jayaweera, J. Alebring, and S. Svanberg, "Versatile Multispectral Microscope Based on Light Emitting Diodes," *Rev. Sci. Instr.* **82**, 123106 (2011).
53. S. W. Hell, "Far-Field Optical Nanoscopy," *Science* **316**, 1153-1158 (2007).
54. M. J. B. Rust, M. Zhuang, X., "Sub-Diffraction-Limit Imaging by Stochastic Optical Reconstruction Microscopy (STORM)," *Nat. Methods* **3**, 793-795 (2006).
55. R. O. Gray and C. J. Corbally, *Stellar Spectral Classification*, (Princeton University Press, 2009).
56. J. B. Campbell, *Introduction to Remote Sensing*, 5th ed., (The Guilford Press, 2011).
57. D. Althausen, D. Muller, A. Ansmann, U. Wandinger, H. Hube, E. Clauer, and S. Zorner, "Scanning 6-Wavelength 11-Channel Aerosol Lidar," *J. Atmospheric & Oceanic Tech.* **17**, 1469 (2000).
58. J. B. Gillespie, D. A. Ligon, P. M. Pellegrino, N. F. F. Jr, and N. J. Wood, "Development of a Broadband Lidar System for Remote Determination of Aerosol Size Distributions," *Meas. Sci. Technol.* **13**, 383-390 (2002).
59. A. W. Nolin and J. Dozier, "A Hyperspectral Method for Remotely Sensing the Grain Size of Snow," *Remote Sensing Environ.* **74**, 207-216 (2000).
60. V. Backman, R. Gurjar, K. Badizadegan, I. Itzkan, R. R. Dasari, L. T. Perelman, and M. S. Feld, "Polarized Light Scattering Spectroscopy for Quantitative Measurement of Epithelial Cellular Structures *in Situ*," *IEEE JSTQE* **5**, 1019-1026 (1999).
61. R. O. Prum, R. Torres, S. Williamson, and J. Dyck, "Two-Dimensional Fourier Analysis of the Spongy Medullary Keratin of Structurally Coloured Feather Barbs," *Proc. R. Soc. B* **266**, 13-22 (1999).
62. S. M. Doucet, M. D. Shawkey, G. E. Hill, and R. Montgomerie, "Iridescent Plumage in Satin Bowerbirds: Structure, Mechanisms and Nanostructural Predictors of Individual Variation in Colour," *J. Exp. Biol.* **209**, 380-390 (2006).
63. R. O. Prum and R. H. Torres, "A Fourier Tool for the Analysis of Coherent Light Scattering by Bio-Optical Nanostructures," *Integr. Comp. Biol.* **43**, 591-602 (2003).
64. R. O. Prum, J. A. Cole, and R. H. Torres, "Blue Integumentary Structural Colours in Dragonflies (Odonata) are not Produced by Incoherent Tyndall Scattering," *J. Exp. Biol.* **207**, 3999-4009 (2004).
65. R. O. Prum, E. R. Dufresne, T. Quinn, and K. Waters, "Development of Colour-Producing Beta-Keratin Nanostructures in Avian Feather Barbs," *J. R. Soc. Interface* **6 Suppl 2**, S253-265 (2009).
66. E. R. Dufresne, H. Noh, V. Saranathan, S. G. J. Mochrie, H. Cao, and R. O. Prum, "Self-Assembly of Amorphous Biophotonic Nanostructures by Phase Separation," *Soft Matter* **5**, 1792 (2009).
67. K. J. McGraw, "Multiple UV Reflectance Peaks in the Iridescent Neck Feathers of Pigeons," *Naturwissenschaften* **91**, 125-129 (2004).
68. H. Yin, L. Shi, J. Sha, *et al.*, "Iridescence in the Neck Feathers of Domestic Pigeons," *Phys. Rev. E* **74**, 051916 (2006).
69. E. Shevtsova, C. Hansson, D. H. Janzen, and J. Kjaerandsen, "Stable Structural Color Patterns Displayed on Transparent Insect Wings," *PNAS* **108**, 668-673 (2011).
70. C. Giacovazzo, H. L. Monaco, G. Artioli, *et al.*, *Fundamentals of Crystallography*, (Oxford University Press, 2002).
71. "Infrared Associates Inc.", retrieved Mar 2012, <http://www.irassociates.com>
72. "Vigo System S.A.", retrieved 2012, <http://vigo.com.pl/>.
73. "Sky-Watcher ®", retrieved Mar 2012, <http://www.skywatcher.com>
74. M. Klaassen, A. Kvist, and Å. Lindström, "Flight Costs and Fuel Composition of a Bird Migrating in a Wind Tunnel," *The Condor* **102**, 444-451 (2000).

75. S. Ward, U. Moller, J. M. Rayner, D. M. Jackson, W. Nachtigall, and J. R. Speakman, "Metabolic Power of European Starlings *Sturnus Vulgaris* During Flight in a Wind Tunnel, Estimated from Heat Transfer Modelling, Doubly Labelled Water and Mask Respirometry," *J. Exp. Biol.* **207**, 4291-4298 (2004).
76. S. Ward, J. M. V. Rayner, U. Möller, D. M. Jackson, W. Nachtigall, and J. R. Speakman, "Heat Transfer from Starlings *Sturnur Vulgaris* During Flight," *J. Exp. Biol.* **202**, 1589-1602 (1999).
77. O. Cangar, J. M. Aerts, J. Buyse, and D. Berckmans, "Quantification of the Spatial Distribution of Surface Temperatures of Broilers," *Poult. Sci.* **87**, 2493-2499 (2008).
78. J. T. Kiehl and K. E. Trenberth, "Earth's Annual Global Mean Energy Budget," *Bulletin Am. Meteorological Soc.* **78**, 197 (1996).
79. K. Barat, *Laser Safety: Tools and Training*, (CRC Press, 2008).
80. A. Godard, "Infrared (2–12  $\mu\text{m}$ ) Solid-State Laser Sources: A Review," *Comptes Rendus Physique* **8**, 1100-1128 (2007).
81. J. R. Albertine, "History of Navy HEL Technology Development and Systems Testing," in *Laser and Beam Control Technologies*, (Proc. SPIE, 2002).
82. D. Schuöcker and B. Holzinger, "CO<sub>2</sub> Laser with 65MW Pulses and 100kW Power, Concept and First Steps of Development," *Proc. SPIE* **7005**, 70051F-70051F-70012 (2008).
83. H. P. Chou, R. C. Slater, and Y. Wang, "High-Energy, Fourth-Harmonic Generation Using CO<sub>2</sub> Lasers," *Appl. Phys. B* **66**, 555–559 (1998).
84. G. C. Bhar, P. Kumbhakar, D. V. Satyanarayana, N. S. N. Banerjee, U. Nundy, and C. G. Chao, "Third Harmonic Generation of CO<sub>2</sub> Laser Radiation in AgGaSe<sub>2</sub> Crystal," *PRAMANA J. Phys.* **55**, 405-412 (2000).
85. Y. Jiang and Y. J. Ding, "Efficient Harmonic Generation of Second, Third, and Fourth Orders from Fourier-Transform-Limited CO<sub>2</sub> Laser Beam at 10.6 $\mu\text{m}$  in GaSe Crystals," *Opt. Comm.* **282**, 1452-1454 (2009).
86. Y. Lu, X. Wang, L. Miao, D. Zuo, and Z. Cheng, "Third-Harmonic and Fourth-Harmonic Generations of CO<sub>2</sub> Laser Radiation in a GaSe Crystal," *Opt. Comm.* **284**, 3622-3625 (2011).
87. Y. M. Andreev, V. V. Butuzov, G. A. Verozub, A. I. Gribenyukov, S. V. Davydov, and V. P. Zakharov, "Generation of the Second Harmonic of Pulsed CO<sub>2</sub>-Laserradiation in AgGaSe<sub>2</sub> and ZnGeP<sub>2</sub> Single Crystals," *Laser Phys.* **5**, 1014 - 1019 (1995).
88. D. Haberberger, S. Tochitsky, and C. Joshi, "Fifteen Terawatt Picosecond CO<sub>2</sub> Laser System," *Opt. Expr.* **18**, 17865-17875 (2010).
89. A. Rogalski, "Infrared Detectors: An Overview," *Infrared Phys. & Technology* **43**, 187–210 (2002).
90. J. L. Bufton, T. Itabe, L. L. Strow, C. Laurence Korb, B. M. Gentry, and C. Y. Weng, "Frequency-Doubled CO<sub>2</sub> Lidar Measurement and Diode Laser Spectroscopy of Atmospheric CO<sub>2</sub>," *Appl. Opt.* **222**, 2592-2602 (1983).
91. L. Fiorani, F. Colao, and A. Palucci, "Measurement of Mount Etna Plume by CO<sub>2</sub>-Laser-Based Lidar," *Opt. Lett.* **34**, 800-802 (2009).
92. R. E. Warren, R. G. Vanderbeek, and J. L. Ahl, "Estimation and Discrimination of Aerosols Using Multiple Wavelength LWIR Lidar," 766504-766509 in *Chemical, Biological, Radiological, Nuclear, and Explosives (CBRNE) Sensing XI*, (Proc. SPIE, **7665**, 2010).
93. "Nextgenn Global Technologies Limited", retrieved Mar 2012, <http://nextgenn.net>.
94. J. M. Missirian and L. Ducruet, *IRST: A Key System in Modern Warfare*, Infrared Technology and Applications XXIII, Pts 1 and 2, Vol. 3061, (Proc. SPIE, Bellingham, 1997).
95. R. T. Hintz, J. Allen, M. Chen, T. Price, and G. Goetz, "UAV Infrared Search and Track (IRST)/Eyesafe Laser Range Finder (Elr) System," 9.1 – 9.14 in *RTO-MP-SET-094*, 2005).
96. J. Sandsten, P. Weibring, H. Edner, and S. Svanberg, "Real-Time Gas-Correlation Imaging Employing Thermal Background Radiation," *Opt. Expr.* **6**, 92-103 (2000).
97. P. Samuelson, "Infrared Spectroscopic Techniques Applied in Ecological Studies," Master thesis (Lund University, Lund Reports on Atomic Physics, LRAP–435, 2011).
98. J. Craven-Jones, M. W. Kudenov, Maryn G. Stapelbroek, and E. L. Dereniak, "Infrared Hyperspectral Imaging Polarimeter Using Birefringent Prisms," *Appl. Opt.* **50**, 1170-1185 (2011).
99. M. W. Kudenov and E. L. Dereniak, "Compact Snapshot Real-Time Imaging Spectrometer," 81860W-81860W-81812 in (Proc. of SPIE **8186**, 2011).
100. M. W. Kudenov, M. J. Escuti, E. L. Dereniak, and K. Oka, "White-Light Channeled Imaging Polarimeter Using Broadband Polarization Gratings," *Appl. Opt.* **50**, 2283-2293 (2011).
101. "A European Aerosol Research Lidar Network to Establish an Aerosol Climatology: EARLINET", retrieved 2012, <http://www.earlinet.org/>.
102. S. Tubasum, D. Thomsson, R. Cogdell, I. Scheblykin, and T. Pullerits, "Polarization Single Channeled Imaging of Circular Photosynthetic Antenna," *Photosynth. Res.* **111**, 41-45 (2012).
103. A. Moore and R. H. Miller, "Automated Identification of Optically Sensed Aphid (*Homoptera: Aphidae*) Wingbeat Waveforms," *Ann. Entomol. Soc. Am.* **95**, 1-8 (2002).
104. L. Mei, Z. G. Guan, H. J. L. J. Zhou, *et al.*, "Agricultural Pest Monitoring Using Fluorescence Lidar Techniques," *Appl. Phys. B* **106**, 733-740 (2011).
105. A. Runemark, M. Wellenreuther, H. Jayaweera, S. Svanberg, and M. Brydegaard, "Rare Events in Remote Dark Field Spectroscopy: An Ecological Case Study of Insects," *IEEE JSTQE* **18**, 1573 - 1582 (2012).

## PAPER XVI

### **Passive unmanned sky spectroscopy for remote bird classification**

P. Lundin, M. Brydegaard, A. Runemark, S. Åkesson,  
L. Cocola, and S. Svanberg  
*Proc. SPIE* **8174**, 81740J (2011).

# Passive unmanned sky spectroscopy for remote bird classification

Patrik Lundin<sup>a</sup>, Mikkel Brydegaard<sup>a</sup>, Lorenzo Cocola<sup>a,b</sup>, Anna Runemark<sup>c</sup>, Susanne Åkesson<sup>c</sup>, and Sune Svanberg<sup>a,d,e</sup>

<sup>a</sup>Atomic Physics Division, Lund University, P.O. Box 118, SE-221 00 Lund, Sweden

<sup>b</sup>Centre of Studies and Activities for Space, University of Padova, CISAS - "G. Colombo", Via Venezia 15, 35131, Padova, Italy

<sup>c</sup>Centre for Animal Movement Research, Department of Biology, Lund University, Ecology Building, SE-223 62 Lund, Sweden

<sup>d</sup>Joint Research Center of Photonics, Zhejiang University-Royal Institute of Technology-Lund University, Hangzhou 310058, China

<sup>e</sup>Center of Optics and Electromagnetic Research, South China Normal University, Guangzhou 510006, China

## ABSTRACT

We present a method based on passive spectroscopy with aim to remotely study flying birds. A compact spectrometer is continuously recording spectra of a small section of the sky, waiting for birds to obscure part of the field-of-view when they pass the field in flight. In such situations the total light intensity received through the telescope, looking straight up, will change very rapidly as compared to the otherwise slowly varying sky light. On passage of a bird, both the total intensity and the spectral shape of the captured light changes notably. A camera aimed in the same direction as the telescope, although with a wider field-of-view, is triggered by the sudden intensity changes in the spectrometer to record additional information, which may be used for studies of migration and orientation. Example results from a trial are presented and discussed. The study is meant to explore the information that could be gathered and extracted with the help of a spectrometer connected to a telescope. Information regarding the color, size and height of flying birds is discussed. Specifically, an application for passive distance determination utilizing the atmospheric oxygen A-band absorption at around 760 nm is discussed.

**Keywords:** Remote sensing, passive optical spectroscopy, bird migration, bird classification, diurnal migration, Fraunhofer line discrimination

## 1. INTRODUCTION

There are still many aspects of bird migration in which we have little knowledge, and ecologists search for ways to learn more about how flight routes are chosen, about the timing of long distance migrations, navigation, and how winds and other weather conditions affect the flights [1,2]. A severe drawback of many studies of migratory birds is that one either have to manipulate the bird by attaching tracking devices to follow them individually in the field, or alternatively, bring the birds into the laboratory and study them in captivity. Both lines of research have limitations, since the birds need to be captured and handled. Remote techniques applied in open field situations to study bird migration are usually limited in terms of what information can be recorded, and it is often not known which species is flying above unless the distance is short enough to visually identify the bird. Advances in remote studies of bird movements and migration are important since birds are vectors for bird-borne diseases such as avian flu, avian malaria and tick-borne diseases, as well as for seeds and aquatic organisms [3, 4]. In addition, bird migration patterns may also reflect global change [e.g. 5].

The primary tools used by ecologists to remotely study birds today are a pair of binoculars or a small telescope. These tools will, with the help of our perception, provide information about the size, shape and flight speed of a bird. With the help of our trichromatic vision, some qualitative spectroscopic information (the color of the bird) is also obtained. However, as birds have a visual system with four color bands as compared to the three bands of humans, more spectroscopic information might pertain and be hidden for us if our vision is not complemented by technology.

Various other methods to remotely study birds have been developed and used, such as tracking and surveillance radars [e.g. 6, 7], ceilometers [8, 9] and infrared cameras [e.g. 10]. The desirable information is carried from the bird to the observer with the help of either electromagnetic waves or sound waves (another transport possibility is falling ordure but it is questionable if this counts as remote sensing...). In the case of sound waves, the flight calls can provide some information about the species but can only crudely give the number of birds in a passing flock of birds. Some migratory songbirds produce distinct flight calls, but the majority of birds are quiet in flight or produce calls which are similar between species, proving it is hard to use sounds alone for migration studies [11, 12]. Coming to the electromagnetic waves, again, the dominant part used has been the visible spectrum for humans, as in the case of standard bird watching. Another much used wavelength range is the radio-wave region, as used by radar stations. Tracking- and surveillance radars are very powerful in providing information about flight height and direction, number of birds and sometimes bird sizes. One way to estimate the size is by identifying the flight speed and wing beat frequency, which both correlate with the body size. On the other hand, radar provides little further species specific information and combination with other techniques is therefore desirable. Some studies with the purpose to compare different methods have drawn conclusions on the advantages and disadvantages of presently existing remote sensing methods [13-15].

As already indicated, traditional unmanned methods offer very limited information about the species of passing birds. It is thus important to develop existing methods further but also to bring new techniques into the field of ornithology. We hope that spectroscopic information can provide intelligence about mainly species, but hopefully also about sex, age and condition of passing migrants. Automatic monitoring techniques which do not require continuous human surveillance would make studies more efficient. Unmanned systems, observing a well-defined part of the sky could also provide more quantitative data on time and number of passing birds.

We have performed a number of previous experiments and field campaigns with the purpose to study flying insects and birds. These studies have mostly dealt with laser induced fluorescence (LIF), using an ultraviolet (UV) pulsed laser beam pointing in a direction where the insects or birds are expected. When the animals pass through the beam, the UV light is absorbed and a broad-band fluorescence light distribution is generated. This spectrally broad light is then re-absorbed in, e.g., the plumage of the bird and the light escaping will thus depend on the pigments in the feathers in this case, in the same way as would be the case in reflectance spectroscopy. The escaping fluorescence is collected with a telescope and analyzed with an array of photomultipliers or a spectrometer. LIF was used to classify damselflies [16, 17], to identify agricultural pests [18] and to study birds [19,20]. In [20] infrared cameras were also used to study spectral signatures in the mid-infrared spectral region, as well as passive spectroscopy similar to the one presented in this paper. Our group also developed dark-field scattering spectroscopy to remotely study insects moving freely in their habitat [21].

In the present paper we explore the use of a spectrometer coupled to a telescope looking vertically up into the sky, waiting for birds to pass by. A bird will not only affect the total intensity received but hopefully also the spectral distribution of the light. The spectrum received depends on the color of the bird and information about this is thus obtained by observing the quick spectral changes induced by the passing bird. Depending on the angle of the incoming sunlight with respect to the bird and the telescope, this can be seen as either absorption- or reflectance spectroscopy (or a mixture). The spectra collected during a time period of days are stored and treated with principal component analysis. The amount and sign of a component associated with a red shift of the spectrum are shown to carry information on the color of the birds. The impact of the absorption depth of a terrestrial Fraunhofer oxygen line is evaluated as a possible way to passively measure the approximate height of the passing bird.

## 2. METHODOLOGY AND THEORETICAL MOTIVATION

The experiments were performed in the Swedish city of Lund (Lat. N 55° 42' 37" Long. E 13° 12' 16") during the time period March 11 to April 5, 2011. Figure 1 shows a schematic illustration of the experimental setup. A compact spectrometer (Ocean Optics, USB4000) covering the wavelength range from 180 to 890 nm was used with a sampling frequency of 50 Hz. Due to atmospheric absorption, however, the spectral region of most interest is between 300 and 800 nm. The slit of the spectrometer was 25  $\mu\text{m}$ , yielding a spectral resolution of 1.5 nm. The spectrometer was connected to a 1-mm optical fiber with the other end placed in the focal point of a 40-cm diameter Newtonian telescope with a focal length of 1 m. The telescope was positioned to look straight up (vertically) to simplify the geometrical conditions as far as possible. The combination of the fiber diameter and the focal length of the telescope determines the divergence of the field-of-view (FOV) to around 1 mrad. Thus, a circular area with a diameter 1 m was viewed at a height of 1 km. A camera (Guppy-503B, Allied Vision Technology, with a MT9P031 sensor from Micron/Aptina) was installed coaxially with the large telescope. The camera was taking photos of the sky approximately every 10th minute and when triggered by sudden intensity changes recorded by the spectrometer. Each time the camera is triggered, two snapshots are taken in an attempt to also provide information about the direction of flight. This commonly used way to obtain velocities of moving objects could in this case, with a well aligned system, principally be simplified by only taking one photo. Since the position of the bird has to be in the centre of the FOV of the camera at the time of triggering (if the FOVs of the telescope and camera are exactly coaxial) the trigger delay and the position in the photo is enough to obtain the velocity.

As long as the sky is clear the intensity and spectral distribution of light reaching the spectrometer will vary only slowly throughout the day. A spectrum representing the blue sky will be recorded (see figure 2) with an intensity which varies solely with the height angle of the sun ( $\theta_s$ ). During the time period of the experiments this angle was at most 40 degrees from horizontal. Since single scattering dominates during clear weather the photons reaching the telescope (which only detects light coming from straight above) can be considered to have been scattered once but at a distribution of heights. A mean height of scattering can be defined which also gives a mean distance through atmosphere that photons have traveled. A way to evaluate this distance is to look at the terrestrial Fraunhofer lines caused by the atmosphere of earth. One such line is due to molecular oxygen A-band absorption at around 760 nm (indicated by the arrow in figure 2). The contrast in this line (i.e. the off-line intensity divided by the in-line intensity) will therefore give an indication about the mean length photons travel through air (the air density as a function of height also has to be considered). The oxygen Fraunhofer absorption lines (there is also a weaker band due to oxygen around 690 nm, the B band, also visible in figure 2) have previously been used for passive detection of marine oil slicks [22] and are being considered for space-based global mapping of vegetation health [23]. Here sun-induced fluorescence adds a broad-band background intensity (free of Fraunhofer line imprint) which leads to a reduced observed contrast of the Fraunhofer lines. In order to analyze the strength of the vegetation fluorescence clearly a good understanding of the strength of the oxygen absorption in view of light propagation through a partly cloudy atmosphere is needed.

When the weather is cloudy the intensity of light will heavily fluctuate as a function of time. In general, the intensity is higher (which at first thought could be a bit surprising) when looking straight up during cloudy conditions than during clear sky observation. As mentioned, the mean distance that photons travel through the atmosphere will change slightly during cloudy conditions, partly because the now introduced multiple scattering but also due to the fact that photons will have a new mean scattering height (which now tends to go closer to the cloud height). Obviously, the spectra recorded by the spectrometer will now be different from those recorded during clear weather (the sky is blue and clouds are white or gray, reflecting the differently strong wavelength dependence of Rayleigh and Mie scattering, respectively). However, even if the intensity fluctuates during cloudy weather, the timescale of these fluctuations is still much longer than for those when a bird flies through the FOV of the telescope. These fast bird-induced intensity changes could therefore be used to trigger the camera. Unfortunately, as the triggering and response of the camera is non-instantaneous, the birds frequently escaped the FOV of the camera. The hope was, that not only the mean intensity would change when a bird flew by, but also the spectral shape of the light recorded.

All data from the spectrometer and from the camera were stored on a computer. In total 165 hours of data were recorded, containing approximately 30 million spectra.

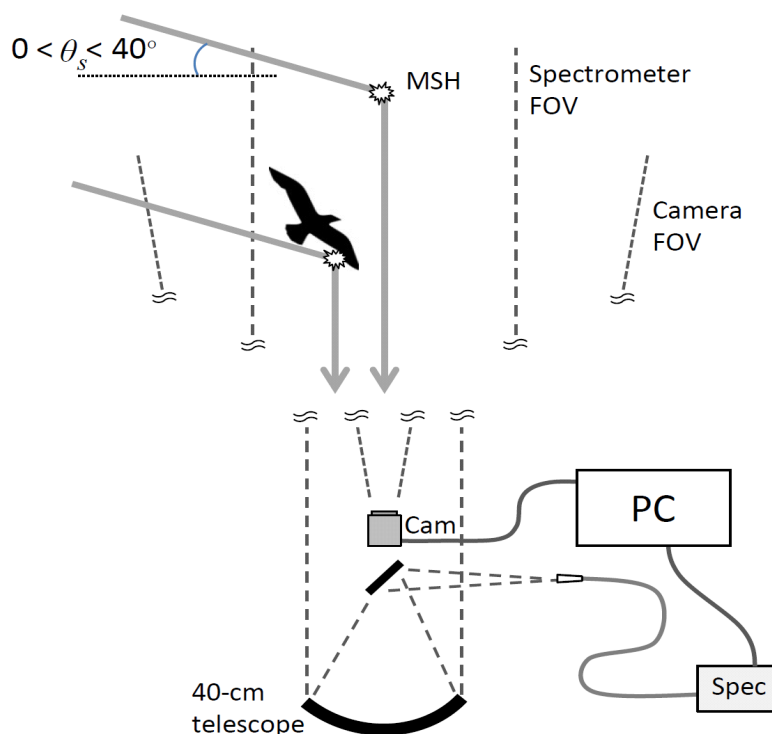


Figure 1. Schematics of the experimental setup. The light from the sun that reaches the telescope has been scattered at a distribution of heights from ground level and up. However, a mean scattering height, MSH, can be found. When a bird enters the FOV of the telescope the light will have an increased probability of being scattered in the bird plumage. This will change the mean scattering height. The light reaching the 40-cm diameter Newtonian telescope will be focused into a 1-mm diameter optical fiber and delivered to the spectrometer, which records spectra at 50 Hz. Sudden intensity changes trigger the camera taking snapshots of the sky.

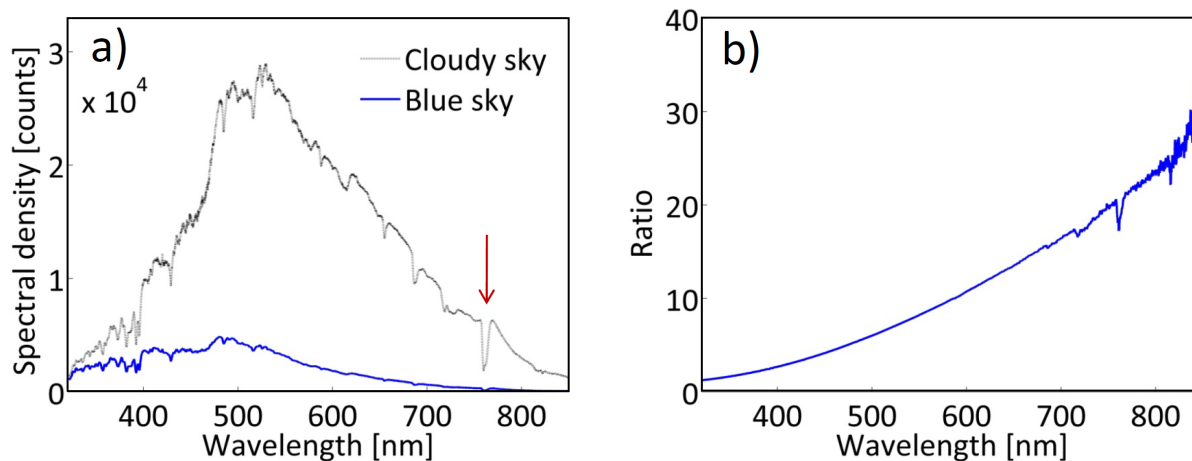


Figure 2. **a)** Example spectra of a cloudy and clear blue sky (recorded at around 10:00 and 16:30 at March 28; see figure 3). It is exemplified how the light intensity of the clear sky is generally lower throughout the spectrum. The vertical arrow points at the atmospheric oxygen A-band absorption at around 760 nm. The dark current (bias) of the spectra has been removed by setting the intensity below 300 nm (where we expect no light due to ozone absorption) to zero. However, the spectra are not white-light calibrated. **b)** The ratio between the cloud spectrum and the clear sky spectrum. As expected, the ratio goes up strongly towards the red side of the spectrum. It can also be noted that we have a slight decrease in the ratio at the oxygen absorption line. This indicates that the light reaching the spectrometer has traveled a longer mean path during the cloudy weather.

### 3. ANALYSIS AND RESULTS

The data from the spectrometer were stored with information on time and spectral distribution in matrices of 3000 spectra, each having 3648 spectral bins. After subtracting the dark current by setting the light intensity below 300 nm to zero, the mean intensity of each spectrum was calculated and plotted as a function of time. For each day of recording a vector of averaged intensity was obtained,  $I$ , as exemplified for March 28 in figure 3a. "Low-pass" filtered versions of these vectors were also created,  $I_{LP}$ , by running a median filter with a certain time span on  $I$ . More specifically, this function will go through the vector  $I$  from top to bottom and take the median value within the specified time span, in our case set to 200 ms (ten sampling points). This median filter will work better than a mean filter (which is the more common way to smooth curves) as fast outliers will be ignored completely. The difference between  $I_{LP}$  (light gray curve in figure 3b) and  $I$  (black curve in figure 3b) can now be thought of as a "high-pass" filtered version,  $I_{HP}$ , of  $I$ . The idea is that a bird quickly entering the FOV of the telescope induces an extreme value in this curve and a deviation beyond a certain threshold is considered as a bird "event". Figure 3c shows a histogram of the absolute values of  $I_{HP}$ . The probability for zero (same value for  $I_{LP}$  as for  $I$ ) is highest and then the probability goes down for larger values of  $I_{HP}$ . A certain limit where the "noise" starts to turn into actual events is seen as a kink in the histogram. This is then an appropriate position to put the threshold for a bird event. If we now go back to figure 3b, this threshold is marked as a light red filled region around  $I_{LP}$ . When  $I$  reaches outside this region, we consider this as a bird event. Such events are marked with magenta colored stars in figure 3a and 3b. Times with heavily cloudy weather, as marked with gray in figure 3a, are at present time ignored in the rest of the analysis due to complicating factors in the analysis during these times. The number of birds detected by the routine depends on the value set on the threshold. We applied a threshold which was allowed to vary slightly during the day due to strong differences in light intensity during the morning/evening and the middle of the day. A total of 77 bird events were found during the clear periods with the threshold values chosen.

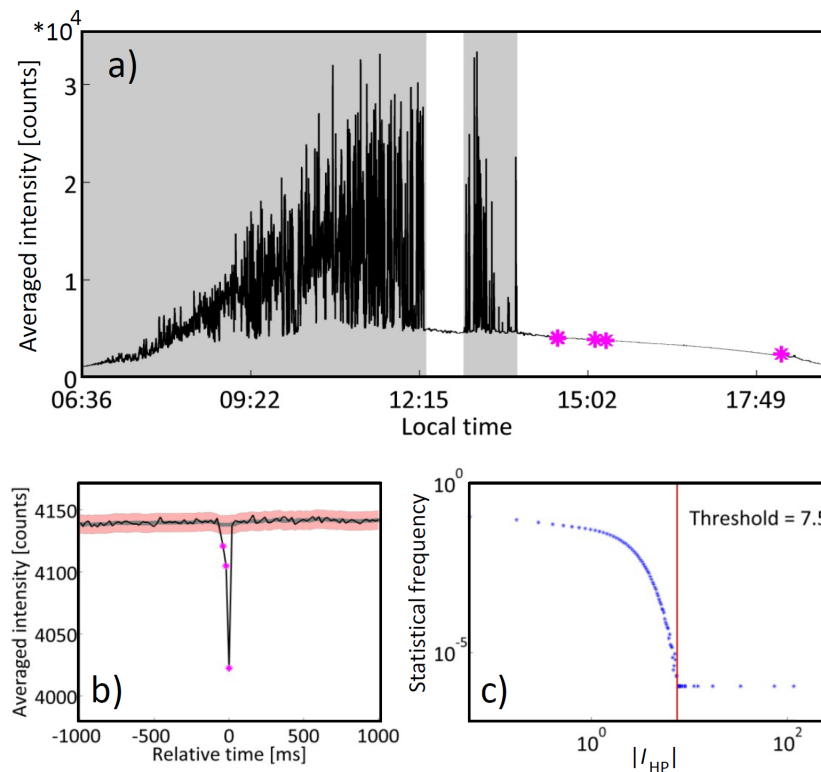


Figure 3. **a)** The spectrally averaged intensity as a function of time of the day (local time, GMT+1, March 28). Cloudy time periods are easily distinguished due to the heavily fluctuating light intensity. For now we ignore these times in the following analysis. The magenta stars mark times when bird events occurred. **b)** A "zoom-in" of the curves around a bird event. When the original intensity curve deviates from the low-pass filtered curve with more than the value of a threshold, events are detected. **c)** Histogram of the absolute difference between the low-pass filtered and original curves during this day of recording. The threshold is put where the decreasing noise amplitude is separated from rare events. In this case we see that 9 events were recorded during the clear period of this day.

Figure 4 shows example photos taken by the camera during two bird events. Each trigger from the spectrometer causes two snapshots to be taken with a certain time separation. This will, if the bird stays in the FOV of the camera during both snapshots, give information about the flight direction and speed. The photos are normalized intensity images where white represents high intensity and black low.

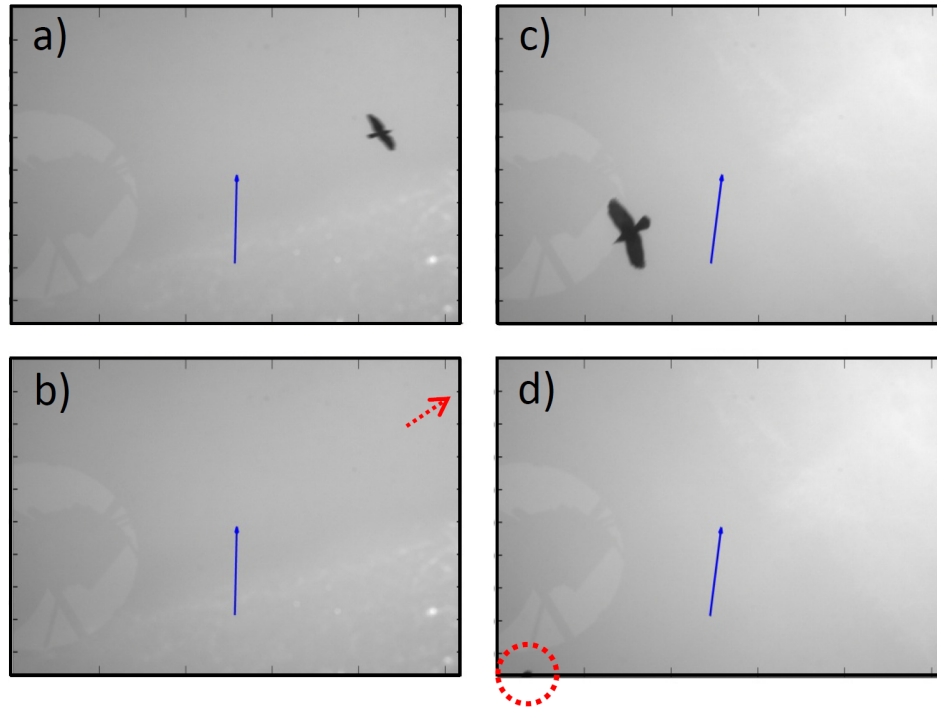


Figure 4. **a)** First image in the series of two taken at March 28. The photo corresponds to the event in figure 3b. The solid (blue) arrow indicates the direction of the incoming sun radiation. The solar height angle was in this example 37.2 degrees at the time 13:00. **b)** the second photo during the same event as in a). The bird has already escaped the FOV of the camera as indicated by the dashed arrow (red). **c)** Another example image obtained during March 24 at 12:17. The height angle of the sun was 35.6 degrees. **d)** Second image in the series; the bird can be seen just about to escape the FOV to the bottom left, as indicated by the circle.

The spectrum for each bird rare event along with the static spectrum of the sky in connection with the event (the mean of the spectra between 600 and 200 ms before the actual event) were stored in matrices (event number in one direction and spectral bin along the other) for further analysis, one with the bird event spectra, **B**, and one with the corresponding static spectra, **S**. The ratio of the values in these matrices were also obtained and stored in a third matrix, **R**. We have chosen to focus the continued analysis on these "spectrum ratios", **R**.

Singular-value-decomposition, SVD, was now applied on the ratio spectra, **R**, to try to extract the important information contained in the ratios. Due to the fact that the intensity of light at the oxygen absorption line previously discussed is differing depending on the height of the bird and weather conditions, the wavelengths above 750 nm were excluded in the SVD analysis (this region will instead be discussed in the next section). Many of the dominant principal components, PCs, would otherwise have to take care of this absorption line. Figure 5a shows the Eigenvalues of the first 20 principal components. As can be seen, basically two components suffice to describe the spectra from all 77 events. The rest of the components more or less take care of noise. Figure 5b shows the first three PCs. The first component,  $PC_1$ , is a very flat line, meaning that the spectrum recorded when the bird is in the FOV is similar in shape to the static sky spectra just before the events (the fact that it is negative has no physical significance). This is expected both because many of the birds only cover a small part of the FOV, and also because the most common chromophores are eumelanin and phaeomelanin which have dull spectral signatures. However, the second PC,  $PC_2$ , is more interesting and shows a slope in the ratio (again the direction of the slope has no physical meaning). This means that the birds do have an impact on the spectral shape of the light recorded by the spectrometer.

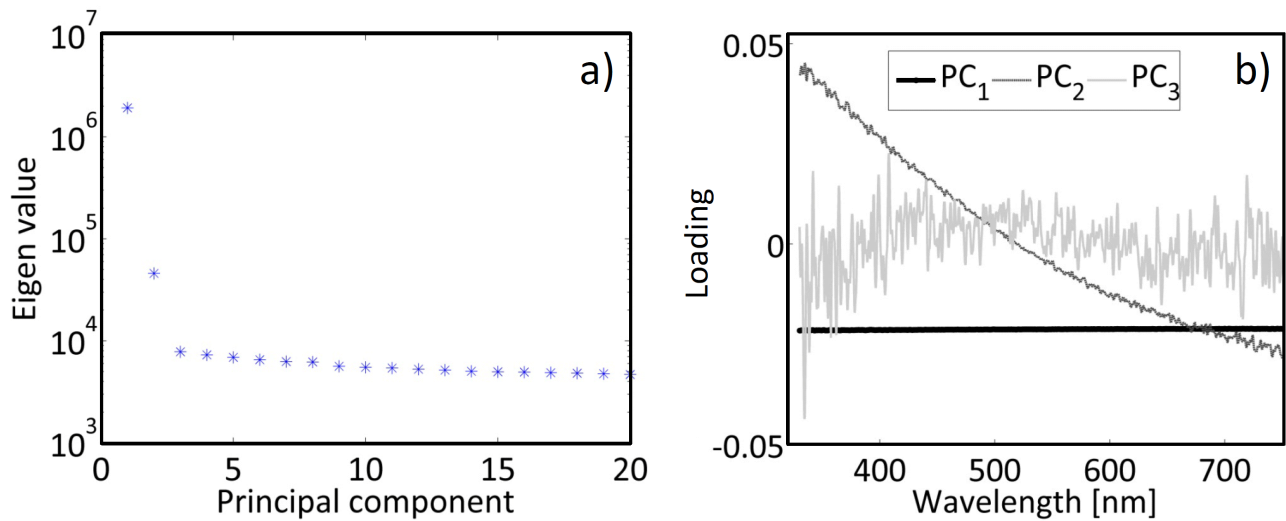


Figure 5. **a)** The Eigenvalues of the first 20 principal components. The first two, PC<sub>1</sub> and PC<sub>2</sub>, stand out from the rest. **b)** The first three principal components. PC<sub>1</sub> is a flat change in intensity while PC<sub>2</sub> seems to take care of spectral shifts to the red or blue in the spectra. PC<sub>3</sub> and the rest mainly consist of noise.

The scores of the different PCs can now be viewed for the different bird events. The value on PC<sub>1</sub> gives an indication of the size of the event, mainly affected by the fraction of the FOV covered. In figure 6a a histogram of the scores of PC<sub>1</sub> for the different ratios is shown. Actually, on the x-axis we have  $(\text{the scores of PC}_1) \times (\text{the mean value of PC}_1) \times (\text{the Eigenvalue of PC}_1) - 1$ ; we define this as the event strength. In this way a strength of 0 means no flat (mean) change to the static spectrum at all. A strength of -1 would mean total light absorption. Values above 0 means an increase in total received intensity; 1 would mean a doubling of the static intensity. As seen in the figure, most birds cause a decrease in received intensity but not all. The value of PC<sub>1</sub> will depend on if the bird is light or dark, the height, the size and if the bird is centered in the FOV or not. If one happens to know that only a single species can be considered, this kind of histogram would mainly depend on the height and could thus give information about the height distribution of the birds, and if the height is instead known, the histogram gives size information. Figure 6b shows a histogram of the ratio between the scores of (negative) PC<sub>2</sub> and the strength, giving an indication of the "reddishness" of the birds.

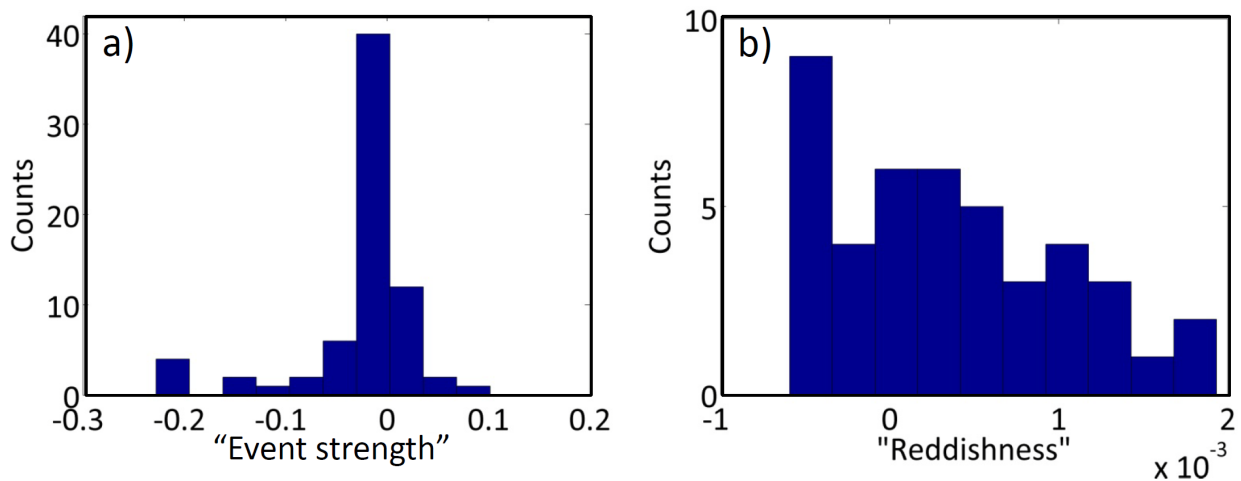


Figure 6. **a)** A histogram of the event strengths defined as  $(\text{the scores of PC}_1) \times (\text{the mean value of PC}_1) \times (\text{the Eigenvalue of PC}_1) - 1$ . A strength of -1 means total intensity loss, 0 means no flat change from the corresponding static preceding spectrum, +1 means that the total intensity is doubled. **b)** Histogram of the "reddishness" of the birds. The values are defined as the negative value of PC<sub>2</sub> divided by the strength.

#### 4. CASE STUDY ON THE OXYGEN LINE

In this section we investigate the possibility of estimating the flying height of a bird by observing the relative change of the absorption fraction in a terrestrial Fraunhofer line during the time when the bird obscures the FOV of the telescope. (It can be noted that in principal there should be no light at all at the exact resonance frequencies of the transition but do the limited resolution of the spectrometer the line will never be completely black.) The difference in path length through atmosphere (see figure 1) for the light scattered in the plumage of the bird could show up as a changed in-line absorption fraction. The effect, however, is expected to be small since only a part of the FOV is covered by the bird and since the relative path length change is small. To start to explore the method, the absorption fraction at the A-band absorption of molecular oxygen at 760 nm for the sky light was found as a function of time. Figure 7 shows a plot of the intensity of light at the line ("in-line") divided with the "off-line light" – the light intensity at the sides of the absorption line (thus the y-values are 1 minus the absorption fractions) as function of hour of the day. The in-line intensity is calculated as the mean of the intensity between 757.8 and 765.0 nm and the off-line is the rest of the range extended to 749.0 and 772.0 nm. The solid line shows the in-line-to-off-line intensity ratio for the sky light during March 28 (corresponding to figure 3a). We see how the absorption fraction, as expected, is larger during morning and evening hours and how it smoothly goes down during the middle of the day when the sun sits higher on the sky. We can also see that even if the clouds (whose presence is clearer in figure 3a) do affect the mean path length, the effect is not very large compared to the changes induced by the hour of the day. The data corresponding to the first part in the morning and the last in the evening were excluded in the analysis due to low light intensities then. Included in the figure is the same ratio for spectra with birds in the FOV, but for bird spectra found during all days of the study. In general we see that the absorption fraction shows both higher and lower values for the bird spectra as compared to the ratio for the background sky light. We have not been able to draw any conclusions about the flying height from these data.

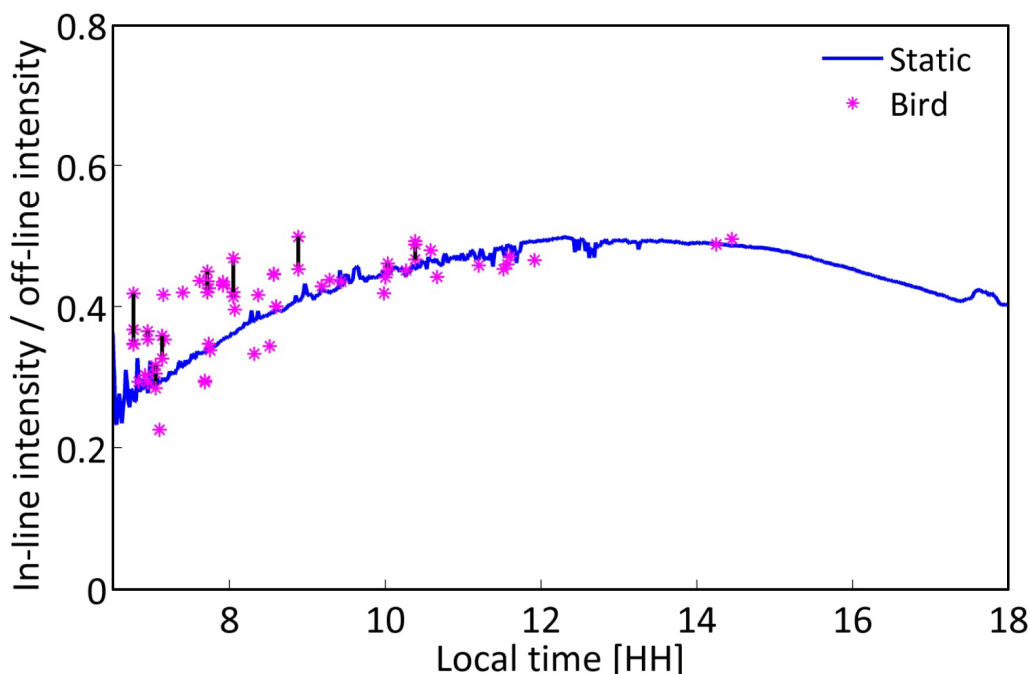


Figure 7. The 760 nm oxygen in-line intensity divided with the surrounding off-line intensity as a function of time of day (local time, GMT+1). The fraction of light absorbed at the line is thus 1 minus the values in the graph. The solid line (blue) shows the described ratio averaged over 1 second of data (3000 spectra) for March 28 (corresponding to figure 3a). We see how, as expected, the path length through atmosphere and thus the absorption fraction decreases towards the middle of the day. The relative strength of the light at the oxygen line thus increases during the middle of the day. The stars show the same ratio for the spectra containing bird signatures. The values are thus for single spectra and included bird spectra found during all days of the study. The black vertical lines connect points obtained for the same bird. We thus see that the same bird even shows up as spectra with different absorption depths.

## 5. DISCUSSION

The study presented was performed in an urban area mainly covered by buildings, roads, parking lots, etc. This situation differs from that in our previous campaign [20] which was performed in a rural area at the Kullaberg nature reserve, also in Sweden. At the latter location the ground was mainly covered by vegetation, something giving an extra aspect to a passive spectroscopic study of passing birds. Vegetation has a strong increase in its reflectance in the wavelength region above 700 nm approximately. As a significant fraction of the light reaching the bottom side of a flying bird is actually reflected sunlight from the earth, the light reflected by the bird will have an increase of intensity in the mentioned wavelength region, as compared to what the sky itself has. This effect was thus not noticed in the present rural study.

It is not obvious that the ratios in the matrix  $\mathbf{R}$  are always the best representatives of how the birds influence the light reaching the telescope. In an ideal situation one would like to take the spectrum recorded by the spectrometer during the time when the bird is in the FOV of the telescope and subtract the light coming from the rest of the sky. These spectra could now be divided with the ones of the light actually illuminating the bird. This would be the actual absorption or reflection spectrum of the bird. Unfortunately we cannot subtract the light from the rest of the sky, nor do we know the exact spectrum of the light illuminating the bird (this is a mixture between direct sun-light, light already having been reflected by earth and clouds, and blue sky light). It can therefore be discussed if  $\mathbf{B}$ ,  $\mathbf{R}$ , or perhaps  $\mathbf{B}\cdot\mathbf{S}$ , gives the best indication about the actual spectrum of the bird. However, the use of  $\mathbf{R}$  is pleasant in the way that some unknown parameters, e.g., the mean intensity is automatically removed, as are slow spectral changes the background light during the day.

Unfortunately, we cannot search, in a satisfying way, for any correlation between the relative change in the oxygen absorption and the altitude of the birds since we lack additional altitude determining equipment. On the other hand we know that the multiple events recorded for each bird in figure 7 (connected with the vertical lines) correspond to the same flying height. Since the values obviously change within the recording for a single bird we cannot hope for a direct correlation between the plotted ratio and the flying height. Possibly the changes in the absorption depth are too small to get a good altitude estimation. Thereby not said that an indirect correlation cannot exist. To have a fair possibility of evaluating the prospects for using the oxygen absorption line as a way to evaluate the flight height of birds, some kind of reference measurement is needed. One way could be to implement the passive spectrometer approach together with a tracking radar or lidar system. Such systems would provide a trustworthy height determination. Another approach that we were hoping to use this time was the triggered photos of the passing birds. By evaluating the partial area covered by the birds and at the same time having a reasonable idea of the true sizes, the heights could have been estimated. Unfortunately, it turned out that many of the birds were not captured by the camera due to the too long triggering delays, so the method could not be used in the present measurement campaign.

## 6. CONCLUSION

We have found that passive surveillance with the help of a spectrometer connected to a telescope can provide information on the color of a bird passing by in flight. We hope to refine the method and to evaluate it further in continued studies. We could not correlate the absorption depth in the oxygen A-band Fraunhofer line with the altitudes of flying birds. An existing method proving a trustworthy altitude to compare to could help in evaluating the approach further.

This work is supported by Linnaeus grants from the Swedish Research Council and Lund University.

## REFERENCES

- [1] Åkesson S., and Hedenström A., "How migrants get there: migratory performance and orientation," *BioScience* 57, 123-133 (2007).
- [2] Alerstam T., and Lindström Å., "Optimal bird migration: the relative importance of time, energy and safety," in [Bird Migration: Physiology and Ecophysiology], E. Gewinner, ed., Springer-Verlag, 331-351 (1990).
- [3] Alerstam T., Hedenström A., and Åkesson S., "Long-distance migration: evolution and determinants," *Oikos* 103, 247-260 (2003).
- [4] Newton I., [The migration ecology of birds], Academic Press, London (2008).
- [5] Cox G. W., [Bird migration and global change], Island Press City (2010).
- [6] Adams D. H. W., "Radar observations of bird migration in Cyprus," *Ibis* 104, 133-146 (1972).
- [7] Parslow J. L. F., "The migration of passerine night migrants across the English Channel studied by inst radar," *Ibis* 111, 48-79 (1969).
- [8] Åkesson S., "Coastal migration and wind drift compensation in nocturnal passerine migrants," *Ornis Scand.* 24, 87-94 (1993).
- [9] Gauthreaux S. A. Jr., "A portable ceilometer technique for studying low level nocturnal migration," *Bird Banding* 40, 309-320 (1969).
- [10] Zehnder S., Åkesson S., Liechti F., and Bruderer, B., "Nocturnal autumn bird migration at Falsterbo, south Sweden," *J. Avian Biol.* 32, 239-248 (2001).
- [11] Farnsworth A., Gauthreaux S. A. Jr., and van Blaricom, D., "A comparison of nocturnal call counts of migrating birds and reflectivity measurements on Doppler radar," *J. Avian Biol.* 35, 365-369 (2004).
- [12] Farnsworth A., and Lovette I. J., "Evolution of nocturnal flight calls in migrating wood-warblers: apparent lack of morphological constraints," *J. Avian Biol.* 36, 337-347 (2005).
- [13] Bruderer B., and Liechti, F., "Quantification of bird migration - different means compared," in *Proc. Bird Strike Committee* 22, Europe, 243-254, (1994).
- [14] Gauthreaux S. A., and Livingston J. W., "Monitoring bird migration with a fixed-beam radar and a thermal-imaging camera," *J. Field Ornithol.* 77, 319-328 (2006).
- [15] Liechti F., Bruderer B., and Paproth, H., "Quantification of nocturnal bird migration by moonwatching: comparison with radar and infrared observations," *J. Field Ornithol.* 66, 457-468 (1995).
- [16] Brydegaard M., Guan Z. G., Wellenreuther M., and Svanberg S., "Insect monitoring with fluorescence lidar techniques: feasibility study," *Appl. Opt.*, 48, 5668-5677 (2009).
- [17] Guan Z. G., Brydegaard M., Lundin P., Wellenreuther M., Runemark A., Svensson E. I., and Svanberg S., "Insect monitoring with fluorescence lidar techniques: field experiments," *Appl. Opt.* 49, 5133-5142 (2010).
- [18] Mei L., Guan Z. G., Zhou H., Lv J., Zhu Z., Cheng J., Chen F., Löfstedt C., Svanberg S., and Somesfalean G., "Agricultural pest monitoring using fluorescence lidar techniques – feasibility study," submitted to *Appl. Phys. B*.

- [19] Brydegaard M., Lundin P., Guan Z. G., Runemark A., Åkesson A., and Svanberg S., "Feasibility study: fluorescence lidar for remote bird classification," *Appl. Opt.* 49, 4531-4544 (2010).
- [20] Lundin P., Samuelsson P., Svanberg S., Runemark A., Åkesson S., and Brydegaard, M., "Remote nocturnal bird classification by spectroscopy in extended wavelength ranges," *Appl. Opt.* 50, 3396-3411 (2011).
- [21] Runemark A., Wellereuther M., Jayaweera H., Svanberg S., and Brydegaard M., "Rare Events in Remote Dark Field Spectroscopy, Case study: A damselfly population," submitted to *Journal of Selected Topics in Quantum Electronics*, IEEE (2011).
- [22] Plascyk J. A., and Gabriel F. C., "The Fraunhofer Line Discriminator MKII – an airborne instrument for precise and standardized ecological luminescence measurement," *IEEE Transactions on Instrumentation and Measurement*, IM-24, 4 (1975).
- [23] Rascher U., Gioli B., and Miglietta F., "FLEX - fluorescence explorer: a remote sensing approach to quantify spatio-temporal variations of photosynthetic efficiency from space," *Photosynth. Res.* 91, 293-294 (2007).